DISTRIBUTION STATEMENT A
Approved for Public Release
Distribution Unlimited

MATERIALS RESEARCH SOCIETY
SYMPOSIUM PROCEEDINGS VOLUME 740

Nanomaterials for Structural Applications

Symposium held December 2–6, 2002, Boston, Massachusetts, U.S.A.

EDITORS:

Christopher C. Berndt
Stony Brook University
Stony Brook, New York, U.S.A.

Traugott E. Fischer
Stevens Institute of Technology
Hoboken, New Jersey, U.S.A.

Ilya Ovid'ko
Russian Academy of Sciences
St. Petersburg, Russia

Ganesh Skandan
Nanopowder Enterprises, Inc.
Piscataway, New Jersey, U.S.A.

Thomas Tsakalakos
Rutgers University
Piscataway, New Jersey, U.S.A.

MRS
Materials Research Society
Warrendale, Pennsylvania

20030812 221

This work was supported in part by the Office of Naval Research under Grant Number N00014-03-1-0054. The United States Government has a royalty-free license throughout the world in all copyrightable material contained herein.

Single article reprints from this publication are available through
University Microfilms Inc., 300 North Zeeb Road, Ann Arbor, Michigan 48106

CODEN: MRSPDH

Copyright 2003 by Materials Research Society.
All rights reserved.

This book has been registered with Copyright Clearance Center, Inc. For further information, please contact the Copyright Clearance Center, Salem, Massachusetts.

Published by:

Materials Research Society
506 Keystone Drive
Warrendale, PA 15086
Telephone (724) 779-3003
Fax (724) 779-8313
Web site: http://www.mrs.org/

Manufactured in the United States of America

CONTENTS

Preface xiii

Materials Research Society Symposium Proceedings iv

FRACTURE AND MECHANICAL PROPERTIES I

* **Deformation and Coble Creep of Nanocrystalline Materials** 3
C.S. Pande and R.A. Masumura

Tensile Deformation and Fatigue Crack Growth in Bulk Nanocrystalline Al-7.5Mg 15
P.S. Pao, H.N. Jones, S.J. Gill, and C.R. Feng

Bimodal Microstructure and Mechanical Properties of Cryomilled Nanocrystalline Al-7.5Mg 21
Zonghoon Lee, David B. Witkin, Enrique J. Lavernia, and Steven R. Nutt

Hardness and Abrasion Resistance of Nanocrystalline Nickel Alloys Near the Hall-Petch Breakdown Regime 27
Christopher A. Schuh and T.G. Nieh

Hybrid Nylon-6/Silica Nanocomposites With Improved Mechanical Properties 33
Monserrat García, Werner E. van Zyl, and Henk Verweij

FRACTURE AND MECHANICAL PROPERTIES II

* **Plasticity in Nanomaterials** 41
Guo-Dong Zhan, Joshua D. Kuntz, Julin Wan, and Amiya K. Mukherjee

Microstructures and Mechanical Properties of Nanostructured Copper-304 Stainless Steel Multilayers Synthesized by Magnetron Sputtering 49
X. Zhang, A. Misra, H. Wang, H. Kung, J.D. Embury, R.G. Hoagland, and M. Nastasi

*Invited Paper

PROCESSING AND MECHANICAL PROPERTIES

Synthesis of Titania Coated Alumina Particles by a Hybrid Sol-Gel Method 57
A.D. Schmidt, S.B. Majumder, P.S. Dobal, R.S. Katiyar, and D.C. Agrawal

Nucleation Induced Nanostructures 63
A. ten Bosch

Hydrogen Stabilization of {111} Nanodiamond 69
A.S. Barnard, N.A. Marks, S.P. Russo, and I.K. Snook

Processing of Clay/Epoxy Nanocomposites With a Three-Roll Mill Machine 75
Asma Yasmin, Jandro L. Abot, and Isaac M. Daniel

The Growth of Bamboo-Structured Carbon Tubes Using a Copper Catalyst 81
B.L. Farmer, D.M. Holmes, L.J. Vandeperre, R.J. Stearn, and W.J. Clegg

Characterization of Mechanical Deformation of Nanoscale Volumes 87
Christopher R. Perrey, William M. Mook, C. Barry Carter, and William W. Gerberich

Coating of Ultrathin Polymer Films on Carbon Nanotubes by a Plasma Treatment 93
Peng He, Jie Lian, Donglu Shi, Lumin Wang, David Mast, Wim J. van Ooij, and Mark Schulz

Electrodeposition of Ni Catalyst on Tungsten Substrates and Its Effect on the Formation of Carbon Nano- and Micro-Coils 101
Erik Einarsson, Jun Jiao, Josie Prado, George M. Coia, Jeremy Petty, and Logan Love

Arc Plasma Synthesis of Nanostructured Fe Powder 107
Gil-Geun Lee and Sung-Duck Kim

Size Reduction of Clay Particles in Nanometer Dimensions 113
Gopinath Mani, Qinguo Fan, Samuel C. Ugbolue, and Isabelle M. Eiff

Effect of Solid-Solution W Addition on the Nanostructure of Electrodeposited Ni 119
Hajime Iwasaki, Kenji Higashi, and T.G. Nieh

Interface Conduction Between Conductive ReO_3 Thin Film and $NdBa_2Cu_3O_6$ Thin Film 125
Manabu Ohkubo, Kumiko Fukai, Kohji Matsuo, Nobuyuki Iwata, and Hiroshi Yamamoto

FRACTURE AND MECHANICAL PROPERTIES III

Characterization of Nanoparticle Films and Structures Produced by Hypersonic Plasma Particle Deposition 133
Christopher R. Perrey, Ryan Thompson, C. Barry Carter, Ashok Gidwani, Rajesh Mukherjee, Thierry Renault, P.H. McMurry, J.V.R. Heberlein, and S.L. Girshick

POLYMER-BASED NANOSTRUCTURED MATERIALS

Biodegradable Polyester/Layered Silicate Nanocomposites 141
Pralay Maiti, Carl A. Batt, and Emmanuel P. Giannelis

Characterization of Metal-Oxide Nanoparticles: Synthesis and Dispersion in Polymeric Coatings 147
Li-Piin Sung, Stephanie Scierka, Mana Baghai-Anaraki, and Derek L. Ho

NANOCOMPOSITES: SYNTHESIS AND PROPERTIES

Mechanical Behavior of Polymer Nanocomposites: A Discrete Simulation Approach 155
E. Chabert, C. Gauthier, R. Dendievel, L. Chazeau, and J.-Y. Cavaillé

Nanophase Alumina/Poly(L-Lactic Acid) Composite Scaffolds for Biomedical Applications 161
Aaron J. Dulgar Tulloch, Rena Bizios, and Richard W. Siegel

Mechanical and Thermoviscoelastic Behavior of Clay/Epoxy Nanocomposites 167
Jandro L. Abot, Asma Yasmin, and Isaac M. Daniel

Preparation and Characterization of Alumina Based TiN_n and SiC_n Composites 173
Mats Carlsson, Mats Johnsson, and Annika Pohl

Synthesis and Characterization of Metal Nanoparticles and the Formation of Metal-Polymer Nanocomposites 179
Anshu A. Pradhan, S. Ismat Shah, and Lisa Pakstis

MODELING AND MEASUREMENT TECHNIQUES

Modeling Mechanical Properties of Carbon Molecular Clusters and Carbon Nanostructural Materials 187
Vadim M. Levin, Julia S. Petronyuk, and Inna V. Ponomareva

Modeling Self-Assembly of Nanoparticle Structures: Simulation of Nanoparticle Chemical Potentials in Polymer-Nanoparticle Mixtures 193
Krishna T. Marla and James C. Meredith

Densification and Sintering of a Microwave-Plasma-Synthesized Iron Nanopowder 199
L.J. Kecskes, R.H. Woodman, and B.R. Klotz

A Semiconductor Nano-Patterning Approach Using AFM-Scratching Through Oxide Thin Layers 205
L. Santinacci, T. Djenizian, and P. Schmuki

Nanoindentation Technique at Investigating of Aluminum Oxide-CrC Nanoparticles Composite Coating 211
Maksim V. Kireitseu

Multilayers by Self-Assembly 217
M. Toprak, D.K. Kim, M. Mikhaylova, and M. Muhammed

Adhesion of HVOF Sprayed Diamond-Containing Nanostructured Composite Coating 223
Maksim V. Kireitseu and Ion Nemerenco

Rheological Behavior and Model of Metal-Polymer-Ceramic Composite 229
Maksim V. Kireitseu

Synthesis of Aerogel-Metal Cluster Composites by Gamma Radiolysis 235
Massimo F. Bertino, Jared F. Hund, Guohui Zhang, Chariklia Sotiriou-Leventis, Nicholas Leventis, Akira T. Tokuhiro, and John Farmer

Synthesis of Zeolite Y Nanocrystals From Clear Solutions 241
Y. Shen, M.P. Manning, J. Warzywoda, and A. Sacco Jr.

Molecular Dynamics Simulations on Nanocomposites Formed by Intermetallic Dispersoids of $L1_2$ Type and Aluminum Matrices 249
Min Namkung, Sun Mok Paik, and Buzz Wincheski

Condensation of Carbon Vapor in the Microwave Oven 255
Oxana V. Kharissova, Israel Nieto Lopez, Ubaldo Ortiz Méndez, Juan A. Aguilar, and Moisés Hinojosa Rivera

Structure and Elastic Properties of Immiscible LDPE-PP Blends: Dependence on Composition 261
Julia S. Petronyuk, Olga V. Priadilova, Vadim M. Levin, Olga A. Ledneva, and Anatolii A. Popov

Deformation-Induced Crystallization and Amorphization of Al-Based Metallic Glasses 267
Rainer J. Hebert and John H. Perepezko

MODELING, SIMULATIONS, AND INTERFACES

Atomistically Informed Continuum Model of Polymer-Based Nanocomposites 275
Catalin R. Picu, Alireza Sarvestani, and Murat S. Ozmusul

Continuum Mechanics-Discrete Defect Modeling and Bubble Raft Simulation of Cracked Specimen Response in Nanoscale Geometries 281
Michael J. Starr, Walter J. Drugan, Maria d. C. Lopez-Garcia, and Donald S. Stone

Interfacial Control of Creep Deformation in Ultrafine Lamellar TiAl 287
L.M. Hsiung

CHARACTERIZATION OF NANOSTRUCTURED MATERIALS

Structure and Characterization of Sol-Gel and Aerogel Materials and Oxidation Products From the Reaction of $(CH_3O)_4Si$ and $C_{16}H_{33}Si(OCH_3)_3$ 295
Thomas M. Tillotson and John G. Reynolds

Red Shift in Optical Absorption Tail and Superparamagnetism of γ-Fe_2O_3 Nanoparticles in a Polymer Matrix 301
John K. Vassiliou, Jens W. Otto, V. Mehrotra, and J.J. Davis

Nanomechanical Characterization on Zinc and Tin Oxides Nanobelts 309
Minhua Zhao, Scott Mao, Zhong Lin Wang, Fengting Xu, and John A. Barnard

* **Anomalous X-ray Scattering for Determination of Nanostructured Alloy Formation and Site-Specific Chemistry of Bragg Peak** 319
G.M. Chow

SYNTHESIS OF NANOSTRUCTURED MATERIALS I

Fabrication of Isolated Ferroelectric Nanostructures 333
S. Bhattacharyya, Soma Chattopadhyay, and M. Alexe

Formation, Mechanical and Electrical Properties of Ni-Based Amorphous Alloys and Their Nanocrystalline Structure 339
Xiangcheng Sun and Tiemin Zhao

Synthesis of Novel Vanadium Oxide Nanotubes and Nanofibers 345
Samuel T. Lutta, Hong Dong, Peter Y. Zavalij, and M. Stanley Whittingham

Silver Nanodisk: Synthesis, Characterization and Self-Assembly 351
Sihai Chen, Zhiyong Fan, and David L. Carroll

*Invited Paper

SYNTHESIS OF
NANOSTRUCTURED MATERIALS II

Radiolytic Synthesis of Bimetallic Nanoparticles With High Aspect Ratio 359
C.M. Doudna, M.F. Bertino, S. Pillalamarri, F.D. Blum, A.T. Tokuhiro, S. Chattopadhyay, and J. Terry

Fluorinated Single Wall Nanotube/Polyethylene Composites for Multifunctional Radiation Protection 365
Merlyn X. Pulikkathara, Meisha L. Shofner, Richard T. Wilkins, Jesus G. Vera, Enrique V. Barrera, Fernando J. Rodríguez-Macías, Ranji K. Vaidyanathan, Catherine E. Green, and Clay G. Condon

Damping and Stiffness Enhancement in Composite Systems With Carbon Nanotubes Films 371
E.A. Lass, N.A. Koratkar, P.M. Ajayan, B.Q. Wei, and P. Keblinski

In Situ Preparation of Polymer-Coated Zirconia Nanoparticles by Decomposition of Zirconium-Tert-Butoxide 377
Michael Schallehn, Volker Lorenzen, Johannes Seydel, and Horst Hahn

NANOSTRUCTURED MATERIALS

Simulation of Carbon Nanotube Pull-Out When Bonded to a Polymer Matrix 385
S.J.V. Frankland and V.M. Harik

A Study of Hydrogen Adsorption in Pretreated Nanocarbon 391
Sang Moon Lee, Satoshi Ohshima, Kunio Uchida, and Motoo Yumura

An Approach to Nanoglasses Through Anodic Oxidation of Sputtered Aluminum on Glass Surface 397
Satoru Inoue, Song-Zhu Chu, and Kenji Wada

Growth of Carbon Nanofibers on Electroless Ni-P Alloy Catalyst 405
T.K. Tsai, W.L. Liu, S.H. Hsieh, and W.J. Chen

Material Properties and Process Compatibility of Spin-On Nano-Foamed Polybenzoxazole for Copper Damascene Process 411
Takashi Enoki, Kenzo Maejima, Hidenori Saito, and Akifumi Katsumura

Ferromagnetic Shape Memory of Nanostructure Fe-Pd Alloy: The Texture Observation Study by Laser and Electronic Microscopes 417
T. Okazaki, T. Kubota, Y. Furuya, S. Kajiwara, and T. Kikuchi

Stoichiometry, Crystallinity, and Nano-Scale Surface Morphology of the Graded Calcium Phosphate-Based Bio-Ceramic Interlayer on Ti-Al-V 423
J.D. Long, K. Ostrikov, S. Xu, and V. Ligatchev

Preferred Orientation in Fibers of HiPco Single Wall Carbon Nanotubes From Diffuse X-ray Scattering 429
W. Zhou, K.I. Winey, J.E. Fischer, S. Ramesh, R.K. Saini, L.M. Ericson, V.A. Davis, M. Pasquali, R.H. Hauge, and R.E. Smalley

Polymer-Attached Functional Inorganic-Organic Hybrid Nano-Composite Aerogels 435
Xipeng Liu, Mingzhe Wang, and William M. Risen Jr.

Nanocomposite Fibers 441
Yong K. Kim, Armand F. Lewis, Prabir K. Patra, Steven B. Warner, Shamal K. Mhetre, Mithun A. Shah, and Daejin Nam

Simulation of Morphology and Surface Vibration in Copper and Gold Nanoparticles 447
Y. Kogure, Y. Kato, T. Nozaki, and M. Doyama

Compressive Behavior for Surface-Nanocrystallized Al-Alloy Material 453
Yueguang Wei, Chen Zhu, and Xiaolei Wu

SYNTHESIS OF NANOSTRUCTURED MATERIALS III

Plastic Relaxation Mechanics in Systems With a Twist-Bonded Layer 461
Catherine Priester and Geneviève Grenet

Author Index 467

Subject Index 471

PREFACE

Symposium I, "Nanomaterials for Structural Applications," held December 2–6 at the 2002 MRS Fall Meeting in Boston, Massachusetts, provided a dynamic overview of current multidisciplinary research in this rapidly growing field, with the primary focus of reinforcing the relationship between basic science and engineering at the nanoscale level. This volume contains selected papers presented at the symposium whose thematic sessions covered nanostructured bulk materials, films, coatings and nanocomposites. These new materials are now being introduced in structural applications, such as wear resistance, plastic forming, and other load bearing applications. Nanophase or nanocrystalline materials are also being used in electronics, refractory, biological and catalytic applications. Progress in a wide range of structural applications for nanomaterials crucially depends on the development of new fabrication and processing technologies, along with a fundamental understanding of the relationship between the structure and properties.

This volume will be of interest to researchers and graduate students in the field of nanostructured materials science and nanotechnologies. It can also be useful for engineers who are involved in production and processing of nanomaterials for structural applications.

We gratefully acknowledge the financial support of this symposium from MRS and the Office of Naval Research. Special thanks go to the officers and staff of MRS for smoothly running the Meeting and for assisting the Symposuim Organizers.

Christopher C. Berndt
Traugott E. Fischer
Ilya Ovid'ko
Ganesh Skandan
Thomas Tsakalakos

February 2003

MATERIALS RESEARCH SOCIETY SYMPOSIUM PROCEEDINGS

Volume 715— Amorphous and Heterogeneous Silicon-Based Films—2002, J.R. Abelson, J.B. Boyce, J.D. Cohen, H. Matsumura, J. Robertson, 2002, ISBN: 1-55899-651-6
Volume 716— Silicon Materials—Processing, Characterization and Reliability, J. Veteran, D.L. O'Meara, V. Misra, P. Ho, 2002, ISBN: 1-55899-652-4
Volume 717— Silicon Front-End Junction Formation Technologies, D.F. Downey, M.E. Law, A. Claverie, M.J. Rendon, 2002, ISBN: 1-55899-653-2
Volume 718— Perovskite Materials, K. Poeppelmeier, A. Navrotsky, R. Wentzcovitch, 2002, ISBN: 1-55899-654-0
Volume 719— Defect and Impurity Engineered Semiconductors and Devices III, S. Ashok, J. Chevallier, N.M. Johnson, B.L. Sopori, H. Okushi, 2002, ISBN: 1-55899-655-9
Volume 720— Materials Issues for Tunable RF and Microwave Devices III, S.C. Tidrow, J.S. Horwitz, J. Levy, X. Xi, 2002, ISBN: 1-55899-656-7
Volume 721— Magnetic and Electronic Films—Microstructure, Texture and Application to Data Storage, P.W. DeHaven, D.P. Field, S.D. Harkness IV, J.A. Sutliff, J.A. Szpunar, L. Tang, T. Thomson, M.D. Vaudin, 2002, ISBN: 1-55899-657-5
Volume 722— Materials and Devices for Optoelectronics and Microphotonics, R.B. Wehrspohn, S. Noda, C. Soukoulis, R. März, 2002, ISBN: 1-55899-658-3
Volume 723— Molecularly Imprinted Materials—Sensors and Other Devices, K.J. Shea, M.J. Roberts, M. Yan, 2002, ISBN: 1-55899-659-1
Volume 724— Biological and Biomimetic Materials—Properties to Function, J. McKittrick, J. Aizenberg, C. Orme, P. Vekilov, 2002, ISBN: 1-55899-660-5
Volume 725— Organic and Polymeric Materials and Devices—Optical, Electrical and Optoelectronic Properties, G.E. Jabbour, N.S. Sariciftci, S.T. Lee, S. Carter, J. Kido, 2002, ISBN: 1-55899-661-3
Volume 726— Organic/Inorganic Hybrid Materials—2002, R.M. Laine, C. Sanchez, S. Yang, C.J. Brinker, 2002, ISBN: 1-55899-662-1
Volume 727— Nanostructured Interfaces, G. Duscher, J.M. Plitzko, Y. Zhu, H. Ichinose, 2002, ISBN: 1-55899-663-X
Volume 728— Functional Nanostructured Materials through Multiscale Assembly and Novel Patterning Techniques, Steven C. Moss, 2002, ISBN: 1-55899-664-8
Volume 729— BioMEMS and Bionanotechnology, L.P. Lee, J.T. Borenstein, R.P. Manginell, M. Okandan, P.J. Hesketh, 2002, ISBN: 1-55899-665-6
Volume 730— Materials for Energy Storage, Generation and Transport, G. Ceder, S.A. Ringel, R.B. Schwarz, 2002, ISBN: 1-55899-666-4
Volume 731— Modeling and Numerical Simulation of Materials Behavior and Evolution, V. Tikare, E.A. Olevsky, A. Zavaliangos, 2002, ISBN: 1-55899-667-2
Volume 732E—Chemical-Mechanical Planarization, S.V. Babu, R. Singh, N. Hayasaka, M. Oliver, 2002, ISBN: 1-55899-668-0
Volume 733E—Polymer Nanocomposites, S. Nutt, R. Vaia, W. Rodgers, G.L. Hagnauer, G.W. Beall, 2002, ISBN: 1-55899-669-9
Volume 734— Polymer/Metal Interfaces and Defect Mediated Phenomena in Ordered Polymers, E.D. Manias, G.G. Malliaras, 2003, ISBN: 1-55899-671-0
Volume 735— Bioinspired Nanoscale Hybrid Systems, G. Schmid, U. Simon, S.J. Stranick, S.M. Arrivo, S. Hong, 2003, ISBN: 1-55899-672-9
Volume 736— Electronics on Unconventional Substrates—Electrotextiles and Giant-Area Flexible Circuits, M.S. Shur, P. Wilson, D. Urban, 2003, ISBN: 1-55899-673-7
Volume 737— Quantum Confined Semiconductor Nanostructures, J.M. Buriak, D.D.M. Wayner, F. Priolo, B. White, V. Klimov, L. Tsybeskov, 2003, ISBN: 1-55899-674-5
Volume 738— Spatially Resolved Characterization of Local Phenomena in Materials and Nanostructures, D.A. Bonnell, J. Piqueras, A.P. Shreve, F. Zypman, 2003, ISBN: 1-55899-675-3
Volume 739— Three-Dimensional Nanoengineered Assemblies, T.M. Orlando, L. Merhari, K. Ikuta, D.P. Taylor, 2003, ISBN: 1-55899-676-1
Volume 740— Nanomaterials for Structural Applications, C. Berndt, T.E. Fischer, I. Ovid'ko, G. Skandan, T. Tsakalakos, 2003, ISBN: 1-55899-677-X

MATERIALS RESEARCH SOCIETY SYMPOSIUM PROCEEDINGS

Volume 741— Nano- and Microelectromechanical Systems (NEMS and MEMS) and Molecular Machines, A.A. Ayon, T. Buchheit, D.A. LaVan, M. Madou, 2003, ISBN: 1-55899-678-8
Volume 742— Silicon Carbide 2002—Materials, Processing and Devices, S.E. Saddow, D.J. Larkin, N.S. Saks, A. Schoener, 2003, ISBN: 1-55899-679-6
Volume 743— GaN and Related Alloys—2002, E.T. Yu, C.M. Wetzel, J.S. Speck, A. Rizzi, Y. Arakawa, 2003, ISBN: 1-55899-680-X
Volume 744— Progress in Semiconductors II—Electronic and Optoelectronic Applications, B.D. Weaver, M.O. Manasreh, C.C. Jagadish, S. Zollner, 2003, ISBN: 1-55899-681-8
Volume 745— Novel Materials and Processes for Advanced CMOS, M.I. Gardner, J-P. Maria, S. Stemmer, S. De Gendt, 2003, ISBN: 1-55899-682-6
Volume 746— Magnetoelectronics and Magnetic Materials—Novel Phenomena and Advanced Characterization, S. Zhang, W. Kuch, G. Guentherodt, C. Broholm, A. Kent, M.R. Fitzsimmons, I. Schuller, J.B. Kortright, T. Shinjo, Y. Zhu, 2003, ISBN: 1-55899-683-4
Volume 747— Crystalline Oxide-Silicon Heterostructures and Oxide Optoelectronics, D.S. Ginley, S. Guha, S. Carter, S.A. Chambers, R. Droopad, H. Hosono, D.C. Paine, D.G. Schlom, J. Tate, 2003, ISBN: 1-55899-684-2
Volume 748— Ferroelectric Thin Films XI, D. Kaufman, S. Hoffmann-Eifert, S.R. Gilbert, S. Aggarwal, M. Shimizu, 2003, ISBN: 1-55899-685-0
Volume 749— Morphological and Compositional Evolution of Thin Films, N. Bartelt, M.J. Aziz, I. Berbezier, J.B. Hannon, S. Hearne, 2003, ISBN: 1-55899-686-9
Volume 750— Surface Engineering 2002—Synthesis, Characterization and Applications, A. Kumar, W.J. Meng, Y-T. Cheng, J. Zabinski, G.L. Doll, S. Veprek, 2003, ISBN: 1-55899-687-7
Volume 751— Structure-Property Relationships of Oxide Surfaces and Interfaces II, X. Pan, K.B. Alexander, C.B. Carter, R.W. Grimes, T. Wood, 2003, ISBN: 1-55899-688-5
Volume 752— Membranes—Preparation, Properties and Applications, V.N. Burganos, R.D. Noble, M. Asaeda, A. Ayral, J.D. LeRoux, 2003, ISBN: 1-55899-689-3
Volume 753— Defect Properties and Related Phenomena in Intermetallic Alloys, E.P. George, H. Inui, M.J. Mills, G. Eggeler, 2003, ISBN: 1-55899-690-7
Volume 754— Supercooled Liquids, Glass Transition and Bulk Metallic Glasses, A.L. Greer, T. Egami, A. Inoue, S. Ranganathan, 2003, ISBN: 1-55899-691-5
Volume 755— Solid-State Chemistry of Inorganic Materials IV, M. Greenblatt, M.A. Alario-Franco, M.S. Whittingham, G. Rohrer, 2003, ISBN: 1-55899-692-3
Volume 756— Solid-State Ionics—2002, P. Knauth, J-M. Tarascon, E. Traversa, H.L. Tuller, 2003, ISBN: 1-55899-693-1
Volume 757— Scientific Basis for Nuclear Waste Management XXVI, R.J. Finch, D.B. Bullen, 2003, ISBN: 1-55899-694-X
Volume 758— Rapid Prototyping Technologies, A.S. Holmes, A. Piqué, D.B. Dimos, 2003, ISBN: 1-55899-695-8
Volume 759— Granular Material-Based Technologies, S. Sen, M.L. Hunt, A.J. Hurd, 2003, ISBN: 1-55899-696-6
Volume 760E—The Undergraduate Curriculum in Materials Science and Engineering, E.P. Douglas, O.D. Dubón Jr., J.A. Isaacs, W.B. Knowlton, M. Stanley Whittingham, 2003, ISBN: 1-55899-697-4
Volume 761E—Molecular Electronics, M-I. Baraton, E.L. Garfunkel, D.C. Martin, S.S.P. Parkin, 2003, ISBN: 1-55899-698-2

Prior Materials Research Society Symposium Proceedings available by contacting Materials Research Society

Fracture and Mechanical Properties I

Mat. Res. Soc. Symp. Proc. Vol. 740 © 2003 Materials Research Society

Deformation and Coble Creep of Nanocrystalline Materials

C.S. Pande and R. A. Masumura
Materials Science and Technology Division,
Naval Research Laboratory,
Washington, DC 20375-5343, USA.

ABSTRACT

Modeling of strengthening by nanocrystalline materials need consideration of dislocation interactions and sliding due to Coble creep, both of which may be acting simultaneously. Such a mechanism is considered in this paper. It is shown that a model based on using Coble creep (with a threshold stress) for finer grains and conventional Hall-Petch strengthening for larger grains, appears to be most successful in explaining experimental results provided care is taken to incorporate into the analysis the effect of grain size distribution occurring in most specimens. A generalized expression relating yield stress to grain size is also proposed.

INTRODUCTION

For relatively large grain sizes (for grains larger than about a micron) relationship between yield stress τ and grain size d, is described very well by the classic Hall-Petch relationship [1,2] *viz.*,

$$\tau = \tau_o + k\, d^{-1/2} \tag{1}$$

where τ_O is the friction stress, and k is a constant often referred to as the Hall-Petch slope which varies from material to material. Masumura *et al.* [3] have plotted some of the available data in a Hall-Petch plot. They find that the yield stress-grain size exponent for relatively large grains appears to be very close to -1/2 and generally this trend continues until the very fine grain regime

(~100 nm) is reached. However in nanocrystalline materials whose grain sizes are of nanometer (nm) dimensions, the applicability and validity of Eq. (1) has been questioned [4,5]. A close analysis of experimental Hall-Petch data in a variety of materials shows that even though the plot of τ *vs.* $d^{-1/2}$ forms a continuous curve, but below a critical grain size Hall-Petch slope is nearly zero (with no increase in strength on decreasing grain size) or in some cases at least where the strength actually decreases with decreasing grain size ("Inverse Hall Petch") [5]. In this paper we are mostly interested in the mechanism or mechanisms responsible for yield stress applicable to whole range of grain sizes but especially for the lowest grain sizes.

DISLOCATION MODELS

For large grain sizes most of the models use a mechanism based on dislocations. They account very well for the grain size dependence of the stress, τ,in Eq. (1); most of these can be rationalized in terms of a dislocation pile up model [6]. In deriving the Hall-Petch relation, the role of grain boundaries as a barrier to dislocation model is considered in various models. In one type of model [7,8,9], the grain boundary acts as a barrier to pile up of dislocations, causing stresses to concentrate and activating dislocation sources in the neighboring grains, thus initiating slip from grain to grain. In the other type of models [10,11] the grain boundaries are regarded as dislocations barriers limiting the mean free path of the dislocations, thereby increasing strain hardening, resulting in a Hall-Petch type relation. (For a survey, see Lasalmonie and Strudel [12].) It is clear that a variety of mechanisms could be postulated. There are several problems with any pile up model. Existence of pile ups in all types of models , both bcc and fcc can not be taken as established. Even in the frame work of a conventional model it can be shown that it cannot be applicable to grains of of small sizes [4]. Pande and Masumura [13] by considering the conventional Hall-Petch model showed that a dislocation theory for the Hall-Petch effect gives a linear dependence of τ on $d^{-1/2}$ only when there are large number of dislocations in a pile-up, which is equivalent to assuming that the grain sizes in the polycrystal under consideration is large. What happens if this assumption is not strictly true? Pande and Masumura [13] have investigated the case where classical Hall-Petch dislocation pile up model

is still applicable with the sole exception that the analysis must take into account of the fact that in the nanometer size grains the number of dislocations within a grain cannot be very large.

If the number of dislocations, n, in a pile up is not too large, the length of the pile up L is not linear in n but an additional term is necessary [14]. Pande and Masumura [13] using a result from Szego [15] give an improved expression *viz.*,

$$L = \frac{A}{2\tau}\left[2(n+m-1)^{1/2} - \frac{i_1 + \varepsilon}{(12)^{1/3}(n+m-1)^{1/6}}\right]^2 \qquad (2)$$

where A = □ $b/(\pi\tau^*)$, G is the shear modulus, b is the Burgers' vector, τ^* is the barrier stress, $i_1/6^{1/3}$ = 1.85575 and ε is a small correction term (ε□□and can be neglected. For small grain sizes this gives additional terms to Hall-Petch relation [13]. This model however cannot explain a drop in $\tau$for very fine grained materials. In what follows, for sake of simplicity we ignore this correction.

One can of course assume that dislocation sources must operate in each grain, and so an additional component of the yield stress exists of at least Gb/d. However as shown by Yamakov *et al.* [16] such a possibility is not likely. There are other dislocation model such as due to Valiev *et al.* [17], Malygin [18] and Gryaznov *et al.* [19]. The latter proposed a generalization of the of Hall-Petch relationship. By making judicious assumptions and approximations, they were able to develop a formulation that can account for yield stress for any grain sizes.

We will not discuss dislocation models any further except to state that at still smaller grain sizes, dislocation mechanism operating in the interior of the grain should cease because for sufficiently small grain size there will be only two dislocations in the pile-up. And eventually for even finer grain sizes the number of dislocations will falls to one and no further increase in the yield stress is possible and it should saturate. This probably happens at grain sizes less than 15nm [3].

Lack of dislocation activity in the interior of the grains of course does not preclude activity in the grain boundaries. Such an activity can lead to some very interesting consequences, which have been investigated by Gutkin and Ovid'ko [20]. They find that such dislocation activity is very much dependent on the mode of preparation of the specimens. If true, this could provide an explanation of the large scatter in the data seen in yield stress for smaller grain sizes

as seen in [3]. Specifically Gutkin and Ovid'ko show that the contribution to yield stress due to grain boundary dislocations is given by,

$$\tau = k_1 + k_2/d \tag{3}$$

where k_1 and k are constants. This expression of course should only be applicable for very fine grains.

MECHANISM INVOLVING COBLE CREEP

Clearly, at sufficiently small grain sizes, the Hall-Petch model based upon dislocations may not be operative except possibly in the grain boundaries. It has however been postulated that in this range of grain sizes, a new mechanism of deformation may be operative akin to the familiar Coble creep or grain boundary diffusional creep, however in this case acting at even room temperatures [22, 3]. Coble creep is a deformation process that leads to homogeneous elongation of grains along the tensile direction. It is believed to be strain rate dependent and where the strain rate is usually given as,

$$\dot{\varepsilon} = \frac{c\,\tau\,\Omega\,\delta_D D_{gb}}{k_B T\, d^3} \tag{4}$$

where δ_D is the width of the diffusing channel (approximately equal to the grain boundary width), D_{gb} is the diffusion constant for a grain boundary, T is the temperature, k_B is Boltzmann's constant, τ is the applied stress, Ω is the activation volume and c is a proportionality constant that depends upon the grain shape. From Eq. (4),

$$\tau = B d^3 \text{ where } B = \frac{\dot{\varepsilon} k_B T}{c\,\Omega\,\delta_D D_{GB}}. \tag{5}$$

Chokshi *et al.* [21] first proposed room temperature Coble creep as the mechanism to explain the so called inverse Hall Petch effect seen in nanocrystalline specimens. Certainly, there is an order of magnitude agreement and the trend is correct, however, the functional dependence of τ on d found by them is incorrect as pointed out by Neih and Wadsworth [22]. Conventional Coble creep demands as shown above that $\tau \sim d^3 = [d^{-1/2}]^{-6}$, *i.e.*, the τ *vs.* $d^{-1/2}$ curve falls very steeply as $d^{-1/2}$ increases. This is not found experimentally [21]. Their data however fits better a relation of the form

$$\tau = \beta - K' d^{-1/2} \tag{6}$$

where β and K' are constants. Eq. (6) cannot be related simply to any known mechanism.

A plausible explanation for this experimental fact was provided by Masumura *et al.* [3]. In their model it is assumed that that polycrystals with a relatively large average grain size obey the classical Hall-Petch relation. For very small grain sizes, it is assumed that Coble creep is active. The statistical nature of the grain sizes in a polycrystal is taken into consideration by using an analysis similar to Kurzydlowski [23]. The volume of the grains are assumed to be log-normally distributed Finally, it is assumed that a grain size d^* exists at which value of grain size the classical Hall-Petch mechanism switches to the Coble creep mechanism, *i.e.*, $\tau_{hp} = \tau_c$ at $d = d^*$. This model gives an analytical expression for τ as a function of the inverse square root of d in a simple and approximate manner that could be compared with experimental data over a whole range of grain sizes.

A major consideration in this approach is what explicit expression to use for Coble creep. Eq. (5) was not found to be suitable since it led to an extremely steep drop of τ with $d^{-1/2}$. In the model of Masumura *et al.* [3] the τ *vs.* d relationship used for Coble creep is given by

$$\tau_c = \frac{B_0}{d} + B d^3 \tag{7}$$

where B_0 is a constant while B is both temperature and strain-rate dependent. This threshold term [27] B_0/d can be large if d is in the nanometer range. For intermediate grain sizes, both

mechanisms (dislocations and Coble creep) might be active if the specimen has grain size distribution, as is usually the case.

We have also considered the expression of Yamakov *et al.* [16] for Coble creep, Eq. (7), for calculating yield stress of nanocrystalline materials. The experimental results are not precise enough to compare the two expressions for Coble creep precisely. We have compared the two expressions by checking which of the two versions are consistent with the experimental finding of Chokshi *et al.* [21] for copper and palladium. The Coble creep expression developed with a threshold stress gives a somewhat better fit unless the values of d^* are relatively small. It should however be noted that the experimental result of Chokshi *et al.* [21] is some what controversial (see references [24] and [25]) and hence further experimental results are needed.

A GENERALIZED EXPRESSION FOR YIELD STRESS

Collecting various terms discussed above, a generalized form of yield stress applicable to any polycrystal is obtained as

$$\tau = \tau_0 + kd^{-1/2} + k_1 + \frac{B_0}{d} + Bd^3, \tag{8}$$

where k_1 and B_0 are as yet undetermined constants. Several points regarding this equation should be noted. Firstly, the first two terms on the left hand side is to be used for grains larger that a given critical size d^*. For grains smaller than d^* the last three terms on the right hand side should be applicable. As before d^* is obtained by the following equation,

$$\tau_0 + k\left(d^*\right)^{-1/2} = k_1 + \frac{B_0}{d^*} + B\left(d^*\right)^3. \tag{9}$$

Secondly, not all the three terms on the right hand side will be significant for every situation. If Coble creep is dominant, the last two terms will be dominant; whereas if grain boundary dislocations are active, the first two terms may be more significant. Eq. (8) differs from the corresponding result used in [3] in two respects. First, it has an additional term k_1 and second, the

B_o/d term, which was introduced in an *ad hoc* fashion in [3], is identified with grain boundary dislocation reactions. Finally, this equation is true provided all the grains are of the same size. In a real polycrystal, we will have a distribution of grain sizes. Hence the averaging procedure given by Masumura *et al.* [3] should be used.

The technique applicable to the present situation is briefly described below. We define a volume average of the system of Eq. (8) following Kurzydlowski [23] as

$$(\tau)_{ave} - \tau_o = \frac{1}{m_v}\int_{d^*}^{\infty} k d^{-1/2} v f(v) dv + \frac{1}{m_v}\int_0^{d^*}\left(k_1 + \frac{B_o}{d} + Bd^3\right) v f(v) dv, \qquad (10)$$

where m_v is the grain volume average and is defined by

$$m_v = \int_0^{\infty} v f(v) dv \approx \gamma \bar{d}^3, \qquad (11)$$

where $\bar{d}$ is the mean grain size and γ is a geometrical factor of the order of 1. The grain volume distribution function $f(v)$ is assumed to be lognormal. All the integrals in Eqs. (10) and (11) can be integrated exactly in terms of error functions [3]. A comparison of the prediction with experiments for copper and nickel is given in [3], where it is shown that the model works well.

In Figs. 1 and 2, we compare the results of this procedure for two cases with a recent experimental results of Volpp *et al.* [26]. In Fig. 1 we assumed that Coble creep is dominant so that k_1=0 and in the other case we assume that Coble creep is negligible so that B = 0. We have plotted the yield stress as a function of grain size rather than as a function of $d^{-1/2}$. These two cases seem to correspond to the experimental case of annealed and as prepared specimen. The agreement with Eq. (8) together with Eq. (9) is very encouraging. We believe these two equations together with an averaging procedure is capable of describing the yield stress of any polycrystal in a functional form. The exact values of the constants have however to be determined in each case.

In Figs. 1 and 2, we have also plotted the derivative of hardness (or yield stress) as a function of average grain size to bring out a specific feature of the model. It is seen that in both

cases, the derivative curve (dotted) shows peaks. We believe this peak is a signature of the $1/d$ term in Eq. (8). The experimental data is, however, not precise enough to corroborate this point.

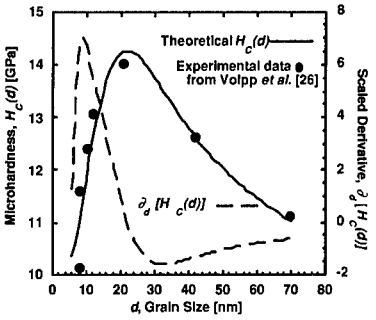


Figure 1. Dominant Coble creep influence.

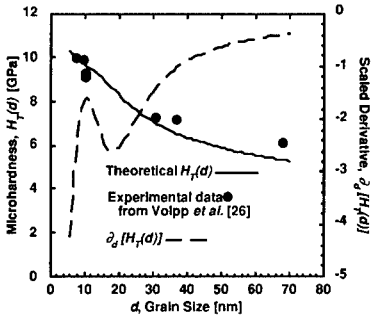


Figure 2. Negligible Coble creep influence.

For practical purposes it might be convenient to have an approximate expression but simpler than developed in [3] for the yield stress as a function of grain size. Towards that goal, we proceed as follows. Eq. (10) can be re-written as

$$(\tau)_{ave} - \tau_o = \frac{1}{m_v}\int_0^\infty k d^{-1/2} v f(v) dv - \frac{1}{m_v}\int_0^{d^*}\left(k d^{-1/2} - k_1 - \frac{B_o}{d} - B d^3\right) v f(v) dv$$

or

$$(\tau)_{ave} - \tau_o = I_1 - I_2. \tag{12}$$

The first integral can be exactly shown to be equal to

$$I_1 = \frac{k \exp\left(-5\sigma^2/72\right)}{(\bar{d})^{-1/2}} = \frac{K}{(\bar{d})^{-1/2}}, \tag{13}$$

where σ is the standard deviation in $\ell n(v)$. The second integral can be expressed in terms of error functions as mentioned before, but we find that for the range of grain sizes from 0 to d^*, a good approximation is given by,

$$I_2 = \frac{M_1}{(\bar{d})^3} \exp\left[-M_2\left\{\ell n\left(\frac{\bar{d}}{d^*}\right)\right\}^2\right], \tag{14}$$

where M_1 and M_2 strictly are functions of d^*. But we find that $M_2 \approx 1$ and M_1 can be obtained from using the fact that the curve of $(\tau)_{ave}$ vs $d^{-1/2}$ should peak around d^*. This gives M_1 as

$$M_1 = \frac{K}{6}(d^*)^{5/2}. \tag{15}$$

Thus finally

$$(\tau)_{ave} = \tau_o + \frac{K}{(\bar{d})^{1/2}} - \frac{K}{6(d^*)^{1/2}}\left(\frac{d^*}{\bar{d}}\right)^3 \exp\left[-M_2\left\{\ell n\left(\frac{\bar{d}}{d^*}\right)\right\}^2\right]. \tag{16}$$

We propose this approximate, semi-empirical equation as a convenient and simple equation to describe the whole range of grain sizes. The first two terms, of course, give the classical Hall-Petch result. The last term is responsible for the Inverse Hall-Petch effect. M_2 is about 1, K (the Hall-Petch slope) can be obtained experimentally and d^* being given by Eq. (10).

It is interesting to note that in this scheme, the mechanisms responsible for the Inverse Hall-Petch effect can, as a first approximation, be represented by d^* alone. In principle d^* can be obtained in terms of $\bar{d}$ from the peak, d_p, of the experimental curve of τ vs. $(\bar{d})^{-1/2}$. If the experimental gain size distribution is very narrow, $d_p \approx d^*$ and d_p *or* d^* is given by Eq. (9). If however the grain size distribution is not narrow, the actual peak d_p of τ vs. $(\bar{d})^{-1/2}$ curve may not coincide with d^*. By using various grain size distributions and using the averaging

procedure given by Masumura *et al.* [3], it is easy to show that $d_p \geq d^*$. In this case, Eq. (15) is only approximately true.

Taking these factors into account, we write Eq. (16) as

$$\tau_{norm} = \xi - M_1 \xi^6 \exp\left[-4 M_2 \left\{\ell n(\xi)\right\}^2\right] , \qquad (17)$$

where

$$\tau_{norm} = \frac{(\tau)_{ave} - \tau_o}{K(d_p)^{-1/2}} \text{ and } \xi = \left(\frac{\bar{d}}{d_p}\right)^{-1/2} , \qquad (18)$$

and because of the reasons stated before, $M_1 \approx 1/6$ and $M_2 \approx 1$. In Fig. (3), we plot Eq. (17) using these values of M_1 and M_2. The right side of the curve will be affected if somewhat different values of of M_1 and M_2 are used.

It is seen that this figure that Eq. (17) is able to account for both the conventional and "Inverse Hall-Petch" regions. We should point out that Eq. (17) is semi-empirical, and is being presented here as a rough approximation to the actual function obtained by the detailed averaging procedure [3] involving complicated error functions. Eq. (17) uses just two constants, M_1 and M_2 whose values are approximately given and uses the normalization of the average grain size with the peak of the curve, which is easily obtained from the experimental data.

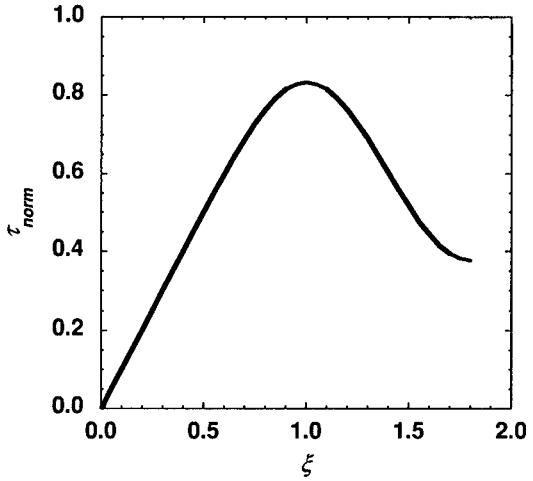


Figure 3. Simplified expression for yield stress (Eq. 17)

SUMMARY AND CONCLUSIONS

We have investigated theoretically, the connection between grain size and yield stress (or microhardness) for polycrystals, especially of nanometer sizes. We obtain an expression for the yield stress as a function of grain size, applicable to any material and for any grain size. Depending on the mode of the preparation, not all the terms in this equation will contribute. Hence for nanocrystalline materials, a large scatter in a Hall-Petch plot is expected, as is experimentally seen. We also specify, which of the terms will dominate for a given mode of preparation of the nanocrystalline material. Finally a semi-empirical equation relating yield stress with average grain size is also proposed.

REFERENCES

1. E. O. Hall, *Proc. Phys. Soc. London* **B64,** 747 (1951).
2. N. J. Petch, *J. Iron Steel Inst.* **174,** 25 (1953).
3. R. A. Masumura, P. M. Hazzledine and C. S. Pande, *Acta Mater.* **46,** 4527 (1998).
4. C. S. Pande, R. A. Masumura and R. W. Armstrong, *Nanostructured Materials* **2,** 323 (1993).
5. P. G. Sanders, J. A. Eastman and J. R. Weertman, *Acta, Mater.* **45,** 4019 (1997).
6. J. C. M. Li and Y. T. Chou, *Met. Trans.* **1,** 1145 (1970).
7. T. E. Mitchell, S. S. Hecker and R. L. Smialek, *Phys.Stat. Sol.* **11,** 585 (1965).
8. R. W. Armstrong and A. K. Head, *Acta Met.* **13,** 759 (1965).
9. C. S. Pande and R. A. Masumura in *Proc. of Sixth International Conf. on Fracture*, (1984) p.857.
10. N. Louat, *Acta Met.* **33**, 59 (1985).
11. A. G. Evans and J. P. Hirth, *Scripta Met.* **26**, 1675 (1985).
12. A. Lasalmonie and J. L. Strudel, *J. Mat. Sci.* **21**, 1837 (1986).
13. C. S. Pande and R. A. Masumura in *Processing and Properties of Nanocrystalline Materials*, edited by C. Suryanarayana, J. Singh and F. H. Froes, (Warrendale, PA, TMS,1996) p.387.
14. Y.T. Chou, *J. App. Physics* **38,** 2080 (1967).

15. G. Szego, *Orthogonal Polynomials,* (American Mathematical Society **23**, Colloquium Publications 1939).
16. V.Yamakov, D. Wolf, S.R.Phillpot and H. Glieter, *Acta Mat.* 50(2002) 61.
17. Z. Valiev, E. V. Kozolv, Yu. F. Inanov, J.Lian, A.A.Nazarov and B.Brandelet, *Acta Mat.* **42,** 2467 (1994).
18. G. A. Malygin, *Phys. Solid State*, **37,** 1248 (1995).
19. V. G. Gryaznov, M. Yu. Gutkin, A. E. Romanov and L. I. Trusov, *J. of Mater. Sci.* **28,** 4359 (1993).
20. M. Yu. Gutkin and I. A. Ovid'ko, private communication, 2002.
21. A. H. Chokshi, A. Rosen, J. Karch and H. Gleiter, *Scripta Met.* **23,** 1679 (1989).
22. T. G. Nieh and J. Wadsworth, *Scripta Met.* **25,** 955 (1991).
23. K. J. Kurzydlowski, *Scripta Met* **24,** 879 (1990).
24. H. V. Swygenhoven, M. Spaczer, A. Caro and D. Farkas, *Phys. Rev. B*, **60,** 22 (1999).
25. H. V. Swygenhoven and A. Caro, *Phys. Rev. B*, **58,** 11246 (1999).
26. T. Volpp, E. Göring, W. M. Kuschke and E. Arzt, *NanoStructured Matls.*, **8**, 855 (1997).
27. S. M. L. Sastry, private communication, 1997.

Mat. Res. Soc. Symp. Proc. Vol. 740 © 2003 Materials Research Society I1.4

Tensile Deformation and Fatigue Crack Growth in Bulk Nanocrystalline Al-7.5Mg

P.S. Pao, H.N. Jones, S.J. Gill, and C. R. Feng
Materials Science and Technology Division, Naval Research Laboratory
Washington, DC 20375, U.S.A.

ABSTRACT

The fatigue crack growth kinetics and tensile deformation of bulk nanocrystalline Al-7.5Mg were investigated. Nanocrystalline particulates were first prepared by mechanically ball milling spray atomized Al-7.5Mg powders in liquid nitrogen. These particulates were then degassed, consolidated by hot isostatic pressing, and extruded into rods. Bulk nanocrystalline Al-7.5Mg has significantly higher fatigue crack growth rates and lower fatigue crack growth thresholds than those of ingot-processed 7050-T7451. The fatigue crack growth thresholds exhibit only a weak stress ratio dependency and can be identified as having a Class I behavior when using the fatigue classification proposed by Vasudevan and Sadananda. In 3.5% NaCl solution, fatigue crack growth rates of bulk nanocrystalline Al-7.5Mg are as much as three times higher than those obtained in air. Tensile fracture of bulk nanocrystalline Al-7.5Mg is preceded by the formation of a localized shear band. In contrast to the low dislocation density in the as-extruded material, the gage section and the shear band region both exhibited a high dislocation density and dislocation cell structure.

INTRODUCTION

Nanocrystalline materials have received considerable attention recently due to the possibility of improved surface, electronic, optical, magnetic, and/or mechanical properties. Because of the difficulties in producing nanocrystalline materials in sufficiently large quantity and quality, however, many studies on nanocrystalline materials have been limited to thin films or very small samples. Mechanical properties of nanocrystalline materials have thus often been deduced indirectly from indentation tests due to the limited amount available. With recent advances in nanocrystalline materials production techniques, such as ball milling at cryogenic temperatures (cryomilling), large quantities of Al-Mg particulates with grain sizes of several nanometers can be successfully produced [1-5]. Good tensile strength and creep properties have been demonstrated for bulk nanocrystalline Al-Mg alloys [1,2]. However, the fatigue crack growth behavior and the effect of very small grain size on the fatigue crack growth kinetics of bulk nanocrystalline aluminum alloys have not been established.

In the present study, the fatigue crack growth kinetics and tensile deformation behavior of a bulk nanocrystalline Al-Mg alloy were determined. The fatigue crack growth rates and fatigue crack growth threshold stress intensity factor ranges (ΔK_{th}) of a bulk nanocrystalline Al-Mg alloy in both air and 3.5% NaCl solution were evaluated and were compared to those of ingot-metallurgy large grained alloy.

EXPERIMENTAL PROCEDURES

The bulk nanocrystalline material used in this study was 101.6-mm-diameter Al-7.5Mg extruded rod. Spray atomized Al-7.5Mg powders with a particle size less than 100 μm were mechanically ball milled in liquid nitrogen for eight hours. Details of the cryomilling processes can be found in [6]. The cryomilled powders were degassed at 317 °C in a 1.33×10^{-4} Pa vacuum, consolidated by hot isostatic pressing (HIP) at 317 °C and 200 MPa, and then extruded at 202 °C into an 101.6-mm-diameter rod with an extrusion ratio of 6.5:1.

For fatigue crack growth studies, 5.08-mm-thick compact-tension (CT) specimens with a width of 38.1 mm and oriented in the C-R direction were machined from as-extruded Al-7.5Mg rod. Fatigue crack growth tests were performed in ambient air (20 °C and 42% relative humidity) and in a flowing 3.5% NaCl solution (exposed to air under an open-circuit condition) at a cyclic load frequency of 5 Hz using a sine waveform and load ratios from 0.1 to 0.8. Details of the fatigue crack growth test procedures can be found in [7]. After fatigue tests, the fatigue-fractured surfaces were studied by scanning electron microscopy (SEM). A profilometer was used to measure the fracture surface roughness of the post-fatigue specimens. Transmission electron microscopy (TEM) was performed to examine dislocation structures.

RESULTS

Microstructures and tensile deformation

The grain size of the as-cryomilled Al-7.5Mg powders was not determined in this study. However, based on the work done at UC-Irvine on a similar alloy under identical cryomilling conditions, the average grain size of the as-cryomilled Al-7.5Mg powders was estimated to be about 25 nm. Following elevated temperature degassing, HIP, and extrusion, the grains coarsened considerably to an average size of about 250 nm. Even though the grains grew during powder processing and extrusion, the average grain size of the bulk nanocrystalline Al-7.5Mg was still more than two orders-of-magnitude smaller than that of typical ingot-metallurgy aluminum alloys. The Al-7.5Mg extrusion also contained sharp fiber texture with {111} planes parallel to the extrusion direction.

Table 1: Tensile Properties of Aluminum Alloys

Material	Yield Strength (MPa)	Tensile Strength (MPa)	% elongation
Al-7.5Mg	553	665	4.2
Al 5083-H321	228	317	16.0
Al 7050-T74	455	510	11.0

Tensile properties in the longitudinal direction (parallel to the extrusion direction) of bulk nanocrystalline Al-7.5Mg are tabulated in Table 1, together with those of ingot-metallurgy Al 5083-H321 (Al-4.4Mg-0.7Mn-0.15Cr) and Al 7050-T74 (Al-6.2Zn-2.25Mg-2.3Cu-0.12Zr). As shown in Table 1, the yield strength of bulk nanocrystalline Al-7.5Mg is more than twice that of Al 5083-H321, and is about 100 MPa more than that of high-strength Al-7050-T74. The tensile

elongation of the bulk nanocrystalline Al-7.5Mg, however, is significantly lower than those of both Al 5083-H321 and Al 7050-T74.

The onset of tensile instability occurred at plastic strains on the order of 0.7% and consisted of the sudden formation of a macroscopic shear band, usually near one of the shoulders of the test specimen. Any further straining beyond this point would induce a flat transverse fracture at the shear band location surrounded by 0.76 mm thick shear lips with a local reduction in area of about 6%. Due to the limited tensile deformation ductility of this material compression tests were conducted to further investigate its deformation behavior. Samples were cut from the undamaged portions of grip section of the tension test specimens. These were then tested in compression at strain rates of 10^{-4} s^{-1} and 10^{-3} s^{-1} between hardened platens in a servohydraulic load frame using a molydisulfide lubricant to reduce barreling of the sample.

The flow behavior of this material in compression exhibited two unusual effects. At plastic strains between 0.8% and 3% the work hardening rate was slightly negative. In addition the flow stress at 10^{-4} s^{-1} was greater by 7 MPa on average than that at 10^{-3} s^{-1} indicating a small negative strain rate sensitivity. These two aspects of the deformation behavior of the material cause it to exhibit a low tensile ductility. While there is evidence of a higher dislocation density in the gage section and the shear band region, the dislocation storage efficiency at plastic strains above 0.8% must be low to account for the low work hardening rate.

Fatigue crack growth kinetics

Fatigue crack growth rates as a function of stress-intensity-factor-range (ΔK) in an ambient air for bulk nanocrystalline Al-7.5Mg are shown in Fig. 1a. Fatigue crack growth rates of ingot-metallurgy Al 7050-T74 under similar test conditions are also included in Fig. 1a for comparison. The fatigue crack growth rate data of Al-7.5Mg exhibits the typical sigmoidal shape in the log-log plot, and can be separated into a near-threshold Stage I and an intermediate Stage II.

As shown in Fig. 1a, in ambient air and at intermediate and high ΔK, the fatigue crack growth rates of Al-7.5Mg are three to five times higher than those of Al 7050-T74 at comparable ΔK. Furthermore, the apparent ΔK_{th} of Al-7.5Mg is only about 1 MPa $\sqrt{m}$, which is significantly lower than the 2.2 MPa $\sqrt{m}$ exhibited by Al 7050-T74. As will be discussed later, the higher fatigue crack growth rates and lower ΔK_{th} of Al-7.5Mg can be attributed to the much smoother fracture surfaces which led to much lower fracture surface roughness induced crack closure levels when compared to Al 7050-T74.

Figure 1b compares the fatigue crack growth rates of Al-7.5Mg in a 3.5% NaCl solution to those obtained in ambient air. As shown in Fig. 1b, at high ΔK, the fatigue crack growth rates in a 3.5% NaCl solution are up to three times faster than those in air. As ΔK decreases, however, the difference between fatigue crack growth rates obtained in a 3.5% NaCl solution and in air progressively diminishes. At ΔK slightly above 2 MPa $\sqrt{m}$, the fatigue crack growth rates are essentially the same in these two environments and the apparent ΔK_{th} in a 3.5% NaCl solution is slightly less than 2 MPa $\sqrt{m}$. That is, the apparent ΔK_{th} observed in a more aggressive 3.5% NaCl solution is actually significantly higher than that obtained in ambient air. This seemingly contradictory behavior is also observed in ingot-metallurgy 2000- and 7000-series alloys and can be attributed to the corrosion product induced crack closure phenomenon which can effectively reduce the crack tip opening driving force and cause apparently higher ΔK_{th} [7,8].

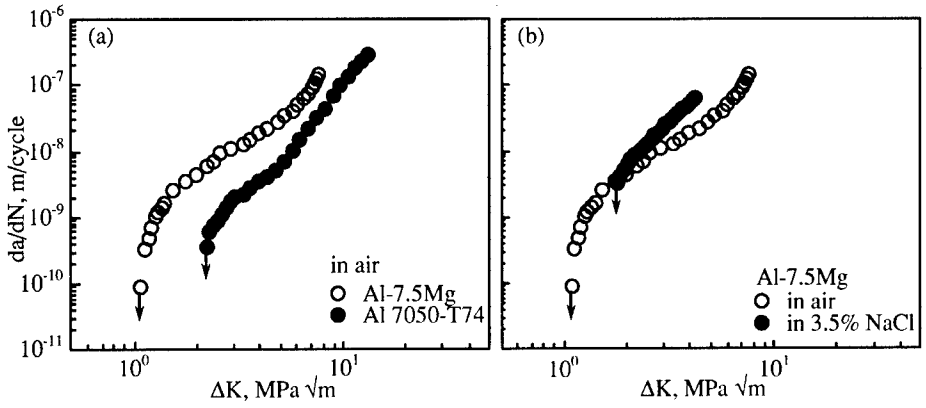


Figure 1. (a) Comparison of fatigue crack growth in air of Al-7.5Mg and Al 7050-T74 and (b) Effect of environment on fatigue crack growth of Al-7.5Mg.

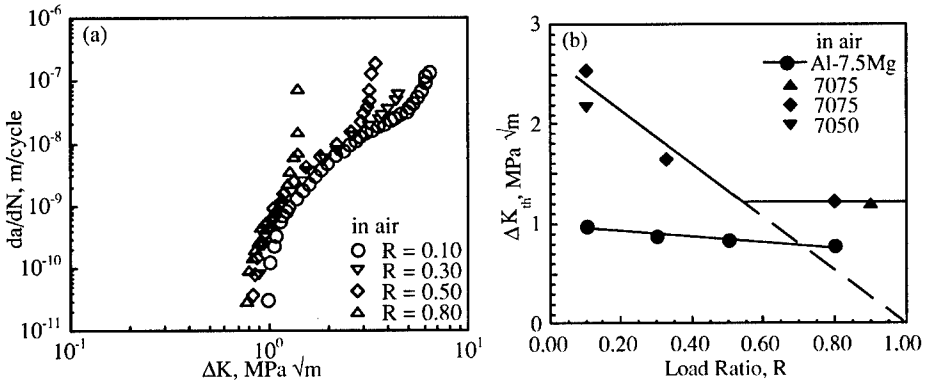


Figure 2. (a) Fatigue crack growth in air of Al-7.5Mg and (b) Effect of load ratio on fatigue crack growth thresholds of Al-7.5Mg, Al 7075, and Al 7050.

To take advantage of the recently developed classification of fatigue crack growth behavior and to elucidate the effect of load ratio on fatigue crack growth, fatigue crack growth kinetics of nanocrystalline Al-7.5Mg in air at load ratios from 0.1 to 0.8 are determined and are shown in Fig. 2a. As shown in Fig. 2a, fatigue crack growth rate curve at each load ratio follows a sigmoidal shape. While there are large divergences at high ΔK, where crack growth approaches instability, the differences in ΔK_{th} are actually small. The effect of load ratio on ΔK_{th} is shown in Fig. 2b together with the data from 7000-series ingot alloys. As shown in Fig. 2b, the fatigue crack growth thresholds of Al-7.5Mg exhibit only weak load ratio dependency and can be

identified as having a Class I behavior when using the fatigue classification proposed by Vasudevan and Sadananda [9]. In contrast, ingot 7000-series alloys exhibit a Class III behavior as their fatigue crack growth thresholds demonstrate strong load ratio dependence from R = 0.1 to 0.5, but remain independent of load ratio at R > 0.5.

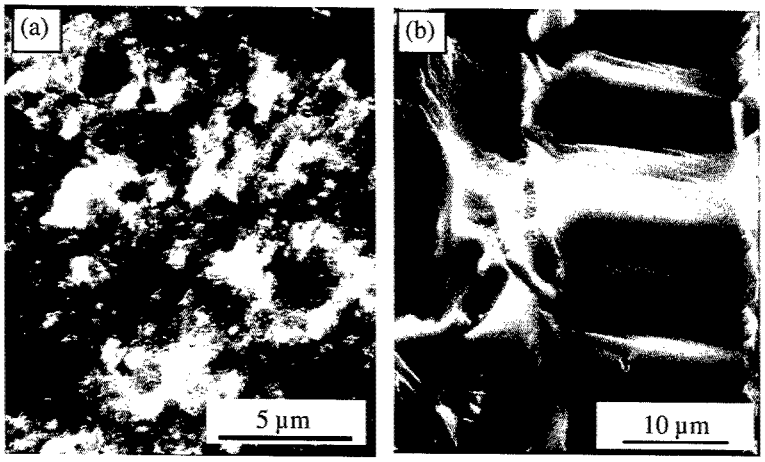


Figure 3. Fatigue fracture surface morphology in air of (a) Al-7.5Mg (at ΔK = 1.1 MPa $\sqrt{m}$) and (b) Al 7050-T74 (at ΔK = 2.2 MPa $\sqrt{m}$).

Figures 3a and 3b compare, respectively, the fatigue fracture surface morphologies of bulk nanocrystalline Al-7.5Mg and Al 7050-T74, both taken in the near-threshold region in an ambient air environment. As shown in Fig. 3b, the fracture surface morphology of Al 7050-T74 is very rough and fracture paths are transgranular and highly tortuous. Many crystallographic steps can be seen across the large elongated pancake grains and some slip traces are also present on these steps. The average surface roughness as measured by profilometer is 24 μm. In contrast, as shown in Fig. 3a, the fatigue fracture surface morphology produced in ambient air of bulk nanocrystalline Al-7.5Mg is largely uncharacteristic with no apparent crystallographic features. The fracture surfaces, even in the near-threshold region of the bulk nanocrystalline Al-7.5Mg, are much smoother than those of Al 7050-T74. The average surface roughness of the bulk nanocrystalline Al-7.5Mg as measured by profilometer is about 0.8 μm, which is thirty times smaller than the 24 μm observed in Al 7050-T74.

The observed difference in fatigue crack growth kinetics in air between the bulk nanocrystalline Al-7.5Mg and Al 7050-T74, as shown in Fig. 1a, therefore, can be attributed largely to the difference in fracture surface roughness induced crack closure levels in these two alloys. The crack closure levels in Al 7050-T74 are significantly higher than those exhibited by Al-7.5Mg. For instance, the crack closure level in the near-threshold region of Al 7050-T74 is about 43% of the maximum applied load whereas it is almost zero for the Al-7.5Mg. If the stress-intensity factor is truncated to account for roughness-induced crack closure and the

effective stress-intensity-factor-range ΔK_{eff} is used as a measure of the fatigue crack driving force, then the difference between the fatigue crack growth rates and the ΔK_{th} is significantly reduced.

SUMMARY

Fatigue crack growth rates through bulk nanocrystalline Al-7.5Mg are significantly higher and the fatigue crack growth thresholds are significantly lower than those of ingot-metallurgy Al 7050-T74. The higher fatigue crack growth rates and lower thresholds can be attributed to the much smoother fracture surface morphology and lower roughness induced crack closure in bulk nanocrystalline Al-7.5Mg. The fatigue crack growth thresholds in air exhibit only a weak stress ratio dependency and can be identified as having a Class I behavior when using the fatigue classification proposed by Vasudevan and Sadananda. At intermediate and high stress intensities, fatigue crack growth rates of bulk nanocrystalline Al-7.5Mg in 3.5% NaCl solution are higher than those obtained in air.

ACKNOWLEDGEMENTS

This work was supported by the Office of Naval Research, and monitored by Dr. A.J. Sedriks. Special thanks are extended to Dr. K. Sadananda of NRL for many helpful discussions, and to Dr. Dan Matejczyk of Boeing and Professor Enrique Lavernia of UC-Irvine for providing bulk nanocrystalline Al-7.5Mg extruded rod.

REFERENCES

1. R. Hayes, V. Tellkamp, and E. Lavernia, Scripta Materialia 41, 743 (1999).
2. V.L. Tellkamp and E.J. Lavernia, Nanostruct. Mater. 12, 249 (1999).
3. J. Rawers, G. Slavens, and R. Krabbe, Nanostruct. Mater. 9, 197 (1997).
4. R.J. Perez, H.G. Jiang, and E.J. Lavernia, Nanostruct. Mater. 9, 71 (1997).
5. M.J. Lau, H.G. Jiang, R.J. Perez, J. Juarez-Islas, and E.J. Lavernia, Nanostruct. Mater. 9, 157 (1997).
6. R.J. Perez, B. Huang, and E.J. Lavernia, Nanostruct. Mater. 7, 565 (1996).
7. P.S. Pao, S.J. Gill, C.R. Feng, and K.K. Sankaran, Scripta Materialia 45, 605 (2001).
8. P.S. Pao, M.A. Imam, L.A. Cooley, and G.R. Yoder, Corrosion 45, 530 (1989).
9. A.K. Vasudevan and K. Sadananda, Metall. Trans. 26A, 1221 (1995).

Mat. Res. Soc. Symp. Proc. Vol. 740 © 2003 Materials Research Society

Bimodal Microstructure and Mechanical Properties of Cryomilled Nanocrystalline Al-7.5Mg

Zonghoon Lee, David B. Witkin[1], Enrique J. Lavernia[2] and Steven R. Nutt
Department of Materials Science, University of Southern California,
Los Angeles, CA 90089-0241, U.S.A.
[1]Department of Chemical Engineering and Materials Science, University of California at Irvine,
Irvine, CA 92697-2575, U.S.A.
[2]Department of Chemical Engineering and Materials Science, University of California at Davis,
Davis, CA 95616, U.S.A.

ABSTRACT

The microstructure and mechanical properties consisting of tensile behavior and hardness of bulk nanocrystalline Al-7.5Mg alloy were investigated. Grain refinement was achieved by cryomilling of atomized Al-7.5Mg powders, and then nanocrystalline powders blended with 15% and 30% coarse-grained Al-7.5Mg powders were consolidated by hot isostatic pressing (HIP) followed by extrusion to produce bulk nanocrystalline Al-7.5Mg alloys. Bimodal structures, which enhance ductility and toughness of nanocrystalline metals, were produced that consisted of nanocrystalline grains and elongated coarse-grain bands. Examination of indentation revealed unusual deformation mechanisms and interactions between the coarse-grain bands and nanocrystalline regions. The ductile coarse-grain bands underwent extensive plastic deformation near indentation, while nanocrystalline regions exhibited limited deformation.

INTRODUCTION

The relations between microstructures and mechanical properties of bulk nanocrystalline metals have been investigated in recent years. Although several materials and microstructures have been developed high strength nanocrystalline metals, nanocrystalline metals still suffer from ductility and toughness reduction in contrast with increasing its strength. In one recent study, elastic-nearly perfectly plastic stress-strain behavior was observed and reported in Al-10Ti-2Cu alloy produced by mechanical alloying using cryomilling [1,2,3]. Such behavior is atypical for coarse-grain alloys of similar composition. Multi-scale structures, which were consisted of nanocrystalline grains and coarse-grain regions, enhanced ductility and toughness of bulk nanocrystalline alloys. In an effort to optimize toughened alloys based on multi-scale microstructures, more thorough understanding of microstructure and of structure-property relations in this structure was required. In the extended study, bimodal structures, which were comprised of nanocrystalline grains separated by coarse-grain regions, were produced to achieve ductile phase toughening in Al-7.5Mg. Thus in this work, the bimodal microstructure of bulk nanocrystalline Al-7.5Mg alloy was investigated using electron microscopy and optical microscopy. The stress-strain behaviors of bimodal Al-7.5Mg were estimated using uniaxial tensile test. In addition, Vickers hardness tests also were performed along the parallel and perpendicular to the extrusion direction to investigate the orientation dependent response of the bimodal microstructures and the interactions between coarse-grain and nanocrystalline regions.

EXPERIMENTAL DETAILS

Spray atomized Al-7.5%Mg in weight percent alloy powders were used to produce materials for this work. Nanocrystalline powder was produced using low-energy mechanical attrition at a cryogenic temperature (cryomilling) with a stainless steel vessel and milling balls with a diameter of 6.4 mm. The ball to charge ratio was 36:1, with stearic acid added at 0.25 percent of the powder weight to moderate the cold welding process. The cryomilling was operated at 180 rpm for eight hours, and maintained at a temperature of –190 °C using flowing liquid nitrogen into the vessel itself, submerging the powder and balls. Cryomilled nanocrystalline powders were combined with coarse-grained Al-7.5Mg powders of 0, 15 and 30 weight percent respectively and were blended to form bimodal samples. These samples were loaded in aluminum cans for vacuum degassing at 400 °C. The cans were sealed and consolidated in hot isostatic press (HIP) at 325 °C and 25 ksi. The consolidated billets were extruded using an extrusion ratio of 6.5:1 and proprietary rate and temperature parameters.

Tensile specimens were machined from the resulting extrusions along the extrusion direction with a gauge length of 13.5 mm and a gauge diameter of 3.5 mm. The tensile tests were performed on a universal testing machine at room temperature, using a nominal strain rate of 10^{-3} s^{-1}. The microstructure of the extrusions was examined using transmission electron microscopy (TEM) and optical microscopy. Vickers hardness measurements were performed on the polished and chemically etched surfaces along the extrusion and transverse directions at 10 gf load for the coarse-grain region and nanocrystalline region respectively, and 1 kgf load for the global region, which covered both coarse-grain and nanocrystalline region. The polished and chemically etched surfaces and indentations were observed using optical microscope and scanning electron microscopy (SEM; Cambridge 360). Thin foils for transmission electron microscopy (TEM) were prepared by tripod polishing to prepare an electron transparent wedge, which provided large thin areas for TEM observation. Samples were examined using a Philips EM420 TEM with EDS. In order to reveal both global and local structure, TEM images were recorded at low and high magnifications using Philips EM420 and Akashi 002B TEMs.

DISCUSSION

The bimodal microstructures comprised of nanocrystalline grains and coarse-grains were prepared by consolidation of powders and extrusion successfully. Bulk nanocrystalline Al-7.5Mg mixed with 15% and 30% coarse-grain had bimodal structures with nanocrystalline region and coarse-grain regions. However, the microstructure of Al-7.5Mg with 0% was uniform with a few percent of residual coarse grains. The global three-dimensional view of bimodal structure of the as-extruded Al-7.5Mg with 30% coarse-grain is shown in figure 1. Coarse-grain regions and nanocrystalline regions are evident in the figure. The bright and dark regions indicate coarse-grain and nanocrystalline regions, respectively, on the figure. Both coarse-grain and nanocrystalline regions extended along the extrusion direction while coarse-grain regions extended in highly elongated bands. The resulting bimodal structures were comprised of nanocrystalline grains separated by coarse-grain bands. The coarse-grain bands, which were dispersed uniformly and were similar in their shape and size, were about 240 μm long and 20 μm wide in Al-7.5Mg with 30% coarse-grain. The spacing, which occupied with nanocrystalline, between coarse-grain bands was about 25 μm. The length and width of coarse-grain bands of Al-

7.5Mg with 15% coarse-grain were shorter than those of Al-7.5Mg with 30% coarse-grain and the spacing between coarse-grain bands of Al-7.5Mg with 15% coarse-grain was bigger than that of Al-7.5Mg with 30% coarse-grain. The coarse-grain bands usually consisted of grains and sub-grains about 1 μm in contrast with nanocrystalline region, which had grains about 200 nm sizes. There were no intermetallic phases detected in both coarse-grain bands and nanocrystalline region. Figure 2 shows the microstructures of the coarse-grain bands and the sub-grains within Al-7.5Mg with 0%, 15% and 30% coarse-grain, respectively. The interfaces between nanocrystalline region and coarse-grain bands looked rather faceted. The ductile coarse-grain bands and nanocrystalline region had the same composition of Al-7.5Mg.

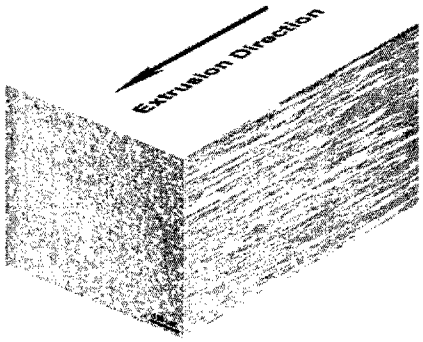


Figure 1. Three-dimensional view of bimodal microstructure of as-extruded Al-7.5Mg alloy with 30% coarse-grain content.

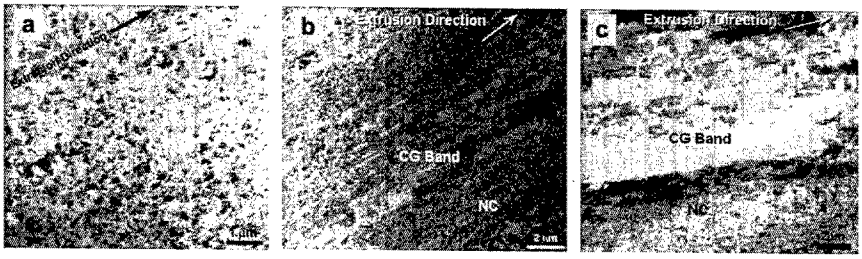


Figure 2. TEM micographs of as-extruded Al-7.5Mg alloy with 0% (a), 15% (b) and 30% (c) coarse-grain content, respectively.

The engineering stress-strain curves obtained from uniaxial tensile tests along the extrusion directions are displayed as a function of coarse-grain content in figure 3. The tensile stress-strain behavior of the Al-7.5Mg with 30% coarse-grain alloy exhibited elastic-nearly perfectly plastic stress-strain behavior in noticeably contrast to that of the Al-7.5Mg with 0% coarse-grain, which showed limited plastic deformation and work hardening. This feature is consistent with the

uniaxial tension stress-strain behavior reported for sintered nanocrystalline Al-Ti-Cu [1,2,3] and Al [5]. The yielding was followed by extended periods of mild work softening. The tensile stress-strain behavior of Al-7.5Mg with 15% coarse-grain exhibited somewhat improved plastic deformation and work softening. The ductility and toughness increased over 200% with coarse-grain content of Al-7.5Mg alloys while the yield stress just decreased about 15% drop. The peak flow stresses of the Al-7.5Mg with 0%, 15% and 30% coarse-grain were about 850 MPa, 760 MPa and 700 MPa at room temperature, respectively, which were remarkable for an aluminum alloy. Elongation to failure of Al-7.5Mg with 30% coarse-grain was about 7 % at room temperature. However, unlike pure ultrafine-grained materials, the strength of the present material cannot be attributed solely to grain size refinement. The small degree of work hardening and work softening is not well understood, but may be related to a change in deformation mechanism stemming from the unusual structure.

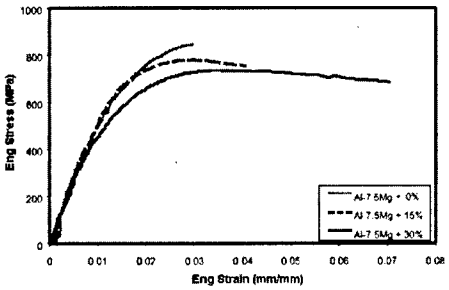


Figure 3. Uniaxial tensile stress-strain behaviours of as-extuded Al-7.5Mg alloy with 0%, 15% and 30% coarse-grain content at room temperature. [4]

The Vickers hardness of bimodal Al-7.5Mg along the extrusion direction was decreased with increasing coarse-grain content from 0% to 30% in figure 4 (b). The hardness is inversely proportional to the coarse-grain content. The ductile coarse-grain phase contributed to decrease the hardness of bimodal Al-7.5Mg using heavy 1 kgf load. The micrograph of 1 kgf indentation on Al-7.5Mg with 30% coarse-grain, as shown in figure 4 (a), is an anomaly, which is unlikely to indent on uniform structure materials. The ductile coarse-grain region showed barrel-shaped indentation faces, which resulted from piling up of the coarse-grain around the faces of indenter, in noticeably contrast to the perfect indentation of nanocrystalline region around the faces of indenter. The hardness of individual coarse-grain and nanocrystalline regions was estimated using a very light 10 gf load, which enabled to indent on coarse-grain region and nanocrystalline region separately as shown in figure 5. The hardness of nanocrystalline region was same on Al-7.5Mg with 15% and 30% coarse-grain, while the hardness of coarse-grain region was decreased and the hardness difference between nanocrystalline and coarse-grain region was increased with increasing coarse-grain content. The hardness of nanocrystalline region was not sensitively related to coarse-grain content. That claims the effective indentation zone of nanocrystalline region was restricted in relatively short range and did not reach to coarse-grain region. Thus, the nanocrystalline region is likely to dissipate its deformation energy in short range. However, the hardness of coarse-grain region was directly depending on the coarse-grain content. The

deformation of ductile coarse-grain region was expanded to nanocrystalline region extensively, which might constraint the deformation of coarse-grain region. The feature is evident on figure 5. The size of plastic zone beneath a hardness indentation will be estimated in ongoing research. The hardness of Al-7.5Mg with 0% coarse-grain was lower than that of nanocrystalline region on Al-7.5Mg with 15% and 30% coarse-grain because Al-7.5Mg with 0% coarse-grain contained a few percent of residual coarse-grain during processing. It might affect small indentations. Consequently the hardness of bimodal microstructures comprised of nanocrystalline grains and coarse-grain bands was depending on coarse-grain content. Moreover, these structures played a significant role in enhancing ductility and toughness by its unusual deformation mechanism in the bulk nanocrystalline alloys.

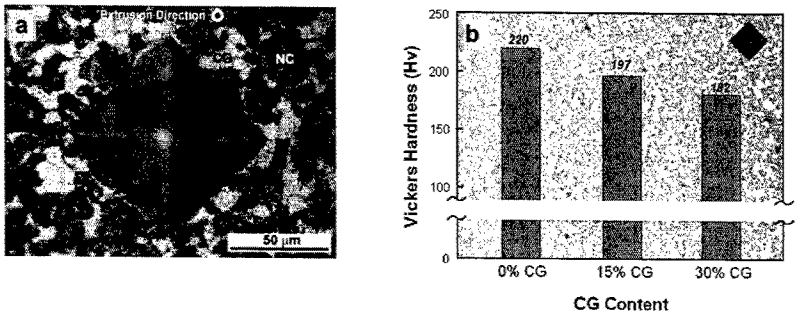


Figure 4. (a) The micrograph of indentation using 1 kgf load on Al-7.5Mg alloy with 30% coarse-grain content along the extrusion direction, (b) Vickers hardness results using 1 kgf load on Al-7.5Mg alloy with 0%, 15% and 30% coarse-grain content along the extrusion direction.

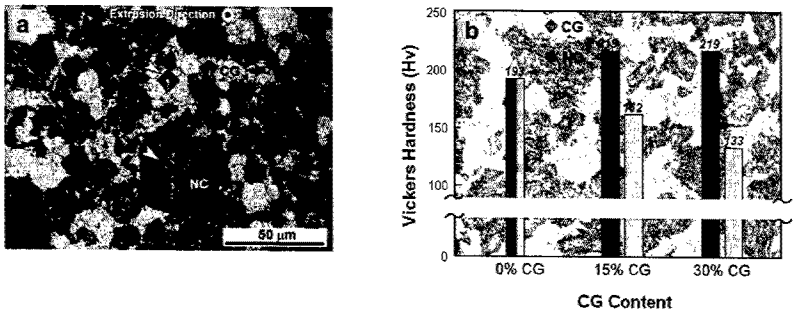


Figure 5. (a) The micrograph of separate indentations using 10 gf load on coarse-grain and nanocrystalline region of Al-7.5Mg alloy with 30% coarse-grain content along the extrusion direction, (b) Vickers hardness results using 10 gf load on coarse-grain (CG) and nanocrystalline (NC) region of Al-7.5Mg alloy with 0%, 15% and 30% coarse-grain content along the extrusion direction.

CONCLUSIONS

In an effort to enhance ductility and toughness of bulk nanocrystalline metals, bimodal structures of Al-7.5Mg comprised of nanocrystalline grains and elongated coarse grains were produced by consolidation of cryomilled powders successfully. Coarse grains were elongated in the extrusion direction and formed ductile coarse-grain bands. Elastic-nearly perfectly plastic stress-strain behavior was observed in tension tests of bulk nanocrystalline Al-7.5Mg with 30% coarse-grain. The unusual absence of work hardening was a noteworthy characteristic of the bimodal Al-7.5Mg alloy. Although the phenomenon is not fully understood at present, it has been reported in other nanocrystalline alloy systems prepared by mechanical alloying, and warrants further investigation. The hardness properties of bimodal Al-7.5Mg alloy revealed the different hardness and deformation behavior between nanocrystalline region and coarse-grain region. Investigation of tensile and hardness test proposes unusual deformation mechanisms and interactions between ductile coarse-grain bands and nanocrystalline regions. The present work has shown that the yield strength can be substantially increased while retaining reasonable ductility, although it was by no means fully optimized. The bimodal microstructure and its ductility toughening effect inspire us to design microstructures and to guide the selection of processing parameters leading to optimal performance characteristics on various nanocrystalline metals.

ACKNOWLEDGEMENTS

This work was supported by a MURI grant from the Office of Naval Research, N00014-01-1-0882.

REFERENCES

1. R.W. Hayes, R. Rodriguez and E.J. Lavernia, Acta Mater., 2001, vol. 49, pp. 4055-68.
2. Z. Lee, R. Rodriguez, E.J. Lavernia and S.R. Nutt, *Ultrafine Grained Materials II*, edited by Y.T. Zhu, T.G. Langdon, R.S. Mishra, S.L. Semiatin, M.J. Saran, and T.C. Lowe, TMS, Seattle, WA, 2002, pp. 653-59.
3. Z. Lee, R. Rodriguez, R. W. Hayes, E. J. Lavernia and S. R. Nutt: Metall. Mater. Trans. A, 2002, accepted.
4. D. Witkin, Z. Lee, S. R. Nutt and E. J. Lavernia: submitted in Scripita Mater.
5. X.K. Sun, H.T. Cong, M. Sun and M.C. Yang: Metall. Mater. Trans. A, 2000, vol. 31A, pp. 1017-24.

Mat. Res. Soc. Symp. Proc. Vol. 740 © 2003 Materials Research Society

Hardness and Abrasion Resistance of Nanocrystalline Nickel Alloys Near the Hall-Petch Breakdown Regime

Christopher A. Schuh[1] and T. G. Nieh[2]
[1] Department of Materials Science and Engineering, Massachusetts Institute of Technology
77 Massachusetts Avenue, Room 8-211, Cambridge, MA 02139, USA
[2] Materials Science and Technology Division, Lawrence Livermore National Laboratory
7000 East Avenue, L-350, Livermore, CA 94550, USA

ABSTRACT

The breakdown of classical Hall-Petch scaling remains an area of scientific interest, and will govern the limiting strength of nanocrystalline alloys for structural applications. In this work we discuss the hardness and scratch resistance of nanocrystalline nickel and nickel-tungsten solid solution alloys, assessed through nanoindentation and nano-scratch techniques. The materials have been prepared by electrodeposition, and are fully dense with grain sizes between 6 and 22 nm. In this range of grain sizes, there is some evidence for a breakdown of Hall-Petch scaling, reflected in both the hardness and abrasion data. The role of solid solution alloying on this breakdown is also discussed.

INTRODUCTION

The grain size of metals can now be varied through a broad range, including the sub-microcrystalline and nanocrystalline regimes, owing to the development of novel processing methods. For example, severe plastic deformation techniques [1, 2] are applicable to most alloys, and can produce grain sizes below one micron. Compaction of nano-powders or nanocrystalline powders offers the possibility of finer grain sizes below 100 nm [3, 4], as do several deposition-based methods such as electrodeposition [5, 6]. The development of nanocrystalline alloys has been driven technologically, by the promise of exceptional properties, as well as scientifically, by the potential breakdown of classical scaling laws and the accompanying need for new materials physics in the nanostructured limit. For example, Hall-Petch strengthening (strength increasing as the inverse square-root of grain size) is expected to break down for grain sizes in the range of 5-30 nm [7] and in fact should give way to a weakening trend toward the amorphous limit. Such an inflection is not only scientifically interesting, but also sets the physical limit for strengthening of nanostructured engineering materials.

Hall-Petch scaling and its possible breakdown in the nanocrystalline regime have been investigated experimentally and theoretically by many authors. The purpose of the present work is to extend the discussion of Hall-Petch breakdown to consider, firstly, the possible roles that solid-solution alloying may play with regard to this effect, and secondly, the implications of Hall-Petch breakdown for abrasion resistance in nanostructured materials. These issues have particular relevance with regard to next-generation micro electromechanical systems made by electrodeposition-based "LIGA" processes.

EXPERIMENTAL PROCEDURES

Foils of nanocrystalline nickel (n-Ni) and nickel-tungsten (n-Ni-W) were fabricated by direct current (DC) electrodeposition, using standard procedures given in more detail in Refs. [8, 9]. In the case of n-Ni, a nanocrystalline structure is induced through the inclusion of a small amount (5 g/L) of saccharine in the plating bath, and for both n-Ni and n-Ni-W alloys the grain size, morphology, and texture of the plated foils can be tailored to some degree through the choice of bath pH and applied current density [8, 9]. The as-deposited foils were characterized by X-ray diffraction, and their grain size determined by applying the Scherrer formula for peak broadening to the (200), (220), or (111) reflections after correction for instrumental line broadening using a silicon standard. Some specimens were also examined by transmission electron microscopy (TEM) in a Philips CM300 or a JEM-4000EX.

Indentation testing was performed in an MTS/Nanoinstruments (Oak Ridge, TN) Nanoindenter-XP, as well as a TriboIndenter instrumented nanoindenter (from Hysitron, Minneapolis, MN), in all cases with a diamond Berkovich indenter. Hardness was determined both by the Oliver-Pharr method and the continuous stiffness method [10], with the instantaneous contact area determined using the calibrated area function of the Berkovich tip. Indentations were performed both on the planar surface and polished cross-sections of the electrodeposited foils; the reported results are average values of more than ten indents.

Abrasive nano-scratch experiments were performed on n-Ni using the Nanoindenter-XP over a travel distance of 500 μm, with a ramping normal load from 20 to $1.5 \cdot 10^5$ μN. The diamond tip was oriented such that an edge of the Berkovich pyramid was pointing in the direction of travel. At least three identical scratches were performed on each material; the scratch profiles were always very consistent.

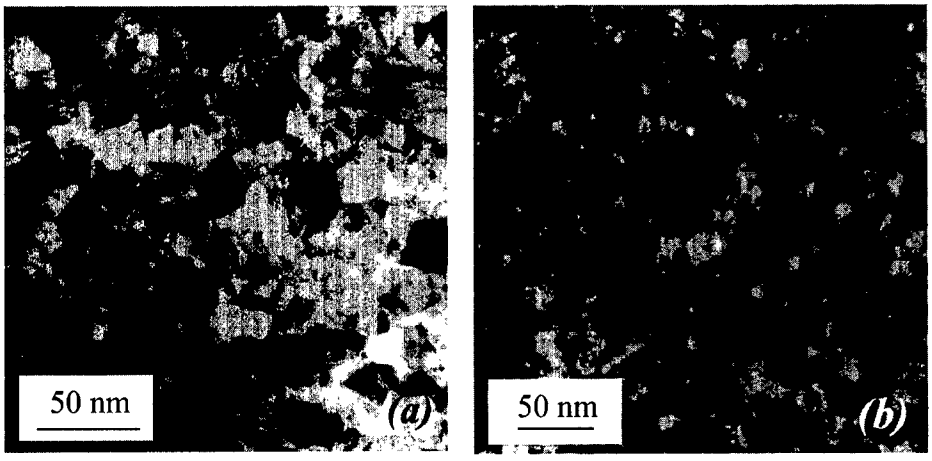


Figure 1: Bright-field TEM images of (a) n-Ni and (b) a n-Ni-W alloy, with nominal grain sizes d = 14 and 7 nm, respectively.

RESULTS AND DISCUSSION

Materials

For nominally pure n-Ni, specimens with grain sizes in the range 12-22 nm were produced by electrodeposition, while for alloyed n-Ni-W alloys the grain size was somewhat smaller, in the range 6-10 nm, as revealed by the x-ray line broadening measurements. 12 and 6 nm are the smallest grain sizes we were able to produce in Ni and Ni-W, respectively; further attempt to reduce the grain size by adding nucleant in the electrodeposition bath was found impossible without producing some amorphous phases. TEM observations of the grain structure were found to give similar values to the x-ray measurements (within ± 2 nm), and additionally verified that the specimens were free of porosity. Typical nanostructures observed in the foil normal direction are illustrated in Fig. 1 for both a pure Ni (a) and a Ni-W alloy (b). Chemical analysis revealed that all of the Ni-W alloys had a similar global composition, Ni–(11.6-14.1 at%)W. Additional details about these materials, their processing and structure are available in Refs. [8, 9].

Hardness and Deviations from Hall-Petch Behavior

The results of the instrumented indentation experiments are summarized as a function of grain size in the Hall-Petch plot of Fig. 2. For comparison, this plot also contains hardness data on nominally pure nickel from the work of Erb et al. [11, 12], who used pulsed-current electrodeposition to produce materials, as well as Ebrahimi et al. [13], who prepared specimens by DC electrodeposition. To a grain size as fine as d = 14 nm and hardness as high as ~6.4 GPa, the present data for n-Ni are in reasonable agreement with the classical Hall-Petch scaling behavior, and complement the data of Ebrahimi et al. [13]. However, between the smallest grain sizes of d = 14 and 12 nm, our data show a significant decrease in hardness, consistent with Hall-Petch breakdown anticipated at these grain sizes [7].

The peak hardness of ~6.4 GPa observed for n-Ni at d = 14 nm is in agreement with the peak hardness measured by Erb et al. [11, 12] near the same grain size (see Fig. 2), as is the observation of a Hall-Petch breakdown. However, our data reflect a rather abrupt breakdown point near $d \approx 14$ nm, while the data of Erb et al. [11, 12] show a much broader transition region, spanning grain sizes from 11-25 nm. A possible explanation for this discrepancy lies in the method of sample fabrication. Although both investigations employed electrodeposition techniques to prepare fully dense n-Ni specimens, the present study used direct current plating whereas Erb et al. [11, 12] used pulsed current plating, in which the current is applied as a rectangular wave-form. These methods produce grain structures with different morphologies; our DC electrodeposited foils have an elongated grain structure in the plating direction, as described in Ref. [8]. Additionally, pulsed-current plating gives a rather broad grain size distribution that would tend to broaden the observed Hall-Petch breakdown in Fig. 1 [11, 12].

As described above, both our data and those of Erb et al. [11, 12] suggest that the Hall-Petch inflection occurs near ~12-15 nm for pure nickel. In contrast, the data for Ni-W shown in Fig. 1 appear to also exhibit an inflection, but at a finer grain size, d ~ 7-9 nm; alloying with W apparently causes a decrease in the inflection grain size. Such a decrease is only possible if the addition of W suppresses the deformation mechanism at the finest grain sizes below the

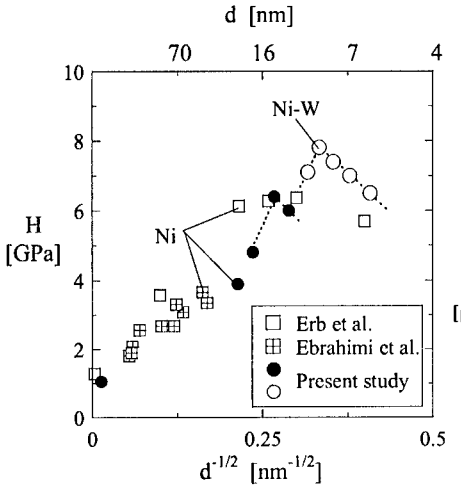


Figure 2: Hall-Petch plot of hardness (H) vs. reciprocal square-root grain size ($d^{-1/2}$) for n-Ni and n-Ni-W alloys, compared with data from Refs. [17-19]

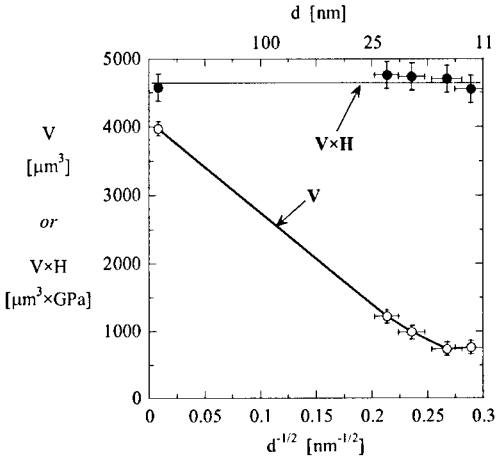


Figure 3: Hall-Petch-style plot of abraded volume (V) vs. reciprocal square-root grain size ($d^{-1/2}$) for n-Ni after identical 500 μm scratches with a Berkovich diamond tip.

inflection. Although the detailed deformation mechanisms associated with Hall-Petch breakdown are still under debate, there is general support for diffusional mechanisms such as grain boundary sliding or Coble creep [14, 15]. For such diffusive mechanisms to occur in solid solution alloys such as Ni-W, all of the atomic species of the alloy must redistribute diffusively in order to maintain chemical homogeneity. In a binary alloy deforming in steady state, the deformation is governed by an effective diffusivity, which is a composite of the majority and minority component diffusivities. Assuming a steady-state Coble-creep mechanism to occur below the inflection grain size, and further assuming that the inflection occurs abruptly at a single grain size, it is possible to make an estimate of the inflection grain size for a given concentration, c, of substitutional element [9]:

$$\frac{d^i_{Ni\text{-}W}}{d^i_{Ni}} \approx \left[\frac{D_W}{D_{Ni}} \cdot (1-c) + c\right]^{2/7} \qquad (1)$$

where D_W and D_{Ni} are the grain boundary diffusivites of Ni and W in α-Ni, and the inflection grain size of the alloy, $d^i_{Ni\text{-}W}$ is predicted relative to the inflection grain size for pure nickel, d^i_{Ni}.

Although there are apparently no quantitative values for the grain boundary diffusion of tungsten in nickel, the volume diffusivity of W in Ni is very much smaller than the self-diffusivity of Ni ($D_W / D_{Ni} \approx 5 \cdot 10^{-5}$ at room temperature) [16]. For such a slow diffusing solid solution element it is reasonable to write:

$$\frac{d^{i}_{Ni\text{-}W}}{d^{i}_{Ni}} \approx c^{2/7} \qquad (2)$$

Using an average value for the atomic W concentration in the present alloys, $c = 0.13$, this rough calculation gives $d^{i}_{Ni\text{-}W} / d^{i}_{Ni} \approx 0.56$, suggesting that the inflection grain size would be reduced by about a factor of two by alloying Ni with 13% W. If the data for Ni-W in Fig. 2 are interpreted as a Hall-Petch breakdown, then the experimental value for this ratio is in the range $d^{i}_{Ni\text{-}W} / d^{i}_{Ni} =$ 0.47-0.60, in excellent agreement with the estimate of Eq. (2). In the case where the diffusional process occurs primarily in the bulk of the nanocrystalline grains (a Nabarro-Herring creep process), the exponent in Eqs. (1,2) would become 2/5. The expected shift in the inflection grain size would then be $d^{i}_{Ni\text{-}W} / d^{i}_{Ni} \approx 0.44$, still in reasonable agreement with the experimental range of $d^{i}_{Ni\text{-}W} / d^{i}_{Ni} = 0.47\text{-}0.60$. Thus, the quantitative predictions of Eq. (2) are relatively insensitive to the exact value of the grain size exponent; the general expectation of an inflection grain size smaller by about half is therefore qualitatively reasonable. The very good agreement between model and data may be largely fortuitous, given the many simplifying assumptions of the model and the paucity of experimental data.

The above concepts are not specific to the Ni-W system, but should be generally applicable to most all substitutional solid solutions. Such alloying is theoretically expected to shift the inflection grain size of the Hall-Petch breakdown to smaller values, provided that the alloying element is a slow diffuser, and a diffusive mechanism is in fact responsible for the Hall-Petch breakdown.

Nano-Abrasion near the Hall-Petch Breakdown

Fig. 3 shows a summary of the major results from the nano-scratch experiments on n-Ni, the total volume of displaced material, V, as determined from atomic force microscope images of the scratches, plotted against $d^{-1/2}$ in Hall-Petch style. The trend shown in this figure is similar to that observed in hardness (Fig. 2), with a generally linear relationship between V and $d^{-1/2}$ from 15 μm down to ~14 nm grain sizes. The Hall-Petch hardness breakdown observed below ~14 nm in Fig. 2 is manifested here as a deviation from this linear relationship for the specimen with d = 12 nm.

For a rigid asperity scratching a substrate, the amount of material dV displaced by abrasion is proportional to the distance of translation dx, and scaled by the projected area of the asperity in the direction of travel. For our experiments, the projected contact area is determined from the ideal geometry of a Berkovich tip, and the applied load increases as a linear function of position, with a proportionality constant $\kappa = 300$ N/m. Under these conditions one can derive [8]:

$$\frac{dV}{dx} = 0.146 \cdot \frac{\kappa}{H} \cdot x \qquad (3)$$

This inverse relationship between hardness and abraded volume can be quantitatively validated by normalizing the wear data in Fig. 3 with the experimental hardness values (from Fig. 2). The solid points in Fig. 3 show the same data, now multiplied by the hardness according to Eq. (3). Whereas the volume of removed material varied by over a factor of five (open points in Fig. 2), normalization with the hardness completely removes this variation to within experimental error.

Thus, although the nanocrystalline nickel specimens used in this work exhibited a broad range of wear resistance, we find that these differences are quantitatively commensurate with the measured change in hardness, even in the limit of the finest grain sizes. Although the breakdown of Hall-Petch strengthening at these grain sizes may be related to a transition in the plastic deformation mechanism, the abrasive wear mechanism appears unchanged through this transition. It is important to emphasize, however, that we have observed an apparent breakdown of Hall-Petch strengthening in pure n-Ni only at a single grain size in this work.

CONCLUSIONS

The Hall-Petch strengthening of nominally pure Ni is found to hold well into the nanocrystalline regime, with the first suggestion of a breakdown near d ~ 14 nm. This value is in agreement with prior data from the literature, and is significantly different than found in Ni-W alloys, which exhibit an apparent Hall-Petch breakdown near d ~ 7-8 nm. If diffusional creep mechanisms operate at the finest grain sizes, we find that this result is indeed expected, provided that the solid solution alloying element is a slow diffuser. The Hall-Petch breakdown in n-Ni is also found to manifest itself in the abrasive scratch resistance, which is inversely proportional to hardness.

ACKNOWLEDGEMENTS

Portions of this work were performed under the auspices of the US Department of Energy by the University of California, Lawrence Livermore National Laboratory, under contract W-7405-Eng-48.

REFERENCES

[1] F. H. Froes, O. N. Senkov and E. G. Baburaj, *Mater. Sci. Eng.* **A301**, 44 (2001).
[2] R. Z. Valiev, I. V. Alexandrov, Y. T. Zhu and T. C. Lowe, *J. Mater. Res.* **17**, 5 (2002).
[3] G. W. Nieman, J. R. Weertman and R. W. Siegel, *Scripta Metall. Mater.* **24**, 145 (1990).
[4] P. G. Sanders, J. A. Eastman and J. R. Weertman, *Acta Mater.* **45**, 4019 (1997).
[5] H. Natter and R. Hempelmann, *Journal of Physical Chemistry* **100**, 19525 (1996).
[6] L. Lu, M. L. Sui and K. Lu, *Acta Mater.* **49**, 4127 (2001).
[7] T. G. Nieh and J. Wadsworth, *Scripta Metall. Mater.* **25**, 955 (1991).
[8] C. A. Schuh, T. G. Nieh and T. Yamasaki, *Scripta Mater.* **46**, 735 (2002).
[9] C. A. Schuh, T. G. Nieh and H. Iwasaki, *Acta Mater.* (2002), in press.
[10] W. C. Oliver and G. M. Pharr, *J. Mater. Res.* **7**, 1564 (1992).
[11] U. Erb, *Nanostructured Materials* **6**, 533 (1995).
[12] A. M. El-Sharik, U. Erb, G. Palumbo and K. T. Aust, *Scripta Metall. Mater.* **27**, 1185 (1992).
[13] F. Ebrahimi, G. R. Bourne, M. S. Kelly and T. E. Matthews, *Nanostructured Materials* **11**, 343 (1999).
[14] V. Yamakov, D. Wolf, S. R. Phillpot and H. Gleiter, *Acta Mater.* **50**, 61 (2002).
[15] H. Van Swygenhoven, M. Spaczer, A. Caro and D. Farkas, *Phys. Rev.* **B60**, 22 (1999).
[16] E. A. Brandes and G. B. Brook, eds. *Smithells Metals Reference Book, Seventh Edition.* 1992, Butterworth-Heinemann: Oxford, UK.

Mat. Res. Soc. Symp. Proc. Vol. 740 © 2003 Materials Research Society

Hybrid nylon-6/silica nanocomposites with improved mechanical properties

Monserrat García, Werner E. van Zyl, and Henk Verweij[1]
Inorganic Materials Science Group, MESA+ Research Institute, University of Twente
P.O. Box 217, 7500 AE Enschede, The Netherlands
[1]Department of Materials Science and Engineering, The Ohio State University,
Columbus, OH 43210-1178, USA.

ABSTRACT

The study involves the development of new strategies to form technically interesting hybrid nanocomposites with improved mechanical properties. In particular, a new 'dissolution' preparative route was developed which incorporates silica nanoparticles (<30 nm) into a nylon-6 matrix. The procedure relies on the judicious choice of organic solvent and pH control. The synthesis involves the dissolution of nylon-6 in formic acid followed by silica particle addition (as an acidified, monodisperse sol) with stirring. Viscous solutions were prepared under cleanroom conditions and casted as thin films which are dried and vacuum treated at ~60ºC. TEM images revealed that the silica particles i.) retained their original shape and size (10-30 nm), ii.) are mono-dispersed and iii.) mainly non-agglomerated. The degree of crystallinity of the composites was determined with XRD as a function of percentage filler added. The nylon-6 phase is semi-crystalline while the silica phase is amorphous. Initial mechanical tests on the composites were conducted and showed with 1wt% silica addition, the E modulus was increased to ~2600 MPa. The increase in mechanical properties may be a result of the nanosize filler particles which has good synergy with the nylon matrix. Friction and wear properties were also investigated on a pin on disk tribometer by running a flat pin of steel against the composite disc.

INTRODUCTION

During the past decades Polyamide-6 (PA-6) has occupied a prominent place in engineering thermoplastics due to its wide spectrum of properties [1]. The mechanical properties of PA can be modified by the addition of inorganic fillers as low cost reinforcement material [2]. Fillers widely used are calcium carbonate, talc, silica and glass fiber, which play an important role in the plastics filler market [3]. The influence of these fillers on the polyamide depend strongly on their shape, particle size, distribution and surface characteristics [4]. A composite with improved properties and a low particle concentration (to preserve the good properties of pure PA) is desired . Since silica (SiO_2) is very versatile [5] and can be modified as required (different particle size, pH, morphology etc.) it is one of the most applied fillers in thermoplastic polymer composites and has been applied for automotive applications, electric engineering, electronics, appliances and consumer goods [6].
It has been established that the filler particle size and degree of dispersion have a pronounced influence on the composite properties. Increased aggregation of fillers with decreasing particle size is a commonly observed adverse effect and control of the dispersion through appropriate processing conditions remains as a major challenge [7].
The aim of the present investigation was to a) seek a general and facile room temperature synthesis strategy by which nanoscale inorganic filler particles can be well dispersed into a

polyamide matrix, b) determine stress-strain relationships and c) friction behavior. The motivation to obtain good dispersion stemmed from the observation that if any properties are to be further improved, then the distribution of the inorganic filler particles in the polymer matrix has to be as homogeneous as possible. Our procedure was based on selecting appropriate reaction conditions, particularly with regard to solvent choice and pH control. The silica dispersion remained stable due to sufficient proton adsorption that maintained a (positively) charged surface in solution. Solvent use was kept to a minimum to ensure concentrated, highly viscous solutions could be cast on clean glass surfaces followed by a combination of vacuum and heat (60-80°C) treatments to remove the solvent.

Another important application of nylon-6 is seen in the rapid growth in the use of thermoplastic as wear resistant materials to substitute metals [8]. Dry polymer-metal sliding bearings are frequently used because of the advantages for example regarding cost and easy assembly in production. By using nanoparticles (high surface area) it is expected to have even better adhesion between polymer and matrix. In addition, factors that exert influence on friction and wear characteristics of the polymer composites are also the particle size of the filler. If the particles are large and hard, they can be easily removed out of the matrix material and contribute to the wear of composites by their abrasive action and cause wear and damage of counterpart material [9]. The easy fall-out of large hard particles under tribological conditions is then avoided.

Silica nanoparticles are currently used for the enhancement of the mechanical properties in polyamide-6 [10]. In this study, the effect of the addition of nano-silica on the tribological performance and on the materials microstructure of the PA-6 was investigated as well.

EXPERIMENTAL DETAILS

Commercial polyamide-6 was used (Aldrich). The inorganic filler used was silica sol (SNOWTEX). The preparation of the polymer solution has been described elsewhere [11]. Nylon films were produced by drawing a steel knive over a pre-treated glass containing a solution of the polymer in formic acid at a rate of 1 mm min-1 using Dr Blade™ equipment. A surface treated glass with ethanol and acetone was used for a better adhesion of the polymer solution to the glass. Film thickness varied slightly due to the presence of a semicrystalline spherulitic microstructure. The composite was left overnight and a film-coating of 0.1 to 0.5 mm was formed on the glass.

Mechanical testing: All samples were prepared with compression moulding. The polymer nanocomposite was melted and given a certain shape by compression of the melt. The samples were dried in a vacuum oven at 80°C for 2 days. Plates of 1 mm thickness were moulded and the test samples were machined out of the plates. The elastic modulus was measured at a tensile speed of 1 mm/min and the displacement was measured with an extensometer with a gauge length of 10 mm. Yield stress, strain-at-yield and strain-at-break were recorded on a Zwick Z010 apparatus.

Tribological measurements: Before tribological measurements the film casted nanocomposites were compressed moulded into sheets of about 19x5.5x1 mm at 250-260°C. Compression was performed in 3 steps: 2 min at 5 MPa and , 3 min at 10 MPa and 5 min at 20MPa at 250°C. The samples were cooled at room temperature. The investigated polymers were cut into discs with diameter of ca. 40 mm and a thickness variation between 0.9 and 1.07 mm. The discs surface

roughness varies from Ra=0.5 to 1.4 μm. The roughness of the pin was Ra = 0.15 μm. Dry sliding wear tests samples were performed with a pin-on-disc tribometer (CSEM, Neuchatel, Switzerland), placed in a climate chamber (Heraeus, HC4057, Balingen, Germany) at 23ºC and 40% relative humidity. The test set-up consisted of a flat round steel pin 100McCrW4 sliding against a rotating polymer sample. The sliding velocity for the nanocomposites was set at 0.1 m/s to avoid the occurrence of a high *PV* value for nylon and of possible thermally induced fracture processes. The load used was 1 N and the mean initial contact pressure was 0.7 MPa with a pin of 1.3 mm. The resulting PV was then 75339 N/m·s The sliding distance of the tests was adapted for each specific measurement to obtain significant wear and to detect possible fatigue. Measurements for nano - composites were set at 10 km of sliding distance. The coefficient of friction was measured on-line by monitoring the ratio between the measured shear force and the applied normal force through measurement of the deflection of the pin-arm (lever) with two inductors. Wear measurements by weight lost of the samples were initially performed but preliminary results indicated that the moisture had a negative influence in the experiments with a varied weight from the sample over time. The wear track depth was measured with a micromap 512 Opto-profiler.

Instrumentation: Transmission Electron Microscopy (TEM) micrographs were obtained using a JEOL 2010F equipped with a field-emission gun operating at 200 kV. TEM samples were prepared by ultramicrotoming thin sections of the polyamide/silica nanocomposite with a diamond knife. These thin sections were then captured on Formvar coated Ni grids. The particles observed in the micrographs were unambiguously identified as silica by using both X-Ray Energy Dispersive Spectrometry (EDAX R-TEM Sapphire detector equipped with a super-ultra thin window) and Energy Filtering (Gatan Imaging Filter 2001) attached to the TEM.
Powder XRD data were collected on a Philips X'Pert-1 PW3710 diffractometer using Cu-Kα (λ=1.542 Å) radiation with a secondary curved graphite monochromator. XRD data verified the amorphous state of the silica particles (no peaks observed) while the nylon-6 was semi-crystalline.
Quantitative XRF was used to determine the amount (as wt.-%) silica present in each bulk sample. Analysis was performed on a Philips PW 1480/10 fluorometer (Eindhoven, The Netherlands). The calculation method used the program FPMulti that has been previously described [12].

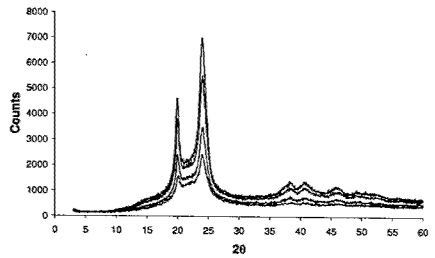


Figure 1. X-Ray diffraction of nylon-6 nanocomposites

RESULTS AND DISCUSSION

Dispersion and mechanical tests

The crystallinity of the formed composites was followed with X-Ray diffraction (XRD) as a function of percentage filler added. The XRD data of a composite containing variable amounts of silica filler percentage is shown in Figure 1. It was observed that the nylon-6 component was semi-crystalline while the silica phase was, with no discernable peaks, amorphous.

For the TEM investigation the sample was microtomed to a thickness (~80 nm) where the silica particles showed good visual contrast with the polymer matrix. Two TEM pictures taken from different sample localities revealed an even distribution of the silica particles throughout the matrix. The TEM micrographs clearly indicated several unique properties of the composite resulting from the improved synthesis method, namely a) silica particles were all in the 10-30 nm size range, b) silica particles were non-agglomerated and c) silica particles were well dispersed (good homogeneity) inside the polyamide matrix. Scheme 1 shows the TEM pictures of a 3wt% sample. We chose filler additions in the range 1-5 mol% because it was evident from current methods that a maximum of 5 mol% filler loadings already leads to optimum mechanical properties [2].

The main difficulty of this technique lies in removing the solvent from the films. This is avoided by treatment of the films in a very high vacuumoven 10^{-7} Mbar. SEM

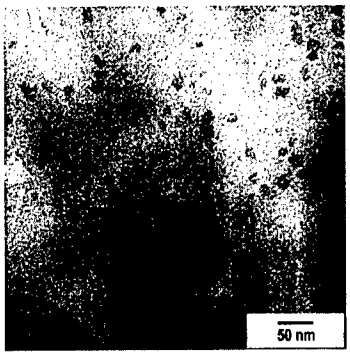


Figure 2. Silica homogeneously dispersed

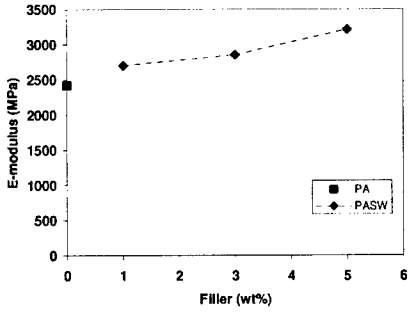


Figure 3. Variation in the elastic modulus for composites with different filler percentages. PA = polyamide (nylon-6), PASW = polyamide with silica (10 – 30 nm) in water media.

Wt% silica	Friction coefficient	Wear rate [mm^3/Nm]
0	0.45	5.29×10^{-5}
2	0.20	2.0×10^{-7}
14	0.40	2.81×10^{-5}

Table I. Wear rate and coefficients of friction of PA6 (C) nanocomposites . Velocity = 0.1 m/s Load=1N, Distance of sliding 10 km.

pictures have also shown the presence of voids in the films. However, if the resulting material is dense, Gardnes impact tests (falling ball impact) could be useful to do the measurements on these films.

The elastic modulus for composites with different filler percentages as tested with an extensometer is shown in Fig. 3. Already with 1 wt.-% silica addition, an increase in E-modulus could be observed; an E-modulus increase for 3 and 5 wt.-% loadings was sustained. Data points represent the average value after four tests for each sample.

Tribology

Table I gives the coefficient of friction and wear rate for PA-6 and its composites while sliding occurred against the steel counterface. The coefficient of friction of 2wt% of SiO_2 filled composite is lower than that of unfilled PA6. For addition of 14wt% of SiO_2, the coefficient of friction value was slightly lower than that of unfilled PA6 after few kilometres of wear track. The filler thus contributed to the reduction in wear rate of PA6 where 2wt% of silica were more effective in reducing the wear rate and was more effective in reducing the coefficient of friction as well.

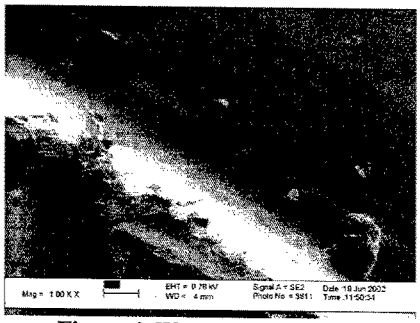


Figure 4. Wear track of 2wt%-silica/PA-6 nanocomposite.

CONCLUSIONS

The synthesis method described can be generally applied to all classes of polyamide-based composites that are susceptible to solvent dissolution. Inorganic filler material can be readily incorporated into the polymer matrix resulting in a hybrid nanocomposite with unprecedented control in particle size, mono-dispersity and homogeneity. An increase in E-modulus as a function of filler percentage added (0-5 wt.-%), a small decrease in yield strength (improvement in impact toughness) and a strain-at-break of >0.5 were obtained.
Furthermore, the addition of nano-silica to the PA-6 led to a lowering of the coefficient of friction and the wear resistance was improved. The minimun wear rate between the samples was obtained with 2wt% of filler addition.

ACKNOWLEDGMENTS

The authors would like to thank B.A.G. Schrauwen for the performance of the mechanical tests B. J. Kooi and J.T. De Hosson for the TEM pictures, H. Koster for the XRD measurements and L. Vrielink for the XRF characterization. This research is supported by the *Netherlands Organisation for Scientific Research* (NWO-PPM).

REFERENCES

1. M. I. Kohan, Nylon, Plastics Handbook. Hanser. New York. (1995)
2. F, Yang, Y. Ou, Z. Yu, *J. Appl. Polym. Sc.* **69**, 355-361 (1998).
3. S. Nago, S. Nakamura, andY. Mizutani, *J. Appl. Polym. Sc.* **45**, 1527 (1992).
4. M. Sumita, T. Shizuma, K. Miyasaka, and K. Ishikawa, *J. Macromol. Sci. Phys.* **B22** (4), 601-618 (1983).
5. M.A. Brook, Silicon in Organic, Organometallic, and Polymer Chemistry ; (John Wiley & Sons 2000).
6. R. Rothon, Particulate-filled Polymer Composites. Essex (Longman 1995).
7. E. Reynaud, C. Gauthier, and J. Perez, *La Revue de Métallurgie-CIT/Science et Génie de Matér.*169-176 (1999).
8. S. Hironaka, *Jpn. J. Tribol.* **42**, 8, 931-939 (1997).
9. J.M. Thorp, *Tribol. Int.* **15**, 59-68 (1982).
10. E. Reynaud, T. Jouen, C. Gauthier, G. Vigier, and J. Varlet, *Polymer* **42**, 8759-8768 (2001).
11. W.E. van Zyl, M. García, B.A.G. Schrauwen, B.J. Kooi, J.T. De Hosson, and H. Verweij, *Macromol. Mater. Eng.* **287**, 106-109 (2002).
12. M.H.J. Bekkers, and H.A. van Sprang, *X-Ray Spectrom.* 26, 122 (1997).

Fracture and Mechanical Properties II

Mat. Res. Soc. Symp. Proc. Vol. 740 © 2003 Materials Research Society

Plasticity in Nanomaterials

Guo-Dong Zhan, Joshua D. Kuntz, Julin Wan, and Amiya K. Mukherjee
Department of Chemical Engineering and Materials Science
University of California, One Shields Avenue, Davis, CA 95616

ABSTRACT

There have been many predictions of the reinforcing effects of carbon nanotubes in various composite matrices but large improvements in properties have not yet been convincingly demonstrated. In the present study, we have successfully realized this possibility in reinforcing nanocrystalline alumina. Fully dense single-wall carbon nanotubes (SWCN)/Al_2O_3 nanocomposites with nanocrystalline alumina matrix have been fabricated at sintering temperatures as low as 1150°C by spark-plasma-sintering (SPS). A fracture toughness of 9.7 $MPam^{1/2}$, nearly three times that of pure nanocrystalline alumina, has been achieved in the 10 vol.% SWCN/Al_2O_3 nanocomposite. Moreover, high-strain-rate superplasticity has been achieved in $Al_2O_3/ZrO_2/MgAl_2O_4$ nanocomposite with truly nanocrystalline grain size of 100 nm. Compression superplastic tests were conducted in the temperature range of 1300-1450°C at strain rates 10^{-3}-10^{-1} s^{-1}. The results generated a stress exponent of ~ 2 and an activation energy of ~ 620 kJ/mol.

INTRODUCTION

The fabrication of nanocrystalline materials is an exciting area of materials research because such bulk materials with grain sizes less than 100 nm exhibit novel properties as compared with their microcrystalline counterparts, such as optical transparency and enhanced superplasticity. However, the brittleness of nanocrystalline ceramics has limited their potential and promise for use in structural applications. Carbon nanotubes, especially single-wall carbon nanotubes (SWCN), should be ideal reinforcing fibers for composites [1]. Theoretical and experimental studies [2,3] showed that carbon nanotubes with very high aspect ratios (length-to-diameter ratio of 1,000 or more) have exceptional mechanical characteristics. SWCN are among the stiffest fibers known, with a measured Young's modulus of ~1.5 TPa [4]. However, to date, the utilization of the extraordinary mechanical properties of carbon nanotubes in composites has not been successfully realized, e.g., in alumina based systems only a 24% increase in toughness has been obtained so far. In the present study, we have successfully realized the potential of carbon nanotubes in significantly reinforcing ceramics for the first time.

Superplasticity is another exciting area for nanocrystalline ceramic materials. High strain rate superplasticity (HSRS) is usually referred to as the demonstration of high ductility at strain rates around 10^{-2} s^{-1} or greater [5,6] . HSRS used to be a phenomenon found exclusively in fine-grained metals and metal matrix composites. For ceramics, the typical superplastic strain rate is in the range of 10^{-5}-10^{-4} s^{-1}. Ceramic HSRS was not observed until very recently [7,8]. Kim et al. [7] reported a composite ceramic material consisting of tetragonal ZrO_2, $MgAl_2O_4$ and α-Al_2O_3 phases that exhibit superplasticity at strain rates up to 1 s^{-1} at 1650°C. While scientifically significant, these results are not of practical importance due to the prohibitively high forming temperature. Additionally, these results did not provide any phenomenological data to account for a deformation mechanism. In the present work, we strive to bring the HSRS deformation

temperature for this triphasic ceramic to 1350°C or lower. Tests were also conducted to establish the strain-rate sensitivity and activation energy of the deformation process, which are two of the three primary characteristic rate parameters required for further modeling of the deformation phenomenon.

EXPERIMENTAL

The alumina powder used in the alumina-SWCN composites, consisting of 80% α-Al_2O_3 and 20% γ-Al_2O_3 with particle sizes of 300 nm (40 nm crystallite size) and 20 nm respectively, was obtained from Baikowski International Corporation (Charlotte, NC 28273). Purified single-wall carbon nanotubes (also called Buckytubes) were obtained from Carbon Nanotechnologies Incorporated (Houston, TX 77084). The SWCN were produced by the HiPco process [9,10] . Two compositions, containing SWCN at 5.7 vol.% and 10 vol.%, were produced. For the superplasticity investigation, the material is targeted the same overall phase composition as reported by Kim et al.: 30 vol.%Al_2O_3, 40 vol.%ZrO_2 and 30 vol.%$MgAl_2O_4$. The starting materials were commercially available nano-sized powders: γ-Al_2O_3 (Nanotechnologies, Austin, TX), with 15 nm particle size; tetragonal ZrO_2 stabilized by 3 mol.% Y_2O_3 (Tosoh, Tokyo, Japan), with 24 nm particle size; MgO (Nanopowder Enterprise Inc., Piscataway, NJ), with 40 nm particle size. The powders were mixed by ball milling for 24 hours using zirconia media in ethanol. The mixed powder is pressed into a 19mm diameter graphite die and sintered with Dr. Sinter® 1050 spark plasma sintering system (Sumitomo Coal Mining Company, Ltd.) under vacuum. After applying the given pressure (63MPa), samples were heated to desired temperatures and held for a few minutes before turning off the power.

The final densities of the sintered compacts were determined by the Archimedes' method. Microstructural observation was carried out using high-resolution scanning electron microscope (SEM). Grain sizes were estimated from XRD and SEM analysis. Additional characterization by analytical electron microscopy and high-resolution transmission electron microscopy (HRTEM) was performed on a Philips CM-200. Indentation tests were performed on a Wilson Tukon hardness tester with a diamond Vickers indenter. The indentation parameters for fracture toughness (K_{IC}) and hardness measurements were a 2.5 Kg load with a dwell of 15 seconds. The fracture toughness was calculated by Antis equation [11].

In the superplasticity investigation, samples with dimensions 5 mm ×3 mm ×3 mm were machined from the sintered material, and subjected to compression tests on a computer-interfaced hydraulic testing machine. Computer control was used to run constant strain-rate tests and step strain-rate tests. The tests were performed in air; in the temperature range of 1300 - 1450°C and strain-rate range 10^{-3}-10^{-1} s^{-1}. Constant strain rate testing was realized by adjusting (decreasing) the crosshead speed in accordance with the instantaneous height of the specimen. These tests were terminated once a pre-set strain was reached. Step-strain rate tests were also conducted in constant strain-rate mode for each segment of the deformation, while the strain-rate was increased to the next higher rate when the strain reached 0.1 at each designated strain rate.

RESULTS AND DISCUSSION

Single-Walled Carbon Nanotubes Toughening

The processing conditions, physical and mechanical properties for pure alumina and nanocomposites are shown in Table I. The pure alumina nanopowders can be consolidated by SPS at 1150°C for 3 minutes to get full density. The microstructure of the pure Al_2O_3 consisted of equiaxed grains with an average value of 349 nm. Measured Vickers hardness and fracture toughness are 20.3 GPa and 3.3 $MPam^{1/2}$, respectively. Note that both 5.7 vol.% SWCN/Al_2O_3 and 10 vol.% SWCN/Al_2O_3 nanocomposites can also be successfully consolidated to their theoretical densities at the same sintering conditions as that for pure alumina, suggesting that the addition of SWCN to the alumina matrix was not detrimental to the sintering process. XRD analysis of the consolidated specimens reveals that the γ-Al_2O_3 has been transformed to α-Al_2O_3 in both the pure alumina and the composites. Most of the alumina grains were in the nanocrystalline range, around 200 nm. It is interesting to note that the introduction of carbon nanotubes leads to refinement of grain size. This refinement is consistent with observations by Laurent et al. [12]. The fracture toughness of the 5.7 vol.% SWCN/Al_2O_3 nanocomposite is over two times higher than that of pure alumina and there is almost no decrease in hardness. A toughness of nearly three times pure alumina was achieved in the 10 vol.% SWCN/Al_2O_3 nanocomposite when sintered under the same conditions. In the open literature [13,14], all the other carbon nanotubes reinforced ceramic composites have been consolidated by hot-pressing methods that require higher temperatures and longer duration than SPS. These sintering parameters must damage the carbon nanotubes in the composites, leading to decreases or total loss in reinforcing effects.

Table I. Processing conditions and the resultant properties of SWCN reinforced nanocrystalline alumina nanocomposites consolidated by spark-plasma-sintering

Materials	Processing conditions	Relative density (%TD)	Grain size (nm)	H_V (GPa)	K_{IC} ($MPam^{1/2}$)
Al_2O_3	SPS 1150°C/3 min.	100	349	20.3	3.3
5.7 vol.% SWCN/Al_2O_3	SPS 1150°C/3 min.	100	~200	20.0	7.9
10 vol.% SWCN/Al_2O_3	SPS 1150°C/3 min.	100	~200	16.1	9.7

Figure 1 shows the dependence of toughness on carbon nanotube content in the alumina nanocomposites. No reinforcing effect was noted in the *in-situ* carbon nanotubes-Fe-Al_2O_3 nanocomposites although the fracture toughness is similar to that of alumina. Moreover, only a marginal increase in fracture toughness can be obtained even by improving the quality and quantity of carbon nanotubes in the latter work [15] . The reasons given were mainly related to the damage of carbon nanotubes during hot-pressing. Also noted was the fact that volume contents of carbon nanotubes in the sintered products are lower than those in the starting powders. So far, the best reported result by Siegel et al. [13] was a 24% increase in toughness in 10 vol.% MWCN/Al_2O_3 nanocomposite. However, it can be seen that fracture toughness increases significantly with the introduction of single-wall carbon nanotubes for the present nanocomposites. The 10 vol.% SWCN/Al_2O_3 nanocomposite is nearly three times as tough as pure nanocrystalline alumina. To date, it is the best result achieved.

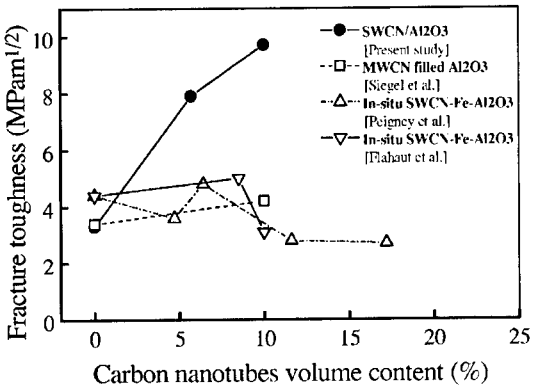


Figure 1. Fracture toughness versus carbon nanotube volume content in alumina based composites as reported in literature

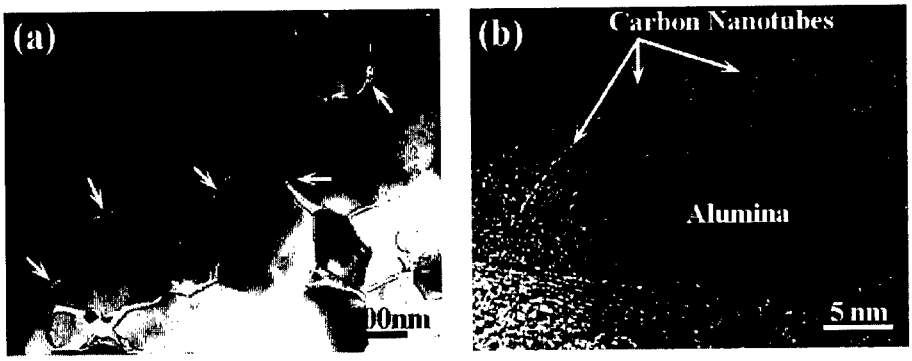


Figure 2. TEM Micrographs of 5.7 vol.% SWCN/Al_2O_3 nanocomposite. (a) Bright-field TEM image and (b) high-resolution TEM image of specimens in the fully dense 5.7 vol.% SWCN/Al_2O_3 nanocomposite. The arrows indicate the SWCN phase.

Figure 2a shows a typical bright field TEM image of the 5.7 vol.% SWCN/Al_2O_3 nanocomposite. It is interesting to note that carbon nanotubes were distributed along grain boundaries to develop a network microstructure. It can be seen that some of carbon nanotubes were entangled with alumina grains and some of them encapsulated alumina nano-scale grains. Intimate contact between carbon nanotubes and alumina was observed in this material, as shown in Figure 2b. XDS profile and spot scans were performed to analyze the chemical composition of the different grains, grain boundaries, and particles in the samples. The interface condition and bonding between the SWCN ropes and the alumina matrix are part of our ongoing study. The present results suggest that the extent of interfacial bonding might be a factor in increasing the toughness of the composites.

High Strain Rate Superplasticity

The microstructure of the as-sintered material is shown in Fig. 3. The material reached 4.63 g/cm^3 (100% theoretical density) after sintering for 3 minutes at 1150°C. XRD results identified the phases as t-ZrO_2, α-Al_2O_3 and $MgAl_2O_4$. The mean grain size is about 100 nm, about half the size of the material reported by Kim et al. [7]. The deformed sample shows larger grain size as compared to the original microstructure. The grain growth, however, has been determined to be mainly due to the time at temperature and not due to the deformation process. Stress-strain results indicate that at lower strain rates, the material undergoes moderate strain hardening (increasing of stress with strain); at intermediate rates, the flow stress remains relatively constant during deformation. At high strain-rates, there is an apparent strain softening (decreasing stress with increasing strain). The strain-hardening effect can be attributed to concurrent grain growth during superplastic deformation and was observed in the high temperature/low strain rate combinations. Strain softening, as established for metallic materials, is most likely to be caused by dynamic re-crystallization, and occurs in the low temperature/high strain rate combinations. In tensile tests, it has also been associated with cavitation. Constant stress deformation at a function of strain can be reached when these two effects balance each other, thus it is observed at intermediate strain rates.

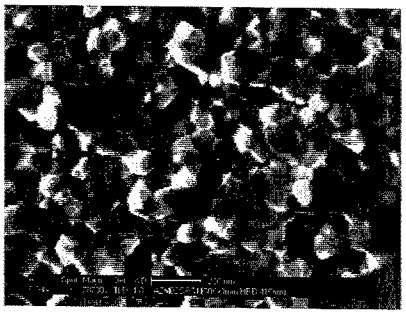


Figure 3. SEM image of fractured surface of SPS-derived $Al_2O_3/ZrO_2/MgAl_2O_4$ nanocomposite

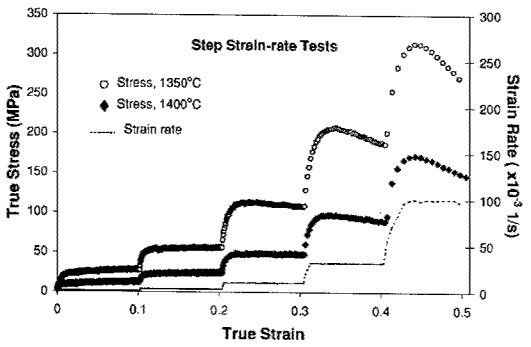


Figure 4. Typical stress-strain curves in the step strain-rate tests

With increasing strain-rate, the trend of shifting from strain hardening to softening can be observed. It is also noticed that this occurs at a higher strain rate if the deformation temperature is higher. The stress-strain rate dependence as measured with step strain rate tests as in Fig. 4 were plotted into double logarithmic charts as in Fig. 5. The slope of the data gives the values of strain rate sensitivity, m. The superplastic deformation of the present material gives a very consistent m value of about 0.55. The constitutive relation for superplastic deformation can be expressed in the form of Mukherjee-Bird-Dorn equation

$$\dot{\varepsilon} = A\frac{D_0 Gb}{kT}\left(\frac{b}{d}\right)^p\left(\frac{\sigma}{G}\right)^n \exp(-Q/RT) \qquad (1)$$

in which G is the elastic modulus, b is the Burgers' vector, k is Boltzmann's constant, T is the absolute temperature, d is the grain size, p is the grain-size dependence coefficient, n is the stress exponent, Q is the activation energy for diffusion, D_0 is a constant and R is the gas constant. The inverse of strain rate sensitivity, m, gives the value of n. The experimentally determined stress dependence of the strain rate n is equal to 2 for this material. This observation narrows the deformation mechanism to two possible choices: (1) Grain boundary sliding accommodated by diffusion, where the interface reaction at grain boundaries controls the deformation rate, as described by Artz-Ashby-Verrall model; (2) Grain boundary sliding accommodated by climbing of lead dislocation in pile-ups in individual grains (Mukherjee model) or in a group of grains (Ball-Hutchison model). The discrimination between these two types of deformation mechanisms requires the determination of other characteristic parameters, namely activation energy Q and grain size dependence p. It is also noticeable in Fig. 5, that for lower temperatures the stress-strain rate curves deviate from the $m = 0.55$ ($n \approx 2$) regime at the high strain-rate end and takes a lower value of strain rate sensitivity. In metals this phenomenon is frequently encountered and is attributable to the transition of mechanism from grain boundary sliding controlled superplasticity to dislocation-climb controlled power-law creep, which has a typical n value of 3-5. In ceramics, the observation of this phenomenon is very rare. In contrast the n value in ceramics, e.g., alumina and zirconia, was found to shift from 2 to 1 as stress and strain rate approach higher values [16,17]. It will be important to find out the reason for this behavior in the present material and this is the subject of continuing research in our laboratory.

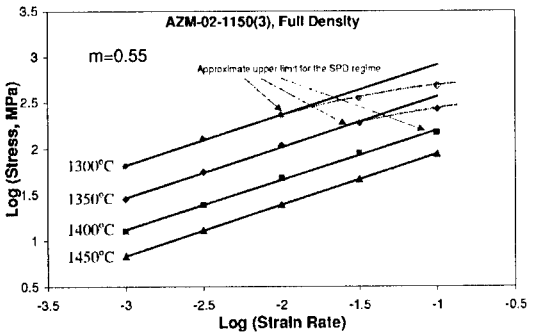


Figure 5. Stress-strain rate relationship, determination of strain rate sensitivity

The dependence of strain rate on temperature at different stress levels (these stress levels were chosen to make sure the deformation is in the m=0.55 superplastic regime) is given in Fig. 6. The activation energy for the superplastic deformation of the $Al_2O_3/ZrO_2/MgAl_2O_4$ composite gives a consistent value of 620 kJ/mol. However, the effort to interpret this activation energy encounters difficulty, mainly owing to the wide scatter of data in the literature concerning the component phases for this material. For instance, for yttria-stabilized zirconia alone, the activation energy for superplastic deformation ranges from 360 to 660 kJ/mol [18]. While in the meantime the activation energy for lattice diffusion of the slower moving cations are 391kJ/mol for Zr^{4+} and 423kJ/mol for Y^{3+}. The grain boundary diffusion activation energy takes values of 309kJ/mol and 293kJ/mol for Zr^{4+} and Y^{3+}, respectively [19]. These values provide poor correlation between phenomenology of superplastic tests and basic diffusion processes. Similar controversies exist for the other two components, alumina, and spinel. More effort on sieving out the literature data, in terms of the differences in purity content, processing route, testing technique as well as microstructural evolution, needs to be conducted. In order to understand the deformation mechanisms in truly nanocrystalline nanocomposites, ongoing investigation to establish the parameter p, the grain size dependence of strain rate, and identify the possible dislocation activities in the deformed samples, is currently underway.

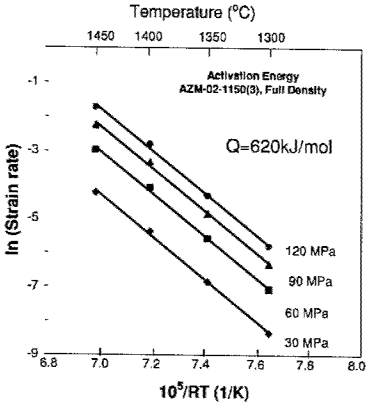


Figure 6. Temperature dependence of strain rate and constant stress.

CONCLUSIONS

(1) This study for the first time demonstrates that ropes of single-wall carbon nanotubes are attractive materials for reinforcement of nanoceramics. The spark-plasma-sintering technique has been found to be a very effective processing method for consolidation of carbon nanotubes composites without accumulating damage. A fracture toughness of 9.7 $MPam^{1/2}$, nearly three times that of pure nanocrystalline alumina, has been achieved in the 10 vol.% $SWCN/Al_2O_3$ nanocomposite. The effective bonding of the SWCN ropes with the matrix plays a central role in the reinforcing effect.

(2) The nanocrystalline $Al_2O_3/ZrO_2/MgAl_2O_4$ ceramic nanocomposite exhibits high-strain-rate superplasticity up to 10^{-1} s^{-1} as low as 1400°C with strain rate sensitivity of 0.55 and activation energy of 620 kJ/mol. These results suggest that grain boundary sliding is the likely mechanism for superplasticity in this nanocomposite.

ACKNOWLEDGEMENTS

This investigation was supported in part by a grant (#G-DAAD 19-00-1-0185) from U.S. Army Research Office with Dr. William Mullins as the Program Manager and in part by the Office of Naval Research grant number N00014-01-C-0370 under contract to Rutgers University. TEM images were obtained at the National Center for Electron Microscopy (NCEM) at the Lawrence Berkeley Laboratory.

REFERENCES

1. G.-D. Zhan, J. D. Kuntz, J Wan, and A. K. Mukherjee, *Nature Materials*, **2**, 38, 2003.
2. P. Calvert, *Nature*, **357**, 365 (1992).
3. S. Subramooney, *Adv. Mater.* **15**, 1157 (1998).
4. M-F. Yu, B. S. Files, S. Arepalli, and R. S. Ruoff, *Phys. Rev. Lett.* **84**, 5552 (2000).
5. O.D. Sherby, T. G. Nieh and J. Wadsworth, *Mater. Sci. Forum*, **243-245,** 11 (1997).
6. T. G. Langdon, *Mater. Sci. Forum*, **304-306,** 13 (1999).
7. B. N. Kim, K. Hiraga, K. Morita and Y. Sakka, *Nature*, **413,** 288 (2001).
8. K. Morita, K. Hiraga, and Y. Sakka, *J. Am.Ceram. Soc.*, **85,** 1900 (2002).
9. M. J. Bronikowski, P. A. Willis, D. T. Colbert, K. A. Smith, and R. E. Smalley, *J. Vac. Sci. Technol.* **19**, 1800 (2001).
10. P. Nikolaev, et al. *Chem. Phys. Lett.* **313**, 91 (1999).
11. G. R. Antis, P. Chantikul, B. R. Lawn, and D. B. Marshall, *J. Am. Ceram. Soc.*, **64**, 533 (1981).
12. Ch. Laurent, A. Peigney, O. Dumortier, and A. Rousset, *J. Euro. Ceram. Soc.* **18**, 2005 (1998).
13. R. Z. Ma, J. Wu, B. Q. Wei, J. Liang, and D. H. Wu, *J. Mater. Sci.* **33**, 5243 (1998).
14. R. W. Siegel, et al. *Scripta Mater.* **44**, 2061 (2001).
15. E. Flahaut, et al. *Acta Mater.* **48**, 3803 (2000).
16. R. M. Cannon, W. H. Rhodes and A. H. Heuer, *J. Am. Ceram. Soc.*, **63,** 46 (1980).
17. L. Clarisse, R. Baddi, A. Baille, J. Crampon, R. Duclos and J. Vicens, *Acta mater.*, **45,** 3843 (1997).
18. M. Gust, G. Goo, J. Wolfenstine and M. L. Mecartney, *J. Am. Ceram. Soc.*, **76,** 1681 (1993).
19. Y. Oishi, K. Ando, and Y. Sakka, in *Advanced Ceramics, **Vol.7**, Additives and Interfaces in Electronic Ceramics.* Edited by M. F. Yan and A. H. Heuer. American Ceramic Society, Columbus, OH, pg. 208 (1993).

Correspondence and requests for materials should be addressed to A. K. Mukherjee.
akmukherjee@ucdavis.edu

Mat. Res. Soc. Symp. Proc. Vol. 740 © 2003 Materials Research Society

Microstructures and Mechanical Properties of Nanostructured Copper-304 Stainless Steel Multilayers Synthesized by Magnetron Sputtering

X. Zhang, A. Misra, H. Wang, H. Kung, J. D. Embury, R. G. Hoagland and M. Nastasi
Materials Science and Technology Division, Mail Stop G755, Los Alamos National Laboratory, Los Alamos, NM 87545

Abstract

Nanostructured Cu/304 stainless steel (SS) multilayers were prepared by magnetron sputtering at room temperature. 304SS has a face-centered cubic (fcc) structure in bulk. However, in the Cu/304SS multilayers, the SS layers exhibited fcc structure for layer thickness of less than or equal to 5 nm. For 304SS layer thickness larger than 5nm, bcc 304SS grains were observed to grow on top of the initial ≈ 5 nm of fcc SS. The maximum hardness of Cu/304SS multilayers was ≈ 5.5 GPa (factor of two enhancement compared to rule of mixtures hardness) achieved at a layer thickness of 5nm, with a decrease in hardness with decreasing layer thickness below 5 nm. The hardness of fcc/fcc Cu/304SS multilayers (layer thickness ≤ 5 nm) is compared with Cu/Ni, another fcc/fcc system, to gain insight on how the mismatch in physical properties such as lattice parameters and shear moduli of the constituent layers affect the peak hardness achieved in these nanoscale systems.

Introduction

Nanostructured multilayers are made up of alternating nanometer scale layers of two different materials. The layer thickness can be well controlled in the scale of 1nm or less by physical vapor deposition (PVD). These nanostructured multilayers have novel mechanical, electrical, magnetic, and optical properties [1-3]. The mechanical properties of these multilayered composites are of particular interest since the strength of these multilayer composites can be significantly increased to about 1/3 of the theoretical strength limit [4]. In the μm to the sub-μm length scale regime, the strengthening in these multilayers can be explained by the Hall-Petch model of dislocation pile-ups at interfaces or grain boundaries. The yield strength, σ_y, is proportional to $h^{-1/2}$, where h is the layer thickness [5,6]. Hall-Petch slope is a measure of the strength of interface barrier for dislocation pile-ups and determines the rate of strength increase with decreasing h. However, in the tens of nanometers regime the Hall-Petch model breaks down [1]. The deformation mechanism may involve glide of single dislocations, in the form of Orowan loops, leading to $\sigma_y \propto \ln(h)/h$ relation [4,7]. In the limit of a few nanometers, the strength of the multilayer may be determined by the stress to transmit a single dislocation across the interfaces. Factors such as shear modulus mismatch and lattice parameter mismatch may determine the transmission stress for single dislocations. For multilayers with a large difference between shear modulus, dislocations in the low shear modulus phase need to overcome a high repulsive stress (Koehler stress) to enter the high modulus phase [8]. Furthermore, coherency stresses within the thin lattice matched multilayers may alternate from tensile to compressive in adjacent layers, and results in an additional barrier for single dislocation transmission across interfaces [9, 10]. The magnitude of coherency stress increases with increasing lattice parameter mismatch. When the interfaces are semi-coherent, the spacing of the misfit dislocations at the interface reduces with increasing lattice parameter mismatch. In some systems, a drop in strength, or softening, is observed [1, 11-13] when the layer thickness is below a few nanometers. The mechanisms for this softening, however, are not well understood.

In this paper, we report the studies on microstructures and mechanical properties of Cu/304SS multilayers. It is previously known that the Cu/304SS multilayers have fcc/bcc structure for a layer thickness larger than 5 nm, while they have fcc/fcc structure for a layer thickness less than 5 nm [14]. At layer thickness of less than 5nm, a reasonable comparison can be made between Cu/304SS and Cu/Ni multilayers to understand the effects of lattice parameter mismatch on the peak hardness. A comparison of mutual solubility, interface misfit and Young's modulus mismatch between Cu/304SS and Cu/Ni (single crystal with cube on cube orientation) is listed in Table 1.

Table 1. A comparison of Cu/304SS ($h \leq 5$ nm) with Cu/Ni multilayer system.

Materials	Mutual solubility	Crystal structure	Lattice parameter mismatch*	E_X/E_{Cu} **
Cu/Ni [11]	completely miscible	fcc/fcc	2.63%	1.99
Cu/304SS	major elements immiscible with Cu^	fcc/fcc	0.48% (fcc SS)	1.82

^ Cu may have limited solubility in fcc SS [15]
* For fcc/fcc systems, % misfit between interplanar spacing of {100}.
** E_{Cu} is the average Young's modulus of polycrystalline Cu and E_X is the average Young's modulus of the other phases. For Cu, Ni, the ratio of the Young's modulus in (100) orientation is calculated.

Experimental

Cu/304SS multilayers were DC sputter deposited at room temperature on Si (100) substrates that have a native SiO_2 layer. The chamber was evacuated to a base pressure of $\leq 5 \times 10^{-8}$ torr prior to deposition. Ar pressures of 5 mtorr and 4mtorr were used for the deposition of 304SS and Cu respectively. Sputtering power of 200W and 100W for 3.95 inch diameter targets were used for the deposition of 304SS and Cu respectively. In all multilayered composites, 304SS was always deposited as the first layer on Si substrate. The thickness of the constituent layers within the multilayers was varied from 1 to 500 nm, and the total number of bilayers deposited was such that the total multilayer film thickness was ≈ 2 μm. Transmission electron microscopy (TEM) was performed on a Philips CM30 microscope at 300kV. The hardness and indentation modulus of the multilayers and 2 μm single layered Cu and 304SS films were measured using an indentation load-depth sensing apparatus, commercially available as Nano Indentor II. Continuous stiffness technique was used for nano-indentation with a displacement rate of 2 nm/s. The nominal indentation depth was 250 nm.

Results and Discussions

Microstructures of Cu/304SS multilayers are studied systematically for all layer thickness with TEM. Selected examples are given in the sequence of increasing layer thickness beginning with the smallest layer thickness of 1nm. Fig. 1 shows that Cu/304SS multilayers with 1 nm layer thickness exhibits a sharp interface between each layer. Columnar grain size, on the average of 33 nm, within each layer is much greater than the layer thickness. The corresponding selected area diffraction pattern (inset in Fig. 1) shows a weak {111} fiber texture for the 304SS

and Cu layers. The lattice parameter of fcc Cu is 0.3615 nm, while it is 0.3591 nm for fcc 304SS. Therefore it is difficult to separate the diffraction rings from these two layers in electron diffraction.

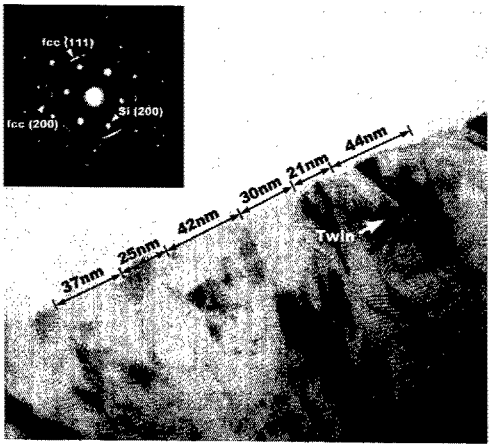


Fig. 1. Cross section TEM micrograph of Cu/304 SS multilayers with an equal layer thickness of 1nm and the corresponding selected area diffraction pattern.

Cu/304SS multilayers with layer thickness ≤ 5nm also exhibited fcc structures in both layers. At layer thickness ≥ 10 nm (Fig. 2), additional diffraction rings corresponding to bcc 304SS (lattice parameter = 0.2866 nm) were also observed. Dark field TEM, not shown here, revealed that the initial ≈ 5 nm thick 304SS from the Cu/304SS interface was fcc and then bcc 304SS grains grew on top of the fcc grains. Thus, higher layer thickness multilayers exhibited predominantly bcc grains (as shown in Fig. 3 for Cu/304SS 100 nm sample) with the much smaller fcc grains confined to the interfacial region. The formation of bcc 304SS is nevertheless a surprising result since 304 austenitic SS has 8-10 % Ni to stabilize the fcc austenite phase.

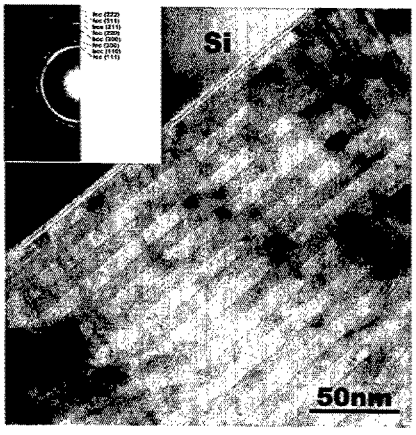


Fig. 2. Bright field TEM micrograph of Cu/304SS multilayers with a layer thickness of 10nm. Compared to Fig. 1, the diffraction pattern shows additional rings from the bcc structure of 304SS.

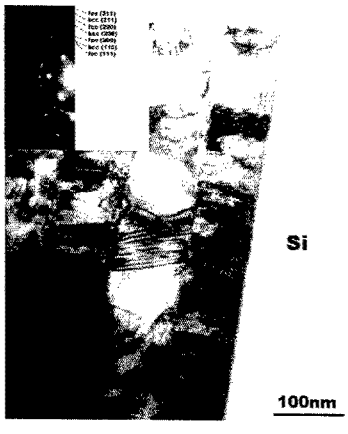


Fig. 3 Bright field TEM micrograph showing the cross section of Cu/304SS multilayers with 100 nm layer thickness. Diffraction pattern (similar to Fig. 2) shows a mixture of bcc and fcc 304SS phases, along with fcc Cu.

The formation of metastable bcc 304SS thin film is proposed to be due to the rapid vapor quenching achieved in the sputtering process [16]. It is speculated that the fcc structure in sputtered 304SS thin films can only be stabilized by epitaxial growth on fcc Cu underlayer [14]. However, we have observed fcc structure in the first few nanometers of the 304SS thin film sputter deposited on other non-fcc substrates as well, e.g., Si with native oxide. It is possible that dc magnetron sputtering of an alloy target that contains primarily Fe, Ni and Cr may not result in a film with identical composition to the target. For 304SS, even a small drop in the Ni to Fe ratio with increasing thickness may lead to the stabilization of the bcc structure. We are investigating this in more detail using Auger depth profiling of the film composition as well as sputtering other austenitic stainless steels that have higher Ni concentration to see what structures are obtained in the thin films, and will report the findings in a separate article later.

The hardness of Cu/304SS and Cu/Ni multilayers are plotted as a function of $h^{-1/2}$ (Hall-Petch plot) in Fig. 4, where h is the layer thickness. Hardness of Cu/304SS multilayers increased almost linearly with $h^{-1/2}$ for $h \geq 100$nm, consistent with the Hall-Petch model. This linear relationship is deviated at smaller layer thickness. A maximum hardness of around 5.5 GPa is reached at h = 5nm. For lower h, hardness drops with decreasing layer thickness, reducing to around 4.7 GPa at h = 1nm. The dashed line corresponding to a hardness value of 2.95 GPa represents the rule of mixtures (ROM) values, i.e., average of the hardness of single layered Cu and 304SS films. Therefore, the maximum hardness of multilayers is around a factor of 2 higher than the ROM hardness. Since 304SS has a mixture of bcc and fcc phases at layer thickness larger than 5nm, a demarcation line is drawn in Fig. 4 to separate the plot into two regimes. The first regime, h > 5nm, consists of a mixture of fcc and bcc 304SS phases, while in the second regime, $h \leq 5$nm, 304SS has fcc phase.

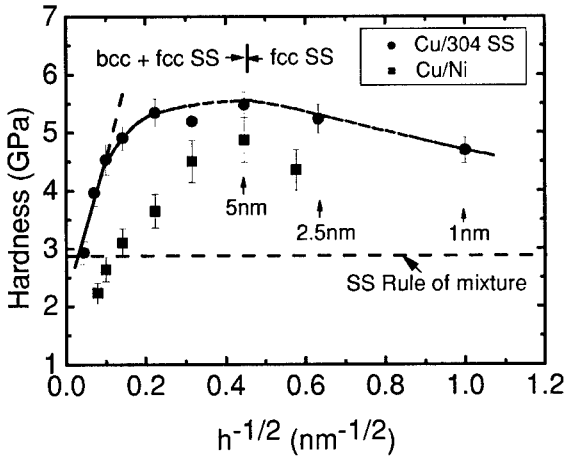


Fig. 4. Hardness of Cu/304SS and Cu/Ni multilayers as a function of $h^{-1/2}$ (h stands for layer thickness). The horizontal dashed line indicates the hardness of Cu/304SS according to the rule of mixtures.

A comparison of mechanical properties of Cu/304SS with previously studied Cu/Ni is listed in table 2, for h $\leq$5nm. The ratio of the maximum yield strength, σ_{max} (estimated as 1/3 of the maximum hardness), to the rule of mixture strength, σ_{rom}, is higher for Cu/304SS as compared to Cu/Ni. Cu/Ni multilayer is expected to be stronger than Cu/304 SS primarily due to a factor of about 5 times larger lattice parameter mismatch. One difference between the two systems that may affect the stress state at the interface is the mutual solubility. Cu and Ni are completely miscible, while Cu and major elements (Fe, Cr) in 304SS are almost immiscible. Therefore the interface between Cu and 304SS could be chemically sharper compared with Cu/Ni. It has been shown that intermixing at the interface over a few monolayers may reduce the interface barrier stress for slip transmission [17]. Another factor that should be taken into account is the crystallinity of the multilayers. Cu/Ni data in Table 2 is for single crystal multilayers with cube-on-cube orientation, while Cu/304SS multilayers were polycrystalline with <111> texture. For coherent Cu-Ni multilayers, MD simulations have shown that the interface barrier stress is higher for {111} twin interfaces than {001} interfaces [10]. A comparison between epitaxial single crystalline Cu/SS304 with Cu/Ni, both with (100) orientation, shall be very valuable for further studies of strengthening mechanism at small layer thickness.

Table 2. A comparison of mechanical properties between Cu/304SS (h $\leq$5 nm) and Cu/Ni multilayers.

Materials	Crystal structure	$\sigma_{max}/\sigma_{rom}$	h at σ_{max} (nm)	Softening
Cu/Ni [11]	fcc/ fcc single crystal (100)	1.61	5	Yes, for h <5nm
Cu/304SS	fcc/fcc polycrystalline <111> texture	1.88	5	Yes, for h < 5nm

The similarity between the two systems is that softening occurred at layer thickness of less than 5 nm. It is suspected that softening observed in Cu/Ni could be related to intermixing at the interface between [16]. As mentioned above, graded interface may have lower barrier strength to dislocation transmission than chemically sharp interface. As the layer thickness decreases to a couple nanometers, the ratio of the intermixed layer at the interface (presumably a few monolayers) to the layer thickness increases and this may account for the drop in the strength with decreasing layer thickness below ~ 5 nm. In the case of Cu/304SS, the major elements (Fe, Cr) in fcc 304SS are immiscible with Cu. However, Cu is reported to have ~4% solubility in fcc 304 SS [15] and this may lead to limited intermixing, although much less than the case of completely miscible Cu-Ni system. Furthermore, softening has been observed in immiscible systems as well, although at layer thickness below ~ 1-2 nm. Therefore, other factors should be considered in explaining the softening in Cu/304SS multilayers. The absence of misfit dislocations at smaller layer thickness may lower the interface barrier to dislocations [10]. Recent molecular dynamics simulations [18] have shown that softening is to be expected when dislocation core width is some fraction of the layer thickness. Our future work will examine the softening at the smallest layer thicknesses in more detail.

Summary

Sputter-deposited Cu/304SS multilayers have fcc Cu/fcc 304SS structure for a layer thickness less than 5 nm, while a mixture of bcc and fcc 304SS with fcc Cu is observed at larger layer thickness. The maximum hardness of Cu/304 SS is 5.5 GPa, approximately a factor of two higher than the rule of mixtures hardness. The peak hardness of Cu/304SS is higher than that of Cu/Ni multilayer even though the latter has a much larger lattice parameter mismatch, and slightly higher shear modulus mismatch. This may be attributed to lowering of interface barrier stress to single dislocation transmission due intermixing at the miscible Cu-Ni interface, and to the differences in the texture in these systems. The decrease in hardness when the layer thickness is reduced from 5 to 1 nm needs to be investigated in more detail.

Acknowledgement

This research is funded by DOE-OBES. XZ acknowledges support from LANL director's funded post-doctoral fellowship. Technical assistance from Caleb Evans and Mark Hollander on sputter deposition is acknowledged.

References

1. B. M. Clemens, H. Kung, S. A. Barnett, MRS Bulletin, **24,** 20 (1999).
2. P. M. Anderson, T. Foecke, P. M. Hazzledine, MRS Bulletin, **24** (1999) 27.
3. G. S. Was, T. Foecke, Thin Solid Films, **286**, 1 (1996).
4. J. D. Embury and J. P. Hirth, Acta Metall. Mater., **42,** 2051 (1994).
5. E. O. Hall, Pro. Roy. Soc. (London). **B64**, 474 (1951).
6. N. J. Petch, J. Iron Steel Inst., **174**, 25 (1953).
7. W. D. Nix, Mater. Sci. Engg., **A234-236**, 37 (1997).
8. J. S. Koehler, Phys. Rev. B., **2**, 547 (1970).
9. M. Shinn, L. Hultman, S. A. Barnett, J. Mater. Res., **7**, 901 (1992).
10. S. I. Rao, P. M. Hazzledine, Phil. Mag. A, **80**, 2011 (2000).
11. A. Misra and H. Kung, Adv. Eng. Mater., **3**, 217 (2001).
12. P. M. Hazzledine and S. I. Rao, MRS Symp. Proc. **434**, 135 (1996).
13. D. M. Tench, J. T. White, J. Electrochem. Soc., **138**, 3757 (1991).
14. K. Parvin and S. P. Weathersby, T. W. Barbee, Jr., T. P. Weihs and M. A. Wall, Mater. Res. Soc. Symp. Proc., **382**, 191 (1995).
15. Jacek Banas, Andrzej Mazurkiewicz, Mater. Sci. Engg., A, **277**, 183 (2000).
16. T. W. Barbee, B. E. Jacobson, and D. L. Keith, Thin Solid Films, **63**, 143 (1979).
17. X. Chu and S. A. Barnett, J. Appl. Phys., **77**, 4403 (1995).
18. R. G. Hoagland, T. E. Mitchell, J. P. Hirth and H. Kung, Phil. Mag. A, **82**, 643 (2002).

Poster Session

Mat. Res. Soc. Symp. Proc. Vol. 740 © 2003 Materials Research Society

Synthesis of Titania coated Alumina Particles by a Hybrid Sol-gel Method

A.D. Schmidt[1], S.B. Majumder[2], P.S. Dobal[2], R.S. Katiyar[2], and D.C. Agrawal[3]
[1]Goshen College, Department of Chemistry, Goshen, IN, USA
[2]Department of Physics, University of Puerto Rico, San Juan, PR 00931-3343
[3]Materials Science Program, Indian Institute of Technology, Kanpur, 208016, India

ABSTRACT

Modifying their surface with a coating of another ceramic material can dramatically alter the properties of ceramic particles. In the present work we have demonstrated that the Al_2O_3 particles can be successfully coated by TiO_2 using a novel sol-gel technique. The nature of these coatings was predicted on the basis of scanning electron microscopy imaging in conjunction with the micro-Raman scattering measurements. The surface morphology of these particles shows that either individual or group of sub-micron alumina particles are coated with the nano-crystalline titania particles. The thickness of the titania coating could be varied by changing the precursor sol concentration. Amorphous titania was converted to anatase phase at 400°C and upon further heating it started transforming to rutile phase, and both these phases coexisted in the coated particles that were heat treated up to 800°C. The mechanical strength of the titania coating was measured qualitatively by ultrasonicating the coated powders for longer duration to observe that titania coatings are strongly adhered with the alumina particles.

INTRODUCTION

Coating a ceramic particle with another material can be useful for a number of applications. One such use is to uniformly coat the ceramic particle with organic binder in order to disperse it uniformly into the ceramic matrix.[1]. The other use has been to distribute sintering aid in ceramic matrix, thus bohemite coating is reported to enhance the green state plasticity and sintered density of Si_3N_4 ceramics [2]. Coating silica on alumina particles are found not only to improve the sintered density of alumina, but also form mullite, an important high strength ceramic compound [3]. In colloidal processing of ceramic composite the interaction forces can be altered by changing the surface properties of ceramic particles by coating with another ceramic material to achieve hetero-coagulation [4]. Sol-gel processing has been found to be effective in coating the ceramic particle with an amorphous gel coating of another ceramic. Metal alkoxide or salts are used as precursor material to prepare an amorphous gel layer around the ceramic particles [5-6]. The effectiveness of the gel coating on ceramic particles are demonstrated through TEM analysis, however, the nature of these coatings after calcinations have not been studied adequately [5]. In this work we have studied the nature of titania coating on alumina particles by calcining these coated particles in a wide range of temperature (as dried at 80°C to 800°C) in air. Titania coating is expected to enhance the sinterability of alumina and these powders could be used as low loss microwave dielectric material. The nature of titania coating has been studied by X-ray diffraction (XRD), scanning electron microscopy (SEM) and micro-Raman spectroscopy. The experimental results clearly indicate the effective coating of

alumina by titania nano-particles. It is also demonstrated qualitatively that the titania is reasonably well adhered to the alumina particles.

EXPERIMENTAL DETAILS

Ti sols (concentration varied from $1X10^{-2}$ M to $1X10^{-3}$M) was prepared by dissolving Ti-isopropoxide in acetic acid (1:1 weight percent). About 2 gm of alumina powders were ultrasonically dispersed in about 30 ml acetic acid to form a stable suspension. The isoelectric point (IEP) of alumina is about 9.2 and therefore maintaining the pH of the suspension in acidic range (~3-4) yield excellent dispersion of alumina. The acetic acid chelated Ti sol was added drop-wise into alumina suspension at room temperature with continuous stirring. The resultant suspension was allowed to settle, and the lighter particles, excess sol and solvents were decanted to separate the heavier particles with an amorphous gel layer. The resultant paste was transferred in a petridish (kept on an ultrasonicate bath) and dried by flowing compressed air at room temperature. The dried powders were heat treated in a temperature range of 200 to 800°C for 2h in air maintaining a heating rate of $5°Cmin^{-1}$. Differential thermal analysis in conjunction with Fourier transformed infra-red spectroscopy (FTIR) of powders heat treated at different temperatures for 2 hours, were performed to characterize the thermal events as a function of temperature. The nature of the coating was analyzed by a combined XRD and SEM studies in conjunction with micro-Raman spectroscopy.

RESULTS AND DISCUSSIONS

Figure 1 shows the FTIR spectra of titania gel coated alumina particles (a) as dried, calcined at (b) 400°C and (c) 800°C for 2 hours in air. The acetate bands attached with Ti (at about 1400 and 1520 cm^{-1}) along with other bending and stretching modes (assigned in Fig. 1a) are clearly seen in as dried powders, however, their absence in powders annealed at higher temperatures (Fig. 1b and 1c) indicated that the organics are completely removed at about 400°C. This is also supported by the DTA analysis (not shown).

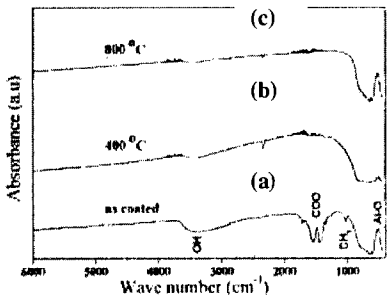


Figure 1 FTIR spectra of titania coated alumina particles calcined at different temperatures

The typical crystallization behavior of titania coating is shown in Fig.2a. As revealed from the XRD results, the titania crystallizes into anatase (tetragonal, indexed according to JCPDS file 21-1272) phase at 400°C. The anatase to rutile (tetragonal File 21-1276) transformation initiates at about 600°C (or less) and both these phases coexist till 800°C. The ratio of rutile: anatase phases, as a function of annealing temperature, was calculated from the X-ray diffractograms and it was shown that the rutile phase content increases with the increase in calcinations temperature for all concentrations of titania precursor sols (Fig.2b). The relative phase contents were calculated as follows : the (101) anatase peak was deconvoluted

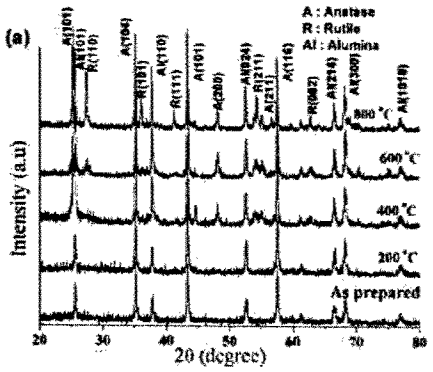


Figure 2(a) X-ray diffractograms of titania coated alumina particles calcined at different

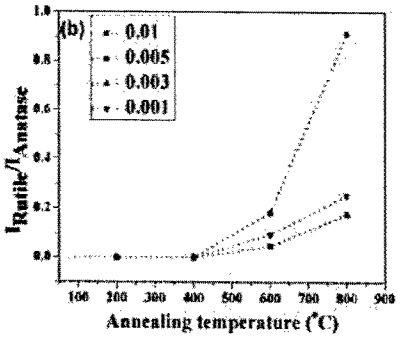


Figure 2(b) Variation of rutile:anatase phase contents as a function of calcination temperature

from (012) diffraction peak of alumina using Pearson VII function. The rutile (110) peak was also fitted using the same function and the ratio of the integrated area of (110) rutile peak: (101) anatase peak was taken to be a measure of the rutile: anatase phase content. The dramatic anatase to rutile conversion (particularly in powder calcined at 800°C) for $5X10^{-3}$M titania coated composition is not well understood. Probably, other factors such as grain growth etc also influence the intensity ratio, and therefore, the ratio of phase contents are not strictly represented only by the intensity ratio of the diffraction peaks of corresponding phases.

X-ray diffraction analysis, however, failed to predict the nature of titania coating on alumina particles. The possibilities of this kind of coating approach have schematically been shown in Fig. 3. Dipping alumina particles in titania sol and subsequent ultrasonication is assumed to uniformly coat alumina with amorphous titania gel. Upon annealing three kind of situations are predicted, crystalline titania are separated from alumina particles (case I), titania could either partially (case II) or fully (case III) coat alumina particles. To observe the nature of titania coating, the surface morphology of the calcined coated powders were characterized by SEM. For this purpose a dilute dispersion of calcined alumina powders and titania coated alumina was made in isopropanol solvent. The concentration of particles was such that it gives a turbid appearance. The pH of the suspension was maintained slightly acidic; and since the IEP of TiO_2 and Al_2O_3 are 6 and 9.2 respectively it is expected that the repulsive force between oxide particles avoid coagulation [7]. The stable suspension drop was taken out by a micro-pipette and put on a mirror polished aluminum stub and the solvents were allowed to evaporate at room temperature. This avoids any undesired particle agglomeration due to forced drying. Fig. 4 (a) shows the micrograph of calcined uncoated alumina. Uncoagulated alumina

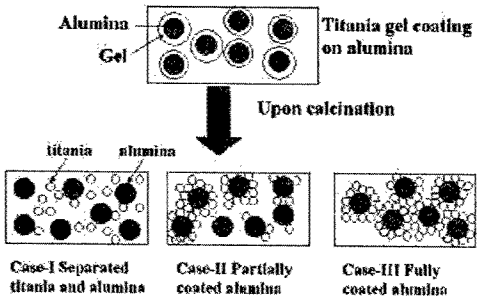


Figure 3 Schematic diagram of the probability of different kinds of coating

particles, in the size range of 0.4-0.5μm, are seen in the micrograph. Fig. 4(b) shows the TiO_2 coated alumina (TiO_2 coating was made from 0.01 M/L precursor sol). It is clearly seen that alumina particles are coated completely with TiO_2 particles. It is worth mentioning here at this point that both these micrographs are the representatives of several SEM pictures taken in many different samples. However, at this stage we are not ruling out the possibility of alumina partially coated with titania, as shown schematically in Fig. 3 (case II).

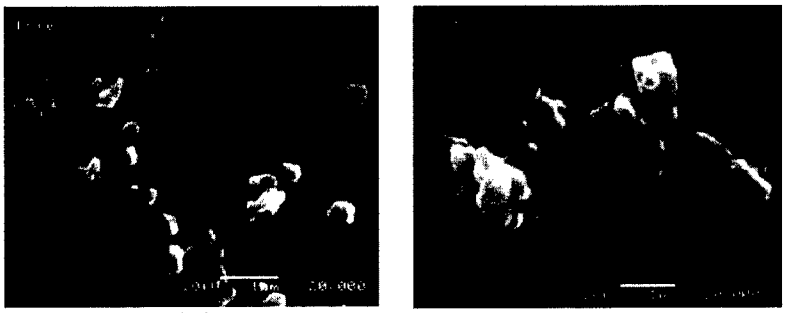


Figure 4 SEM micrographs of (a) bare and (b) 0.01M titania coated alumina particles both calcined at 800^0 C for 2 h

Micro-Raman spectroscopy has been used as an effective characterization tool to draw a definite conclusion about the nature of titania coating on alumina. Figure 5 shows the Raman spectra of as prepared and titania coated alumina, heat treated at different temperatures for 2h in air. Note that up to 200°C the Raman spectra are featureless indicating the alumina particles are fully coated with the titania gel since no characteristics band of alumina is apparently observed. The titania coating is crystallized into anatase phase upon heat treatment at higher temperature as indicated by the Raman spectra and the absence of any characteristic band of alumina clearly indicated that alumina particles are fully coated with titania particles. We have done these measurements for other titania coated particles prepared with different titania alkoxide concentration and the outcome was identical as reported in Fig.5. Also Raman measurements were performed in different regions of these samples and the results show that the alumina particles are completely coated with titania as predicted in Fig. 3 (case III).

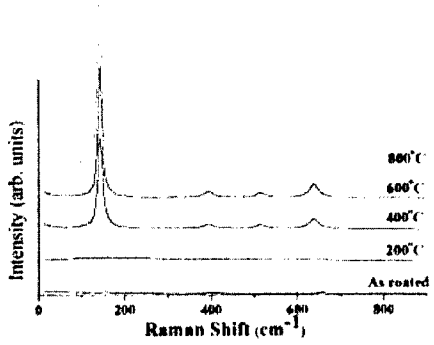


Figure 5 Raman spectra of titania coated alumina annealed at various temperature for 2h.

Finally, we tested qualitatively the strength of the adhesion of the titania coating on alumina particles. For this purpose a dilute suspension of coated powders were ultrasonicated for extended period of time (up to 2h) and Fig. 6 shows the Raman spectra of coated powders prepared from 0.01 and 0.001 M/L Ti sol. As shown in the Figure, the appearance of only titania bands in the recorded Raman spectra even after 2 h of ultrasonication, clearly indicates the strong adherence of the

coating on alumina. However, the appearance of a very broad band of alumina in case of titania coated from the thicker sol indicates that dilute concentration of the coating sol could have more effect for efficient coating. More systematic studies are required to understand these issue better.

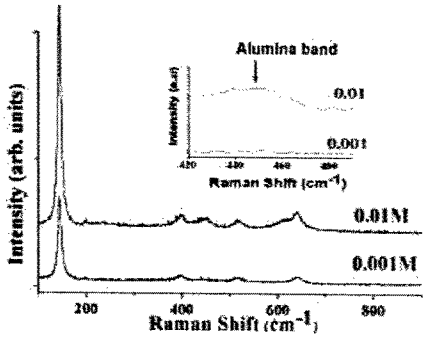


Figure 6 Raman spectra of titania coated alumina after ultrasonication for 2h

CONCLUSIONS

A hybrid sol-gel technique has been described to prepare titania coated alumina powders. Through a combined study of SEM and micro-Raman we have demonstrated that alumina particles are completely covered by titania. Preliminary characterizations show that these coatings are reasonably well adhered to alumina particles. More systematic studies are required to understand the growth behavior of titania as a function of precursor sol concentration and heat treatment conditions. Moreover, the sinterability and the high frequency (> GHz) dielectric characteristics of these materials are also interesting to study for the possible use in microwave devices.

ACKNOWLEDGMENTS

Part of this work was supported by NSF-REU 0097768 and NSF-INT 0097018 grants

REFERENCES

1. M.A. Buchta and W.H. Shih, *J. Am. Ceram Soc.* **79** 2940 (1996).
2. W.H. Shih, L.L. Pwu, and A.A. Tseng, *J. Am. Ceram Soc.* **78**, 1252 (1995)
3. M.D. Sacks, N. Bozkurt, and G.W. Scheiffele, *J. Am. Ceram. Soc.* **74**, 2428 (1991).
4. E.P. Luther, T.M. Kramer, F.F. Lange, and D.S. Pearson, *J. Am. Ceram. Soc.* **77**, 1047 (1994).
5. C.Y. Yang, W.Y. Shih, and W.H. Shih, *J. Am. Ceram. Soc.* **83**, 1879 (2000).
6. S. Mei, J. Yang, R. Monteiro, R. Martins, J.M.F. Ferreira, *J. Am. Ceram. Soc.* **85**, 155 (2002).
7. J.S. Reed, "Principles of Ceramic Processing" 2nd Ed. (John Wiley & Sons, Inc., 1995) pp 150-171.

Mat. Res. Soc. Symp. Proc. Vol. 740 © 2003 Materials Research Society

Nucleation Induced Nanostructures

A. ten Bosch
Laboratoire de Physique de la Matière Condensée, CNRS 6622, Parc Valrose, F-06108,Nice Cedex 2, France

ABSTRACT

Numerical simulations in films and aggregates have repeatedly shown the presence of vibrations during a phase transition and/or the appearance of periodic structures. A phase transition could be controlled and novel nanostructures created by astute manipulation of such phenomena. In order to study the occurrence and effect of wave-like phenomena, the dynamics of a first order phase transition is described using kinetic theory. At a first order phase transition, the initial phase is replaced in time by the new phase on propagation of a density front through the sample. The dynamic stability analysis studies the transition to the uniform phase by propagation of the front and provides the conditions for the formation of transient periodic structures by a local increase of density. The results apply also to spherical geometry and a discussion of cluster dynamics follows the planar case.

INTRODUCTION

In a first order phase transition, the emerging stable phase displaces the original phase by the dynamic process of nucleation and growth. Between the two phases, a contact forms which propagates as an interfacial profile, providing a practical method to produce materials in thin layers. Applications are well known in thin films and coatings of metals, semiconductors and polymer materials for use in electronics, optics and in the surface modification of materials to improve mechanical or chemical properties.[1]

A phase transition could be controlled and novel nanostructures created by excitation of waves. Numerical simulations in films and aggregates have repeatedly shown the presence of vibrations during a phase transition and/or the existence of specific wave-like motions[2-6] which effect the shape, the morphology and the propagation of the interface.

THEORY

In order to study the occurrence and effect of wave-like phenomena, the dynamics of a first order phase transition is described using kinetic theory [7] for the evolution of the probability distribution of particles $f(\mathbf{r}, t)$ or the number density $n(\mathbf{r},t)= nf(\mathbf{r},t)$, n being the total number of particle per volume. The function $n(\mathbf{r}, t)$ measures the probability for a particle to arrive at position $\mathbf{r}$ after a time t and fulfills the equation of continuity:

$$\frac{\partial n(\vec{r},t)}{\partial t} = -\frac{\partial}{\partial \vec{r}} \cdot \vec{j}(\vec{r},t) \qquad (1)$$

The evolution of the flux j (**r**,t) = n(**r**,t) v(**r**,t) , v(**r**,t) being the average velocity of the particles of mass m, is described by the dynamic flux equation,

$$\frac{\partial \vec{j}}{\partial t} = -\beta \vec{j} - \frac{1}{m} n(\vec{r},t) \frac{\partial}{\partial \vec{r}} \mu(\vec{r},t) \qquad (2)$$

The friction forces of the medium are included in β. We concentrate on the dynamics of a system which, having achieved uniform temperature, is dominated by particle flow. The driving force of the transition is the gradient of the local chemical potential μ(**r**,t). The chemical potential is enslaved by the density and in the effective interaction model [8]:

$$\mu(\vec{r},t) = \mu(n) - \frac{\kappa}{2} \Delta n(\vec{r},t) \qquad (3)$$

The function μ (n) is the bulk chemical potential, the second term takes local variations of the density into account. The constant κ is related to the range of the interaction potential between particles.

At a first order phase transition, the initial phase is dynamically unstable and is replaced in time by the new stable phase on propagation of a density front through the sample. The transition from the two phase "kink" solution of eq. (1) and (2) , as described below, to the final phase of uniform density is of interest to the dynamics of the phase transition which proceeds by propagation of the front. The velocity of the front, its shape, stability and the structure that is left behind are studied.

RESULTS

In heterogeneous nucleation the phase transition is initiated on the interface. The new emerging phase may grow and replace the initial phase under certain conditions which will be defined by analysis of the dynamic stability for different initial conditions. The dynamic stability analysis will show that the "kink" of density $n(x,t) = n_1$, $x < L(t)$; $n(x,t) = n_0$, $x > L(t)$ is linearly unstable to a long range local increase of density at the surface. The function L(t) determines the boundary between the phases, the initial phase of density n_0 and the new emerging phase of density n_1, and describes the propagation of the kink.

The two kinetic equations are combined by taking the time derivative of (1), inserting (2) and using (3):

$$\frac{\partial^2 \eta}{\partial t^2} = -\beta \frac{\partial \eta}{\partial t} + c_0^2 \left[\frac{\partial^2}{\partial x^2} \eta(x,t) - \xi^2 \frac{\partial^4}{\partial x^4} \eta(x,t)\right] \qquad (4)$$

The dynamic equation (4) is linear in a small perturbation $\eta(x,t) = n(x,t) - n_0$ for $x>0$ and its derivatives and valid in the region close to the state of density n_0 for $x>0$ and $\eta(x,t) = 0$ for

x<0 . The velocity of sound in the initial uniform medium is $c_0^2 = \frac{n_0}{m}\frac{\partial \mu(n_0)}{\partial n_0}$ and ξ is the density correlation length.

In one possibility, the initial phase wets the emerging phase and the initial conditions are η (x,t=0) = η_0 exp(-q x), j(x,0) =0. The resulting perturbation is exponential and $\eta(x,t) \propto \exp[-qx + \omega t]$. The left hand side of (4) determines the dispersion relation ω(q):

$$\omega(q) = \frac{1}{2}(-\beta \pm \sqrt{\beta^2 + F(q)})$$
$$F(q) = 4q^2 c_0^2 (1 - \xi^2 q^2) \qquad (5)$$

Different behavior is found for different values of wetting layer thickness and a critical length emerges. The critical wave vector is q_c for which Im $\omega(q_c) = 0$ or $1+F(q_c)/\beta^2 = 0$.

For $q>q_c$, The solution is a damped vibration which causes the initial wetting layer to vanish with time. $\eta(x,t) = \eta_0 \exp[-qx - \beta t/2][\cos(\Omega_q t) - \frac{\beta}{2\Omega_q}\sin(\Omega_q t)]$. The dispersion relation of the elastic vibration is $\Omega_q = \frac{1}{2}\sqrt{-\beta^2 - F(q)}$. The kink is dynamically stable, the transition will not be triggered by this small scale perturbation.

For $1/\xi < q < q_c$, the dispersion relation is real and negative and translation sets in. For example for $q \approx 1/\xi$, the perturbation front recedes with a velocity v_ξ and decays with time.

$$\eta(x,t) = \eta_0 \exp[-q(x + v_\xi t)]\exp(-\frac{v_\xi t}{\xi})$$
$$v_\xi = \frac{2c_0^2}{\xi\beta}$$

For $q < 1/\xi$, the dispersion relation is real and positive. For $q\xi << 1$, the perturbation front advances with a positive velocity v:

$$\eta(x,t) = \eta_0 \exp[-q(x - vt)]$$
$$v = \frac{c_0^2 q}{\beta}(1 - q^2\xi^2)$$

For stationary total number of particles, the velocity of the interface dL/dt must be equal to the average flux of the particles normal to the interface [9] and

$$dL/dt = - j_x (L,t) / (n_1 - n_0 - \eta (L,t)) \qquad (6)$$

When the density of new phase is larger than that of the initial phase (such as on condensation or crystallization) $n_1 > n_0$ and $\eta_0 > 0$. For $1/\xi < q < q_c$ the value of the density at the front edge decreases as the n_1 front propagates into the initial phase. The front

motion L(t) is initially linear in time and advances slower than the perturbation. After a sufficiently long time, the motion ceases as the initial perturbation is incorporated into the front. For a fluctuation with $q < 1/\xi$, the profile edge L(t) recedes and the n_1 phase vanishes. The value of the density at the profile edge increases with time to conserve particle number. A convective instability occurs; the localized perturbation grows while moving away from its initial location although at a fixed location it appears to decay.[9] The discussion is similar when the density of new phase is smaller than that of the initial phase (such as on evaporation or melting) with $n_1 < n_0$ and $\eta_0 < 0$.

The phase transition can be also induced by periodic deformation of the initial phase. Setting $q \rightarrow iq$, the dispersion relation $\omega(q)$ is obtained from (4). There is a critical wave vector Q_c with Im $\omega(Q_c) = 0$. The solution is a damped wave for a periodic fluctuation in the initial phase of small wave length or $q > Q_c$ and the initial profile is stable. For a wave length larger than the critical length or wave vector $q < Q_c$, the dispersion relation is real and positive and the solution is a front which advances as the periodic deformation decays.

The results can be applied to spherical geometry and the discussion of cluster dynamics follows the planar case. The linear stability of the classical cluster, defined as $n(r,t) = n_1$ $(r<a)$ and $n(r,t) = n_0$ $(r>a)$, to a local increase of density at the surface r = a of the cluster proceeds as before. For a fluctuation $\eta(r,t) = 0$ for r<a and $\eta(r,t) = \frac{\eta_0}{r}\exp[-qr + \omega t]$, r>a, which increases the density near the surface, the linear equation (4) is obtained in radial coordinates for the function $\eta(r,t)r$. For stationary particle number, the dynamics of the cluster radius a is given by the radial flux at the surface: $da/dt = - j_r(a,t) / (n_1 - n_0 - \eta(a,t))$ [4]. The cluster is stable and damped vibrations are induced for $q > q_c$. For $1/\xi < q < q_c$, front propagation sets in, the cluster will start to grow with a decreasing density at the cluster surface[10]. For an initial thick layer of width $q<1/\xi$, the cluster is unstable with possibly a transition to nonspherical shapes. In contrast, for the solution described in [11], the unfavorable surface to bulk ratio always inhibits growth in small clusters.

CONCLUSIONS

In experiments or numerical simulation, the boundary and initial conditions within the cell determines the dynamics observed. To start a phase transition by wetting, the parameters of importance are ξ^{-1} and $\xi\beta/c_0$ in the initial phase. If favorable, a large range of possible fluctuations causes the initial phase to become dynamically unstable and propagation and growth of the new phase sets in. Vibrations are excited for small scale initial fluctuations at the onset of a phase transition. In real systems, a complex signal will emerge but the resulting turmoil dies down after β^{-1}. The characteristic time is sufficiently long in polymer systems to freeze the transient states, resulting in small scale periodic micro- or nanostructures.

ACKNOWLEDGEMENTS

Helpful discussions with E. Dehaudt, who made his results available before publication, are gratefully acknowledged.

REFERENCES

1. M. Ohring, *Materials Science of Thin Films* (Academic Press, San Diego, 1992)
2. S.Waar, L. Woodcock, Faraday Discuss.,**95**, 329 (1993)
3. L. Bartell, J.Mol.Structure, **445**,59(1998)
4. A. Ludu, J.P. Draayer, Phys.Rev.Letters **80** ,2125 (1998)
5. D. Zhukhovitskii, J. Chem. Phys.**110** ,777 (1999)
6. E. Dehaudt, *Fusion et cristallisation des paraffines et polyethylenes*, Thesis Ecole des Mines de Paris 2001 and to be published
7. S.A. Rice,P. Gray, The Statistical Mechanics of Simple Liquids (J.Wiley, New York,1965); A.ten Bosch, Phys.Rev. E , to be published (2003)
8. R. Evans, Adv. Physics, **28** ,143 (1979)
9. D. Walgraef, *Spatio-Temporal Pattern Formation* (Springer Verlag, New York,1997)
10. A. ten Bosch, J. Chem. Phys.**110**, 12251 (1999)
11. M. Mouti, A. ten Bosch, J. Chem. Phys.**99**,1796 (1993)

Mat. Res. Soc. Symp. Proc. Vol. 740 © 2003 Materials Research Society

Hydrogen Stabilization of {111} Nanodiamond

A.S. Barnard[1], N.A. Marks[2], S.P. Russo[1] and I.K. Snook[1]
[1]Department of Applied Physics, RMIT University,
Melbourne, Victoria, 3001, Australia
[2]Department of Applied Physics, School of Physics, University of Sydney,
Sydney, New South Wales, 2006, Australia

ABSTRACT

Presented here are results of ab initio Density Functional Theory (DFT) structural relaxations performed on dehydrogenated and monohydrogenated nanocrystalline diamond structures of octahedral {111} and cuboctahedral morphologies, up to approximately 2nm in diameter. Our results in this size range show a transition of dehydrogenated nanodiamond clusters into carbon onion-like structures, with preferential exfoliation of the C(111) surfaces, in agreement with experimental observations. However, we have found that this transition may be prevented by hydrogenation of the surfaces. Bonding between atoms in the surface layers of the relaxed structures, and interlayer bonding has been investigated using Wannier functions.

INTRODUCTION

With the advent of nanotechnology related research in recent years, many studies have sought to understand the formation of the carbon clusters, and the dynamic phase changes and stability relationship between graphite and nanodiamond clusters. It has been observed experimentally [1-3], that upon annealing nanodiamond particles transform into onion-like carbon, from the surface inward (with the transformation temperature dependant on the size of the particle). Such observations reveal preferential graphitization and exfoliation of the diamond C(111) surfaces over other lower index surfaces, and the transformation of complete dehydrogenated nanodiamonds into onion carbon. This transition has also been modelled theoretically using semi-empirical [2,4-7] and ab initio methods [8,9]. Presented here are structural relaxations of hydrogenated nanodiamonds with octahedral and cuboctahedral morphologies. It is anticipated that saturation of the nanodiamonds surfaces with hydrogen will passivate the surfaces and stabilize the structures and preserve the diamond structure.

AB INITIO METHOD

The hydrogenated nanodiamonds have been relaxed using the Vienna Ab initio Simulation Package (VASP)[11,12]. We used ultra-soft, gradient corrected Vanderbilt type pseudo-potentials [13] as supplied by Kresse and Hafner [14], and the valence orbitals are expanded in a plane-wave basis up to a kinetic energy cut-off of 290eV. The crystal relaxations were performed in the framework of DFT within the Generalized-Gradient Approximation (GGA), with the exchange-correlation functional of Perdew and Wang (PW91)[15]. A detailed description of this technique may be found in references [16,17]. We have successfully applied this technique to the relaxation of dehydrogenated [8-10], hydrogenated [18] and doped [10] nanodiamond structures in the past, with results showing excellent agreement with experiment and all-electron methods [19].

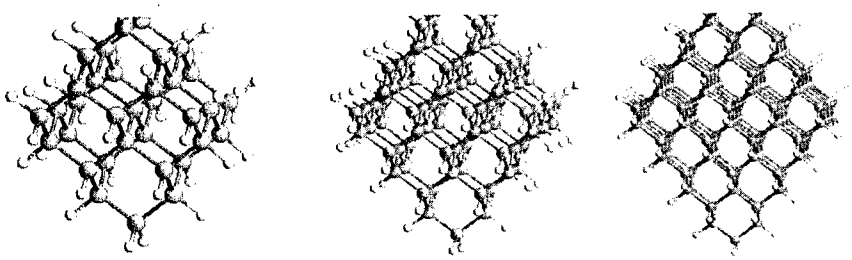


Figure 1. The $C_{35}H_{36}$, $C_{84}H_{64}$ and $C_{165}H_{100}$ octahedral nanodiamond crystals after the relaxation process.

RELAXATION RESULTS

Three octahedral nanodiamond crystals have been generated by 'cleaving' fragments from a bulk diamond lattice, and are denoted C_{35}, C_{84} and C_{165}. These structures have C(111)(1x1) single dangling bonds surfaces, which have then been terminated with hydrogens to produce the $C_{35}H_{36}$, $C_{84}H_{64}$ and $C_{165}H_{100}$ nanodiamonds (see Figure 1). Each nanodiamond has then been relaxed, and the final structure compared to the previously obtained results [8,9] for the dehydrogenated C_{35}, C_{84} and C_{165} nanodiamonds. Following relaxation, the carbon framework of the $C_{35}H_{36}$ structure was found to be almost identical to the initial cleaved fragment, showing no adoption of the rounded shape observed in the relaxed C_{35} cluster. Also, although the C_{84} and C_{165} nanodiamonds have previously been found to transform into a two-shell carbon-onions [9], the hydrogenated structures do not. The $C_{84}H_{64}$ and $C_{165}H_{100}$ nanodiamonds retain the original 'cleaved' diamond framework (with no exfoliation of the C(111) surfaces), and exhibit little change in the length of surface bonds. The surface structure was found to alter slightly during the structural relaxation, but finally relaxed to the bulk-like positions. All evidence of the phase transition characteristic of the dehydrogenated {111} nanodiamonds has been eliminated.

Two nanodiamonds with cuboctahedral structure have also been considered. These are the $C_{29}H_{24}$ and $C_{142}H_{72}$ nanodiamonds, which are characterised by C(111)(1x1):H and C(100)(2x1):H surfaces (see Figure 2). Previously published results of the C_{29} nanodiamond show a transformation of the nanocrystal into the C_{28} fullerene, with an endohedral carbon atom ($C@C_{28}$)[9]. The $C_{29}H_{24}$ nanodiamond was however found to be stable, and although the bond lengths and angles varied slightly during the relaxation, the diamond lattice was preserved (see Figure 2). Similarly, the C_{142} nanodiamond has been found to exhibit preferential graphitization of the C(111) surfaces [9], producing fullerenic 'cages' on the surface. These fullerenic cages were observed briefly in the initial stages of the relaxation of the $C_{142}H_{72}$ nanodiamond, however following a rearrangement of the hydrogens, the crystal relaxed back into the bulk diamond-like structure (see Figure 2).

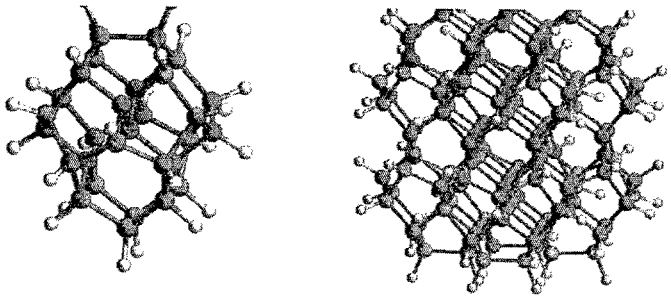


Figure 2. $C_{29}H_{24}$ and $C_{142}H_{72}$ cuboctahedral nanodiamond crystals after the relaxation process.

Wannier functions and analysis of bonding

Wannier functions provide a local and chemical view of the bonding, and are related to the occupied Kohn-Sham orbitals via a unitary transformation [20]. In periodic (super-cell) systems this transformation is non-unique due to Bloch phase factors and Brillouin Zone sampling, leading Marzari and Vanderbilt [21] to propose *maximally localised* Wannier Functions for which the total spatial spread

$$S = \sum_n \left(\langle r^2 \rangle_n - \langle \mathbf{r} \rangle_n^2 \right) \qquad (1)$$

is minimized. In equation 1, the brackets indicate expectation values with respect to individual Wannier functions $w_n(\mathbf{r})$. Two key pieces of information are then available: the Wannier Function Center (WFC) defined as the expectation value of the position operator, and the localisation defined by the square root of the variance [22]. When the Kohn-Sham orbitals are doubly occupied (as in this work), these two quantities reveal the location and spatial extent of each bond.

The Wannier analysis was performed using the Car-Parrinello Molecular Dynamics package [23], taking as input the relaxed coordinates from VASP. All calculations used the BLYP exchange-correlation functional [24], Martins-Trouiller pseudo-potentials [25], and a plane-wave basis set with a wavefunction cut-off of 476 eV. Results for C_{29} and $C_{29}H_{24}$ are presented in Figure 3, showing the WFC as small black circles, and the carbon and hydrogen atoms as dark and light grey respectively.

In the hydrogenated structure the WFC are located on the midline joining atom pairs, and so indicate a bond. For C-C bonds the WFC lies at the midpoint, indicating a symmetric charge density, whereas C-H bonds have more charge at the hydrogen end of the bond. In either case the WFC localisation is small (less than 1.7 Å), indicating that the WFC is associated with only two atoms. The Wannier picture thus confirms σ-bonding with hydrogenation, as expected.

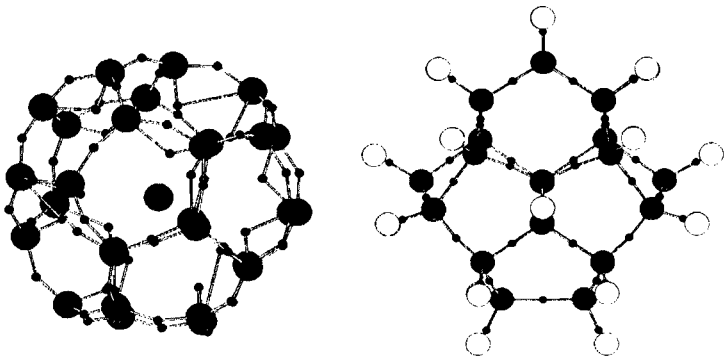


Figure 3. Atoms and Wannier Function Centers for C_{29} (left) and $C_{29}H_{24}$ (right). Carbon and hydrogen are shown as dark and light grey respectively, while small black circles denote the Wannier Function Centers.

A very different situation is evident for the dehydrogenated C_{29} structure, where the absence of hydrogen leads to bent σ-bonds, distorted π-bonds and an ionic central atom. Atom pairs connected via a single WFC indicate σ-bonds, and have localisations very similar to the hydrogenated case. However, none of these WFCs lie on the midline, but instead are projected radially outward, with the carbon atoms subtending an angle of approximately 140°. The absence of atom pairs connected by two WFCs indicates that no π-bonding is present. Instead, the inner WFCs are bent towards the central atom and are significantly more delocalised (~2.6 Å compared to 1.7 Å for the outer WFCs). In a category of it's own is a single WFC with an intermediate localisation of 1.9 Å, and connected only to the central atom. This indicates the presence of ionic character in C_{29}, in agreement with detailed ab initio calculations by Jackson et al [26].

DISCUSSION

Using WC analysis it has been shown that hydrogenation of C(111) nanodiamond surfaces promotes a bulk diamond-like surface structure and bonding. As a preliminary test of the effects of surface hydrogenation on the structural properties nanodiamond, the cohesive energy has been considered. In a previous study [8] the cohesive energy of dehydrogenated nanodiamond was calculated using the total (spin-polarization corrected) energy per ion plotted against the fractional ratio of dangling bonds (N_d/N_t), for a series of dehydrogenated nanocrystal structures. We note that, for example, a dehydrogenated cuboctahedral nanodiamond of ~8.5nm diameter would have $N_d/N_t \sim 0.07$, therefore by extrapolating to the limit $N_d/N_t \rightarrow 0$ using a linear fit the intercept gives an estimate of the cohesive energy. The cohesive energy of dehydrogenated nanodiamond has been calculated to be 7.71eV[8].

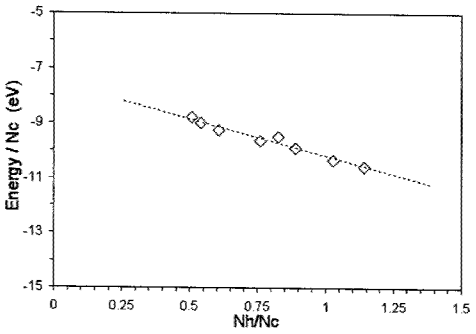


Figure 4. Prediction of the cohesive energy of relaxed hydrogenated nanodiamond from the linear fit to the total energy per atom versus the number of hydrogens per carbon.

This procedure was repeated for the relaxed hydrogenated nanocrystals, by plotting the total energy per carbon atom versus the number of hydrogen atoms per carbon atom N_h/N_c as shown in Figure 4. By extrapolating the nanocrystal energies as a function of the hydrogen to carbon ratio (in the limit as $N_h/N_c \rightarrow 0$) the cohesive energy for relaxed, hydrogenated nanodiamond was predicted to be 7.52eV. This value is considerably closer to the calculated bulk diamond value of 7.39eV[8], indicating that hydrogenation of nanodiamond also induces a more bulk-like cohesive energy at the nano-scale.

CONCLUSION

It has been shown that hydrogenation of nanodiamonds C(111) surfaces eliminates the nanodiamond to carbon-onion transition, and promotes the bulk-diamond structure and bonding. This has been illustrated by comparing the hybridization of bonds present in the relaxed hydrogenated and dehydrogenated nanocrystals via calculation of Wannier functions. These calculations confirm that while the dehydrogenated structures contain distorted σ and π-bonds, all of the corresponding hydrogenated nanocrystals were found to be entirely σ-bonded. Therefore, although it was found previously that dehydrogenated nanodiamonds with C(111) faces were energetically unstable, these structures may be stabilised by saturating the surfaces following cleaving. Hydrogenation of the surfaces of the nanodiamond structures investigated here serves not only to passivate the surfaces, but also to stabilize the bulk diamond-like structure, making nanodiamond a suitable possibility for the nanodevices of the future.

ACKNOWLEDGEMENTS

We would like to acknowledge the Victorian Partnership for Advanced Computing and the Australian Partnership for Advanced Computing in support of this project.

REFERENCES

[1] V. L. Kuznetsov, A. L. Chuvilin, Y. V. Butenko, I. Y. Mal'Kov and V. M. Titov, Chem. Phys. Lett., **209**, 72 (1994).

[2] V. L. Kuznetsov, I. L. Zilberberg, Y. V. Butenko, A. L. Chuvilin and B. Seagall, J. Appl. Phys., **86**, 2, 863 (1999).

[3] S. Tomita, T. Sakurai, H. Ohta, M. Fujii and S. Hayashi, J. Chem. Phys., **114**, 17, 7477 (2001).

[4] F. H. Ree, N. W. Winter, J. N Glosli and J. A. Viecelli, Physica B, **265**, 223 (1999).

[5] N. W. Winter and F. H. Ree, J. Comp. Aided Mat. Design, **5**, 279 (1998).

[6] F. Fugaciu, H. Hermann and G. Seifert, Phys. Rev. B, **60**, 15, 10711-10714 (1999).

[7] H. Hermann, F. Fugaciu and G. Seifert, Appl. Phys. Lett., **79**, 1, 63-65 (2001).

[8] A. S. Barnard, S. P. Russo and I. K. Snook, Phil. Mag. Lett. **83**, 1, 39-45 (2003).

[9] A. S. Barnard, S. P. Russo and I. K. Snook, Diamond Relat. Mater., (2002) (in press).

[10] A. S. Barnard, S. P. Russo and I. K. Snook, J. Chem. Phys., (2002) (submitted).

[11] G. Kresse and J. Hafner, Phys. Rev. B, **47**, RC558 (1993).

[12] G. Kresse and J. Hafner, Phys. Rev. B, **54**, 11169 (1996).

[13] D. Vanderbilt, Phys. Rev. B, **41**, 7892 (1990).

[14] G. Kresse and J. Hafner, J. Phys.: Condens. Matter., **6**, 8245 (1994).

[15] J. Perdew and Y. Wang, Phys. Rev. B, **45**, 13244 (1992).

[16] G. Kresse and J. Furthmüller, Comp. Mat. Sci., **6**, 15 (1996).

[17] J. Furthmüller, J. Hafner and G. Kresse, Phys. Rev. B, **53**, 7334 (1996).

[18] S. P. Russo, A. S. Barnard and I. K. Snook, Surf. Rev. Lett., (2002) (in press).

[19] A. S. Barnard, S. P. Russo and I. K. Snook, Phil. Mag. B, **82**, 17, 1767-1776 (2002).

[20] W. G. Wannier, Phys. Rev. B, **52**, 191 (1937).

[21] N. Marzari and D. Vanderbilt, Phys. Rev. B **56**, 12847, (1997)

[22] P. L. Silvestrelli, N. Marzari, D. Vanderbilt and M. Parrinello, Solid State Comm. **107**, 7, (1998).

[23] CPMD Code, J. Hutter, A. Alavi, T. Deutsch, M. Bernasconi, S. Goedecker, D. Marx, M. Tuckerman and M. Parrinello, MPI fur Festkoerperforschung, IBM Zurich Research Laboratory, 1995 - 2002

[24] A. D. Becke, Phys. Rev. A **38**, 3098 (1988); C. L. Lee, W. Yang and R. G. Parr, Phys. Rev. B **37**, 785 (1988).

[25] N. Troullier and J. L. Martins, Phys. Rev. B, **43**, 1993 (1994).

[26] K. Jackson, E. Kaxiras and M. R. Pederson, Phys. Rev. Lett., **48**, 23, 17556-17561 (1993)

Mat. Res. Soc. Symp. Proc. Vol. 740 © 2003 Materials Research Society I3.7

Processing of Clay/Epoxy Nanocomposites with A Three-Roll Mill Machine

Asma Yasmin, Jandro L. Abot and Isaac M. Daniel
Center for Intelligent Processing of Composites, Northwestern University,
Evanston, IL 60208-3040, U.S.A.

ABSTRACT

In the present study, a three-roll mill machine was used to disperse/exfoliate the nanoclay particles in an epoxy matrix. The compounding process was carried out with varying mixing time and concentrations of clay particles (1 to 10 wt.%). It was found that the longer the mixing time, the higher the degree of intercalation. Mechanical properties, XRD and TEM were used to characterize the nanocomposites. Elastic modulus was found to increase with increasing clay content, however, the tensile strength was not found to vary accordingly. Compared to conventional direct and solution mixing techniques, the compounding of clay/epoxy nanocomposites by a three-roll mill was found to be highly efficient in achieving higher levels of intercalation/exfoliation in a short period of time and also environmentally friendly.

INTRODUCTION

Over the last decade, polymer based composites containing nano-scale layered silicate clay particles have drawn significant attention [1-11]. This is mainly because the addition of a small amount of clay particles (<5 wt.%) can show significant improvement in mechanical, thermal and barrier properties of the final composite without requiring special processing techniques. These composites are now being considered for applications ranging from food, electronic, automotive to aerospace industries. It is generally believed that the improvement of properties of nanoclay composites is directly related to the complete exfoliation of silicate layers in the polymer matrix. However, a processing technique that produces complete exfoliation is still a technical challenge. This may be due to the high viscosity of the resin and the strong tendency of nanoclay particles to agglomerate [3]. It is also reported that the degree of exfoliation depends on the structure of clays, curing temperature and curing agent [4]. The commonly used techniques to process clay-epoxy nanocomposites are: direct mixing and solution mixing [4-7]. However, these techniques produce intercalated or intercalated/exfoliated composites rather than exfoliated composites. Vaia et al. have suggested that the degree of exfoliation can be improved through the aid of conventional shear devices such as extruders, mixers, ultrasonicators etc. [8]. In the present study, a three-roll mill machine was used as a means of applying an external shearing force to exfoliate the stacked layers of silicate clay in the epoxy matrix. The correlation between degree of exfoliation and mechanical properties of the nanocomposites is also discussed here.

EXPERIMENTAL

A diglycidyl ether of bisphenol A (DGEBA) epoxy resin cured with methyl tetrahydrophthalic anhydride hardener from Vantico was used as the matrix. 1-Methylimidazole was used as an accelerator. They were in proportions of 100:90:1 (phr) respectively. The reinforcing nanoclay particle was Nanomer I.28E commercially available from Nanocor, Inc. It

is a natural montmorillonite (MMT) modified with a quaternary amine. It has a surface area of about 750 m^2/g, an aspect ratio of 200-500 and a platelet thickness of 1 nm [12].

In this study, a three-roll mill machine (Ross Bench Top Model 52M 2.5″ x 5″) was used to disperse and exfoliate the nanoclay particles in the epoxy matrix. First, the epoxy resin (DGEBA) was placed between the feed and center rolls. Once the rolls started moving, the clay particles were spread gradually on the resin to get direct and maximum contact with the rolls. The dispersion was achieved by the shear forces generated between the adjacent rolls. Compounding was carried out at room temperature for 3 h, with a rotation speed of 500 rpm and a feed rate of 120 g/h. It was observed that the mixture became viscous and opaque as the silicate layers dispersed and expanded with time. However, when the dispersion was completed, it produced a clear and transparent mixture. The final product from the mixer was then collected and mixed with hardener at 60 °C for 1 h on a hot plate. After adding accelerator and mixing for a few minutes, the solution was left overnight for degassing. After degassing, the mixture was poured in an aluminum mold and cured in an oven at 148 °C for 1 h. Nanocomposites were prepared with clay concentrations from 1 to 10 wt.%.

The tensile samples were prepared following ASTM standard D638-99 and tested on an Instron 8500 servohydraulic machine at a crosshead rate of 0.127 mm/min. Small angle X-ray scattering (SAXS) was performed on both clay and uncured nanocomposites, whereas, wide angle X-ray diffraction (WAXD) was performed on cured nanocomposites to evaluate the degree of clay exfoliation. SAXS was carried out on a Bruker AXS solid-state detector with CuKα radiation (λ = 1.541 Å) and operating at 30 kV and 13 mA. The 2D-diffraction pattern for each sample was collected for 1.5 h. WAXD was carried out on a RIGAKU diffractometer with CuKα radiation (λ = 1.541 Å) with a scanning speed of 0.5°/min and operating at 40 kV and 20 mA. The degree of exfoliation was further confirmed using a JEOL TEM operating at an accelerating voltage of 100 kV. The ultra-thin TEM sample with a thickness of 60 nm was cut using a microtome at room temperature. The fracture surfaces of tensile specimens were examined using a Hitachi S4500 FE scanning electron microscope. The fracture surfaces were gold coated prior to SEM investigation to avoid charging and were examined at 3 kV accelerating voltage.

RESULTS AND DISCUSSION

Figure 1a shows the SAXS patterns of 3 wt.% clay nanocomposites prepared using the mixer at 1000 rpm. The patterns reveal the effect of mixing time on intercalation. The stronger peak obtained after 1 h mixing compared to 0.5 h mixing implies that an ordered intercalated nanocomposite was formed. This also indicates that an optimum balance between residence time and level of shear is required to facilitate the intercalation/exfoliation and dispersion of layered silicates. The pure Nanomer shows a characteristic diffraction peak corresponding to the (001) plane at 2.4 nm (figure 1b). The increase in d-spacing from 2.4 to 3.34 nm (~40% higher) after mixing just for 0.5 h indicates that the mixer is highly efficient in making an intercalated nanocomposite within a short period of time.

In earlier investigations [13], nanocomposites were also prepared using both direct and solution methods. In the direct method, clays were mixed in an epoxy resin at 60 °C for 3 h using a magnetic stirrer and a hot plate. In the solution method, clays were dissolved in acetone for 3 h using an ultrasonic bath prior to mixing in an epoxy resin. Figure 1b shows a comparison in SAXS patterns of 3 wt.% nanocomposites under all processing methods. Both direct and solution methods show weaker peaks as well as lower d-spacing (3.17 and 3.25 nm respectively)

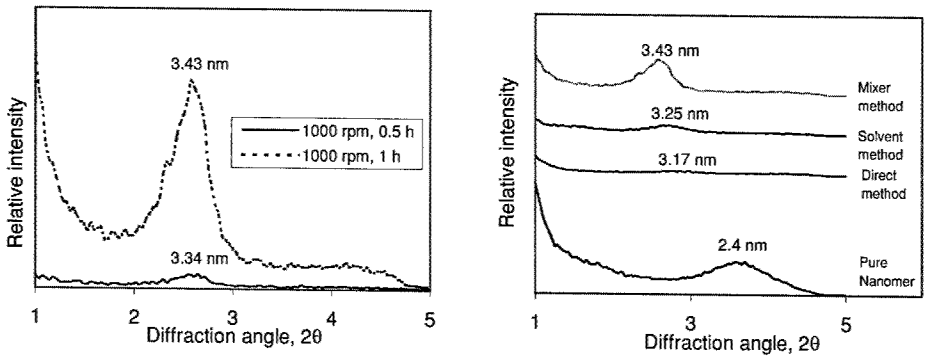


Figure 1. SAXS patterns of 3 wt.% clay nanocomposites. (a) Effect of mixing time (b) Effect of processing techniques.

compared to the mixer method (3.43 nm). It is thus clear that the shear force between adjacent rolls acts as a driving force to disperse and intercalate the clay platelets, whereas, no such shear effect is present in other methods. Furthermore, as the mixing time increases the viscosity of the mixture increases, which in turn may provide an extra shear force to disperse the clay platelets [11]. Therefore, it can be suggested that the mixer produces a good intercalated nanocomposite in a more efficient way compared to both direct and solution methods.

Figure 2 shows the WAXD patterns of nanocomposites containing 1 to 10 wt.% of clay prepared using the mixer for 3 h at 500 rpm. The nanocomposite with 1 wt.% clay shows a shallow peak with d-spacing of 3.66 nm, whereas, the nanocomposite with 2 wt.% of clay shows no peak which is indicative of an exfoliated structure. Since the viscosity of 2 wt.% clay nanocomposite is higher than that of 1 wt.% clay, the extra shear force in the former case may cause better exfoliation of clay platelets in the epoxy resin as suggested elsewhere [11]. However, the nanocomposites with higher clay content (>2 wt.%) show pronounced peaks from silicate basal planes (d_{001}) with d-spacing slightly lower than the composite containing 1 wt.% of clay. Therefore, the absence of peak in the case of 2 wt.% clay nanocomposite needs further confirmation by SAXS or low speed WAXD patterns. In general, the lower d-spacing at higher

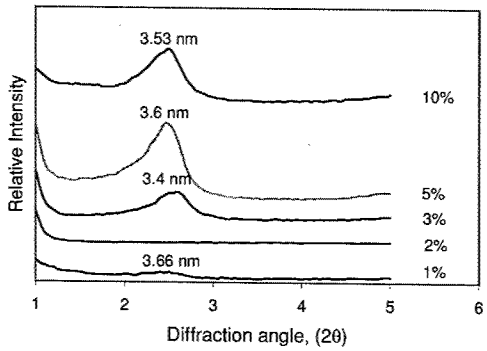


Figure 2. WAXD patterns of nanocomposites with varying clay contents.

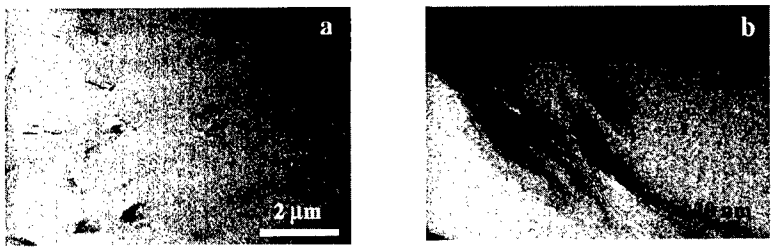


Figure 3. TEM images of 1 wt.% clay nanocomposite. (a) Low mag.: (b) high mag.

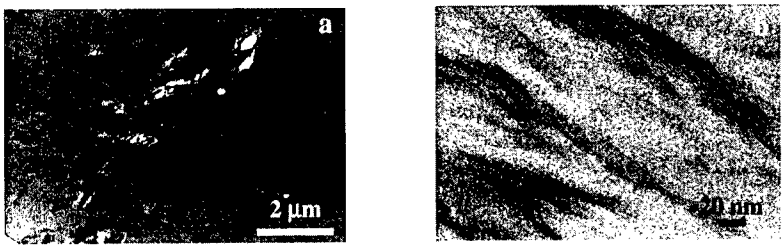


Figure 4. TEM images of 10 wt.% clay nanocomposite. (a) Low mag.: (b) high mag.

clay content is attributed to the increased intercalating sites with increased clay content that might impede the exfoliation of individual silicate layers [9]. Therefore, it can be suggested that the 2 wt.% clay nanocomposite shows complete exfoliation with respect to the shear force and residence time applied in this study, whereas, the addition of higher clay content produces ordered intercalated nanocomposite. It is of interest to mention that the compounding of Cloiste 30B (Southern Clay Products Inc.) in the same epoxy matrix and identical conditions shows complete exfoliation regardless of clay content [13]. This indicates that the degree of exfoliation depends on the type of clay and its surface modification.

The TEM images of nanocomposites containing 1 and 10 wt.% of clay are presented in figures 3 and 4 respectively. The dark lines in figures 3b and 4b are the intersections of silicate layers of 1 nm thick. Both composites show intercalated structures with an average distance between two platelets of 3.6 nm and therefore, in good agreement with the WAXD results (figure 2). Figure 4a shows nano voids inside the silicate clay layers and this is an indication of improper degassing due to high viscosity of the mixture at high clay concentrations.

The variation of elastic modulus with the percentage of clay content is shown in figure 5. It is found that the modulus of the composite increases continuously with increasing concentration of clay. An improvement of about 34% is observed just for an addition of 2 wt.% of clay. However, the improvement of only 42 and 52% for an addition of 5 and 10 wt.% of clay respectively, signifies that the rate of improvement decreases at higher concentrations. The improvement in elastic modulus can be attributed to the well dispersion of nano-size clay particles as well as to the good interfacial adhesion between the particles and the epoxy matrix [3]. Therefore, the clay particles will restrict the mobility of polymer chains under loading. The orientation of silicate

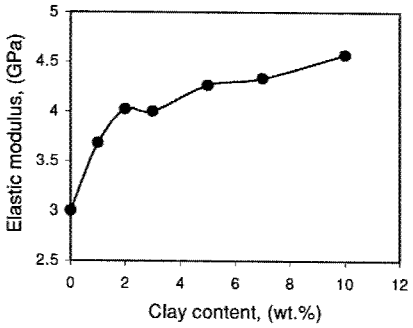


Figure 5. Effect of clay content on elastic modulus of clay/epoxy nanocomposites.

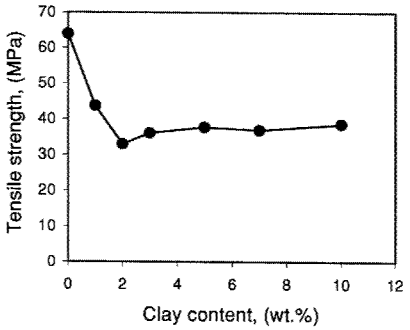


Figure 6. Effect of clay content on tensile strength of clay/epoxy nanocomposites.

layers and polymer chains with respect to the loading direction can also contribute to the reinforcement effects [10]. However, the decreasing rate of elastic modulus improvement with higher clay content can be attributed to the presence of unexfoliated aggregates [10].

Figure 6 shows the variation in tensile strength with the percentage of clay content. Unlike the elastic modulus, nanocomposites with any clay concentration show a lower tensile strength than the pure epoxy. This is similar to the results reported by Zerda et al [5] but in contrast to the tensile strength values of nanocomposites reported elsewhere [3,10,11]. However, the failure of all nanocomposites at strengths lower than the pure epoxy can be assumed to be compounding process related. As mentioned before, the compounding process of nanoclay in an epoxy matrix with a three-roll mill produces a highly viscous and foamy material, and the higher the clay content the higher the viscosity. The Nanomer particles treated with ammonium ions also accelerate the curing process of epoxy resin [12]. Therefore, the mixture becomes highly viscous with time and hinders the complete degassing before casting. It is also observed that the degassing problem becomes critical for nanocomposites containing more than 5 wt.% of clay, which in turn, produces nanocomposites with nano to micro-level voids. The presence of nano-voids in 10 wt.% clay nanocomposites (figure 4a) confirms this. The other source of voids could be trapped air during pouring of highly viscous material onto the mold. The failure of all specimens at the same strength level (30 to 40 MPa) also indicates the possibility of crack

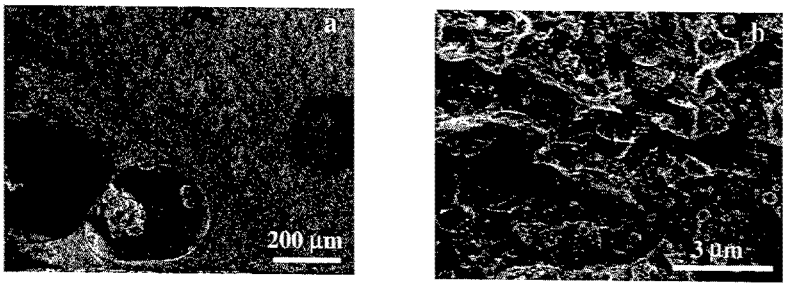


Figure 7. SEM fractographs of 10 wt.% clay nanocomposite.
(a) Crack initiation from voids (b) Fracture surface at higher magnification

initiation from similar type of defects. Therefore under tensile loading, cracks should initiate from these tiny voids and cause the specimen to fail at relatively low strain. Figure 7a confirms the crack initiation from such micro-voids during tensile testing of a 10 wt.% clay/epoxy nanocomposite. Figure 7b shows the same fracture surface at higher magnification. The bright spots correspond to clay aggregates and finely dispersed in the material. This observation further confirms the incomplete exfoliation or inevitable aggregation of clay layers in this nanocomposite. The presence of such clay aggregates in the microstructure of nanocomposite is also reported by Kornmann et al. [7]. These loose clusters or unexfoliated nanoparticles in the matrix may act as additional crack initiation sites by splitting up easily under applied load [5]. A better degassing and exfoliation technique is, therefore, very important and is now under investigation to improve the tensile strength of clay/epoxy nanocomposites.

CONCLUSIONS

The compounding of nanoclay composites with a three-roll mill machine is found to be highly appealing and environmentally friendly since no solvent is required. Compared to direct and solution methods, the mixer is found highly efficient in achieving a higher degree of intercalation/exfoliation within a short period of time. It is also found that the longer the mixing time, the higher the degree of intercalation. The complete exfoliation in 2 wt.% clay nanocomposite indicates that an optimum balance between clay content, residence time and level of shear is required to facilitate the exfoliation and dispersion of layered silicates. The elastic modulus of the composites is found to increase with increasing concentration of clay content. The highest rate of improvement in modulus in 2 wt.% clay nanocomposite confirms the direct relation between degree of exfoliation and mechanical properties in such systems. However, the apparent lower tensile strength of the nanocomposites with respect to pure epoxy can be attributed to the clustering of nanoparticles as well as to the nano to micro-size voids in the microstructure generated due to inadequate degassing of the mixture.

ACKNOWLEDGEMENT

The authors are thankful to Dr. Didier Lefebvre for his advice and help with regard to three-roll mill machine.

REFERENCES

1. Z. Wang, and T.J. Pinnavaia, *Chem. Mater.* **10**, 3769 (1998).
2. R.A. Vaia, H. Ishii and E.P. Giannelis, *Chem. Mater.* **5**, 1694 (1993).
3. C.L. Wei, M.Q. Zhang, M.Z. Rong and K. Friedrich, *Comp. Sci. Tech.*, **62**, 1327 (2002).
4. L. Jiankun, K. Yucai, Q. Zongneng, and Y. Xiao-Su, *J. Polym. Sci: Part B*, **39**, 115 (2001).
5. A.S. Zerda, and A.J. Lesser, *J. Polym. Sci: Part B*, **39**, 1137 (2001)
6. P.C. LeBaron, Z. Wang, and T.J. Pinnavaia, *J. App.Clay Sci.*, **15**, 11 (1999).
7. X. Kornmann, H. Lindberg, and L.A. Berglund, *Polymer* **42**, 1303 (2001).
8. R.A. Vaia, K.D. Jandt, E.J. Kramer and E.P. Giannelis, *Chem. Mater.*, **8**, 2628 (1996).
9. P.H. Nam, P. Maiti, M. Okamoto, T. Kotaka, N. Hasegawa and A. Usuki, *Polymer*, **42**, 9633 (2001).
10. X. Liu and Q. Wu, *Polymer*, **42**, 10013 (2001).
11. T.D. Fornes, P.J. Yoon, H. Keskkula and D.R. Paul, *Polymer*, **42**, 9929 (2001).
12. Nanocor, Inc., Technical data.
13. A. Yasmin, *Unpublished work.*

Mat. Res. Soc. Symp. Proc. Vol. 740 © 2003 Materials Research Society

The Growth of Bamboo-Structured Carbon Tubes Using a Copper Catalyst

B.L. Farmer, D.M. Holmes, L.J. Vandeperre, R.J. Steam and W.J. Clegg
Ceramics Laboratory, Department of Materials Science and Metallurgy,
University of Cambridge, Pembroke Street, Cambridge, CB2 3QZ.

ABSTRACT

Catalytic decomposition of methane has been used to grow bamboo-structured carbon tubes at temperatures ranging from 1233 K to 1291 K. No tube growth was observed at temperatures less than 1233 K, whilst above 1291 K pyrocarbon was the dominant product. It is shown that the average size of the copper catalyst particles was influenced by the reaction temperature, with the reciprocal of the maximum size of the copper particle decreasing linearly with temperature. This is consistent with the idea that the melting point can be reduced by surface energy effects. Observations show that under the conditions here the catalyst particle penetrates into the carbon fibre and a mechanism is proposed for development of the bamboo structure based upon the energy changes that take place.

INTRODUCTION

A wide range of carbon structures can be formed by the catalytic decomposition of hydrocarbons or the disproportionation of CO including various types of tubes and fibres as well as shells and stacks. In this paper hollow carbon fibres grown from copper catalyst particles are described. The most striking feature of these bamboo fibres is the repeating nature of the structure due to the formation of a transverse wall of carbon across the tube at regular intervals. Several authors have suggested that this structure might involve capillary forces causing the liquid or solid metal catalyst to move suddenly up the carbon tube [1-5], although the detailed mechanism is not understood. In this paper we describe some experiments using a copper catalyst and how capillary forces may give rise to such a sudden movement of the liquid catalyst enabling the bamboo structure to form.

EXPERIMENTAL DETAILS

A copper catalyst was produced by precipitation from a solution of hydrated copper nitrate, $Cu(NO_3)_2 \cdot 3H_2O$, and ammonium hydrogen carbonate, NH_4HCO_3. The precipitate was removed using a centrifuge and dried at 378 K for 12 hours. The resulting particles were then ground with a pestle and mortar before placing a small quantity on an alumina substrate. This was placed in a tube furnace and calcined at 673 K in air for 4 hours before purging with Ar then H_2. The furnace was then heated to the desired reaction temperature. At 25 K below the final temperature CH_4 was introduced. The flow rates for H_2 (99.995% pure) and CH_4 (99.999% pure) were 1.4 l min^{-1} and 0.2 l min^{-1} respectively through a tube with a 60 mm internal diameter. The tube was held at constant temperature for 1 hour and then cooled under flowing Ar. The carbon grown was examined using a Jeol JSM-6340F field emission scanning electron microscope (SEM) and a Jeol JSM 2000FX transmission electron microscope (TEM). For SEM the samples were examined directly and for TEM the carbon products were scraped off the substrates on to gold supported amorphous carbon grids.

RESULTS AND DISCUSSION

Carbon fibres only grew at temperatures between 1233 K and 1291 K. At high reaction temperatures pyrocarbon formed, whilst below 1233 K no reaction occurred. Within this temperature range the lengths of the fibres after 1 hour were approximately 2 μm at 1233 K, but were many hundreds of micrometers at 1291 K. However the most striking feature of the fibres that formed was that they had walls lying perpendicular to the direction of growth forming a regular cell structure which can be seen in figure 1(a). At a given temperature, the shape of the segments and the segment aspect ratio was independent of fibre diameter.

The copper catalyst particles could be seen at the ends of the fibre, as can be seen in detail in figure 1(b). The catalyst particles have a diameter larger than the fibre with which they are associated and there is a fixed ratio between the catalyst particle diameter and the fibre diameter, see figure 2.

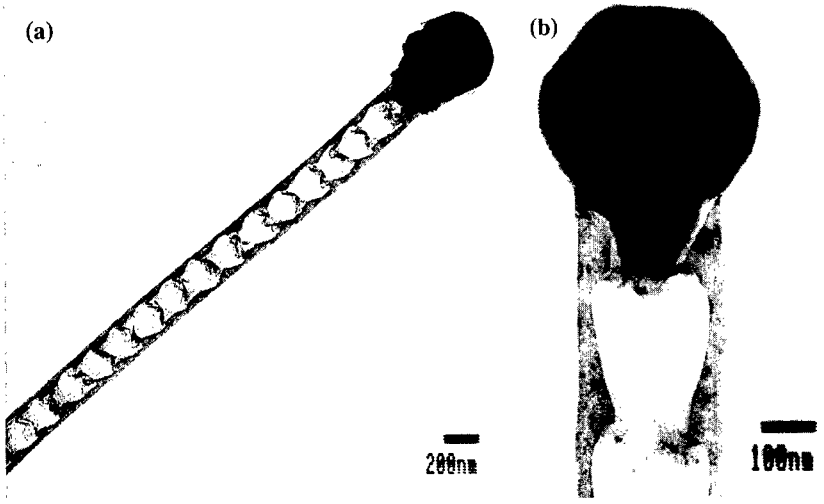


Figure 1(a). A TEM micrograph of a bamboo fibre grown at 1278 K showing the repeating internal structure and a copper catalyst particle at the tip. **Figure 1(b).** A TEM micrograph showing a catalyst particle with a conical shaped tail sat inside a conical carbon cell grown at 1278 K.

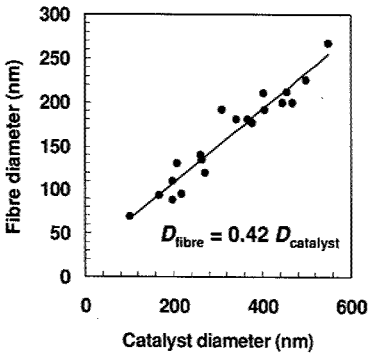


Figure 2. The variation of the fibre diameter with the diameter of the catalyst particle for fibres grown at 1278 K.

The maximum size of the catalyst particles that were observed increased with increasing temperature as shown in figure 3. Extrapolating the experimental data gives an intercept on the abscissa of 1356 K compared with the bulk melting temperature of copper of 1357 K. These observations are consistent with the idea that the catalyst particles are molten at the reaction temperature, where the suppression in melting point being associated with effects due to surface tension.

Increasing the reaction temperature decreases the diameter of the fibre that forms on a given volume of catalyst particle, the fibre size being approximately 0.64 of the catalyst particle diameter at 1233 K but only 0.42 of the catalyst particle diameter at 1291 K.

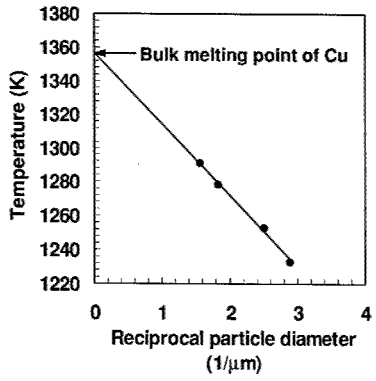


Figure 3. A plot of the maximum observed catalyst particle diameters over a range of temperatures plotted as a reciprocal versus temperature. The line of best fit intercepts the abscissa at a temperature of 1356 K, close to the bulk melting temperature of pure copper of 1357 K.

Figure 1(b) shows that the catalyst particle does not just sit as a spherical particle on top of the fibre, but has a 'tail' that penetrates into the cell structure. The surface area of the overall particle is therefore slightly greater than it would have been if it had remained completely spherical. This can only occur if there is a reduction in the energy of the surfaces of the particle that is when

$$\Delta A_{\text{particle}}\gamma_{Cu/g} + \Delta A_{\text{tail}}\left(\gamma_{Cu/C} - \gamma_{C/g}\right) \leq 0 \qquad (1)$$

where $\gamma_{Cu/g}$ is the energy of the interface between copper and the gaseous environment, $\gamma_{C/g}$ is the energy of the interface between carbon fibre and the gaseous environment, $\gamma_{Cu/C}$ is the energy of the surface between copper and carbon, $\Delta A_{\text{particle}}$ is the change in area of the spherical portion of the particle and ΔA_{tail} is the area of the surface of the tail that was formed within the tube.

From the above expression three types of behaviour are evident. Where $\gamma_{Cu/g} < (\gamma_{Cu/C} - \gamma_{C/g})$, the catalyst will form a spherical particle at the end of the fibre. If instead $\gamma_{Cu/g} >> (\gamma_{Cu/C} - \gamma_{C/g})$ the catalyst will be contained entirely within the carbon tube. There is also an intermediate range of surface energies where equation 1 is obeyed, when the liquid flowing into the tube causes an initial reduction in the energy of the system as the reduction in surface energy outweighs the increase in surface area. However, as the liquid extends further into the narrowing tube, the increase in surface area eventually outweighs the change in surface energies, giving a curve as shown in figure 5, so that a tail of equilibrium length, l_e, is predicted to form. The extent of this penetration depends on the relative surface energies and on the internal shape of the tube.

Simply allowing the catalyst particle with its tail of equilibrium length to move upward at a constant rate would not give the observed cell structure, but rather a solid fibre or possibly an empty tube. The formation of the cell structure in these fibres would seem to require that the tail expanded and contracted whilst the carbon fibre was growing.

One might therefore consider a possible mechanism for the formation of the bamboo structure as follows. Consider a growing carbon tube containing truncated conical cells, as observed in figure 1(b), with a catalyst particle on top and with the surface energies such that a tail of an equilibrium length, l_e, is formed at time t_0, as shown in figure 5. The transverse wall can form by the precipitation of carbon on the underside of the drop at t_1 as shown in figure 6, lowering the overall energy of the system from its initial value at t_0. By t_2 further precipitation causes lengthening of the tube whilst also reducing the internal dimensions elongating the metal particle so that the overall energy of the surfaces further increases.

Eventually the increase in the energy of the surfaces caused by this growth of the tube and reduction of the internal dimension is such that it becomes energetically favourable for the tail to reform and the process begins again. This overall process allows the formation of the transverse wall and for the liquid adjacent to it to move rapidly up the tube giving a repeating process.

All of the changes in the energy of the surfaces are measured from the situation where the catalyst particle sits on top of the carbon tube as a sphere.

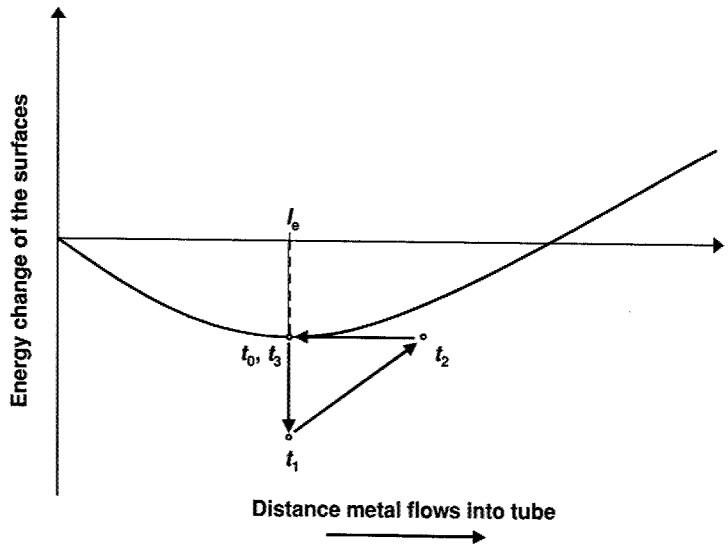


Figure 5. The change in energy of the surfaces during the steps shown in figure 6. The curve shows the energy change that occurs when the liquid catalyst flows into the initial carbon cone. The energy and position of the initial equilibrium tail formed is at t_0. This energy is reduced by the precipitation of the transverse wall at t_1. Further precipitation causes the dimensions of the drop to change until eventually the energy of the surfaces is equal to that at t_0, whereupon the liquid moves rapidly up the tube. The position of zero energy change is where the droplet forms a sphere on top of the fibre.

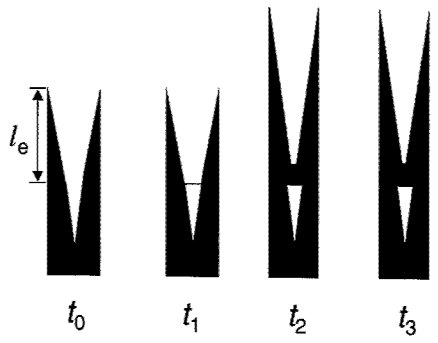


Figure 6. A schematic representation of a sequence of events during the growth of a bamboo carbon fibre.

The process shown in figure 5 illustrates a particular case where the new tail formed is of the same dimension as that of the original one and the growth process is therefore at a steady-state. If the initial conditions are that steady-state growth does not occur immediately, it is found that the cell changes shape until a steady-state is reached. For a fixed catalyst volume and fibre diameter, the cell shape produced during steady state growth is dependent on the ratios of the surface energies and the rate at which the tube lengthens compared with the rate at which the internal dimensions decrease, and it is independent of the shape of starting cone used.

This repeating process will only work within certain limits of surface energies, tube dimensions and geometries. For instance, the process can break down if the rate at which the tube lengthens compared with the rate at which the internal dimensions decrease is very high. When this occurs the energy of the system at t_2 is never greater than the energy at t_3 and there is no driving force for the catalyst to move from the position at t_0 to that at t_3, so that the catalyst particle will tend to completely envelope within the tube. Also, if the internal dimensions are very small, the energy changes required to form a tail are much greater, so that solid fibres and tubes tend to form instead. This is consistent with observations elsewhere[3].

CONCLUSIONS

The growth of hollow bamboo fibres using a copper catalyst in CH_4 and H_2 gas at temperatures in the range 1233 to 1291 K has been studied. Observation of the size of the largest observed catalyst particle suggests that the copper is molten during fibre growth. A model based upon changes of the energies of the surface has been proposed which gives a mechanism for the formation of bamboo-structured carbon fibres and which also shows that transitions to tubes and fibres can be easily obtained.

REFERENCES

1. Y. Li, J. Chen, Y. Ma, J. Zhao, Y. Qin, and L. Chang, Chem. Commun. 1141-1142 (1999).
2. C. J. Lee and J. Park, App. Phys. Lett. **77**, 3397-3399 (2000).
3. J. Chen, Y. Li, Y. Ma, Y. Qin, and L. Chang, Carbon **39**, 1467-1475 (2001).
4. X. X. Zhang, Z. Q. Li, G. H. Wen, K. K. Fung, J. Chen, and Y. Li, Chem. Phys. Lett. **333**, 509-514 (2001).
5. L. T. Chadderton and Y. Chen, J. of Cryst. Growth **240**, 216-169 (2002).

Mat. Res. Soc. Symp. Proc. Vol. 740 © 2003 Materials Research Society

Characterization of Mechanical Deformation of Nanoscale Volumes

Christopher R. Perrey, William M. Mook, C. Barry Carter*, William W. Gerberich
Department of Chemical Engineering and Materials Science
University of Minnesota, 421 Washington Ave. S.E., Minneapolis, MN 55455
* corresponding author: carter@cems.umn.edu

ABSTRACT

The mechanical properties of nanoscale volumes and their associated defect structure are key to many future applications in nanoengineered products. In this study, techniques of mechanical testing and microscopy have been applied to better understand the mechanical behavior of nanoscale volumes. Nanoindentation has been used to investigate important mechanical material parameters such as the elastic modulus and hardness for single nanoparticles. New sample preparation methods must be developed to allow the necessary TEM characterization of the inherent and induced defect structure of these nanoparticles. Issues of chemical homogeneity, crystallinity, and defect characteristics at the nanoscale are being addressed in this study. This integration of investigative methods will lead to a greater understanding of the mechanical behavior of nanostructured materials and insights into the nature of defects in materials at the nanoscale.

INTRODUCTION

Testing and characterization of small volumes has become increasingly important for numerous applications. For instance, the mechanical properties of silicon components in micro-electromechanical systems (MEMS) can depend on the specific small-scale geometries being used [1]. This dependence needs to be understood to predict failure modes and to improve both device reliability and design [2]. Both molecular dynamic simulations [3] and indentation experiments of small volumes [4-6] indicate that nanostructured materials can support larger stresses than their bulk counterparts. This phenomena is known as the indentation size effect [7-9]. An explanation of this effect is the dislocations that develop at high pressures are confined by the small volume or nanostructure being probed and are forced close together; thus resulting in extremely high stresses.

The consequences of these very high internal stresses have potential for the design of nanostructured materials with enhanced mechanical properties. However, to evaluate properties via nanoindentation, it is necessary to accurately determine contact area, crystal orientation, and the inherent and induced defect structure within the small volume. Ideally, it should be possible to nondestructively image an individual nanoparticle before and after indentation using transmission electron microscopy (TEM). The results can then be compared to molecular dynamic simulations of equal volume with identical composition, structure and boundary conditions. This study is the first step in that process and details the direct mechanical response of single nanospheres of silicon with radii between 20 to 50 nm, as well as the characterization of similar nanospheres using TEM.

EXPERIMENTAL

The particles studied here are synthesized by injecting vapor-phase $SiCl_4$ into an Ar-H_2 thermal plasma, which is expanded to low pressure through a nozzle, driving homogenous nucleation of silicon nanoparticles [10]. This synthesis approach has previously been used in a process known as hypersonic plasma particle deposition [11] to deposit continuous SiC films with hardnesses in the range 30-40 GPa [12]. In the work reported here, the substrate for continuous film deposition is removed, and the particles instead enter an aerodynamic lens system fully described by Liu [13] and Di Fonzo [14], forming a beam of nanoparticles. This focused beam of nanoparticles was rastered across both a sapphire wafer and TEM support films mounted on a computer-controlled substrate translation system, thereby depositing lines of nanoparticles.

Typically after one pass of the sapphire substrate and TEM support film, the deposited line is tens of microns wide and a few microns high at its center. A sparse distribution of nanoparticles can be accessed near the edge of the line with a scanning probe microscope (SPM) based nanoindenter (Hysitron TriboScope™, Hysitron Inc., Edina, MN). Mechanical characterization of an isolated silicon nanoparticle is preformed by indenting (i.e. compressing) the nanoparticle with a diamond tip. The diamond tip of the nanoindenter has a 1000 nm radius of curvature and an elastic modulus of 1100 GPa while the sapphire substrate has a modulus of 450 GPa. Since the radius of curvature of the tip is orders of magnitude greater than the nanoparticle radius, it is assumed the particle is compressed uniaxially between two rigid, flat platens. The TEM analysis was performed using a Philips CM30 and a Philips CM200 field-emission TEM operated in scanning TEM (STEM) mode for chemical analysis.

RESULTS

The spherical nature of the nanoparticles was confirmed using TEM. Figure 1a shows a bright-field TEM image of a typical Si nanoparticle. The spherical shape is evident, and the selected-area diffraction pattern of this particle is in agreement with the [$1\bar{1}2$] zone

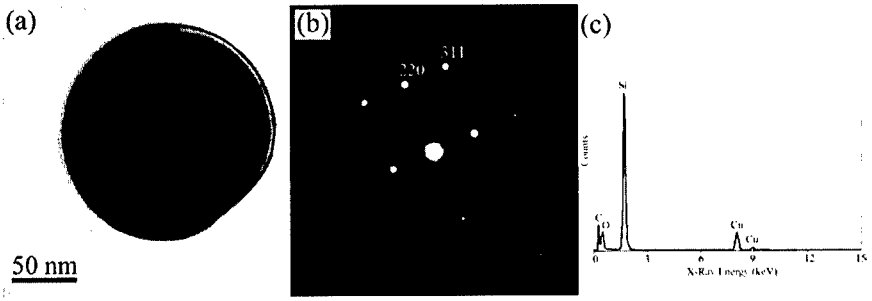


Figure 1: Nanosphere observations. (a) Bright-field TEM image showing an 80 nm radius Si nanosphere without obvious defects. (b) The selected area diffraction pattern from this particle, consistent with the [$1\bar{1}2$] zone axis of Si. (c) XEDS analysis of this particle confirms it is Si; the Cu and C peaks are from the TEM support grid.

of diamond-cubic Si (Figure 1b). The chemical identity of the nanoparticle was confirmed using X-ray energy dispersive spectrometry; the resulting spectrum is shown in Figure 1c. The Si and O peaks originate from the nanoparticle, while the C and Cu signals are from the C support film and Cu grid.

A thin layer of non-crystalline material surrounding the surface of the nanoparticle is evident in Figure 1a. The size and chemical identity of this surface layer was investigated using analytical TEM. Figure 2a is an annular dark-field STEM image of isolated silicon nanoparticles from this deposition. In this image, the crystalline material diffracts strongly and appears bright, while the amorphous layer around the particle exhibits less intensity. The line that is drawn across the nanoparticle denotes the location of an elemental line scan, where the electron beam is moved a discrete distance along the line and an electron energy loss spectrum (EELS) is collected for each point. In this manner, a profile of the elemental signals along the line can be created using EmiSpec Vision™ software. These profiles are shown in Figure 2b for Si and O for a line length of 150 nm and 1 sampling point/nm. It is evident that the oxygen signal is the greatest at the edges of the particle, where the largest amount of amorphous layer is sampled by the electron beam without signal dampening from the bulk crystalline Si nanoparticle. The width of the oxide layer is approximately 5-15 nm.

Individual nanoparticles were scanned and indented repeatedly with the nanoindenter at increasing loads. An example of load-displacement curves for a nanoparticle originally 50 nm in height (i.e. diameter) can be seen in Figure 3a. It should

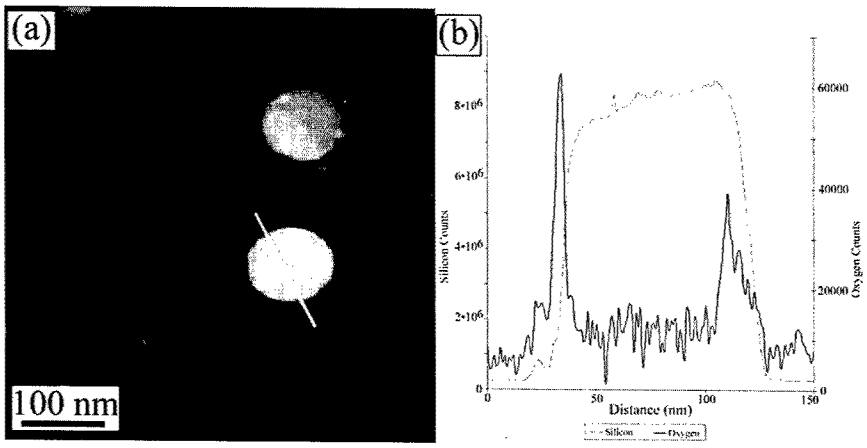


Figure 2: PEELS STEM analysis. (a) Annular dark field STEM image denoting the location of an analytical line scan across a Si nanoparticle. (b) Electron energy loss spectra for Si and O as a function of distance along the line scan. The elemental signals indicate the presence of a 5-15 nm thick oxide layer surrounding the Si nanoparticle core.

be noted that the particle was scanned and its height was recorded before each indentation. The associated SPM profiles of the particle show the initial and final cross sectional scans in Figures 3b and 3c respectively. In these scans, the lateral dimension of the nanoparticle of approximately 1 μm is an artifact due to the large tip radius. After repeated indentations, the nanoparticle has fractured as seen in the final cross section in Figure 3c.

The hardness of a nanoparticle was determined by dividing the maximum indentation load by the contact area. At maximum load, the sphere has deformed both elastically and plastically. Therefore the contact area will be somewhere between Hertzian (perfectly elastic) and geometric (perfectly plastic) treatments. A modified version of geometric contact was chosen here because it will overestimate the area, thus providing a conservative estimate of nanoparticle hardness. This contact area was also in close agreement with molecular dynamic simulations of similar silicon nanospheres [15]. The normal geometric contact radius, $a_{geom.}$, is divided by two because contact is occurring at both the top and bottom of the nanoparticle where

$$a_{geom.} = \left[\delta R - \frac{\delta^2}{4}\right]^{1/2} \quad ; \quad \delta = \delta_p + \delta_{max} \ , \ \delta_p = d_o - d \qquad \text{Eq. 1}$$

such that δ is the indentation depth and accounts for previous particle deformation, R is the initial particle radius, d is the particle height before indentation, d_o is the initial spherical particle height, δ_p is the previous plastic displacement (deviation from the sphere), and δ_{max} is the maximum displacement during the indentation. Therefore, contact area is just $A_c = \pi(a_{geom.})^2$ and hardness is $H = P_{max}/A_c$, where P_{max} is the maximum load for the given run.

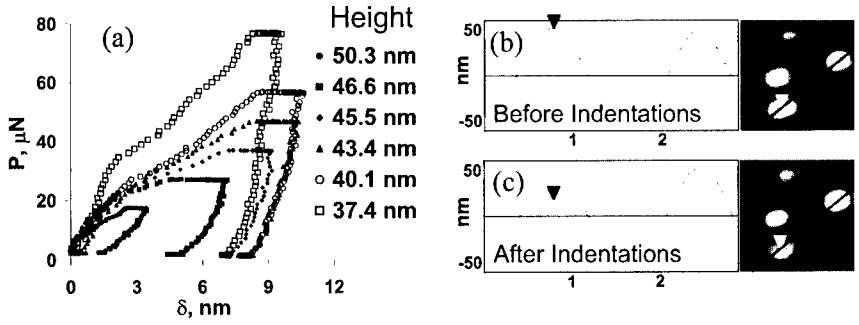


Figure 3: Nanoparticle mechanical test data. (a) Repeated indentation of single silicon nanoparticle which was originally 50 nm in diameter. (b) Initial SPM cross section of particle before indentations. (c) Final fractured particle cross section after indentations were complete.

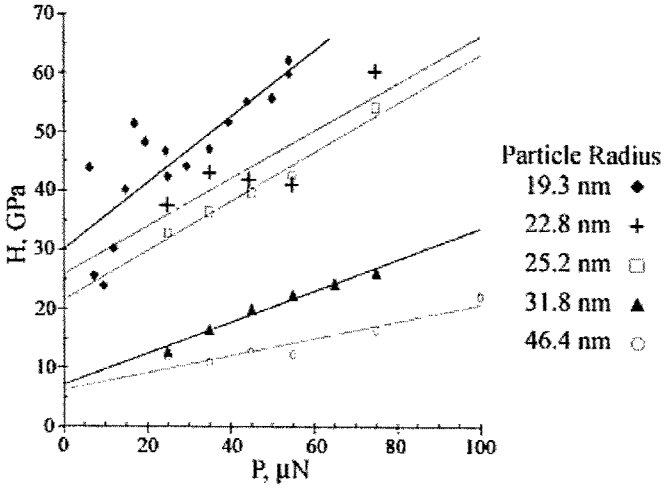


Figure 4: Hardening curves for five nanoparticles of increasing size. Trend lines are a least squares fit to the data.

Hardening curves for individual nanoparticles are shown in Figure 4. A least squares fit has been added to the figure to identify experimental trends. Five particles of various diameters are repeatedly indented at increasing loads similar to the 50 nm particle data shown in Figure 3. Each point on the graph represents an individual indentation run. It is proposed that as the sphere deforms plastically, discrete dislocation loops are nucleated and glide toward the sphere's center. The oxide layer covering the nanoparticle prevents the dislocation loops from gliding through the sphere and exiting the other side. Consequently, the hardness of a nanoparticle that is indented repeatedly will increase due to the increasing dislocation density within it. Hardness values at zero load can be interpreted as the intrinsic hardness of a defect-free particle. As particle sizes decrease, both intrinsic hardness and hardening rate increase.

CONCLUSIONS

This work has shown that mechanical phenomena at the nanoscale is an area that contains many features. Using silicon nanospheres, superhard behavior has been demonstrated. This is additional evidence for scale effects in small volumes. When these results are combined with mechanical deformation theory and computational results, connectivity from the nm to the mm scale can be achieved. The application of TEM to the characterization of structure and chemistry for these nanoparticles provides further insights for refinement of models and theory for future work.

ACKNOWLEDGEMENTS

This work was supported by the National Science Foundation under grant DMI-0103169 and an NSF-IGERT program through grant DGE-0114372. The authors

gratefully acknowledge the members of the University of Minnesota's HPPD program, particularly A. Gidwani, R. Mukherjee, T. Renault, J. V. R. Heberlein, S. L. Girshick, and P. H. McMurry for many helpful discussions. CRP and CBC thank Jim Bentley from Oak Ridge National Laboratory for assistance with the analytical TEM. Research at the ORNL SHaRE Collaborative Research Center was supported by the Division of Materials Sciences and Engineering, U.S. Department of Energy, under contract DE-AC05-00OR22725 with UT-Battelle, LLC.

REFERENCES

1. D.A. LaVan and T.E. Buchheit. Conference on MEMS Reliability for Critical and Space Applications - SPIE 1999;**3880**: 40-44.
2. D.M. Tanner, N.F. Smith, L.W. Irwin, W.P. Eaton, K.S. Helgesen, J.J. Clement, W.M. Miller, J.A. Walraven, K.A. Peterson, P. Tangyunyong, M.T. Dugger and S.L. Miller. (January 2000), Sandia National Laboratory.
3. V. Yamakov, D. Wolf, M. Salazar, S.R. Phillpot and H. Gleiter. Acta Materialia 2001;**49**: 2713-2722.
4. J.J. Kim, Y. Choi, S. Suresh and A.S. Argon. Science 2002;**295**: 654.
5. S.P. Baker, R.P. Vinci and T. Arias. MRS Bulletin 2002;**27**: 26.
6. S. Veprek and A.S. Argon. Surfaces and Coatings Technology 2001;**146-147**: 175-182.
7. W.D. Nix and H. Gao. Journal of the Mechanics and Physics of Solids 1998;**46**: 411-425.
8. M.F. Horstemeyer, M.I. Baskes and S.J. Plimpton. Acta Materialia 2001;**49**: 4363.
9. W.W. Gerberich, N.I. Tymiak, J.C. Grunlan, M.F. Horstemeyer and M.I. Baskes. Journal of Applied Mechanics 2002;**69**: 433-442.
10. N. Rao, B. Michael, D. Hansen, C. Fandrey, M. Bench, S. Girshick, J. Heberlein and P. McMurry. Journal of Materials Research 1995;**10**: 2073.
11. N.P. Rao, N. Tymiak, J. Blum, A. Neuman, H.J. Lee, S.L. Girshick, P.H. McMurry and J. Heberlein. Journal of Aerosol Science 1998;**29**: 707.
12. N. Tymiak, D.I. Iordanoglou, D. Neumann, A. Gidwani, F.D. Fonzo, M.H. Fan, N.P. Rao, W.W. Gerberich, P.H. McMurry, J.V.R. Heberlein and S.L. Girshick. (1999) in 14th International Symposium on Plasma Chemistry (M. Hrabovsky, M. Konrad and V. Kopecky, eds.), Vol. **4**, pp. 1989, Institute of Plasma Physics, Academy of Sciences of the Czech Republic, Prague.
13. P. Liu, P.J. Ziemann, D.B. Kittleson and P.H. McMurry. Aerosol Science and Technology 1995;**22**: 293.
14. F.D. Fonzo, A. Gidwani, M.H. Fan, D. Neumann, D.I. Iordanoglou, J.V.R. Heberlein, P.H. McMurry, S.L. Girshick, N. Tymiak, W.W. Gerberich and N.P. Rao. Applied Physics Letters 2000;**77**: 910-912.
15. W.W. Gerberich, W.M. Mook, C.R. Perrey, C.B. Carter, M.I. Baskes, R. Mukherjee, A. Gidwani, J.V.R. Heberlein, P.H. McMurry and S.L. Girshick. Journal of the Mechanics and Physics of Solids **(in press)**.

Mat. Res. Soc. Symp. Proc. Vol. 740 © 2003 Materials Research Society

Coating of Ultrathin Polymer Films on Carbon Nanotubes by a Plasma Treatment

Peng He, Jie Lian[1], Donglu Shi, Lumin Wang[1], David Mast[2], Wim J. van Ooij, and Mark Schulz[3]
Dept. of Chemical and Materials Engineering, [2]Dept. of Physics, [3]Dept. of Mechanical Engineering, University of Cincinnati
Cincinnati, OH 45221
[1]Dept. of Nuclear Engineering and Radiological Science, University of Michigan
Ann Arbor, MI 48109

ABSTRACT

Ultrathin polymer films have been deposited on both single- and multi-wall carbon nanotubes using a plasma polymerization treatment. HRTEM experiments showed that an extremely thin film of the pyrrole layer (2-7 nm) was uniformly deposited on the surfaces of the nanotubes including inner wall surfaces of the multi-wall nanotubes. Time-of-Flight Secondary ion mass spectroscopy (TOFSIMS) experiments confirmed the nanosurface deposition of polymer thin films on the nanotubes. The deposition mechanisms and the effects of plasma treatment parameters are discussed.

INTRODUCTION

Nanotubes are used in many applications because of their desirable bulk properties. Unfortunately, the surface of the nanotubes is often not ideal for the particular application. The ability to deposit well-controlled coatings on nanotubes would offer a wide range of technological opportunities based on changes to both the physical and chemical properties of the nanotubes. Atomic layer controlled coatings on nanotubes, for example, would allow nanotubes to retain their bulk properties but yield more desirable surface properties. These ultrathin coatings could act to activate, passivate or functionalize the particle to achieve both desirable bulk and surface properties. For instance, nanophase polymers typically consist of a hard phase dispersed in a soft phase to achieve specific enhanced properties. "Hard" nanotube serves as the hard phase. By manipulation of the physical, chemical and optical properties of the "hard" phase nanotubes, tunable materials properties can be achieved. A key aspect of being able to manipulate the properties of the nanotubes is the surface treatment of the nanotubes by various processing techniques. This technology produces high-tech properties with the low cost normally associated with plastics.

Another example is the consolidation at low temperatures via so-called nanoglue. When an adhesive thin film is coated on the nanotube surfaces, these nanotubes can be consolidated at a temperatures. However, this method requires the adhesive thin film to be extremely thin and uniform. Therefore the volume percent of the polymer is limited to only a few percent. In this way, the bulk mechanical properties can be maintained.

Depositions of ultrathin films with unique physical, chemical and biological properties on nanotubes can also have great potential in many engineering applications.

On the surface of the nanotubes, an extremely thin layer of polyacrylic film can be coated by a plasma treatment. The polyacrylic film will react with metallic ions in water. As a result of the high surface-to-volume ratio of these nanostructured clusters, the efficiency of ion exchange in the water flux is much higher than other types of traditional reactors. Therefore, tailoring the nanotube surface structure becomes of ultra importance in today's nanotechnology. The broad range of these properties due to nano surface structures include electro-magnetic conductivities, uniformity, index of refraction, high reflectance, low absorption, stress, and the adhesion of the film structure to the substrate. All these properties are determined by new parameters such as interfaces between the ultrathin film and the nanotube, nanotube surface morphology, and structures of the film.

EXPERIMENTAL DETAILS

In this experiment, we used Pyrograf III PR-24-PS and PR-24-HT (17) nanotubes as substrates. These are the multi-wall carbone nanotubes (MWCNT). Single-wall carbon nanotubes (SWCNT) were also used for plasma treatment. These nanotubes have the same structure and purchased from Pyrograf products Inc. The schematic diagram of the plasma reactor for thin film deposition of nanotubes is shown in Fig. 1. The vacuum chamber of the plasma reactor consists of a Pyrex glass column about 80 cm in height and 6 cm in internal diameter. The carbon nanotubes are vigorously stirred at the bottom of the tube and thus the surfaces of nanotubes can be continuously rotated and exposed to the plasma for thin film deposition during the plasma polymerization process. A magnetic bar was used to stir the powders. The gases and monomers were introduced from the gas inlet during the plasma cleaning treatment or plasma polymerization. The system pressure was measured by a thermocouple pressure gauge. A RF power generator operating at 13.56 MHz was used for the plasma film deposition (7,8).

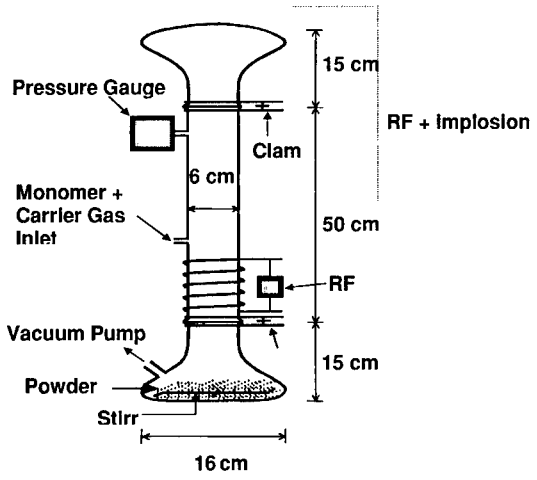


Figure 1. *Schematic diagram of the plasma reactor for thin polymer film coating of the nano-particles.*

Before the plasma treatment, the chamber pressure was pumped down to less than 5 Pa at which time the monomer vapors were introduced into the reactor chamber. The operating pressure was adjusted by the mass flow controller. Pyrrole was used as the monomer for plasma polymerization. To be able to distinguish the deposited polymer thin film and the surface of carbon nanotubes, we introduced a small fraction of C_6F_{14} to co-polymerize with the pyrrole monomer. In this way, we will be able to characterize the deposited thin film in the TOFSIMS experiments. During the plasma polymerization process, the RF power was 15 W and the system pressure was 30 Pa. The plasma treatment time was 30 minutes per batch of 0.3 grams of powder.

After the plasma treatment, the carbon nanotubes were examined using transmission electron microscopy (TEM) and Time-of-Flight secondary ion mass spectroscopy (TOFSIMS). The high-resolution TEM experiments were performed using a JEOL JEM 2010F electron microscope with a field emission source. The accelerating voltage was 200 kV. The nanotubes were dispersed in methanol and suspended on a perforated carbon film supported by Cu grids. Bright-field and high-resolution imaging techniques were used to characterize the features of both the original and the coated carbon nanotubes. TOFSIMS was performed on a Ion-Tof model IV equipped with a 25 keV 69Ga+ source. The mass resolution of the instrument was 8,000 at amu 28. Positive and negative spectra were collected in the mass range 0-1000 amu. The spectra were acquired by rastering the beam over an areas of 300 x 300 μm of bundle of the untreated or treated carbon nanotubes.

Fig. 2 shows the bright-field TEM images of the original uncoated Pyrograf III PR-24-HT (Fig. 2A) nanotubes and the Pyrograf III PR-24-PS carbon nanotubes (Fig. 2B). As can be seen in this figure, both Pyrograf III carbon nanotubes have similar size features with a hollow channel. The Pyrograf III PR-24-HT nanotubes have slightly smaller outside diameters averaging about 70 nm, and they are quite uniformly distributed. The Pyrograf III PR-24-PS carbon nanotubes have outside diameters ranging between 40 nm and 120 nm. Some nanotubes become curved during their growth with the open ends. An HRTEM image (Fig. 3A) of the original Pyrograf III PR-24-HT carbon nanotubes shows the graphite structure with the interlayer spacing d_{002}=0.34 nm. Based on the bright-field TEM and HREM images, the wall thickness of the nanotubes can be estimated to be about 20~30 nm for both the Pyrograf III PR-24-HT and Pyrograf III PR-24-PS carbon nanotubes. Nanotubes with axially parallel graphite layers (not shown here) and nanotubes with axially parallel graphite layers oriented at an angle to the tube axis (Fig. 3A) were observed. The edge dislocations can be seen due to the disorder of the graphite layers (002). It is noticed that both the outer and inner surfaces terminate at the graphite (002) layer without the addition of a surface layer, for the originally uncoated nanotubes (Fig. 3A). The bright field and high-resolution TEM images of these nanotubes after plasma treatment are shown in Fig. 3B (Pyrograf III PR-24-PS PR-24-HT nanotubes). An ultrathin film amorphous layer can be clearly seen covering both the inner and outer surfaces of the Pyrograf III PR-24-HT nanotubes (Fig 3B). The thin film is uniform on both surfaces, however, with a larger thickness on the outer wall (7 nm) than on the inner wall (1~3 nm) surface (Fig. 3B). The thickness of ultrathin film is approximately 2~7 nm all the way surrounding the nanotube surfaces for both the Pyrograf III PR-24-HT and Pyrograf III PR-24-PS carbon nanotubes. The film is also thicker and more uniform than the roughness (<1 nm) on the outer surface of the carbon

nanotubes (Fig. 3A). The lattice image of graphite can be clearly seen with an extremely thin layer of polymer film on its surface.

Figure 4a is the HREM image of the coated SWCNT. Compare to Figure 2 and 3, one can see a much thinner nanotube with a diameter of only 1.4 nm. Figure 4b is the HRTEM image of coated SWCNT in a bundle. Due to high surface energies, these SWCNT's tend to cluster together in an aligned form. The polymer film, however, is deposited on the outer surface of the bundle as show in Figure 4b.



Figure 2 *Bright-field TEM images of the original uncoated carbon nanotubes of Pyrograf III PR-24-PS PR-24-HT (A) and Pyrograf III PR-24-PS (B).*

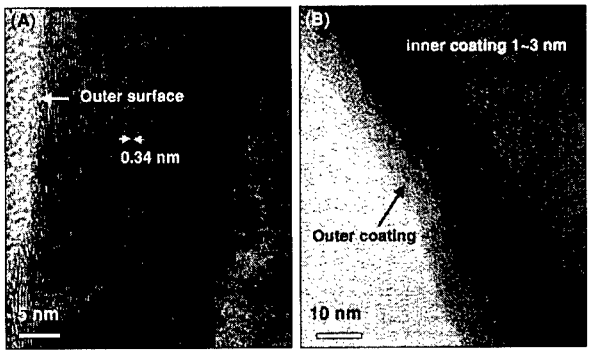


Figure 3. *HRTEM images of yrograf III PR-24-PS PR-24-HT nanotube: (A) The fragments of the wall with inclined planes (002) showing lattice space on the outer and inner surfaces of uncoated Pyrograf III PR-24-PS PR-24-HT nanotubes with slight roughness (<1 nm) on the surface; (B) An ultrathin film of pyrrole can be observed on both outer and inner surfaces of coated Pyrograf III PR-24-PS PR-24-HT nanotubes.*

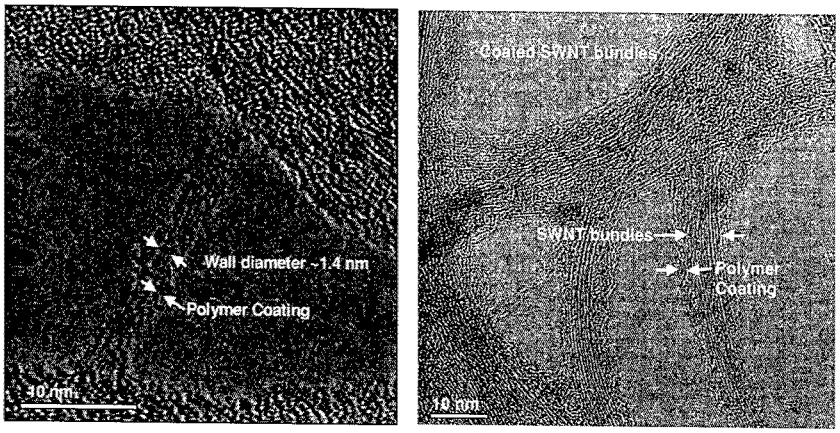


Figure 4. *HRTEM images of single wall carbon nanotubes: (A) an isolated SWCNT coated with pyrrole; (B) a bundle of SWCNT coated with pyrrole.*

To confirm the TEM observations shown in Fig. 2-4, TOFSIMS was carried out to study the surface films of the nanotubes. Fig. 5a shows part of the TOFSIMS spectra of untreated Pyrograf III PR-24-HT carbon nanotubes. The spectrum of the untreated nanotubes show an appreciable intensity of carbon, hydrogen, and oxygen, which is a characteristic of a un-treated natural surface. In Fig. 5b one can see that the treated nanotubes have strong carbon-fluorine peaks indicating the surface coating of the nanotubes and consistent with the HRTEM data presented in Fig. 2-4. In particular, the spectrum in Fig. 5b shows carbon-fluorine in the forms of $C_4F_7^+$, $C_3F_7^+$, $C_4F_6^+$, $C_5F_7^+$ indicating highly branched and cross linked polymer structure in the deposited thin film. It is to be noted that the fluorine shown in the TOFSIMS spectrum can only be part of the monomer introduced during the plasma coating process, a strong indication of polymerized film on the carbon nanotubes.

During coating, the polymer is introduced as a vapor and the collision frequency increases with the gas pressure. The rate of polymer condensation on the nanoparticle surfaces may be influenced by many parameters such as electron density, temperature, and energy density. To achieve a thin and uniform coating on such small nanoparticles, all these synthesis parameters must be optimized. Although a systematic study on the optimization of synthesis parameters has not yet been carried out, the preliminary experimental data have indicated that the coating polymer must be stable and not reactive with the substrate during coating. The gas pressure must be moderate for a low collision rate on the nanoparticle surfaces. In addition, polymerization should take place relatively fast after the condensation on the particle surfaces. These will ensure a uniform coating on the order of 1-2 nm for all particle sizes.

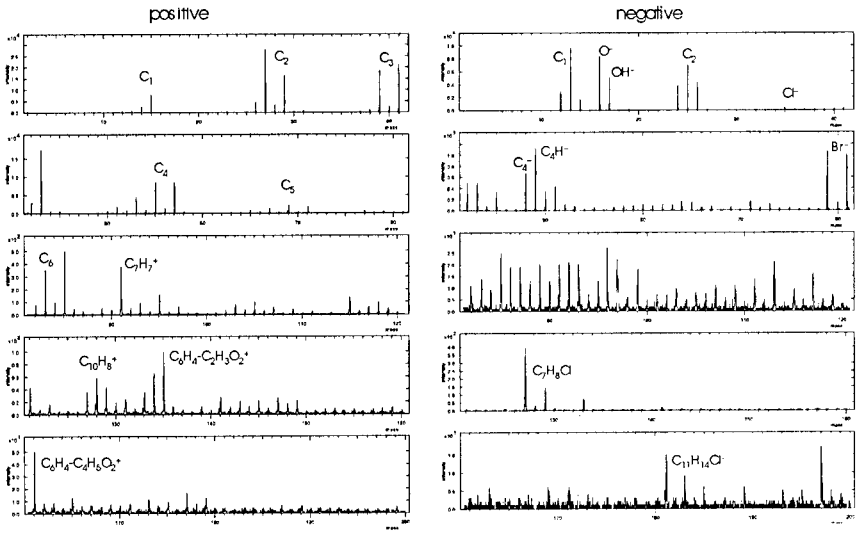


Figure 4. SIMS data showing uncoated MWCNT's..

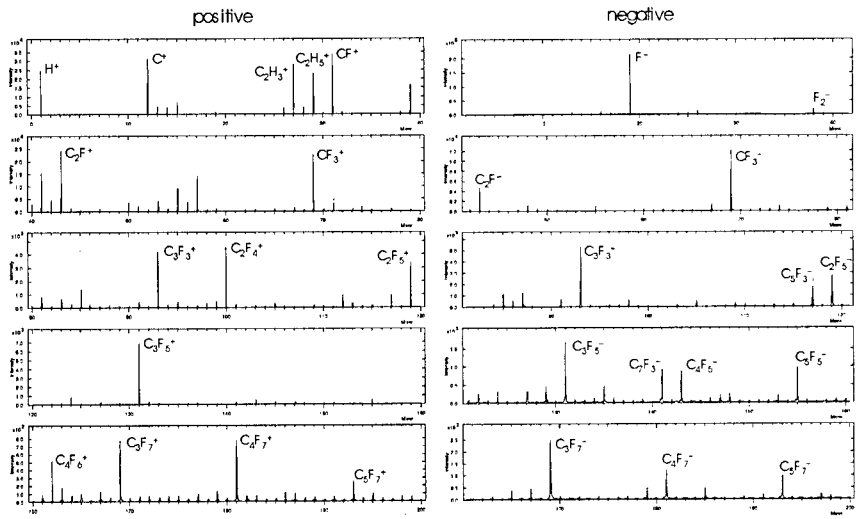


Figure 5. SIMS data showing coated MWCNT's.

In summary, we have deposited an ultrathin polymer film on the inner and outer surfaces of carbon nanotubes by means of a plasma polymerization treatment. The polymer layer is not only uniform on both inner and outer surfaces, but it is also deposited in an extremely thin layer of 2~7 nm. TOFSISM spectra confirmed the polymer nature of the deposited thin films. By controlling the plasma coating conditions, the deposition rate can be closely controlled so that the film thickness on both the inner and outer wall surfaces is uniform and nearly identical.

REFERENCES

1. R. W. Siegel, *Nanostructured Materials*. **3**, 1 (1993).
2. G. C. Hadjipanayis and R. W. Siegel, *Nanophase materials, Synthesis-properties-applications* (Kluwer Press, Dordrecht, 1994).
3. G. M. Whitesides, J. P. Mathias, and C. T. Seto, *Science*, **254**, 1312 (1991).
4. C. D. Stucky, and J. E. MacDougall, *Science*, **247**, 669 (1990).
5. H. Gleiter, *Nanostructured Materials*, **6**, 3 (1995).
6. *Nanotechnology*, A. T. Wolde, ED. (STT Netherlands Study Center for Technology Trends, The Hague, The Netherlands, 1998).
7. G. Timp, "Nanotechnology," AIP Press, Springer, 1998.
8. Y. Bar-Cohen, "Electroactive Polymers as Artificial Muscles - Reality and Challenges", *42nd AIAA Structures, Dynamics, and Materials Conference (SDM), Gossamer Spacecraft Forum (GSF)*, Seattle WA, 2001) 1-10.
9. D. D. Mazzoldi and R. H. Baughman, "Electro-mechanical behavior of carbon nanotube sheets in electrochemical actuators", *Electroactive Polymer Actuators and Devices* (SPIE Proceedings, 2000) 25-32.
10. J. Fraysse, A. I. Minett, G. Gu, S. Roth, *et al.*, "Towards the demonstration of actuator properties of a single carbon nanotube," *Current Applied Physics*, 1, 407-411 (2001).
11. N. G. Lebedev, I. V. Zaporotskova, and L. A. Chernozatonskii, "On the Estimation of Piezoelectric Modules of Carbon and Boron Nitride Nanotubes," 2001, Volograd State University, 400062 Volgograd, Russia, and Institute of Biochemical Physics of RAS, 117334, Moscow, Russia
12. D. Shi and W. J. v. Ooij, "Uniform Deposition of Ultrathin Polymer Films on the Surface of Aluminum Nanoparticles by a Plasma Treatment," *Appl. Phys. Lett.*, 78, 1243 (2001).
13. N. Inagaki, S. Tasaka, and K. Ishii, *J. App. Poly. Sci.*, **48**, 1433 (1993).
14. C. Bayer, M. Karches, A. Mattews and P. R. Von Rohr, *Chem. Eng. Technol.* **21**, 427 (1998)
15. S. Eufinger, W. J. van Ooij, and T. H. Ridgway, *Journal of Appl. Pol. Sci.*, **61**, 1503 (1996).
16. W. J. van Ooij, S. Eufinger, and T. H. Ridgway, *Plasma and Polymers*, **1**, 231 (1996).
17. Applied Sciences, Inc., 141 W. Xena Ave., P.O. Box 579, Cedarville, OH 45314-0579

Mat. Res. Soc. Symp. Proc. Vol. 740 © 2003 Materials Research Society I3.20

Electrodeposition of Ni Catalyst on Tungsten Substrates and Its Effect on the Formation of Carbon Nano- and Micro-coils

Erik Einarsson, Jun Jiao, Josie Prado[1], George M. Coia[2], Jeremy Petty, and Logan Love
Department of Physics, Portland State University
Portland, Oregon 97207, U.S.A.
[1] Department of Chemical Engineering, Oregon State University
Corvallis, Oregon 97331, U.S.A.
[2] Department of Chemistry, Portland State University
Portland, Oregon 97207, U.S.A.

ABSTRACT

Carbon micro-coils and nano-coils were produced in high yield from nickel catalyst particles electrochemically deposited onto tungsten substrates. Various electrochemical deposition techniques were used to produce the nickel catalyst particles. These particles catalyzed the chemical vapor deposition (CVD) of acetylene at 800°C, resulting in growth of carbon micro- and nano-coils. Linear-sweep (cyclic) voltammetry produced catalyst particles which resulted in single-filament coils intermixed with thin nanotubes over most of the substrate surface. Passing the same amount of charge by constant current electrolysis produced nickel particles that decomposed carbon but did not grow coils. Catalyst particles deposited by constant current electrolysis grew nanocoils similar to linear-sweep voltammetry but in small, localized, high-yield patches. The coils produced were either spring-like micro-coils of low pitch and large diameter or rope-like nano-coils of higher pitch and smaller diameter. High-resolution transmission electron microscopy (HRTEM) showed typical graphite fringes in the filaments, but did not reveal an internal tubular structure. Catalyst particles were often detected at the ends of the coils.

INTRODUCTION

Their uniqueness and interesting properties have prompted many researchers to investigate carbon coils [1-4]. Not unlike other carbon micro- and nano-structures, carbon coils have many potential applications such as micro-springs, micro-sensors, magnetic beam generators, and electromagnetic shielding materials [5]. For some applications the substrate on which these coils are grown would play an important role. Tungsten is a very practical substrate because of its strength, high melting point, and use as a high-performance material. Various catalyst-substrate combinations have been used to grow carbon micro- and nano-coils, but we are the first to produce carbon coils from nickel catalyst electrochemically deposited onto tungsten. In this research, the effects of various electrochemical techniques used to deposit nickel onto tungsten substrates were investigated.

EXPERIMENT

Nickel (Ni) catalyst particles were electrochemically deposited onto tungsten (W) by three different electrochemical deposition techniques: linear-sweep voltammetry, constant current

electrolysis, and constant potential electrolysis. The electrolyte solution was 1.0 M in NaCl, 1.0 M in NH_4Cl, and 10 mM in $Ni(NO_3)_2 \cdot 6H_2O$, and was basified to pH 8.3 by addition of concentrated NH_4OH [6]. A three-compartment glass electrochemical cell was used, and the electrolyte was deoxygenated by sparging with N_2 before Ni deposition. The working electrode was a polished W rod of 4 mm in diameter, cleaned in an ultrasonic bath prior to deposition. The reference electrode was a Ag wire immersed in saturated aqueous KCl solution and isolated by a porous vycor plug, and is referred to here as the Ag/AgCl reference. The auxiliary electrode was a coiled Pt wire.

Using the linear-sweep voltammetry technique, Niwas deposited by sweeping the potential of the working electrode linearly from -0.25 V to -1.2 V vs. Ag/AgCl at a scan rate of 30 mV/s. The presence of Ni was verified by reversing the scan from -1.2 V back to -0.25 V and observing a stripping peak at -0.38 V. The presence of this stripping peak indicates the removal of Ni from the electrode. The potential of the W electrode was scanned once again from -0.25 V to -1.2 V vs. Ag/AgCl, then reversed, stopping at a potential of -0.75 V to complete deposition without removing any Ni. Using the constant current electrolysis technique, Ni was deposited by applying a constant current for a designated time interval. Using constant potential electrolysis, a potential of –1.5 V was applied to the working electrode for different time intervals. All deposition processes were controlled by a computer-interfaced potentiostat/galvanostat designed in-house.

To grow carbon nano-coils the W substrates were placed in a ceramic boat, which was inserted into a CVD chamber. The chamber was heated to 700 °C where 385 sccm (standard cubic centimeters per minute) H_2 was introduced for 15 minutes to activate the Ni catalyst. The samples were then heated to 800 °C at which both 385 sccm H_2 and 25 sccm C_2H_2 were introduced for 10, 15, or 20 minutes. The pressure was maintained at 100 mbar throughout the growth process. After cooling to room temperature, the samples were removed from the reaction chamber. Black soot visible on the W surface indicated deposition of carbon on the substrate.

An FEI 611 focused ion beam (FIB) microscope and an ISI-SS40 scanning electron microscope (SEM) were used to characterize the morphologies of the samples. An FEI Tecnai F-20 field emission high-resolution transmission (and scanning transmission) electron microscope (HRTEM/STM) equipped with a high angle annular dark field detector (HAADFD) and an energy dispersive x-ray (EDX) spectrometer was used to examine the internal structures and the chemical compositions of the coils. TEM samples were prepared by carefully scratching some soot from the W substrates and dispersing it in a small amount of acetone, several drops of which were then applied to a lacy-carbon coated copper TEM grid.

RESULTS AND DISCUSSION

When the above experiment was run using a clean W substrate with no deposited Ni, no growth of any carbon structures occurred. This indicates pure W does not catalyze carbon coil or nanotube growth. Both nanotubes and carbon coils, however, were synthesized via chemical vapor deposition of acetylene at 800 °C when Ni was electrochemically deposited onto the W substrates, identifying the deposited Ni particles as the growth catalyst. Figure 1 below shows coils produced from catalyst deposited by the linear-sweep voltammetry technique. Thin carbon nanotubes, having diameters between 10 and 50 nm, are visible. These were often co-synthesized with the carbon coils, growing in among them. This technique deposited Ni catalyst particles in a fairly uniformly distributed fashion on the W surface.

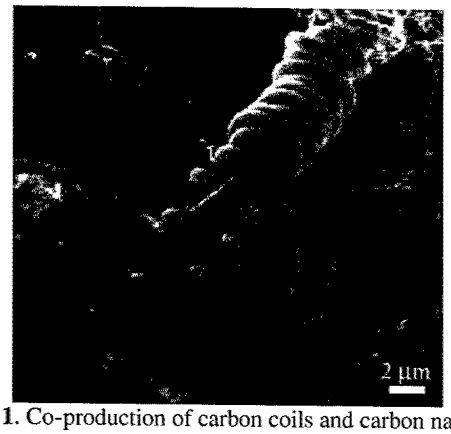


Figure 1. Co-production of carbon coils and carbon nanotubes

This growth was fairly uniform over the substrate surface. Under the same growth conditions we also observed the production of carbon coils from pure Ni, indicating the Ni itself is important in coil growth. The presence of Ni catalyst particles is necessary for growth, but the particle's size and shape seem to determine the actual growth structure.

Figure 2(a) shows a micro-coil grown from Ni nanoparticles deposited via linear-sweep voltammetry. These micro-coils had diameters between 1 µm and 5 µm, while the filament thicknesses were between 250 and 700 nm. Rope-like nano-coils were also produced by this deposition method, as seen in Figure 2(b). The diameters of these coils were between 50 and 250 nm and the average thickness of their filaments was less than 100 nm. Comparing Figures 2(a) and 2(b) one easily sees the pitch of the micro-coils tends to be much larger and much more irregular than that of the nano-coils. The presence of Ni, which was often found at the tip of the coils, was confirmed by energy dispersive x-ray analysis (EDX).

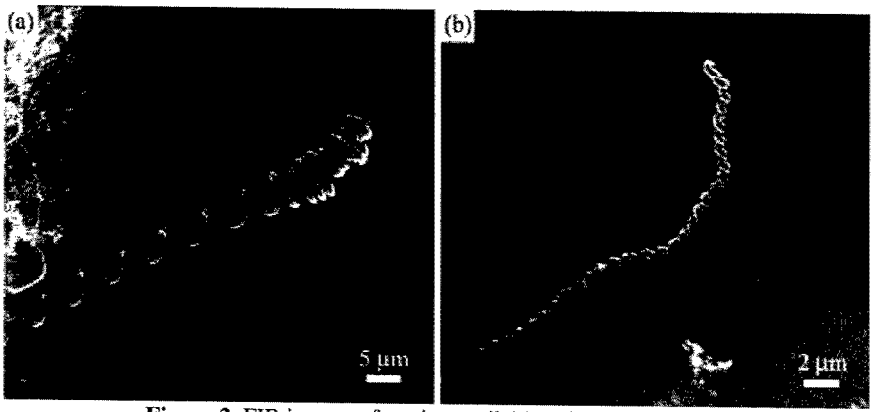


Figure 2. FIB images of a micro-coil (a) and a nano-coil (b).

The production and yield of carbon coils, however, was not always the same. Changing the electrodeposition technique used to deposit Ni had a noticeable effect on coil production. In this study we have shown that different techniques of electrochemical Ni catalyst deposition influence the production of carbon coils. When constant potential electrolysis was used to deposit the catalyst particles, growth of carbon coils was dependent upon deposition time. Our research indicates carbon coils are grown from large catalyst clusters [6], thus a longer deposition time would be needed for the Ni particles to grow large enough to be able to produce nano- and micro-coils. Other studies have shown that the size of electrochemically deposited Ni catalyst particles is controllable by adjusting various deposition parameters such as current, potential, and deposition time [7-8], specifically a constant potential applied for a longer time interval yields larger Ni clusters [7]. This is in agreement with our coil growth hypothesis. The constant potential technique worked only when done over a long enough time to grow large clusters. Figure 3(a) below shows coil production resulting from Ni deposition by constant potential electrolysis.

The linear-sweep voltammetry technique applies a linearly-varying potential to the working electrode for a relatively long time interval (~1 minute). As a result, deposited Ni particles have plenty of time to nucleate into large clusters. This explains why this deposition method was always effective in growing carbon coils. The constant current electrolysis technique, on the other hand, applied a current to the working electrode for a much shorter time, 2 seconds or less, in order to pass the same amount of charge as was passed in the linear-sweep voltammetry technique. This allowed much less time for Ni particles to cluster. Consequently this deposition technique produced few, dispersed carbon nanotubes from small Ni clusters, but no carbon coils. When using the constant potential electrolysis technique, whether or not the deposited Ni particles produced carbon coils depended on deposition time. Deposition over a short time interval resulted in no coil growth, while a longer deposition time produced carbon coils. Results similar to those from the linear-sweep voltammetry technique were observed by applying a potential of -1.2 V for 20 s. The main difference was that the Ni particles were not deposited evenly over the substrate surface, but instead in small bunches.

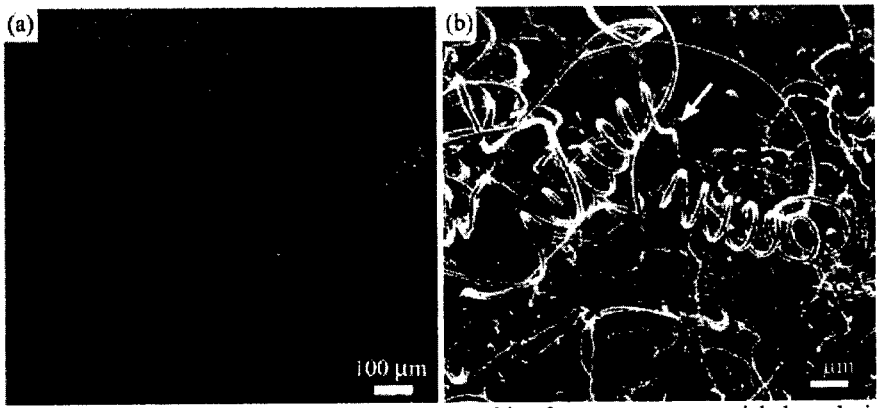


Figure 3. (a) Localized, high-yield coil growth resulting from constant potential electrolysis catalyst deposition. (b) A close-up view of Figure 3(a), showing a high-yield of coils.

This non-uniform distribution of catalyst grew patches of coils and carbon nanotubes. The coil yield in these patches was slightly higher than from linear-sweep voltammetry (Figure 3 above). When the deposition time was reduced to 4 seconds, smaller Ni catalyst particles were deposited, growing thin carbon nanotubes but no coils.

Generally, carbon coils exhibited exclusively right- or left-handed helicity, but some coils actually changed helicity during growth. An occurrence of this in a micro-coil is indicated by the arrow in Figure 3(b). An example of a nano-coil changing helicity is shown by the arrow in Figure 4.

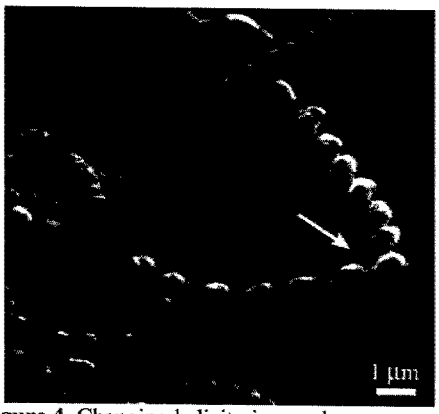


Figure 4. Changing helicity in a carbon nano-coil.

HRTEM images showed the internal structure of a carbon micro-coil to be typical graphite fringes, but revealed no internal tubular structure. Graphite fringes in a micro-coil are shown below in Figure 5.

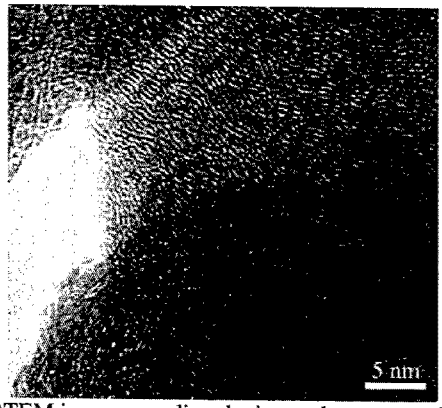


Figure 5. HRTEM image revealing the internal structure of a carbon coil

CONCLUSIONS

Carbon micro- and nano-coils were grown from Ni catalyst particles via the chemical vapor deposition of acetylene at 800 °C. Different Ni deposition techniques and their effects on the production of carbon coils were investigated. It was found that both linear-sweep voltammetry and constant potential electrolysis were effective in producing carbon coils, whereas constant current electrolysis yielded only thin carbon nanotubes. These results, however, do not imply the constant current technique cannot deposit coil-producing catalyst particles. Our results show electrochemical deposition techniques that deposit sufficiently large catalyst particles produce carbon micro- and nano-coils. A constant potential was applied for both 4 and 20 s in the constant potential technique, while the linear-sweep technique took more than one minute to deposit Ni. The constant current technique, on the other hand, in order to pass the same amount of charge as was passed in the linear-sweep voltammetry technique, applied a constant current for only a very short time period (less than two seconds). This resulted in very little time for Ni catalyst particles to nucleate. If this technique were used to apply the same current for a longer time, Ni particles large enough to produce carbon coils should be produced. Based on these results, this study suggests that adjusting the catalyst deposition parameters can influence the production of coils on W substrates. Additional research needs to be done to determine the role of the substrate on the production of carbon coils.

ACKNOWLEGEMENTS

The authors would like to thank Dr. Y.C. Wang at FEI Company for his help with HRTEM/HAADF images. Financial support for this work was provided by the National Science Foundation under awards ECS-0217061 and DMR-0097575 and the American Chemical Society Petroleum Research Fund of award No. PRF-38108-G5.

REFERENCES

1. S. Motojima, M. Kawaguchi, K. Nozaki, and H. Iwanaga, *Appl. Phys. Lett.* **56**, 321 (1990).
2. X. Chen, and S. Motojima, *J. Mate. Sci.* **34** (22), 5519 (1999).
3. X. Chen, W. In-Hwang, S. Shimada, M. Fujii, H. Iwanaga, and S. Motojima, *J. Mater. Res.* **15**, 808 (2000).
4. W. In-Hwang, T, Kuzuya, H. Iwanaga, and S. Motojima, *J. Mater. Sci.* **36**, 971 (2001)
5. L. Pan, M. Zhang, and Y. Nakayama, *J. Appl. Phys.* **91**, 10058 (2002).
6. J. Jiao, E. Einarsson, J. Prado and G. M. Coia, submitted to *J. Appl. Phys.* (2002)
7. M. P. Zach and R. M. Penner, *Adv. Materials*, **12** (12), 878 (2000).
8. Y. Tu, Z. P. Huang, D. Z. Wang, J. G. Wen, and Z. F. Ren, *Appl. Phys. Lett.* **80**, 4018 (2002).

Mat. Res. Soc. Symp. Proc. Vol. 740 © 2003 Materials Research Society I3.22

Arc Plasma Synthesis of Nanostructured Fe Powder

Gil-Geun Lee and Sung-Duck Kim
Div. of Materials Science and Engineering, Pukyong National University,
San 100, Yongdang-Dong, Nam-Gu, Busan 608-739, Korea

ABSTRACT

To investigate the effect of the parameters of the arc plasma process on the characteristics of the iron nano powder, the hydrogen volume fraction in the powder synthesis atmosphere was changed from 10% to 50%. The particle size, phase structure and magnetism of the synthesized iron powder were studied using the FE-TEM, XRD and a vibration magnetometer at room temperature. The particle size increased simultaneously with the increase in the hydrogen volume fraction, and the particle size ranged from about 20nm to 100nm with the change of the hydrogen volume fraction increasing from 10% to 50%. The synthesized iron powder particle had a shell-core structure composed of the crystalline α-Fe in the core and the crystalline Fe_3O_4 in the shell. The iron nano powder synthesized under the high hydrogen volume fraction condition had a higher saturation magnetism and lower coercive force than the values of the one synthesized under the low hydrogen volume fraction condition.

INTRODUCTION

Metal nano particles with a diameter between 10nm and 100nm have a wide range of potential application, including magnetic recording media, catalyst, electric conductive or resistive paste, ferrofluids, and others [1]. The iron is one of the main elements for the application of metal nano particles in the various industrial fields. Nano size iron particles are of particular interest in the fundamental studies of magnetism. The magnetic properties of nano sized iron particles, prepared by varied methods at varied conditions are very different [2,3]. The physical and chemical properties of metal nano particles strongly depend on the particle and surface properties, including size, morphology, surface area, surface oxide, and others. The practical application of metal nano particles should be to verify the relationship between the preparing process parameters and those properties.

Nano particles can be produced by several different methods, such as colloidal precipitation, mechanical attrition and the gas condensation process [4]. The latter is the most used method at present, for the advantages of being relatively simple to be extended to large-scale and high-rate production. The gas condensation processes typically involve nucleation and

growth of nano sized particles from a supersaturated vapor produced either by evaporation of bulk materials or by chemical reaction of gas-phase precursors. The arc plasma process can be preparing metal, ceramic and their composite nano particles by vaporization-condensation of metals or alloys in an active atmosphere using a DC arc-plasma. The nano particles prepared by this process are well dispersed and free of anion contamination compared to those prepared by the wet process.

In the present study, nano iron particles were prepared by the arc plasma process with changing process parameters, and then the morphology, phase structure and magnetism of synthesized iron particles at different process parameters were studied by using the FE-TEM, XRD and a vibration magnetometer at room temperature.

EXPERIMENTAL DETAILS

The preparing apparatus of nano particles by the arc plasma method mainly consisted of a vacuum chamber, tungsten cathode and a copper anode, a gas flow system and a DC power supply. The pure iron (above 99.99% purity) bulk was used as a raw material. The vacuum chamber was pumped to 10^{-5} torr and then was backfilled with a hydrogen/argon mixture gas to 300 torr. Then the arc plasma was initiated between the tungsten cathode and the iron bulk on the copper anode under the arc current 60A, arc voltage 21~25V, and a reaction time of 1 hour. The mixing ratio of the hydrogen/argon was changed from 1:9 to 5:5. The atom smoke of the iron was subsequently generated around the arc spot area of the molten iron. The nano iron particles were formed by a collision between the quenched iron atoms due to a collision with atmosphere gas atoms. Then the formed nano iron particles were separated with working gas. Before the particles were taken out of the chamber, they were passivation treated under an argon/oxygen mixture atmosphere at room temperature for 12 hours to prevent a rapid spontaneous combustion. The variation of microstructure, phase structure and magnetic properties of synthesized iron particles with the change of the mixing ratio of the hydrogen/argon were studied using the FE-TEM, XRD and a vibration magnetometer at room temperature.

RESULTS AND DISCUSSION

Figure 1 shows X-ray diffraction patterns of synthesized powder with the volume fraction of hydrogen gas in the powder synthesis atmosphere. In the case of a 10vol.% of hydrogen, synthesized powder was composed of α-Fe and Fe_3O_4 phases. The relative intensity of the diffraction peak of Fe_3O_4 decreased with an increase in the volume fraction of hydrogen, and the diffraction peak of Fe_3O_4 disappeared at above about a 30vol.% of hydrogen. The Fe_3O_4 phase

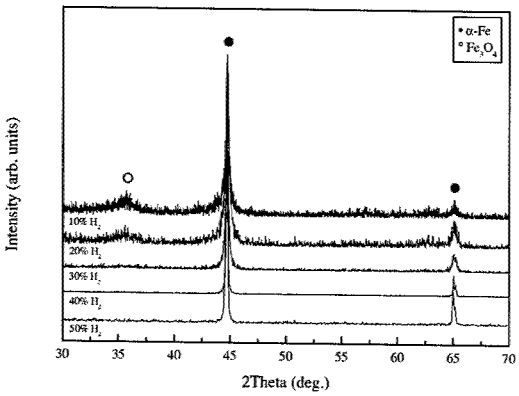


Figure 1. The variation of X-ray diffraction patterns of synthesized powder with the volume fraction of hydrogen.

was formed due to the surface oxidation reaction of the iron particles by the oxygen atoms during the passivation treatment. The surface oxidation reaction of the particles depends on the particle size and the relative amount of the particle to the oxygen concentration in the passivation atmosphere. Figure 2 shows the variation of the powder generation rate with the volume fraction of the hydrogen in the powder synthesis atmosphere. The powder generation rate slowly increased with an increasing of hydrogen volume fraction until at about a 20vol.%, and then dramatically increased at about a 30vol.% of hydrogen, and then had saturated values about 3.5g/h at above a 40vol.% of hydrogen. By the Uda [5], the hydrogen molecular promotes the evaporation of the metal vapor from the molten metal in the arc plasma process by the dissolving and evaporation action. This promoting action of the hydrogen molecular increased with increasing the volume fraction of the hydrogen in the powder synthesis atmosphere by Sievert's

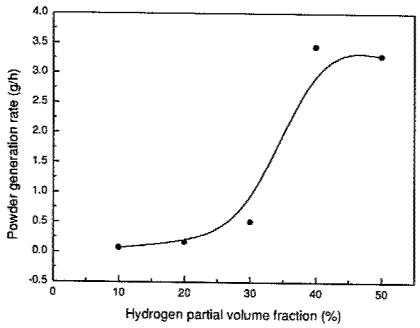


Figure 2. The variation of the powder generation rate with the volume fraction of hydrogen.

law. Also, the powder generation rate increases with increasing the melt temperature at a constant chamber pressure. The thermal energy of the arc plasma depends on the gas atmosphere and shape of one's column. The shape of the arc plasma column that was changed from a spread shape has low thermal energy to a concentration shape and has a high thermal energy with increasing of the volume fraction of the hydrogen. It knows that the synthesis condition was changed from a small amount of powder generation condition to a large amount of powder generation condition with increasing of the volume fraction of the hydrogen in the powder synthesis atmosphere. The oxygen concentration in the chamber was constantly maintained during the passivation treatment. The high powder generation rate on the powder synthesis step has an effect of increasing the relative amount of powder to oxygen concentration on the passivation treatment step. Figure 3 shows the TEM micrographs of the synthesized powder with the hydrogen volume fraction of (a) 20% and (b) 40%. As shown in figure 3, the particle size has about 20nm at a 20vol.% of hydrogen, and has about 80nm at a 40vol.% of hydrogen. It knows that the particle size of the synthesized iron powder increased with increasing of the volume fraction of the hydrogen. As shown in figure 2, the powder generation rate increased with an increasing of the volume fraction of the hydrogen. This means that the concentration of the iron vapor in the chamber was increased with an increasing of the volume fraction of the hydrogen. The higher iron vapor concentration gives a higher collision probability between the cooled iron atoms, and then formed larger iron particles. The larger particle has less sensitivity on oxidation than the smaller particle due to the relatively small surface area per unit volume. It was considered that the phase change of the synthesized iron powder with the hydrogen volume fraction as shown in figure 1, was due to the change of the relative amount of the powder generation and particle size with the hydrogen volume fraction.

Figure 4 shows the FE-TEM micrograph of the synthesized iron nano particle at 20vol.% of the hydrogen. The synthesized iron nano particle had a shell-core structure composed of α-Fe

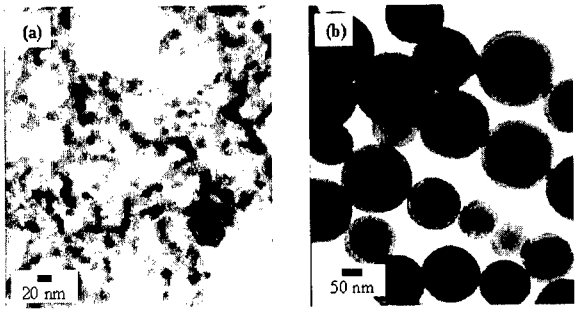


Figure 3. TEM micrographs of the synthesized powder with the hydrogen volume fraction of (a) 20% and (b) 40%.

in the core and Fe_3O_4 in the shell. The oxide layer has a crystalline structure, and the thickness of one layer was about 2nm at a 20vol.% of the hydrogen. The oxide thickness decreased from about 2.5nm to 1nm with increasing of the volume fraction of the hydrogen from 10% to 50%.

Figure 5 shows the magnetization hysteresis loops of the synthesized iron nano powder with the hydrogen volume fraction of (a) 20% and (b) 40%. In the case of a 20vol.% of the hydrogen, the saturation magnetization and coercive force have about 120emu/g and 750Oe, respectively. In the case of a 40vol.% of the hydrogen, the saturation magnetization and coercive force have about 180emu/g and 150Oe, respectively. The iron nano powder synthesized under the high hydrogen volume fraction condition had a higher saturation magnetism and lower coercive force than the values of the one synthesized under the low hydrogen volume fraction condition. It thinks that these changes of the saturation magnetization and coercive force of the synthesized iron nano powder comes from the change of the relative amount of composing phases (α-Fe and Fe_3O_4) and particle size with the volume fraction of the hydrogen [6,7]

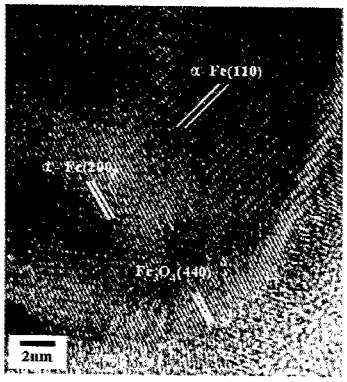


Figure 4. FE-TEM micrograph of the synthesized iron nano particle.

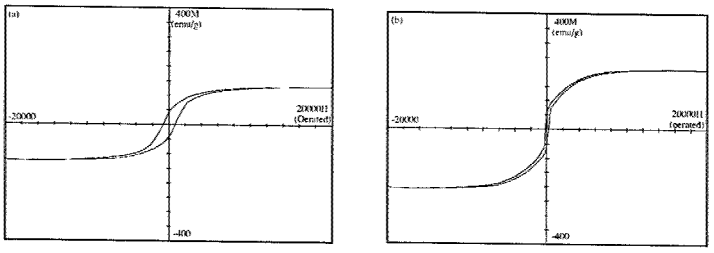


Figure 5. The magnetization hysteresis loops of the synthesized iron nano powder with the hydrogen volume fraction of (a) 20% and (b) 40%.

CONCLUSIONS

The iron nano powder could be synthesized by the arc plasma process and this powder has a stable surface characteristic on the rapid spontaneous combustion. The powder generation rate and particle size were increased with increasing of the hydrogen volume fraction in the powder synthesis atmosphere. The particle size ranged from about 20nm to 100nm with the change of the hydrogen volume fraction increasing from 10% to 50%. The synthesized iron powder particle had a shell-core structure composed of the crystalline α-Fe in the core and the crystalline Fe_3O_4 in the shell. The thickness of the oxide layer decreased simultaneously with the increase in the hydrogen volume fraction in the powder synthesis atmosphere. This thickness ranged from about 2.5nm to 1nm with the change of the hydrogen volume fraction increasing from 10% to 50%. The iron nano powder synthesized under the high hydrogen volume fraction condition had a higher saturation magnetism and lower coercive force than the values of the one synthesized under the low hydrogen volume fraction condition.

ACKNOWLEDGMENTS

This work was supported by grant No. R05-2001-000-00784-0 from the Basic Research Program of the Korea Science & Engineering Foundation.

REFERENCES

1. R. W. Siegel, *Mater. Sci. Eng.* **A168**, 189(1993).
2. Y. Fukano, *Jpn. J. Appl. Phys.* **13**, 1001(1974)
3. M. Kusunoki and T. Ichihashi, *Jpn. J. Appl. Phys.* **25**, 219(1986).
4. K. E. Gonsalves, S. P. Rangarajan and J. Wang in *Handbook of Nanostructured Materials and Nanotechnology* edited by H. S. Nalwa, (Academic Press 24-28 Oval Road, London, 2000) pp.1-52.
5. M. Uda, *Bull. Metal. Soc. Japn.* **22**, 412(1983).
6. T. A. Yamamoto, R. D. Shull and H. W. Hahn, *Nanostr. Mater.* **9**, 9530(1977).
7. A. E. Berkowitz, R. H. Kodama, S. A. Makhlof, Ft. Parker, F. E. Spada, E. J. McNiff and S. Foner, *J. Magnetism and Magnetic Mater.* **196-197**, 591(1999).

Mat. Res. Soc. Symp. Proc. Vol. 740 © 2003 Materials Research Society

Size Reduction of Clay Particles in Nanometer Dimensions

Gopinath Mani, Qinguo Fan, Samuel C. Ugbolue, and Isabelle M. Eiff, Department of Textile Sciences, University of Massachusetts Dartmouth, North Dartmouth, MA.

Abstract

This research work focuses on combining ball milling and ultrasonication to produce nano-size clay particles. Our work also emphasizes on increasing the specific surface area of montmorillonite clay particles by reducing the particle size to nanometer dimensions. We have characterized the as-received clay particles by using particle size analysis based on laser diffraction and found that the size of the clay particles is not consistent and the particle size distribution is very broad. However, after the unique treatment and processing, the clay particles were obtained in nanometer dimensions with narrowed particle size distribution.

Introduction

Particle size is not only a crucial parameter for polymer nanocomposites but also it plays a vital role in paints, pigments, inks, toners, chemicals, talc, drugs, pharmaceuticals, cosmetics, confectionery, chocolate liquor, etc. When the particle size gets reduced, the specific surface area is increased and it would increase the chemical activity of the inorganic materials[1]. When the high specific surface area of the particles is exposed to the polymer molecules, various properties[2,3] of the polymer nanocomposites are changed. Ball milling[4] is a widely used technique for particle size reduction. But the problem of agglomeration[5] is always there when it is in dry powder form. One of the main mechanical effects caused by the ultrasonication[6,7] is the disaggregation and deagglomeration of the particle assembly. Cavitation[7] is the important phenomenon in ultrasonication. A combination of ball milling and ultrasonication can lead to an effective particle size reduction.

Experimental Details

Cloisite-15A (Southern Clay Products Inc, Texas) is the organophilic montmorillonite clay used in our study. Glass balls in 3 and 5 mm, stainless steel balls in 5 and 8 mm were also used. Thumblers tumbler (Tru-Square metal products, WA) was used for ball milling. Ultrasonic Processor CPX 750 (Cole-Parmer Instruments, IL) was used for ultrasonication process. Particle size analyzer-Mastersizer 2000 (Malvern Instruments), Scanning Electron Microscope JSM 5610 were used to characterize the particle size.

Thumblers tumbler is a steel hexagon barrel with removable rubber lining and it is 9 cm in diameter and 8 cm in depth. A glass bottle, 5.5 cm in height and 2.5 cm diameter, is used inside the tumbler for the ball milling of clay. Effect of the different materials (glass and stainless steel) and different sizes (3mm, 5mm, 8mm) of balls on particle size reduction and distribution were studied. The milled particles were dispersed in xylene. Again ultrasonication was done on milled particles in xylene. An investigation on the amplitude, pulsation rate and time of the ultrasonication process was done with respect to particle size distribution and the optimum conditions in our laboratory were determined. Particle size analyzer was used to characterize the nanoparticles based on the principles of laser diffraction and morphological studies.

RESULTS AND DISCUSSION

The speed of the tumbler was maintained at 20 rpm in the ball milling operations. The slow speed is preferred in order to increase the possibility of the balls making contact with many particles; hence the impact energy is even and the centrifugal forces would not overcome gravity. The ratio of balls-to-clay particles in the tumbler media was 100:2.5 (grams) and it was allowed to run for 24 hours. 3 mm glass balls are found to give better results than the other balls used.

Kinetic Energy (K.E.) produced by a single ball = ½ (mv^2), where m is the mass of the ball and v is the velocity of the tumbler. The total kinetic energy is approximately the same for all the types of balls used even though they are different in size and nature (Table. 1). In the case of 3 mm glass balls, which have higher surface area, more contact with the particle occurs. When the glass bottle is rotating inside the tumbler, because of its lower mass (0.0363 gm), more number of balls reaches the maximum height, hits the top surface of the bottle and fell down. When the balls reach the bottom surface of the bottle and accelerates (i.e.) at h=0, all the potential energy is converted to kinetic energy. K.E is considered to be acting on the defects (internal pore, surface cracks, micro cracks and surface fissure) in the particles, which ultimately results in particle size reduction.

Types of balls	Mass of a Single ball (kg)	K.E produced by a Single ball (Joules)	No of balls in 100 grams	Total K.E (Joules)
3 mm glass balls	0.0363×10^{-3}	2.02×10^{-6}	2754	5563.08×10^{-6}
5 mm glass balls	0.142×10^{-3}	7.89×10^{-6}	704	5554.56×10^{-6}
5 mm s.steel balls	0.432×10^{-3}	2.4×10^{-5}	231	5544×10^{-6}
8 mm s.steel balls	1.069×10^{-3}	5.99×10^{-5}	94	5630×10^{-6}

Table 1 Total kinetic energy produced by different types of balls

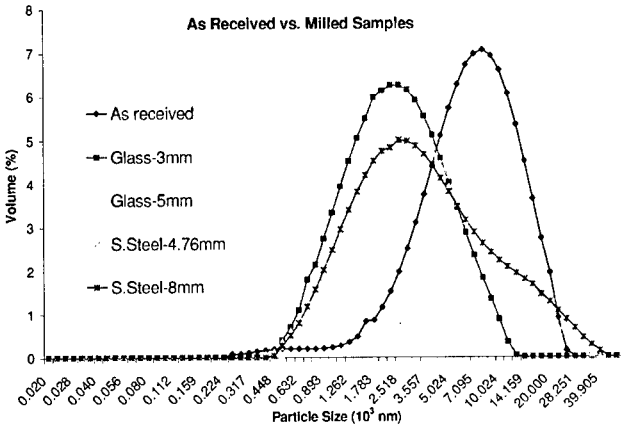


Figure 1. Particle Size Distribution Curves for the As-received and milled particles

The Particle Size Distribution (PSD), Specific Surface Area (SSA), Surface Weighted Mean (SWM) and Volume Weighted Mean (VWM) of as-received particles and ball-milled particles were determined using the Particle Size Analyzer. In a particle size distribution with a lot of fine particles, the SWM is very sensitive to the presence of finer particles. The VWM shows sensitivity to the presence of coarser particles. Thus, the direct use of as-received clay particles is not considered suitable for these applications of nanotechnology. So we decided to reduce the particle size and to narrow the size distribution by a combination of ball milling and ultrasonication techniques.

Properties	As-received nano-clay particles
PSD	0.02 to 2000 μm
SSA	1.22 m^2/g
SWM	4.9 μm
VWM	8.451 μm

Table II Properties of the As-received clay particles

Properties	Milled Samples (Effect of different types of balls on the particles)			
	3mm-Glass balls	*5mm-Glass balls*	*5mm-S.Steel balls*	*8mm-S.Steel balls*
PSD	0.63 to 14μm	0.35 to 41μm	0.44 to 50μm	0.44 to 55μm
SSA	2.92m^2/g	2.55m^2/g	2.2m^2/g	2.35m^2/g
SWM	2.052m^2/g	2.348m^2/g	2.724m^2/g	2.548m^2/g
VWM	3.172m^2/g	4.818m^2/g	5.830m^2/g	5.762m^2/g

Table III Effect of different types of balls on the As-received clay particles

Dry particles usually consist of aggregates and agglomerates that must be dispersed in xylene to produce individual units of the particle. When the particles were dispersed in xylene, there was a drastic change in the particle size and particle size distribution. The PSD, SSA, SWM, and VWM of the ball-milled clay particles dispersed in xylene are 0.5 μm to 33.570 μm, 36.8 m^2/g, 0.163 μm, and 1.022 μm respectively.

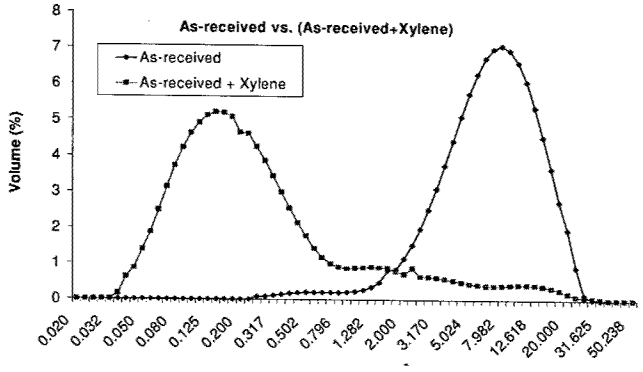


Figure 2. Particle Size Distribution curves for the As-received and milled particles.

Ultrasonication was done on the milled particles in xylene. The particles in xylene are considered the nuclei for the cavitation of bubbles. The high energy produced due to the collapse of bubbles at very high temperature was responsible for breaking the particles. The so-generated shock waves can cause the particles to collide against one another with great force. Since these are same charged particles, problem of agglomeration is greatly reduced. An investigation on the amplitude, pulsation rate and time of the ultrasonication process was done with respect to particle size distribution. Amplitude is directly proportional to the intensity, which is a measure of amount of energy available per unit volume of liquid. Hence as the amplitude increases, a higher energy is imparted to the cavitation bubble giving rise to greater intensity of the energy released in the implosion of that bubble. When the amplitude is increased from 80% to 90%, with pulse rate 5 sec. on and 5 sec. off, the SSA increases from 35.38m^2/g to 46.98m^2/g in 4 hours.

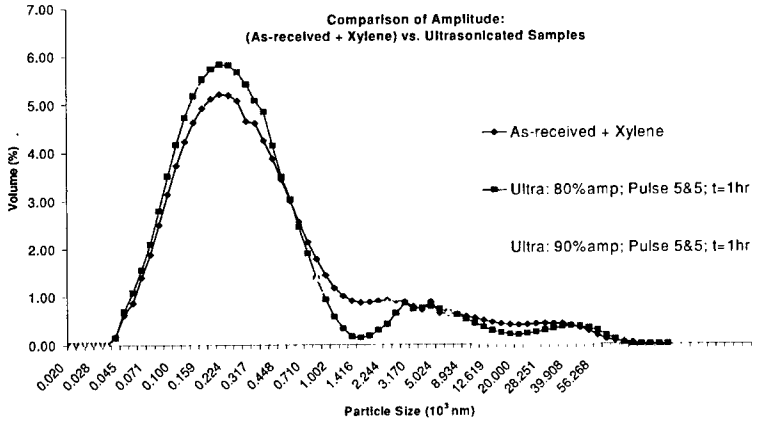


Figure 3.1 - Particle Size Distribution curves showing that higher amplitude is better (1 hour ultrasonication time)

The particle size distribution curve (span) becomes narrowed for the 90% amplitude curves compared with other curves (Fig 3.1 and Fig 3.2). The span expresses the width of the distribution curve regardless of the actual size of the material.

Time is another vital factor. The longer the time allowed for ultrasonication, the better the results of particle size reduction. When the ultrasonication time is changed from 15 min. to 1 hour and to 4 hours, the SSA increases from 38 m^2/g to 45.4 m^2/g and to 46.9 m^2/g respectively. The PSD of the treated samples also decreased accordingly. When the pulsation rate is changed from 5 sec. on and 5 sec. off to 8 sec. on and 4 sec. off, for 4 hours, the SSA increases from 35.5 m^2/g to 49.5 m^2/g. The span is also greatly reduced which indicates narrower particle size distribution (Fig 4).

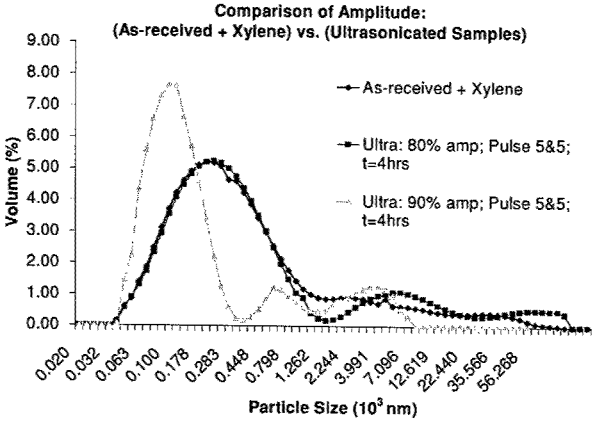


Figure 3.2 - Particle Size Distribution curves showing that higher amplitude is better (4 hours ultrasonication time)

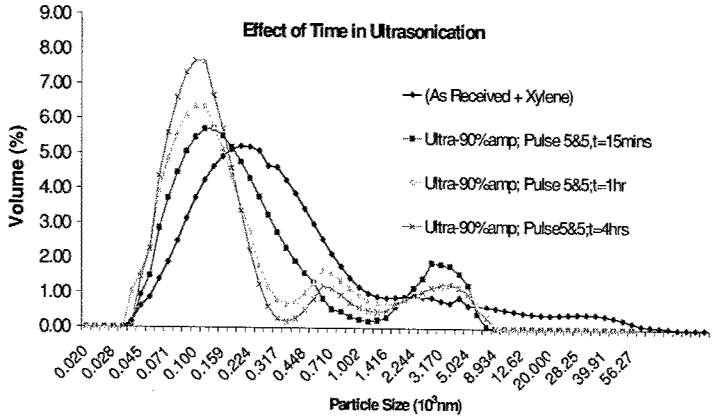


Figure 4 - Particle Size Distribution curves showing that when the ultrasonication time is increased, particle size and the span gets decreased.

The treated clay particles (after ball milling, dispersed in xylene and ultrasonication) were obtained in nanometer dimensions. Table IV summarizes the PSD, SSA, SWM and VWM of the clay particles before and after processing;

Parameters	As-received clay particles	Reduced size clay particles
PSD	0.02 μm to 2000 μm	50 nm to 350 nm
SSA	1.22 m^2/g	48.2 m^2/g
SWM	4.9 μm	128 nm
VWM	8.451 μm	650 nm

Table 1V As-received clay particles Vs. Reduced size clay particles

Conclusion

The optimum conditions for the ultrasonication process in our laboratory were determined; 90% amplitude, 8 second on and 4 second off pulsation rate, and 4 hours. The processed clay particles were obtained in nanometer dimensions. The average reduced particle size range is from 50 nm to 350 nm, average specific surface area is dramatically increased to 48.2 m^2/g, average surface weighted mean and average volume weighted mean are drastically decreased to 128 nm and 650 nm respectively.

Acknowledgements

The authors would like to thank National Textile Center for supporting this study.

References

1. Brian, H.K., Characterization of Powders and Aerosols; Wiley: New York, 1999.
2. Ou, Y., Yang, F., Journal of Polymer Science Part B: Polymer Physics, 1998, 36.
3. Emmanuel, P.G., Advanced Materials, 1996, 8(1), 29-35.
4. Hendry, H. H. Handbook of Powder Metallurgy; Chemical Publishing Co, Inc: New York, 1973.
5. Goettler, L. A., and Rechtenwald, D.W. Proceedings of Additives'98, Orlando, FL, February, 1998.
6. Wedlock, D. J., Controlled Particle, Droplet and Bubble Formation; Butterworth Heinemann: New York, 1994.
7. Kenneth, S. S., Ultrasound Its Chemical, Physical, and Biological Effects; VCH publishers: Weinheim, 1988.

Mat. Res. Soc. Symp. Proc. Vol. 740 © 2003 Materials Research Society I3.28

Effect of Solid-Solution W Addition on the Nanostructure of Electrodeposited Ni

Hajime Iwasaki, Kenji Higashi[1] and T. G. Nieh[2]

Department of Materials Science & Engineering, Himeji Institute of Technology
2167 Shosha, Himeji, Hyogo 671-2201, Japan
[1] Department of Metallurgy and Materials Science, College of Engineering, Osaka Prefecture University, Sakai 599-8531, Japan
[2] Lawrence Livermore National Laboratory, L-350, PO Box 808, Livermore, CA 94551, USA

ABSTRACT

Electrodeposition method was employed to produce freestanding Ni-W alloy foils. The foils consist of nanograins. The structure of the foil, e.g. texture, grain morphology, size distribution, and the nature of grain boundaries, were characterized using X-ray diffraction and high-resolution electron microscopy. The deposited foils exhibit an equiaxed nanocrystalline structure having a grain size value of about 6 nm. Two types of grain boundary structure were observed. One type of grain boundary is essentially one atomic layer thin and another type consists of a structureless layer of about 0.5-1 nm in thickness. Angular dark field (Z-contrast) image of the deposited foils showed an inhomogeneous distribution of W solutes. In some local regions, the W content actually exceeds the equilibrium solid solution limit. Many grain boundaries with a structureless layer of about 0.5-1 nm are probably a result of local supersaturation of W.

INTRODUCTION

The technological development of nanocrystalline alloys has been driven by the promise of exceptional properties. Scientifically, the study of nanocrystalline materials is also of great interest because the potential breakdown of classical scaling laws and the accompanying need for new materials physics in the nanostructured limit. However, materials with grain sizes below about 10 nm are still extremely difficult to produce. Electrodeposition is a viable method to produce fine-structured material. However, to produce nanocrystalline materials using electrodeposition, fine grain sizes apparently require a compromise in purity. For example, the addition of a nucleation agent during electrodeposition can reduce the grain size of the nanocrystalline product, but it also increases the carbon and sulfur content of the alloy [1,2]. Alternatively, finer grain sizes can be achieved via alloying, as demonstrated in Fe-Ni [3,4] and other systems [5,6]. Alloying has long been recognized as an effective method to increase glass-forming ability and, in fact, is critical for the production of bulk amorphous metals and devitrified nanocrystalline alloys [7]. Considered collectively, the above studies suggest that fine-structured nanocrystalline metals (from amorphous to ~10 nm grain size) are achievable through the use of a low-temperature single-step production process and a careful selection of alloy composition.

In the present work, we study the grain and grain boundary structures of nanocrystalline Ni-W alloys with grain sizes below 10 nm produced by direct current (DC) electrodeposition. Prior research has shown that Ni-W alloys can be refined to a fully amorphous structure by judicious design of the plating bath [8]. Thereby, this system offers the potential to observe the transition in mechanical properties from the nanocrystalline to the amorphous state. Additionally, Ni-W alloys have been targeted for the application of micro-fabrication technologies, where their improved hardness and abrasion resistance are attractive [9].

EXPERIMENTAL DETAILS

Electrodeposition of Ni-W alloys has been discussed at length previously [8,9]. Here we have used a similar method to produce foils about 20 μm thick; the composition of the plating bath is given in Table I. Citric acid and ammonium chloride were introduced to form complexes with Ni and W, while sodium bromide was used to improve conductivity. An electro-polished copper sheet of 25 x 30 x 1 mm was used as the plating substrate, and the anode was high purity platinum. A 500 mL bath was maintained at 72° C, and the applied DC current density was constant at 0.05, 0.10 or 0.15A/cm^2. A new plating bath was made of analytical reagent-grade chemicals and pure water for each experiment.

After plating, the Cu substrate was dissolved in an aqueous solution containing 250 g/L of CrO_3 and 15 cm^3/L H_2SO_4. All electrodeposited foils were degassed in vacuum at 80°C for 24 h. Chemical analysis of the electrodeposited alloys was carried out by means of spectroscopic analysis in an inductively coupled argon-plasma (to determine metal content), and for one foil the oxygen and hydrogen content were assessed by measuring the amount H_2O formed after melting the alloy. Structural analysis was also performed by means of X-ray diffraction (XRD) using Cu-Kα radiation in a Rigaku RINT –1500 operating at 40 kV and 200 mA.

Microstructural observations were performed using high-resolution electron microscopy (HREM) on the normal plane of the electrodeposited foils. The high-resolution transmission electron microscopy is JEM-4000EX, operated at 400 kV.

DISCUSSION

Table I: Composition of the plating bath for Ni-W electrodeposition.

Nickel Sulfate ($NiSO_4$-$6H_2O$)	0.06 mol/L
Citric Acid ($Na_3C_6H_5O_7$-$2H_2O$)	0.5 mol/L
Sodium Tungstate (Na_2WO_4-$2H_2O$)	0.14 mol/L
Ammonium Chloride (NH_4Cl)	0.5 mol/L
Sodium Bromide (NaBr)	0.15 mol/L

Table II: Chemical and physical properties of Ni-W electrodeposits.

Current Density (A/cm^2)	W content (at%)	XRD grain Size (nm)	TEM grain Size (nm)	Texture (<110> ‖ thickness)
0.05	11.6	7	~5	Strong
0.10	11.8	-	4.5-6.2	Moderate
0.15	12.4	-	~4	Near Random

Composition and nano-structure

The chemical and physical properties of the electrodeposited Ni-W films, as well as the current density used to produce the films, are listed in Table II. All of the alloys exhibited a W content in the narrow range of 12.0 ± 0.4 at%, slightly increases with an increasing applied current density. Analysis from the specimen synthesized at a current density of 0.10 A/cm^2 indicated low impurity levels of 1350 and 780 ppm for H and O, respectively.

XRD and electron diffraction patterns indicated that all of the Ni-W foils were single-phase with an FCC structure, suggesting a solid solution alloy. Although the equilibrium phase diagram of the Ni-W system is speculative at room temperature, W is expected to dissolve in Ni up to ~12.5 at% [10]. The electrodeposited foils listed in Table II are noted to be very close to this limit. Grain sizes of the Ni-W foils were determined either directly from HREM images, or indirectly, from the XRD data. The results, included in Table II, are found to be well clustered in the range below 10 nm.

The structure of the Ni-W alloy deposited at a current density of 0.10 A/cm^2, which exhibits the main features of all of the specimens investigated, is shown in Fig. 1. The grain shape is apparently isotropic, and there is no obvious tendency for grains with a similar orientation to cluster together. Presumably, grain boundaries are mostly of the high-angle variety.



Fig. 1 Bright field image of nanocrystalline Ni-W alloy deposited at a current density of 0.10 A/cm^2.

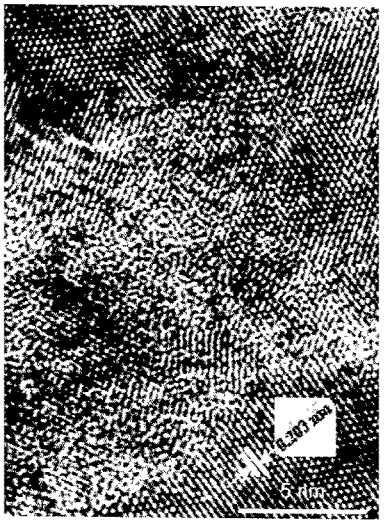


Fig. 2 A high-resolution image of the same Ni-W foil from Fig. 1.

A high-resolution image of Fig. 1 showing the detailed structure of the Ni-W foil is presented in Fig. 2. This figure is filled with fine domains of lattice fringes with a spacing of 0.203 nm, which is the spacing of the {111} plane of Ni. The grain size is estimated to be about 4.5-6.2 nm, and the intercrystalline regions (i.e., grain boundaries and triple junctions) are manifested as structureless bands about 0.5-1 nm wide. The images also indicate that the grains are approximately equiaxed, with no notable morphological anisotropy.

The effect of applied current density on the nanostructure of the Ni-W alloys is illustrated in Figs. 3 and 4, which are planar views of the specimens deposited at (a) 0.05 and (b) 0.15 A/cm^2, respectively. These figures can be directly compared with Fig. 2, which is the corresponding image from sample produced with an intermediate current density of 0.10 A/cm^2. Although the current density has little effect on the grain size and the global concentration of W in the alloys (Table II), these figures show that current density greatly affect the texture of the deposited films, and generally a higher current density results in a more random orientation (Fig. 4).

Existence of structureless region

As discussed in Fig. 2, grain boundaries and triple junctions exhibit as structureless bands (or amorphous bands). High-resolution images taken from Figure 1 show that, in fact, there are two types of grain boundary. One type of grain boundary is a high-angle boundary but does not exhibit a band structure (marked by arrows in Fig. 5a), i.e. crystal lattices of neighboring grains have an intimate contact. Another type is the grain boundary exhibiting as a structureless band surrounding a grain (marked in Fig. 5b), i.e. the crystal lattices of neighboring grains are separated by structureless bands. The former is a typical grain boundary for nanocrystalline pure Ni produced by electrodeposition, while the latter is for alloyed Ni.

Prior research has shown that Ni-W alloys can be refined to a fully amorphous structure [8]. A corresponding dark field image of Fig. 1 is shown in Fig. 6. Grain size is estimated to be

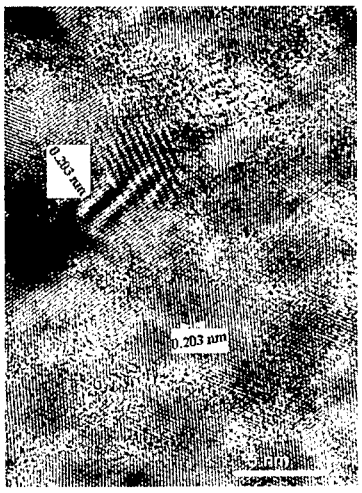


Fig. 3 High-resolution image of nanocrystalline Ni-W alloys deposited at a current of 0.05 A/cm^2.

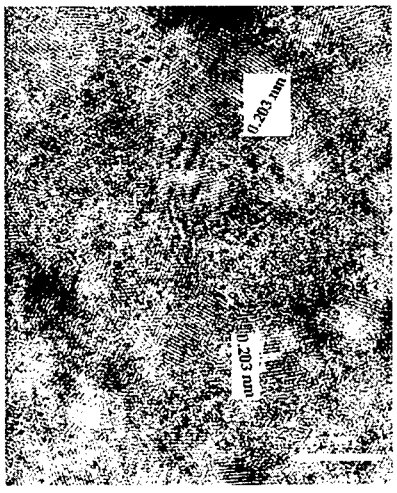


Fig. 4 High-resolution mage of nanocrystalline Ni-W alloy deposited at a current of 0.15 A/cm^2.

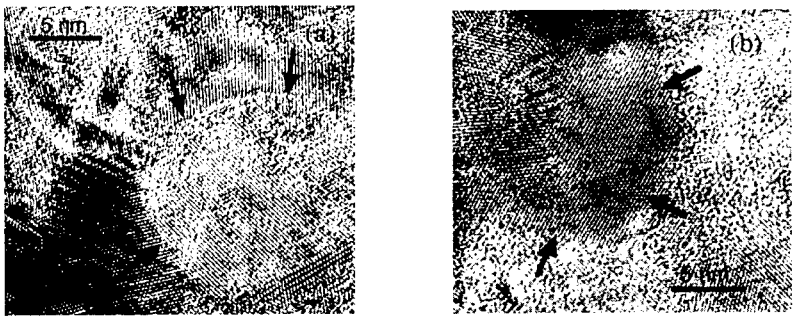


Fig. 5 High-resolution image of nanocrystalline Ni-W alloy deposited at a current density of 0.10 A/cm^2, showing high-angle boundaries without structureless layer (a) and grain boundaries with a structureless phase separating two neighboring grains (b).

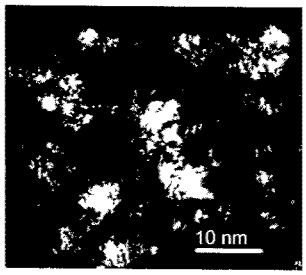


Fig. 6 Dark field image taken from the sample used for Fig. 1.

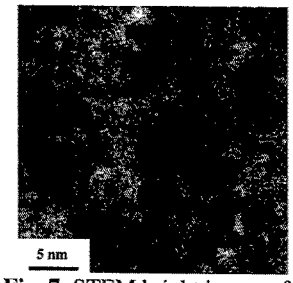


Fig. 7 STEM bright image of the sample used for Fig. 6.

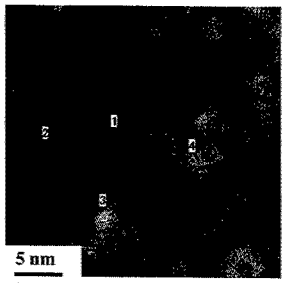


Fig. 8 HAADF image showing Z contrast caused by density difference.

about 5 nm. A close inspection of this figure shows the existence of many very small bright spots. These bright spots are structureless phase includes very short-range ordered crystals.

To further investigate the W distribution, a STEM image from the sample used for Fig. 1 is shown in Fig. 7. This figure does not show the lattice image because STEM observation is not available for taking the image. The angular dark field image (i.e. Z-contrast) of Fig. 7 is shown in Fig. 8. In Fig. 8, the dark field contrast that arises from the difference of local density in the material; specifically, a brighter spot indicates a higher density. Chemical analyses were subsequently carried out at a dark region (Point 1) and a bright region (Point 4) in Fig. 8, and the results are shown in Fig. 9. From the intensities at 1.774 keV for W and 7.471 keV for Ni, the atomic percents were calculated at Points 1 and 4. Tungsten contents were 8 at% and 14 at% at Points 1 and 4, respectively. It is noted that the tungsten content at Point 4 is over the equilibrium solubility limit of 12.5 at% at room temperature. Electrodeposition is, in principle, like rapid solidification process, which usually produces metastable phase or even amorphous phase. The structureless bands shown in Fig 5b is thereby proposed to be a metastable phase caused by the local supersaturation of W in Ni. Watanabe [14] recently reported that if the affinity between an alloying element and the matrix element is stronger than that between the same elements, the alloying system has high potential to produce an amorphous phase. His simulations showed that amorphous-like structure occurs in a binary system when the alloying content is about 20 at%. The mixed phase structure obtained in this study is in a transitional stage from nanocrystalline state to amorphous state.

CONCLUSIONS

Nanocrystalline Ni-W alloys were synthesized using an electrodeposition method, and their structure investigated. The main results of this work are:

1) The Ni-W alloys all have similar composition (~13 at% W) and grain size (d ~ 4-9 nm), and the texture of the foils varies depending on the deposition current density.

2) There are two types of grain boundaries in nanocrystalline Ni. One type of grain boundary is of one atomic layer thin and another type consists of a structureless layer of about 0.5-1 nm in thickness.

3) The formation of structureless phase is characteristic for the electrodeposited Ni-W alloys. The structureless band is probably a metastable phase caused by the local supersaturation of W in Ni.

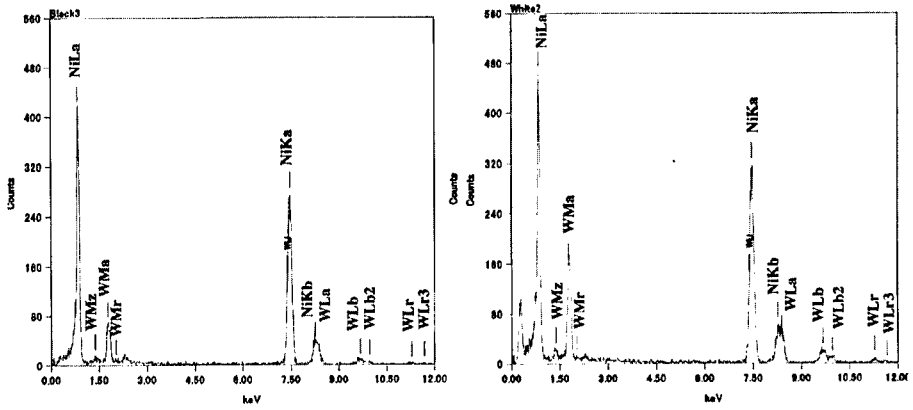


Fig. 9 Chemical analysis from Points 1 and 4 in Fig. 8. The W content at Point 4 is higher than that at Point 1.

REFERENCES

1. R.T.C. Choo, J.M. Toguri, A.M. El-Sharik, U.Erb, *Journal of Applied Electrochemistry* **25**, 384 (1995).
2. H. Natter, M. Schmelzer, R. J. Hempelmann, *Mater. Res.* **13**, 1186 (1998).
3. M.L. Trudeau, *Nanostructured Materials* **12,** 55 (1999).
4. D.L. Grimmett, M. Schwartz, K. Nobe, *Journal of the Electrochemical Society* **140,** 973 (1993).
5. U. Erb, *Nanostructured Materials* **6,** 533 (1995).
6. U. Erb, A.M. El-Sharik, G . Palumbo, K.T. Aust, *Nanostructured Materials* **2,** 383 (1993).
7. A. Inoue, *Acta Mater.* **48,** 279 (2000).
8. T. Yamasaki, R. Tomohira, Y. Ogino, P. Schlossmacher, K. Ehrlich, *Plating and Surface Finishing* **87,** 148 (1999).
9. T. Yamasaki, *Scripta Mater.* **44,** 1497 (2001).
10. *ASM Handbook: Alloy Phase Diagrams.* Vol. 3. 1992, Metals Park, OH: ASM.
11. T. Watanabe, *Materialia Japan* **40,** 871 (2001).

Mat. Res. Soc. Symp. Proc. Vol. 740 © 2003 Materials Research Society I3.30

Interface Conduction between Conductive ReO_3 Thin Film and $NdBa_2Cu_3O_6$ Thin Film

Manabu Ohkubo, Kumiko Fukai, Kohji Matsuo, Nobuyuki Iwata and Hiroshi Yamamoto
Department of Electronics & Computer Science,
College of Science & Technology, Nihon University
7-24-1 Narashinodai, Funabashi-shi, Chiba 274-8501, Japan

ABSTRACT

The Re oxide films were deposited on quartz glasses by RF reactive sputtering from a Re metal target. The lowest resistivity was observed in the film *in-situ* annealed at 200°C in Ar atmosphere and showed the order of 10^{-4} Ωcm of which the value was still about 10 times as large as that of a single crystal ReO_3. The temperature dependence of the resistivity revealed a metallic behavior. A superconductivity did not take place in the bilayered film of ReO_3 / $NdBa_2Cu_3O_6$. In the interface region the resistivity minimum probably caused by the Kondo effect was observed in the neighborhood of 120K.

INTRODUCTION

Most high-*Tc* cuprates superconductors have two-dimensional multilayered structures with CuO_2 planes. The cuprates show superconductivity when enough carriers are doped to the CuO_2 planes from a charge reservoir block (CRB). We have been interested in rhenium (Re) oxides [1] as the candidate of a CRB because multi-valences, +2 ~ +7, of Re ions are noticeable in various Re oxides. We propose the multilayered films with ReO_3 (CRB) and cuprates superconductors in order to synthesize novel high-*Tc* superconductors. Especially an infinite layered cuprates is expected to become the candidate of the pair material for Re oxides.

It is well known that the ReO_3 reveals extremely high conductivity comparable to that of Ag. The structure of ReO_3 is simple as shown in Figure 1. It was, however, difficult to obtain Re oxide films due to vigorous sublimation at comparatively low temperature.

The purposes of this work are to prepare the Re oxide thin films and to study the resistivity of the ReO_3 thin film, and to evaluate it as the material of a CRB. As a preliminary research we

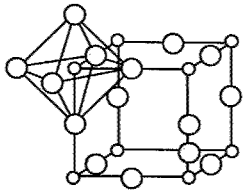


Figure 1. The structure of ReO_3.

have carried out the deposition of ReO_3 thin films on reduced nonsuperconductive $NdBa_2Cu_3O_6$ films, and discussed the transport properties of the bilayered film.

EXPERIMENTAL

We prepared the rhenium oxide thin films by reactive RF sputtering from the targets which were compressed Re powder or a metal Re disk. The substrates were quartz glasses. The distribution of temperature on the substrate was kept constant and uniform by using a copper sheet between the substrate and its holder. The RF electric power was about 100 W. The reactive and sputtering gases were O_2 and Ar, respectively. The pressure of the gas was Ar / O_2 = 90 / 10 mTorr. The substrate temperature was changed from ambient to 240°C. In the case of ambient, the prepared films were *in- situ* annealed in the temperature range from 150°C to 300°C for 30 minutes after the film deposition.

Superconductive $NdBa_2Cu_3O_7$ films were prepared by a pulsed Laser ablation deposition. The detailed preparation conditions will appear elsewhere. The deposition of ReO_3 was carried out on the reduced nonsuperconductive $NdBa_2Cu_3O_6$ film. The deoxidization of the $NdBa_2Cu_3O_7$ thin film was carried out by the annealing at 300°C in a vacuum. By deoxidization in the vacuum the lattice parameter **c** of the $NdBa_2Cu_3O_{7-\delta}$ thin film changed from 11.73Å to 11.86Å. The **c** value after the annealing was almost equivalent to that of $NdBa_2Cu_3O_6$.

The crystal structure of the films was analyzed by reflected x-ray diffraction (XRD). The surface of film was observed by a scanning electron microscope (SEM). The resistivity was measured by a four-probe technique. The current value was set up so that changes of the voltage by the noise came within about 1% of measurement voltage values.

RESULTS & DISCUSSION

The Re oxide films did not grow on the substrates at substrate temperatures above 100°C because of the strong sublimation of Re oxides. It was quite difficult to control a suitable substrate temperature in order to obtain the film.

The deposited films on ambient substrates deliquesced in air and were yellow in color. These properties were consistent with the features of Re_2O_7. The film was amorphous, which was confirmed by XRD. Then, post annealing was done in order to proceed with the crystallization and reduction of as-prepared films.

The prepared films were annealed in Ar atmosphere in the temperature range from 150°C to 300°C for 30 minutes. Figure 2 shows the typical XRD spectra of the annealed films. The peaks observed were assigned as those of the ReO_3 phase.

Figure 3 shows the peak intensity ratio of ReO_3 (100) / ReO_3 (110) and the full width at half

maximum (FWHM) as a function of annealing temperature. The peak intensity ratio is about 7 at annealing temperatures above 200°C, while it is less than 2 at the annealing temperature of 150°C. The FWHM reveals the minimum value, 0.15° in the film annealed at 220°C.

The crystal growth at 150°C was low probably because of the poor reduction of Re_2O_7. When the annealing was carried out above 200°C the films changed to ReO_3 films with the preferential orientation of (100) planes.

Figure 4 shows the annealing temperature dependence of color change of Re oxides. The color of ReO_3 changed from blue to green with increase of annealing temperature. It is thought that the degree of oxidation of ReO_3, which changed slightly by annealing temperature, influenced the color of the films.

Figure 5 shows the typical resistivities of thin films with the ReO_3 phase as a function of temperature. The resistivity slightly decreases with decreasing temperature. Metallic behavior was observed in the all annealed films. The film annealed at 260°C shows a

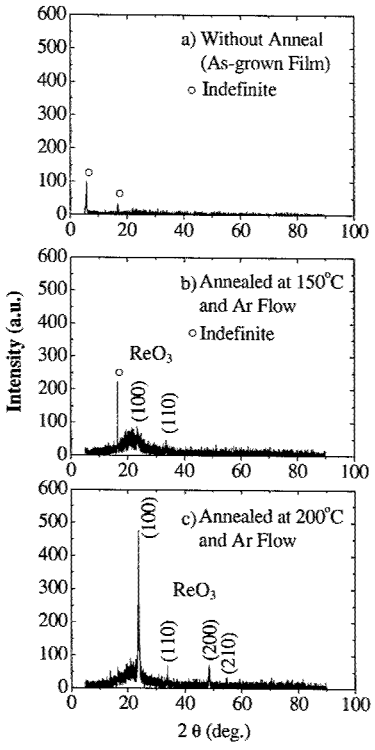


Figure 2. XRD spectra.

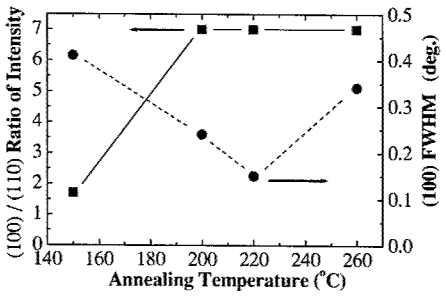


Figure 3. Annealing temperature dependence of the intensity ratio of ReO_3(100)/(110), and the full width at half maximum.

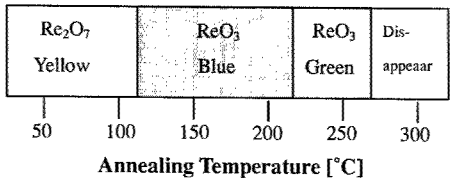


Figure 4. Annealing temperature dependence of color changes of Re oxides.

comparatively high resistivity. This was thought to be caused by the decrease of the degree of the oxidation.

In Figure 6 the room temperature resistivity are summarized with the change of annealing temperature. In the annealing temperature range from 200°C to 260°C, the resistivity of the films increases as the annealing temperature increases. Then the crystallinity decreased as indicated by the increase of FWHM in the temperature range of 220 ~ 260°C. The ReO_3 film may be changing to form a more reduced, lower conductivity phase as shown by the decrease in conductivity.

Conclusively, the optimum annealing condition to obtain conductive ReO_3 thin films was at around 200°C. The resistivity of the single-crystal bulk ReO_3 was very low [2], 10^{-5} to 10^{-7} Ω cm, and showed metallic conduction with a large resitivity ratio, R (300K) / R (100K) of about 10. The resistivity of the ReO_3 film was, however, still several ten times larger than that of the single crystal. The higher crystallinity and the optimum oxidation are indispensable in order to acquire the higher conductivity.

Figure 7 shows the SEM photograph of the cross section of the ReO_3 film on the quartz glass. It was confirmed that the ReO_3 film was deposited and grown uniformly on the substrate. Therefore we can discuss a transport phenomenon in the interface of the film and the substrate.

The bilayered film with $NdBa_2Cu_3O_6$ and ReO_3 was studied in order to investigate the doping effect from ReO_3 to the nonsuperconductive cuprate layer. The resistivity of $NdBa_2Cu_3O_6$ in the room temperature became about 10^3 times as large as that of the ReO_3 thin film. For this reason, the resistivity on the surface of a bilayered film is dominated by the resistivity of the ReO_3 thin film.

Figure 8 shows the resistivity of ReO_3 thin film and the bilayered film. The superconductivity expected in the temperature range above 77K was not observed. The value and the temperature dependence of the resistivity are almost the same as those of the ReO_3 thin

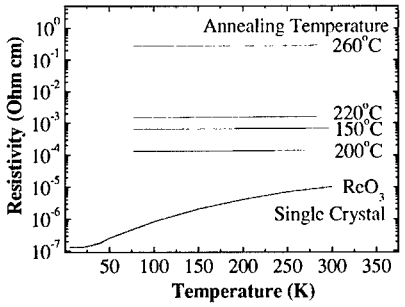


Figure 5. The temperature dependence of resistivity of ReO_3 thin films, and single crystal [2].

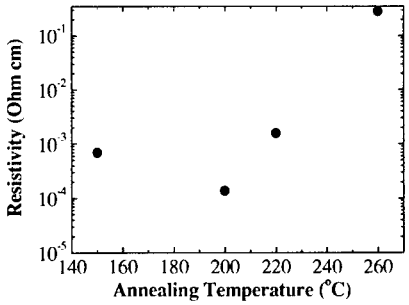


Figure 6. The change of the 300K resistivity depending on annealing temperature.

film. It should be, however, noticed that the "resistivity minimum" appeared at a temperature of about 120 K. It is believed that the spins of the $NdBa_2Cu_3O_6$ influences the resistivity of the ReO_3 in the near the interface. When the spin reorientation takes place corresponding to the antiferromagnetic phase transition of the $NdBa_2Cu_3O_6$ film, the resistivity observed may be changed. The resistivity minimum is expected appear at the temperature below a Néel temperature.

As is well known with respect to the Kondo effect [3], the magnetic impurities in metals establish the resistivity minimum. In the present case, it is possible that the antiferromagnetic ordering of spins produces the same phenomenon. We think that scattering of conductive electrons are influenced by the magnetic moments through Kondo effect in the interface of the bilayered film. The order-disorder of magnetic moment of Cu strongly is related to the appearance of high temperature superconductivity. The results observed in the interface of the bilayered film give us a novel material system to investigate mechnaisms of a high temperature superconductivity.

CONCLUSIONS

Since Re oxides are easily sublimed, it was difficult to obtain the as-grown ReO_3 film. The ReO_3 thin film was prepared by adopting a post-annealing process. The crystal growth of the ReO_3 phase and preferential (100) orientation depended on the annealing temperature. The metallic conductivity of the ReO_3 thin film was confirmed for the first time. From the influences of crystallinity and the degree of reduction, a higher conductivity ReO_3 thin film was obtained by post-annealing at about 200°C. The expected superconductivity was not observed



Figure 7. The SEM photograph of the cross section of the ReO_3 film on the quartz glass.

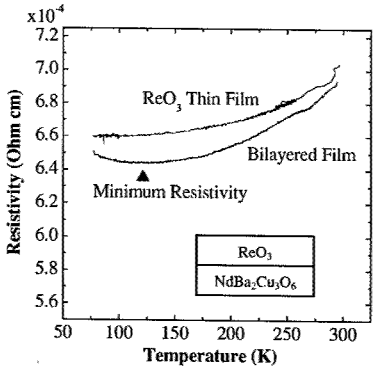


Figure 8. The temperature dependence of the resistivity of the bilayered film

in the bilayered ReO_3 / $NdBa_2Cu_3O_6$ thin film. On the other hand, the resistivity minimum appeared in the bilayered film. Therefore, we conclude that the interesting interface phenomenon which takes place in the conductive electron systems strongly depends on spin ordering.

REFERENCES

1. J. Feinleib, W. J. Scouler, A. Ferretti, *Physical Review*, **165**, 765(1968).
2. T. P. Pearsall and C. A. Lee, *Physical Review B*, **10**, 2190(1974).
3. J. Kondo, *Prog. Theor. Phys.*, **32**, 37(1964).

Fracture and Mechanical Properties III

Mat. Res. Soc. Symp. Proc. Vol. 740 © 2003 Materials Research Society

Characterization of Nanoparticle Films and Structures Produced by Hypersonic Plasma Particle Deposition

Christopher R. Perrey, Ryan Thompson, C. Barry Carter*, Ashok Gidwani[1], Rajesh Mukherjee[1], Thierry Renault[1], P. H. McMurry[1], J. V. R. Heberlein[1], and S. L. Girshick[1]

Department of Chemical Engineering and Materials Science
University of Minnesota, 421 Washington Ave. S.E., Minneapolis, MN 55455
[1] Department of Mechanical Engineering
University of Minnesota, 111 Church Street S.E., Minneapolis, MN 55455
*corresponding author: carter@cems.umn.edu

ABSTRACT

There is great potential for the use of nanostructures in numerous applications. Investigation of nanoparticle films and structures is an important area of research for the production of nanoengineered devices. However, for these devices to become a reality, a production method that can yield high-rate synthesis of nanostructured powders is necessary. The hypersonic plasma particle deposition (HPPD) process has been shown to be capable of such high-rate production of nanoparticle films and structures. Versatile in its ability to manufacture nanoparticles of different chemistries HPPD also has the capability of in situ particle consolidation and assembly. In this study, chemically diverse films and structures have been produced by HPPD on a variety of substrates. Using novel specimen preparation techniques, these nanoparticles have been characterized by TEM. Fundamental issues of importance have been investigated for both the nanoparticle structure and the constituent nanoparticles. These issues include nanoparticle crystallinity and defect structure. The chemical homogeneity and structural characteristics of the deposition are also investigated. This application of microscopy to aid process development has resulted in insights into the nanoparticle formation process and the dynamics of the HPPD process.

INTRODUCTION

There is currently great interest in the synthesis and processing of nanostructured materials, which are materials with grain sizes less than about 100nm. Such materials are often found to have properties superior to those of conventional bulk materials. Examples of enhanced properties include greater strength, hardness, reactivity, etc. Past developments in production and determination of the properties of these materials have been summarized in extensive reviews [1, 2]. The potential applications of these materials include wear resistant coatings, microparts for MEMS , ductile ceramics, new electronic and optical devices, and catalysts.

This work demonstrates the ability of hypersonic plasma particle deposition (HPPD) to produce deposits of nanostructured materials. Characterization of these deposits has led to a greater understanding of nanoparticle formation and the dynamics of the HPPD process.

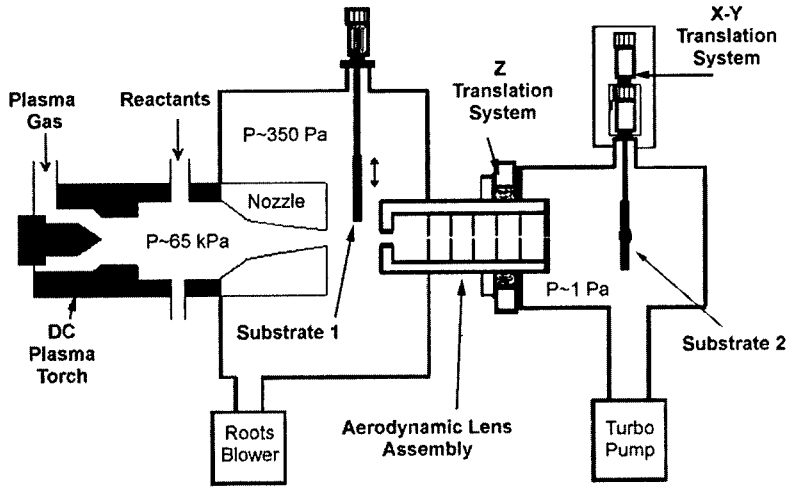


Figure 1: Schematic of the HPPD apparatus

EXPERIMENTAL DETAILS

Hypersonic Plasma Particle Deposition (HPPD) involves a one-step process in which nanoparticles are both synthesized and deposited. The experimental set-up is shown schematically in Figure 1. The details of the experimental apparatus and operating conditions have been described previously [3, 4] and are briefly explained here. A 10 kW DC plasma torch operates with typical plasma forming gas feed rates of 30-37.5 slm of argon and 2-7.5 slm of hydrogen. The arc current varies between 200-275 A. The gas phase reactants are injected downstream of the plasma torch, where the temperatures are sufficiently high (> 4000K) to dissociate the precursor vapors into their atomic form. The resulting gas mixture is then quenched through a converging boron nitride nozzle, leading to super saturation of vapors and subsequent nucleation of particles. The particle-laden gas is then accelerated by a free expansion into the vacuum chamber (maintained at about 2 Torr). The particles impact a substrate in one of the following two ways to form a deposit.

In the first process, called "continuous film deposition", a molybdenum substrate is positioned normal to the flow, and particles as small as a few nanometers in diameter impact the substrate at high velocity to form a dense, nanostructured coating as seen in Figure 2. For example, a 20 nm particle is predicted by numerical calculations to impact the substrate with a velocity of about 1700 m/s. The typical growth rates for these films are 5-7 μm/min.

In "focused beam deposition", the second process, the molybdenum substrate is replaced by an aerodynamic lens assembly, which "focuses" [5] the particles to a narrow beam, with beam widths of the order of a few tens of microns. A second-stage substrate is placed downstream of the exit nozzle of the lens assembly. If this substrate is held stationary the nanoparticle beam

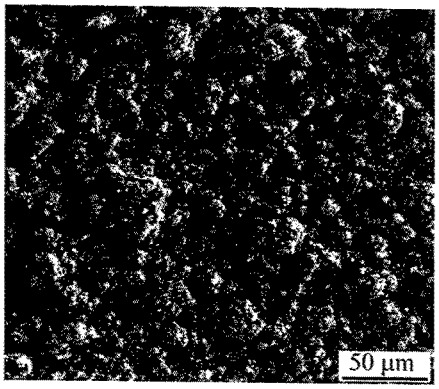


Figure 2: SEM image of the surface of a Ti-Si-N nanoparticle film deposited at 700 °C. The complex structure of the film is evident even at low magnifications.

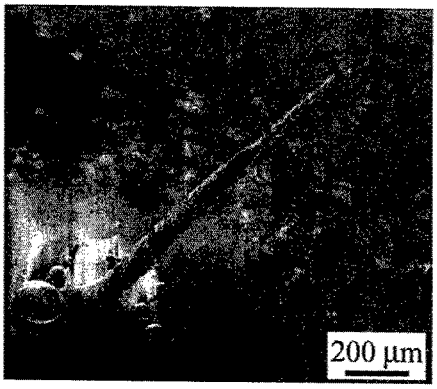


Figure 3: A SiC nanoparticle tower, approximately 2 mm tall with a 40 μm half-height width, deposited with focused particle beam on a stationary substrate in 4 minutes. This implies a growth rate of approximately 8 μm/min for this structure.

forms a high-aspect-ratio "tower" (Fig. 3). By translating the substrate one can use the particle beam to deposit lines and patterns. It is possible to deposit on a variety of substrates in this stage. So far, Si wafers, Al_2O_3 wafers, and TEM support films have been used.

The HPPD process has deposited nanostructured films composed of elements from among the following: Si, Ti, C, and N. The reactants for pure Si and Ti deposits are $SiCl_4$ and $TiCl_4$, respectively, while CH_4 is injected to produce carbides and N_2 (in the plasma) or NH_3 (in the reaction zone) to produce nitride deposits. Average particle sizes for the HPPD process are in the range 10–30 nm.

Nanoparticle films were prepared for TEM analysis using a FEI DB 235 focused ion beam (FIB) tool. Both the lift-out and self-supporting techniques for the FIB were employed [6-9]. Conventional TEM characterization was carried out using a Philips CM30. Analytical TEM and high-resolution TEM (HRTEM) were performed using a Philips CM200 and a spherical aberration-corrected Philips CM20, respectively.

DISCUSSION

The surface of a Ti-Si-N nanoparticle film produced by HPPD (utilizing the "continuous film deposition" process) is shown in Figure 2. At low magnification, the film appears relatively uniform; however, at higher magnifications, the nanostructure of the film becomes evident. In order to characterize the sub-surface features of the films by TEM, special preparation techniques have been developed. The use of TEM is necessary for nanoscale characterization due to the versatility and resolution of the characterization techniques [10, 11]. However, the TEM specimens are required to be less than 3 mm in diameter and thin, with the final thickness dependent on the analysis desired [11]. For this study, the FIB was used to produce electron-transparent cross section specimens of the films: Figure 4 is a SEM image of a completed lift-out specimen of a β-SiC nanoparticle line produced with the focused beam deposition stage. It is

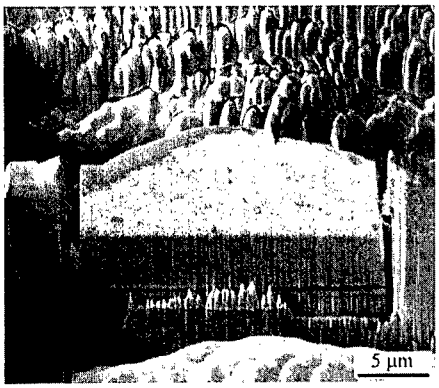


Figure 4: SEM image of a β-SiC nanoparticle structure prepared by the FIB lift-out technique. The specimen structure is maintained for subsequent TEM analysis.

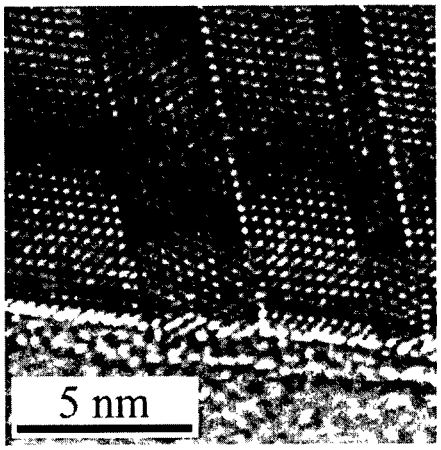


Figure 5: Bright-field HRTEM image of microtwins in a β-SiC nanoparticle.

important to maintain the film-substrate interface and internal porosity of the structure, as these factors influence the properties of the film. It must be noted that the use of traditional TEM specimen preparation methods would require these pores filled with epoxy to stabilize their structure. Here, the FIB provides a precise method that does not require such procedures, and provides a large intact electron transparent area for subsequent TEM analysis [12].

In addition to the characterization of nanoparticle films, individual nanoparticles produced by HPPD have been analyzed. Using the focused beam deposition stage of the HPPD apparatus, it is possible to deposit lines of nanoparticles directly onto TEM support films. The center of a line is densely populated by nanoparticles; however, if the specimen is examined away from the line, a sparse distribution of nanoparticles is found, allowing the examination of single nanoparticles. Atomic level analysis is then possible using HRTEM. An example of this characterization is illustrated in Figure 5, which is a bright-field HRTEM image of microtwins in a β-SiC nanoparticle. The changes in atomic stacking are evident across the twin boundaries. Here, the use of spherical aberration correction in the HRTEM provides direct imaging of defect structure without the need for extensive image reconstruction, and will allow for a more complete understanding of growth- and mechanically-induced defects in nanoscale materials.

Analysis of the identity of chemically distinct surface layers is possible using analytical TEM. Figure 6 is a scanning TEM (STEM) image which denotes the path of an electron energy loss spectrum (EELS) line scan across a Si nanoparticle. A spectrum was collected every 1 nm along the path. The Si and O signals are shown in Figure 7 as a function of distance for the line scan. The shape of the oxygen profile is expected for a nanoparticle composed of a Si core that has oxidized at the surface. At the edge of the particle, only the oxide layer is sampled by the electron beam, leading to a large O signal. Conversely, the diminished oxygen signal in the bulk of the particle is due to the interference of the bulk Si core, which effectively masks the oxide signature. As oxide layers are deleterious to some potential nanoscale applications, identifying the presence of certain chemical species in nanoparticles has great importance for the development of the HPPD process.

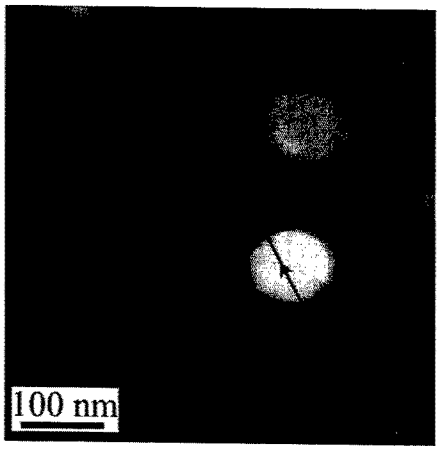


Figure 6: Annular dark-field STEM image designating the path of a line spectrum across a Si nanoparticle.

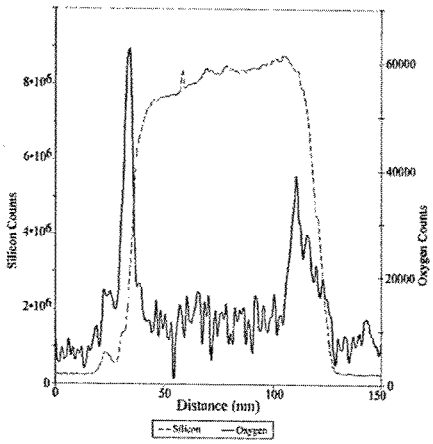


Figure 7: Electron energy loss spectra for the line scan shown in Figure 6. The oxygen signal indicates the presence of a surface oxide layer for the Si nanoparticle.

CONCLUSIONS

This study has illustrated the ability to produce and characterize both nanoparticle films and individual nanoparticles. The HPPD system is capable of high-rate deposition of chemically diverse structures. The techniques described for sample preparation and analysis provide opportunities for understanding nanoparticle formation and structure, as well as facilitating feedback on the performance of the HPPD apparatus. This combination will lead to tailoring the HPPD system for the production of nanoparticle-based functional structures. Further structural and chemical analysis of nanostructures will provide information to investigate material properties at the nanoscale.

ACKNOWLEDGEMENTS

This work was supported by the NSF NIRT program through grant NSF/DMI-0103169. The authors thank James Bentley of Oak Ridge National Laboratory for assistance with the analytical TEM, and Paul Kotula and Joseph Michael of Sandia National Laboratory for access to the FIB. Research at the ORNL SHaRE Collaborative Research Center was supported by the Division of Materials Sciences and Engineering, U.S. Department of Energy, under contract DE-AC05-00OR22725 with UT-Battelle, LLC. Work at Sandia was supported through the U.S. Department of Energy under contract DE-AC04-94AL8500. Sandia is a multiprogram laboratory operated by Sandia Corporation, a Lockheed-Martim Company, for the U.S. Department of Energy.

REFERENCES

1. R.W. Siegel. Materials Science and Engineering 1993;**A168**: 189.
2. H. Gleiter. Progress in Materials Science 1989;**33**: 223-315.
3. N.P. Rao, N. Tymiak, J. Blum, A. Neuman, H.J. Lee, S.L. Girshick, P.H. McMurry and J. Heberlein. Journal of Aerosol Science 1998;**29**: 707-720.
4. J. Blum, N. Tymiak, A. Neuman, Z. Wong, N.P. Rao, S.L. Girshick, W.W. Gerberich, P.H. McMurry and J.V.R. Heberlein. Journal of Nanoparticle Research 1999;**1**: 31.
5. F. DiFonzo, A. Gidwani, M.H. Fan, D. Neumann, D.I. Iordanoglou, J.V.R. Heberlein, P.H. McMurry, S.L. Girshick, N. Tymaik, W.W. Gerberich and N.P. Rao. Applied Physics Letters 2000;**77**: 910-912.
6. F.A. Stevie, C.B. Vartulo, L.A. Giannuzzi, T.L. Shofner, S.R. Brown, B. Rossie, F. Hillion, R.H. Mills, M. Antonell, R.B. Irwin and B.M. Purcell. Surface and Interface Analysis 2001;**31**: 345-351.
7. J.K. Lomness, L.A. Giannuzzi and M.D. Hampton. Microscopy and Microanalysis 2001;**7**: 418-423.
8. D.M. Longo, J.M. Howe and W.C. Johnson. Ultramicroscopy 1999;**80**: 69-84.
9. T. Yaguchi, H. Matsumoto, T. Kamino, T. Ishitani and R. Urao. Microscopy and Microanalysis 2001;**7**: 287-291.
10. K.C. Grabar, K.R. Brown, C.D. Keating, S.J. Stranick, S.-L. Tang and M.J. Natan. Analytical Chemistry 1997;**69**: 471-477.
11. D.B. Williams and C.B. Carter. Transmission Electron Microscopy, Plenum Press, New York (1996).
12. C.R. Perrey, C.B. Carter, P.G. Kotula and J.R. Michael. Microscopy and Microanalysis 2002;**8**: 1144CD.

Polymer-Based Nanostructured Materials

Mat. Res. Soc. Symp. Proc. Vol. 740 © 2003 Materials Research Society

Biodegradable Polyester / Layered Silicate Nanocomposites

Pralay Maiti[1], Carl A. Batt[2] and Emmanuel P. Giannelis[1]
[1]Department of Material Science and Engineering, [2]Department of Food Science, Cornell University
Ithaca, NY 14853, U.S.A.

ABSTRACT

Nanocomposites of α-hydroxy polyester, polylactide (PLA) and β-hydroxy polyester, polyhydroxybutyrate (PHB) with layered silicates have been successfully prepared by melt extrusion of PLA and PHB with organically modified montmorillonite (MMT) and fluoromica. The mechanical properties of the nanocomposites are improved compared to the neat polymers. Storage modulus increase up to 40% compared with the pure polymers by adding only 2-3 wt% nanoclay. Biodegradation can be controlled by the choice of the nanoclay used.

INTRODUCTION

Concerns over the persistence of plastics in the environment, shortage of landfill space, increased cost of solid waste disposal, emissions during incineration, and negative impact on wildlife through ingestion and entrapment have increased research and development efforts on biodegradable polymers. The challenge remains to design biodegradable alternatives to conventional plastics that combine the mechanical and physical properties of the latter, yet they are susceptible to microbial and environmental degradation without adverse effect on the environment. Improvements in biodegradability typically, however, come at the expense of performance and trade-offs often need to be made in achieving performance while maintaining biodegradation.

Recently, polylactides (PLA) and polyhydroxybutyrate (PHB) have received much research attention as biodegradable polymers [1-4]. However, their strength as well as thermal stability, gas barrier, and solvent and flame resistance are not sufficient for end use. Polymer nanocomposites made by incorporating inorganic nanoparticles such as nanoclays into a polymer matrix have been shown to improve materials properties. In addition, the nanocomposites can avoid trade-offs in materials properties and, thus, design materials with a unique set of properties that cannot be realized in conventional filled polymers and composites.

A typical challenge in synthesizing polymer nanocomposites is the inherent incompatibility between the polymer matrix and the inorganic nanoparticles. To circumvent this problem the nanoparticles are organically modified. For example, nanoclays can be ion-exchanged with different alkyl ammonium or phosphonium ions to render them organophilic and, thus, more compatible with the polymer [5-9].

In this paper we report the synthesis and properties of both PLA and PHB nanocomposites with different nanoclays prepared by melt intercalation. The microstructure, mechanical properties and biodegradability are presented and discussed.

EXPERIMENTAL

Polylactide (PLA) ($M_w = 1.87 \times 10^5$, $M_w/M_n = 1.76$ and *D*-content = 1.1-1.7%) was supplied by Dow Cargil Company and dried under vacuum at 80°C before use. Montmorillonite (MMT) and fluoromica (dimethyl dialkyl ammonium, MAE, and dipolyoxyethylene alkyl ammonium, MEE) were used as received. Nanocomposites were prepared by melt extrusion using a twin screw, bench top microextruder operated at 190°C. The extruded and palletized strands were dried under vacuum at 80°C to remove residual water. The inorganic content was measured by measuring the residue after heating at 950°C in a furnace. The numbers in the nanocomposite sample notation represent the percent nanoclay content. Unless otherwise specified the nanocomposites are based on C_{18}-MMT.

X-ray diffraction experiments were performed using a θ-θ diffractometer (Scintag) equipped with a germanium detector using CuK_α radiation and a graphite monochromator (wavelength, λ = 0.154 nm). The generator was operated at 45 kV and 40 mA. Dynamic mechanical measurements were performed using $15 \times 4 \times 1.5$ mm^3 samples on a TA Instrument (DMA 2980) in tension. The temperature was ranged from –50 to 150°C using a heating rate of 2°C/min. Biodegradation experiments were performed be measuring the weight loss of $2 \times 2 \times 0.5$ mm^3 sheets immersed in compost manure at 60°C and 90% humidity in a closed chamber.

RESULTS AND DISCUSSION

Microstructure

Wide angle X-ray diffraction (WAXD) patterns of the nanocomposites based on octadecyl ammonium exchanged montmorillonite are shown in Figure 1. The peak position of the nanocomposites shifted towards a lower diffraction angle when compared to the base nanoclay suggesting that spacing of the silicate layers increases by intercalation of polymer chains in the galleries. A small decrease in d-spacing with increasing silicate content is also seen.

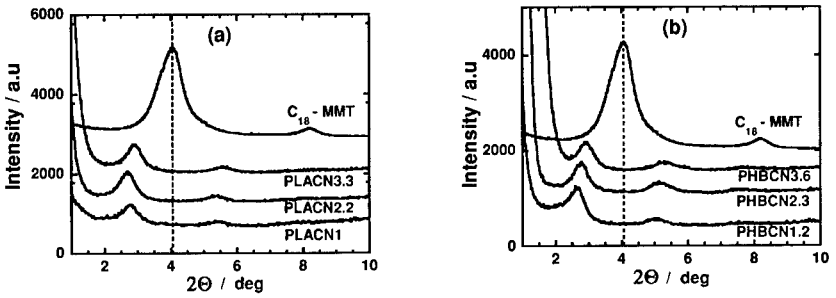


Figure 1. WAXD patterns of PLA (left) and PHB (right) nanocomposites. The pattern of the base nanoclay is included for comparison. The numbers on the sample notation indicate the percent inorganic content in the nanocomposite.

The peaks in the X-ray diffraction patterns are evidence of intercalated nanocomposites in which the spacing increases as a result of polymer intercalation while the regular stacking of the silicate layers is maintained. Transmission electron microscopy also reveals the presence of intercalated nanocomposites in agreement with the X-ray diffraction experiments. The nanocomposites based on fluoromica show similar behavior.

Dynamic Mechanical Property

The storage modulus of PLA and PHB nanocomposite as a function of temperature is shown in Figure 2. The modulus, E′, increases with increasing nanoclay content in both systems. The storage modulus at 20 ºC and percent increment with respect to the pure polymers are summarized in Table I. In general for the same amount of nanoclay the fluoromicas lead to higher increases in modulus compared to montmorillonite. The nanocomposites show about a 40% increase with ~ 3 wt.% nanoclay. Another interesting feature lies in the temperature behavior of the two systems. At the glass transition temperature, T_g, the modulus decreases significantly, almost one order of magnitude, for PLA and its nanocomposites while a slight decrease is observed for PHB and its nanocomposites.

Using differential scanning calorimetry (DSC) we find that PHB is highly crystalline (ΔH = 105 J/g, ~70 % crystallinity [10]) while PLA shows only ~35% crystallinity (ΔH = 35 J/g [11]). The DSC study also shows that the crystallinity does not change in the nanocomposites compared to the neat polymer. We attribute the smaller decrease in modulus for PHB to the higher amount of crystallinity in that system.

The montmorillonite based nanocomposite exhibits a slightly lower Tg from the corresponding fluoromica and neat PHB. The lower Tg is due to the drop in molecular weight from 110K to 60 K in the montmorillonite based nanocomposite. No such degradation is observed for the fluoromica nanocomposite. The difference in behavior between the two nanoclays is probably due to their different surface chemistries (see below).

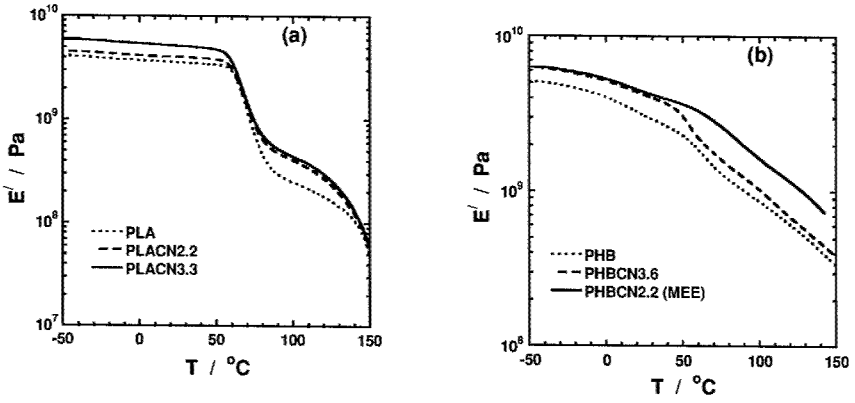


Figure 2. Storage modulus, E′, of samples annealed at 120 ºC as a function of temperature (a) PLA (b) PHB system.

Table I. Storage Modulus of PLA and PHB Nanocomposites

System	E′ / GPa at 20°C	% Increment w.r.t. PLA	System	E′ / GPa at 20°C	% Increment w.r.t. PHB
PLA	3.63	-	PHB	3.25	-
PLACN1.0	4.00	10	PHBCN1.2	3.69	13
PLACN2.2	4.07	12	PHBCN2.3	4.00	23
PLACN3.3	5.26	44	PHBCN3.6	4.38	35
PLACN2.2(MAE)	3.55	no increment	PHBCN2.0(MAE)	4.31	33
PLACN2.1(MEE)	4.26	17	PHBCN2.2(MEE)	4.55	40

Biodegradation in Compost Media

Figure 3 shows the weight loss of PHB and the corresponding nanocomposites as a function of time. Apparently, the degradation starts just after 1 week and at the initial stage the weight loss is almost the same for the pure PHB and the fluoromica based nanocomposite. But after 3 weeks of exposure the rate of degradation is much higher for the neat polymer compared to the nanocomposites. Interestingly, the montmorillonite based nanocomposite shows a higher initial

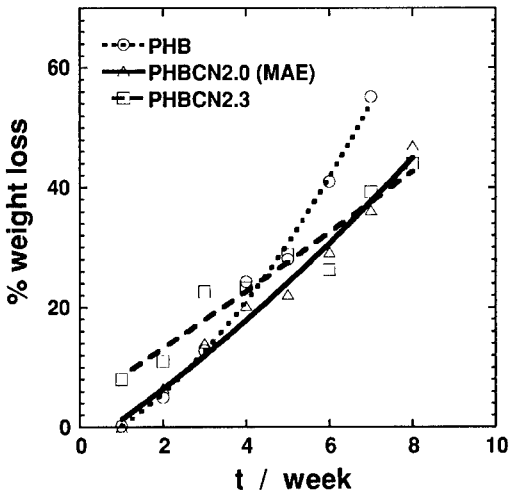


Figure 3. Percentage weight loss of PHB and its nanocomposite in the compost media at 60°C and 90% humidity as a function of degradation time.

decomposition rate compared even to the neat PHB. This is probably because of the presence of Al Lewis acid sites in the octahedral layers of montmorillonite and/or the presence of surface hydroxyl groups, which can catalyze the hydrolysis of the ester linkages in the polymer. Fluoromica contains Mg in the octahedral sites and much fewer surface hydroxyl groups. The decrease in polymer degradation after some point is attributed to the better barrier properties of the nanocomposites, which prevents oxygen and moisture from reaching the sample. Degradation occurs with the hydrolysis of ester linkages in the presence of moisture and subsequently weight loss appears from the consumption of oligomers by the microorganisms. The different mechanisms operating in the different systems are also evident in the surface roughening of the samples. Work is in progress to establish the degradation mechanism of polymer/silicate layer nanocomposites.

CONCLUSIONS

PLA and PHB form well-ordered intercalated nanocomposites with organically modified silicates. The mechanical properties of the nanocomposites are improved compared to the neat polymers. Storage modulus increase up to 40% compared with the pure polymers by adding only 2-3 wt% nanoclay. Biodegradation can be controlled by the choice of the nanoclay used.

ACKNOWLEDGEMENT

This work was supported by NASA and Rohm and Haas.

REFERENCES

1. D. W. Grijipma and A. Pennings, *J. Macromol. Chem. Phys.* **195**, 1649 (1994).
2. R. G. Sinclair, *J. Macromol. Sci., Pure Appl. Chem.* **A33**, 585 (1996).
3. A. Steinbuechel, "Novel material from sources," *Biomaterials*, ed. D.B. Byron (Macmillan, 1996).
4. H. M. Muller and D. Seebach, *Angew. Chemi Inter. Ed.* **32**, 477 (1993).
5. R. A. Vaia, H. Ishii and E. P. Giannelis, *Chem. Mater.* **5**, 1994 (1993).
6. E. P. Giannelis, *Adv. Mater.* **8**, 29, (1996).
7. R.A. Vaia and E.P. Giannelis, *MRS Bulletin* **26**, 394, (2001).
8. P. Maiti, K. Yamada, M. Okamoto, K. Ueda, and K. Okamoto, *Chem. Mater.* **14**, 4654 (2002).
9. S.S. Ray, P. Maiti, M. Okamoto, K. Yamada and K. Ueda, *Macromolecules* **35**, 3104 (2002).
10. P.J. Barham, A. Keller, E.L. Otun and P.A. Holmes, *J. Mater. Sci.* **19**, 2781 (1984).
11. E.W. Fischer H.J. Sterzel, and G. Wegner, *Kolloid Z. Z. Polym.* **25**, 980 (1973).

Mat. Res. Soc. Symp. Proc. Vol. 740 © 2003 Materials Research Society I5.4

Characterization of Metal-Oxide Nanoparticles: Synthesis and Dispersion in Polymeric Coatings

Li-Piin Sung, Stephanie Scierka, Mana Baghai-Anaraki, and Derek L. Ho
National Institute of Standards and Technology
Gaithersburg, MD 20899, U.S.A.

ABSTRACT

Metal-oxide nanoparticles can be used to optimize UV absorption and to enhance the stiffness, toughness, and probably the service life of polymeric materials. Characterization of the nano- and microstructure dispersion of particles is necessary to optimize the structure-property relationships. Characterizations of both TiO_2 particles dispersed in an acrylic-urethane matrix and TiO_2 nanostructured films obtained through sol-gel synthesis are discussed. Experimental methods include microscopy (confocal, AFM) and small angle neutron scattering (SANS). Results from SANS experiments, which yield information about the cluster size of the nano-TiO_2 particles and the spatial dispersion in various nanoparticle/polymer samples are presented and compared to the results of microscopy studies.

INTRODUCTION

Metal-oxide particles (or pigments), such as TiO_2 and ZnO, serve many functions in the various polymeric materials. Traditionally, they have been used as pigments to enhance the appearance and improve the durability of polymeric products, and usually they have been considered to be inert. As nanosized particles, these materials exhibit broad band UV absorption, a benefit that currently has been exploited only in sunscreen applications. Also, the addition of nanoparticles would likely enhance the stiffness, toughness, and service life of polymeric materials, for example, in applications in which mar resistance is important. Optimizing the material properties of metal-oxide nanoparticle/polymer composites, the microstructure and dispersion (sizes and spatial distribution) of nanoparticles must be characterized as a function of different process conditions.

In this project, non-destructive characterization methods, such as small angle neutron scattering (SANS), laser scanning confocal microscopy (LSCM) and atomic force microscopy (AFM), were used to determine the spatial dispersion of nano-pigments (mainly TiO_2) in polymeric binders and in nanostructured TiO_2 samples prepared using a sol-gel method. For the nanoparticle/polymer composites, particle sizes, dispersion time, and pigment concentration were varied. The results will be compared to these obtained via transmission electron microscopy (TEM).

EXPERIMENTAL DETAILS*

* Certain instruments or materials are identified in this paper in order to adequately specify experimental details. In no case does it imply endorsement by NIST or imply that it is necessarily the best product for the experimental procedure.

Materials

The particulate materials used in this study included: pigmentary TiO_2 (CR-800, Kerr McGee) and nano-TiO_2 (P-25, Degussa). The average diameters (provided by manufacturers) of these particles were 190 nm and 25 nm for CR-800 and P-25, respectively. TiO_2 particle/polymer films were prepared by dispersing TiO_2 into an acrylic-urethane binder by hand or using a dispermat mixer (BYK Gardener) and then applying the mixture onto release paper using a draw-down blade. The films were cured at room temperature for at least one day. Various particle concentrations and processing conditions were used to examine and improve the dispersion. Additionally, to improve organic compatibility for the dispersion, P-25 was silanized using octyltrichlorosilane (OTS) to obtain a nanoparticle slurry [1]. Nanostructured TiO_2 films obtained using sol-gel synthesis were also studied. Two types of sol-gel processes were used: hydrolysis (sol-product) [2] and condensation (gel-product) [3]. Reactants include titanium tetraisopropoxide (Aldrich), isopropanol (Mallinkrodt), nitric acid (JT Baker), and deionized water. Different sol-gel processing conditions, such as TiO_2 concentration and sintering temperature were examined.

Microscopy

Laser scanning confocal microscope (LSCM)

A Zeiss model LSM510 laser scanning confocal microscope (LSCM) was used to characterize dispersion and microstructure in the film samples. An oil immersion objective (100×/1.3) was used to minimize the scattered intensity from the polymer-air surface. The scanning area of each confocal micrograph was about 18.4 μm × 18.4 μm at 0.18 μm/pixel, with a scanning time of 8 s/frame. The calculated transverse and depth resolutions (point-to-point spread function) for an objective with a numerical aperture (N.A.) of 1.3 are 155 nm and 286 nm, respectively, for a scanning laser wavelength of 543 nm [4].

Atomic Force Microscopy (AFM)

A Dimension 3100 Scanning Probe Microscope with Nanoscope IIIa controller from Digital Instruments was operated in tapping mode to characterize the surface morphology (nanostructure) of TiO_2 films. Silicon microcantilever probes (TESP, Digital Instruments) were used. Topographic and phase images were obtained simultaneously using a resonance frequency of approximately 300 kHz for the probe oscillation and a free-oscillation amplitude of 62 nm ± 2 nm. The set-point ratio (the ratio of set point amplitude to the free amplitude) ranged from 0.60 to 0.80.

Small angle neutron scattering (SANS)

Small angle neutron scattering measurements were performed at the NIST Center for Neutron Research using the 30 m SANS instrument with a combination of various wavelengths and a special focusing neutron optics-device [5] to achieve a wide range of size scale from 1 nm to 1 μm. After standard calibrations and accounting for the sample transmission and film thickness, two-dimensional scattering images were averaged azimuthally to produce a one-dimensional absolute scattering intensity curve as a function of the scattering wave vector q. Here, $q = 4\pi\sin(\theta/2)/\lambda$, where θ is the scattering angle and λ is the wavelength. Because TiO_2 has a higher neutron scattering cross section than the polymeric binder, the neutron scattering intensity is proportional to the differences in TiO_2 concentration within the sample.

The total coherent scattered intensity (from micro-domain), I(q), can be modeled as:

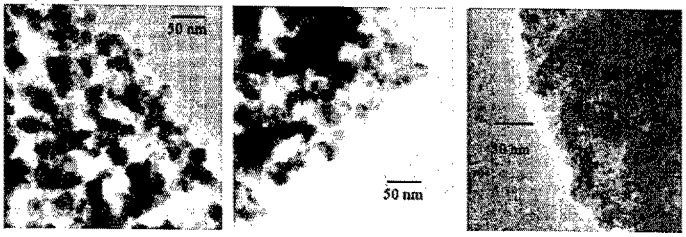
$$I(q) = I(0)\, P(q)\, S(q) \qquad (1)$$

where P(q) is the single particle form factor and S(q) is the structure factor [6]. I(0) is proportional to the scattering amplitude (scattering contrast between the particles and the polymer matrix) and the concentration of particles. The form factor P(q) is characteristic of the size and shape of the particles. The structure factor, S(q), is related to the correlation function describing the radial distribution function between particles or micro-domains. A peak in the scattering profile at a scattering wave vector q indicates the existence of micro-domains with a characteristic average length $d = 2\pi/q_{peak}$. The estimated extended uncertainties (k=2) in the SANS data presented in this paper are smaller than the size of symbols.

RESULTS AND DISCUSSION

Dispersion of TiO_2 particle in polymeric coatings

Traditionally, transmission electron microscopy (TEM) has been used to measure the particle size of metal oxides before dispersion into polymer resins. In Figure 1, conventional TEM micrographs are shown for the TiO_2 samples used in this study. The images were taken on an FEI CM30 transmission electron microscope equipped with a Noran energy dispersive spectrometer. The images were collected at 300 kV and were recorded on a Gatan Model 679 slow scan CCD camera. The samples were prepared by dipping a carbon-coated grid into the sample powders. No grinding or suspension of the powder was performed. The images clearly show that TEM only provides a rough estimate of the particle size and shows that the oxides aggregate into polydispersed clusters.



(a) (b) (c)

Figure 1. TEM micrographs of TiO_2 samples: (a) P-25, (b) organic silanated treated P-25, and (c) gel product (150 g/L, RT, air-dried).

For the particle/polymer composite films, various TiO_2 particle concentrations and processing conditions were carried out to examine the dispersion of particles in the polymeric binder. In Figures 2a –h, LSCM images are shown for TiO_2 composite films. These micrographs are two dimensional (2D) intensity projections, which consists of a stack of Z- slices with 150 nm thickness increments. Figures 2a-b, films with CR-800 (190 nm diameter) particles are shown for two different concentrations: 1 % vs. 2.5 %. Here, the "%" denotes the particle volume concentration (PVC), calculated as 100×(volume of particles/volume of the sample). In Figures 2c-d, films with P-25 (25 nm diameter) are shown for PVC of 1 % and 2.5 %, respectively. For PVC of 2.5 %, changes in distribution are shown in Figures 2e-h for dispermat mixing times of 5 min, 10 min, 20 min, and 40 min, respectively. Note that the scattered intensity from particles is proportional to r^6, where r is the radius of particle, so that a single nanoparticle of 25 nm is not

visible in the LSCM images. All particles observed in the P-25 samples are thus aggregated clusters. All 1 % PVC samples appear to have slightly poorer dispersion compared to the 2.5 % samples, and the P-25 nanoparticles dispersed poorly in all cases in spite of increasing dispersion times (see Figure 2 e-h.)

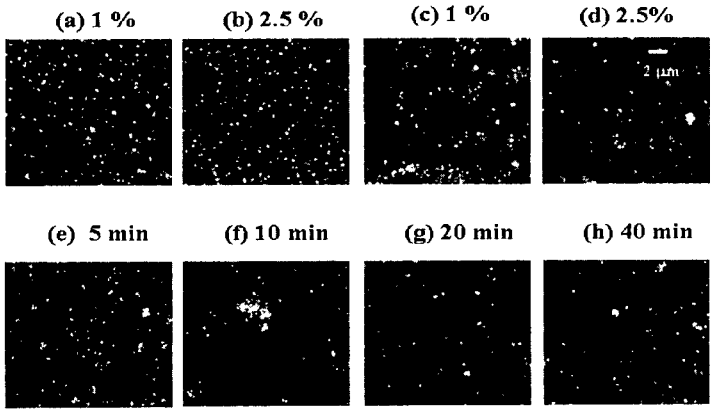


Figure 2. LSCM micrographs of TiO_2 in polymeric binder: (a) and (b) pigmentary TiO_2 particle films. (c) and (d) TiO_2 nanoparticle films; (e)-(h) show TiO_2 nanoparticle (2.5 % PVC) distribution in the polymer films after 5 min to 40 min dispersion times using Dispermat.

Microscopy results represent local and near-surface structures (for example, the probing depth without changing optical contrast is about 8 μm for P-25, 2.5 % PVC samples,) and it is laborious to analyze the particle/cluster sizes from large number of images to obtain sufficient statistics with reasonable resolution. To analyze the dispersion of TiO_2 in the polymeric coatings, SANS was used to characterize the microstructure of the TiO_2/polymer system (Figure 3). From the intensity profile, I(q), in this measurable q-range, the overall cluster size of the sample containing P-25 particles mixed by hand was found to be similar to that of the sample containing pigmentary particles (≈ 190 nm diameter) mixed by hand. In general, the particle cluster size in the sample containing organic silanated treated P-25 mixed using a Dispermat mixer is smaller than those samples containing P-25 without treatment, and was much smaller than in the sample mixed by hand. To determine the averaged sizes and spatial distribution of TiO_2 clusters, the general scattering law was applied as indicated in Eq (1), with the assumption that the scatterers (particles/ clusters) are "sufficiently dilute." In this case, the structure factor $S(q) = 1$ and the form factor P(q) can be generalized using the Guinier approximation [6] for the SANS data in the $q < R_g^{-1}$ region (i.e. for the q values smaller than the turn-over point (q*) to a plateau region of the log-log plot). The R_g is defined as the radius of gyration of the cluster regardless of the shape of TiO_2 clusters.

However, most of the intensity profiles shown in Figure 3 do not show the clear turn-over plateau region, thus the averaged sizes can not be determined accurately. Nevertheless, we can estimate the average size, $R_g > 21$ nm for the sample containing organic silanated treated P-25 /mixed using Dispermat and $R_g > 31$ nm for the sample without treatment. Current work aimed to improve dispersion using surfactants and other treatments will be combined with SANS, xray

scattering measurements in the lower q region to quantitatively characterize the dispersion of nano-TiO_2 particles in the polymeric coatings.

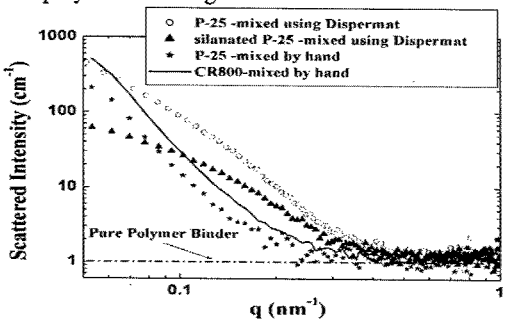


Figure 3. SANS measurements of nano-particles in polymeric binder under different processing conditions. SANS results on the pigmentary particle (CR800) and pure polymeric binder are also shown as reference. The PVC of TiO_2 was 2.5 % in all samples.

TiO_2 network nanostructures prepared through sol-gel synthesis

In addition to using commercially available nano-TiO_2 particles, various sizes of nano-TiO_2 network nanostructures were synthesized by varying and controlling its final particle concentrations and sintering temperatures in sol-gel processing. In Figure 4a, SANS results of the TiO_2 nanostructures prepared using the hydrolysis (sol-product) process are shown for different final particle concentrations. The initial "stock" solution contained titanium isopropoxide, isopropanol, deionized water, and HNO_3 had a calculated concentration of 40 g (TiO_2)/L. Using heat and evaporation, a sol-product (still in a solution form) were prepared with final concentrations of 60 g/L, 124 g/L, and 150 g/L. Similar to the nanoparticle /polymer composite films in the previous section, the R_g of the nanostructure was calculated. Values of $R_g \approx 40$ nm $\pm$ 2 nm were determined at the initial concentration (40 g/L) and decreased slowly to $R_g \approx 8$ nm $\pm$ 0.6 nm at the final particle concentration (150 g/L). SANS results indicated that the size of the nanostructure decreased as the particle concentration of the solution increased. The SANS result of the final dry film made from 150 g/L solution is also plotted in Figure 4a. The size of film structure is consistent with that of the solution at higher q, however with noticeable increasing intensity at $q < 0.1$ nm^{-1} (a indication of larger structure). The micro/nano-structure of the film was observed using AFM, and an image of the 150 g/L TiO_2 dry film is shown in Figure 4b. The topographic image (left image) shows various network structure with various sizes of clusters and pores. The phase image (right image) reveals uniformly fine structure.

In Figure 4c, SANS results are shown for the TiO_2 network nanostructures prepared using condensation process (gel-product) for various sintering temperatures. All samples are in the dry powder state and have a final TiO_2 particle concentration of 150 g/L in the solution state before the condensation process. Noticeably the intensity profiles of the gel product at sintering temperatures above 300 °C exhibit more complex shape and a broad peak formed at large q, which moves to a lower q value with increasing sintering temperature. The peak in I(q) can be attributed to the presence of homogeneous regions with an averaged diameter $d = 2\pi/q_{peak}$. The "d" value is estimated to be 12.5 nm at 300 °C and increased to 38.5 nm at 500 °C. This "homogeneous" region is probably related to the pores (between particles) of the network

structure, at which the pore size increases with increasing sintering temperature. In the low q region, the SANS data follows a $I(q) \sim q^{-4}$ scaling law (Porod law [6]), and this scattering profile indicates the formation of larger cluster sizes, in the size which can not be determined in this q range. Overall, the scattering profile of the gel product can be modeled using two length scales. Further analysis of SANS data will be performed and compared to detailed results obtained from TEM and X-ray scattering /diffraction.

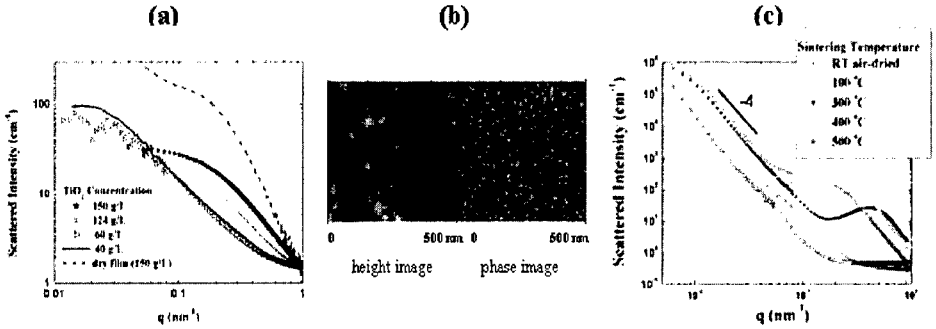


Figure 4. (a) SANS results for TiO_2 sol samples with different concentrations. (b) AFM image (500 nm x 500 nm) of a TiO_2 dry film (150 g/L). (c) SANS results for gel samples prepared using different sintering temperatures.

SUMMARY

We have controlled TiO_2 concentrations and sintering temperatures in the sol-gel process to synthesize various size scales of TiO_2 network nanostructure and improve particle dispersion in the polymeric coating systems by organic silanated treatment. Nanostructure information obtained from SANS allows for designing and implementing techniques to improve the material properties. In combination with microscopic data and modeling of SANS data, the neutron scattering is a powerful tool for non-destructive characterization of the structure and dispersion of nanoparticle/network systems.

ACKNOWLEDGMENTS

The authors thank Professor Chang-lin Lin and Dr. Shirley Turner for helping with the microstructure characterization using AFM and TEM.

REFERENCE

1. S.E. Berger, G.A. Salensky, US Patent 4,061,503 (1977).
2. B. O'Regan, J. Moser, M. Anderson, M. Gratzel, J. Phys.Chem., **94**, 8720-8726 (1990)
3. Y. Haga, H. An, R. Yosomiya, J. Mat.Sci. **32**, 3183-3188 (1997).
4. T.R. Corle, G.S. Kino, G.S., *Confocal Scanning Optical Microscopy and Related Imaging Systems* (Academic Press 1996).
5. S.M. Choi, J.G. Barker, C.J. Glinka, Y.T. Cheng, P.L. Gammel, J Appl Cryst **33**, 793 (2000).
6. J.S. Higgins, H.C. Benoit, *Polymers and Neutron Scattering* (Clarendon Press: Oxford, UK, 1994).

Nanocomposites: Synthesis and Properties

Mat. Res. Soc. Symp. Proc. Vol. 740 © 2003 Materials Research Society I6.1

Mechanical Behavior of Polymer Nanocomposites : a discrete simulation approach

E. Chabert[1], C. Gauthier[1], R. Dendievel[2], L. Chazeau[1] and J.-Y. Cavaillé[1]
[1] GEMPPM-INSA Lyon, 7 Avenue Capelle, 69621 Villeurbanne Cedex
[2] GPM2-INPG, 101 Rue de la Piscine, 38402 Saint Martin d'Hères Cedex

ABSTRACT

This work reports the dynamic mechanical characterization of nanocomposites based on a poly(butyl acrylate) matrix filled with spherical particles of either polystyrene or silica both of diameter around 100 nm. A discrete numerical simulation, taking into account the microstructure and the nature of contact between reinforcing particles has been developed. This simulation enables to quantify the effect of interactions between filler particles on the elastic modulus, and in a more general sense, to clarify the concept of mechanical percolation. It gives results in very good agreement with experimental data.

INTRODUCTION

Nanocomposite materials consist of a nanometer-scale phase in combination with another phase acting as a matrix. Work about polymer nanocomposites has exploded over the last few years. Their properties are reported to be different from that of their micro-scale counterparts [1,2]. The specific features in nanocomposites are (i) the large interfacial area which can reach 100-1000 m^2/g, (ii) the average distance between particles, down to a value comparable with the macromolecule coils. This can favor the short-distance filler-filler interactions leading, above a threshold fraction, to the formation of a network (percolation). Moreover, the presence of an interphase polymer layer near the inorganic surface with properties differing dramatically from the bulk polymer is often assumed. Due to the large surface area of the nanofillers, the interphase polymer is expected to dominate the properties of the nanocomposites. Though significant progress has been made in developing nanocomposites with different polymer matrices, a general understanding has yet to emerge. A major challenge to further development of nanocomposites is the lack of structure - properties modeling taking into account the influence of filler-filler and filler-matrix interactions.

MATERIALS AND EXPERIMENTAL RESULTS

Nanocomposites materials were prepared using the emulsion polymerization route. PS and PBuA latexes were blended varying the PS content (from 10 to 45 vol. %). After film formation (35°C, 90 % of relative humidity), this process leads to rigid spherical PS fillers (d=110nm) randomly dispersed in a soft PBuA polymer matrix (these films are referred as "as dried" films). When PS-PBuA films have undergone an annealing treatment at 140°C (i.e. above the glass transition of the PS) for several hours, films were designated "annealed". Silica particles (Stöber synthesis [3]) with similar diameter (125 nm) were also introduced in the same PBuA matrix.

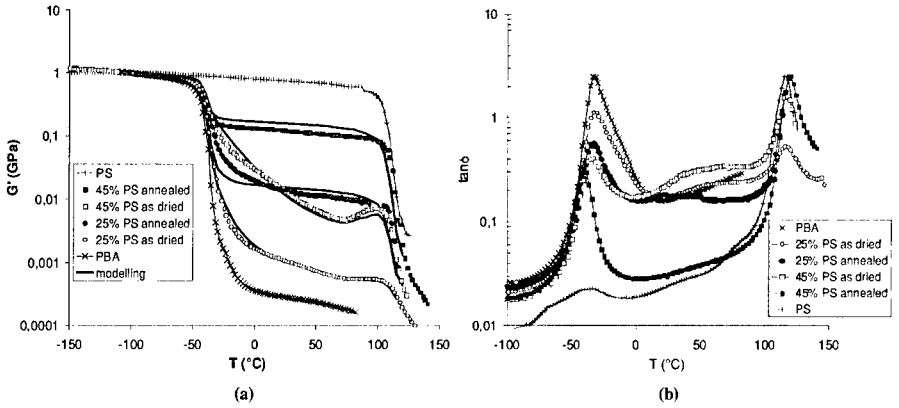


Figure 1: (**a**) Elastic shear modulus of "as dried" and "annealed" PS/PBuA nanocomposites versus temperature (1 Hz, 1°C/min). Lines: modeling using the discrete numerical simulation.

(**b**) loss factor of "as dried" and "annealed" PS/PBuA nanocomposites against temperature

Dynamic mechanical analysis of the samples have been performed in torsion [4] in the temperature range [-170; 150 °C] with a heating rate of 1°C/min at a fixed frequency of 1 Hz.

Figure 1a shows the temperature dependence of the storage shear modulus of the PS and PBuA phases and of various PS-PBuA composites. The behavior of "as dried" films can be described as follows: (i) a glassy plateau where the modulus of both phases and composites films are about 1 GPa; (ii) above the α relaxation of the PBuA (-50°C), a large drop in modulus followed by a continuous decrease and (iii) around 70 °C, an increase of the modulus until the PS main relaxation. These two counteracting phenomena lead to the presence of a bump in the loss factor curve, located between the peaks associated to the main relaxation of PBuA and PS phases (**Figure 1b**). Above -50°C, at a given temperature, the modulus is observed to strongly increase with the filler content. In the case of the "as dried" nanocomposites, the dependence of G' with temperature in the range [-50; 70°C] is more pronounced when the filler content is higher. After the annealing treatment, the PS/PBuA nanocomposites exhibit a much higher modulus (compared to as dried) with temperature dependence very close to that of the PS at the same temperature. These results are thought to be the consequence of the formation of a stiff network of PS. Actually, in the case of spherical filler, the percolation threshold is about 20 vol. %. Thus, before annealing ("as dried" samples), for filler content above 20 vol.%, a percolated network of filler is likely to be present in the sample but the interactions between the particles are probably softer, even punctual. Thus, these experimental results feature the difference between geometrical and mechanical percolation.

In the case of silica (**Figure 2**), the dependence of the modulus on filler content is observed in both the glassy and the rubbery plateaus since the shear modulus of silica is about 30 times that of the glassy polymer. Above the main relaxation of the PBuA, silica-filled

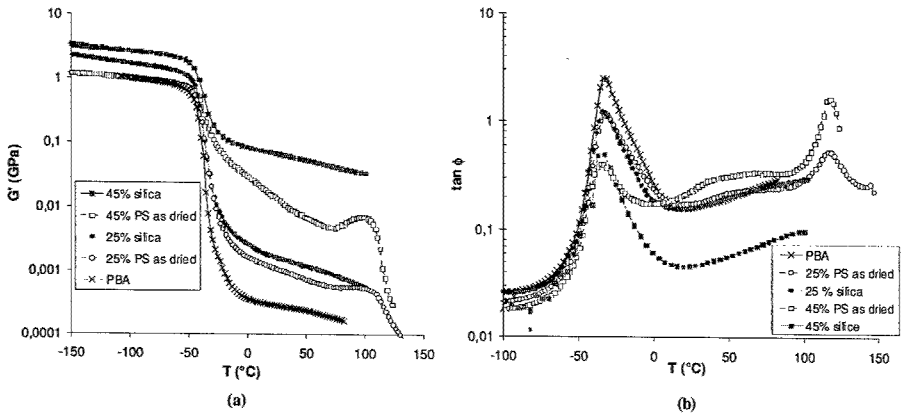


Figure 2: (a) Elastic shear modulus and (b) internal friction of "as dried" PS/PBuA nanocomposites and silica/PBuA nanocomposites as a function of temperature (1 Hz, 1°C/min).

nanocomposites display higher moduli than that filled with PS. This can be attributed to the presence of hydrogen bonds assumed to take place between silica particles (instead of Van der Waals bonds in the case of PS). Moreover, the modulus increase around 70°C is no longer observed in the case of silica filler. That indicates that this phenomenon has to be related to the interactions existing between PS fillers (and/or between PS and PBuA) and that these interactions are temperature-dependent.

To sum up, the mechanical behavior of the PS-PBuA and Silica-PBuA nanocomposites in the rubbery plateau is ruled by the filler content and the strength of the contacts between particles.

DISCRETE NUMERICAL APPROACH

Experimental results have shown a major influence of the nature of interactions between fillers on the linear mechanical behavior. In that case, classical homogenization methods based on mean field-type approximations fail to predict the modulus increase. As a consequence, we have developed a discrete numerical approach based on a composite assembly of spherical particles, which explicitly takes into account the microstructure and the nature of contact between reinforcing particles.

This model, described in detail in [5], is in fact based on the scheme developed by Jagota [6] to model the viscosity of composite packing of hard and soft spheres. Calculations are made on a close packing of monodisperse spheres, which represent either the filler particles or the PBuA matrix particles (≈1000 spheres with a packing density ≈ 0.57, **Figure 3**). At each contact between neighboring spheres, three forces and three moments are transmitted. These efforts are expressed as a linear function of the displacements and the rotations of the connected spheres, exhibiting different "contact stiffness" (normal, tangential, flexural and torsion). These

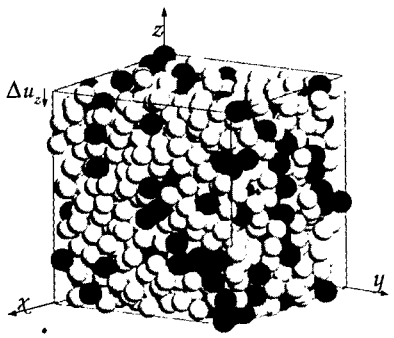


Figure 3: Example of random packing of monodisperse hard and soft spheres used to calculate the effective modulus.

stiffness depend both on the modulus of each connected sphere and on a geometrical parameter α defined as $\alpha=(R_c/R)^2$, where R_c and R are the contact radius and the sphere radius respectively. In fact, the larger α (i. e. the contact area), the higher the transmission of moments through the contact.

Three kinds of contact are thus considered: soft/soft, hard/hard and soft/hard contacts. α^{ss} for soft/soft contacts is taken equal to 1, since the PBuA matrix of nanocomposites materials is continuous. For hard/hard contacts, we used a variable α^{hh} in order to quantify the effect of the strength of filler-filler interactions on the effective modulus. Soft/hard contacts result from a serial law between hard/hard contacts (with $\alpha^{hh}=1$ since the PBuA matrix totally wets filler particles) and soft/soft contacts ($\alpha^{ss}=1$). The effective modulus is then numerically deduced by applying adequate boundary conditions, corresponding to a compression test.

Simulation results

The evolution of the packing modulus with the site fraction *p* of hard inclusions is plotted in **Figure 4** considering, in a first time, a huge contrast between soft and hard particles: $G_f/G_m=10^{12}$. When filler-filler interactions are strong (so called "bonded" case with high contact area: $\alpha^{hh}=1$), the effective modulus increases suddenly at the geometrical percolation threshold $p_c=0.325$. On the other hand, when filler-filler interactions are weak ("bonded" case with $\alpha^{hh}=10^{-6}$), i. e. when the rolling of hard particles is allowed, there is no discontinuity at the percolation threshold. Moreover, the modulus obtained for 100% of hard particles is lower than the modulus of bulk filler. Like in reference [6], we have also defined a "sliding" contact, where hard/hard contacts resist only to normal efforts with the properties of filler material, the others efforts being transmitted like in soft/soft contacts. **Figure 4** shows that in that case, the effective modulus increases only a little: the packing behaves like a sand pile.

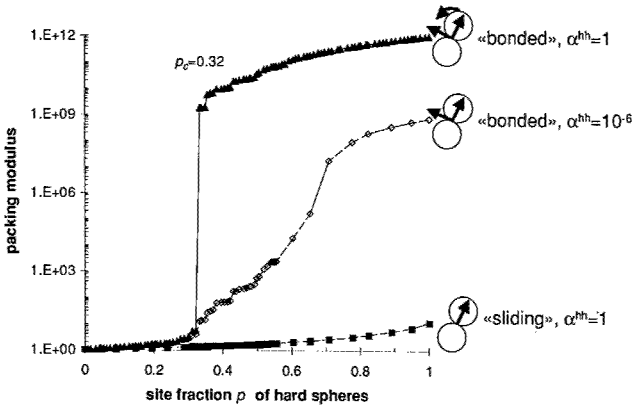


Figure 4: Evolution of the packing modulus as a function of the site fraction p of hard spheres for different cases of hard/hard contacts (1000 spheres, $G_f/G_m=10^{12}$).

This simulation shows clearly the differences between geometrical percolation and mechanical percolation: the mechanical percolation occurs only when filler-filler interactions are strong enough (transmission of moments). In contrast, when filler-filler interactions are weak, the contribution of the formation of a macroscopic filler network has little effect on the modulus.

Application to PS/PBuA nanocomposites

This model has been applied to PS/PBuA nanocomposites. After the annealing treatment, PS particles are strongly bonded. As a consequence, calculations have been made with $\alpha^{hh}=1$ (efforts and moments are transmitted as in bulk PS). Simulation results plotted in **Figure 1** are in very good agreement with experimental data. Before the annealing treatment, the strength of filler-filler contact is unknown and evolves with temperature. Therefore, the variation of α^{hh} with temperature has been adjusted in order to agree well with the experimental data for the nanocomposite containing 25% PS. Then, keeping the same law for $\alpha^{hh}(T)$, calculations have been made for 45% PS. As shown on **Figure 1**, the prediction is very close from experimental result.

CONCLUSIONS

The main influence of the presence of the nanosized filler in a poly(butyl acrylate) matrix are observed in the rubbery plateau. In this temperature range, the contrast between the modulus of the different phases is huge and the mechanical behavior seems to be essentially governed by the microstructure and the strength of the links between the filler, these links being either direct contacts or indirect contacts via the matrix in between. To account for the observed increase of modulus and its evolution with temperature, a discrete model of spheres assembly taking into account the local filler/filler and matrix/filler contacts is proposed. This approach agrees well

with the experimental data and allows to better understand the reinforcement when the percolation threshold is crossed.

ACKNOWLEDGEMENTS

This work was performed under the auspices of "Programme Matériaux" from CNRS under contract n°13. One of the authors (E. Chabert) was supported through the Brite project BE 97-4448 administrated by the European Community.

REFERENCES

[1] E.P. Giannelis, *Adv.Mater.* **8**, 29 (1996)
[2] L. Chazeau, C. Gauthier, G. Vigier, J.Y. Cavaillé, *in "Handbook of Organic-Inorganic Hybrids Materials and nanocomposites"* Edited by H.S. Nalwa, American Scientific Publishers, (2003)
[3] W. Stöber, A. Fink , E. Bohn, *J. Colloid Interf. Sci.*, **26**, 62 (1968).
[4] S. Etienne, J.Y.Cavaillé, J. Perez, Rev. Sci. Instrum. **53**-8, 1261 (1992)
[5] E. Chabert, R. Dendievel, C. Gauthier and J.-Y. Cavaillé, *submitted to Compos. Sci. Technol.*.
[6] A. Jagota and G. W. Sherer, *J. Am. Chem. Soc.* **78**, 521 (1995).

Mat. Res. Soc. Symp. Proc. Vol. 740 © 2003 Materials Research Society

Nanophase Alumina/Poly(L-Lactic Acid) Composite Scaffolds for Biomedical Applications

Aaron J. Dulgar Tulloch[1,3], Rena Bizios[2,3], and Richard W. Siegel[1,3]
[1]Department of Materials Science and Engineering, [2]Department of Biomedical Engineering, and [3]Rensselaer Nanotechnology Center
Rensselaer Poytechnic Institute, Troy, NY 12180-3590 USA

Abstract

Three-dimensional composites of nanophase alumina and poly(L-lactic acid) with an interconnected porous network and an overall porosity in excess of 90% are cytocompatible. Osteoblast proliferation on the nanophase ceramic/polymer composites is a function of time of cell culture and of nanoceramic loading in the biomaterial substrates.

Introduction

Biomaterials are an integral part of biomedical applications, such as tissue engineering and prosthetic devices, that constitute alternative strategies in addressing the increasing clinical need for replacement tissue. Such materials also provide the potential for alleviating the limitations of autologous tissue availability and the medical problems associated with allografts.

Among the most promising recent biomaterial developments, nanophase ceramics and their composites with polymers have been shown to exhibit selectivity for, and promoted enhancement of, osteoblast (the bone-forming cell) functions pertinent to new bone tissue formation.[1-6] To date, however, the potential of these novel material formulations has only been explored using essentially two-dimensional substrates. Because of the three-dimensional nature of native tissues, and of the pertinent construction requirements for tissue engineering applications, the current study focused on the preparation, characterization, and cytocompatibility of three-dimensional nanophase alumina/poly(L-lactic acid) composite scaffolds in an effort to provide improved material formulations for biomedical applications.

Materials and Methods

Scaffold Preparation Three-dimensional, porous composite scaffolds were prepared using a thermal phase separation process according to established methods.[7] Briefly, poly(L-lactic acid) (PLLA) with a molecular weight of 100,000 (Polysciences) was dissolved in 1,4-dioxane (Sigma-Aldrich) by magnetic stirring at 70 °C for two hours to obtain a 5% (w/v) solution. Appropriate amounts of either nanophase alumina (grain size of 38 nm; Nanophase Technologies) or micron-size alumina (grain size of 1 μm; Sigma-Aldrich) were blended into the polymer solution by vortexing and then stirring at 70 °C for one hour to obtain 50/50, 60/40, 70/30, or 80/20 (w/w) percent ceramic/polymer composites. Each composite was frozen at –20 °C for 2 hours and then at –70 °C overnight, before being freeze-dried at -98 °C and 7 mTorr for 48 hours (to remove the dioxane). All scaffolds were stored in a dessicator for a maximum of 7 days prior to use. Pure PLLA scaffolds were constructed similarly, but without the addition of ceramic, and were used as controls.

Scaffold Architecture and Properties Scaffolds (12.5 mm in diameter and 25.0 mm in height) were cut in half along their diameter, sputter-coated with gold, and visualized using a field-emission scanning electron microscope (JEOL JSM-6330F). Pore architecture and size were determined from measurements on random fields of selected low magnification (x50) SEM images. Porosity was measured on a minimum of 5 scaffolds of each type using a helium pycnometer (Micromeritics AccuPyc 1330). Compression properties were determined using a United SSTM-1-PC testing machine according to established protocols.[8] Scaffold degradation was examined in the absence of cells under static conditions, in phosphate buffered saline, in a humidified, 37 °C, 5% CO_2/95% air environment, and was quantified by determining weight loss over a four week period.

Osteoblast Isolation and Culture The cytocompatibility of the materials examined in this study were investigated using an *in vitro* model. For this purpose, osteoblasts were isolated from neonatal rat calvariae according to established protocols and characterized by alkaline phosphatase activity, synthesis of collagen, and accumulation of calcium in their extra-cellular matrix.[9] These osteoblasts were cultured in Dulbecco's Modified Eagle Medium (DMEM, Gibco) supplemented with 10% fetal bovine serum (FBS, Gibco) and 1% penicillin/streptomycin (P/S, Gibco) under standard cell culture conditions (a static, humidified, 37 °C, 5% CO_2/95% air environment). The medium was changed every other day.

Osteoblast Seeding and Proliferation on Scaffolds Osteoblasts (260,000 cells) of population number three were seeded onto each scaffold (10x10x3 mm^3) under a 50 Torr vacuum for 5 minutes, followed by the addition of 1 mL of fresh medium. The initial distributions of cells throughout the scaffolds were confirmed after 16 hours by washing the scaffolds three times with phosphate buffered saline (PBS), fixing the cells in methanol for 30 min, staining the cells with Ethidium Homodimer – 1 (Molecular Probes Inc.), cutting the scaffold into consecutive 20 μm sections with a cryotome (Richard-Allan Sci. Microm MH 505 E), and visualizing the cells using fluorescence microscopy. Osteoblast proliferation was monitored at 3, 7, and 14 days. At these times, each scaffold was washed three times in PBS, mechanically pulverized, and then treated with 1 mL of a papain solution (0.125 mg/mL in phosphate buffered EDTA with 10 mM cysteine) at 60 °C for 16 hours (to release the DNA from the cells). Cellular and synthetic material debris were removed by centrifugation at 3,000g at room temperature for 10 minutes. The extracted DNA present in each supernatant was then labeled with Hoechst 33258 (Bio-Rad) and quantified using a fluorometer (TD-360; Turner Designs) according to manufacturer's instructions.

Results

Scaffold Architecture and Properties All scaffolds tested, namely the pure PLLA, 50/50 micron-size alumina/PLLA composites, and 50/50 nanophase alumina/PLLA composites, exhibited similar pore architecture (Figure 1). These pores were irregular in size (average diameter about 150 μm), shape and orientation, and had a high degree of interconnectivity throughout each scaffold. The porosity of the scaffolds was in excess of 90%. The PLLA scaffolds exhibited a significantly ($p < 0.05$) higher porosity than either the micron or nanophase 50/50 composite scaffolds; these composite scaffolds had similar porosities (Table 1). Compression modulus and yield strength for the pure PLLA scaffolds were significantly ($p <$

0.05) lower than those of either the micron or nanophase 50/50 composites. The mechanical properties of the micron and nanophase 50/50 composites tested were similar (data not shown). None of the scaffolds tested during the present study exhibited weight loss over the four week period examined (data not shown).

Osteoblast Distribution As illustrated by the micrographs shown in Figure 2, the technique used to seed the osteoblasts resulted in the distribution of viable cells throughout the three-dimensional scaffolds tested at early times (up to 16 hours) of culture. However, beyond 24 hours and under the static cell culture conditions used for these experiments, osteoblasts in the center of the scaffolds did not survive. In contrast, cells present in the outermost (approximately 500 μm from the nearest surface) region of each scaffold remained viable for all durations (up to 7 days) tested (data not shown).

Cytocompatibility As evidenced by the results of the osteoblast proliferation experiments (Figures 3 and 4), all materials tested in the present study were cytocompatible. In fact, compared to results obtained on pure PLLA scaffolds, osteoblast proliferation on the 50/50 nanophase alumina/PLLA composites was significantly ($p < 0.05$) higher for all durations (3, 7, and 14 days) tested (Figure 3). In addition, osteoblast proliferation was significantly ($p < 0.05$) higher on the nanophase than on the micron-size 50/50 alumina/PLLA composites after 3 and 7 days (Figure 3). Furthermore, osteoblast proliferation increased significantly ($p < 0.05$) with nanophase alumina loading (Figure 4).

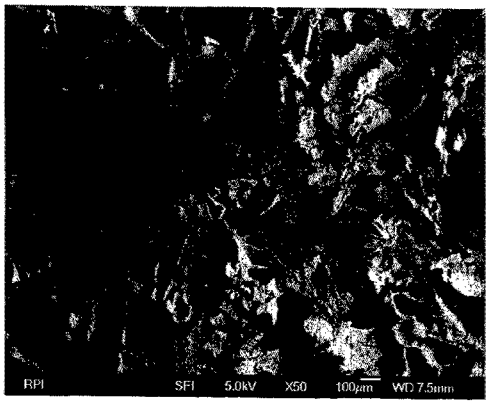


Figure 1. Representative scanning electron micrograph illustrating the porous architecture of the scaffolds tested in the present study. This picture is of a 50/50 nanophase alumina/PLLA composite. Bar = 100μm.

Table I
Pore-size and Open-porosity of PLLA and Alumina/PLLA Composites

	Pore-size (μm)	Porosity (%)
PLLA	145 ± 48	93.6 ± 0.3
50/50 micron-size alumina/PLLA	183 ± 68	91.9 ± 0.3
50/50 nanophase alumina/PLLA	152 ± 48	92.2 ± 0.3

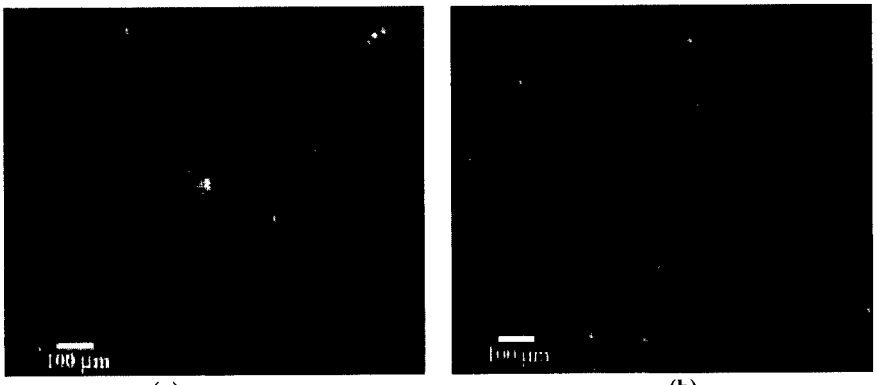


Figure 2. Representative fluorescence micrographs illustrating the osteoblast (light spots) distribution on a 50/50 nanophase alumina/PLLA composite 16 hours after seeding: (a) scaffold surface (0.5 mm from the scaffold edge); (b) scaffold center (5.0 mm from the scaffold edge). Bar = 100 µm.

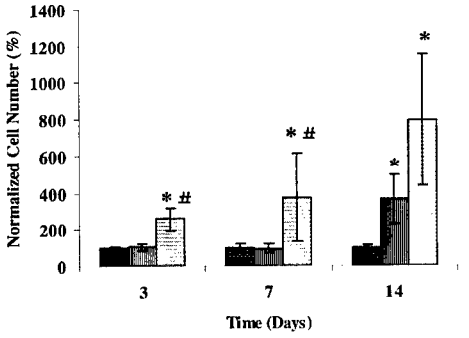


Figure 3. Time course of osteoblast proliferation on ■ pure PLLA (controls), ■ 50/50 micron-size alumina/PLLA, and ▤ 50/50 nanophase alumina/PLLA. The data were normalized against the cell proliferation results obtained on pure PLLA at the respective times. Values are mean ± SEM; n = 3; *p < 0.05 and #p < 0.05 compared to PLLA and micron-size composites, respectively (two-sample t test).

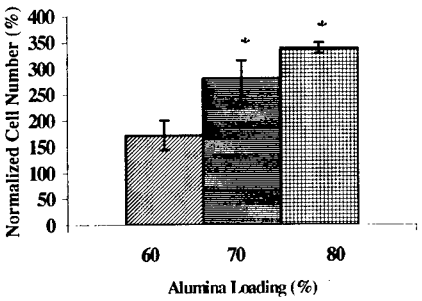


Figure 4. Osteoblast proliferation on ▨ 60/40 nanophase alumina/PLLA, ■ 70/30 nanophase alumina/PLLA, and ▤ 80/20 nanophase alumina/PLLA composites after 7 days of culture. The data were normalized against the cell proliferation results obtained on pure PLLA at day 7. Values are mean ± SEM; n = 3; *p < 0.05 compared to 60/40 nanophase alumina composites (two-sample t test).

Discussion

The present study was successful in preparing three-dimensional nanophase and micron-size alumina/PLLA composite scaffolds with pore-size, porosity, and compressive mechanical properties comparable to those reported in the literature for pure PLLA and micron-size hydroxyapatite/PLLA composites prepared using the same thermal phase separation technique.[7] Additionally, the absence of detectable degradation for all scaffold types is in agreement with literature reports of no significant weight loss for porous PLLA scaffolds under conditions similar to those used for the present study for durations of less than 50 days.[10]

In contrast to the differences observed in bending modulus for two-dimensional, non-porous nanophase and micron-size composites of alumina with either PLLA or poly(methyl-methacrylate),[2] the mechanical properties of all three-dimensional scaffolds examined by the present study were similar. An investigation of the underlying mechanisms for this discrepancy was outside the scope of the present study, but a possible explanation for these results is that the porous structure of the scaffolds masks the advantages provided by the nanophase materials tested.

Necrosis of cells in the center of three-dimensional scaffolds has been a problem encountered by investigators working in tissue engineering. For example, Ishaug et al. (1997) reported that cells further than 240 μm from the surface of poly(D,L-lactic-co-glycolic acid) scaffolds (disks 7 mm in diameter and 1.9 mm in height) did not survive during 56 days of culture.[11] Ma et al. (2000) reported cell necrosis in the center of pure PLLA scaffolds, but not in the center of micron-size hydroxyapatite/PLLA scaffolds (disks 10 mm in diameter and 1.5 mm in height).[12] In the present study, while osteoblasts in the center of alumina/PLLA scaffolds (10x10x3 mm^3) did not survive, cells present in the outermost (approximately 500 μm from the nearest surface) region of each scaffold remained viable for all durations (up to 7 days) tested. The exact causes for these observations are not known. However, since the scaffold degradation results of the present study preclude decreases in the media pH (due to polymer degradation), the observed cell necrosis is most likely due to limited diffusion of oxygen and nutrients under the static cell-culture conditions utilized routinely for such studies; this explanation was proposed by Sikavitsas et al. who have attempted to engineer bone tissue using cultures of marrow stromal cells on three-dimensional, porous scaffolds of 75/25 (w/w) percent poly(D,L-lactic-co-glycolic acid).[13]

The increased proliferation of osteoblasts on three-dimensional, nanophase alumina/PLLA composites reported in the present study is in agreement with a similar cell proliferation trend observed on essentially two-dimensional substrates of nanophase alumina/PLLA composites containing 30 - 50% alumina.[2] Important contributions of the present study are, therefore, the successful preparation of composites with nanophase alumina content as high as 80%, and the evidence that these formulations maintain the select and enhanced cytocompatibility first observed on essentially two-dimensional nanoceramics and on their composites with polymers.[2-4] The mechanism(s) behind the observed increased osteoblast proliferation as a function of alumina content is not known. Previous work in our laboratory, however, suggests that enhanced calcium adsorption may result in calcium-mediated binding and conformational changes of select proteins on both nanoceramic and nanoceramic/polymer composite surfaces; since proteins mediate cell interactions on substrates, these events play a key role in the subsequent cell adhesion, as well as in other osteoblast functions that are pertinent to new bone formation.[5]

Overall, the present study is the first to investigate some aspects of the use of three-dimensional, porous, nanophase alumina/PLLA scaffolds, which are pertinent to tissue engineering and implantable biomaterials. Undoubtedly, further research is needed to determine the optimal conditions under which these novel material formulations perform best in biomedical applications.

Acknowledgements

The authors would like to thank Ms. Katerina Leventis for her assistance with the cell experiments, Dr. Harry Kimelberg and Ms. Carol Charniga for the rat calvariae (source of the osteoblasts used in the cell experiments), Dr. Dennis Metzger for permission to use the cryotome in his laboratory, and Nanophase Technologies Corporation for their donation of the nanophase alumina. This project was supported by grants from Philip Morris U.S.A. and from the Nanoscale Science and Engineering Initiative of the National Science Foundation under NSF Award Number DMR-0117792.

References

1. Webster, T.J., Siegel, R.W., Bizios, R., Nanostruct. Mater. 12:983 1999
2. McManus, A.J., Master's Thesis, Rensselaer Poytechnic Institute, Troy, NY 2001
3. Webster, T.J., Siegel, R.W., Bizios, R., Biomaterials 20:1222 1999
4. Webster, T.J., Siegel, R.W., Bizios, R., Biomaterials 21:1803 2000
5. Webster, T.J., Ergun, C., Doremus, R.H., Siegel, R.W., Bizios, R., J. Biomed. Mater. Res. 51:475 2000
6. Webster, T.J., Schadler, L.S., Siegel, R.W., Bizios, R., Tissue Eng. 7:291 2001
7. Zhang, R., Ma, P.X., J. Biomed. Mater. Res. 44:446 1999
8. ASTM D 1621-00
9. Puleo, D.A., Holleran, L.H., Doremus, R.H., Bizios, R., J. Biomed. Mat. Res. 25:711 1991
10. Lam, K.H., Nieuwenhuis, P., Molenaar, I., Esselbrugge, H., Feijen, J., Dijkstra, P.J., Schakenraad, J.M., J. Mater. Sci.: Matls. in Med. 5:181 1994
11. Ishaug, S.L., Crane, G.M., Miller, M.J., Yasko, A.W., Yazemski, M.J., Mikos, A.G., J Biomed. Mater. Res. 36:17 1997
12. Ma, P.X., Zhang, R., Xiao, G., Franceschi, R., J. Biomed. Mater. Res. 54:284 2001
13. Sikavitsas, V.I., Bancroft, G.N., Mikos, A.G., J. Biomed. Mater. Res. 62:136 2002

Mat. Res. Soc. Symp. Proc. Vol. 740 © 2003 Materials Research Society

Mechanical and Thermoviscoelastic Behavior of Clay/Epoxy Nanocomposites

Jandro L. Abot, Asma Yasmin and Isaac M. Daniel
Robert McCormick School of Engineering and Applied Science, Northwestern University, Evanston, IL 60208, U.S.A.

ABSTRACT

The study of organic-inorganic nanocomposites has become relevant in recent years since these materials exhibit synergistic properties derived from the two components. Thermosetting polymers like epoxies that have high mechanical properties provide a baseline for further improvement with the addition of nanoclay particles. These nanocomposites can be used as the matrix of a fiber reinforced composite and lead to higher matrix dominated mechanical properties including elastic modulus, strength and fracture toughness. This study concentrates on the mechanical and thermoviscoelastic properties in the glassy regime of nanocomposites prepared by direct mixing. The elastic modulus of the nanocomposites was found to improve with respect to the pure epoxy modulus at the expense of both tensile strength and ductility regardless of clay content. The glass transition temperature was also found to decrease as well. The morphology of the nanocomposites was studied and correlated with the aforementioned properties.

INTRODUCTION

Nanocomposites formed by the intercalation or exfoliation of inorganic fillers of the order of 1-100 nm into polymers are of particular interest because of their demonstrated improvement of the physical and mechanical properties relative to the unmodified polymer. Microfillers are used quite extensively but the use of nanofillers is limited because of dispersion problems and viscosity build-up related to strong interparticle interactions. Layered silicate/polymer nanocomposites and clay/epoxy nanocomposites in particular have been studied over the last decade [1]. The morphology of these materials plays a key role and many papers have been written about the characterization of nanocomposites in the nanoscale describing the different layer separations. However, a characterization in the mesoscale and microscale is necessary to determine the orientation and content fluctuations. According to Vaia and Liu [2], the spatial characterization of nanocomposites over six orders of magnitude is a challenge and inconsistencies are likely to appear among different techniques such as scattering spectroscopy and electron microscopy. From the structural point of view, there exist two types of nanocomposites, the intercalated one where the polymer is inserted between the silicate layers forming well-ordered multilayers and the exfoliated one where the silicate layers break into single platelets and orient themselves forming a random pattern. A detailed study of the intercalation and exfoliation behavior of clay/epoxy materials was performed by Lü et al [3].

Several studies on the mechanical behavior of clay/epoxy nanocomposites have been performed. Lan and Pinnavaia [4] reported more than a 10-fold increase in both elastic modulus and strength of an exfoliated nanocomposite consisting of a diglycidyl ether of bisphenol A (DGEBA) epoxy of subambient glass transition temperature (T_g) with 5% weight of montmorillonite. The authors showed that no big improvements were obtained for epoxies with

higher T_g in the glassy region. Giannelis et al. [5] reported the formation of nanocomposites with epoxies cured with different anhydrides and amines, and dynamic mechanical analyses (DMA) showed an improvement of the storage modulus of 58% below T_g and 450% above T_g. Zilg et al. [6,7] performed tests with anhydride cured epoxy and montmorillonite particles and they report almost no improvement for four different particle contents. There was a slight decrease in the elastic modulus of about 10 % and a decrease of the strength of about 50%. However, for 10 wt % of clay the elastic modulus increased by 116 % and the strength decreased slightly. Although T_g was not determined for these nanocomposites, a decrease was observed for mica nanocomposites.

This paper intends to provide a detailed characterization of the mechanical properties of clay/epoxy nanocomposites in the glassy regime at room temperature. Montmorillonite clay particles and an anhydride-cured epoxy were the selected materials and the nanocomposites with 2 to 20 % clay content were formed by a direct mixing method. Special emphasis was placed on the optimization of strength and toughness by way of careful processing.

EXPERIMENTAL

Materials

Epoxy

Epoxy was selected because it is a low creep polymer with high mechanical properties, high heat distortion temperature and excellent dimensional stability. For these reasons, it is also the most common polymer used in fiber and filler reinforced polymers for structural applications. The epoxy system considered here is an anhydride-cured epoxy consisting of a DGEBA epoxy resin cross-linked by methyl tetrahydrophtalic anhydride (MTHPA) with the help of a 1-methylimidazole accelerator. All chemicals were purchased from Vantico Inc. and used in proportions of 100:90:1 (phr) respectively.

Clay

Montmorillonite/smectite (Hydrated Sodium Calcium Aluminum Magnesium Silicate Hydroxide) was selected because it is a relatively inexpensive clay with good intercalation capabilities. It consists of very small platy crystals and it is a subgroup of the clays which are a group of the phyllosilicates which are silicate rings of tetrahedrons, linked by shared oxygen to other rings in two dimensional planes that produce a sheet-like structure, that contain varying amounts of water and allow substitution of their cations. The selected clay particles for this study were Nanomer I.28E from Nanocor and Cloisite 30B from Southern Clay Products (table I). In order to allow dispersion of the clay in an organic medium like an epoxy polymer, a surface modification of the clay is necessary to make it organophilic. Rendering the normally hydrophilic inorganic host surface into a hydrophobic host requires ion exchanging the hydrated inorganic gallery cations with cationic organic surfactants such as alkylamines. Both types of particles used for this study had been treated with quaternary amines and they were dispersed as received. However, it has been shown that protonated amines in contrast to quaternary amines react with epoxy resins thus enhancing both swelling and compatibility [4]. The length of the alkyl chain plays also a key role in increasing the basal spacing of the particles [4].

Table I. Properties of clay particles.

	Nanomer I.28E	Cloisite 30B
Specific density	1.9	1.98
Mean particle size (μm)	8-10	6
Basal spacing (Å)	24	18.5

Nanocomposite formation

A direct method like curing agent dispersion [8] was employed to disperse the particles in the epoxy matrix to form the nanocomposite. It consisted of mixing the clay particles with the hardener for 15 h followed by the addition of the epoxy resin and the accelerator and subsequent mixing for 1 h. The mixing was carried out with a magnetic stirrer in a hot plate at 50ºC. The resulting mixed material was degassed under deep vacuum until no bubbles were observed and then cured in a Teflon mold at 150ºC for 1 h. Several curing cycles with varying temperature and time were also considered and it was found that extending the curing cycle for more than 1 h at 150°C would not improve the mechanical properties substantially. Different amounts of clay were added to the epoxy: 1, 2, 5, 10, 15 and 20% by weight. Interfacial adhesion of the layered silicates results from adsorption, i.e. the binding of polymer molecules to the platelet surface. The motion of the polymers in the interlayer is the process that dictates the intercalation kinetics and effective diffusion of the confined polymer inside the platelet is the governing factor [9]. This diffusion becomes increasingly hindered with increasing particle content because of both the viscosity build-up and the catalytic effect of the particles making processing more difficult.

Characterization

Nanocomposite formation is accompanied by increased interlayer distance as evidenced by x-ray scattering and transmission electron microscope (TEM). Small angle x-ray scattering (SAXS) performed in a machine with a solid state detector with CuKα radiation was employed to monitor the change in the basal spacing (d-spacing) and intercalation patterns of the particles. Wide angle x-ray diffraction (WAXD) performed on a diffractometer with CuKα radiation was used to determine the basal spacing of pure Cloisite. Scanning electron microscopy (SEM) was used to determine the presence of clay aggregates in the nanocomposites.

Testing

Nanocomposite specimens for testing under uniaxial tension were prepared according to ASTM standards. They were bonded to fiberglass tabs with an epoxy-based adhesive (Hysol™ EA9430) and cured at room temperature under vacuum. The mechanical properties were determined through quasi-static tests performed in a servo-hydraulic testing machine under displacement control. It was found that the strain gage instrumentation would damage the surface of the specimens by generating thermal cracks that would trigger early failures. Extensometers were used instead to record the strains. The elastic modulus, strength and ultimate strain were measured. The thermoviscoelastic behavior was studied in a DMA with double cantilever specimens sweeping across a temperature range of 30-200 ºC and for a single frequency (1 Hz). The storage and loss moduli and the glass transition temperatures were recorded.

RESULTS AND DISCUSSION

Morphology

The diffraction patterns of the cured nanocomposites for various clay contents can be seen in figure 1. It can be seen that the epoxy wets completely the Nanomer particles and increases their initial d-spacing of 24Å to 34 Å for all nanocomposites regardless of clay content. The nanocomposites with Cloisite particles show complete exfoliation regardless of particle content. Kornmann [9] argues that the lack of peaks could rather be attributed to a large distribution of basal spacings as confirmed by TEM analysis. Large aggregates as observed in SEM (bigger than 10 μm) can act as load-concentrating defects leading to a reduction in ductility.

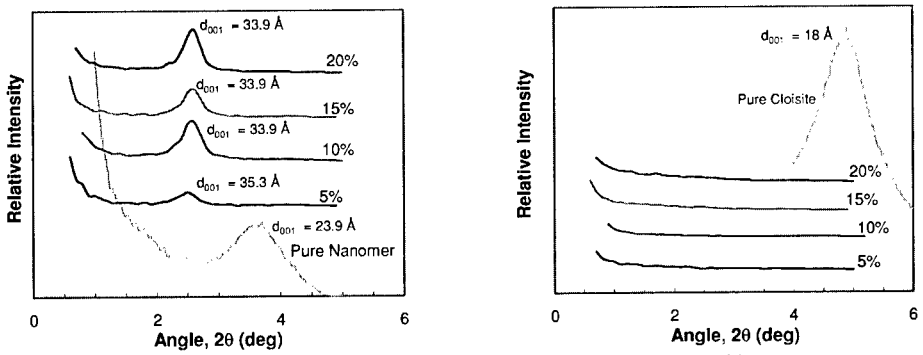


Figure 1. X-ray diffraction patterns of epoxy nanocomposites: a) Nanomer; b) Cloisite.

Mechanical and thermoviscoelastic behavior

The stress-strain behavior of the Nanomer/epoxy and Cloisite/epoxy nanocomposites under uniaxial tension is presented in figure 2. The pure epoxy shows a linear behavior up to 0.7% strain followed by a stress-softening region that approaches a tensile strength plateau. All nanocomposites behave similarly compared to pure epoxy. The tensile behavior of Nanomer nanocomposites approaches the behavior of pure epoxy while Cloisite nanocomposites show a stronger behavior. Their elastic moduli increase continuously with clay content and this rate of variation increases also with clay content. Cloisite particles consistently give higher modulus nanocomposites than Nanomer particles but this difference decays markedly with increasing clay content. The nanocomposite strengths decrease with clay content. Although all measured tensile strengths were lower than the pure epoxy strength, it was the particle clusters as evidenced by SEM pictures that prevented Cloisite/epoxy from reaching higher strengths. The nanocomposites with 2% clay content did not follow the trend and showed higher elastic modulus and lower ductility than the nanocomposites with 5% clay content. Yasmin et al. [11] reported higher improvements of elastic moduli for low clay contents of nanocomposites prepared by mixing in a roll mill. The d-spacings of both particles after nanocomposite formation were identical to the corresponding ones for nanocomposites prepared by the direct method employed here. This suggests that the microstructure rather than the nanostructure determines the elastic behavior of these materials.

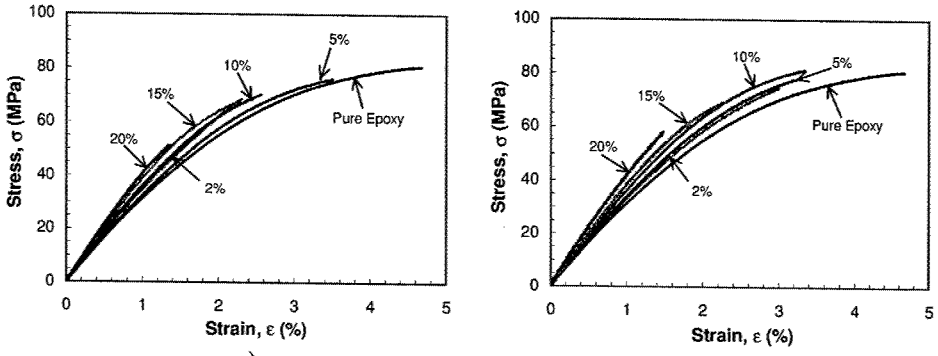


Figure 2. Stress-strain behavior of nanocomposites under uniaxial tension: a) Nanomer/epoxy; b) Cloisite/epoxy.

The thermoviscoelastic behavior of all nanocomposites is characterized by an increase of storage modulus in the glassy region with respect to the pure epoxy and by a decrease of T_g, both for increasing clay content (figure 3). The storage modulus at room temperature varies with clay content similarly to the elastic modulus. Although it was not experimentally confirmed, the reduction in T_g could be attributed to a disruption of the crosslinks making the polymer more flexible at higher temperatures.

The modeling of all the described mechanical and thermal properties in terms of the filler volume fraction is an important task. It can be said that the elastic modulus follows the Reuss model for low clay fractions (less than 0.07) and models such as Halpin-Tsai or Mori-Tanaka with low aspect ratios appear to describe better its behavior for higher filler volume fractions. Table II gives the mean thermomechanical properties for all nanocomposites (T_g calculated from *tan* δ).

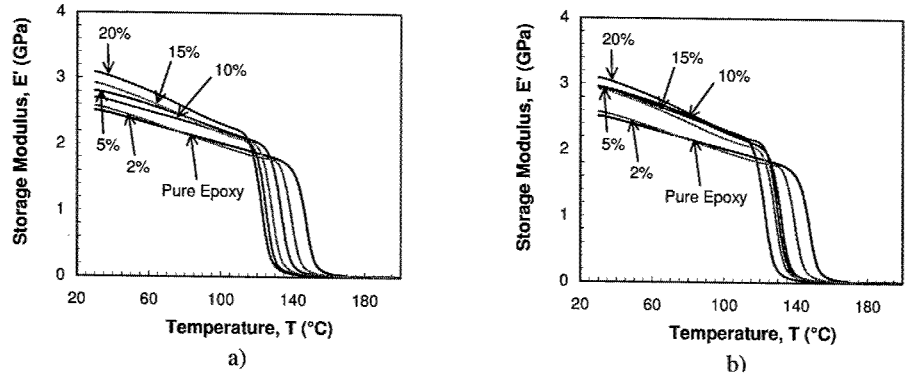


Figure 3. Storage modulus-temperature behavior of nanocomposites: a) Nanomer/epoxy; b) Cloisite/epoxy.

Table II. Thermomechanical properties of clay/epoxy nanocomposites.

	Nanomer I.28E				Cloisite 30B			
	E (GPa)	F_t (MPa)	ε_{ult} (%)	T_g (°C)	E (GPa)	F_t (MPa)	ε_{ult} (%)	T_g (°C)
0%	3.4	81	4.85	152.4	3.4	81	4.85	152.4
2%	3.7	64.1	2	144.7	3.65	74.8	3.0	140.7
5%	3.5	76.1	3.5	137.6	3.55	78.1	3.5	137.5
10%	3.6	70.1	2.6	131.2	3.85	81.4	3.4	133.9
15%	3.95	67.4	2.25	133.3	4.05	69.2	2.3	135.9
20%	4.35	62.1	2	129.2	4.45	58.2	1.5	129.6

SUMMARY AND CONCLUSIONS

A study of the mechanical and thermoviscoelastic behavior of clay/epoxy nanocomposites and their corresponding morphologies was performed. Two different types of clay particles were intercalated as received in the epoxy matrix by a direct mixing method. It was found that the elastic modulus of the nanocomposites increases and their tensile strength and ductility decrease with increasing clay content. The modulus improvements are more pronounced for higher clay contents. Cloisite particles exfoliate and give nanocomposites with slightly higher mechanical properties than nanocomposites with Nanomer particles that intercalate and increase their basal spacing. These results are in agreement with previous observations on particulate-filled glassy epoxies and semicrystalline polymers, where increased stiffness leads to a decrease of ductility and toughness. It has been reported that nanocomposites from the same materials with identical basal spacing but formed by applying extensive shear loading produces nanocomposites with much higher elastic modulus. This fact reinforces the idea that the microstructure rather than the nanostructure determines the elastic behavior of these nanocomposites.

REFERENCES

1. T. J. Pinnavaia and G. W. Beall, *Polymer-Clay Nanocomposites*, (Wiley, Chichester, 2000) pp. 127-149.
2. R. D. Vaia and W. Liu. *J. Polym. Sci.: Part B: Polym. Phy.* **40**, 1590 (2002).
3. J. Lü, K. Yucai, Q. Zongneng and Y. Xiao-Su. *J Polym. Sci., Part B: Polym. Phy.* **39**, 115 (2001).
4. T. Lan, T. J. Pinnavaia. *Chem. Mater.* **6**, 2216 (1994).
5. E. P. Giannelis and P. B. Messersmith, U.S. Patent No. 5 554 670 (10 September 1996).
6. C. Zilg, R. Mülhaupt and J. Finter. *Macromol. Chem. Phys.* **200**, 661 (1999).
7. C. Zilg, R. Thomann, R. Mülhaupt and J. Finter. *Macromol. Mater. Eng.* **280/281**, 41 (2000).
8. P. Messersmith and E. P. Giannelis. *Chem. Mater.* **6**, 1719 (1994).
9. E. Manias, H. Chen, R. Krishnamoorti, J. Genzer, E. J. Kramer and E. P. Giannelis. *Macromol.* **33**, 7955 (2000).
10. X. Kornmann, H. Lindberg and L. A. Berglund. *Polym.* **42**, 1303 (2001).
11. A. Yasmin, J. L. Abot and I. M. Daniel. "2002 MRS Conference" (2002).

Mat. Res. Soc. Symp. Proc. Vol. 740 © 2003 Materials Research Society

Preparation and Characterization of Alumina based TiN_n and SiC_n Composites

Mats Carlsson[1], Mats Johnsson[1] and Annika Pohl[2]
[1]Dept. Inorg. Chem., Stockholm University, SE-106 91 Stockholm, Sweden
[2]Dept. Mater. Chem., The Ångström Lab., Uppsala University, SE-751 21 Uppsala, Sweden

ABSTRACT

Ceramic composites containing 2 and 5vol. % of nanosized commercially available TiN and SiC particles in alumina were prepared via a water based slurry processing route followed by spark plasma sintering (SPS) at 75 MPa in the temperature range 1200-1600°C. Some of the samples could be fully densified by use of SPS already after five minutes at 1200°C and 75 MPa. The aim was to control the alumina grain growth and thus obtain different nano-structure types. The microstructures have been correlated to some mechanical properties; *e.g.* hardness and fracture toughness.

INTRODUCTION

The weakest link in a chain determines the strength. This is an expression, which is applicable to most areas within the subject of materials science. It becomes especially obvious in the case of ceramics since these materials exhibit a brittle behaviour. In order to obtain improved toughness of ceramics one have to find ways to make the material homogeneous and free from cracks, pores and inclusions. Except for these fundamental but also unattainable details introducing reinforcement material in the matrix can also increase the toughness. Particles of a second phase in a matrix can act as reinforcement by different toughening mechanisms depending on *e.g.* composition, particle size, powder-processing route and thermal expansion properties.

Nano-sized particles have higher intrinsic sintering activities than micron sized ones and therefore a lower sintering temperature is expected to be required when sintering such particles. Nano-composites have proved to exhibit very good mechanical properties, with new toughening mechanisms. During the last decade an increasing interest for the nano sized region have been raised. Niihara and co-workers managed in the early 90´ies to obtain nano-sized particles embedded in or in-between larger alumina grains [1]. The mechanical properties were outstanding, but the results have been difficult to reproduce for other research groups.

Both TiN and SiC are used in construction ceramics as reinforcement of alumina. However, since the thermal expansion are different; TiN having a higher, and SiC having a lower thermal expansion than that of alumina, the expected properties should be different. For instance, at room temperature after sintering, in the case of SiC/alumina composites, the SiC particles are compressed and the matrix is tensile stressed. The conversed scenario is expected for TiN/alumina. But, however, that implies strong inter granular bonds between TiN and alumina. Therefore the surface properties *e.g.* the degree of surface oxidation or impurities plays important roles for the internal stress fields and therefore mechanical properties. This ought to be especially crucial for nano composites since the grain boundaries become more and more prominent when the particle size reduces.

The aim of this project was to obtain homogeneous powder mixtures with 2 vol.% and 5 vol.% nano-sized TiN and SiC particles dispersed in fine-grained alumina, to sinter them fully densified with spark plasma sintering (SPS) and to correlate the microstructures to mechanical properties. By applying different sintering parameters, in this case the temperature, attempts to tailor the microstructure were planned.

Alumina reinforced with TiN or SiC nano particles have been extensively reported earlier *e.g.* [1-3], but not this processing route. It was shown in a former investigation [3] that an admixture of 10 vol.% of TiN nano particles in alumina was too much in order to have the particles separated, while 5 vol.% seemed to be suitable. In the present study we added 5 vol.% of nanoparticles but also investigated the effect of a further decrease (to 2 vol.%) in the nanoparticle admixture. Measurements on zeta potentials on similar ceramic powders have shown that the pH_{iep} is about 3-5 for TiN [3-5], and 2.5-3 for SiC [6] whereas it is about 9 for Al_2O_3 [3,6]. However when adding a small amount (0.5 wt.%) of a poly acrylic acid (PAA) dispersant to an alumina/water suspension the pH_{iep} is decreased to about 3 and furthermore the dispersant yields a pH of about 9. This means that well dispersed low viscous composite slurries can be obtained without further controlling the pH. This behaviour was utilized for the preparation of both TiN and SiC composites.

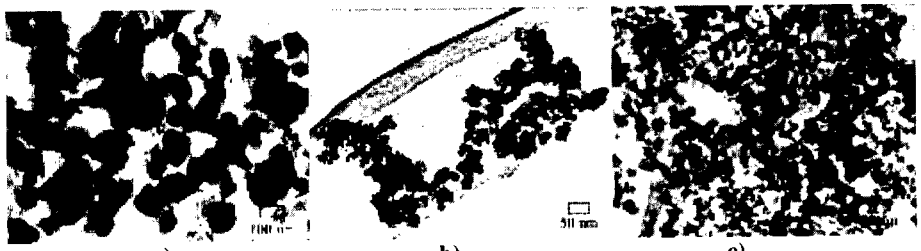
EXPERIMENTAL

The powders used in this study are given in table I. The powder morphologies were studied at 200kV in a TEM (Jeol, 2000FX, Japan). The samples were prepared by putting droplets of powder/ethanol suspensions onto copper grids and letting the ethanol evaporate (figure 1 a-c). Due to the small size and the dry state of samples, the particles tend to form agglomerates, which are deagglomerated during the processing.

The nano sized TiN powder is pyrogenic and was therefore handled in a glove box under nitrogen and suspended in ethanol-water mixture to obtain a slow surface oxidation. Then the solvent was evaporated at 50°C so that the powder could be handled in air. The SiC nanoparticles were suspended directly into alumina/water slurries according to the following powder processing scheme (figure 2).

Table I. The powders used in this investigation.

	TiN_{nano}	β-SiC_{nano}	α-Al_2O_3
Manufacturer	H. C. Starck (Germany)	MTI Corporation (U.S.A)	Taimei Chemicals Co. Ltd (Japan)
Powder Grade	Nano TiN	Nano β-SiC	Taimicron TM DAR
Particle size (nm)	30 (BET equivalent spherical diameter)	30	100
Purity (%)	*	95	99.99



a) **b)** **c)**

Figure 1 a-c. TEM images showing the powders used in this investigation; **a)** Al_2O_3 **b)** TiN and **c)** SiC.

Alumina powder, deionised water, and 0.5wt. % of poly acrylic acid (Dispex A40, Allied Colloids, USA) were mixed for 30 minutes at 400 rpm in a planetary ball mill (Pulverizette 6, Fritsch GmbH, Germany) equipped with a 250ml SiAlON milling jar and SiAlON milling spheres. Then 2 vol.% and 5 vol.% of the reinforcement phases were added and the slurries were milled for another 10 minutes. After equilibration the slurries were freeze granulated by spraying the slurry through a nozzle into liquid nitrogen. The granules were finally freeze dried in a freeze dryer (Hetosicc, Heto-Holten A/S, Denmark).
According to the former investigation [3] we could obtain homogeneous composites without additions of grain growth inhibitors like MgO and sintering in a hot press furnace. In the present investigation a finer alumina powder was used and the powder mixtures were sintered in another manner. In the sintering experiments of this investigation the dry powder mixture was poured directly into a graphite dye, which were put in the Spark plasma-sintering (SPS, Dr. Sinter, Japan) device. The heat increment in the SPS was maintained by using a pulsed DC according to figure 3a. A typical sintering cycle is represented in figure 3b.

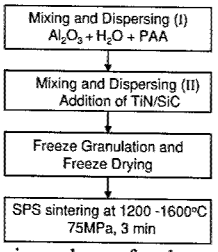


Figure 2. Processing scheme for the composite preparation.

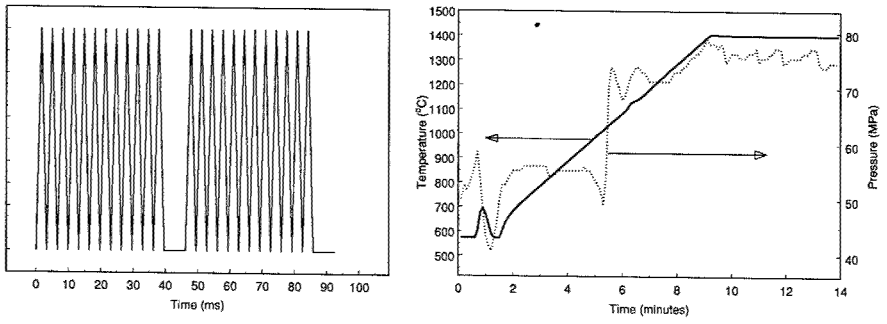


Figure 3. a) Schematic illustration showing the used SPS pulse duration for the sintering experiments. **b**) Temperature and pressure profiles for a typical SPS sintering cycle.

The samples were exposed to 1200, 1400 and 1600°C with the pressure 75MPa for 5 minutes. The densities of the sintered samples were measured by Archimedes principle using tap water. The theoretical density of the composites were calculated assuming a density of 3.97g*cm^{-3} for Al_2O_3, 3.22g*cm^{-3} for SiC, and 5.21g*cm^{-3} for TiN. For mechanical measurements pieces were

polished and the Vickers hardness were measured using a square based diamond for indents with an indenter using the load 5kg parallel to the pressing direction. The Vickers hardness was calculated using the expression (2):

$$H=1.8544*P/a^2 \qquad (2)$$

Where P is the load in Newton and a is the length in metres of the diagonal of the obtained indentation.

The mode 1 fracture toughness was determined measuring the lengths of the yielded cracks according to [7](3):

$$K_{1C}=A*(E/H)^{1/2}(P/C^{3/2}) \qquad (3)$$

Here, A is a constant and was set to 0.016, C is the mean crack length (meter), H is the hardness from (1), P is the load (Newton) and E is the Young´s modulus which was assumed to have a constant value of 390GPa for all composites. This is consistent with values of a similar investigation [8].

In order to reveal the microstructure of the samples fracture surfaces were prepared by crushing the composites. The samples were put onto a conductive tape and investigated in a FEG SEM (Leo 1550, Germany) at 10kV (without any additional sputtered conductive layer) and a SEM (Jeol, 880, Japan) at 20kV (with a sputtered layer of gold).

RESULTS AND DISCUSSION

After sintering it was found that the SiC composites required at least 1400°C for densification while the TiN nano-composites could be almost fully densified already after sintering at 1200°C (table II). But, however the 5 vol. % TiN composite exhibited a lower density at 1600°C. The explanation to this may be found in the PAA additions. The dispersant was not burnt of before sintering and at least two different scenarios could be considered; There could be carbon containing remnants at the grain boundaries which in contact with surface oxides produces CO(g) which then could be trapped in the structure because of the rapid sintering cycle. The other scenario is that gaseous decomposition products from the dispersant it self is trapped in the matrix. However, this does not explain why the SiC composites do not show the similar behaviour. The actual reason remains to be solved.

Table II. Percent of theoretical density, hardness, and fracture toughness.

Composite	1200°C			1400°C			1600°C		
	$\%\rho_{th}$	H_{V5} (GPa)	K_{1C} ($MPam^{1/2}$)	$\%\rho_{th}$	H_{V5} (GPa)	K_{1C} ($MPam^{1/2}$)	$\%\rho_{th}$	H_{V5} (GPa)	K_{1C} ($MPam^{1/2}$)
2vol.% TiN	99.9	20.3	3.7	98.9	16.7	3.8	99.0	15.5	*
5vol.% TiN	98.7	20.7	3.2	97.9	17.0	3.4	96.2	13.9	4.1
2vol.% SiC	92.5	(15.2)	(3.5)	99.4	20.6	2.8	99.9	19.3	2.8
5vol.% SiC	89.8	(11.5)	(3.9)	97.4	19.8	3.0	99.4	19.8	2.5

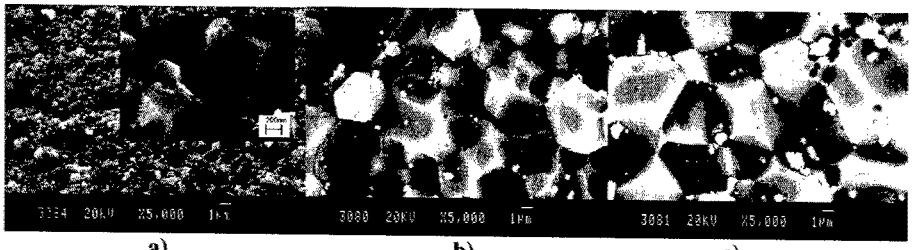
*Immeasurable cracks. Values in brackets are misleading because the samples are not fully dense.

As the sintering temperature increases the (alumina) grains are expected to grow (especially without additions of MgO). This was also found in the present investigation and is obvious in the fracture surface images for e.g. the 2 vol.% TiN and SiC composites (figures 4 a-c and 5 a-c). The resolution of the FEG SEM is high enough to reveal the nanoparticles in the 1200°C composite. It is evident in fig 4a that the alumina grains have grown somewhat already after the short sintering at 1200°C and some nano particles seem to be within the alumina grains. The rapid heating by means of SPS sintering involves very high electric currents through the material. This enhances surface diffusion and could also lead to closed porosity. As the temperature increase also the nanoparticles grow to agglomerates (figure 4b-c). This is also reflected in the mechanical behaviour. Both the hardness and fracture toughness tend to decrease with increasing sintering temperature (table II). It is evident from figures 4 and 5 that SiC composites show more transgranular fracture surface features than the TiN_n composites and they exhibit SiC agglomerates implying a less homogeneous powder mixture. The reason for this is not clear. Generally, the SiC composites are harder but have somewhat lower fracture toughness than TiN composites. It should be noted that these data are not to be considered as absolute values, but rather as a base for internal comparison. However, from these results it could be concluded that low sintering temperature is desirable, but the reinforcement admixture (2 or 5 vol %) is less important. For the TiN composites sintered at higher temperatures a strange indent behaviour showed up which involved absence of sharp indent profiles. A plausible explanation to this phenomenon could be found in the larger thermal expansion difference at elevated temperatures giving rise to stress fields in the material, which is released during the indentations but also in probable closed porosity.

A subsequent annealing of the compacts after sintering has been suggested for improving the mechanical behaviour by ordering of dislocation structures [1,9]. The role of such annealing has not been investigated in this study.

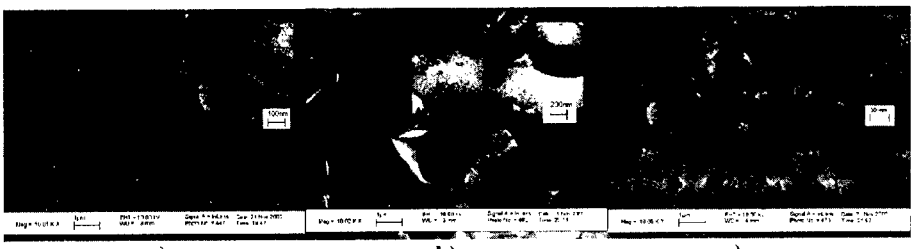
CONCLUSIONS

Fully densified nano composites comprising alumina and well dispersed nanoparticles of TiN or SiC could be obtained using a water based processing scheme followed by SPS sintering at 75MPa. The TiN composites sintered already at 1200°C whereas the SiC composites required higher temperatures. An unexpected drop in density for the TiN composites sintered at higher temperature is not yet explained.



a) **b)** **c)**

Figure 4a-c. BSE SEM images showing fracture surfaces of 2 vol.% TiN/Al_2O_3 composites sintered at 75 MPa for 5 minutes at **a)** 1200°C (where the microstructure is revealed by the FEG SEM inset) **b)** 1400°C, and **c)** 1600°C. Note the substantial temperature dependent grain growth of alumina (dark grains) and agglomeration of TiN particles at 1400°C and higher (lighter spots).



a) **b)** **c)**

Figure 5a-c. FEG SEM images with magnified insets showing fracture surfaces of 2 vol.% SiC/Al_2O_3 composites sintered at 75 MPa for 5 minutes at **a)** 1200°C, **b)** 1400°C, and **c)** 1600°C. These composites show more of transgranular fracture surfaces than the TiN_n composites and the SiC_n particles are less homogeneous dispersed than TiN_n composites.

Measurements of hardness and fracture toughness showed that the lowest possible sintering temperatures are desirable from mechanical properties point of view. No great differences between 2vol% and 5vol % composites could be observed for either TiN- or SiC-composites. When fully dense, the SiC composites were harder than TiN composites, but had somewhat lower fracture toughness. The measurements were hard to perform on some of the composites because a strange behaviour of the indents, probably depending on stress fields in the composites.

REFERENCES

1. K. Niihara, *J. Ceram. Soc. Jpn.* **99** (10) 974-982 (1991)
2. L. Gao, H. Z. Wang, J. S. Hong, H. Miyamoto, K. Miyamoto, Y. Nishikawa, S. D. D. L. Torre. *J. Eur. Ceram. Soc.* **19** (5), 609-613 (1999)
3. E. Laarz, M. Carlsson, B. Vivien, M. Johnsson, M. Nygren, and L. Bergström, *J. Eur. Ceram. Soc.* **21,** 1027-1035 (2001)
4. R. Nass, S. Albayrak, M. Aslan, H. Schmidt: "Colloidal Processing and Sintering of Nanoscale TiN" in *Ceramic Transactions Vol. 51*, ed. H. Hausner, G. L. Messing, S.-I. Hirano, (Am.Ceram. Soc. 1995) pp 591-595.
5. R. Wäsche, G. Steinborn, F. Baader, *Fortschrittsber. DKG (1995) pp. 151-158 (in german).*
6. S. C. Deevi, C. K. Law, A. S. Rao, Process Technology Proceedings, 7 (Interfacial Phenom. Biotechnol. Mater. Process.) ed. Y.A. Attia, B.M. Moudgil and S. Chandler, (Elsevier, 1988) pp. 201-215
7. G.R. Anstis, P. Chantikul, B.R. Lawn and D.B. Marshall, *J. Am. Ceram. Soc.* **64** (9), 533-538 (1981)
8. B. Baron, C.S. Kumar, G. Le Gonidec, and S. Hampshire, *J. Eur. Ceram. Soc.* **22,** 1543-1552 (2002)
9. R. J. Brook and R. A. D. Mackenzie, Mater.World 1(1), 27-30 (1993)

ACKNOWLEDGEMENTS

We are grateful to Dr. Eric Laarz at the Institute for Surface Chemistry, Stockholm, Sweden for preparing the composite slurries and to Ms Mirva Heinonen, Stockholm University, Sweden for assistance with some of the sintering experiments.

Mat. Res. Soc. Symp. Proc. Vol. 740 © 2003 Materials Research Society I6.10

Synthesis and Characterization of Metal Nanoparticles and the Formation of Metal-Polymer Nanocomposites

Anshu A. Pradhan,[1,3] S. Ismat Shah[1,2,3] and Lisa Pakstis[1]

[1] Department of Materials Science and Engineering

[2] Department of Physics and Astronomy
University of Delaware, Newark, DE 19716, USA

[3] Fraunhofer Center for Manufacturing and Advanced Materials, Newark, DE 19711, USA

ABSTRACT

Metal nanoparticles are highly prone to oxidation due to their high surface energy and affinity for oxygen which can lead to the complete oxidation of the particles. Studying and utilizing the unique properties of metal nanoparticles requires minimizing their interaction with the atmosphere. We have used the co-condensation technique to synthesize suspensions of metal nanoparticles in isopropanol. The solvent protects the nanoparticles from the atmosphere and minimizes agglomeration of the nanoparticles. The particles showed a lognormal distribution and the average particle size was below 20nm. Polymer-metal nanocomposites were made by dispersing the metal nanoparticles in PMMA matrix by spin coating and solution casting. Adherent films, fibers and free standing films could be obtained by varying the process conditions. The SEM images show that the nanoparticles in the spun coated films were non-agglomerated and well dispersed over a wide area. Morphology of the spun coated films was different from the solution cast films. Electrically conducting films having interconnected silver particle network could be obtained. Cytotoxicity studies show that the silver nanoparticles and the PMMA-Ag nanocomposite films are antibacterial in nature. We have also dispersed the nanoparticle into pump oil and measured the thermal conductivity of the resultant mixture. The thermal conductivity of the oil could be increased by over 50% by adding an extremely small fraction of the silver nanoparticles.

INTRODUCTION

Metal nanoparticles have received tremendous interest due to their unique optical, electrical and magnetic properties.[1-4] Several chemical and vacuum techniques have been used to synthesize metal nanoparticles.[5,6] In general, chemical techniques produce smaller nanoparticles with a narrower particle size distribution, while vacuum techniques produce higher purity nanoparticles. In this paper, we report on the synthesis of silver nanoparticles by Co-Condensation (COCON) technique which combines the advantages of chemical and vacuum routes of nanoparticle synthesis. COCON is derived from an earlier technique called Vacuum Evaporation onto a Running Oil Substrate (VEROS) demonstrated by Yatsuya and his co-workers[7]. The technique was modified by Klablunde[6,8] who used an organic liquid in place of the oil used in VEROS. The COCON technique involves the co-deposition of metal vapors from an evaporation source, and a suitable solvent onto the cryogenically cooled walls of an evacuated chamber. The supercooling of the metal vapors as they move away from the evaporation source leads to the formation of metallic nuclei. These nuclei are deposited on the chamber walls together with the remaining metal vapors and the solvent. No growth occurs on

cold chamber wall, however, on warming the reactor the nuclei grow to form metal nanoparticles. The solvent molecules surround the growing metal nuclei and prevent agglomeration. This solvation effect is critically important as it not only disperses the nanoparticles within the liquid medium, it also prevents oxidation of the nanoparticles which is a common problem in the synthesis of metal nanoparticles. The COCON technique is also easily scalable. We have used a scaled up reactor to produce silver nanoparticle suspensions. The nanoparticles were dispersed into a poly-methyl methacrylate (PMMA) matrix by spin coating and solution casting. These films have non-agglomerated silver nanoparticles dispersed over a wide area and allow the exploitation of the large surface area of the nanoparticles. In addition, process conditions can be varied to yield conducting films. It is also known that silver nanoparticles are antibacterial in nature.[9,10] Thus, the PMMA-Ag nanocomposites can be used as low cost flexible antibacterial surfaces.

EXPERIMENT

A schematic of the COCON reactor is shown in Fig. 1. The reactor is 2m long and 0.4m in diameter. An effusion cell acts as the source of metal vapors. The reactor is pumped down after which the liquid nitrogen and the flow of 2-propanol is started. The pumping is then stopped and the low pressure is maintained by the solvent freezing along the sides of the reactor. The crucible is heated to a temperature of around 1400°C which causes the metal to vaporize. The growth of the nanoparticles occurs both in the vapor phase as the metal vapor travels towards the reactor wall and when the frozen solvent layer with the embedded metal nuclei melts. The nanoparticles are obtained in a suspension with the solvent. The particle size was determined by Transmission Electron Microscopy (TEM) and by X-Ray Diffraction (XRD).

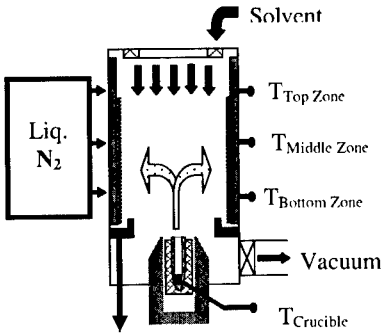


Fig. 1: Schematic of the COCON

To form metal-polymer nanocomposites, PMMA (MW = 88K) was dissolved in a 1:1 mixture of the methyl ethyl ketone (MEK) and the silver suspension. The polymer concentration was between 8 mg/mL and 30 mg/mL. Films on silicon and glass substrates were fabricated by either spin casting at 600rpm or solution casting by allowing the solvent to evaporate slowly by saturating the atmosphere around the films with the solvent. The silver concentration in the suspensions and the films was determined with Thermo Gravimetric Analysis (TGA). The films were imaged by SEM and optical microscopy. The sheet resistance of the films was measured with a 4-point probe. Antibacterial studies were carried out by placing E.Coli cells grown to the mid log phase in contact with the films and the nanoparticles. For the suspensions, the 2-propanol was evaporated to eliminate the effect of the solvent. The cells were placed in an incubator at 37 °C for 24 hours. The number of colony forming units (CFUs) was then counted to determine the antibacterial nature of the particles and the films.

RESULTS AND DISCUSSION

Fig. 2a shows a TEM micrograph of the nanoparticles deposited with the crucible temperature of 1380°C. The particles show a log-normal distribution (Fig. 2b). Since vacuum phase synthesis of nanoparticles commonly show a log-normal distribution[11], this suggests that at least a part of the growth occurs in the vapor phase. The particle size increases slightly with temperature while the size distribution gets narrower at higher temperatures (Fig. 2c). Fig. 3

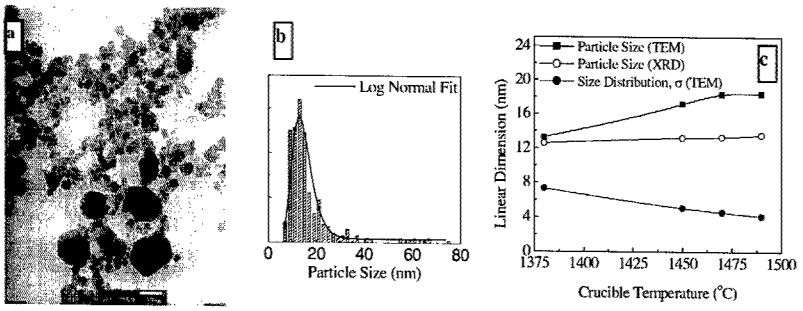


Fig 2: Variation of the particle size and size distribution of the nanoparticles

shows a high resolution TEM image of the silver nanoparticle and the associated diffraction pattern. It can be seen that the nanoparticle is a single crystal with few defects.

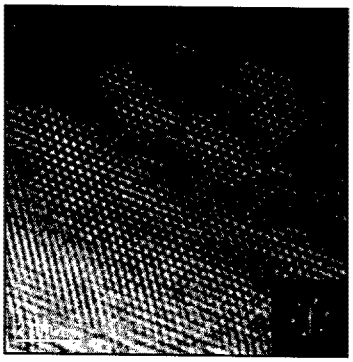


Fig. 3: HR-TEM image of a silver

To form the metal-polymer nanocomposites, PMMA was chosen since it is a commonly used transparent polymer and is soluble 1:1 mixture of 2-propanol and MEK. As the solvent used in the COCON process was also 2-propanol, PMMA was dissolved in 1:1 mixture of MEK and 2-propanol. Fig. 4a shows the SEM images of the films deposited by spin coating from the PMMA-Ag solution. The silver nanoparticles can be seen as lighter regions in the darker PMMA matrix. It can be seen that the nanoparticles are non-agglomerated and well dispersed over a large area. At high polymer concentrations (30 mg/mL), fibers are formed in addition to the films during spin coating. The fibers are a few cms long and 0.5 mm in diameter. SEM of the fibers (Fig. 4b) also shows that the individual nanoparticles are dispersed in the polymer matrix. The SEM images are very different from TEM images of the silver nanoparticles (Fig. 2a). This suggests that the agglomeration seen in the TEM image is due to the capillary force which concentrates the nanoparticles into an ever-decreasing volume as the solvent evaporates. The film obtained by spin coating shows a "snapshot" of the silver nanoparticles in the suspension because the rate of solvent loss is higher. Thus, it can be seen that the solvation of the metal nanoparticles, which prevents the

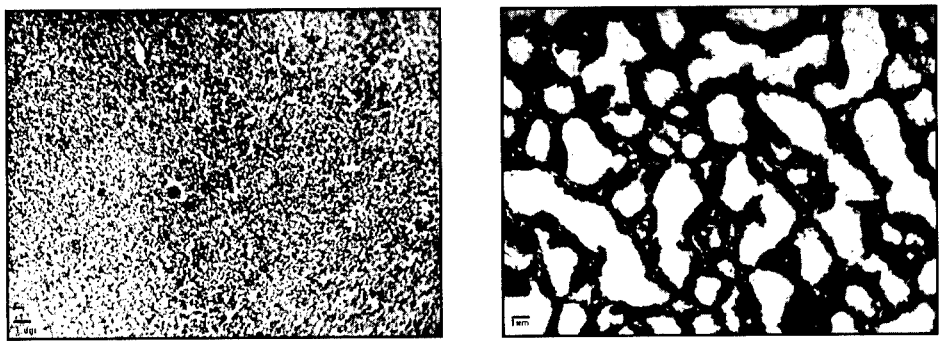
agglomeration of nanoparticles in the suspension, leads to the dispersion of the nanoparticles in the films. These nanocomposite films hold the nanoparticles in a stable matrix and allow us to take full advantage of the large surface area of the nanoparticles.

The films deposited by solution casting (Fig. 5) show a considerably different morphology from the spun cast films. In addition, the morphology is strongly dependent on the PMMA-Ag ratio. Fig. 5a shows an optical micrograph of a film deposited from a 1mL solution containing 30mg PMMA and 1.5mg Ag, while Fig. 5b is of a film deposited from a 1mL solution containing 15mg PMMA and 1.5 mg Ag. The film dimensions were 3cm x 3cm and the thickness was approximately 5μm. Since the techniques used to form these films are non-specific, the silver nanoparticles can be imbedded in almost any polymer matrix. Films deposited at higher polymer concentrations contain individual sub-micron silver regions distributed in a PMMA matrix. We believe that the slow evaporation of the solvent decreases solvation of the nanoparticles which allows the agglomeration of the nanoparticles. This



(a) (b)

Fig 4: SEM micrographs of spin coated PMMA-Ag



(a) (b)

Fig. 5: Optical micrographs of solution cast PMMA-Ag films

hypothesis was tested by gently heating the silver nanoparticle suspension. The silver immediately precipitated out of the suspension, which suggests that reduction in solvation by

providing kinetic energy to the solvent molecules that allows increased interaction amongst the nanoparticles leading to agglomeration of the nanoparticles. Films having a connected silver network (Fig. 5b) were found to be electrically conducting. The sheet resistance of the PMMA-Ag nanocomposite was around 4500 Ω/□ which is 11 orders of magnitude lower than the sheet resistance of PMMA (10^{15} Ω/□). Thus, these films can be used for applications such as transparent large area collectors for solar cell, soft electrically conducting bio-electrical interfaces, etc. The spun coated films (Fig. 2) and the solution cast films with discrete silver islands (Fig. 5a) were electrically insulating. Therefore, varying the solution evaporation rate makes it possible to control the properties and the morphology of the nanocomposite films.

Cytotoxicity studies were carried out to determine the effect of silver nanoparticles on bacterial growth. Fig. 6 shows the effect of the silver nanoparticle concentration on bacterial growth. It can be seen that addition of 10^{-4}g of silver leads to complete elimination of E.Coli colony forming units. Solution cast films containing the silver nanoparticles are also cytotoxic and inhibit bacterial growth.

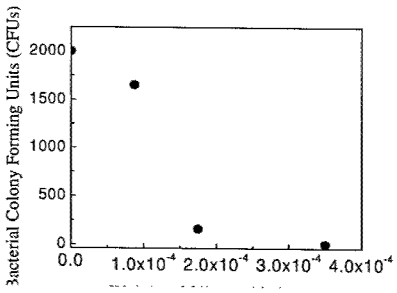


Fig. 6: Effect of silver concentration on the antibacterial properties of PMMA-Ag films

We have also added silver nanoparticle suspensions obtained from the COCON reactor to enhance its thermal conductivity. Fig 7 shows the variation of the thermal conductivity of the mixture with the silver concentration. The thermal conductivity of a mixture of pump oil and 2-propanol was also measured to determine the effect on the solvent on the thermal conductivity. The addition of $2x10^{-4}$ wt% silver increases the thermal conductivity of the mixture by over 50%. The heat capacity and the electrical conductivity of the mixture remain unchanged. The oil-silver nanoparticle mixture is ideally suited for application such as lubricant in electrical motors, which require high thermal conductivity without jeopardizing the electrical properties.

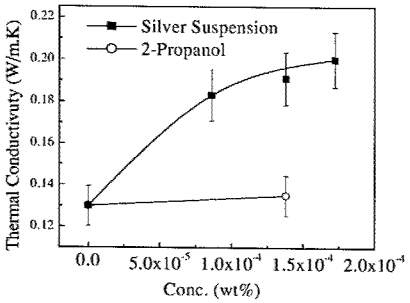


Fig. 7: Variation of the thermal conductivity of pump oil with addition of silver suspension

CONCLUSION

We have used the COCON technique to synthesize suspensions of silver nanoparticles in 2-propanol. The particles had a log-normal distribution and the particle size was below 20nm. Polymer-metal nanocomposites were made by dispersing the silver nanoparticles in a PMMA. The morphology of the films could be varied from having individual isolated nanoparticles in a

polymer matrix to interconnected silver web structures. Films with the interconnected silver network were found to be electrically conducting. Cytotoxicity studies carried out on the films proved that the nanocomposites were antibacterial in nature. Silver nanoparticle suspension was also added to pump oil to enhance its thermal conductivity. The thermal conductivity increased by 50% on addition of 10^{-4}wt% of silver.

REFERENCES

1. T. W. Ebbesen, H. J. Lezec, H. F. Ghaemi, T. Thio, and P. A. Wolff, Nature **391,** 667 (1998).
2. R. Elghanian, J. J. Storhoff, R. C. Mucic, R. L. Letsinger, and C. A. Mirkin, Science **277,** 1078 (1997).
3. J. P. Alivisatos, Science **271,** 933 (1996).
4. R. P. Cowburn, J. Phys. D **33,** R1 (2000).
5. D. L. Feldheim and C. A. J. Foss, *Metal Nanoparticles* (Marcel Dekker, Inc., New York, 2002).
6. K. J. Klabunde, *Free Atoms, Clusters, and Nanoscale Particles* (Academic Press, San Diego, 1994).
7. S. Yatsuya, T. Hayashi, H. Akoh, E. Nakamura, and A. Tasaki, **17** (2), 355 (1978).
8. K. Matsuo and K. J. Klabunde, J. Org. Chem. **47** (5), 843 (1982).
9. S. M. Modak and C. L. Fox, Biochem. Pharmacol. **22** (19), 2391 (1973).
10. T. J. Berger, J. A. Spadaro, S. E. Chapin, and R. O. Becker, Antimicrob. Agents Chemother. **9** (2), 357 (1976).
11. R. C. Flagan and M. M. Lunden, Mater. Sci. Eng. A-Struct. Mater. Prop. Microstruct. Process. **204** (1-2), 113 (1995).

Poster Session

Mat. Res. Soc. Symp. Proc. Vol. 740 © 2003 Materials Research Society

Modeling mechanical properties of carbon molecular clusters and carbon nanostructural materials

Vadim M.Levin, Julia S.Petronyuk, Inna V.Ponomareva
Lab. of Acoustic Microscopy, Inst.of Biochemical Physics, Russian Academy of Sciences,
4 Kosygin St., Moscow, 119991, Russia

ABSTRACT

The concept of 2D elasticity of a graphene sheet together with the idea of stiffness of a single sp^3 bond have been applied to theoretical evaluating elastic properties of diverse carbon states. 2D elastic moduli have been extracted from data on elastic moduli of crystalline graphite. Stiffness of the sp^3 bond has been estimated from data on the elastic modulus of diamond. Efficiency of Van-der-Waals interaction has been taken from the elastic modulus C_{33} of crystalline graphite. Characteristics of single fullerene deformability have been computed by the molecular dynamics method. Theoretical estimations have been performed for single molecular clusters, pristine fullerite, HPHT phases of polymerized C_{60}, etc. The estimations are in good agreement with experimental data on elastic properties and nanoscale structure of carbon states. The approach is effective for establishing interrelation between nanostructure and elastic properties, for prediction and classification of nanostructure in novel carbon materials.

Three types of hybridized covalent bonds between of carbon atoms (sp^3, sp^2 and sp) give rise a variety of macromolecular clusters and carbon nanostructural solids, which are essentially distinguished in their mechanical properties. Diversity of mechanical characteristics stems from the variability in nanostuctural organization and from combination of different types of covalent bonds (sp^2 and sp^3) with Van-der-Waals interaction between molecular clusters. The purpose of the paper is to explain the elastic property diversity in the frame of simple mechanical models of different nanoscale structures using, in the main, data on elastic properties of well-known carbon states – graphite and diamond. Analysis of these models makes it possible to follow variations in elastic characteristic of carbon states in transition from one form of nanostructural organization to another.

The most of carbon states are formed by *2D* structural units – plane or curved graphene sheets or closed molecular clusters (fullerenes, nanofilaments, etc) originated from these sheets. Van-der-Waals forces or covalent sp^3 bonds provide *3D* linkage between the *2D* graphite-like nanostructural elements. Diversity of carbon states actually results from two specific peculiarities of hybridized C-C bonds. The first is high lability – interatomic distances and valent angles are liable to vary over relatively wide range. Stressed sp^2 bonds cause bending graphite sheets – curved atomic sheets are inherent in many carbon states: carbon fibers, fullerenes, nanotubes and so on. The other feature of carbon is concurrent participation of different types of C-C bonds in formation of carbon states. Normally the spatial structure of carbon materials is formed by Van-der-Waals interaction between graphene sheets or molecular clusters. This interaction results in formation of soft and fragile materials (crystalline graphite and graphite materials, pristine fullerites, carbon nanotube paper). Under extreme conditions sp^3 bonds link molecular clusters

forming hard and ultrahard HPHT fullerene phases, neutron irradiated graphite, diamond-like films, etc.

Our mechanical models for evaluating elastic properties of solid carbon states include: (1) graphene sheets and *2D* closed molecular clusters (fullerenes and nanofilaments) as elements of spatial construction, (2) Van-der-Waals interaction and (3) diamond-like sp^3 bonds as factors to assemble these structural elements into an integral construction. It allows discussing the mechanical properties in terms of *2D* graphene sheet elasticity, stiffness of individual diamond-like bond and efficiency of Van-der-Waals force.

Carbon molecular clusters involve a significant number of atoms to treat them as macroscopic systems and to speak about their elastic properties. The surface elastic moduli $\tilde{C}_{11}$ and $\tilde{C}_{12}$ establish interrelation between the tensions τ_1, τ_2 and strains ε_1, ε_2 in the sheet plane:

$$\tau_1 = \tilde{C}_{11}\cdot\varepsilon_1 + \tilde{C}_{12}\cdot\varepsilon_2, \qquad \tau_2 = \tilde{C}_{12}\cdot\varepsilon_1 + \tilde{C}_{11}\cdot\varepsilon_2 \tag{1}$$

Following to Ruoffs [1], the *2D* elasticity of graphene sheets is evaluated from the in-plane elastic moduli C_{11} and C_{12} of crystalline graphite referred to a single sheet. The sheet density N in a graphite stack is derived from the interlayer distance d_0. Using experimental data (C_{11} =1020GPa, C_{12} = 180 GPa and d_0 = 0.335 nm [2]) we arrive at the surface moduli of a graphene sheet:

$$\tilde{C}_{11} = C_{11}\cdot d_0 = 341{,}7\ \text{Pa·m}, \qquad \tilde{C}_{12} = C_{12}\cdot d_0 = 60{,}3\ \text{Pa·m} \tag{2}$$

The moduli $\tilde{C}_{11}$ and $\tilde{C}_{12}$ have been used in [1] to estimate the bulk elastic modulus $B_{C_{60}}$ of a single C_{60} molecule:

$$B_{C_{60}} = \frac{2}{3}\left(\tilde{C}_{11} + \tilde{C}_{12}\right)\cdot\frac{1}{R_{C_{60}}} = \frac{2}{3}\left(C_{11} + C_{12}\right)\cdot\frac{d_0}{R_{C_{60}}} \approx 800\,\text{GPa}, \tag{3}$$

R_{C60} = 0,35 nm is the fullerene radius. The off-plane elastic characteristics (bending resistance) of the graphene sheet could not be estimated from properties of graphite. Response of an atomic layer to bending could not be considered as ordinary reaction of a macroscopic body: compression of the area below the neutral line and dilatation of the upper layers. To evaluate the response theoretical computation has been performed in the frame of molecular dynamics methods [3,4] for spherical configuration of a graphene sheet because of our special interest to elastic properties of superhard HPHT phases of C_{60}. The bending stiffness k of a graphene shell has been introduced to describe correlation between the point force f and the displacement ΔR_{C60} of the shell induced this point load:

$$f = k\cdot\Delta R_{C_{60}}/R_{C_{60}}. \tag{4}$$

The calculated value of k is $57.6\cdot10^{-8}$ N.

Elasticity of a single sp^3 bond is characterized by stiffness K_{sp^3} of elementary tetrahedron associated with the bond with respect to the force f acting along the tetrahedron axis:

$$f = K_{sp^3}\cdot\varepsilon_h, \qquad \varepsilon_h = \Delta h/h \tag{5}$$

The applied force induces the change Δh of the tetrahedron height h that we consider as the length of the intercluster link. Value of K_{sp^3} may be evaluated from magnitude of the elastic modulus $C_L^{<111>}$ of diamond along the <111> direction. Diamond lattice is treated as an arrangement of parallel layers consisted of diamond tetrahedrons oriented along <111> direction. Normal stress applied to the {111} plane provides the force $f = \sigma \cdot S_0$ acting on an individual tetrahedron; $S_0 = \sqrt{3}/4 \cdot a^2$ is area of the {111} plane associated with a single tetrahedron, a is length of *fcc* diamond lattice. The deformation ε_h of the elementary tetrahedron is equal to deformation induced by the applied stress in diamond

$$\varepsilon_h = \varepsilon^{<111>} = \sigma / C_L^{<111>}. \tag{6}$$

Starting from the value of $C_L^{<111>}$=1200 GPa [5] the single sp^3 bond stiffness has been calculated:

$$K_{sp^3} = f / \varepsilon_h = C_L^{<111>} \cdot S_0 = \sqrt{3}/4 \cdot a^2 \cdot C_L^{<111>} = 6.58 \cdot 10^{-8} \text{ N}. \tag{7}$$

Efficiency of Van-der-Waals interaction is taken from the graphite elastic modulus C_{33} responsible for interlayer interaction between atomic sheets in crystalline graphite.

Elementary structural units described above are employed for the assessment of elastic properties in diverse carbon states. The attention is focused on evaluation of the bulk elastic modulus B (inverse compressibility). The bulk modulus is a natural elastic characteristic of a matter. The bulk modulus can be evaluated in the frame of the models for all feasible carbon states. Estimation of shear elastic characteristics requires more detailed description of interatomic interaction.

Let start the consideration from soft and fragile carbon states that are formed by plane or curved graphene sheets linked by Van-der-Waals forces. Crystalline and turbostratic graphite, pristine fullerite and nanotube materials represent this kind of the structural organization. Weak molecular forces between sheets, graphite clusters or fullerene molecules give the main contribution into elastic response of a matter. In crystalline graphite Van-der-Waals interaction hold together the stack of two-dimensional graphene sheets. Hydrostatic pressure p applied to a graphite sample above all else induces change of the distance between graphene sheets. So the bulk modulus B is close to the interlayer component C_{33} of the elastic matrice of graphite:

$$B_{gr} \approx C_{33} = 36 \text{ GPa}.$$

In turbostratic graphite and molecular crystals of pristine fullerite weak Van-der-Waals forces are responsible for interaction between graphite clusters or fullerene molecules in all directions uniformly. The bulk modulus B in these materials should be approximately 3 times smaller comparing with the value of B in crystalline graphite because hydrostatic pressure is able to change intercluster distances in three orthotropic directions. For a cubic molecular crystal of pristine fullerite the Hook equation gives values of strains ε_i (i =1,2,3) induced by hydrostatic pressure p: $\varepsilon_i \approx p / C_{33}$; here the unidirectional elastic modulus of fullerite is approximated by the interlayer module C_{33} of graphite. The bulk deformation ε_V determines the value of the bulk modulus of crystalline C_{60}:

$$\varepsilon_V = \Delta V/V = \cdot\varepsilon_1 + \varepsilon_2 + \varepsilon_2 = 3 \cdot p / C_{33}; \qquad B_{pris} = C_{33}/3 = 12 \text{ GPa}. \tag{8}$$

The theoretically estimated value of B is in good agreement with the experimentally obtained magnitude of 11 GPa. The little difference caused by curvature of fullerene molecules because the basis of our estimations is the molecular interaction between the plane graphene sheets.

The next group of carbon states includes substances in which covalent sp^3 partly replace the Van-der Waals interaction between molecular clusters. The substitution results in progressive stiffening carbon materials as increasing quantity of sp^3 covalent bonds. Mixture of sp^2 and sp^3 is characteristic for many graphite and diamond-like materials. But our consideration will be focused on high-pressure high-temperature (HPHT) phases of polymerized fullerite. Under HPHT conditions fullerites C_{60} and C_{70} undergo an intricate series of successive transformations caused by covalent sp^3 bonding of fullerene clusters. Mechanical properties of HPHT phases follow structural transformations. Polymerized fullerenes demonstrate a wide spectrum of phases with diverse nanostructure, elastic properties of that are available [6] to compare with our modeling estimations.

At first stages of polymerization fullerene balls are linked together into linear chains or planar structures [7] by pairs of sp^3 bonds (2+2 cycloaddition mechanism). Molecular chains and planes are held together by means of Van-der-Waals forces. Chains of polymerized C_{60} are aligned parallel into orthorhombic crystalline structure, planes provides tetrahedral or rhombohedral structure of *2D* polymerized C_{60}. Van-der-Waals interaction between chains or planes of polymerized balls is much weaker than sp^2 and sp^3 bonds that form individual chains of fullerene molecules. Compressibility of the *1D* or *2D* polymerized states is determined by changing distances between chains and planes in directions perpendicular to the direction of alignment. Their bulk elastic moduli B should be close to the value specific for pristine crystalline fullerite or graphite (10 ÷ 40 GPa). The real values of B depend on topology of material structure. In pristine C_{60} Van-der-Waals interaction is responsible for all of three deformation ε_1, ε_2 and ε_3 induced by hydrostatic pressure along the coordinate axes. Elastic response along each of the axes is described by the elastic coefficient C, which is close to the interlayer elastic parameter C_{33} of graphite: $C \approx C_{33}$. Because the bulk deformation ε_V involves all three values ε_1, ε_2 and ε_3:

$$\varepsilon_V = \cdot\varepsilon_1 + \varepsilon_2 + \varepsilon_2; \qquad \varepsilon_1 \sim \varepsilon_2 \sim \varepsilon_3 \sim p \,/\, C,$$

we have arrived at the value $B_{prist} = C/3 \approx 12$ GPa in (8).

In *1D* polymerized C_{60} hydrostatic pressure produces two strain ε_1 and ε_2 only, the third strain ε_3 along the direction of molecule alignment vanishes ($\varepsilon_3 << \varepsilon_{1,2}$). So the bulk elastic modulus B_{1D} of *1D* polymerized C_{60} is by 1,5 time higher than the modulus of pristine C_{60}:

$$B_{1D} = p/(\varepsilon_1 + \varepsilon_2) = C/2 = (3/2)\cdot B_{prist.} \approx 17 \text{ GPa} \qquad (9)$$

In *2D* polymerized state nanostructure is easily deformed only along one direction – perpendicular to the planes of covalently bounded fullerene molecules ($\varepsilon_{2,3} << \varepsilon_1$). The sp^3 covalent bonding makes *2D* polymerized C_{60} 3 times stiffer comparing with pristine fullerene:

$$B_{2D} = p/\varepsilon_1 = C = 3\cdot B_{prist.} \approx 35 \text{ GPa} \qquad (10)$$

Elastic modules of *1D* and *2D* polymerized C_{60} have been measured by the pulse time-resolved method of acoustic microscopy [6]. The experimental values of the bulk elastic modulus B for *1D* and *2D* polymerized C_{60} fullerites (B_{1D} = 27 GPa and B_{2D} = 45 GPa) are close to our estimations – 17 and 35 GPa respectively. Divergence of the experimental and calculated values

shows our calculations should be considered, as a qualitative way for estimating because real features of interaction between polymerized clusters has not been taken into account. Principally new situation arises when sp^3 covalent bonds pack up fullerene molecules into a *3D* system. This type of C_{60} polymerization is realized at quite high pressure (9 ÷ 12 GPa) and temperature (higher 1000 ^{0}C). Elastic properties of *3D* polymerized fullerites have been measured by acoustic microscopy technique [6] and Brillouin scattering method; it was been shown the hardness and bulk modulus of some *3D* polymerized phases are compared with these parameters of diamond. It necessary to underline *3D* polymerized phases in practice are observed in crystalline (actually,polycrystalline) or partly disordered states. A few theoretical models of *3D* crystalline structure of C_{60} fullerites has been proposed [8,9].

For our estimations we employ the simplest model of a cubic *3D* structure formed by fullerene molecules that are held together with double sp^3 covalent bonding (2+2 cycloaddition) in three perpendicular coordinate directions x_1, x_2, x_3. The primary unit of this *3D* structure is a fullerene molecule plus six perpendicular double sp^3 bonds. Elastic response of the structure to a stress applied along any of the coordinate axes is determined by the combined stiffness K of the series system of elastic elements involved a pair of covalent sp^3 bonds and bending resistance of the elastic sphere to a point force. Elastic characteristics of these elements have been described above. Using the bending stiffness k of a graphene shell and stiffness K_{sp^3} of a single sp^3 bond the expression for combined stiffness of the primary structural unit is written:

$$K = \frac{k \cdot \left(2K_{sp^3}\right)}{\frac{l_1}{L} \cdot \left(2K_{sp^3}\right) + \frac{l_2}{L} \cdot k}, \tag{11}$$

l_1 – fullerene ball diameter (~ 7Å [10]), l_2 – sp^3 tetrahedron height (~ 2Å), L – lattice parameter of *3D* polymerized C_{60} (~ 8,5 Å). According to our previous estimations: $k = 57.6 \cdot 10^{-8}$ N and $K_{sp^3} = 6.6\ 10^{-8}$ N. The resulting value of the combined stiffness $K = 31.3$ N gives an elastic characteristics of the *3D* polymer C_{60} structural unit. To pass to material properties we should transfer from the stiffness K to the elastic modulus C_{11}, characterizing one-dimensional elastic response of a matter dividing the stiffness K by area $S_{3D} = L^2$ of the lattice unit:

$$C_{11} = K/S_{3D} \approx 450 \text{ GPa}. \tag{12}$$

Estimation of the bulk elastic modulus B_{3D} for the simple cubic *3D* structure ($\varepsilon_1 \sim \varepsilon_2 \sim \varepsilon_3 \sim p/C_{11}$) is:

$$B_{3D} = p/\varepsilon_V = C_{11}/3 \approx 130 \text{ GPa} \tag{13}$$

The value of B_{3D} has been calculated in approximation $C_{11} >> C_{12}$. It gives the minimum of the value. Approximation $C_{11} \approx C_{12}$ leads to the maximum value of $B_{3D} \approx 400$ GPa. For the most solids $C_{11} \sim 2\,C_{12}$ and B_{3D} is about 260 GPa. Experimental values of bulk elastic modulus $B_{3D} \sim$ 160 ÷ 450 GPa [6] are in a good agreement with our calculations.

Experimental data point to existence of HPHT fullerene states with values of elastic moduli that are much bigger values calculated above. To explain these experimental results we propose a new model of structural organization and mechanical properties of HPHT phases. At very high pressure (11÷13GPa) and temperature (1200÷2000 ^{0}C) fullerenes are linked through incorporation of sub-units of one cluster into cages of others (reaction of polycondensation [11]).

The cluster coalescence results in formation of rigid and tight-packed *3D* graphene sheet network. We model the structure as a *3D* system of mutually intersected graphene sheets packed parallel to *x*-, *y*-, *z*-directions and connected one to another by common atoms along lines of their intersections. The model seems to be a good approximation to estimate elastic response of ultra-hard fullerite materials.

The elastic response of the model system is expressed through the surface elastic moduli $\tilde{C}_{11}$ and $\tilde{C}_{12}$ of a single graphene sheet and density $N = 1/b$ of graphene sheet package along each of the principal directions of packing (b – is a mean distance between neighbor atomic sheets along a given direction). Hydrostatic pressure p induces principal strains ε_1, ε_2 and ε_3 along the principal axes. In each of three orthogonal directions the elastic response is caused by in-plane deformation of two orthogonal systems of intersecting sheets. For direction 1:

$$p = 2 \cdot \tilde{C}_{11} \cdot 1/b \cdot \varepsilon_1 + \tilde{C}_{12} \cdot 1/b \cdot (\varepsilon_1 + \varepsilon_3); \tag{13}$$

the same equations may be written for direction 2 and 3. This system of equations makes it possible to express the bulk deformation ε_V through the pressure p and to obtain the equation for the bulk elastic modulus B of the structure:

$$B = 2/3 \cdot (C_{11} + C_{12}) \cdot (d/b), \tag{14}$$

where C_{11}, C_{12} – in-plane elastic moduli of graphite; d and b – interlayer distances in graphite and in the model system accordingly. When the average size of the cluster units equals to the fullerene radius $R_0 = 0.355$ nm the expression (14) coincides with Rouffs' calculations for the bulk elastic modulus of a free fullerene molecule: $B = 800$ GPa. The ultimate value of $B = 950$ GPa arises when the average interlayer distance b coincides with the one in graphite. Calculated values are able to explain extremely high values of the bulk elastic modulus of ultrahard fullerites $B = 550 \div 800$ GPa having been observed in experiments [6].

REFERENCES

1 R.Ruoff, *Nature*, **350,** 663-664. (1991)
2 O.L. Blakslee, D.G. Proctor, E.J.Seldin, G.B. Spence and T.Weng, *J. Appl.Phys.* **41,** №8, 3373-3382 (1970).
3 W.Burcert, N.L.Allinger, *Molecular Mechanics*, Amer. Chem. Soc., Washington, 1982.
4 D.W. Brenner, *Phys.Stat.Sol. (B)* **217,** 23 (2000).
5 *The properties of natural and synthetic diamond*, ed. J.E.Field, *London*, 1992.
6 V.M. Levin, V.D. Blank, V.M. Prokhorov, Ja.M. Soifer, N.P. Kobelev *J.Chem.and Phys.of Solids* 61 (2000) 1017–1024.
7 M.Nunez-Regueiro et.al., *Phys.Rev.Lett. 74* (2) (1995) 278-281.
8 M. O'Keeffe; *Nature*, **352** (1991) 674.
9 L.A. Chernozatonskii, N.R. Serebryanaya, B.N. Marvin *Chem.Phys.Lett.* 316 (2000) 199-204.
10 T.D.Burchell, *Carbon Materials for Advanced Technologies*, PERGAMON, 1999.
11 Bineta Keita and Louis Nadjo, V.A Davydov et.al., *New J.Chem.* 19 (1995) 769-772.

Mat. Res. Soc. Symp. Proc. Vol. 740 © 2003 Materials Research Society

Modeling Self-Assembly of Nanoparticle Structures: Simulation of Nanoparticle Chemical Potentials in Polymer-Nanoparticle Mixtures

Krishna T. Marla and James C. Meredith
School of Chemical Engineering, Georgia Institute of Technology
Atlanta, GA 30332-0100, U.S.A.

ABSTRACT

The expanded ensemble Monte Carlo (EEMC) simulation method has been applied to calculation of the chemical potential of nanocolloidal particles in the presence of polymeric surface modifiers. Two general classes of surface modifiers have been studied – nonadsorbing and freely-adsorbing. For both systems, the infinite dilution colloid chemical potential was calculated as a function of the colloid diameter and the modifier chain length. The colloid chemical potential was found to decrease with increasing modifier chain length for both types of modifiers, albeit for different reasons. Empirical power-law scaling relationships were found to represent the simulation results well. A physical interpretation was proposed for the power law exponents obtained in the case of adsorbing modifiers.

INTRODUCTION

Nanoscale colloidal dispersions play an important role in most synthesis and processing steps for nanoscale structural materials. Applications include catalysts, adsorbents, polymer nanocomposites for high-strength barrier and flame resistant materials, and nanocrystals for photonics and electronics. These nanostructures can be prepared not only via nucleation and arrested growth processes, but also as equilibrium products, allowing thermodynamic control of crystal lattice structure and feature size. Many experimental approaches utilize short-chain organic modifiers to promote nanoparticle stability and to influence the lattice structure and size. Examples of common organically-modified nanocolloids include noble metal nanoparticles stabilized with poly (2-hydroxyl methacrylates) [1], two- and three-dimensional arrays of Pd or CdSe nanocrystals modified with alkanethiols [2, 3], and polymer-silica nanocomposites that mimic natural organic-inorganic materials. [4, 5] Unfortunately, the present knowledge of organically-modified nanoparticle self-assembly is inadequate for precise thermodynamic control of these structures. A breakthrough in rational predictive strategies for nanoscale structural material synthesis would be the development of molecular-models that account for the effect of surfactants on the thermodynamic and transport properties of nanoparticles.

Towards this goal, we have recently developed a novel application of the expanded ensemble Monte Carlo (EEMC) simulation method, which allows accurate calculation of the chemical potentials of organically-modified nanoparticles. Chemical potential (μ) is the free energy of inserting a molecule (collection of molecules in the case of a nanoparticle) into a system of interest relative to a reference state. Knowledge of the modifier chain length, concentration and particle size dependence of μ can be used to predict self-assembly and dispersability (phase behavior) in these systems. The traditional Widom [6] method for calculating μ using computer simulations works well for small molecules and moderate densities, but severe difficulty arises for polymers and other molecular aggregates such as colloids, due to the high probability of steric overlaps. As a result the Widom method samples almost exclusively the high-energy overlap contributions to the chemical potential. EEMC is a powerful approach

that overcomes these sampling limitations in free energy calculations. [7-14]Additional ensemble variables are introduced to define a reversible and efficient path between two desired states of free energy measurement. These states are sampled according to probabilities determined from the partition function. We have adapted this method to polymer-nanocolloid mixtures by inserting nanoparticles into the system incrementally in a series of smaller diameter increments. [15]

In this paper we have applied the EEMC method for calculating nanoparticle chemical potentials in the presence of two broad classes of polymeric modifiers: nonadsorbing and freely adsorbing. We use the hard sphere (HS) potential to model nonadsorbing modifiers and the Lennard-Jones (LJ) 6-12 potential to model freely adsorbing modifiers. In each of these cases we calculate infinite dilution nanoparticle chemical potential as a function of both modifier chain length (n) and particle diameter (σ_c) and discuss the physical interpretation of these dependencies. Finally, we present empirically-derived scaling relationships which describe nanoparticle chemical potential as a power law function of n and σ_c.

THEORY

To adapt the EEMC approach to nanoparticle-polymer mixtures, the particle diameter (the "expansion variable") is allowed to vary between zero (fully removed) and full size via increments and decrements. These increments or decrements are accepted according to a Metropolis type acceptance criterion. A predefined number of intermediate diameters of the particle are allowed by prescribing them as the different "states" of the EE. Incremental chemical potentials, calculated at each diameter describe the free energy of increasing diameter from d_i to d_{i+1}. The full chemical potential is recovered by summing the incremental values from zero to the desired particle size. The statistical mechanical details of this method have been presented in a recent publication. [15]

SIMULATION DETAILS

The simulations were performed in a cubic box with periodic boundary conditions. In all cases our system consisted of a single colloidal particle dispersed in a dilute polymer solution. Polymer chains are fully flexible and consist of tangent segments with a constant bond length of σ_p (bead spring model). The polymer segment density ρ_p is maintained constant for all the simulations at $\rho_p = 0.05$, which corresponds to a packing fraction of $\Phi = 0.026$. The chain length of the polymer was varied from $n = 2$ to a maximum of $n = 60$. The effect of colloid size on the chemical potential was also studied by varying σ_c from $1\sigma_p$ to $15\sigma_p$. In all of the simulations, the box length L (typically $40\sigma_p$) was greater than $n/2$ and σ_c, to prevent artificial intrachain or intraparticle interactions.

RESULTS

Nonadsorbing modifiers (HS potential)

The HS potential, used here to model nanoparticles in the presence of nonadsorbing modifiers in a good solvent, gives purely the entropic or configurational contribution to the chemical potential. The HS model system provides a stringent test of EEMC chemical potential

calculation since the configurational contribution is the most difficult part of the calculation. In addition it has been shown that self-assembly can be driven by entropic depletion forces in the presence of nonadsorbing polymer. [16, 17] Figure 1 shows the infinite dilution chemical potential, $\beta\mu_c^{ex}$ versus the colloid diameter σ_c for polymer chain lengths of $5 < n < 60$. In general $\beta\mu_c^{ex}$ increases as a cubic polynomial in σ_c for all chain lengths, reflecting the increase in the probability of overlaps and excluded volume. Figure 1 compares the simulation results with the predictions of the PRISM-based colloid-polymer model of Fuchs and Schweizer (FS model). [18, 19] The FS model compares very well with the simulations except that at chain lengths above 30 the FS model slightly overpredicts the chemical potential, and at chain lengths less than 30, the predictions are slightly lower than the simulated results. Minor quantitative deviations are due to the assumed Gaussian intramolecular polymer structure factor in the model. Results from a field-theoretic (FT) model are also shown for comparison.[20]

Figure 2 shows the effect of the polymer chain length on the infinite dilution chemical potential, $\beta\mu_c^{ex}$, for different colloid diameters σ_c. The chemical potential decreases with chain length for all particle sizes. For a constant polymer segment density, longer chain length (i.e., lesser number of chains) results in less excluded volume for the particle due to chain connectivity constraints on the location of polymer segments. This explains the decrease of chemical potential with chain length. From Figure 2 we observe that for all particle sizes, there is a sharp decrease in colloid chemical potential from $n = 2$ to $n = 20$. In this regime inserting the colloid particle requires the free energy of creating additional volume by doing work against the polymer fluid osmotic pressure. However for larger chain lengths only an internal section of the polymer chain needs to be rearranged as the colloid particle sees only a part of the chain. Hence we see that for $n > 20$ the change in chemical potential is comparatively small. This is an interesting result since it tells us that firstly, even in the absence of attraction, a large reduction in

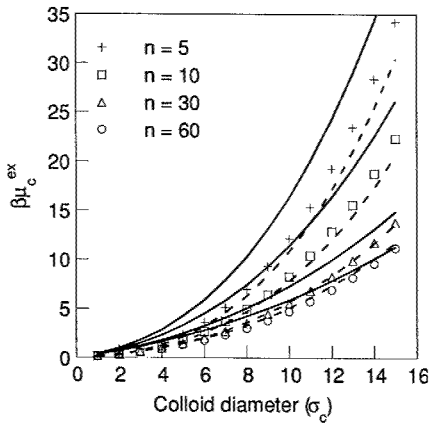


Figure 1. Infinite dilution HS colloid chemical potential vs. colloid diameter in a dilute HS polymer solution at different polymer chain lengths (n). Dotted line: FS model. Solid line: FT model.

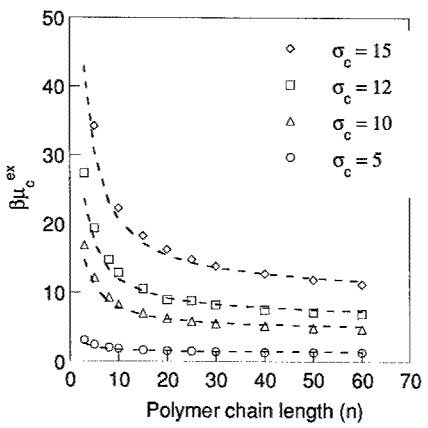


Figure 2 Infinite dilution HS colloid chemical potential vs. polymer chain length in a dilute HS polymer solution for different colloid diameters. The dotted lines are predictions from the FS model.

the colloid chemical potential can be brought about by adding short chain polymers (modifiers) and secondly, increasing polymer chain length beyond a particular value yields little additional reduction in chemical potential. In addition, the chemical potential reduction effect from adding polymer chains increases as particle size increases.

Freely adsorbing modifiers (LJ 6-12 potential)

The LJ 6-12 potential, used to model freely adsorbing homopolymer modifiers incorporates attraction and chain adsorption effects. The LJ model captures the essential physical features of many organic molecules and remains sufficiently general to be of broad, predictive value. All the simulations were performed at a reduced temperature of $T^* = 3.0$ ($T^* = Tk_B/\varepsilon$) and LJ energy parameters $\varepsilon_{cc} = \varepsilon_{pp} = \varepsilon_{cp} = 1$, where ε_{cc}, ε_{pp} and ε_{cp} are the colloid, polymer and colloid-polymer LJ interaction parameters respectively. Figure 3 shows a plot of infinite dilution chemical potential, $\beta\mu_c^{ex}$ versus the colloid diameter σ_c for polymer chain lengths of $5 < n < 30$. For all chain lengths, $\beta\mu_c^{ex}$ decreases with σ_c and shows a cubic dependence on σ_c. The chemical potential decreases with σ_c because the LJ attractive energy increases linearly with σ_c and this results in stronger attractive (negative) interactions between the particle and the polymeric modifiers and thereby, a lower chemical potential. These results demonstrate that in the case of strongly adsorbing modifiers, attractive energetics dominate the repulsive and excluded volume interactions that are predominant in nonadsorbing modifier systems.

The effect of chain length of adsorbing modifiers on particle chemical potential is shown in Figure 4. As in the case of nonadsorbing modifiers, here too we observe that for all particle diameters, $\beta\mu_c^{ex}$ decreases with increasing chain length. However, more than the decrease in excluded volume due to chain connectivity constraints, it is chain adsorption on the particle surface that leads to lowering of particle chemical potential in this case. As we increase the chain length, the entropy loss associated with chain adsorption decreases and hence more chain segments get adsorbed onto the particle surface. This results in the particle getting a larger number of attractive negative interactions and thus, a lower chemical potential.

Scaling relationships

The chemical-physics of nanocolloid-polymer mixtures can be described by simplified scaling relationships which capture the dependence of thermodynamic properties on physical molecular parameters. These relationships reflect the physics that is observed in the simulations and could be used to compare, interpolate of extrapolate experimental data. With this motivation we performed power law regression of the chemical potential data for the two classes of modifiers using σ_c and n as the functional molecular parameters and arrived at the following relationships:

Nonadsorbing modifiers $\quad \beta\mu_c^{ex} = 0.13\sigma_c^{2.34}n^{-0.48}$

Freely adsorbing modifiers $\quad \beta\mu_c^{ex} = -0.012\sigma_c^{3.07}n^{0.44}$

For nonadsorbing modifiers modeled with the HS potential it has been shown that the chemical potential shows a cubic polynomial dependence on σ_c/R_g where R_g is the radius of gyration of the polymer. [15, 18, 19] Hence the empirical power law scaling exponents shown above have little physical significance and are a mathematical consequence of reducing a cubic

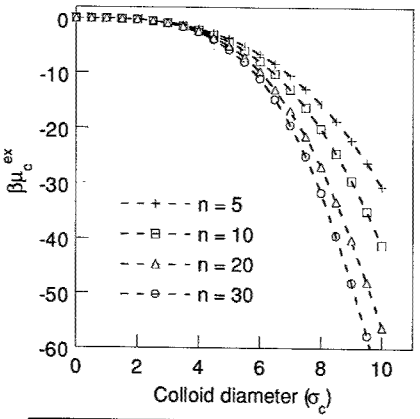


Figure 3 Infinite dilution LJ colloid chemical potential vs. colloid diameter in a dilute LJ polymer solution at different polymer chain lengths. The line is a guide to the eye.

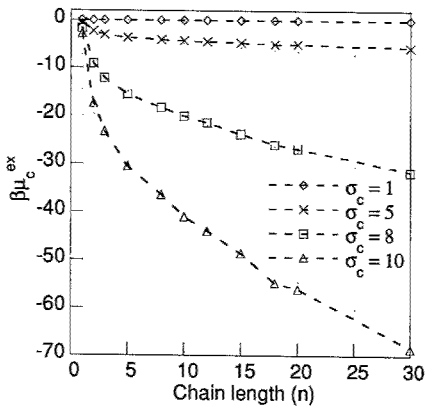


Figure 4 Infinite dilution LJ colloid chemical potential vs. polymer chain length in a dilute LJ polymer solution for different colloid diameters. The line is a guide to the eye.

polynomial to a power law function of the independent molecular parameters. However, for the freely adsorbing modifiers, we believe that a physical import can be attributed to the exponents in the scaling relationship. The cubic dependence on σ_c is essentially a product of a linear term (σ_c) and a square term (σ_c^2). The linear dependence represents *unit particle-polymer interaction energy* since the LJ attractive energy varies linearly with the particle diameter. The square term is a surface area effect which is indicative of the number of chains that adsorb on the particle i.e., the *number of particle-polymer interactions*. The chain length exponent arises out chain adsorption and represents the thickness of the adsorbed layer. For chains that are anchored on a surface in a theta solvent, the mean field theory predicts that the thickness of the adsorbed layer scales with $n^{0.5}$. [21] In the case of freely adsorbing modifiers, the chains would tend to swell a little more compared to tethered chains and hence one would expect that the exponent would be slightly lower than 0.5. In addition, since the adsorbed chains are closely packed near the particle surface, the attractive and repulsive interactions between the chain segments would be relatively balanced, thereby simulating close to theta solvent conditions.

CONCLUSIONS

The EEMC method was adapted and applied to calculate the infinite dilution nanoparticle chemical potential in the presence of organic surface modifiers as a function of particle diameter and modifier chain length. Two broad classes of organic modifiers were explored: nonadsorbing modifiers and freely-adsorbing modifiers. For both cases it was shown that the addition of short chain organic modifiers ($n < 20$) brings about a substantial reduction in the chemical potential, compared to pure monomer solvent at the same volume fraction. The dependence of particle chemical potential on polymer chain length and particle diameter was found to be represented well by empirical power law scaling relationships of the form $\beta\mu_c^{ex} \alpha \sigma_c^a n^b$ for both types of

modifiers. For nonadsorbing modifiers the σ_c and n dependencies arise purely out of excluded volume and entropic contributions. However for adsorbing modifiers, the LJ attraction energy, surface area and chain adsorption are responsible for the dependence of $\beta\mu_c^{ex}$ on σ_c and n. These scaling relationships, though empirical, could be used to guide experiments and efforts towards theoretical development of chemically specific equations of state for these complex nanoparticle-polymer mixtures.

ACKNOWLEDGEMENTS

We gratefully acknowledge partial support of this project by the Georgia Institute of Technology Molecular Design Institute, under ONR contract N00014-95-1-1116.

REFERENCES

1. A. B. R. Mayer, J. E. Mark, *Polymer* **41**, 1627-1631 (2000).
2. P. J. Thomas, G. U. Kulkarni, C. N. R. Rao, *J. Phys. Chem. B.* **104**, 8138-8144 (2000).
3. C. B. Murray, C. R. Kagan, M. G. Bawendi, *Science* **270**, 1335-1338 (1995).
4. Y. Lu, Y. Tang, A. Sellinger, M. Lu, J. Huang, H. Fan, R. Haddad, G. Lopez, A. Burns, D. Y. Sasaki, J. Shelnutt, C. J. Brinker, *Nature* **410** (2001).
5. A. Sellinger, P. M. Weiss, A. Nguyen, Y. Lu, R. A. Assink, W. Gong, C. J. Brinker, *Nature* **394**, 256-260 (1998).
6. B. Widom, *J. Chem. Phys* **39**, 2808-2812 (1963).
7. A. P. Lyubartsev, A. A. Martsinovski, S. V. Shevkunov, P. N. Vorontsov-Velyaminov, *J. Chem. Phys* **96**, 1776-1783 (1992).
8. N. B. Wilding, M. Muller, *J. Chem. Phys* **101**, 4324 (1994).
9. F. Escobedo, J. J. de Pablo, *J. Chem. Phys.* **103**, 2703-2710 (1995).
10. J. J. de Pablo, M. Laso, U. W. Suter, *J. Chem. Phys.* **96**, 2395-2403 (1992).
11. K. S. Kumar, I. Szleifer, A. Z. Panagiotopoulos, *Phys. Rev. Lett.* **66**, 2935-2938 (1991).
12. J. I. Siepmann, *Mol. Phys.* **70**, 1145-1158 (1990).
13. G. C. A. M. Mooij, D. Frenkel, *Mol. Phys.* **74**, 41-47 (1991).
14. F. Escobedo, J. J. de Pablo, *Mol. Phys.* **89**, 1733-1754 (1996).
15. K. T. Marla, J. C. Meredith, *J. Chem. Phys* **117**, 5443-5451 (2002).
16. E. J. Meijer, D. Frenkel, *J. Chem. Phys* **100**, 6873 (1994).
17. E. J. Meijer, D. Frenkel, *Physica A* **213**, 130-137 (1995).
18. M. Fuchs, K. S. Schweizer, *J. Phys.: Condens. Matter* **14**, R239-R269 (2002).
19. M. Fuchs, K. S. Schweizer, *Phys. Rev. E* **64**, 021514 (2001).
20. E. Eisenriegler, A. Hanke, S. Dietrich, *Phys. Rev. E* **54**, 1134 - 1152 (1996).
21. *Handbook of Surface and Colloid Chemistry*. K. S. Birdi, Ed. (CRC Press, ed. 1st., 1997). pp. 373

Mat. Res. Soc. Symp. Proc. Vol. 740 © 2003 Materials Research Society I7.7

Densification and Sintering of a Microwave-Plasma-Synthesized Iron Nanopowder

L. J. Kecskes, R. H. Woodman, and B. R. Klotz
U.S. Army Research Laboratory, Weapons and Materials Research Directorate
Aberdeen Proving Ground, MD 21005-5069, USA

ABSTRACT

Powder compacts made from microwave-plasma-synthesized iron (Fe) nanopowder (Materials Modification Inc., Fairfax, VA) were sintered under hydrogen (H_2). Results showed that without the application of pressure, the powder could not be sintered to full density. In subsequent experiments, the powder was consolidated to final densities near 80% of the theoretical full density, using plasma pressure compaction (P^2C). To provide an explanation for the difficulty in attaining full densification, the precursor powder and compacted pellet characteristics were examined by several methods. These included residual porosity by mercury pycnometry, surface area measurement by Brunauer, Emmett, and Teller (BET) analysis, and structural change by x-ray diffraction (XRD) and scanning electron microscopy (SEM). It was observed that the nanosized primary particles were aggregated into micrometer-sized dendritic structures, with the appearance of tumbleweeds. The observed limitations in the densification and associated porous microstructures of the pressureless-sintered and P^2C-densified compacts were rationalized in terms of the behavior of the dendritic aggregate structures rather than that of the nanosized primary particles.

INTRODUCTION

A widely accepted method for preparation of full-density nanograined material entails comminution of micrometer-sized powder to nanoscale by high-energy ball milling followed by sinter forging [1]. However, the fabrication of large, fully dense nanostructured metal bodies remains an unrealized goal. A promising alternative to comminution is the direct synthesis of the nanopowder by microwave plasma synthesis (MPS). Iron (Fe) bodies of 95% theoretical density (TD) have been reported by moderate-pressure consolidation of precursor powder by plasma pressure compaction (P^2C) at 850 °C [2]. The mean particle size of the precursor was measured to be ~500 nm, the grain size of the final part was on the order of 10 μm. The primary advantage of P^2C, also known as plasma activated sintering (PAS), is the ability to apply large DC or AC currents through a powder sample, causing the formation of a plasma arc, whereby the interior temperatures rise rapidly. The plasma causes the evolution of impurities, and a simultaneous application of moderate pressure densifies the sample material. Detailed descriptions of PAS can be found in several references [3,4].

A representative lot of MPS Fe nanopowder was obtained from Materials Modification Inc., Fairfax, VA. Fe nanopowder green compacts were pressureless sintered in a hydrogen (H_2) atmosphere with the objective of relating the precursor characteristics and properties to its sintering behavior. Results showed that without pressure, there was difficulty in attaining full density samples. Subsequently, several attempts were made to further densify the Fe using P^2C.

The nanoprecursor was examined by nitrogen sorption, x-ray diffraction analysis (XRD), and field emission scanning electron microscopy (FESEM). Density of the sintered compacts was determined by mercury pycnometry, and the microstructure was examined by scanning electron microscopy (SEM). The pressureless sintering and P^2C results, in context of the precursor characteristics and with implications for the production of bulk samples, are discussed.

EXPERIMENTAL PROCEDURE

The bulk tap density was determined by weighing the as-received Fe powder and dividing by the filled container volume. FESEM was performed on a Hitachi S4700 F-SEM (Nissei Sangyo America, Gaithersburg, MD). Nitrogen gas adsorption analysis was performed on a Micromeritics ASAP 2010 Accelerated Surface Area and Porosimetry System (Micromeritics, Norcross, GA). Two samples, outgassed at 200 °C under vacuum, were subjected to six-point Brunauer, Emmet, and Teller (BET) surface area analysis. Another full adsorption isotherm was collected as well. A Philips APD1700 Automated Powder Diffractometer System (Philips Analytical, Natick, MA) was used for the line broadening XRD analysis, scanning the most intense Fe peaks; the net peak height under each peak was at least 10,000 counts. The instrumental broadening was determined by scanning characteristic peaks of LaB_6 near the Fe peaks. After subtracting the instrumental broadening contribution, Scherrer's equation [5] was used to determine the particle size.

Several 1-g green compacts were pressed uniaxially at 55 MPa. Density was determined based on measurements of the compact thickness and diameter. Pressureless sintering was performed at 300, 500, 700, or 900 °C for 30 min under a 10 l/min flow of dry H_2. The sintered pellets were halved. One half was used to determine pellet density using mercury pycnometry in a Micromeritics Autopore IV Model 9510 Mercury Porosimeter Analyzer (Micromeritics, Norcross, GA). The other half was mounted and polished for SEM examination; the polished surfaces were etched with 2% Nital to reveal the microstructure.

Similarly sized green compacts were loaded in a 1.27-cm inner diameter graphite die assembly. A two-color optical pyrometer was focused on the center of the die to measure the external temperature as the power level through the sample was raised. In each P^2C run, DC current was ramped at 100 A/min such that the target temperature was reached in a few minutes. At the same time, a 127-MPa constant pressure was applied to the samples. Higher pressures caused the dies to crack or shatter. When a predetermined time elapsed at the selected temperature, the current was ramped down to 0 A, and the pressure was released. After cooling, the P^2C samples were extracted and analyzed in the same manner as those obtained from pressureless sintering.

RESULTS AND DISCUSSION

Powder Characteristics

FESEM images, depicted in Figure 1, show a particle size of 50-80 nm. There are no isolated Fe particles; instead, grains appear to be fused to each other, forming chainlike tentacles, with an average size of 0.3-1 μm. Note that the particle-particle necks are a strong evidence of sintering

during MPS. BET plots were linear, with a BET c constant of 42, implying that the powders were free of fine pores and that an effective diameter may be calculated from a hard-sphere model. Using the BET surface area of 13,866 or 15,079 m^2kg^{-1}, a hard-sphere model, and a 7,870 kgm^{-3} density for Fe, the equivalent diameter range was found to be 50 or 56 nm. This is consistent with the FESEM results. XRD line-broadening analysis of each of the four Fe peaks yielded a smaller average crystallite size of about 20 ± 3 nm.

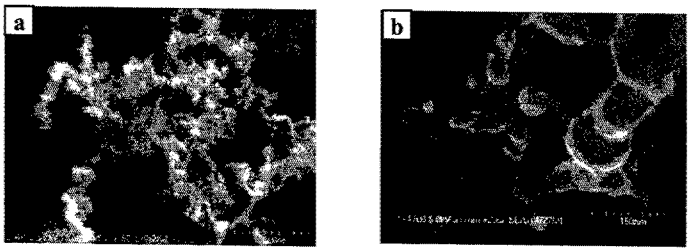


Figure 1. FESEM micrographs of the Fe powder are shown with the aggregate structure in (a) and the individual particles in (b).

Pressureless Sintering Results

The bulk density of the powder was 0.13 gcm^{-3}, or 1.6 %TD of Fe. The powder proved to be pyrophoric, sometimes combusting during die filling or compaction. Green density of the compacts was approximately 40 %TD. Regardless of sintering temperature, the consolidated pellets delaminated, though the macroscopic appearance improved with increasing temperatures. At the lower two temperatures, the pellets were black and rough. At the higher two temperatures, the pellets had only one or two lateral delaminations, but were blistered with a silvery exterior surface. Interior surfaces were also shiny.

As shown in Figure 2, there is little or no coarsening of the individual Fe particles at 300 °C. The dendritic aggregate structure of the Fe clusters is still present. In some isolated areas, necking and the onset of coarsening were observed. At 500 °C, further coarsening and banding takes place. Once 700 °C is exceeded, any remaining evidence of the initial dendritic structure and morphology is lost. Submicrometer voids, or closed pores, remain at the triple points between the 3-4-μm-sized grains. Finally, heterogeneous grain growth at 900 °C of the recrystallized Fe grains dominates the microstructure. (There are a few polishing scratches in some of the soft grains.) Submicrometer voids also coalesce into 5-10-μm void agglomerates or void bands. Summarized in Table I, the effect of temperature is limited on the density; full- or near-full density could not be achieved. Note the extreme grain growth with temperature. Despite a lack of densification, as shown in the table, the grain size of the consolidated Fe pellets dramatically increases with temperature. Assuming an Arrhenius behavior for atom diffusion and associated grain growth, a least squares fit to the data yields an activation energy of 62 ± 6 kJ/mol, which is only one-fourth of that for the self-diffusion of Fe [6].

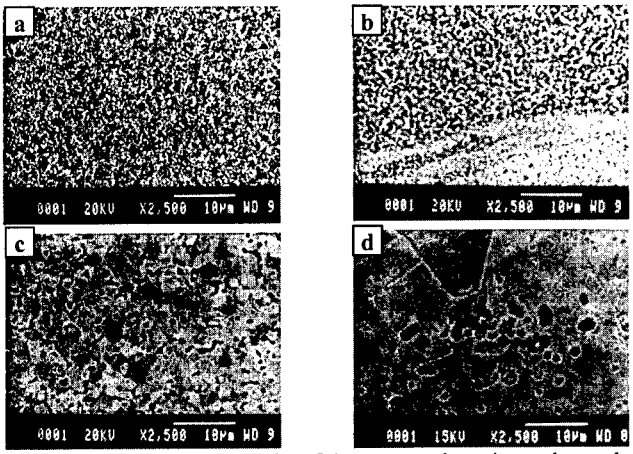


Figure 2. Backscattered electron micrographs of the pressureless sintered samples are shown with 300 °C in (a), 500 °C in (b), 700 °C in (c), and 900 °C in (d).

Table I. Pressureless Sintering Results

Temperature (°C)	Density (gcm^{-3})	Density (%TD)	Average Grain Size (μm)
300	3.52	44.7	0.05
500	4.52	57.4	1.
700	5.87	74.6	5.
900	5.87	74.6	50.

P^2C Results

Unlike the pressureless sintered samples, the P^2C samples were not delaminated. Results of the experiments are listed in Table II. As apparent, the variations of time or temperature have a relatively minor effect on the overall density of the samples. Under moderate pressure, the initially isotropic agglomerates form highly oriented (transverse to the compaction axis), filamentary structures of alternating dense and porous strata (see Figure 3). At 600 °C, the interior of these filaments consists of dendritic aggregates that sintered into a coarsened, yet porous spongy structure. Note the formation of anomalously more dense regions. A comparison of the two samples at 600 °C shows that at low temperatures, the effect of time is negligible on the microstructure. At higher temperatures, especially at 800 and 1000 °C, these filamentary layers grow denser. The interior of these bands consists of 2-3-μm grains, interspersed with isolated submicrometer-sized porosity. Particles in less dense regions coarsen as well, resulting in a random distribution of isolated fine, nanosized droplets.

It has been postulated that increased interfacial and surface-free energies in nanosized particles would enhance diffusion and thereby facilitate sintering at lower temperatures [7]. The well

bonded particles within the dendritic arms seem to support this argument. However, no enhanced low-temperature, solid-state sintering or concomitant densification occurs during pressureless sintering. Gain in density is seen only above the secondary recrystallization temperature of Fe (450 °C). Additionally, the observed coarsening and densification behavior are consistent with a thermally activated process and follow the behavior of larger, conventionally sized powders [8]. The use of the P^2C provides a little gain in densification, but with an added extrinsic, current-induced structural asymmetry that is imparted to the sintered body.

Table II. P^2C Results

Temperature (°C)	Time (min)	Density (gcm^{-3})	Density (%TD)
600	1	6.20	78.8
600	15	6.25	79.4
800	5	5.90	75.0
1000	1	6.06	77.0

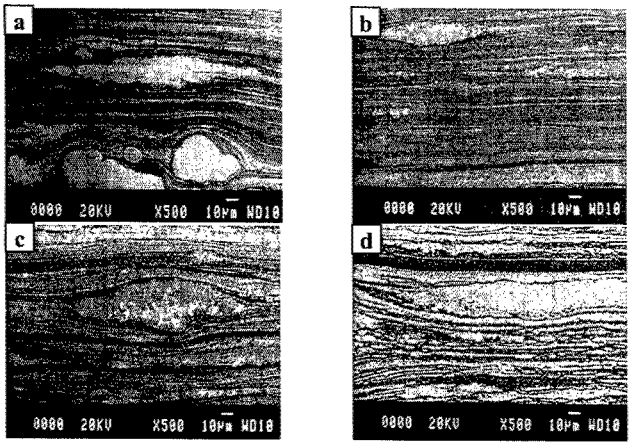


Figure 3. SEM images of the P^2C samples are shown with 600 °C, 1 min in (a), 600 °C, 15 min in (b), 800 °C, 5 min in (c), and 1000 °C, 1 min in (d).

The sintering properties of this MPS powder vis-á-vis a conventional powder can be understood in terms of the dendritic structures shown in Figure 1. Both pressureless sintered and P^2C samples' structural heterogeneity (i.e., banding) is a result of the dendritic agglomerates. That is, although initially enhanced sintering takes place between adjacent particles, the open structure of extended dendritic arms prevents any further possible coalescence and collapse of the partly necked and coarsened structure. It is suspected that because of shorter cycling times, there is less grain growth during P^2C, however, the pressure brought to bear on the green body as to break up the agglomerates is insufficient to fully densify the P^2C samples.

CONCLUSIONS

A MPS Fe nanopowder, consisting of 0.3-1 μm dendritic agglomerates of 50-60 nm spheroidal particles, was sintered using P^2C. The pressureless sintering behavior of this powder indicated that the dendritic structure of the nanopowder hindered solid-state sintering into a fully dense body. No enhanced sintering below the recrystallization temperature was observed. The initial size and morphology of the Fe, however, were completely lost at 500 °C. Using P^2C (high DC current and low pressure), the structure was stratified with suppressed grain growth, but without an increase in density. The implications were twofold: on one hand, if the nanostructure was to be retained, sintering had to be conducted below this temperature. On the other hand, direct sintering of nanopowders to dense bodies required more careful control of the MPS process to avoid formation of low-density agglomerates. While it may be possible to introduce further processing steps, for now, conventional pressing and pressureless sintering of such agglomerates to full-density bodies is extremely difficult.

ACKNOWLEDGMENTS

We note the assistance of Ms. Sara White at Nissei Sangyo America with the use of the FESEM and Mr. George Dewing in the operation of the P^2C. BRK was supported, in part, by an appointment to the research participation program at the U.S. Army Research Laboratory (USARL) administered by the Oak Ridge Institute for Science and Education through an interagency agreement between the U.S. Department of Energy and USARL.

REFERENCES

1. He, L., Allard, L.F., Breder, K., and Ma, E., "Nanophase Fe Alloys Consolidated to Full Density from Mechanically Milled Powders," *J. Mater. Res.* **15** [4], 904-912 (2000).
2. Kalyanaraman, R., Yoo, S., Krupashnkara, M.S., Sudarshan, T.S., and Dowding, R.J., "Synthesis and Consolidation of Iron Nanopowders," *Nanostructured Materials* **10** [8], 1379-1392 (1998).
3. Groza, J.R., "Filed-Activated Sintering," *ASM Handbook; Powder Metallurgy*, Vol.7, ASM, Materials Park, OH, 583-589 (1998).
4. Jones, G., Groza, J.R., Yamazaki, K., and Shoda, K., "Plasma Activated Sintering (PAS) of Tungsten Powders," *Mater. Manuf. Proc.* **9** [6], 1105-1114 (1994).
5. Cullity, B.D., *Elements of X-Ray Diffraction*, Addison Wesley, Reading, MA, 284 (1978).
6. Askeland, D.R., *The Science and Engineering of Materials*, PWS-Kent Publishing Company, Boston, MA, 123 (1989).
7. Groza, J.R., and Dowding, R.J., "Nanoparticulate Materials Densification," *Nanostr. Mater.* **7** [7], 749-768 (1996).
8. Goetzel, C.G., *Treatise on Powder Metallurgy*, Vol. 1, Interscience Publishers, Inc., New York, NY, 515 (1949).

Mat. Res. Soc. Symp. Proc. Vol. 740 © 2003 Materials Research Society

A Semiconductor Nano-Patterning Approach Using AFM-Scratching Through Oxide Thin Layers

L. Santinacci[1],[a] T. Djenizian and P. Schmuki
University of Erlangen-Nuremberg
Department of Materials Science - LKO
Martensstrasse 7, D-91058 Erlangen, Germany

ABSTRACT

AFM-scratching was performed through thin oxide layer which was either a native oxide layer (1.5 – 2 nm thick) or a thermal oxide layer (10 nm thick). Due to their insulating properties, the SiO_2 films act as masks for the metal electrochemical deposition. In the scratched openings copper deposition can take place selectively and thus nano-scale metal lines could be successfully plated onto the p-type silicon substrates. Using particularly, if sufficiently thick thermal oxide has advantages over the native oxide, it allows a H-termination of the Si within the grooves (HF treatment) without eliminating the oxide layer on the rest of the surface.

INTRODUCTION

Since the recent incorporation of electrodeposited copper into electronic devices, a renewal of interest for electrodeposition and related technologies have found new applications in electronics manufacturing, especially for packaging and magnetic recording [1]. Usually photolithography is used in industrial processes to pattern surfaces in the micrometer range. However miniaturization and the promising properties of nano-scaled materials ("quantum confinement") have stimulated research groups to explore alternative patterning techniques. Most of these structuring methods are based on lithography requesting therefore a masking process. Based on this principle high resolution patterning can be performed using electron-beam, x-rays, or scanning probe microscopies to sensitized the resist layer (see e.g., Ref. [2-4]). The other approaches consist of direct selective reactions at the semiconductor surfaces. Different techniques are proposed such as pre-sensitization of the surface by focused ion beam followed by selective electrochemical deposition or dissolution at the implanted locations [5,6]. Another example is the use of an electrochemical-scanning tunneling microscope (EC-STM) to deposit nanometer scaled metallic clusters onto metal and semiconductor surfaces [7]. Under the scanning of the optical tip of a scanning near-field optical microscope (SNOM), it is also possible to use the light to generate and control the local photocurrent that triggers the electrochemical reactions at the scanned locations with a high lateral resolution [8]. Other techniques are reported in literature and a review of these techniques is proposed in Ref. [9]. In a previous paper, an atomic force microscope (AFM) was used to created nano-scratches onto silicon surface covered by the native oxide layer. Due to the masking properties of this oxide film, it was possible to selectively deposit copper within the grooves with a sub-micrometer

[1] On leave from: Swiss Federal Institute of Technology Lausanne (EPFL), Dept. Materials Science, LTP, CH-1015 Lausanne, Switzerland
[a] Present address: University of Provence – CNRS, Dept. Matter Sciences, MADIREL Lab., Centre Saint-Jérome, F-13397 Marseille Cedex 20, France.

lateral resolution [10,11]. The present work investigates the use of this AFM-scratching method through a thin thermal oxide layer to optimize the process.

EXPERIMENTAL

Experiments were carried out on p-Si (100) wafers (1 to 10 Ω·cm) that were thermally oxidized (thickness 10 nm). Samples were degreased by subsequently sonicating in acetone, isopropanol, methanol and rinsed with distilled water. The back contact to the Si electrodes was established by smearing InGa eutectic (99.99%). The electrochemical cell consisted of three-electrodes configuration with Pt gauze as counter electrode and a Haber-Luggin capillary with a Ag/AgCl electrode as reference electrode. The electrochemical deposition was performed in 0.01 M CuSO4 + 0.05 M H_2SO_4 using a Jaissle 1002 T-NC potentiostat. The electrochemical cell was placed in a black box in order to avoid non-controlled photo-electrochemical effects. AFM scratching and imaging were carried out using a PicoSPM microscope from Molecular Imaging driven by a Nanoscope E controller from Digital Instruments. The device was equipped with a three-sided pyramidal single-crystalline diamond tip provided by Digital Instruments (more details about the procedure can be find in Ref. [10]). Chemical analysis was performed by Auger electron spectroscopy (AES) using a Physical Electronics PHI 670. During these experiments, the probe was scanned, line by line, over the sample in the perpendicular direction of the scratches, monitoring the Si LMM signal at 1621 eV and Cu LMM at 922 eV. X-ray photoelectron spectroscopy (XPS) was used to determine the thickness of the silicon dioxide layer after different etching times in HF 1%. The XPS analyzer was a Physical Electronics PHI 5600 series instrument with a monochromatic Al K_α x-ray source. The Si 2p peaks at 99.5 and 104 eV were monitored during the Ar^+ sputtering. Ellipsometric measurements of the oxide film thickness were performed with a Sentech Instruments SE 800 spectrometric ellipsometer equipped with a Xe lamp. Scanning electron microscope (SEM) images were acquired with a JEOL 6400 equipped with tungsten filament.

RESULTS AND DISCUSSION

Figure 1a shows an AFM image of a series of scratches carried out at a constant normal applied force (50 μN) for various number of cycles (N = 10, 20,30,40, 50, 60) on oxide-covered silicon. The scratches are well defined and little debris is visible because the abraded particles are swept out of the observation window by the tip. The protrusions along the sides of the scratches result of surface deformation induced by the mechanical treatment and indicate the presence of stress. The cross section, presented in Figure 1b, gives information about the scratch geometry. The grooves have a V-shape and as expected the scratch size increases with N : between 14 nm to 38 nm in depth and between 183 nm to 265 nm in width. In a previous work [10], the influence of the load on the scratch morphology has been investigated. From those experiments, obtained on native oxide layer-covered silicon wafers, it is apparent that the scratch sizes increase linearly with the normal applied force. The plastic deformation threshold was estimated to be near 14 μN.

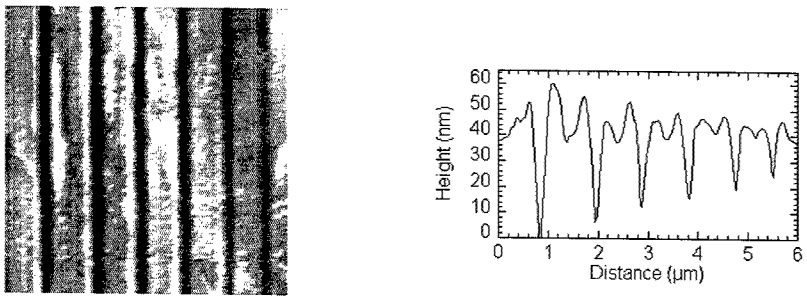


Figure 1: (a) AFM top view of a scratched Si surface (6×6 μm). The 6 AFM-scratches are 20 μm long. Number of cycle varies from left to right: 60, 50, 40, 30, 20, 10. Normal applied force is 50 μN, scan rate is 40 μm/s. (b) Cross section of the top view presented in (a). From Ref. [12].

It was shown before [10] that AFM scratches performed onto p-Si are activated locations for electrochemical deposition. However undesired deposition near the scratches was observed and the sample preparation method was therefore modified. The H-termination of the Si surface by dip in HF 1% was eliminated and thus the native oxide layer present on the Si was not dissolved. In this case, AFM-scratching was carried out through the native oxide layer into the semiconductor substrate. After scratching, the samples were transferred as quickly as possible to the electrochemical cell in order to minimize the regrowth of the oxide layer within the scratches and thus to create two zones on the silicon surface, one "passivated" by the native oxide layer and one "activated" (Si surface within AFM-scratches). Figure 2 shows copper deposit performed at – 500 mV (vs. Ag/AgCl) during 1 s for native oxide layer covered samples. It is clear that highly selective metal deposition is obtained for this type of samples. Copper deposition occurs only at the scratch locations and no copper clusters are observable on the intact surface.

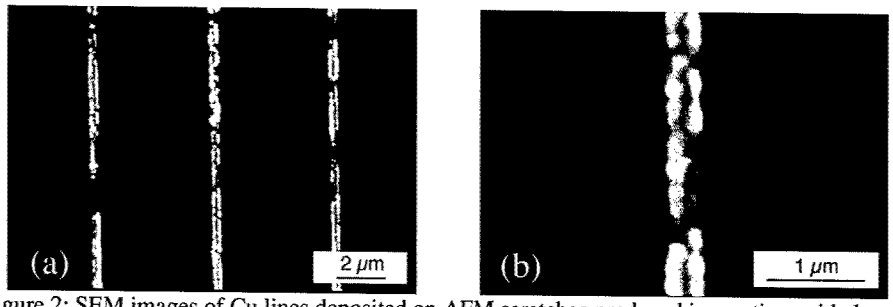


Figure 2: SEM images of Cu lines deposited on AFM scratches produced in a native oxide layer covered p-Si surface. The scratches were made with a force of 15 μN. Deposition was carried out from 0.01 M $CuSO_4$ + 0.05 M H_2SO_4 electrolyte applying a potential step to – 500 mV (vs. Ag/AgCl) during 1 s. (b) Higher magnification of a Cu line presented in (a).

As the deposition time was short (1 s) these images provide information about the initial step of the copper growth. These images show that deposition is initiated on the scratch edges. At

short deposition times, there are two copper lines apparent on one scratch. It was observed that for longer deposition time coalescence of the two lines into a single Cu line occurs. For longer deposition times, copper overgrowth of the insulating native oxide layer can occur. The crystallite morphology suggests that initiation and growth of the 3D metal (Me) phase follows the Volmer-Weber or island growth mechanism. This is in line with the observation of generally weak Me_{ads}-Semiconductor interactions [13].

Native oxide reformation in the scratches appeared to be a possible limiting factor to achieve homogeneous metallic lines especially for short deposition time. Thus an optimization of the process was investigated. A thin oxide layer with a thickness of 10 nm was thermally grown in order to authorize a H-termination of the Si within the grooves by dipping the wafer in HF 1% just after the AFM-scratching step. Note that by this techniques, it was possible to store the scratched sample as the air-formed oxide is surely dissolve just before the electrochemical step. This process is described in Figure 3.

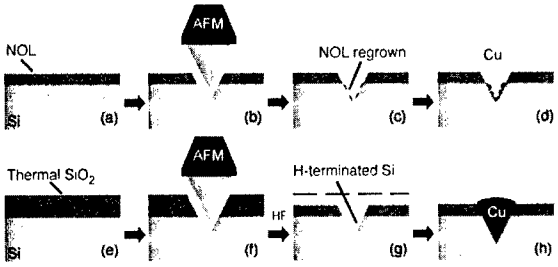


Figure 3: Schematic of the approaches for selective electrochemical deposition of metal within AFM-scratches. First process: (a) Si covered by the native oxide layer (~2 nm), (b) AFM-scratching through the native oxide layer, (c) oxide regrowth within the scratch, (d) selective electrochemical deposition of Me within the scratches hampered by the reform oxide. Second process: (e) Si covered by a dry oxide (10 nm), (f) AFM-scratching through the oxide layer, (g) removal of the native oxide regrown in the scratch and H-passivation, (h) selective electrochemical deposition of Me within the scratch.

The etching rate of the oxide was studied in order to optimize the HF (1%) dip duration. The film thickness measured by XPS and ellipsometry after the immersion of the oxide-covered sample in HF (1%) for different times. An etching time of 30 s was found to be the adequate time. Approximately 4 nm of the thermal oxide layer are removed leaving a 6 nm thick oxide film on the surface while the native oxide layer within the scratches is fully removed, and there, the Si is H-terminated. Additional experiments performed on native oxide covered wafers have confirmed that the dissolution rate of the two types of oxides is similar. Preliminary experiments were carried out on oxide-covered samples scratched with a micro-indentor equipped with a diamond tip for Vickers test. The normal applied load was 49 mN creating scratches of 3 µm in width and 300 nm in depth. Potential step deposition performed at – 500 mV during 10 s are shown in Figure 4.

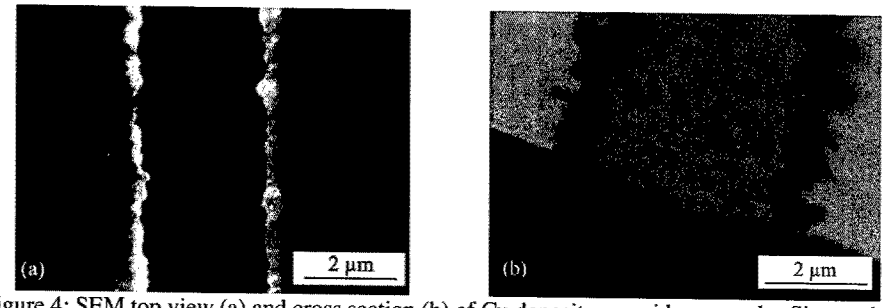


Figure 4: SEM top view (a) and cross section (b) of Cu deposits on oxide covered p-Si scratched with a micro-indentor with a normal applied force of 49 mN. Cathodic potential steps carried out in $CuSO_4$ (0.01 M) + H_2SO_4 (0.05M) at – 500 mV for 10 s.

These SEM pictures confirm the considerable role of the scratch edges during the nucleation phase. On these larger scratches the deposit is exclusively located on each sides of the grooves and only few crystallites are observed within the scratches. It seems that either the Si/SiO_2 interface is an activating location for copper nucleation or the oxide layer is deteriorated by the scratching process in the vicinity of the groove allowing deposition at these sites. In both cases a high defect concentration seemed to activate the metal deposition. At smaller scale (AFM scratching) this effect is less visible due to the earlier coalescence of the metallic lines.

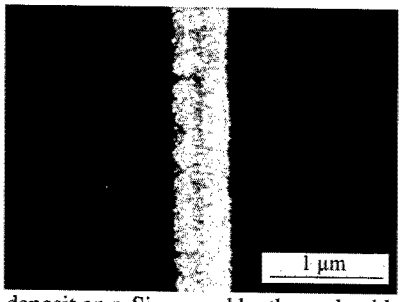


Figure 5: SEM image of Cu deposit on p-Si covered by thermal oxide. Cathodic potential steps carried out in $CuSO_4$ (0.01 M) + H_2SO_4 (0.05M) at – 500 mV for 10 s.

Deposition on thermal oxide covered p-Si is presented in Figure 5. The homogenous Cu line is smaller than in the case of the native oxide covered sample. On the thermal oxide covered silicon it was possible to reach smaller Cu line dimension (480 nm). It can be explained by several factors. In this case, indeed, the Si surface in the scratch is fully H-terminated and therefore the oxide regrowth is prevented and due to the higher thickness of the oxide film, the active size of the groove is smaller than the one for native oxide covered sample. The copper is then more confined in the groove, metal overgrowth is limited and homogeneity is better.

AES mapping for Cu obtained on Cu lines deposited on oxide-covered p-Si has confirmed that the deposition takes place with a very high degree of selectivity. No Cu is detected outside the scratched location. Even when a $\approx 16\ \mu m^2$ square area situated between two copper lines was

analyzed with high integration time, the presence of copper could not be detected. This demonstrates that metal deposition occurs only in the AFM-scratches.

CONCLUSION

The work clearly shows that a thin oxide layers can efficiently be used for masking metal deposition on p-type Si. Scratches produced through this oxide layers using an AFM can be used to open "activated" patterns on the Si surfaces. Onto these patterns metal electrodeposition can be performed selectively, and hence can be used for semiconductor patterning and functionalization by selective electrodeposition in the sub-micrometer range. From the results presented here, it appears clearly that using a thin thermal oxide film as mask, a higher resolution and particularly a better homogeneity can be reached. Copper nucleation is initiated at the groove edges indicating either a high degree of reactivity of the Si/SiO_2 interface or that the oxide layer is deteriorated by the scratching at these locations. This technique should essentially be applicable to any material that can be electrochemically deposited and thus bears the potential to create nano-patterns of a large palette of materials.

ACKNOWLEDGMENTS

The authors would like to acknowledge the financial support of this work by the Swiss National Science Foundation (SNF) and German Research Foundation (DFG). Serge Ecoffey and Haroun Mokdad (EPFL) are acknowledged for their meticulous help.

REFERENCES

1. D. Landolt, *J. Electrochem. Soc.*, **149**, S9 (2002).
2. H. G. Craighead, R. E. Howard, L. D. Jackel, and P. M. Mankiewich, *Appl. Phys. Lett.*, **42**, 38 (1982).
3. C. R. Friedrich, R. Warrington, W. Bacher, W. Bauer, P. J. Coane, J. Göttert, T. Hanemann, J. Hausselt, M. Heckele, R. Knitter, J. Mohr, V. Piotter, H. J. Ritzhaupt-Kleiss, and R. Ruprecht, in *High Aspect Ratio Processing, in Microlithography, Micromachining and Microfabrication, SPIE*, (1997) p. 301.
4. E. A. Dobsiz and C. R. K. Marrian, *Appl. Phys. Lett.*, **58**, 2526 (1991).
5. P. Schmuki, L. E. Erickson and D. J. Lockwood, *Phys. Rev. Lett.*, **80**, 4060 (1998)
6. P. Schmuki and L. E. Erickson, *Phys. Rev. Lett.*, **85**, 2985 (2000).
7. R. Ullmann, T. Will, and D. M. Kolb, *Chem. Phys. Lett.*, **209**, 238 (1993).
8. H. Diesinger, A. Bsiesy) and R. Hérino, *J. Appl. Phys*, **90**, 4862 (2001).
9. P. Schmuki, S. Maupai, T. Djenizian, L. Santinacci, A. Spiegel and U. Schlierf, "Techniques in Electrochemical Nanotechnology" in *Encyclopedia of Nanotechnology*, H. S. Nalwa Ed. (American Scientific Publishers, in press).
10. L. Santinacci, T. Djenizian and P. Schmuki, *J. Electrochem. Soc.*, **148**, C640 (2001).
11. L. Santinacci, T. Djenizian and P. Schmuki, Appl; Phys. Lett., **79**, 1882 (2001).
12. L. Santinacci, T. Djenizian, S. Ecoffey, H. Mokdad, T. Campanella and P. Schmuki, *Electrochim. Acta*, submitted.
13. E. Budevski, G. Staikov, and W. J. Lorenz, *Electrochemical Phase Formation and Growth* (VCH, Weinheim, 1996).

Mat. Res. Soc. Symp. Proc. Vol. 740 © 2003 Materials Research Society I7.9

Nanoindentation Technique at Investigating of Aluminum Oxide - CrC Nanoparticles Composite Coating

Maksim V. Kireitseu
Department of Mechanics and Tribology
Institute of Mechanics and Machine Reliability (INDMASH),
National Academy of Sciences of Belarus
Lesnoe 19 - 62, Minsk 223052, Belarus
E-mail: indmash@rambler.ru

ABSTRACT

In this paper fatigue and fracture of Al-Al_2O_3-CrC nanostructured composite coatings was investigated by nanoindentation technique and in-situ experiments performed by a scanning electron microscope to permit examination of freshly exposed surfaces. Crystallographic and morphological textures were characterized and fracture resistance was measured. CrC layer improves fracture resistance of alumina layer. CrC layer produced by pyrolitic deposition (CVD) may effectively heal pores and defects of alumina layer. It resulted in high load rating of the composite coating. Experiments reveal that in all cases, the detection of an acoustic signal corresponded to the appearance of a circular cracks seen on surface; in a very few cases, examination of surface after detection of a signal revealed presence of two ring cracks. Degree of toughening associated with crack healing is determined by a number of healed defects and an effectiveness of an individual healing.

INTRODUCTION

Aluminum oxide-based nanocomposites are useful as structural elements of micro machines and devices because of its high hardness and load rating, low wear rate, high stiffness-to-weight ratio, and high-temperature stability, but suffer from low fracture resistance. When aluminum oxide layers are formed by micro arc oxidizing, extremely high adhesion (350-400 MPa) to aluminum substrates are achievable [1]. Enhanced hardness has been reported for aluminum oxide matrixes containing alpha and gamma phases of aluminum oxide, both for single-crystal superlattices inspected [2] as well as for polycrystalline nanostructured multilayers studied by Chu et al. [3].

In polycrystalline aluminum oxide matrix, high hardness is explained by the presence of dislocation between the nanostructured interfaces that are resulted from the difference in the shear module of the materials and coherency strains for small periodicity superlattices with significant lattice mismatch between the layers as shown by M. Shinn et al. [2].

Known technology of micro arc oxidizing uses high current densities (up to 40 A/dm^2) when aluminum oxide grows up on aluminum substrate [4]. The current may induce large defects, micro voids and pores in formed aluminum oxide structure [5]; however, aluminum oxide layer consists of two principal phases: alpha and gamma [6]. This may result in its superior mechanical properties. Nevertheless, the structural dismatches do depreciate benefits of oxide aluminum structure while its application as wear protective coating or thermal barier layer.

An objective of the paper was to investigate the possibility to improve physical and mechanical properties of aluminum oxide-based coating by CrC-based nanoparticles produced by a metal organic chemical vapor deposition (CVD). In the present paper, nanoindentation has been used to investigate fracture and fatigue of Al-Al_2O_3-CrC composite coatings. Indentation technique was used as a perfect tool for characterizing the performance and durability of the composite coating.

EXPERIMENTAL PROCEDURE

The combination of an AFM and a nanoindenter (for example, MicroSystems, UK) is a further development of the traditional Vickers microhardness testing device. This instrument allows for two measurement modes. It provides a surface topography of constant contact force in AFM mode and a force displacement curve in nanoindentation mode using the same tip. This feature provides a high spatial resolution to position the tip on the microstructure of interest. The sample is mounted on a scanner that allows for a movement in the plane normal to the axial motion of the tip. The transducer consists of a three-plate capacitor on whose central plate a tetrahedral diamond

Berkovich-tip is mounted. A nanoindentation curve plotted a loading phase where the tip is pressed into the material up to a maximal force, a holding period where the tip creeps into the material and an unloading phase where the force on the material is released. The loading and holding phases result in both plastic and elastic deformation that cannot be distinguished. The unloading phase shows the elastic recovery of the material while the load is released. The contact area Ah is determined by a procedure derived by Oliver et al.[7, 8].

The 5054 aluminum alloy as it's referred in the MIL specifications was substrate on which Al_2O_3 layer was produced by micro arc oxidizing. Al_2O_3 layer has up to 10 % pores on the outside of a sample. Pores diameter ranges between 0.5 and 4.5 μm. The thickness of the alumina layer was 250 μm, its microhardness was between 16 and 18 GPa and its Young's modulus was 290 GPa.

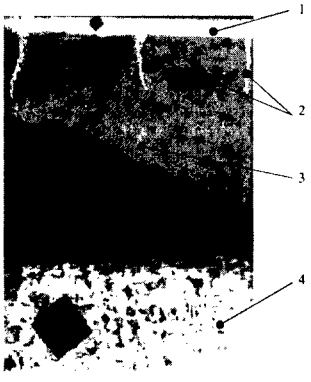


Figure 1. Al-Al_2O_3-CrC nanostructured composite coating

Pyrolysis technology or CVD may deposit CrC nanoparticles on aluminum oxide surfaces. Pyrolitic deposition was performed by a pyrolysis of a metal-organic liquid (Barhos) consisting of Cr-organic compounds under vacuum in pressure range between 4 and 8 Pa. Principal pieces of equipment are a vertical quartz tube reactor, a feeder of a liquid composed of Cr-organic compounds and two cylinder furnaces located inside an internal space of a reactor. Reactor is connected with a vacuum pump through an entrainment separator. Chromium-organic liquid is fed into an upper furnace and evaporates in its inner volume. Vapors of chromium-organic compounds are then delivered to aluminum oxide substrate placed on a special holder inside a lower furnace, where they decompose forming a coating. Temperature of aluminum oxide surface was between 430 and 450°C.

Produced Al-Al_2O_3-CrC composite coating have pores and defects of alumina layer filled by the CrC nanoparticles (see indexes on fig. 1). The nanoparticles form hard CrC layer having low residual strains. Thickness of CrC layer ranges from 10 to 50 μm, its microhardness was 17,5 GPa and its Young's modulus was 300 GPa.

Nanoindentation response of aluminum oxide-CrC nanoparticles multilayed composite coating and homogeneous aluminum oxide coating were determined using a NanoIndentory II instrument. The measurement procedure was as follows: load to maximum, unload to 10% of maximum load, hold for 50 s, load to maximum, hold for 200 s, and completely unload. The maximum load was 10 or 50 mN and a maximum of ten indents sequences were used for each maximum load. The data from the first hold segment ~50 s was used to correct the load-displacement data for thermal drift. The triangular Berkovich diamond indentor tip was calibrated following the procedure described in Ref. [7, 8].

RESULTS & DISCUSSION

The main topics for this section are (1) to explain hardness increase when additional CrC nanoparticles are introduced into the aluminum oxide layer creating aluminum oxide-CrC multilayered composite coating, as compared to few reported hardness enhancement for both a single aluminum oxide layer and may be polycrystalline nanostructured aluminum oxide composite, and (2) to discuss the fracture behavior of aluminum oxide-CrC composite coating. Before discussing these topics, however, I briefly address the phase structure and the residual stress state of the as-deposited CrC nanoparticles. In both cases, superstructure strengthening-hardening is explained based on dislocation glide across nanostructure limited by the shear modulus difference and dislocation glide within individual layers and/or multilayers.

Figure 1 shows that the CrC nanoparticles deposited on Al_2O_3-based layer fill its pores and other structural defects like cracks. CrC nanoparticles and whole CrC layer have high adhesion to aluminum oxide substrate since no exfoliation is visible in the fracture of the coated specimens at applied technological regimes. The composite coating is characterized by a fine-grained globule-like structure. It should be pointed out that one structure may consist of several grains, CrC nanoparticles or subgrains, therefore size of CrC nanoparticle is actually less than width of a pore.

X-ray analysis revealed that CrC top layer consists of generally chromium carbides (Cr_3C_2 and Cr_7C_3). CrC layer heals various surface defects, pores and voids on aluminum oxide surface (see fig. 1), which was deeply determined by studying a coating-substrate interface with an aid of SEM.

Electrochemical studies and SEM investigations revealed that aluminum oxide-CrC composite coating is very dense and virtually defect-free. The healing is resulted by CrC nanoparticles that fill the most defects of aluminum oxide structure. Single oxide aluminum layer was formed; however, the failure is initiated by "opening" defects of aluminum oxide structure. It results in a poor fracture resistance of an aluminum oxide against an initiation and propagation of micro and nanocracks through its defects and pores.

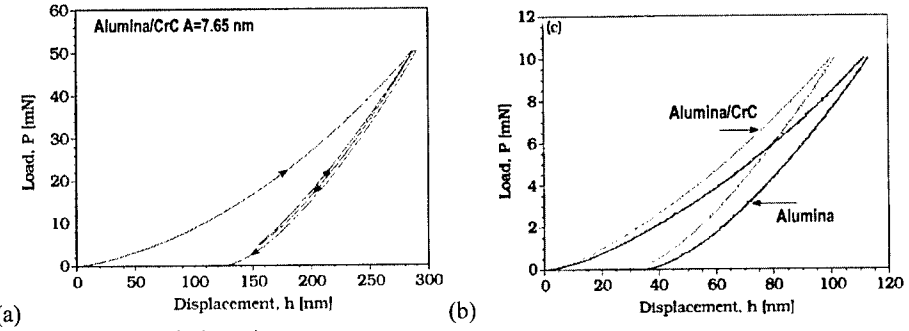


Figure 3. Nanoindentation curves

Figure 3a,b show nanoindentation load-displacement curves from aluminum oxide-CrC multilayed composite coating. A typical curve obtained with 50 mN maximum load is shown for the composite coating at Fig. 3a,b and for a single oxide aluminum structure at Fig. 3b.

The initial loading segment contains an elastic-plastic displacement. The first unloading curve and the second loading curve differ substantially and form a hysteresis loop with a larger displacement rather during unloading than loading. The data from the first hold segment was used for correction of the load-displacement data for thermal drift and the second for investigating creep like dislocation nucleation and glide plastic behavior. Approximately 5-8 nm maximum load creep occurred at the maximum load hold segment in Fig. 3.

Aluminum oxide-CrC-based nanostructured composite coating has the maximum displacement between 270 and 280 nm. It is less then that of single aluminum oxide layer. The first and the second unloading curves from the coatings show actually the same elastic behavior with a small creep. However, the elastic response from the coatings may differ and thus result in the different apparent hardness. Single aluminum oxide layer exhibited the largest percentage of elastic recovery from maximum displacement during the second unloading.

Hardnesses of the aluminum oxide layer was in the range of published nanoindentation hardness data between 16 and 26 GPa, depending on coating microstructure and hardness evaluation procedure. Hardnesses of aluminum oxide-CrC composite coating was in the range of data between 20 and 28 GPa, depending on coating microstructure, thickness of its layers and hardness evaluation procedure.

Higher standard deviations found in previous nanoindentation studies were probably associated with averaging over multiple samples. Despite of this, the results indicated that, in first approximation, the composite coating may be seen as a nanoassembly of CrC nanoparticles and aluminum oxide particles with distinct oxide and carbide phases between them, but rather homogeneous mechanical properties within the same nanostructured elements. This finding has

potentially important implications in the process of fracture propagation that is clearly related to composite coating structure and its heterogeneity.

Major limitation of nanoindentation data analysis remains the hypothesis of isotropy of tested material. In fact, the indentation curve depends to a widely unknown extent on all anisotropic elastic constants of the tested material. Since aluminum oxide-CrC nanostructured composite coating and most probably also single aluminum oxide layer are elastically anisotropic, the reported results are some weighted average of the elastic moduli along the various material orientations.

CONCLUSION

CrC nanoparticles and all CrC coating deposited with the aid of metall-organic CVD on aluminum oxide coating, which is composed of a mixture of Cr and chromium carbides, has good microhardness as high as 20 GPa, fracture resistance and an adhesion to the substrate. CrC layer may have very strong chemical and structural interaction with aluminum oxide substrate when depositing. CrC nanoparticles leads to healing various surface defects and pores of aluminum oxide layer and retardation of the crack initiation and its propagation in the near-surface.

Fracture of Al-Al_2O_3-CrC nanostructured composite coating have been investigated by nanoindentation in-situ experiments. CrC layer may effectively improve the fracture resistance of Al_2O_3 layers by healing defects of aluminum oxide structure such as its pores, internal voids, cracks etc. The degree of toughening associated with crack healing is determined by the number of healing defects and the effectiveness of the individual healing. It may result in enhanced strength, fracture toughness, and microhardness of coated aluminum oxide ceramic specimens.

In general, damage of Al-Al_2O_3-CrC composite coating is suppressed, in contrast to that of single Al-Al_2O_3 coating. Principally, the effect of healing results in high load rating of the Al-Al_2O_3-CrC composite coating, but the contact strains at loading may be higher then that of a single layer. CrC nanoparticles and clusters deflect corresponding to deformation plastic material flow. Deformation may take place in radial spreading of contact zone under indenter with initiation of local cracks.

Nanoindentation technique is powerful approach to investigate fracture mechanics of the coatings. It is expected that nanoindentation modeling for a contact of an indenter and a body would be effectively modified by rheological equations [9, 10]. Therefore, rheological analysis and principal Hertzion equations may be applied together to consider not only elastic and plastic properties of contacted materials, but also viscous properties of a sample and an indenter.

REFERENCES

1. Kireitseu M.V. and Basenuk V.L. *in Proc. of 2001 TMS Fall Meeting: "2nd Int. symposium on modeling the performance of engineering structural materials (MPESM – II)"*, Ed. Dr. Lesurer. – 18-21 October, Akron, OH, USA, 2001. 355 – 364, (2001).
2. M. Shinn, L. Hultman, and S. A. Barnett. *J. Mater. Res.* **7**, 901, (1992).
3. X. Chu, M.S. Wong, W.D. Sproul, S.L. Rhode, and S.A. Barnett. *J. Vac. Sci. Technol.* A **10**, 1604, (1992).

4. K.H. Muller. *Phys. Rev. B* **35**, 7906, (1987).
5. H. Ljungcrantz, L. Hultman, J.-E. Sundgren, and L. Karlsson. *J. Appl. Phys.* **78**, 832, (1995).
6. M.S. Wong, W.D. Sproul, X. Chu, and S.A. Barnett *J. Vac. Sci. Technol.* A **11**, 1528, (1993).
7. W.C. Oliver and G. M. Pharr. *J. Mater. Res.* **7**, 1564, (1992).
8. W.C. Oliver, C. J. McHargue, and S. J. Zinkle. *Thin Solid Films* **153**, 185, (1987).
9. Kireitseu M.. *Journal of Particulate Science & Technology (PS&T)*, vol. **20** (3), 1-15, (2003).
10. Kireitseu M.. *Journal of Engineering Physics and Thermophysics (JEPTER)*, vol. **76** (1), 8-18, (2003).

Mat. Res. Soc. Symp. Proc. Vol. 740 © 2003 Materials Research Society I7.10

MULTILAYERS BY SELF-ASSEMBLY

M. Toprak, D.K. Kim, M. Mikhaylova, M. Muhammed
Dept. of Material Science and Engineering, Royal Institute of Technology, Sweden.

Nanoparticles, as building blocks, are important for the development of advanced, functional composite materials. Recent developments have shown that self-assembly of nanoparticles is a promising technique for the fabrication of complicate nanostructured materials. Self assembly of the nanoparticles into ordered structures on a substrate can be achieved through chemical treatment of the particle and/or substrate surface. The assembled nanoparticles can have a dramatic effect on the physical properties of the composite. A μCP technique has been employed to form a SAM of bifunctional silane (APTMS) in the region of contact. The stamps for the μCP are prepared by polymerization of polydimethysiloxane (PDMS) on a flat surface. Glass substrates have been used for optical absorption measurements. Oxide or metallic particles have been assembled on the patterned surface after a surface treatment. The self-assembled layer was subsequently treated with bifunctional molecules and multilayers of the same material or composites have been thus obtained.

INTRODUCTION

Chemical synthesis of nanostructures and hybrid organic-inorganic materials represent the fastest growing topics of today's chemistry. Being at the interface of traditional disciplines, these areas of science present rich research grounds with potentially strong fundamental and technological impact. The self-assembly of nanoparticles into useful morphologies is a much anticipated development in the nanotechnology as it offers the promise of creating materials from well-characterized, nanometer-scale constituents with interesting properties [1]. Self-assembled mono- and multilayer films on solid substrates have generated considerable interests recently because of the potential for controlling the molecular architecture and chemical and physical properties of layered assemblies on surfaces. Self-assembly (SA) means spontaneous molecular assemblies on a substrate forming an ultrathin molecular film by the treatment of the substrate with a solution of an active organic molecules. The technique provides an ordered thin film fabricating in molecular level. Self-assembled monolayer (SAM)s are stabilized by various interactions in the monolayer. The first part is the head group that provides the most exothermic process, i.e., chemisorption on the substrate surface. As a result of the exothermic head group-substrate interactions, molecules try to occupy every available binding site on the surface, and in this process they push together molecules that have already adsorbed. The second part is the alkyl chain, and the energies associated with its interchain van der Waals interactions are order of few. The third molecular part is the terminal functionality, which governs surface properties and makes it possible to form multilayer films.

Sarathy et al. prepared heterostructures consisting of alternate layers of semiconductor and metal nanoparticles [2]. Colvin et al. have made use of self-assembly of semiconductor nanocrystals to construct an optoelectronic device [3]. Murray et al. have demonstrated the self-organization of CdSe nanocrystallites into a three dimensional superlattice. Multilayers of semiconductor CdS nanoparticles have also been deposited on a glass substrate using the self-assembly of dithiol molecules [4]. There has been some effort to obtain regular arrangements of metal nanoparticles in different dimensions. Two-dimensional arrays of metal nanoparticles are

readily prepared by using alkanethiols. Whetten et al. have described gold nanocrystals stabilized by thiols [5].

This work is a part of the research on the preparation of thin films from nanoparticles and the investigation of their optical, electrical, thermal and mechanical properties. The self assembly is the thin film preparation technique that is employed in this work. Two examples of multilayer is presented: Au/magnetite (Fe_3O_4) and thermoelectric $CoSb_3$ -which can be used for heat-electrical energy interconversion- that are prepared by employing the solution synthesis for the nanoparticles and the self assembly method for the film formation.

EXPERIMENTAL DETAILS

Materials:

Mercaptoptopyl trimethoxy silane (MPTMS), dodecandithiol, ethanol, $HAuCl_4$, $NaBH_4$, $FeCl_2{\cdot}4H_2O$, $FeCl_3{\cdot}6H_2O$, $Co(OH)_2$, $SbCl_3$, HCl, NH_3 and NaOH were obtained from Merck. PDMS Sylgard-184 was obtained from Dow-Corning. Hexane was obtained from Aldrich.

Preparation of Au nanoparticles:

Au nanoparticles are prepared by $NaBH_4$ reduction of $HAuCl_4$ in the presence of trisodiumcitrate as the encapsulating reagent.[6]

Preparation of Fe_3O_4 nanoparticles:

Thermodynamic modelling of the reaction conditions has been performed for the synthesis of ferrite with the required composition.[7] Solutions of Fe^{2+} and Fe^{3+} are prepared and mixed with the Fe^{2+} / Fe^{3+} ratio of 1:2. The modelling results showed that the precipitation of magnetite is possible at a pH above 11. The reaction was performed by the slow addition of a mixture of metal chlorides and NaOH to a continuously mechanically mixed reactor, keeping the pH above 11.

Preparation of $CoSb_3$ nanoparticles:

A solution chemical method was developed [8] for the synthesis of skutterudite, $CoSb_3$, nanoparticles. A thermodynamic modelling of the reaction conditions was performed for the synthesis of a precursor composed of cobalt and antimony oxalates with a ratio of 1:3. The precursor, then, is calcined to oxide, subsequently reduced and alloyed under hydrogen atmosphere. Thus obtained skutterudite nanoparticles are used for the assembly of multilayers.

Functionalizing Surfaces:

Glass substrates were employed in order to perform absorption measurements subsequent to assembly of nanoparticles. The substrates were subject to ultrasound in acetone, boiled in Piranha solution (3:1 H_2SO_4:H_2O_2) for 1 hr to clean any organic impurity on the surface, and thoroughly rinsed with deionized water prior to use. The substrates were functionalized with APTMS or MPTMS in two ways: *i*) derivating the substrate in ethanolic solution of APTMS, *ii*) using the μCP technique. The structure of functional molecules are shown in Figure 1.

Printing:

PDMS stamps were fabricated by mixing an elastomer with curing agent at a ratio of 10:1. This mixture was poured on Petri dishes to obtain flat stamps. After curing at 60 °C for 3 hrs, the

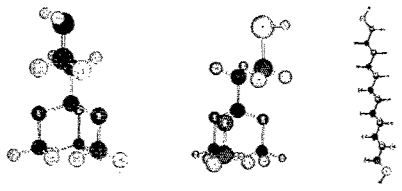


Figure 1: Bifunctional molecules for the functionalization of surfaces, for subsequent self-assembly of nanoparticles. From left to right; APTMS, MPTMS and dodecandithiol.

stamps were peeled away from the master and exposed to liquid ink to transfer silane from solution to the elastomeric stamp. In practical terms, the inker pad is equilibrated for 1 hr with a solution of silane in ethanol, then is withdrawn from solution, dried with a stream of N_2, to take away excessive silane. The stamp is then transferred to the substrate and contacted for 5 min. The elasticity and surface characteristics of the stamp promote good conformal contact between the PDMS surface and the substrate, favouring the formation of a continuous interface through which the homogeneous transfer of silane to the substrate surface is possible. All printing work was performed in N_2 atmosphere, since silanes are very sensitive to humidity and can easily polymerize in the presence of water. Figure 2 shows the overall procedure for functionalization of the substrates and formation of multilayers through stepwise functionalization.

Self-Assembly:

MPTMS molecules were transferred to the substrate surface using the μCP technique with prepared PDMS stamps (Fig. 2. First layer of gold was assembled was attained by dipping the substrate in the colloid solution for 3 hrs. The pH of the colloid solution was adjusted to 5-7 to increase the interaction of nanoparticles and end groups. The derivatizations successfully yielded self-assembly of colloidal Au nanoparticles at MPTMS functionalized surfaces through covalent bonding between the gold surface and –SH groups on the substrate. In the case of $CoSb_3$, the substrate was derivatized in a toluene solution containing skutterudite nanoparticles. The substrates were then ultrasonicated to remove particles adsorbed at unsilanized surfaces.

Depending on the material to be assembled on the second layer, different functional groups can be used to adjust the chemistry for the self assembly process. For the Au/Fe_3O_4 multilayer formation, the assembled Au surface was functionalized with MPTMS. However, the orientation of molecules is reversed, i.e. $-(OCH_3)_3$ groups should point upwards, since they can be attached to oxide surface through the cleavage of $O-CH_3$ bonds. There is no special effort to align the bifunctional molecules, since they will align themselves easily due to the functionality on the substrate surface. Then the substrate was dipped into Fe_3O_4 colloid in toluene and held for another 3 hrs. The assembly of this type of multilayers can be easily performed by the same bifunctional, MPTMS, molecule provided that the target sequence is metal/oxide/metal/oxide etc. Skutterudite multilayer needs a different bifunctional molecule, which is capable of binding the same type of particles in both ends. The commonly used dithiol molecules are very convenient for that purpose. First layer of skutterudite surface was functionalized with dodecandithiol and the substrate was held in $CoSb_3$ dispersed in hexane to self-assemble the second layer.

The characterization of self-assembled surfaces has been performed using Atomic Force Microscope (AFM) in the tapping mode with a Nanoscope IIIa system (Digital Instruments, USA) using a silicon tip.

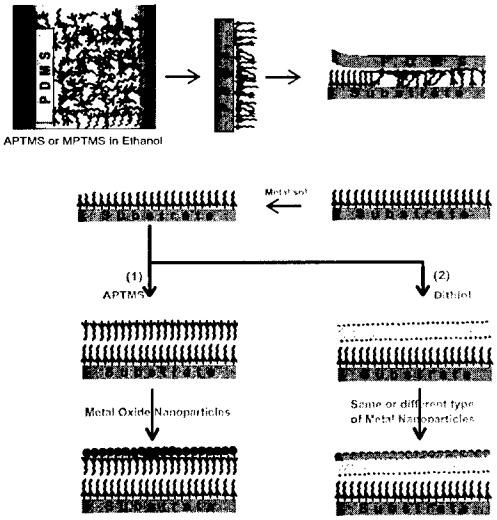


Figure 2: Schema of functionalization of surfaces with contact inking and multilayer formation.

RESULTS AND DISCUSSION

The morphology of self-assembled films was examined by AFM at different processing stages. Figure 3 and 4 shows the AFM images and section analysis of Au/Fe_3O_4 multilayer at first and fourth layers. First layer shows a very high coverage of the substrate surface with highly monodispersed Au nanoparticles. The size of Au nanoparticles is about 200 nm as can be seen from the section analysis of the AFM image. Image analysis of the fourth layer, Fe_3O_4, also shows a very high coverage of the lower surface with highly monodispersed nanoparticles of about 250 nm, as measured from the section analysis of the AFM image.

The assembled multilayer shows interesting optical behaviour as observed from UV-Vis analysis. The absorption spectra for the Au/Fe_3O_4 multilayer -4 layers- is given in Fig. 5. The same slide was used for the same set of measurements after processing stages, in order to

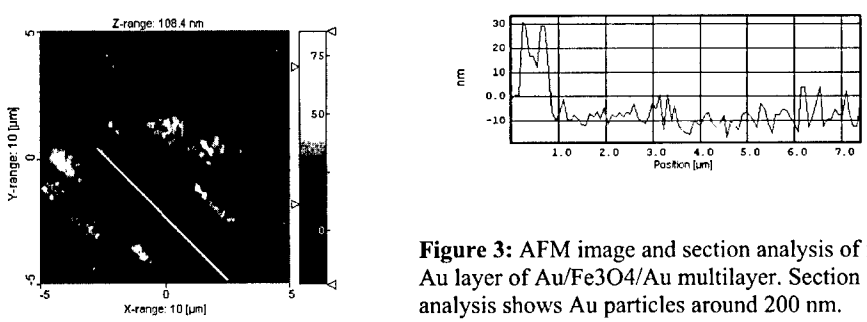


Figure 3: AFM image and section analysis of first Au layer of Au/Fe3O4/Au multilayer. Section analysis shows Au particles around 200 nm.

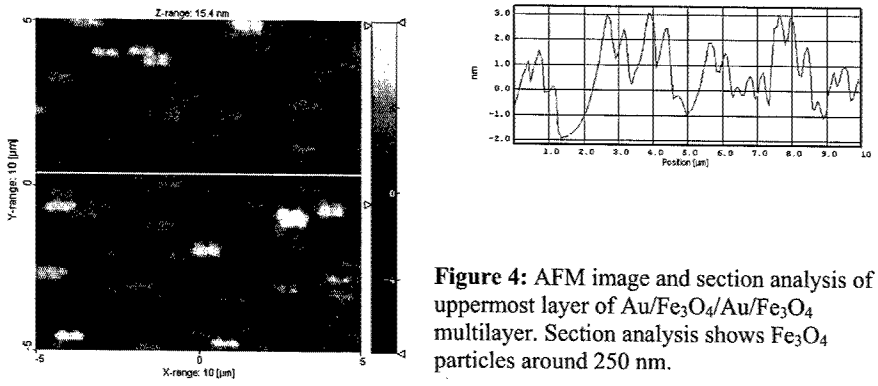


Figure 4: AFM image and section analysis of uppermost layer of $Au/Fe_3O_4/Au/Fe_3O_4$ multilayer. Section analysis shows Fe_3O_4 particles around 250 nm.

eliminate the experimental errors from different batch of samples. The first layer of gold shows a broad absorption in the 600-800 nm range. Magnetite does not have any absorption band in the measured wavelength range. The first magnetite layer simply enhances the absorption of this wide band. The third layer, Au, shifts the absorption maxima towards 520, where the plasmon absorption of Au takes place. The fourth layer, Fe_3O_4, shifts the absorption band to higher wavelengths and higher order contributions of the scattering give rise to formation of new shoulders at 700 and 850 nm. The plasmon absorption of gold at 520 nm also becomes clearly visible as the layer thickness is increased.

An important part of the work is to study the confinement of phonons in low dimensional structures, making a film of TE from nanoparticles. It has been theoretically suggested[9], and experimentally observed[10] that phonons are highly diffracted when the particle size is comparable to the phonon mean free path. Any reduction in the thermal conductivity of the system, provided that electronic properties negatively affected, will directly enhance the material's TE performance. A two-layer skutterudite film was prepared for this purpose and analyzed microstructure and morphology of the film is examined with AFM. The AFM image, given in Fig. 6, shows an interesting arrangement of particles, which was also observed by the

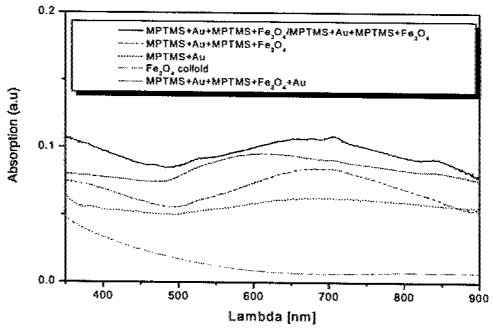


Figure 5: UV-Vis Absorption spectra for $Au/Fe_3O_4/Au/Fe_3O_4$ multilayer system. As the layer thickness increases interesting features are observed with new absorption satellites.

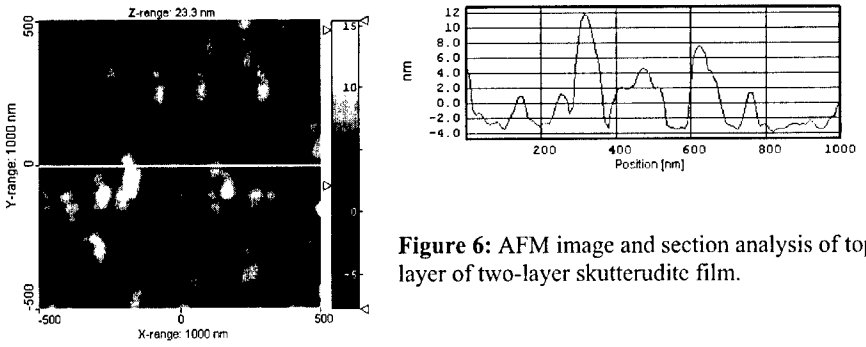


Figure 6: AFM image and section analysis of top layer of two-layer skutterudite film.

TEM analysis. The surface is highly covered but there are still porous regions and there is no registry between the layers. The average particle size of $CoSb_3$ was measured as 60 nm from the section analysis of the image, which is quite reasonable (TEM analysis ~45-50 nm) considering the convolution of AFM tips. Electrical conductivity measurements on the assembled films would give an idea about the porosity of the film, but did not succeed due to contact problems to the nanogranular fragile surface. Mono and multilayer assemblies of TE nanoparticles are currently under detailed investigation and results will be published in future.

CONCLUSION

Self-Assembly was successfully used to prepare metallic and nonmetallic composite multilayer films. The surface chemistry of assembled layers was changed by employing bifunctional molecules and thus the same or different type of nanoparticles were assembled. The thickness of layers can be controlled by using larger nanoparticles and the total thickness by the number of self-assembled layers. Prepared Au/Fe_3O_4 multilayer exhibits interesting optical behavior. Thermoelectric film was successfully prepared by, first time to our knowledge, the self-assembly of TE nanoparticles, and the properties are under investigation.

REFERENCES

1. S.L. Westscott, S.J. Oldenburg, T. R. Lee, N.J. Halas, *Langmuir* **14**, 5396(1998).
2. K.V. Sarathy, P. John Thomas, G.U. Kulkarni, C.N.R. Rao, *J. Phys. Chem. B* **103**, 399(1999).
3. V.L. Colvin, M.C. Schlamp, A.P. Alivisatos, *Nature* **370**, 354(1994).
4. T. Nakanishi, B. Ohtani, K. Uosaki, *J. Phys. Chem.* **B102**, 1571(1998).
5. R.L. Whetten et al. *Adv. Mater.* 1996, 8, 428.
6. K.C. Grabar, K.J. Allison, B.E Baker, *Langmuir* **12**, 2353(1996).
7. D.K. Kim et al., *Scripta Mater.* **44**, 1713(2001).
8. M. Toprak, Y. Zhang, M. Muhammed, A.A. Zakhidov, R.H. Baughman, I. Khayrullin, *18th Int. Conf. on Thermoelectrics*, 382(1999).
9. H.J. Goldsmid, A.W. Penn, *Phys. Lett.* **27A**, 523(1968).
10. L. Bertini, C. Stiewe,M. Toprak, S. Williams, D. Platzek, A. Mrotzek, Y. Zhang, C. Gatti, E. Müller, M. Muhammed, M. Rowe, to be published in *J. Appl. Phys.* Feb. 2003.

Mat. Res. Soc. Symp. Proc. Vol. 740 © 2003 Materials Research Society I7.11

Adhesion of HVOF Sprayed Diamond-Containing Nanostructured Composite Coating

Dr. Maksim V. Kireitseu and Ion Nemerenco
Department of Mechanics and Tribology
Institute of Mechanics and Machine Reliability (INDMASH),
National Academy of Sciences of Belarus
Lesnoe 19 - 62, Minsk 223052, Belarus
E-mail: indmash@rambler.ru

ABSTRACT

In the present paper mechanical properties of HVOF sprayed diamonds-containing aluminum oxide composite coating have been investigated. Crystallographic and morphologic texture was measured. Diamonds nanoparticles may improve fracture resistance of aluminum oxide-based coating. Investigations of thermally sprayed coatings by the test revealed high accuracy, speed and reliability of the test. It is also thought that the composite coatings will have better thermal conductivity and thermal shock resistance than that of aluminum oxide-based coatings.

INTRODUCTION

Ultra-dispersed diamonds (UDD) are the new synthetic diamond powders produced by chemical purification of explosion products. Nanoparticles of UDD have spherical and isometric form with no crystalline facets and a fractional structure of clusters [1, 2]. They may be presented as a high-dispersed powder. The diamond nanoparticles are being used for many applications because of its highest known hardness, excellent wear resistance and high thermal conductivity.

On the other hand, applications of single diamond-containing coating are still limited because of its poor fracture resistance and adhesion to substrates. Needless to say, fracture and adhesion strength between coating and substrate are the most important parameters to characterize its quality and effectiveness of related technologies. In general, adhesion may determine reliability and durability of the coatings.

Adequate coating-substrate adhesion under service conditions is a prerequisite to the satisfactory performance of any thermally sprayed ceramic-coated-metal system. Were the coating-substrate bond to fail in a given case and detachment of the coating from its substrate to occur as a consequence, the purpose for which the coating was applied would not likely be served. Thus, it becomes plain that the nature of the coating-substrate bond and the mechanisms by which it may fail must be known and understood clearly.

Researches [1-8] indicates that the adhesion generally decays with time at a rate that depends on mechanical loads, temperature and chemical makeup of the environment, the coating porosity, and the state of stress at the coating-substrate interface and within the coating. Moreover, it has been studied [3-14] that adhesive and/or cohesive failure of thermally sprayed ceramic-metal systems proceeds by means of a complex set of rate processes. It follows that investigations of coating-substrate adhesion should be conducted under actual and/or closely simulated service conditions to the extent feasible. This becomes particularly difficult when the coating-substrate system must be subjected to elevated applied load, localized stresses and temperatures during

service; for example, when the coating is to act as a protective wear resistant coating, heat barrier in the hostile, high-temperature environments encountered in advanced energy systems such as bearings, jet engines, or gas turbines.

Objective of the work was to investigate adhesion of thermally sprayed HVOF coatings consisting of dimonds, aluminum oxide and substrate.

TECHNIQUE OVERVIEW

Successful efforts to better understanding of adhesion of thermally sprayed ceramic-coated-metal systems requires an accurate method to measure either the adhesion itself and/or the work of adhesion. There are known simple techniques: a glue-based technique and a pull off-based technique [10, 14-17]. The former is based on pulling out glued together coated samples. The technique may result in rough values of adhesion force. To minimize errors a glue composition should be carefully studied and applied because it may fill pores and voids of a coating. The later, so-called pull-off technique, have been applied in experiments. Ferber [9] observed that mechanical and rheological properties of a medium used to grip a coating significantly affected a measured adhesion value. Alternative technique is based on scratching a coating by a diamond microhardness indenter (or other sharp tool), and/or impacting a coating with a projectile or a hammer. Its application shows that there may be significant regression between experimental data and real adhesion forces because of Van der Waals forces.

In the present researches improved pull-off technique [9] was used to measure an adhesion force of the coatings. Adhesion force was calculated by equation (1) as it follows:

$$\sigma_{adh} = P_H / S = P_H / (\pi \cdot R^2) \qquad (1)$$

Where P_H is force of peeling off a coating [Pa]; mathematical constant π is 3,1415; R is a radius of a ball [m], S is square of an indentation track [m^2].

Microstructure of the coatings was investigated by X-ray diffraction (XRD) and scanning electron microscopy (SEM) techniques. XRD measurements were performed on polished samples in a conventional X-ray automatic powder diffractometer (PW-1820 Philips) with a cuata tube, operated at 40 mA and 40 kV. Scans were acquired from 20° to 90° with a step size of 0.025° and exposure times of 4 s per step. The overall chemical composition of the specimens was determined by quantitative energy dispersive X-ray spectroscopy (EDS) measurements in a SEM (JSM 840, Nikon, Japan) equipped with an EDS detector (Model 6506, Micronix, England) which possesses an atmosphere thin window for light element detection ($z > 4$).

A detailed study of the microstructure of the specimen was carried out by conventional TEM using selected area diffraction (SAD). The chemical composition and structure of the phases and grain boundaries were analyzed by analytical TEM and high-resolution TEM. Conventional and analytical TEM were performed on a 200 kV microscope (Model 2000, Pentax, Japan) equipped with an EDS (Model 6506, Micronix, England) and a parallel electron energy-loss spectrometer (peels) detector. High-resolution TEM was conducted on a 300 kV microscope (Model 3010, Nikon, Japan) with a point resolution of less than 0.16 nm. Microhardness was measured with Vickers indentation at load on the indenter of 0.5 N for 30 seconds. Micro-

stresses, grain size and orientation index (texture degree) were calculated. Roughness and microrelief of the coatings were measured by the profilograph-profilometer.

SAMPLES PREPARATION

Steel was substrate of a sample on which alumina-based composite coating containing up to 70% of α-phase of oxide aluminum was produced. Alumina layer has up to 12% pores on the outside of the sample. Diameter of pores ranges from 0.8 to 3.4 μm. The thickness of the alumina-based layer was 300 μm, its microhardness was up to 16 GPa and its Young's modulus was 310 GPa.

Prior to thermal HVOF spraying a base surface was prepared by grinding with water jet contained SiC, oxide aluminum particles with average size of 2 mm. Then surface was preheated. Air consumption was 0.4-0.45 m^3/min. Distance of spraying was between 120 and 140 mm. Thickness of sprayed coating may be up to 3-5 mm.

Table I. Characteristics of ultra dispersed diamonds particles

Principal chemical composition of UDD nanoparticles	82 – 92 % carbon, 1 – 3 % of nitrogen, 1 – 2% of hydrogen, and up to 1 % of other additives.
Phase composition of UDD nanoparticles	80 – 100 % of cubic diamond, 0 – 10 % of hexagonal diamonds, and up to 20 % of diamond as X-ray amorphous carbon.
UDD nanoparticles size	4.0 to 8.0 nm
Size of aggregated UDD clusters	20 - 30 nm
Surface area of UDD nanoparticles	300±30 m^3/gr
Density of UDD nanoparticles	3.1 - 3.2 gr/cm^3
Thermo-stability until oxidation	400 - 450 °C
Thermo-stability until graphitization	1000 - 1100 °C

Ultra dispersed diamonds of 6.0 nm in average size of nanoparticles have been used in experiments to strengthen alumina-based layer. Diamonds were synthesised in strong non-equilibrium conditions of a detonation surge. The diamond nanoparticles look like isometric fragments. Table 1 lists some characteristics of ultra dispersed diamonds.

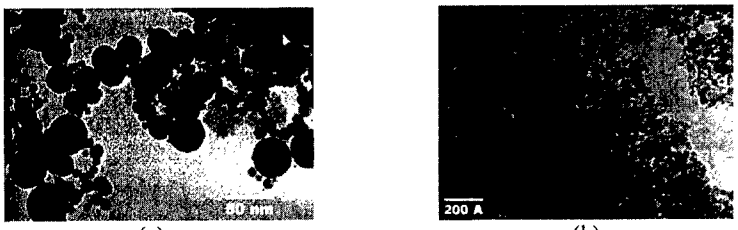
RESULTS & DISCUSSION

Table II shows an effect of UDD nanoparticles on mechanical properties of the composite coating. Diamonds concentration in aluminum oxide-based coating may affect on its size, porosity and roughness (table II). Roughness of the coating decreases up to 0.5-0.3 μm (fig. 1b). Single aluminum oxide structure has generally axial texture. Grains principally orientated in <111> direction.

Table II. Mechanical properties of the aluminum-based diamond containing coating

Thickness from top surface to substrate, μm	Poro-sity, %	UDD-aluminum oxide phases, %	Roughness, μm	Relative UDD con-centration in the coat-ing, %	Size of UDD clusters, nm	Max. hardness, GPa	Internal stress, $1O^8$ N/m^2	Adhe-sion, MPa
10	7-12	35-54	2.0-1.0	0.01-0.09	5.10-6.20	12-14	0.06	109.2
20	4-9	34-58	1.4-0.9	0.1-0.34	2.51-3.02	13-17	0.11	123.5
40	5-7	56-63	1.2-0.9	0.5-0.94	3.51-3.81	17-22	0.08	131.8
100	7-9	63-74	1.2-0.9	1.21-2.14	2.12-2.32	21-23	0.146	145.4
200	5-9	51-72	0.55-0.43	1.5-2.3	3.74-3.97	23-25	0.266	124.1
400	4-8	47-71	0.7-0.45	1.7-2.1	4.78-4.99	21-23	0.289	103.8
600	4-8	53-67	0.54-0.39	1.4-1.6	3.84-4.12	20-21	0.278	124.9
800	3-7	54-57	0.75-0.5	1.2-1.8	3.87-4.21	18-23	0.305	124.3
1000	5-6	31-39	0.5-0.3	1.3-1.6	5.72-7.02	12-15	0.333	133.6

UDD nanoparticles increase both internal stresses (up to $0.119 \cdot 10^8$ N/m^2) and microhardness (up to 25 GPa) in all studied cases. UDD nanoparticles are distributed in aluminum oxide-based coating. Nanoclusters (fig. 1a) and single UDD nanoparticles may diffuse into the aluminum oxide-based coating that results in strengthening it. The presence of diamond particles in the composite structure was also indicated by EDS analysis near the surface of the film (fig. 2). Many crystallized centers and clusters of UDD nanoparticles, aluminum oxide hard phases are observed in structure of the coating (fig. 1a,b).



(a) (b)

Figure 1. UDD clusters (a) and nanoparticles (b).

Near the surface of the coating (fig. 2) can be observed strong pudding rocks containing UDD clusters as it is shown at a high-resolution micrograph of diamond nanoparticles. Single UDD nanoparticles and its clusters may conglomerate with aluminum oxide hard phases.

The incident beam was parallel to the <111> axis, with the plane predominantly parallel to the interface. The heavily irradiated region was observed at 10 μm from the surface. High strain and dislocations were observed at thickness of 10-35 μm. However, there was no difference in lattice constants that was distinguished in the Fourier transform (FT) images obtained from the near surface region, damaged region, and deeper-lying region. Presumably, the lattice parameter value was determined to be constant in all studied regions. This may assure that no new original clusters were in the structure.

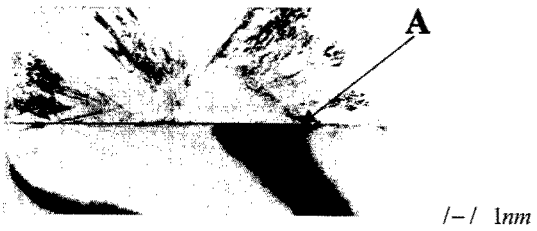


Figure 3. Segment of UDD nanoparticle

Size of the UDD clusters and its distribution in the coating depends on UDD concentration and shape of nanoparticles. Rounded shape of nanoparticles may be invited. In addition, UDD nanoparticles do not affect on HVOF process, but they may affect on mechanism of crystallization and a growth rate of the coating.

CONCLUSION

Ultra dispersed diamond (UDD) nanoparticles effects on roughness, microstructure and hardness of the aluminum oxide-based composites were studied. Roughness decreases up to Ra 0.5-0.3 μm. UDD clusters were found distributed in aluminum oxide-based coating. Hardness of the composite coating is up to 25 GPa at 0.1% UDD concentration; however, UDD nanoparticles may increase internal stresses of the coating. Also UDD nanoparticles may improve adhesion and microhardness of Al_2O_3–based coatings by nanotexturing its structure. Such physical characteristics suggest a number of possible commercial applications for the composite coatings, particularly for wear-resistant and related applications.

REFERENCES

1. Volkov K.V., Kirthats D, and Fritlend F. 1990. Synthesis of Diamond. *The Physics of Combustion and Explosion* 12: 1128-1131.
2. Bachmann P. K. and W. van Enckevort. 1992. Diamond Deposition Technologies. *Diamond Relat. Mater.* 1(1): 1021-34.
3. J.L. Drummond, M. R. Simon, and S. D. Brown, *in Corrosion and Degra-duation of Implant Materials.* Ed. by B. C. Syrett and A. Acharya (ASTM, Philadelphia, 1979), 89.
4. S.D. Brown, J.L. Drummond, M.K. Ferber, and D.P. Reed, *in Mechanical Properties of Biomaterials,* ed. by G. Hastings and D. Williams (Wiley, Chichester, 1980), Vol. II, 249.
5. M. K. Ferber, Brown, *J. Am. Ceram. Soc.* **64**, 737 (1981).
6. M. K. Ferber and S. D. Brown, *in Fracture Mechanics of Ceramics*, edited by R. C. Bradt, A. G. Evans, D. P. H. Hasselman (Plenum, New York, 1983), Vol. **6**, 523.
7. S. D. Brown, Thin Solid Films **119**, 127 (1984).
8. J. E. Randall and D. Dowson, *in Engineering in Medicine* (MEP Ltd., England, 1984), **13**, 67.
9. M. K. Ferber, Ph.D. th, Univ. of Illinois, Urbana, IL, (1981).

10.D. P. Reed, M.S. thesis, University of Illinois, Urbana, IL, (1978).
11.C. M. Baldwin and J. D. Mackenzie, *J. Biomed. Mater. Res.* **10**, 445 (1976).
12.Berndt & H. Herman. *Thin Solid Films* **108**, 427 (1983).
13.N.R. Shankar, C. C. Berndt, and H. Herman. *in Advances in Materials Characterization, Materials Science Research*, edited by D. R. Rossington, R. A. Condrate, and R. L. Snyder (Plenum, New York, 1983), Vol. **15**, 473.
14.C.C. Berndt and R. McPherson, *in The 9th International Thermal Spraying Conference,* edited by J. H. Zaat (Netherlands Institut voor Lastenick, The Hague, NL, 1980), 310.
15.Adhesion or Cohesive Strength of Flame-Sprayed Coatings, American Society for Testing and Materials, Standard Test Method C633-69, (ASTM, Philadelphia, 1969).
16.C. A. Andersson. *In Fracture Mechanics of Ceramics.* Ed. by R. C. Bradt, (Plenum, New York, 1983), Vol. 6, 497.
17.M.V. Kireitseu and V.L. Basenuk, *in the book of SEM Annual Conference 2002.* (Session 63, Paper #89, June 10-12, 2002, Hyatt Regency Milwaukee, Wisconsin, USA, 2002), 210.

Mat. Res. Soc. Symp. Proc. Vol. 740 © 2003 Materials Research Society I7.12

Rheological Behaviour and Model of Metal – Polymer - Ceramic Composite

Dr. Maksim V. Kireitseu
Department of Mechanics and Tribology
Institute of Mechanics and Machine Reliability (INDMASH),
National Academy of Sciences of Belarus
Lesnoe 19 - 62, Minsk 223052, Belarus
E-mail: indmash@rambler.ru

ABSTRACT

In the present paper rheological behaviour of composite coating consisting of Aluminum Oxide -Polymer – Chrome Carbide was examined by using rheological models for principal Hertzian contact of a sphere and a plate. The crystallographic and morphologic texture was characterized and the fracture resistance was measured using fracture-mechanics. A rheological model of the composite coating has been proposed and confirmed by in situ experiments. Several requirements to rheological models were formulated regarding an adequate strain-deformation state of the composite coating. Load rating revealed ultimate strain-deformation rates. Analysis of the models and experimental results revealed better understanding of composite failure and degradation mechanics.

INTRODUCTION

The fracture toughness of brittle coatings and composites are among the most important mechanical properties. Determination of fracture toughness value is a complicated process, involving preparation of specimens with well-defined sharp cracks of known length. Recent review articles [1, 2] have presented a summary of available techniques.

However, one method was conspicuously absent - that of Hertzian indentation using rheological model. In the present paper, Hertzian indentation and rheological models have been used to investigate fracture of composite coating consisting of aluminum oxide -polymer – chrome carbide. The crystallographic and morphological textures were characterized and fracture resistance of the coating was measured using fracture-mechanics and fundamentals of rheology.

EXPERIMENTAL TECHNIQUE

Detailed study of the microstructure of the specimen was carried out by conventional TEM using selected area diffraction (SAD). The chemical composition and structure of the phases and grain boundaries were analyzed by analytical TEM and high-resolution TEM. High-resolution TEM was conducted on a 300 kV microscope (Model 3010, Nikon, Japan) with a point resolution of less than 0.16 nm. Microhardness was measured with Vickers indentation.

The metallographic analysis of the cross-sectional micro-sections of the coated samples was made with a microscope. Microhardness was measured with Vickers indentation at load on the indenter of 0.5 N for 30 s. Then a diagonal of indentation track was measured and microhardness of the layers was calculated. Porosity of the oxide hard layer was measured by the linear method

(method of secant line). The coating of texture image analysis "Leitz-TAS" (Germany) and optical microscope "Ortoplan" was used to study porosity of the oxide ceramic layers.

RHEOLOGICAL MODELING OF NANOCOMPOSITE

To investigate mechanical properties of composites there were suggested many rheological elastic-viscous-plastic coatings described by Rudnitski et al., Shulman et al., Izraelian et al., and Reiner, [3-6]. However, despite some advantages the known models were not applied to developed composite coating and were not experimentally confirmed.

Based on recent researches of mechanical properties of aluminumoxide-based ceramics [7, 8], polymers [8-11] and its composites, a few requirements to a rheological models were formulated [19, 20]. It is expected that "chrome carbide- oxide aluminum - aluminum or its alloy" composite coating can be presented by "elastic-viscous-plastic" rheological model (model 1). The mechanical prototype of the model is shown in fig. 1a. "Steel-elastic-viscous polymer layers – aluminum – oxide aluminum layer" coating can be presented by rheological model consisting from two elastic elements and a viscous element (model 2, fig. 1b). Prototype of the model may be represented by parallel connection of the Maxwells' model and an elastic element. Final rheological equations usually depend on a level and a form of applied stress to the models. Integral deformation of sequentially joined models is calculate as follows:

$$\varepsilon = \varepsilon_1 + \varepsilon_2 \qquad (1)$$

If loaded coating has strain condition $\sigma > \sigma_0$, than rheological equation of the composite coating (model 1 in fig. 1a) can be written by:

$$\sigma = \sigma_0 + E_1\varepsilon_1 + \eta_1 \frac{d\varepsilon_1}{dt} \qquad (2)$$

where σ_0 σ, are strains at initial and final time of loading respectivelly; E_1 is modulus of elasticity; η is coefficient of viscosity; ε is deformation.

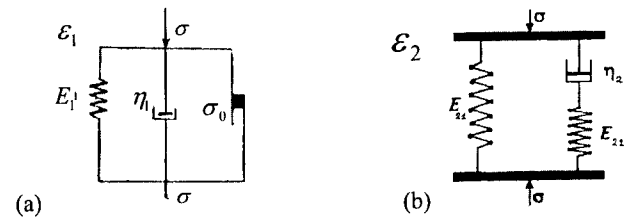


Figure 1. Rheological models of the composite coatings

For the model 2 at fig. 2b representing viscouselastic polymer-based layers, differential equation is defined by:

$$\frac{d\sigma}{dt}+\frac{E_{22}}{\eta_2}\sigma=(E_{21}+E_{22})\frac{d\varepsilon_2}{dt}+\frac{E_{21}E_{22}}{\eta_2}\varepsilon_2 \tag{3}$$

where E_0, E_1 are modulus of elasticity of materials; η is coefficient of viscosity.

Principal rheological equation of sequencially joined models at randomly driven loading is given by:

$$\frac{\eta_1}{E_{22}}\frac{d^2\sigma}{dt^2}+\left(\frac{E_1}{E_{22}}+\frac{\eta_1}{\eta_2}+\beta\right)\frac{d\sigma}{dt}+\frac{E_1+E_{21}}{\eta_2}\sigma-\frac{E_{21}}{\eta_2}\sigma_0=\beta\eta_1\frac{d^2\varepsilon}{dt^2}+\left(\frac{\eta_1}{\eta_2}E_{21}+\beta E_1\right)\frac{d\varepsilon}{dt}+\frac{E_1E_{21}}{\eta_2}\varepsilon \tag{4}$$

Equations from 1 to 4 describe rheological behavior of the composite coating including hard aluminum oxide -based layer, aluminum and viscouselastic polymer layers. By applying the rheological models to the composite coatings the strain-deformation mode of the coating may be studied. It should correlate with rheological and mechanical properties (plasticity, elasticity and viscousity), microstructure and composition of the coatings. Adequate rheological model should be confirmed by experimental results.

MODELLING OF INDENTATION TECHNIQUE

Lawn, (1993, 1998), Frank and Lawn, (1967), Collins, (1993), Pharr et al., (1993) [12-17] described that a deformation rate and a loading rate of materials is a function of indentation track diameter (a) and diameter of indenter (D). Previous works [7, 8, 19, 20] revealed that hertzian indentation technique may be effectivelly modified by rheological models to examine a stress - deformation state of composites and consolidated coatings. Here we will study rheological behavior by proposed models.

The function of stress-deformation mode of the composite coating in fig. 1a is defined by equation (2) at linear correlation of deformation rate vs. loading time. Therefore, the function of strain-deformation mode of model is defined by:

$$\sigma(t)=\sigma_0+E_1\varepsilon_0+\eta_1\dot{\varepsilon}\ (0)+E_1\dot{\varepsilon}\ (0)\cdot t \tag{5}$$

The rheological function (5) uses E_1, σ_0 and η_1 parameters that characterize mechanical properties of the coating. Function of strain-deformation mode of the composite coating in fig. 1b will be expressed by integrating the equation (3) at the linear correlation of deformation rate vs. loading time. The function of stress-deformation mode of model (fig. 1b) is defined by:

$$\sigma(t)=E_{21}[\varepsilon(t)-\varepsilon_0]+\eta_2\dot{\varepsilon}(t)-\frac{3k\eta_2}{2t_1}e^{-t/\tau}+\frac{k\eta_2^2}{E_{22}t_1^2}\left(1-e^{-t/\tau}\right) \tag{6}$$

where $\tau=\eta_2/E_{22}$, $t_1=R/V$; $k=4/(3\pi\cdot(1-\mu^2))$.

Principal Hertzian equation for a contact of spherical indenter and a sample can be written as the following function:

$$P(t)=\sigma(t)\left[\pi RVt+\frac{\pi d^2(t)}{4}\right] \tag{7}$$

where R is indenter radius, V is velocity of loading, t is time of loading, d(t) is function of indentation track depth vs. applied load, $\sigma(t)$ is rheological function (1-6).

Recent results [8] revealed that the initial angle depends on Young modulus of a polymer layer and initial diameter of the track d0 resulted from a roughness of the layer. Therefore, based on experiments on stress relaxation by polymer layers it was calculated that E_{21} = 80 MPa, given value η_2 = 8 MPa·s, and then it was found that E_{22}=2 MPa ($\tau = \eta_2/E_{22}$= 4 s).

To confirm the proposed rheological models Hertzian spherical indentations were done by indentation techniques at five points on the following samples. Size of the sample was 25×10×5 mm coated by "steel base – damping viscouselastic polymer – aluminum alloy – Al_2O_3 layer – chrome carbide layer" composite coating. The indentation was done by the spherical steel balls with diameter of 3.978 mm. Five sets of load-unload data were obtained at each point, with the maximum load being increased from P_1=1 N to P_2=1000 N. For each indentation, unloading was continued to up to 5% of the maximum load. After each indentation, the contact radius (a) was measured from the residual contact trace on the top layer. Then, the plot of indentation stress ($\sigma(t)$) versus indentation track depth (α, mm) was obtained and plotted at fig. 2a. According to Hertz theory these two parameters should show a linear relationship within the zone.

Figure 2a shows indentation depth vs. load curve. The measured values plotted in line 1 in fig. 2a are convex down because of uncounted effects in the experiments such as roughness, structural defects etc.; however, the deviation of the results is unexpectedly little. It should be noted that loading conditions, geometry of contacted surfaces and its mechanical properties may be included in rheological equations to be used in particular case or trial tests. However, the equations may take difficult mathematical forms and their handmade and quick application in practice would be hard. The calculated curve in line 2 is concave down that resulted from accepted conditions in the rheological equations and applied technique of its approximation. Ultimate contact stress for the composite coating with polymer layers was about 1.5 GPa. Polymer layers significantly decreased strength and stiffness of the coatings.

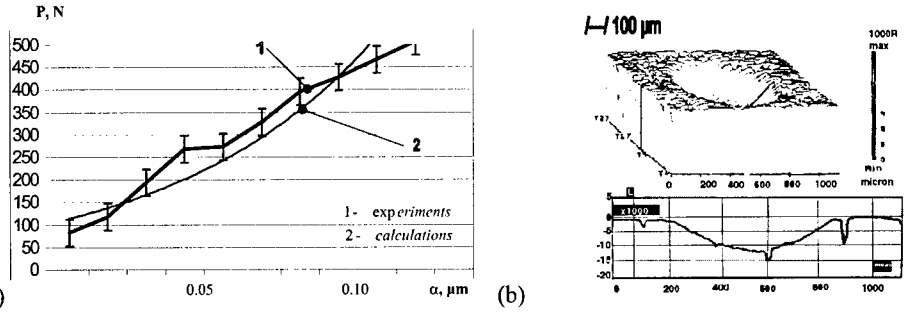


Figure 2. Stress-deformation rating and indentation track

At unloading the coating may show an effect of retardation of deformations (so-colled elastic return) because of damping properties of viscous-elastic polymer material. It could be shown in a figure as a downfall curve. The plotted relations of experimental data and calculated data with the equations (2, 5, 6) are shown good agreement of developed rheological model and mechanical behavior of the composite. Deviation from this line indicates the onset of irreversible deformation. The above stated conditions are found to be used in investigations of mechanical and rheological properties of "oxide aluminum-aluminum- viscous-elastic material (polymer) – steel" composite coatings.

Figure 2b shows indentation track obtained on surface of the composite coating. Diffuse damage, traditional cone and ring cracks have been observed, but fracture features have different impact on the coating. Strains may distribute not only through top CrC and/or oxide aluminum layers, but also relaxed by undernear polymer layer. It was found that strains principally concentrate around porous zones, internal voids and micro-defects of the coating resulted from its structural mismatches. In addition, strains may initiate crack propagation and fracture of the coatings. However, CrC layer naturakky strenghtened aluminum oxide-based coating.

CONCLUSION

The present work revealed rheological behavior and fatigue of advanced composite coatings like «steel – polymer – aluminum - oxide aluminum». Rheological models have been proposed with several requirements to modeling of the coatings. The models been confirmed by in-situ experiments using Hertzian theory for spherical indentation. Hertzian indentation technique effectively modified by rheological models is a powerful approach to investigate fracture mechanics of the coatings. The rheological analysis can consider not only elastic properties of materials, but also plastic and viscous properties of the composite heterogeneous coating. In addition, it may be possible to investigate correlation between rheological properties (plasticity, elasticity and viscous), microstructure and composition of the coatings. Rheological models may give reliable explanation of contact mechanics and rheological behavior of the coatings at loading up to 500 N. They could be used for analysis of its strength and load rating characteristics. It was discovered that ultimate contact stress of the coating included elastic-viscous polymer layers depreciate the ultimate stress to as low as 1.5 GPa. In future it is expected that upcoming investigations on this research will concentrate on smart nanostructured composites based on oxide aluminum ceramics and new composites strengthen by ultra hard nanoparticles such as diamonds.

REFERENCES

1. Sakai M. and Bradt R.C. *Int. Met. Rev.* **38**: 53-78, (1993).
2. Lawn B.R. *J. Am. Ceram. Soc.* **81** (9): 2394–2404, (1998).
3. Markov G.A. *Vestnik of Moscow St. Univ., Mashinostroenie*, **1**. 32-45, (1992).
4. Rudnitski V.A., Kren A.P. and Shilko S.V. *Wear*, Vol. 22, **5**, 502-508, (2001).
5. Reiner M. Rheology. Moscow., Nauka, (1965).
6. Shulman Z.P. Rheophysics. – Nauka, Minsk, (1977).

7. Shulman Z.P. and Smolski B.S. Rheodynamic of non-linear viscous –plastic materials. – Minsk, (1970).
8. Basenuk V., Kireytsev M. and Fedaravichus A. *in Proc. of the Symposium of Materials & Construction Failure*. 23-25May 2001 Augustov, Poland, 12, (2001).
9. Kireitseu M., and Yerakhavets S. *in Proc. of International conference on metallurgical layers and thin films - ICMCTF 2002*. Ed. Dr. B.Sartwell. - San Diego, California, USA, 156-165, (2002).
10. Bezuhov N.P. Fundamentals of elasticity, plasticity and flow theories. - Moscow: Vishaya shkola, (1968).
11. Golberg D.I. Mechanical behavior of polymers. Moscow, Chemistry, (1970).
12. Gul V.E. Structure and strength of polymers. Moscow., Nauka, (1971).
13. Frank C. and B. R. Lawn. *in Proc. R. Sac. London*, A**299**. 291-306, (1967).
14. Lawn B. R. *J. Appl. Phys*., **39**, 4828-4836, (1968).
15. Lawn B. R. Fracture of Brittle Solids. - Cambridge Univ. Press. Cambridge, U.K, (1993).
16. Lawn B. R.. *J. Am. Ceram. Soc*., vol. 81, **9**, 394-404, (1998).
17. Pharr G.M., D.S. Harding, W.C. Oliver, in: M. Nastasi et al., (Ed.): Mechanical Properties and Deformation Behaviour of Materials Having Ultra-Fine Microstructures. – Kluwer, Netherlands, 449-461, (1993).
18. Collins J. Failure of Materials in Mechanical Design. 2nd ed., John Wiley&Sons, NY, (1993).
19. Kireitseu M.. *Journal of Particulate Science & Technology (PS&T)*, vol. **20** (3), 1-15, (2003).
20. Kireitseu M.. *Journal of Engineering Physics and Thermophysics (JEPTER)*, vol. **76** (1), 8-18, (2003).

Mat. Res. Soc. Symp. Proc. Vol. 740 © 2003 Materials Research Society

Synthesis of Aerogel-Metal Cluster Composites by Gamma Radiolysis

Massimo F. Bertino[1] Jared F. Hund[1] Guohui Zhang[2], Chariklia Sotiriou-Leventis[2], Nicholas Leventis[2], Akira T. Tokuhiro[3], and John Farmer[4]
[1]Department of Physics, University of Missouri-Rolla,
Rolla, MO 65409, USA
[2]Department of Chemistry, University of Missouri-Rolla,
Rolla, MO 65409, USA
[3]Department of Nuclear Engineering, University of Missouri-Rolla,
Rolla, MO 65409, USA
[4]MURR, University of Missouri-Columbia,
Columbia, MO 65211, USA.

ABSTRACT

Noble metal clusters (Ag, Au) were formed in a silica aerogel matrix by gamma irradiation of hydrogel precursors loaded with aqueous solutions containing Ag^+ or $[AuCl_4]^-$ ions. Hydrogels exposed to gamma rays assumed the color expected for colloidal suspensions of Ag (respectively Au) clusters. The hydrogels were subsequently washed and supercritically dried, without any evident change in color, indicating that the metal clusters were not removed during drying. Typical gamma ray doses were between 3 and 3.5 kGy, and achieved complete reduction of hydrogels containing metal ion concentrations in the 10^{-4}-10^{-3} M range. Metal clusters in the aerogel monoliths were characterized with optical absorption, transmission electron microscopy, X-ray diffraction, scanning electron microscopy, and X-ray photoelectron spectroscopy. These techniques have shown that the clusters have a crystalline fcc structure. Au clusters consist of pure Au, while surface oxidation of Ag clusters was observed with XPS.

INTRODUCTION

In situ formation and entrapment of metal clusters in aerogels is desirable for application in catalysis[1,2], sensors[3], waste disposal[4,5], and electromagnetic shielding. Metal clusters have been formed in aerogels by adding to a hydrogel a precursor, generally an organometallic compound that does not leach out during the wash cycles required prior to the final supercritical drying procedure. High temperature treatment of the dry aerogel leads to reduction and deposition of the metal particles.[1,2] Alternatively, colloidal metal particles have been added directly into the sol during gelation, and remain trapped all the way to the final aerogel.[6,7]

Another efficient method of reducing metal ions to form homo- and heteronuclear clusters of transition metals is via gamma radiolysis of aqueous solutions.[8-15] That process is initiated by formation of solvated electrons, e_{aq}^- (eq 1), which reduce metal ions M^{m+} to metal atoms (eqs 2, 3). Metal atoms eventually form aggregates, M_n (eq 4).

$$H_2O \xrightarrow{\gamma\text{-radiation}} e_{aq}^-,\ H_3O^+,\ H^\bullet,\ OH^\bullet,\ H_2O_2 \qquad (1)$$

$$e_{aq}^- + M^{m+} \longrightarrow M^{(m-1)+} \qquad (2)$$

$$e_{aq}^- + M^+ \longrightarrow M_0 \qquad (3)$$

$$nM_0 \longrightarrow M_2 \longrightarrow \ldots\ldots M_n \qquad (4)$$

In this paper we describe the formation of nanoscopic metal clusters induced by gamma irradiation of a hydrogel in which the gelation solvent (CH_3OH) has been exchanged by an aqueous solution containing ions of the desirable metal (Ag and Au). Typical work-up of the resulting metal cluster embedded hydrogels leads to aerogel-noble metal cluster nanocomposites. The materials were characterized with optical absorption, transmission electron microscopy, X-ray photoelectron spectroscopy, and X-ray diffraction. Our results show that the noble metal clusters have crystalline fcc structure with lattice parameters comparable to those of the bulk materials, and a cluster size distribution between 10 and 200 nm. Au clusters are free of contamination, while surface oxidation of the Ag clusters has been observed.

The main advantage of our technique is its versatility. For example, it is known that radiolysis allows formation of non-equilibrium alloy clusters such as Au cores surrounded by a Ag shell.[9] Such structures are not accessible by simple impregnation methods, where cluster formation is achieved through high temperature treatment, which leads to equilibrium structures. Furthermore, radiolysis can be used to synthesize clusters out of a wide array of noble and transition metals, like Ni, Co, and Pb.[10]

Experimental Details

Silica aerogel composites were prepared by a modification of previously published procedures in which the contents of vial A (4.514 mL of tetramethoxysilane; 3.839 mL of methanol) and of vial B (4.514 mL of methanol; 1.514 mL of water, and 20 μL of concentrated NH_4OH) are mixed thoroughly to form a sol that gels at room temperature in 10-15 min.[3] The gels were left to age at room temperature then were removed from their molds and soaked in water. The water-washed gels were washed again, with an aqueous solution of the desired metal ion. Such solutions were prepared using $AgNO_3$, $HAuCl_4$, and 2-propanol. The metal ion concentrations varied from 10^{-4} M to 1 M. 2-propanol was added with a typical concentration of 0.2 M to scavenge the $H^\bullet$ and $OH^\bullet$ radicals generated during irradiation, eq 1. After the fourth washing, the solution surrounding the gels was decanted. The vials were closed tightly to avoid loss of solvent (water) by evaporation, and they were placed in close proximity of the core of the campus nuclear reactor. At the end of the irradiation period, the gels were visibly darker (depending on the concentration and chemical identity of the metal ions). The vials were filled with water and the gels were allowed to equilibrate for 12 hrs. Subsequently, the metal-impregnated gels were washed with acetone. The pore-filling acetone was removed by supercritical drying with CO_2.[3]

The samples were irradiated with γ radiation from the fission products of the campus' nuclear reactor (a pool reactor with a maximum power of 200 kW that employs ^{235}Ur fuel rods.) Typical total doses were up to about 3.5 kGy per run, as measured by Thermoluminescent Dosimeters (TLD) placed in vials adjacent to those containing the samples. Typically, gamma rays yield 6 solvated electrons per 100 eV of deposited energy, or, equivalently, 6×10^{-7} M per joule of adsorbed energy. Thus, a dose of 1 kGy can reduce about 5.7×10^{-4} M of Ag^+, and our typical doses of 3-3.5 kGy achieved 100% metal ion reduction for Ag^+ samples with a concentration below about 2×10^{-3} M. Alternatively, a few samples were irradiated with a ^{60}Co source located at University of Missouri-Columbia, which generates dose rates of about 18 kGy/h. It was employed to prepare aerogel/cluster composites with high metal concentrations, whose reduction would otherwise require an excessively long time.

Optical absorption was measured with a Cary 500 spectrophotometer. X-ray photoelectron spectroscopy (XPS) was carried out on a Kratos Axis 165 scanning spectrometer equipped with a 225 Watt Mg monochromatized X-ray source. Surveys were taken over areas as large as 120 square microns to ensure that noble metal clusters were distributed uniformly throughout the aerogel volume. X-ray diffraction (XRD) was measured with a Scintag PadX diffractometer (with a Cu Kα source). Transmission electron microscopy (TEM) was carried out with a Philips EM430T microscope, operated at 300 keV. Selected area electron diffraction (SAED) was used to characterize cluster structure and determine lattice parameters. Local chemical composition was determined with energy dispersive X-ray chemical analysis (EDS). BET surface area measurements were carried out with a Quantachrome Autosorb-1 instrument.

DISCUSSION

Gamma irradiation deeply affects the color of metal-loaded hydrogel monoliths. Hydrogels with low metal concentrations (10^{-4} to 10^{-2} M) irradiated with gamma rays (mostly from Source A) assume the typical color of colloidal suspensions of metal clusters, i.e., pink for Au, brownish for Ag. Hydrogels with higher metal concentration ($\geq 10^{-1}$ M) become opaque. The color of the monoliths does not change after supercritical drying, indicating that the metal clusters are firmly embedded in the silica matrix. Table 1 shows properties of several aerogels containing varying concentrations of Ag and Au.

Reduced Amount (M)	Metal	Density (g/cm^3)	Surface Area (m^2/g)	Mean pore diameter (nm)	Monolith Color	Metal Loading (%w/w)
10^{-4}	Ag	0.108	734±100	8.24±1	Brown	0.01
10^{-3}	Ag	0.108			Dark Brown	0.1
0.18	Ag	0.128	776±100	6.80±1	Opaque	15
1	Ag	0.1347			Opaque	75
10^{-4}	Au	0.116			Pink	0.02
10^{-4}	Au	0.133	879±100	9.62±1	Pink	0.015
10^{-3}	Au	0.156			Pink	0.126

Table 1. Densities, surface areas, and mean pore diameter of aerogel composites loaded with Ag and Au at different concentrations.

The structure of the aerogels was not fundamentally affected by the synthesis procedure, or by the presence of the clusters. In SEM micrographs of the Ag-aerogel composites, the bead structure of silica is evident, and similar to that reported for native silica aerogels.[3] The density values of the metal doped aerogels are larger, but still comparable with those of pure silica aerogels (0.003-0.010 g/cm^3).[7] Surface areas and mean pore sizes are in the 700-900 m^2/g and 7-10 nm range respectively, close to the values reported for native silica aerogels (700-1000 m^2/g and, 8-14 nm, respectively).[3,7,19,20]

Figure 1 shows typical optical absorption spectra of Au- and Ag-loaded silica aerogel monoliths. The absorption maximum of the Ag-doped aerogels is at 385 ± 2 nm, while the maximum of the Au-doped aerogels is at 518 ± 2 nm. These values lie within the range of values previously reported for the plasmon absorption of Au and Ag metal clusters,[18,19] and confirm

the presence and chemical identity of metal clusters in both irradiated hydrogel and aerogel composites.

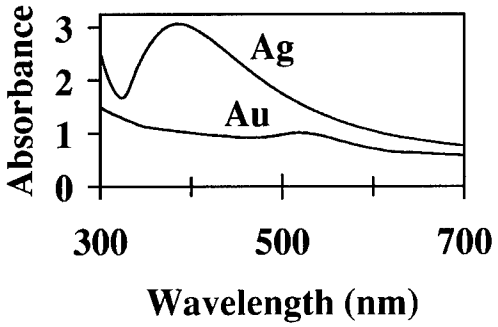


Figure 2. Optical absorption of Ag- and Au- doped aerogel composites obtained by irradiation with Source A of hydrogels made out of solutions having concentrations $[Ag^{+}] = 10^{-4}$ M, and $[Au^{III}] = 10^{-4}$ M, respectively.

TEM images of Ag- and Au-loaded silica aerogels are reported in Figure 4. Figure 4a shows several metal particles embedded in a large silica flake. SAED and EDS showed that the metal clusters are free of contamination, and have fcc structure. Size distributions of metal particles were determined by measuring a large number of particles from several different images. These are reported in Figure 4b-d for Ag^{+} concentrations in the bathing solutions varying from 10^{-4} M to 0.18 M. The mean particle size increases with increasing $[Ag^{+}]$, from about 45 nm at 10^{-4} M to about 65 nm at 5×10^{-2} M, to about 170 nm at 0.18 M. This particle size dependence on concentration is an indication that cluster growth dominates on cluster nucleation, i.e., nuclei form in the initial stages of reduction, and keep growing, without any (or few) new nuclei being added. Figure 4e shows the size distribution of a sample originating from a solution with $[Au^{III}] = 10^{-4}$ M. Particles are somewhat smaller than those in the Ag sample coming from the same bath concentration, and the mean Au particle size is about 30 nm.

XPS analysis of a 0.5 M $[Ag^{+}]$ aerogel revealed the binding energy of the 3*d* states is shifted towards lower energies compared to the bulk. Such shifts are characteristic of oxidized Ag species.[22] Ag oxidation is understandable, considering that the supporting matrix is an oxide and that the synthesis mechanism proceeds, in basic medium, via an Ag_2O intermediate.[21] Oxide states are probably superficial, since XRD analysis is consistent with a fcc structure with the lattice parameter of bulk Ag.

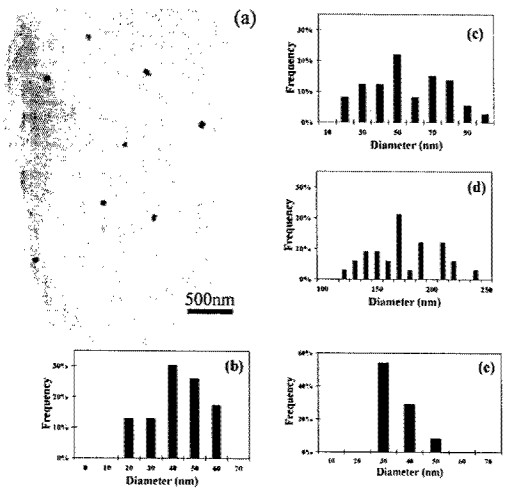


Figure 4. (a) Bright field TEM micrograph of a 5.7×10^{-2} M [Ag^{+}] aerogel. (b) Size distribution histogram of a 10^{-4} M [Ag^{+}] aerogel (23 particles measured). (c) Size distribution of a 5.7×10^{-2} M [Ag^{+}] aerogel (73 particles measured). (d) Size distribution histogram of a 0.18 M [Ag^{+}] aerogel (25 particles measured). (e) Size distribution histogram of a 10^{-4} M [Au^{III}] aerogel (24 total particles). Samples irradiated with UMR reactor

CONCLUSION

In conclusion, we have described a method for the synthesis of metal cluster/aerogel composites. The new materials retain the characteristics of aerogels with a metal content of up to 75% w/w. Work is under way to demonstrate the ability of our method to synthesize clusters of non-noble metals, like Ni, and alloys. These are well known characteristics of the radiolysis technique, and can be employed to tailor the physical and chemical properties of aerogel/metal composites.

ACKNOWLEDGMENT

We thank Mr. W. Bonzer for his assistance with irradiation. We also thank Dr. S. Miller for his assistance with the TEM analysis, and Dr. T. Schuman for helpful discussions. Support from the Department of Energy through the Reactor Instrumentation and Reactor Sharing Grant Program is gratefully acknowledged. This work was supported in part by the Petroleum Research Fund (grant No. 35154-AC5 N. L.; C. S.-L.).

REFERENCES

1. G. Piccaluga, A. Corrias, G. Ennas, A. Musinu, *Sol-Gel Preparation and Characterization of Metal-Silica and Metal Oxide-Silica Nanocomposites*, Materials Science Foundations, Trans Tech Publications (2000).
2. Suh, D. J.; Park, T.-J.; Lee, S.-H.; Kim, K.-L. *J. of Non-Cryst. Solids* **285**, 309 (2001).
3. Leventis, N.; Elder, I. A.; Rolison, D. R.; Anderson, M. L.; Merzbacher, C. I. *Chem. Mater.* **11**, 2837 (1999).
4. Woignier, T.; Reynes, J; Phalippou, J; Dussossoy, J. L.; Jacquet-Francillon, N. *J. of Non-Cryst. Solids* **225**, 153 (1998).
5. Reynes, J.; Woignier, T.; Phalippou, J. *J. of Non-Cryst. Solids* **285**, 323 (2001).
6. Tai, Y.; Watanabe, M.; Kaneko, K.; Tanemura, S.; Miki, T.; Murakami, J.; Tajiri, K. *Adv. Mater.* **13**, 1611 (2001).
7. M. L. Anderson, C. A. Morris, R. M. Stroud, C. Merzbacher, D. R. Rolison, *Langmuir* **15**, 674-681 (1999).
8. J. Belloni, M. Mostafavi, H. Remita, J.L. Marignier, M.O. Delcourt,*New J. Chem.1998*,1239.
9. Treguer, M.; de Cointet, C.; Remita, S.; Khatouri, M.; Mostafavi, M.; Amblard, J.; Belloni, J. *J. Phys. Chem. B* **102**, 4310 (1998).
10. Marignier, J. L.; Belloni, J.; Delcourt, M. O.; Chevalier, J. P. *Nature* **317**, 344 (1985).
11. Remita, H.; Khatouri, M.; Treguer, M.; Amblard, J.; Belloni, J. *Z. Phys. D* **40**, 127 (1997).
12. Remita, H.; Mostafavi, M.; Delcourt, M. O. *Radiat. Phys. Chem.* **47**, 275 (1996).
13. Doudna, C. M.; Hund, J. H.; Bertino, M. F. *Int. Jou. Mod. Phys.* B. **15**, 3302 (2001).
14. Doudna, C. M.; Bertino, M. F., Tokuhiro, A. T *Langmuir*, **18**, 2434 (2002).
15. Henglein, A. *Israel J. Chem. 33*, 77 (1993).
16. Schatz, T.; Cook, A. R.; Meisel, D. *J. Phys. Chem. B* **102,** 7225 (1998); **103**, 10209 (1999).
17. Zacheis, G. A.; Gray, K. A.; Kamat, P. V. *J. Phys. Chem. B* **103**, 2142 (1999).
18. Kreibig U.; Gartz M.; Hilger A. *Ber. Bunsenges. Phys. Chem.* **101**, 1593 (1997).
19. Liz-Marzan, L. M.; Giersig, M.; Mulvaney, P. *Langmuir* **12**, 4329 (1996).
20. Leventis, N.; Elder, I. A.; Long, G. J.; Rolison, D. R. *Nano Lett.* **2**, 63 (2002).
21. Huang, Z.-Y.; Mills, G.; Hajek, B. *J. Phys. Chem.* **97**, 11542 (1993).
22. Moulder, J. F.; Stickle, W. F.; Sobol, P. E.; Bomben, K. D. *Handbook of X-ray Photoelectron Spectroscopy*; Chastain, J., Ed.; (Perkin Elmer: Eden Prairie, MN, 1992).

Mat. Res. Soc. Symp. Proc. Vol. 740 © 2003 Materials Research Society

Synthesis of Zeolite Y Nanocrystals from Clear Solutions

Y. Shen, M.P. Manning, J. Warzywoda, and A. Sacco Jr.
Center for Advanced Microgravity Materials Processing
Northeastern University
Boston MA 02115 USA

ABSTRACT

Synthesis of zeolite nano-sized crystals has attracted much attention because of their properties, some of which maybe different from the normal sized crystals. A synthesis adopted by Voltchev and Mintova was used as the starting point: 0.078 Na_2O: 4.35 SiO_2: 1.0 Al_2O_3: 2.35 $(TMA)_2O$: 248 H_2O. Both the silicate and aluminum starting solutions were clear. Zeolite Y nanocrystals with zeolite A nanocrystals as an impurity were obtained with a size range of 20-100 nm through this synthesis technique.

INTRODUCTION

There has been considerable research over the years in synthesis of large zeolite crystals with sizes approaching the sub-millimeter range. This interest was driven by specific technological applications favoring larger crystals or because crystal structure – property relations could be better determined using larger crystals. Zeolite Y, in particular, plays an important role today in the field of cracking process catalysis - hence, this work focused on this zeolite.

There have been several reports recently on the synthesis of small zeolite crystallites, such as zeolites A, X, L, Beta, ZSM-5 and Silicalite [1-7]. However, there are only few articles about synthesis of nano-sized zeolite Y [1,2]. Those articles explored the possibility of the synthesis of nano-sized particles [1] and the effect of Na_2O/Al_2O_3 on the particle size [2]. The influence of the Si/Al ratio, aging time, the sodium content and TMA content in starting solution on the purity, crystal size, Si/Al ratio in crystals and yield of nano-sized zeolite Y was investigated.

EXPERIMENTAL

In this synthesis, zeolite Y nanocrystals were grown from clear aluminosilicate solutions with different composition. The following reagents were used: Ludox SM-30 colloidal silica (30 wt% SiO_2, 0.56 wt% Na_2O, 0.01 wt% NaCl, 0.03 wt% Na_2SO_4, 69.4 wt% H_2O, Aldrich), aluminum isopropoxide ($Al(OiPr)_3$, 98+%, Aldrich), tetramethylammonium hydroxide (TMAOH, 25 wt% aqueous solution, Aldrich), and deionized water. From the literature in which nanocrystals were obtained Ludox SM-30 has always been used as the silica source. Deionized water was filtered twice through 0.2 and 0.1 μm membrane filters to reduce the particulate sources of undesired ions. All other reagents were used as received. The synthesis mixtures were prepared from two clear precursor solutions. Solution I was prepared in a 60 ml HDPE bottle by adding $Al(OiPr)_3$ into the double-filtered deionized water and TMAOH mixed solution. A white precipitate appeared in solution I upon addition of $Al(OiPr)_3$, and therefore the mixture was stirred at room

temperature using a magnetic stirrer until a clear solution formed. Solution II was formed by combining Ludox SM-30 with double-filtered deionized water in 30 ml HDPE bottle. The precursor solutions were mixed together in a 125 ml HDPE bottle, hand shaken, and put into a 95°C oven. After predetermined times the solids from the synthesis were recovered by centrifugation at 3300 rpm. Between centrifugation cycles supernatants were decanted and solids re-dispersed in deionized water. These processes were repeated about four times until the pH of the decanted solution was between 7 and 8.

RESULTS AND DISCUSSION

The effect of Si/Al ratio in the synthesis mixture on the zeolite Y nanocrystals. Samples, with the reactant solution composition of 0.078 Na_2O: 4.35 SiO_2: 1.0 Al_2O_3: 2.35 $(TMA)_2O$: 248 H_2O, were synthesized by crystallizing in a 95 °C oven for 3 days. By comparing the product X-ray pattern shown in figure 1 with a standard X-ray pattern of zeolite A and that of zeolite Y, it can be concluded that the sample is a mixture of mostly zeolite Y and some zeolite A. In the scanning electron microscope, cubic and octahedral crystal shapes were found as shown in figure 2. Most of the crystals are octahedral zeolite Y nanocrystals with a small amount of zeolite A as impurity.

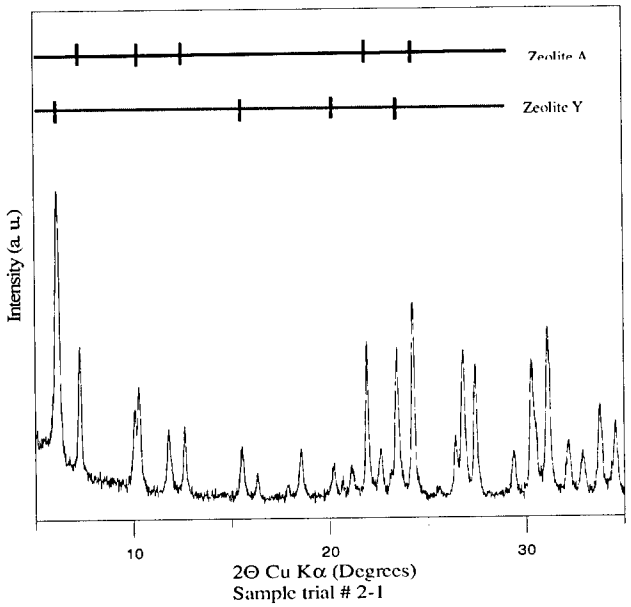


Figure 1. XRD pattern of sample

The results of experiments aimed at finding the relation between the Si/Al ratio in the starting solution and the Si/Al ratio in the final crystals are shown in Table 1. From Table 1, we can see that the

higher the Si/Al ratio in the starting solution, the higher this ratio in the final products. It was also found that the higher this ratio, the less zeolite Y and the more zeolite A in the final product. When the SiO_2/Al_2O_3 ratio is 5.44, about 90% of the final crystals are Zeolite Y. However, when SiO_2/Al_2O_3 ratio is 7.6, 90 percent of products are zeolite A. Figure 3 shows the Si/Al ratio in the zeolite Y crystals increased as the Si/Al ratio in the starting solution increased.

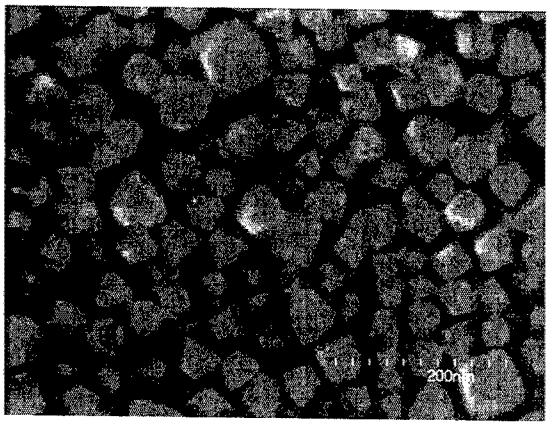


Figure 2. SEM of sample

Table 1: Results for the experiment Trial # 2

Sample No.	SiO_2/Al_2O_3 ratio in the starting solution	SiO_2/Al_2O_3 ratio of zeolite Y in the crystal products [b]	Yield (%)[a]	Size (nm)		Products purity (wt %)	
				Zeolite Y	Zeolite A	Zeolite Y	Zeolite A
# 2-1	4.35	3.3	1.20	50±30	80	60	40
# 2-2	5.44	4.16	1.40	50± 25	150±50	90	10
# 2-3	6.53	4.5	2.47	50± 25	150±50	40	60
# 2-4	7.62	5.56	2.79	50± 25	120±20	10	90

[a]: the calculation is based on the mass of the chemicals without water.

[b]: SiO_2/Al_2O_3 ratio of zeolite A is 1.48

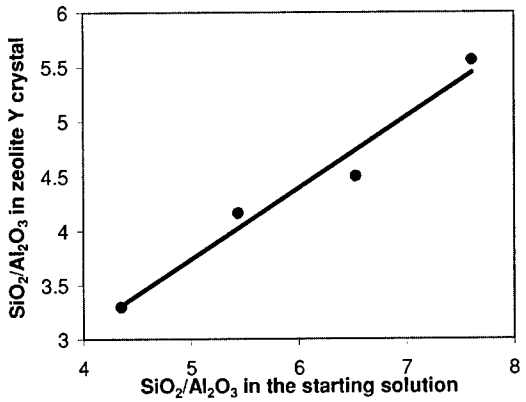


Figure 3. The effect of SiO_2/Al_2O_3 in the starting solution

The effect of Na_2O/Al_2O_3 ratio on the crystalline phase of nanocrystals. Since Ludox SM-30 contains 30 wt % SiO_2, 0.56 wt % Na_2O, and 69.4 wt % water, the amount of Na_2O content increases as the amount of SiO_2 increases. In order to find out whether SiO_2/Al_2O_3 ratio or the Na_2O/Al_2O_3 ratio affects the product purity, a series of experiments, trial # 3 were performed. This was done to investigate the effect of the sodium content in the synthesis mixture on the crystalline phase obtained and on the ultimate particle size of colloidal zeolite particles. Three different chemicals were used as the silica source: Ludox SM-30, Ludox LS-30 and Cab-O-Sil. The results are shown in Table 2. Experiment 3-1 was performed with Cab-O-Sil to have no sodium in the starting solution, but with otherwise unchanged composition compared to samples 3-2, 3-3 and 3-4. Except for sample 3-1, lower sodium contents in the synthesis

Table 2. Effect of Na_2O/Al_2O_3 on the product purity.

Sample number	Na_2O/Al_2O_3 ratio in the starting solution	SiO_2/Al_2O_3 ratio in the starting solution	Yield (%)	Size (nm)		Products purity (wt %)	
				Zeolite Y	Zeolite A	Zeolite Y	Zeolite A
# 3-1	0	4.35	12.45	N [a]	N [a]	Unconfirmed crystals	
# 3-2	0.014	4.35	0.38	50± 25	80	90	10
# 3-3	0.04	4.35	1.07	50± 25	100±30	70	30
# 3-4	0.078	4.35	1.10	50± 25	80	60	40

mixture results in a lower yield as shown in Table 2. Lower sodium content produces more zeolite Y than zeolite A nanocrystals. Zeolite Y is the main product from samples 3-2, 3-3 and 3-4 with zeolite A as the impurity. The result from sample 3-1 is not as expected. An unknown product material was formed other than zeolite A or zeolite Y.

The effect of aging time on the crystalline phase of nanocrystals. Samples 7-A, 7-B, and 7- C were aged at room temperature for 4, 6 and 9 days separately with crystallization at 95 °C for 3 days. Sample 14 and 17 were aged for 15 days and 25 days separately and crystallized at 95 °C for 4 days. Sample 11, 15 and 18 aged for 0 day, 15 days and 25 days with crystallization for 9 days. From Table 3, it can be concluded that longer aging time results in lower yields. But the particle size does not change a lot with the variation of aging time.

Table 3. Results on investigation of aging time

Trial Number	Aging (days)	Crystallization (days)	Yield [a]	Size of Crystals (nm) (From SEM)	
				Zeolite Y	Zeolite A
# 7- A	4	3	2.89	50 ± 30	100 ± 10
# 7- B	6	3	2.98	50	60 ± 10
# 7- C	9	3	2.33	60 ± 20	100 ± 40
# 14	15	4	2.15	40	N/A
# 17	25	4	2.00	50 ± 20	90
# 11	0	9	2.97	60 ± 20	80
# 15	15	9	2.45	50	100 ± 25
# 18	25	9	1.86	55	100± 20

[a]: Mass of product/Mass of chemicals used in the starting solution except water

The effect of crystallization time on the crystalline phase of nanocrystals. Experimental results are presented in Table 4 and Figure 4. Samples # 2-2, # 11, # 12 and # 13 were crystallized for 5, 9, 12 and 16 days at 95 °C oven separately without aging. Sample # 14, # 15 and # 16 were aged at room temperature for 15 days and crystallized at 95 °C for 4, 9, 16 days. # 17 and # 18 aged for 25 days and crystallized for 15 days. From the results it can be seen that the longer the sample stayed in the oven for crystallization, the larger of the yield.

In conclusion, the higher the SiO_2/Al_2O_3 ratio is in the starting solution, the higher this ratio in the final products. It was also found that the higher this ratio, the less zeolite Y and the more zeolite A in the final products and yield. When the SiO_2/Al_2O_3 ratio is 5.44, about 90% of the final crystal is zeolite Y. However, when SiO_2/Al_2O_3 ratio is 7.6, 90 percent of products are zeolite A. Since aging time enhanced the nucleation, crystals obtained after longer aging time are more uniform and the size is smaller. Yield of the crystals increased with longer crystallization time. In these experiments, no relationship was observed between the amount of zeolite Y product and the crystallization time.

Table 4. Effect of crystallization time on crystalline phase

Sample Number	Crystallization (days)	Aging (days)	Yield of crystals *(%)	Production (%) #		Size of crystals (nm)	
				Zeolite Y	Zeolite A	Zeolite Y	Zeolite A
# 2-2	5	0	1.40	90	10	50± 25	150±50
# 11	9	0	2.97	60	40	60 ± 20	80
# 12	12	0	2.30	75	25	50± 30	120
# 13	16	0	5.63	80	20	50	80-200
# 14	4	15	2.15	60	40	40 ± 10	120± 20
# 15	9	15	2.45	55	45	45 ± 10	100± 25
# 16	16	15	6.46	95	5	50	N/A
# 17	4	25	2.00	65	35	40	90
# 18	9	25	1.86	25	75	55	100± 20

*: The yield is based on the mass of feeding chemicals except H_2O.

#: Estimated from X-ray diffraction pattern.

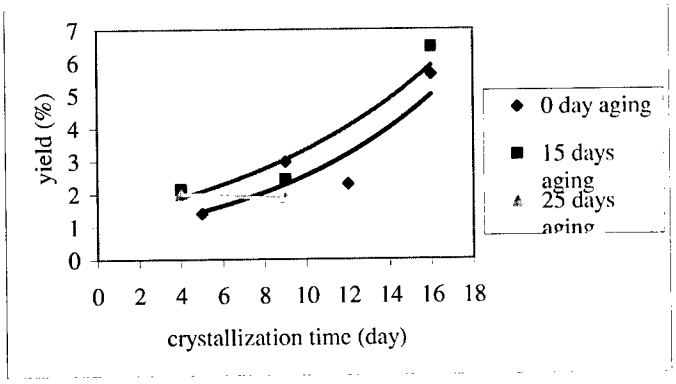


Figure 4. Effect of crystallization time on crystalline phase

REFERENCES

1. V. Valtchev and S. Mintova, *Microporous and Mesoporous Materials*, **43**, 41-49 (2001).
2. B. J. Schoeman, J. Sterte, and J.-E. Otterstedt, *Zeolites*, **14**, 110-116 (1994).
3. S. Mintova, N. H. Olson, V. Valtchev and T. Bein, *Science*, **283**, 958 (1999).
4. I. Schmidt, C. Madsen, and C. J. H. Jacobsen, *Inorg. Chem.*, **39**, 2279-2283 (2000).
5. N. B. Castagnola, and P. K. Dutta, *J. Phys. Chem. B*, **102**, 1696-1702 (1998).
6. M.A. Camblor, A. Corma and S. Valencia, *Microporous and Mesoporous Materials*, **25**, 59 (1998)
7. A. E. Peterson, B. J. Schoeman, J. Sterte, and J.-E. Otterstedt, *Zeolites*, **15**, 611-619 (1995).

Mat. Res. Soc. Symp. Proc. Vol. 740 © 2003 Materials Research Society I7.20

Molecular Dynamics Simulations on Nanocomposites Formed by Intermetallic Dispersoids of $L1_2$ Type and Aluminum Matrices

Min Namkung, [1]Sun Mok Paik, and Buzz Wincheski
NASA Langley Research Center
Hampton, VA 23681
[1]Kangwon National University
Chunchun, Korea

ABSTRACT

Molecular dynamics simulations were performed to characterize the lattice morphology in the region adjacent to the interfaces in nanocomposite systems of a Ni_3Al dispersoid embedded in Al matrix (Ni_3Al/Al) and an Al_3Nb dispersoid embedded in aluminum matrix (Al_3Nb/Al). A nearly perfect coherent interface is obtained in the Al_3Nb/Al system with the lattice planes of dispersoid and matrix aligned parallel in all directions. The simulation results show the presence of the matrix atom-depleted regions near the dispersoid boundary for most cases. Detailed analysis revealed that certain sites immediately next to the dispersoid are energetically favored for the matrix atoms to occupy. The matrix atoms occupying these sites attract other atoms producing the depleted regions. In certain specific situations of Al_3Nb/Al system, however, the wetting of a rotated dispersoid is overwhelmingly complete prompting the need of further study for better understanding. The order parameters of dispersoids calculated for Ni_3Al in aluminum is nearly constant while that for Al_3Nb in aluminum is rapidly decreasing function of temperature in the range of 300 to 1800K.

INTRODUCTION

Second phase particles that are mixed and uniformly distributed within a matrix are called dispersoids. By selecting appropriate type, size, morphology, and concentration of these dispersoids in a matrix, it may be possible to develop structural components that are capable of actively indicating their physical/chemical states and are optimized for best performance based on given application purpose. For example, the magnetic properties of Ni_3Al particles can be affected by the local stress states that may be indicative of the changes in other material states. At the same time, when mixed with a substantial volume fraction, the small nearest neighbor distance between such densely populated dispersoids may prevent the dislocation loop formation while being highly resistant to cutting by dislocations [1]. The current series of investigation concentrates on the morphology of such composites to establish a foundation for systematic study on nanocomposite systems of damage indicating capabilities and prolonged service lives.

Our previous study clearly showed that a Ni_3Al dispersoid, which is coherent with the aluminum matrix, causes a substantial degree of local lattice distortion in the vicinity of matrix/dispersoid interface [2] that is known to enhance the strength of alloys [1]. An unresolved problem of the study was the appearance of lattice atom-depleted regions near the interface in the composite system with a rotated dispersoid and its origin was not well understood. Therefore, the purpose of the present study is to find ways of minimizing the

regions of matrix atom depletion near the interface and closely investigate the nature of these regions.

The lattice structure of Ni_3Al is known as $L1_2$ which possesses a cubic symmetry. Being paramagnetic in nanosize [3], the magnetic field effects of Ni_3Al particles are not considered in the present simulation. The stable phase of Al_3Nb is known to be $D0_{22}$ structure which is tetragonal instead of cubic $L1_2$ [4]. Nevertheless, we choose the metastable $L1_2$ phase of Al_3Nb in the present study for two reasons. First, maintaining the cubic symmetry of the system, the simulation results can be directly compared between the two systems of Ni_3Al/Al and Al_3Nb/Al. Second, by varying the physical and chemical states of the metastable system, some unexpected but interesting facts may be found.

DETAILS OF SIMULATIONS

For each system of Ni_3Al/Al and Al_3Nb/Al, a dispersoid is constructed at the center of a cubic block of pure aluminum. Simulations are first performed by arranging the lattice planes of dispersoid and matrix parallel in all three axes of Cartesian coordinates. Then the dispersoid lattice is rotated with respect to that of the matrix. As an initial investigation of a systematic study on nanocomposites, the rotation of the dispersoids in the present study is limited to the x-y plane and three angles of rotation, i. e., 15^o, 30^o and 45^o. Also in this study, the dispersoid lattice spacings are initially set to be very close to their real values, i. e., 0.357 nm for Ni_3Al and 0.384 nm for Al_3Nb compared to 0.405 nm for pure aluminum. The inner radius of matrix and the outer radius of dispersoid are chosen to allow partial overlap between two lattices. The overlapping lattice points are removed to ensure a minimum separation among the atoms in the interface region. With further adjustment of these radii, the two-dimensional dispersoid boundaries in the x-y planes are selected to be Ni-only edges for Ni_3Al/Al and Al-only for Al_3Nb. The simulations are performed in the temperature range of 300 -1800K based on the temperature-independent parameter values for a modified embedded atom method (EAM) potential given by Baskes [5].

RESULTS AND DISCUSSION

Fig. 1 shows the results of simulations performed at 300 K on the Ni_3Al/Al system with their lattice planes arranged parallel in all three directions. Shown are the atoms in three planes of (001) centered at $z = 0$. The hexagons and tiny dots in this figure represent Ni and Al atoms, respectively. Similar results obtained at 900 K are shown in Fig. 2. The presence of the matrix atom-depleted regions around the dispersoid is clear in the results of these two figures. One of the goals of the present study is to find the origin of such matrix atom-depleted regions at the interface, and a simple model has been established and applied to the results of Figs. 1 and 2, as explained in the following.

The dispersoids shown in Figs. 1 and 2 are almost octagons and two types of edges are found in their boundaries; those consisting of four nickel atoms and the others consisting of five nickel atoms, which we call the four-atom edges and five-atom edges, respectively, for brevity. Upon a close inspection, one finds that three matrix aluminum atoms are lined up immediately next to the four-atom edges.

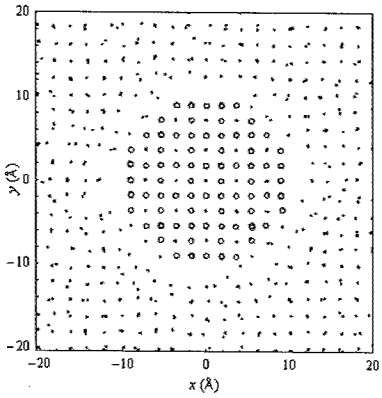


Figure 1. Simulation results of the Ni_3Al/Al composite system at 300K without rotating the dispersoid.

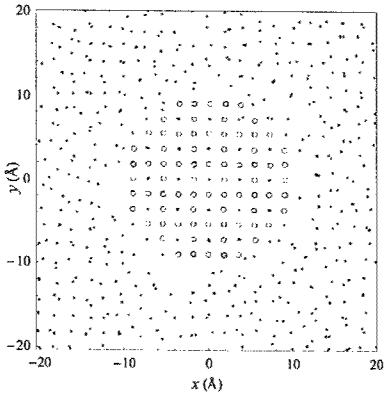


Figure 2. Simulation results of the Ni_3Al/Al composite system at 900K without rotating the dispersoid.

Fig. 3 shows lattice sites near the interface for the matrix aluminum atoms to occupy. Referring the results of Figs. 1 and 2, it is clear that the sites A and A's next to a four-atom edge are energetically more favored than B and B' which are next to a five-atom edge. In Fig. 3, one can see that an aluminum atom in site A has four dispersoid Ni atoms, denoted by x, at the nearest neighbor distance. The same applies to an aluminum atom occupying site B. The important difference is that a complete two-dimensional unit cell is formed when an aluminum atom occupies site A. Once this occurs, A' is the next favorite site for occupation since there are four nickel atoms at the nearest neighbor distance and there exists an aluminum atom at site A to lower the energy of site A'. Along the other edge, however, both B and B' sites have to be occupied by two aluminum atoms simultaneously to form a unit cell and such an occurrence has a much lower probability than that of occupying sites A and A' in sequence. In addition, site B' has only two Ni atoms at the nearest neighbor distance and the probability of occupation is even lower for this site. Hence, the matrix aluminum atoms tend to occupy the sites immediately next to the four-atom edges. This argument is based on a two-dimensional picture but it is trivial to extend the logic to a three-dimensional situation.

The aluminum atoms executing random motion in the interface region arrive at sites A and A'. Once the aluminum atoms occupy sites A and A', they attract other aluminum atoms causing matrix atom-depleted regions near the other edges of dispersoid boundary. The validity of this argument is supported by the absence of such unit cell formation activity by the matrix aluminum atoms when the symmetry of the system is reduced as shown in the results of Fig. 4 obtained with the dispersoid lattice rotated by 15° about the z-axis. Nevertheless, the strongest evidence for the above argument comes from the results of 45° rotation shown in Fig. 5. Here, the five-atom edges are compatible with matrix lattice and the unit cell formation along these edges is clearly seen. Such site preference vanishes at elevated temperature as shown in the simulation results of Fig. 6 for the Ni_3Al/Al system at 900K with the dispersoid rotated by 30° where a significant reduction of the matrix atom depletion is seen.

Fig. 7 shows the results of the Al_3Nb/Al system at 300K obtained without rotating the dispersoid. The system under this situation forms a perfect coherent interface without any noticeable lattice strain in the interface region. Fig. 8 shows the results with the dispersoid rotated by 30° about the z-axis. Here again, the matrix atoms are found to occupy the sites to form unit cells as discussed in the descriptions of the model shown in Fig. 3.

The most unexpected results are found for the 15° and 45° rotation cases as seen in Figs. 9 and 10. The two-dimensional shape of the dispersoid in these two figures is much different from that appeared in the results of Figs. 7 and 8. Here, the dispersoid/matrix bonding is

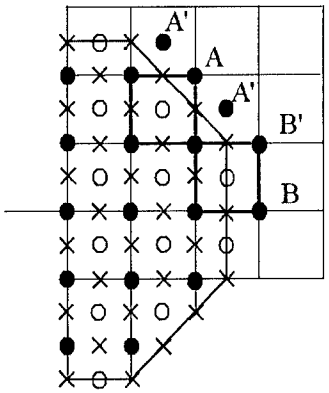


Figure 3. Sites favored (A &A') and less favored (B & B') by matrix atoms. ✕ is for Ni at z = ±a/2, O for Ni at z = 0 and ● for Al at z = 0.

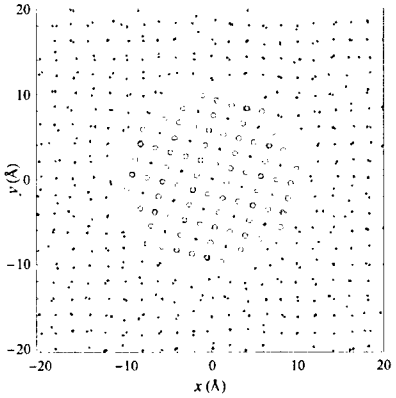


Figure 4. Simulation results of the Ni_3Al/Al system at 300K with the dispersoid rotated by 15° about the z-axis.

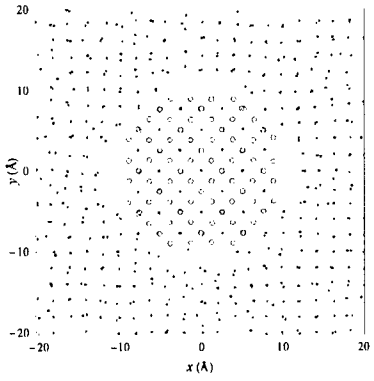


Figure 5. Simulation results of the Ni_3Al/Al system at 300K with the dispersoid rotated by 45° about the z-axis

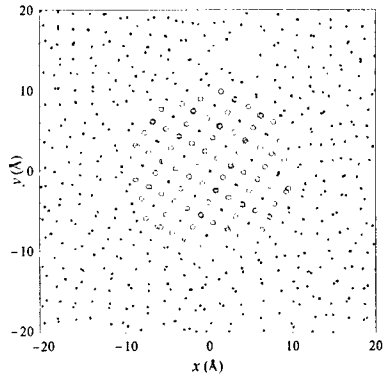


Figure 6. Simulation results of the Ni_3Al/Al system at 900K with the dispersoid rotated by 30° about the z-axis

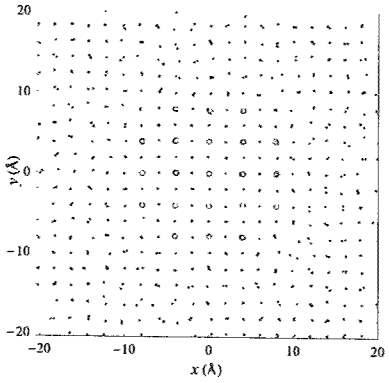


Figure 7. Simulation results of the Al_3Nb/Al system at 300K without rotating the dispersoid.

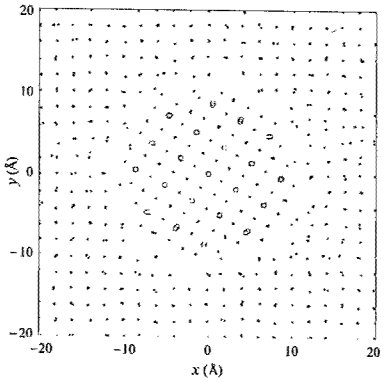


Figure 8. Simulation results of the Al_3Nb/Al system at 300K with the dispersoid rotated by 30° about the z- axis.

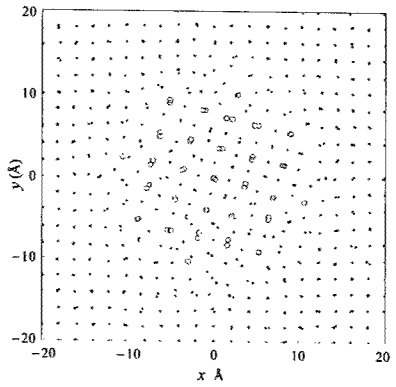


Figure 9. Simulation results of the Al_3Nb/Al composite system at 300K with the dispersoid rotated by 15° about the z-axis.

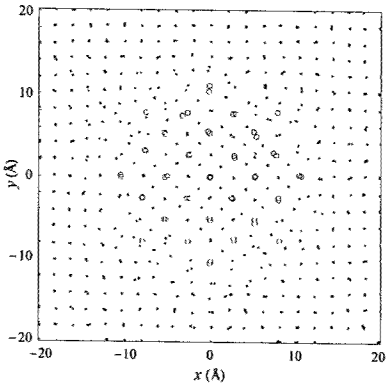


Figure 10. Simulation results of the Al_3Nb/Al composite system at 300K with the dispersoid rotated by 45° about the z-axis.

complete as if they were interdiffused into each other. Such a change in the dispersoid geometry may or may not be related to the fact that the currently assumed $L1_2$ structure of Al_3Ni is a metastable phase. No explanation is available at the moment and systematic study is needed to understand the results of these figures. Finally, the order parameters calculated for systems with unrotated dispersoids over a range of temperature are shown in Figs. 11 and 12 for Ni_3Al/Al and Al_3Nb/Al, respectively. It is seen that the Ni_3Al dispersoid is thermally stable while Al_3Nb is not. This is puzzling since the melting temperature is considerably higher in Al_3Nb than Ni_3Al (1953K vs. 1673K). The melting behavior of a particle embedded in a matrix can be strongly

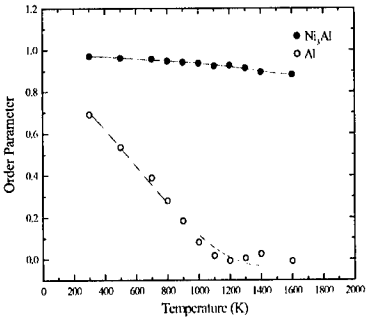


Figure 11. Temperature dependence of order parameters of the unrotated dispersoid and matrix in the Ni_3Al/Al system.

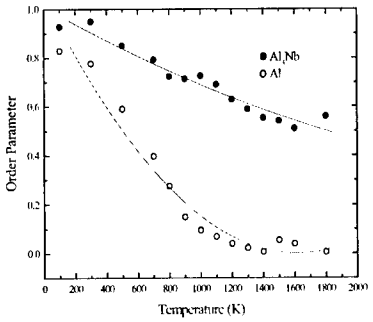


Figure 12. Temperature dependence of order parameters of the unrotated dispersoid and matrix in the Al_3Nbl/Al system.

dependent on the surrounding environment and the temperature dependence of the order parameter needs to be evaluated under various situations to make a general statement.

SUMMARY AND CONCLUSION

The simulation results of the present study show the general trend of unit-cell formation in the matrix if the lattice planes of the matrix and dispersoid are appropriately aligned. The case of 15° and 45° rotations of the dispersiod atoms produce matrix atom-concentrated and depleted regions near the dispersoid. It was found that a perfectly coherent interface forms between Al_3Nb and aluminum matrix under appropriate conditions. Also in the Al_3Nb/Al system, the dispersoid geometry is significantly changed while its wetting with the matrix remains perfect for particular dispersoid orientations. The underlying mechanism for such perfect wetting needs further systematic study along with the temperature effects and stability of the composite systems.

REFERENCES

[1]. T. H. Courtney, *Mechanical Behavior of Materials*, McGraw-Hill (New York, 2000).
[2]. M. Namkung, S. Paik and B. Wincheski, On-line Proceeding of International Conference on Computational Nanostructures (ICCN), San Juan, Puerto Rico (April, 2002).
[3]. S. N. Kaul and Anita Semwal, "Exchange-enhanced Pauli spin paramagnetism in nanocrystalline Ni_3Al", Phys. Rev. B **62**, 13892 (2000).
[4]. M. Yamaguguchi and Inui, in *Structural Applications of Intermetallic Compounds*, edited by J. H. Westbrook and R. L. Fleischer, John Wiley and Sons (New York, 2000).
[5]. M. I. Baskes,"Modified EAM potentials for cubic materials and impurities", Phys. Rev. B **46**, 2727 (1992).

Mat. Res. Soc. Symp. Proc. Vol. 740 © 2003 Materials Research Society I7.25

Condensation of Carbon Vapour in the Microwave Oven

Oxana V. Kharissova[1], Israel Nieto Lopez[1], Ubaldo Ortiz Méndez[2], Juan A. Aguilar[2] and Moisés Hinojosa Rivera[2].
[1]Facultad de Ciencias Físico-Matemáticas, Universidad Autónoma de Nuevo León, *San Nicolás de los Garza, N.L., México, C.P.66450.* **E-mail okhariss@ccr.dsi.uanl.mx**
[2]Facultad de Ingeniería Mecánica y Eléctrica, Universidad Autónoma de Nuevo León, *San Nicolás de los Garza, N.L., México, C.P.66450.* **E-mail uortiz@ccr.dsi.uanl.mx**

ABSTRACT

This work is devoted to microwave heating of graphite for studying the processing of carbon nanotubes (CNTs) by graphite vaporization. We have applied heating by microwaves (MW) (power 800W, frequency 2.45 GHz) in air at 20-90 min. The oven temperature was approximately 1200°C. The condensed material was collected on a fused silica target. After deposition, the morphology of carbon nanotubes was studied by Scanning Electron Microscopy (SEM), Atomic Force Microscopy (AFM), and Transmission Electron Microscopy (TEM). The samples were found to contain nanotubes, nanoparticles and fibers (at 1.30-2.80 micrometers to 6-11 micrometers) which appeared to be highly graphitized. It was observed that multi-walled nanotubes (MWNT´s) were produced by this method.

INTRODUCTION

Multi-walled carbon nanotubes (MWNT´s) were first discovered in 1991 [1]. The walls of this kind of nanotubes consist of multi-layered coaxial cylinders of carbon atoms. In 1993, the other kind of nanotubes, called single-walled carbon nanotubes (SWNT´s), was discovered by NEC and IBM, respectively. Unlike MWNT´s, the walls of SWNT´s have only a single-layer of carbon atoms. Composed of pure carbon, carbon nanotubes are hollow cylinders with a few nanometers in diameter. The honeycomb structure of carbon atoms on the cylinder walls is similar to that of graphite. Due to such special arrangement of carbon atoms, several distinctive properties of carbon nanotubes have been extensively studied. Numerous potential applications, such as flat panel displays [2], chemical sensors [3], hydrogen storage [4], etc., have been proposed. A number of methods such as arc discharge [5], laser vaporization [6], pyrolysis [7,8], plasma-enhanced [9,10] or thermal chemical vapor deposition (CVD) [11,12], have been developed for the production of CNTs.

The synthesis of CNT´s is often accompanied by the formation of other forms of carbon, such as fullerenes, polyhedral particles and amorphous forms of carbon. In many instances purification of CNT´s (removal of side products) is necessary [13].

The microwave (MW) irradiation technique is widely applied in some areas of chemistry [14] and technology to produce or degrade various materials and chemical compounds [15], as well as in the study of chemical processes. Some of its advantages are: a) rapid heating is simply achieved; b) the energy is accumulated in the material; c) the environment do not need to be heated, so energy savings are possible; d) there is no direct contact between the energy source and the material; e) the heating can be easily automated.

A new synthesis method of fullerenes using microwave-induced naphthalene-nitrogen plasma at atmospheric pressure was reported in 1995 [16]. Some positive results were reported in 1999 by MW-heating of chloroform in presence of argon[17].

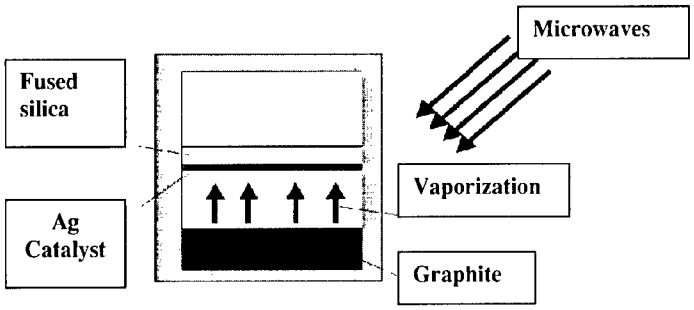


Fig.1. Experimental scheme of heating by microwaves.

The objective of this work is to obtain nanotubes using MW-heating and perforne their characterization by Scanning Electron Microscopy (SEM), Transmission Electron Microscopy (TEM) and Atomic Force Microscopy (AFM).

EXPERIMENTAL DETAILS

Preparation of nanotubes was carried out in a domestic MW-oven (power 800 W and frequency 2.45 GHz). The MW-action allows the graphite heating without direct contact with the energy source; the process control is achieved varying the power and heating time from 20 to 90 min. The samples were prepared from powdered graphite (99 %) and put into a crucible, allowing the heating up to approximately 1200°C. Silver was used as a catalyst simplifys the condensation of carbon vapor and accumulation of nanoparticles. This catalyst was used on the fused silica targets. Fig.1 illustrates the scheme of the experiment.

The obtained samples were characterized by Scanning Electron Microscopy (SEM), Transmission Electron Microscopy (TEM) and Atomic Force Microscopy (AFM). The AFM images were recorded in the contact mode in air at room temperature.

RESULTS AND DISCUSSION

It is well-known that materials absorb microwaves in different manners. In particular, graphite does not need a preliminary heating to absorb microwaves, so it can be directly MW-heated (Fig.2).

Table I. Heating time of the samples.

Sample number	Time (min)	Target	Observation
1	20	Fused silica	No CNT´s
2	20	Fused silica and Ag	Few CNT´s
3	30	Fused silica	Few CNT´s
4	30	Fused silica and Ag	CNT´s
5	40	Fused silica	CNT´s
6	40	Fused silica and Ag	CNT´s
7	60	Fused silica	CNT´s
8	60	Fused silica and Ag	CNT´s
9	90	Fused silica	Crucible was melted.

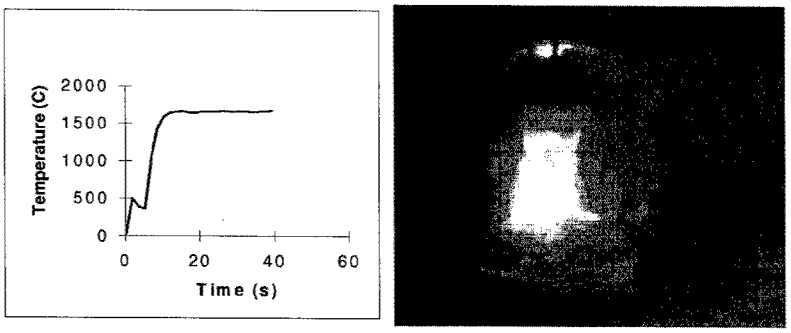
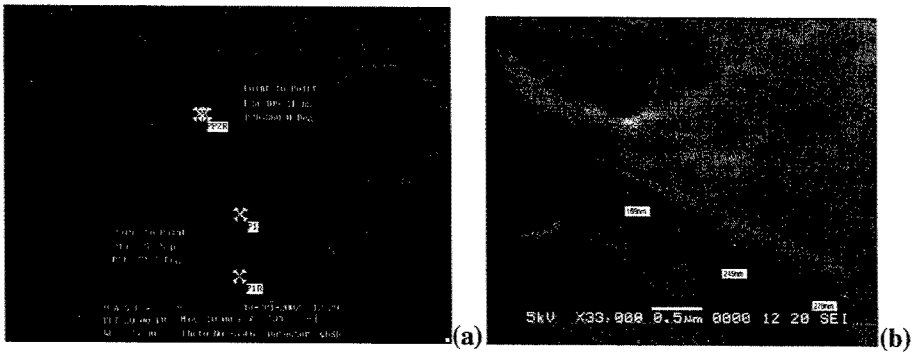


Fig.2. Microwave heating of graphite.

Various graphite samples with weight of 8 g were heated for 20, 30, 40, 60, and 90 min. As it is shown in Table I, the condensation was carried out through carbon vaporization and the process was completed in 60 min. The next step was the deposition of Ag catalyst on the fused silica targets; a series of similar experiments was carried out (Table I). It was established that, when using use of Ag as a catalyst, the deposition time averaged 30 min (Fig.3). The SEM observation of the obtained samples allowed to conclude that the size of the nanotubes are increased with heating time.

The diameter of formed CNTs about is10 nm; others investigators have reported that when using a coating with Co/SiO_2, the diameter may reach up to 0.5 μm [18]. In our experiments, the surface was covered with silver; the diameter of nanotubes increases from 168 nm to 400 nm (Fig.3(b)). The diameters of nanotubes slightly increases with increasing growth time in the range 30-60 min. Since the microwave energy is selectively absorbed by the different materials, the absorbed energy increases with the heating time.

The average growth rate calculated is about 0.3 μm/min. After heating for 20 min, cracks appear in some parts of the surface of the fused silica target, its surface even can be destroyed when the heating is applied for 60 min. Fig.4 shows a TEM image of the CNTs. Most of the carbon nanotubes are closed at both ends. The TEM images are coincident with the images of SEM. The tubes have a bamboo-like structure (Fig.4(b)).



(a) (b)

Fig.3. (a) SEM image of MWCNT's on the target heated for 60 min with catalyst; (b) Image for the bamboo-like structured CNT's grown on the target heated for 30 min with catalyst.

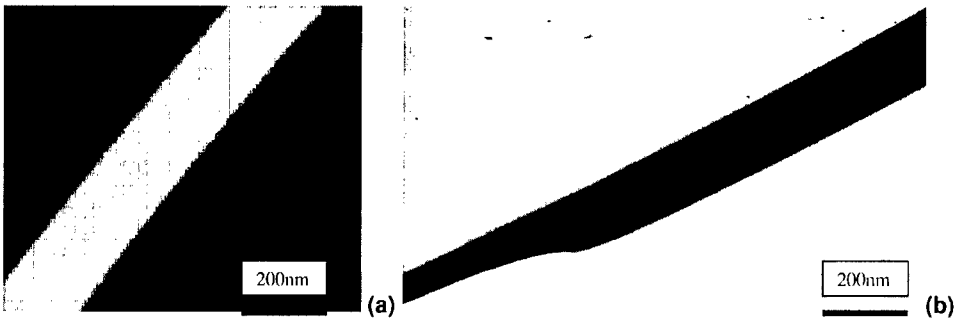


Fig.4. (a) TEM image of CNT on the target heated for 30 min with catalyst; (b) a CNT with a bamboo-like structure.

We measured TEM images of the CNTs to investigate the structure dependence on the catalyst (Table II). The CNTs exhibit exclusively a multi-walled bamboo-like structure for the Ag calatyst. The CNTs have a closed tip without not encapsulated catalyst particle and open tip without encapsulated catalyst (Fig.5). The tip with the particle is open. The tubes are the result of tip growth and metal particles are lifted-up as the tubes grew. This phenomenon has been observed and it has been postulated that the metal nanoparticles were in liquid state during nanotube growth [19].

To investigate the structure of nanotubes obtained by microwaves heating, CNT's were analyzed by AFM. According to AFM studies (Fig.6), carbon vaporization via microwave treatment produces multi-layer nanotubes (thickness 117 Å). As it is seen, the catalyst increases the diameter of tubes (Table II). The tube contains approximately 20 graphite wall layers. This result agrees well with the results of Zhang et.al. [19].

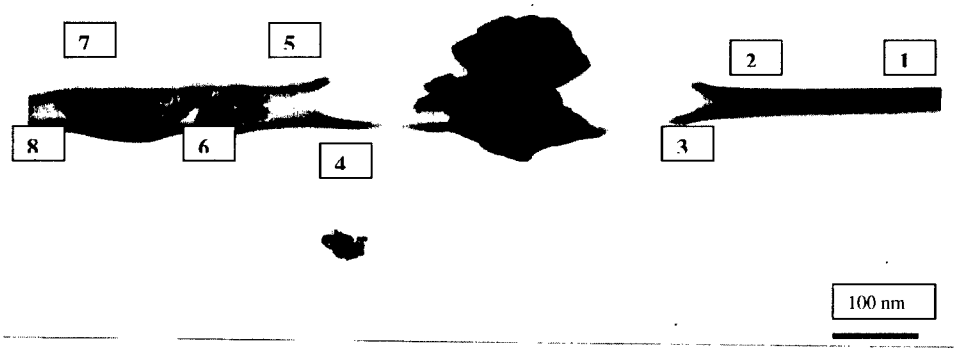


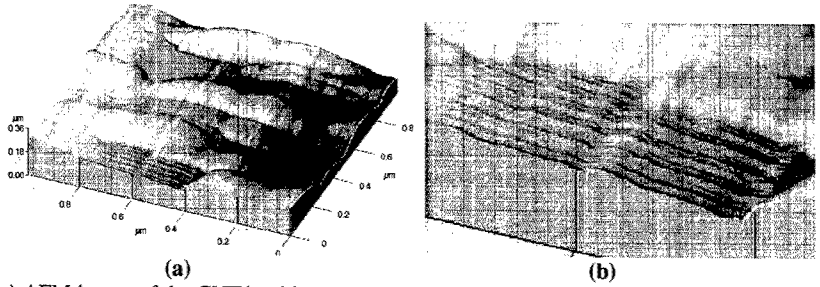
Fig.5. TEM image of CNT tip with a Ag particle in the tube and opened tip (the numbers correspond to entries in Table II).

Table II . Dependence of the diameter of CNT on presence of Ag catalyst.

Entry	Diameter of CNT, nm	Graphite sheets, nm	Channel diameter, nm	Observations
1	55 nm	18.5 nm	17 nm	Without catalyst.
2	66 nm	20 nm	26 nm	Without catalyst. Close to the open tip.
3	99.2 nm	19 nm	61 nm	Open tip.
4	110.3 nm	19 nm	82 nm	Open tip.
5	82.2 nm	20 nm	42.2 nm	With catalyst. Close to the open tip.
6	103.7 nm	17.7 nm	68.3 nm	With catalyst.
7	112.5 nm	18.5 nm	75.5 nm	With catalyst.
8	71.1 nm	19.7 nm	31.7 nm	With catalyst. Far from the Ag particles.

An easy way was reported for improving the purity of nanotubes using a domestic multimode microwave oven [20]. In the present investigation, we noted that the CNTs appeared to be highly graphitized. The nanotubes, obtained by this technique do not require further purification. The diameter of hollow CNT is constant over a long distance.

The SEM analysis of crucible surfaces allowed to observe that the heating for 60 min provokes the formation of carbon fibers with diameters up to 11.87 μm (Fig.7).



(a) **(b)**

Fig.6. (a) AFM image of the CNT´s with a one open MWCNT , (b) image of the CNT layer.

CONCLUSIONS

The vaporization technique by microwaves allows to produce nanotubes. The optimal time is 60 min. The presence of silver as a catalyst permits to decrease heating time to 30 min. As a contribution of this method, the aligned multi-layer carbon nanotubes were obtained. Their diameter is from 50 to 400 nm and the length is from 1 μm to 10 μm. Layer size is about 117 Å.

The CNTs have bamboo-like structure with empty closed compartments inside the nanotube. When we use silver as a catalyst, carbon nanotubes contain Ag particles inside and one tip is open. When nanotube diameters decreased, the layers between compartments appear more compressed. In some cases, the CNT´s are aligned in fibers up to a diameter of 5-12 μm.

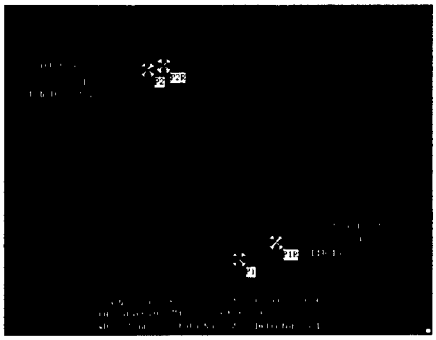


Fig. 7. SEM images of a fiber on a crucible's surface after heating for 60 min.

ACKNOWLEDGMENTS

The authors are very grateful to the CONACyT-Mexico (grant No. I39207U) and the Universidad Autónoma de Nuevo León (Monterrey, Mexico, grant No.CA804-02) for financial support, as well as to Eng. Javier Solís Rodríguez (Magnekon Company) and M.S.Claudia López Gonzalez (FIME, UANL) for technical assistance.

REFERENCES

1. S. Iijima, *Nature*, **354** (1991) 56.
2. W.B.Choi, Y.W.Jin, H.Y.Kim, S.J.Lee, M.J.Yun, J.H.Kang, Y.S.Choi, N.S.Park, N.S.Lee, J.M. Kim, *Appl. Phys. Lett.* **78** (2001)1547.
3. C.Liu, Y.Y.Fan, M.Liu, H.T.Cong, H.M.Cheng, M.S.Dresselhaus, *Science* **286** (1999) 1127.
4. J.Kong, N.R.Franklin, C.W.Zhou, M.G.Chapline, S.Peng, K.J.Cho, H.J.Dai, *Science* **287**(2000) 622.
5. D.S.Bethune, C.H.Kiang, M.S.de Vries, G.Gorman, R.Savoy, J.Vazqurz, R.Beyers, *Nature* **363** (1993) 605.
6. A.Thess, R.Lee, P.Nicolaev, H.Dai, P.Petit, J.Robert, C.Xu, Y.H.Lee, S.G.Kim, A.G.Rinzler, D.T.Colbert, G.E.Scuseria, D.Tomanek, J.E.Fisher, R.E.Smalley, *Science* **273** (1996) 483.
7. M.Terrones, N.Grobert, J.P.Zhang, H.Terrones, J.Olivares, W.K.Hsu, J.P.Hare, A.K.Cheetham, H.W.Kroto, D.R.M.Walton, *Chem. Phys. Lett.* **285** (1998) 299.
8. M.Nath, B.C.Satishkumar, A.Govindaraj, C.P.Vinod, C.N.R.Rao, *Chem. Phys. Lett.* **322** (2000) 33.
9. Jin Lee, Cheol and Park, Jeunghee, School of Electrical Engineering, *Kunsan National University, Kunsan*, (2000) 573-701.
10. Byszewsri, P. and Klusek, Z., *Optoelectronics Review*, **9** (2001) 203-210.
11. X.Ma, E.G.Wang, *Appl. Phys. Lett.* **78** (2001) 978
12. S.L.Sung, S.H.Tsai, C.H.Tseng, F.K.Chaiiang, X.W.Liu, H.C.Shih, *Appl. Phys. Lett.* **78** (1999) 197
13. E.G.Rakov, *Russ. Chem. Rev.* **70**(10) (2001) 827-863
14. Kharissova, O.V., Ortiz, U., Hinojosa, M., *Mat. Res. Soc.*, **654** (2001) AA.3.14.1-6.
15. Teooreanu I.F., *Revue Roum. Chim.*, **40**(10) (1995) 965.
16. Tesuya Ikeda, Toshiihiro Kamo, Minoru Danno, *Appl. Phys. Lett*, **67**(7) (1995) 900.
17. Su-yuan Xie, Rong-bin Huang, La-jia Yu, Jie Ding, and Lan-sun Zheng, *Applied Physics Letters*, **75**(18) (1999) 2764-2766.
18. V.Ivanov, A.Fonseca, J.B.Nagy, A.Lucas, P.Lambin, D.Bernaerts and X.B.Zhang, *Carbon*, **33**(1995) 1727.
19. W.D.Zhang,J.T.L.Thong,W.C.Tjiu,L.M.Gan, *Diamond and Related Materials*, **11**(2002) 1638-1642.
20. R.Avetik, Pradhan Bhabendra K, Chang Jiping, Chen Gugang, Eklunnd Peter C, *J. Phys. Chem. B*, **106**(34) (2002) 8671-8675

Mat. Res. Soc. Symp. Proc. Vol. 740 © 2003 Materials Research Society I7.26

Structure and elastic properties of immiscible LDPE-PP blends: dependence on composition

Julia S. Petronyuk, Olga V. Priadilova, Vadim M. Levin, Olga A. Ledneva, Anatolii A. Popov

Institute of Biochemical Physics, Russian Academy of Sciences,
119991, 4 Kosygin St., Moscow, Russia

ABSTRACT

Local elastic properties and microstructural features of low-density polyethylene-polypropylene (LDPE-PP) blends have been studied by microacoustical technique, differential scanning calorimetry and infrared spectroscopy. Focused ultrasonic beam of acoustic microscope has been employed to measure elastic wave velocities, bulk and shear elastic moduli and Poisson ratio. The experiments show that the mechanical properties of immiscible LDPE-PP blends are non-additivily changeable in relation to ones of primary gomopolymers. Maximum of the moduli values is achieved with small addition of LDPE to PP. Additional drawing of bipolymer shows essential increasing of orientation ability for PP chains in 5/95 – 10/90 % LDPE-PP compositions. DSC curves show no significant deviations in melting temperature and crystallinity degree for different compositions of PP and LDPE phases. Internal microstructure has been imaged for the blends by acoustic microscopy technique. It allows revealing dispersivity of components over the blend body.

INTRODUCTION

Mixing of the polymers leads to production of materials with positive properties omitting more expensive stages of the new polymer synthesis. Polyolefins are the main components of plastic wastes and scrapes [1] and their regeneration as a blend has a practical importance. One of the most extensively studied polyolefins are polyethylene and isotactic polypropylene. Many papers are devoted to investigations of the polyethylene-polypropylene blends [2-4]. Mechanical property of the blends and their relation to structural organization is one of the most attractive topic of consideration. Polymer mixing can lead to improvement of the properties [5]. Variation in properties depends on blend composition, morphology and interaction between phases as well as synthesis conditions [6,7].

A series of structure sensitive methods was used in this study – DSC, IR-spectroscopy and acoustic microscopy techniques (AM). In particular, modern ultrasound methods appear a valuable tool for the local elastic property characterization (compressive as well as shear elastic moduli) and monitoring of internal microorganization [8].

EXPERIMENTAL

Material

Isotactic polypropylene (PP) (T_m = 159.6 °C, χ = 47%, ρ = 0.9076g/cm^3, M_w = 400 000, M_n = 150 000, M_w/M_n = 2.7) and polyethylene (PE) (T_m = 106.1 °C, χ = 22%, ρ = 0.9271g/cm^3, M_w = 80 000, M_n = 30 000, M_w/M_n = 3) were the objects under investigation. The extrusion method of the blend preparation is described in [9]. Isotropic films have been fabricated by pressing with

cellophane substrate at temperature of 190 °C with following quenching in water (0 °C). Thickness of PE-PP films was ~ 200 μm.

Acoustic microscopy

Methods of quantitative acoustic microscopy have been applied to measure local elastic properties and their distribution in polymer blends [8,10]. Short probing pulses of high-frequency focused ultrasound (with pulse duration 30-70 ns and operation frequency 50 MHz) are excited in a coupling fluid and interact with a specimen placed in the focal region (focal spot was 50-90 μm diameter). The probing beam partly reflects from the specimen face, partly penetrates into the specimen as two convergent beams of longitudinal (*L*) and transverse (*T*) waves. Both of the beams undergo reflection and mode conversion (*LT*) at the back surface of the specimen. The output signal of the acoustic microscope is a series of echo pulses. The pulses are separated in time by intervals τ_L, τ_{LT}. Values of sound velocities in a specimen under investigation (d – specimen thickness) are expressed through these intervals:

$$c_L = \frac{2 \cdot d}{\tau_L}; \; c_T = \frac{d}{\tau_{LT} - \frac{1}{2} \cdot \tau_L}. \qquad (1)$$

Data on acoustic wave velocities can be applied to elastic moduli calculation [11].

The technique demands solid identification of echo-signals. If a specimen possesses bulk microstructure (for instance, contains extended defects, pores, phase interfaces and so on) the output signal of the acoustic microscope involves additional sets of echo pulses stemming from reflection at these details. The additional signals can be used to form acoustic imaging (C-scans) for studding topology of the inclusions inside of the specimen body. Another type of acoustic images is B-scans that are formed as traces of echo signals along scanning direction.

Differential scanning calorimetry (DSC)

Degree of crystallization and melting temperature has been studied by DSC technique [12,13]. DSC thermograms were obtained on a DSM-2M differential scanning calorimeter by heating at 8 °C/min. Average value of the melting temperature was measured by maximum of the melting peak in DSC thermograms.

Polarised infrared spectroscopy (IR)

IR-spectra of polymer blend and undiluted components were carried out on "Specord IR-71" spectrophotometer. Degree of orientation was characterized by band dichroism at 840 cm^{-1} and 710 cm^{-1} for PP and PE, correspondingly [14,15].

RESULTS AND DISCUSSION

Acoustic microscopy

Basing on time-delays (τ_L, τ_{LT}) measuring and geometry (d) data the longitudinal C_L and transverse C_T wave velocity have been calculated (equation 1). Poisson's ratio μ, bulk K and shear G elastic moduli have been derived from the data on sonic velocity and density for different compositions of the LDPE-PP blend. Density ρ was measured by the Archimedian principle (accuracy was 0,005 g/cm^3). Results of the measuring and calculations are presented in Table I. The data is given after averaging over three samples for each composition. Elastic moduli show higher

values than those found in tensile tests [2]. This difference can be result from variation in polymer morphology, methods of preparation and, probably, from probably influence of relaxation processes [16]. The employed frequency of 50 MHz is much higher than characteristic frequencies for many relaxation processes in PP and PE.

Our experiments give values of the elastic moduli of LDPE-PP blend are essentially higher than moduli of individual homopolymers in the wide range of compositions. It means the rule of additivity is invalid for the LDPE-PP mixture. Starting from pure PE increasing the PP content in blend composition results in growth of elastic moduli. The growth is accompanied by oscillations that form series of intermediate maxima and minimuma. These features are inherent in all types of the moduli - bulk K and shear G moduli and Young modulus E. In our experiments 10, 35, 70 and 95 wt% PP containing blends are characterized by occurrence of local maximums of the velocity value and moduli. Absolute maximum of elastic property is achieved for the blend with 95% PP. Figure 1 shows behavior of elastic wave velocity in depend on the blend composition. We plot values of sonic velocity for three identical specimens for each composition. It can be seen that values of local maxima and minima are varied a little from one sample to another but the general character of the dependence remains the same. Earlier papers reported about the same behavior of elastic moduli for LDPE-PP blends with growth the PP content [17-21]. Position of the absolute maximum can vary and correspond to a little different bipolymer composition. The difference between experimental data shows that the mechanical properties of blends are probably affected by the mixing conditions.

Variation of elastic characteristics observed in our experiments can be evidence that the different PE-PP compositions possess a diverse structural organization. The correlation between mechanical properties and PE-PP blend morphology has been studied by *Lovinger A. et.al.* [2], which showed that the PE could be considered as an agent of stiffness increasing for PP matrix. The recent article [22] report about structural transformation of polyethylene phases in PE-PP blends; some authors [23] reported that polypropylene and polyethylene could be miscible at some crystallization temperatures.

Values of elastic characteristics for the blend with small PE addition surpass the elastic moduli of pure PP and PE.

Table I. Longitudinal C_L and transverse C_T velocities for different composition of PE-PP blend Accuracy of measurement 2,5% and 1% for longitudinal and transverse wave velocities respectively; K and G are bulk and shear elastic moduli; E is Young modulus; μ is Poisson ratio.

PP-PE %	ρ, g/cm^3	C_L, km/s	C_T, km/s	K, GPa	G, GPa	E, GPa	μ
0/100	0.93	2.09	0.83	3.15	0.62	1.75	0,41
10/90	0.93	2.24	0.99	3.37	0.90	2.48	0.38
20/80	0.93	2.09	0.91	2.96	0.76	2.11	0.38
35/65	0.92	2.51	1.10	4.28	1.10	3.04	0.38
50/50	0.92	2.26	1.00	3.43	0.92	2.53	0.38
70/30	0,92	2.53	1.11	4.38	1.13	3.11	0.38
80/20	0.91	2.38	1.07	3.78	1.06	2.91	0.37
90/10	0.91	2.52	1.14	4.29	1.20	3.30	0.37
95/5	0.91	2.63	1.17	4.68	1.27	3.50	0.38
100/0	0.91	2.20	0.94	3.11	0.83	2.28	0.38

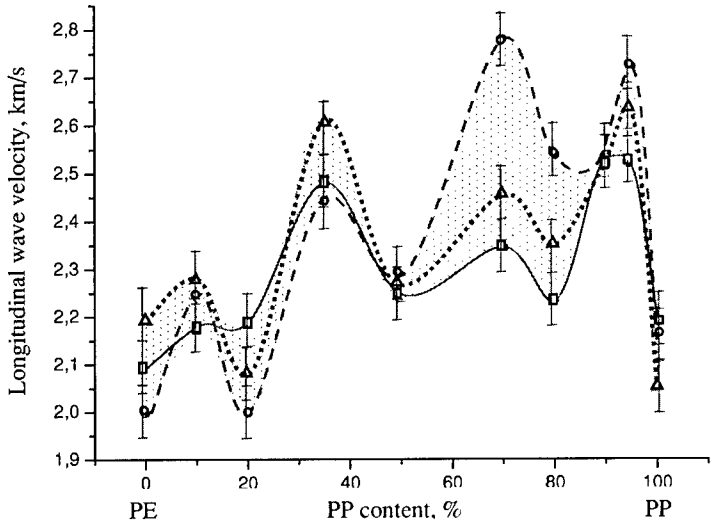


Figure 1. Effect of the PE-PP blend composition on elastic wave velocity. Longitudinal wave velocity has been measured for the three sets of the blend compositions. Different lines show values for different samples.

This peculiarity can result from increasing elastic moduli of blend components caused caused by mutual influence of one components to structure of the other. It is possible strong affect of interfacial layers between phase domains on acoustic property of the blend.

LDPE-PP mixtures tend to separate into individual phase clusters. The acoustic images (B- and C-scans) of the 50-50 wt% PE-PP composition are presented in figures 2a,b. The B-scan gives a cross-section of a blend sample; the C-scan visualizes structure of a internal layer parallel to the specimen face.

The images are formed by echoes are recorded within a fixed time interval. The interval can include echo signals from the whole specimen (1D scanning in this case gives the B-scan shown in figure 2a) and only a part of it (2D scanning over the specimen in this case gives the C-scan shown in figure 2b). Contrast of acoustic images is caused by variations in signal amplitudes and, accordingly, in reflectivity of phase interfaces.

Acoustic images 2a and b include reflections from interphases, which are seen as bright lines or domains. Sizes and distribution of these details characterize the phase dispersion of the blend. The same internal structure with numerous interfaces is characteristic for quite a wide range of concentrations: 30-70 wt% PE-PP ...35-65 wt% PE-PP. Number of details in acoustic images diminishes for low concentration of PE or PP.

It is difficult to associate directly the remarkable PE-PP blend morphology with variations in elastic moduli. Stiffening the blend for high PP content as well as the moduli oscillations could originate as from formation of interphase compatibilized transition layers so from bulk effects of mutual influence of polymer networks.

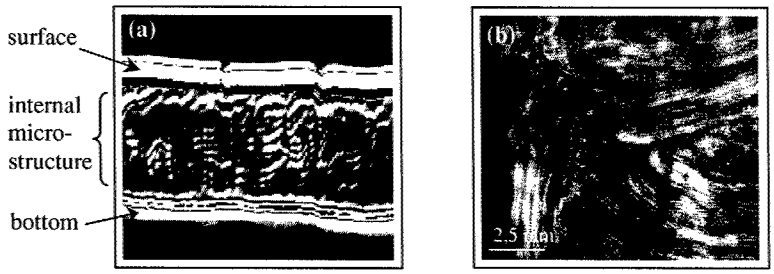


Figure 2. Acoustic images of PE-PP blend with 50-50 wt.% composition: **(a)** B-scan with numerous internal microreflections; **(b)** C-scan with phase or elastic properties distribution of the blend.

Differential scanning calorimetry (DSC)

The melting temperature for the undiluted PP and PE is different ($T_{m\,PP}$ = 159.6 °C and $T_{m\,PE}$ = 106.1 °C); as a result their structures are formed separately. The DSC curves have been used to detect melting temperature and crystalinity dependence on the blend composition. Results of investigation are presented in Table II. DSC curves show no significant deviations in melting temperature and crystallinity degree for different compositions of PP and LDPE phases.

PP-PE wt%	Crystalinity degree, %		Melting temp., ^{0}C	
	PP	PE	PP	PE
0/100	–	22	–	106.1
10/90	42	21	159.6	106.6
20/80	43	22	159.1	106.6
35/65	41	18	159.1	107.1
50/50	45	17.5	160.6	106.6
70/30	42	16	159.6	105.6
90/10	41	18	160.1	107.6
95/5	44	15	160.1	105.6
100/0	47	–	159.6	–

Table II. Melting temperature and crystalinity degree dependence on the PE-PP blend composition,

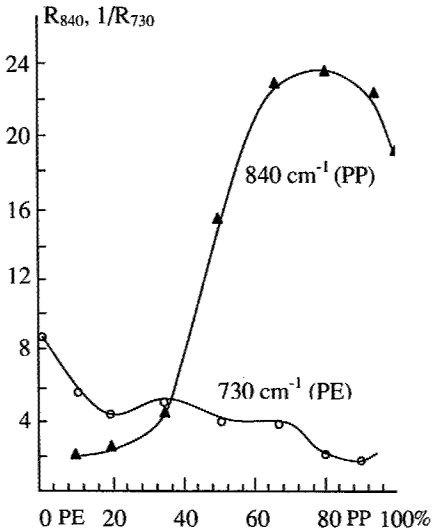


Figure 3. Effect of the PE-PP blend composition on orientation degree R.

Infrared spectroscopy (IR)

The study of the oriented PE-PP system by IR-spectroscopy shows that increase of orientation degree for the PP starts nearby 35 wt% and achieves the maximum for the 80-20 wt% PP-PE blend (figure 3). At small percents PP does not form continuous structure and is involved in PE matrix as discrete structural elements. In this case, the applied stress induces orientation processes in PE matrix while PP grains are weakly deformed only.

CONCLUSIONS

Study of elastic properties for the PE-PP blend carried out by microacoustical technique shows non-monotonical dependence on blend composition. As increasing the PP content elastic moduli of the blend are growing accompanied by formation of intermediate maxima and minima. The absolute maximum is achieved for high PP content but not for pure PP. Apparently, the PE-PP mixture is not absolutely immisible as accepted. The components influence mutually on their state. Acoustic images of the blend microstructure show laminate dispersion of the polymer phases. Poor adhesion at interphases as well as formation of a new stiffer phases can cause presence of numerous reflectors in the specimen body of the PE-PP system. Results of our elastic moduli measurements force us to support the second explanation.

REFERENCES

[1] Paul D.R., Viscon C.E. and Rose E.E. *Polym.Eng.Sci.* **1972** 12,157
[2] Lovinger A. et.al. *J.Appl.Polym.Sci.* **1980** v.25, p 1703-1713
[3] Kruszewski M., Galeski A., Pakula T., Gralowika J. *J.Colloid and Interface Sci. A*, **1973**, v. 44, №2, p. 85.
[4] Titova N.M., Popov V.M. et.al. *Compos.Mater*, USSR, **1982** №12, p.11
[5] Hourston D.J., Schafer F-U *Polymer* **1996**, 37(16) 3521-30.
[6] R.C.Willemse et.al.*Polymer* **1999,** 40, 6651–6659
[7] R.C.Willemse et.al.*Polymer* **1999,** 40 827–834
[8] R G.Macv, Levin V.M. et.al. *IEEE Trans.*, UFFC, **1997** v.44, №6, pp.1224-1231
[9] Ledneva O.A., Popov A.A., Zaikov G.E. *High Molec.Sys.*,USSR.B **1990** E32 №10,p. 785.
[10] Q.L. Zhang, V.M. Levin, et.al. *Progress in Natural Science*, **2001**v.11,suppl.,p.160,
[11] W.P.Meson *Phys.Acoustics*, **1964** v.1
[12] Bershtein V.A., Egorov V.M. *Differential scanning spectroscopy in chemical physics of polymers*, **1990** S.-Petersburg.
[13] Cipitoiu A.,et.al. *IUPAC, Macro83*, Budapesht, **1983** Sec.4, p.727
[14] Dechant J.,et.al. *Ultrarotspectroscopische untersuchungen an polymeren*, **1972**Berlin
[15] Schmidt. G.G. *J.Polym.Sci.A*, **1963** v.1, №7 p.2317
[16] K.Adachi, G.Harrison, J.Lamb, A.M. North, R.Petrick, *Polymer* **1981**, 22, 1032
[17] Plochocki A.P.et. al. *Polymer* **1965**, 10, p.23
[18] O.F.Noel and J.F.Carley *Polym.Eng.Sci.* **1975**15,117 ()
[19] R.D.Deanin and M.F.Sansone *Polymer.Prep.Am.Chem.* **1978**19(1), 211
[20] Wilkinson A.N. and Ryan A.J. Polymer processing: structure development (Kluwer, Dordrecht, The Netherlands, **1998]**
[21] Slonimskii J.J.et. al. *Polym.Sci.* **1964**USSR, 6, p.900
[22] J.Li, R.A. Shanks, Y.Long *Polymer* 42 **2001** 5321-5326
[23] M. Naiki, T. Kikkawa *Polymer* 42 **2001** 1941-1951

Mat. Res. Soc. Symp. Proc. Vol. 740 © 2003 Materials Research Society I7.27

Deformation-induced crystallization and amorphization of Al-based metallic glasses

Rainer J. Hebert and John H. Perepezko
Department of Materials Science and Engineering, University of Wisconsin-Madison, Madison, WI 53706, U.S.A.

ABSTRACT

A main requirement for the application of nanostructured materials for structural applications is their thermal stability. Structural materials are often exposed to mechanically-induced stress states. Nanomaterials for structural applications should therefore retain their microstructure not only within a defined temperature range but also under applied load. Cold-rolling experiments with melt-spun $Al_{87}Ni_{10}Ce_3$ ribbons containing a dispersion of nanocrystallites in an amorphous matrix demonstrate that during the continued deformation through repeated rolling and folding crystallization as well as amorphization reactions could be induced. The results indicate that in addition to the microstructure control through annealing of precursor materials, deformation processing represents an effective approach to the synthesis of amorphous and nanophase composite materials.

INTRODUCTION

Strengthening mechanisms based on the dispersion of second-phase particles or fibers are fundamental to many structural materials. Among the latest examples for composite materials are amorphous, Al-based alloys containing nanocrystallites. The high density (approximately 10^{21} to 10^{22} m^{-3}) of primary Al-nanoparticles or quasicrystals dispersed in the amorphous matrix contributes to an exceptional specific strength. For example, a tensile strength of 1560MPa has been measured for $Al_{88}Ni_9Ce_2Fe_1$ melt-spun ribbons [1,2]. The nanocrystallites are induced through annealing of amorphous precursor materials. Of particular interest are therefore marginal glass-formers, i.e. amorphous systems that reveal a primary crystallization reaction of Al. The temperature range for primary crystallization reactions is between 170ºC and 280ºC for most Al-based systems. Due to the high cooling rates of 10^5-$10^6$$Ks^{-1}$ that are necessary to avoid growth of nuclei or nucleation reactions during the melt-spinning process [3] bulk samples can not be processed directly for the alloys used so far.

Current efforts to produce bulk amorphous Al alloys focus mainly on the compaction and extrusion of amorphous, atomized powders [4,5]. In many cases the deformation of amorphous phases was observed to yield a crystallization reaction, for example upon cold-rolling of Al-Y-Fe and Al-Sm based amorphous ribbons [6], upon bending of different Al-based amorphous ribbons [7], warm-extrusion of gas-atomized amorphous powders [4,5] if the extrusion ratio exceeds a critical value or nanoindentation of a Zr-based glass [8]. A different approach towards bulk amorphous nanocomposites is the continued rolling and folding of crystalline, elemental multilayer arrays [9,10]. After several rolling and folding cycles of Al-Sm multilayer samples, for example, a glass-transition could be detected [11]. The observation of cold-rolling induced crystallization reactions of melt-spun amorphous ribbons on one hand and the amorphization of crystalline multilayers on the other hand suggests that a cyclic crystalline-to amorphous transformation might occur during the deformation processing, similar to the cyclic

transformation behavior of ball-milled Co-Ti and Al-Zr powders [12]. In this work results of rolling experiments with partially crystalline $Al_{87}Ni_{10}Ce_3$ ribbons are highlighted. The partially crystalline structure of the $Al_{87}Ni_{10}Ce_3$ ribbons is useful in testing whether the crystalline fraction in the amorphous matrix is enhanced or dissolved with cold-rolling. The rolling of the ribbons serves therefore as a tool for a systematic investigation of changes in the microstructure and the crystallization behavior upon deformation.

EXPERIMENTAL PROCEDURE

Melt-spun ribbons with a length of about 2.5cm, each, were aligned parallel to each other as a first layer. Shorter ribbon pieces were then arranged in a second layer on top of the first layer such that the shorter ribbons in the second layer were perpendicular to the first layer and covered the ribbons of the first layer entirely. This bilayer sample was then rolled between steel sheets in a first step. This process leads to flow and compaction of the ribbons into one piece. Afterwards, the piece was rolled directly in the rolling mill at the highest deformation level (distance between the rollers set to zero). Then the piece was cut into 2 or 3 smaller pieces that were subsequently stacked on top of each other. This stacked array was then rolled again between steel sheets, and eventually without the sheets, directly in the mill. This procedure was then repeated. The strain was calculated by measuring the thickness after the stacking, before the rolling, and after the rolling. For example, when the thickness after the stacking was 3 units and after the rolling 1unit, the strain was determined as ln3.

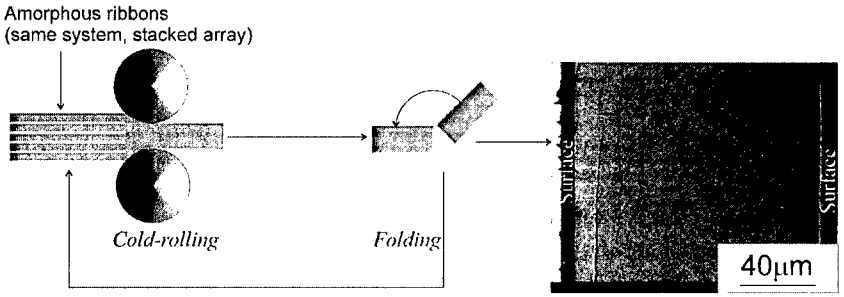


Figure 1. Schematic illustration of the folding and rolling process (left). The SEM image (right) depicts a cross-section of $Al_{85}Ni_{10}Ce_5$ ribbons that were processed according to the schematic illustration. The strain for the sample is approximately –10.

The X-ray analysis was performed with a Cu-Kα source, the DSC results were obtained in a Perkin-Elmer DSC-7 system. For the TEM analysis, samples were ion-milled at a final milling angle of 11° with a total current of approximately 2.5mA. All samples were cooled with liquid nitrogen during the TEM sample preparation. The TEM images were taken with a Philips CM-200 TEM . All ribbons were melt-spun in a single-roller melt-spinner with a copper wheel of 30cm in diameter and a wheel-speed of 55m/s. All ribbons used for the rolling experiments were examined by XRD for crystallinity prior to the rolling. For the experiments that entailed a comparison between as-spun and cold-rolled ribbons from the same system, different pieces

from the same ribbon have been used for all experiments. This ensured that the structure of the samples prior to the experiments were nearly identical.

The rolling procedure is illustrated schematically in figure 1. Added in figure 1 is a SEM cross-sectional image of an $Al_{85}Ni_{10}Ce_5$ melt-spun sample that was cold-rolled several times to a total strain of approximately –10. The thickness of the sample in figure 1 is approximately 130μm while the initial ribbon thickness was about 30μm. The SEM image shows that aside from two cracks no layer structure is visible suggesting that this method of repeated folding and rolling of ribbons is capable of providing sheet material.

RESULTS

Partially crystalline melt-spun $Al_{87}Ni_{10}Ce_3$ ribbons were selected for the current experiment (figure2(a)). In addition to a broad amorphous peak, the Al(111) and Al(200) peaks are visible as well as additional peaks with low intensities. The X-ray patterns of the cold-rolled samples demonstrate that the crystalline fraction in the sample decreases until crystalline peaks are no longer visible at a strain of approximately –4.3 and –7.9. In the X-ray patterns of the samples that were rolled at a strain of –4.3 and –7.9 a distinctive shoulder is observed at an angle of 45º 2Θ.

The isochronal DSC traces for the as-spun and cold-rolled samples are shown in figure 2b. The trace of the as-spun ribbon reveals a strong exothermic signal at temperatures below 110ºC followed by a primary crystallization reaction with an onset of 180ºC. At 340ºC an additional exothermic reaction occurs. The analysis of the peak onset for the primary crystallization peak shows a decrease in the onset temperature from 180ºC to 175ºC at a deformation level of –4.3. Upon further deformation the onset temperature of the primary crystallization peak shifts to approximately 150ºC while the minimum of the peak decreases only from 200ºC to 195ºC, i.e. the primary crystallization peak broadens.

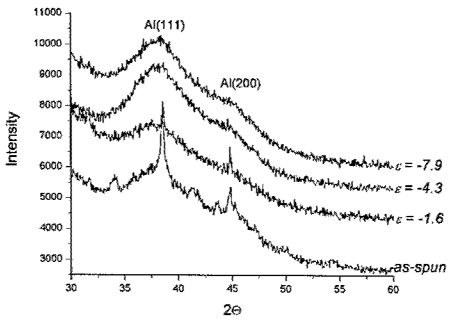


Figure 2(a): X-ray patterns of the $Al_{87}Ni_{10}Ce_3$ ribbons in the as-spun state and at different cold-rolled levels.

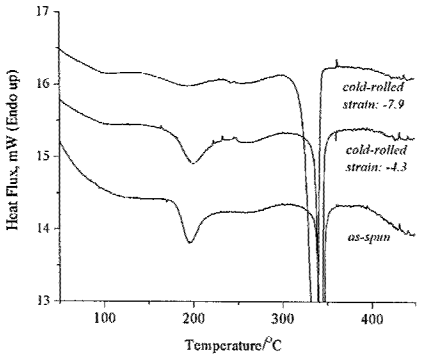


Figure 2(b): DSC traces of as-spun ribbon and after cold-rolling (heating rate 20K/min).

From the XRD measurements it is evident that the as-spun sample contains at least two crystalline phases that gradually vitrify during the rolling process. The shift of the primary

crystallization peak in the DSC trace to lower temperatures between the sample rolled at –4.3 and –7.9 is similar to the behavior observed for the $Al_{88}Y_7Fe_5$ sample that was fully amorphous in the as-spun state but crystallized with rolling [6]. This suggests that the $Al_{87}Ni_{10}Ce_3$ sample could crystallize with further rolling once the crystalline phases have dissolved. The bright-field (BF) TEM images in figures 3-6 help to gain a better understanding of the deformation-induced structural changes in the sample. Figure 3 depicts the as-spun sample. It is apparent that crystallites exist on two different size-scales: one class with a size in the 7-15nm range, the size range of the bigger particles between 25nm and approximately 100nm (particles with a size of about 100nm were observed, but are not shown in the image). In figure 4 three different positions of the sample rolled at a strain of –1.6 are shown. Figure 4(a) is similar to the structure of the as-spun sample. Figure 4(b) shows a transition between a structure similar to the as-spun sample and a structure with very small particles (mostly <6nm). Moreover, the dark particles in the transition region (indicated by arrows) reveal an elongation in the same direction. A similar directionality is observed in figure 4(c). Here, the particles are not only elongated, but

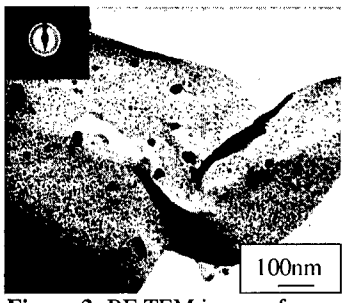


Figure 3: BF-TEM image of as-spun $Al_{87}Ni_{10}Ce_3$ ribbon. Inset shows selected area electron diffraction pattern (SAEDP).

aligned in rows. The particles in the rows break into smaller units. In between the rows, nearly particle-free regions can be observed.

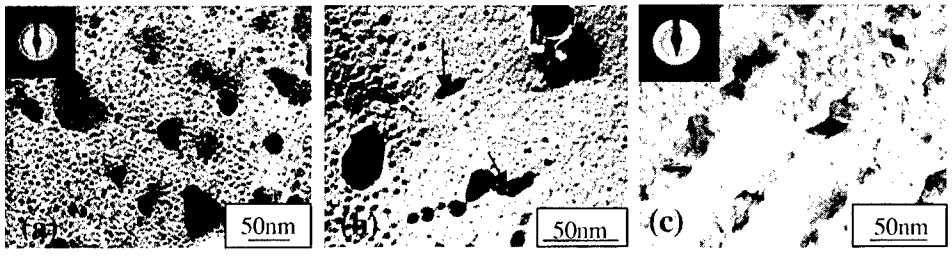


Figure 4: BF-TEM images of the rolled sample at a strain of –1.6. Insets show SAEDP.

The electron diffraction pattern in the BF-TEM image of the sample at a strain of –4.6 (figure 5) shows that at this strain level, the sample is mostly amorphous. Although no peaks can be identified in

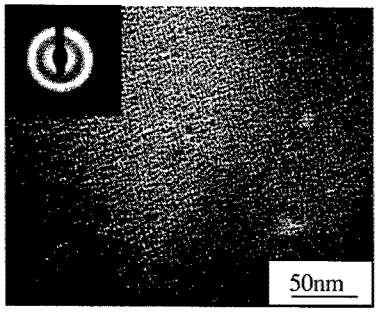


Figure 5: BF-TEM image of the sample rolled at a strain of –4.3. Inset shows SAEDP.

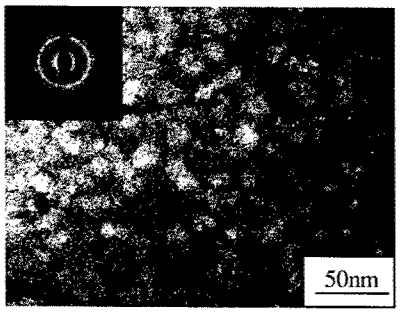


Figure 6: BF-TEM image of the sample rolled at a strain of –7.9. Inset shows SAEDP.

the X-ray pattern, particles are observed in the TEM images, albeit at a lower density than in the as-spun state. Figure 6 demonstrates that upon continuation of the deformation to a strain of -7.9 the particle density increases again. Both, figures 4 and 5 are representative for the microstructures at the respective strain levels as the survey of several different locations in the sample during the TEM monitoring indicated.

DISCUSSION

The main shift in the onset temperature of the DSC primary crystallization peak occurs in the $Al_{87}Ni_{10}Ce_3$ sample between a strain of –4.3 and –7.9 At a strain of –4.3 the shift in the onset of the primary crystallization temperature is only 5K towards lower temperatures, but at a strain of –7.9 the onset temperature has shifted about 20K towards lower temperatures compared with the onset temperature of the as-spun sample. The X-ray and TEM experiments suggest that the slow change in the DSC behavior between the beginning of deformation and a strain of about –4.3 could be related to the transformation of the partially crystalline structure to an amorphous state with a low particle density (figure 5). The mechanism of this transformation appears to be based on a deformation-induced elongation of the particles with subsequent rupture. This would mean that the particles that crystallized during the melt-spinning process can undergo plastic deformation. Figure 4 furthermore demonstrates that during the deformation-induced dissolution of the particles at a given strain only parts of the samples are transforming while other parts still retain their as-spun structure (figure 4, left image). This is in agreement with the idea of localized deformation of amorphous structures in shear-bands at lower temperatures [13]. However, the lateral extension of the areas revealing a band structure as displayed in figure 4, right image, is of the order of several hundred nanometers. The thickness of shear-bands in bent $Al_{90}Gd_5Fe_5$ ribbon is reported to be 10-15 nanometers [14]. The transformation does therefore not proceed in individual shear-bands.

An important finding is the observation that the dissolution of the crystalline phases with rolling is converted at higher strain levels. The selected area electron diffraction pattern (SAEDP) in figure 6 shows clearly the presence of crystalline particles while the SAEDP in figure 5 is more indicative of an amorphous phase. A cyclic crystalline-to amorphous transformation behavior was observed for ball-milled Co-Ti or Al-Zr [12] powders suggesting that upon further deformation of the ribbons the crystalline fraction might decrease again, but the strain regime beyond a strain of –8 has not yet been explored.

As an alternative to a cyclic transformation behavior the microstructure of the ribbon may evolve towards a steady-state that depends on the external forcing condition that scales with the strain-rate as well as on an average relocation distance per strain increment which is a material property [16]. For the strain-rate used in the rolling experiments the steady-state structure would be an amorphous phase containing Al nanoparticles with a size of about 5-20nm as observed for $Al_{88}Y_7Fe_5$ ribbons [6] and in this work for $Al_{87}Ni_{10}Ce_3$ partially crystalline ribbons.

SUMMARY

Cold-rolling experiments with melt-spun $Al_{87}Ni_{10}Ce_3$ ribbons containing fcc-Al nanocrystals and an additional crystalline phase dispersed in an amorphous phase resulted in an amorphization reaction followed by an increase in the crystalline fraction with continued rolling. The results show that the microstructure during the amorphization reaction is heterogeneous. While some areas reveal a banded structure with particles aligned in rows that are parallel to each other, some parts of the sample are not yet affected by the deformation. The TEM images suggest that the amorphization reaction occurred by deformation-induced fracture/rupture of the particles in the matrix. The rolling experiments with melt-spun amorphous Al-based alloys show that deformation processing offers the opportunity to control their microstructure.

ACKNOWLEDGEMENTS

The continued support and encouragement of Dr. W. Mullins, Army Research Office, for the study of the deformation-induced crystallization behavior of Al-based amorphous materials is most gratefully acknowledged (DAAD 19-01-1-0486).

REFERENCES

1. Y.H. Kim, A. Inoue, T. Masumoto, *Mat. Trans. JIM* **31**, 747 (1990).
2. Y.H. Kim, A. Inoue, T. Masumoto, *Mat. Trans. JIM* **32**, 599 (1991).
3. J.H. Perepezko, R.J. Hebert, *JOM* **54**, 34 (2002).
4. Y. Kawamura, H. Kato, A. Inoue, T. Masumoto, *Int. J. Powder Met.* **33**, 50 (1997).
5. D.J. Sordelet, E. Rozhkova, P. Huang, P.B. Wheelock, M.F. Besser, M.J. Kramer, M. Calvo-Dahlborg, U. Dahlborg, *J. Mater. Res.* **17**, 186 (2002).
6. R.J. Hebert, J.H. Perepezko, *Mater. Sci. Engr. A* (in press).
7. H. Chen, Y. He, G.J. Shiflet, S.J. Poon, *Nature* **367**, 541 (1994).
8. J.-J. Kim, Y. Choi, S. Suresh, A.S. Argon, *Science* **295**, 654 (2002).
9. M. Atzmon, J.D. Verhoeven, E.D. Gibson, W.L. Johnson, *Appl. Phys. Lett.* **45**, 1052 (1984).
10. F. Bordeaux, A.R. Yavari, P. Desré, *Mat. Sci. Engr.* **97**, 129 (1988).
11. G. Wilde, H. Sieber, J.H. Perepezko, *Scripta Mat.* **40**, 779 (1999).
12. M. Sherif El-Eskandarany, "Mechanical Alloying" (William Andrew Publishing, 2001), pp. 209-225).
13. C.A. Pampillo, *J. Mater. Sci.* **10**, 1194 (1972).
14. Y. He, G.J. Shiflet, S.J. Poon, *Acta Met. Mat.* **43**, 83 (1995).
15. M. Sherif El-Eskandarany, K. Aoki, K. Sumiyama, K. Suzuki, *Acta Mat.* **50**, 1113 (2002).
16. R.A. Enrique, P. Bellon, *Phys. Rev. Lett.* **84**, 2885 (2000).

Modeling, Simulations, and Interfaces

Mat. Res. Soc. Symp. Proc. Vol. 740 © 2003 Materials Research Society

Atomistically Informed Continuum Model of Polymer-Based Nanocomposites

Catalin R. Picu, Alireza Sarvestani and Murat S. Ozmusul
Department of Mechanical, Aerospace and Nuclear Engineering
Rensselaer Polytechnic Institute, Troy, NY 12180

ABSTRACT

A model polymeric material filled with spherical nanoparticles is considered in this work. Monte Carlo simulations are performed to determine the polymer chain conformations in the vicinity of the curved interface with the filler. Several discrete models of increasing complexity are considered: the athermal system with excluded volume interactions only, the system in which entropic and energetic interactions take place while the filler is a purely repulsive sphere, and the system in which both filler-polymer and polymer-polymer energetic interactions are accounted for. The total density, chain end density, chain segment preferential orientation and chain size and shape variation with the distance from the filler wall are determined. The structure is graded, with the thickness of the transition region being dependent on the property and scale considered. Hence, the polymer in the vicinity of the filler is represented in the continuum sense by a material with graded properties whose elasticity is determined based on the local structure. Homogenization theory is the used to obtain the overall composite moduli. The filler size effect on the composite elasticity is evaluated.

INTRODUCTION

Polymer-based nanocomposites form a new class of reinforced polymers in which the fillers have at least one dimension less than 100 nm. These materials have macroscopic properties significantly different from those of conventional composites of same filler volume fraction [e.g.1,2]. For example, the dispersion of only 2% volume fraction of nanoparticles in thermoplastics almost doubles the yield stress and increases the Young's modulus.

The mechanisms responsible for the enhanced properties are not fully understood and controlled. It appears that interesting properties are obtained when the filler size and/or the filler wall-to-wall distance become comparable with the chain radius of gyration. Two principal ideas have been promoted in this connection: the novel properties are either due to chains connecting several fillers (the double network theory), or to the special distribution and density of entanglements in the confined polymer matrix. In all situations, it is generally accepted that the structure of polymeric chains confined between fillers and their binding to the wall are the major elements controlling the properties of the composite.

This work is part of an ongoing effort to relate the polymer structure to the macroscopic nanocomposite properties. We consider a model polymer filled with spherical impenetrable particles. The chain structure in the vicinity of fillers is determined by Monte Carlo simulations. The elasticity of the matrix is determined based on the local structure. The composite is homogenized for its overall elastic properties. We first review the main features of the polymer structure at the wall, then we present the procedure by which the continuum model is calibrated based on the discrete structure, and finally, we discuss the filler size effect on composite moduli.

Polymer structure in the vicinity of fillers

Lattice Monte Carlo simulations are performed to determine the polymer structure in the vicinity of fillers. A simulation cell containing a single filler is used (with periodic boundary conditions). The polymers are represented by a "pearl-necklace" model. The beads are free to move on a lattice surrounding the filler, the chain connectivity and the excluded volume conditions being enforced at all times. The model and the simulation procedure are described in detail in [3]. The parameters of the model are the chain size (N), the filler radius (R) and the filler volume fraction. Various types of interactions are considered in separate models: excluded volume only, excluded volume and energetic interaction in bulk polymer, excluded volume and energetic interaction between polymers and the filler. The results reported here are for the system with R = 8, N = 100 (R_g = 4.7) and filler-to-filler distance L = 32 (wall-to-wall distance of 16, i.e. twice the chain size, $4R_g$). All dimensions are in multiples of the bond length (equal to the unit of length used in the Lennard-Jones potential representing non-bonded interactions).

The total bead number density normalized by the bulk density is shown in Fig. 1a for the case in which no filler-polymer interactions are imposed. The curve labeled "athermal" corresponds to the purely entropic system in which only excluded volume interactions are allowed. This corresponds to the "high temperature" situation in which the entropic component of the free energy dominates. The curve labeled "energetic" corresponds to the system in which cohesive interactions in the bulk polymer are considered. An ample depletion layer forms next to the filler, and effect also observed in lattice MC simulations of structure next to flat interfaces. We note that continuous space discrete models predict strong density oscillations next to the wall due to packing and no depleted layer. The effect seen here is pronounced in the energetic case (low temperatures), while in the athermal system it is absent, the bead density being constant.

An entropic driving force exists for chain end segregation in the interface. The chain end number density is shown in Fig 1a for the energetic system. The end segregation has no effect on the elastic moduli of the matrix. The effect of the various model parameters is discussed in [3].

The chain number density is evaluated based on the position of the chain centers of mass with respect to the wall (Fig. 1b). The volume surrounding the filler is divided in spherical bins (concentric layers) of thickness equal to 2. The data points represent the density in each layer normalized with the bulk chain number density. The chain density is lower at the wall than in the bulk, an effect due to the excluded volume of the filler. The depletion is also driven by the

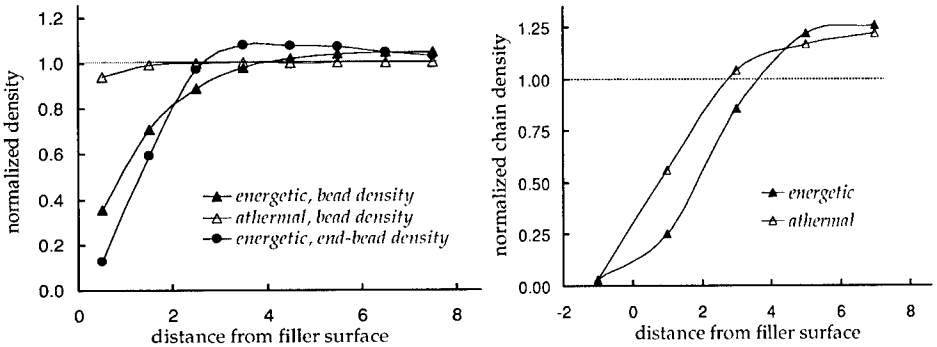


Figure 1. Bead (a) and chain (b) number density profile next to the spherical filler.

entropic force that retracts the chains from the wall (spherical or planar), and by the densification effect of the cohesive interactions in the bulk polymer (see the difference between the "energetic" and "athermal" curves). A small number of chains that wrap around the filler have their centers of mass within the particle (negative distance from filler surface).

The chain size was determined by computing the gyration tensor for chains having their centers of mass at various distances from the filler surface. In the bulk, chains have an ellipsoidal shape, the semi-axes of the ellipsoid being given by the eigenvalues of the gyration tensor. The results obtained for the present system are shown in Fig. 2. The three semi-axes of magnitude in the bulk $\lambda_1 = 3.89$, $\lambda_2 = 1.84$ and $\lambda_3 = 1.14$, are shown in Fig. 2a. Interestingly, chains having their centers of mass in the first bin next to the wall have dimensions similar to those in the bulk. The few chains having their centers of mass within the filler are swollen.

The orientation of the long semi-axis of the ellipsoidal chains is random in the bulk. As the chain center of mass approaches the wall, the chains tend to align with their large semi-axis in the direction tangential to the interface (a "docking" transition previously observed next to a flat wall). Fig. 2b shows the second moment of the orientation distribution of the long semi-axis (labeled "chain"). Perfect orientation in the tangential direction corresponds to a value of –0.5 of this measure. Preferential orientation is observed on all scales, from the bond to the chain scale. The orientation of bonds and chain end-to-end vectors is weaker than that of the coil (Fig. 2b).

Higher confinement induced by a further reduction of the wall-to-wall distance leads to a reduction of chain dimensions, with chains "docking" to the wall in all cases [3]. This result is in agreement with data published by Vacatello [4], but disagree with the model advanced by Mark and collaborators [5]. Our data are discussed against both sets of results in [3].

Elastic moduli of the system of chains

The elasticity of the system of chains is derived here based on the free energy of the system. The total free energy, W, contains three energetic and an entropic term: $W = U^{nb} + U^{b} + U^{f} - TS$ The energetic terms are due to non-bonded interactions, between beads not directly connected along a chain, to bonded interactions, between directly connected beads, and to the energetic interaction between the filler and the matrix. The stiffness of the system of chains in the model

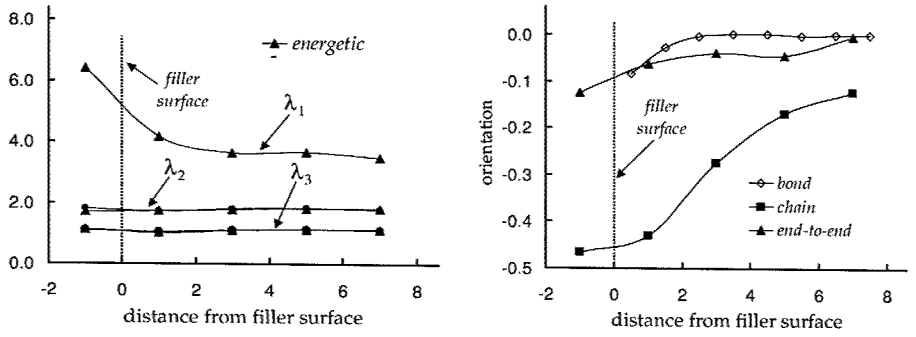


Figure 2. (a) Semi-axes of the ellipsoidal chains as a function of the position of their centers of mass with respect to the wall. (b) A measure of the preferential orientation of chains, bonds and chain end-to-end vector in the direction tangential to the spherical filler.

results as the second derivative of the free energy density ($w = W/V$) with respect to the deformation gradient tensor $\mathbf{F}$, $C_{ijkl} = \partial^2 w / \partial F_{ij} \partial F_{kl}$. Hence, the stiffness has 4 components corresponding to the respective terms in the free energy.

The total energy due to non-bonded interactions, U^{nb}, reads

$$U^{nb} = \int_{V_m} u^{nb} dV_m = \int_{V_m} \frac{1}{\Omega} \int_{V_r} n^{nb}(r_{RA}, \theta_{RA}, \varphi_{RA}) \phi^{nb}(r_{RA}) dV_r dV_m , \qquad (1)$$

where u^{nb} represents the non-bonded energy density, and V_m is the volume of the polymer matrix within the simulation cell. The non-bonded energy density may be expressed as the energy due to non-bonded interactions (cohesive energy) of a representative atom, RA, divided by the atomic volume Ω. In the integral expression of this term, ϕ^{nb} is the interatomic potential and n^{nb} stands for the density of non-bonded neighbors of the RA. The energy U^{nb} is estimated here within the local approximation. The inner integral in eqn. (1) is evaluated by neglecting the dependence of n^{nb} on $(\theta_{RA}, \varphi_{RA})$, i.e. considering that an atom located in bin p has a neighborhood similar to that of an RA located in a homogeneous bulk of density $\rho(r_p)$, where r_p denotes the radial position of bin p with respect to the coordinate system centered at the center of the filler. The function $\rho(r_p)$ is shown in Fig. 1a. For an atom located in a homogeneous material of uniform density ρ, the function n^{nb} may be expressed as $n^{nb} = \rho\, g(r_{RA})$, where $g(r_{RA})$ is the pair distribution function of non-bonded neighbors about the RA. Then, the energy density due to non-bonded interactions in bin p may be written

$$u^{nb,p} = \frac{1}{\Omega} \frac{\rho_p}{\rho_{bulk}} \int_{V_r} \rho_{bulk}\, g(r_{RA}) \phi^{nb}(r_{RA}) dV_r = \frac{\rho_p}{\rho_{bulk}} u^{nb,bulk} . \qquad (2)$$

Hence, the local stiffness in bin p, associated with non-bonded interactions, results from the stiffness of the bulk by scaling with the ratio of the local and bulk densities $C_{ijkl}^{nb,p} = (\rho_p / \rho_{bulk}) C_{ijkl}^{nb,bulk}$ Since the density varies with the distance from the wall, this relationship suggests that the matrix may be represented in the continuum sense by a material with graded elastic constants.

The contribution to stiffness of bonded interactions may be evaluated by a similar procedure. In the model considered here, the bonds are assumed to be rigid and hence, $U^b = 0$.

No energetic interactions between the filler and polymers are considered. Hence, $U^b = 0$. The more realistic case in which the polymers are attracted to the filler, while cohesive interactions are enabled in the bulk, is discussed in [6].

The entropic contribution to stiffness may be evaluated based on the classical formulation of stress production in polymeric systems and the entropic spring idea. The entropy of a chain is related to the probability distribution of the end-to-end vector, R^{ee}. For Gaussian chains (an assumption shown to be valid in the system discussed here), the entropic contribution to the free energy per chain reads $W = (3/2)kTR^{ee^2}/(C_\infty b^2 N)$. A deformation described by the deformation gradient tensor $\mathbf{F}$ changes the end-to-vector from $\mathbf{R}_0^{ee}$ in the undeformed configuration into $\mathbf{R}^{ee} = \mathbf{F} \cdot \mathbf{R}_0^{ee}$. Then, the contribution of a chain to the stiffness tensor becomes

$$C^{entr}_{iJkL} = \frac{\partial^2 w}{\partial F_{iJ}\partial F_{kL}} = \frac{3}{2}\rho^c kT \frac{2\delta_{ik}}{C_\infty b^2 N} R^{ee}_{0\,J} R^{ee}_{0\,L}, \qquad (3)$$

where ρ^c is the chain number density (given in Fig. 1b), and δ_{ik} is the Kronecker delta. The total entropic contribution to the stiffness results by integrating over the whole chain orientation distribution. In the bulk, the chains are randomly oriented in space and the entropic contribution is given by $C^{entr}_{iJkL} = \rho^c kT \delta_{ik}\delta_{JL}$. In the neighborhood of the filler, the end-to-end chain vector is preferentially oriented in the direction tangential to the filler (Fig. 2b) which leads to an anisotropic C^{entr}_{iJkL}. As discussed in [6], the anisotropy is rather weak and hence is neglected in this analysis. It results that the entropic contribution to stiffness in bin p is proportional to the entropic contribution in the bulk, the proportionality factor being the ratio of the chain number density in bin p to that in the bulk,

$C^{entr,p}_{iJkL} = (\rho^c_p / \rho^c_{bulk}) C^{entr,bulk}_{iJkL}$.

Hence, the stiffness in bin p normalized by the bulk stiffness reads

$\frac{C^p_{iJkL}}{C^{bulk}_{iJkL}} = (\rho_p / \rho_{bulk})Q_1 + (\rho^c_p / \rho^c_{bulk})\delta_{ik}\delta_{JL}Q_2$, where $Q_1 = C^{nb,bulk}_{iJkL} / C^{bulk}_{iJkL}$ and $Q_2 = C^{entr,bulk}_{iJkL} / C^{bulk}_{iJkL}$.

The variation of the two density ratios with the distance from the wall is shown in Figs. 1a and b, while Q_1 and Q_2 are constants, independent of the distance to the wall. The two terms Q_1 and Q_2 represent the fraction of the total stiffness of the bulk due to energetic and entropic interactions, respectively. Their magnitude depends on temperature and bulk density. Here, we take these quantities as parameters (note that $Q_1 + Q_2 = 1$). At low temperatures, the entropic component is small and the first term dominates. As the temperature increases, the second term becomes important. The stiffness gradient in the neighborhood of the filler corresponding to 3 pairs (Q_1,Q_2) is shown in Fig. 3a.

Once the stiffness tensor is defined in each layer, homogenization theory may be used to evaluate the moduli of the composite. For this purpose, the multi-inclusion model proposed by Nemat-Nasser and Hori [7] was used. The expression for the overall composite stiffness tensor is given by $\overline{\mathbf{C}} = \mathbf{C}^{bulk}[\mathbf{I} + (\mathbf{S} - \mathbf{I})\Phi^R](\mathbf{I} + \mathbf{S}\Phi^R)^{-1}$, where $\mathbf{C}^{bulk}$ is the stiffness tensor of the bulk, $\mathbf{S}(\Omega;\mathbf{C}^{bulk})$ is Eshelby's tensor for a spherical inclusion Ω embedded in a solid of stiffness $\mathbf{C}^{bulk}$, and $\Phi^R = \sum_{p=1}^{n}(f^p - f^{p-1})\Psi^p(\Omega;\mathbf{C}^{bulk},\mathbf{C}^p)$, $\Psi^p = -[\boldsymbol{S}(\Omega;\boldsymbol{C}^{bulk}) + (\boldsymbol{C}^p - \boldsymbol{C}^{bulk})^{-1}\boldsymbol{C}^{bulk}]^{-1}$ [7].

Filler size effect

Decreasing the size of the filler (R) at constant volume fraction requires a proportional reduction of the cell size and of the wall-to-wall distance between fillers. In this process, the thickness of the graded layer, which is essentially a function of the chain length N, does not scale. Hence, the volume fraction occupied by the graded material increases and a size effect in the overall composite moduli is evidenced. The bulk and shear moduli of the composite are evaluated for the system with 6.5% filler volume fraction. The result for the shear modulus is shown in Fig. 3b for three (Q_1, Q_2) pairs. The composite modulus is normalized by the modulus of the corresponding conventional composite, with no graded region, and having the same filler volume fraction. In the limit of large fillers, the modulus tends to that of the conventional composite (to 1 in Fig. 3b). As the minimum wall-to-wall distance between fillers becomes

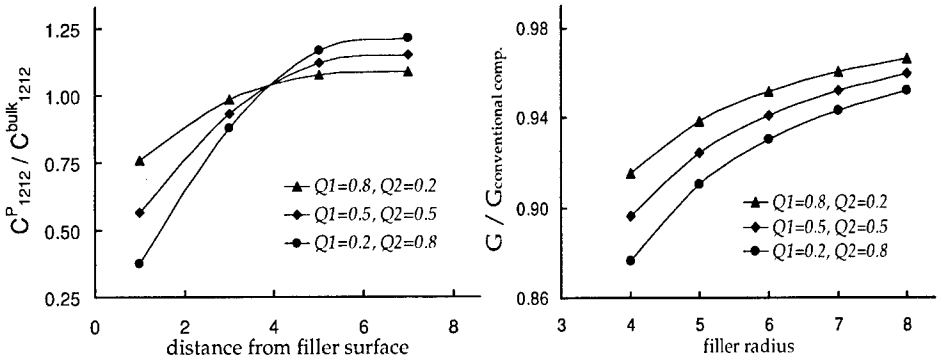


Figure 3. (a) Variation of matrix shear modulus with the distance from the wall. The variation is mainly due to reduced bead and chain number density at the wall. (b) Scaling of the composite shear modulus with the size of the filler (R) at constant filler volume fraction (6.5%).

smaller than about $5R_g$, the modulus departs from that of the conventional composite exhibiting a sensible size effect. The minimum filler separation considered was about 2Rg (which corresponds to R = 4) in order for the graded regions of neighboring fillers not to overlap. The shear modulus decreases as the filler size is reduced. The bulk modulus has a similar variation.

CONCLUSIONS

The structure of the polymer matrix in the close neighborhood of a spherical nanofiller in polymer-based nanocomposites is studied. It is shown that the chains having their center of mass close to the filler, rotate without deforming with their large semiaxis in the direction tangential to the filler. The chain number density is reduced at the wall. The stiffness tensor of this graded material was derived based on the free energy of the system which, in turn, was evaluated based on the atomic and molecular structure. The composite was represented by a multi-phase continuum model and homogenized using the homogenization theory. The effect on the overall composite moduli of reducing the filler size at constant filler volume fraction was evaluated.

ACKNOWLEDGMENTS

This work was supported by the Office of Naval Research through grant N00014-01-1-0732.

REFERENCES

1. C. Becker, H. Krug and H. Schmidt, Mat. Res. Soc. Symp. Proc. 435, 237 (1996).
2. C. Ng, L.S. Schadler and R.W. Siegel, Nanostruct. Mat. **12**, 507 (1999).
3. R.C. Picu and M.S. Ozmusul, Macromolecules, submitted (2003).
4. M. Vacatello, Macromolecules **34**, 1946 (2001); Macromolecules, **35**, 8191 (2002).
5. A. Kloczkowski, M.A. Sharaf and J.E. Mark, Chem. Eng. Sci., **49**, 2889 (1994).
6. R.C. Picu, A. Sarvestani and M.S. Ozmusul, in *Trends in Nano-Scale Mechanics*, edited by V.M. Harik, L.S. Luo and M.D. Salas (Kluwer Academic Press, Dordrecht, 2003).
7. M. Hori and S. Nemat-Nasser, Mech. Mater., **14**, 189 (1993).

Mat. Res. Soc. Symp. Proc. Vol. 740 © 2003 Materials Research Society

Continuum Mechanics-Discrete Defect Modeling and Bubble Raft Simulation of Cracked Specimen Response in Nanoscale Geometries

Michael J. Starr[1], Walter J. Drugan[2†], Maria d. C. Lopez-Garcia[3], and Donald S. Stone[2‡]
[1]Structural Dynamics Research Department, Sandia National Laboratories,
Albuquerque, NM 87185-0847, U.S.A.
[2]Mechanics and Materials Program, University of Wisconsin-Madison,
Madison, WI 53706, U.S.A.
[†]Department of Engineering Physics [‡]Materials Science and Engineering
[3]Department of Chemical Engineering, University of Puerto Rico-Mayaguez, Mayaguez, P.R.

ABSTRACT

In a continuation of prior work, a new group of Bragg bubble model experiments have been performed to explore the effects of nanoscale crack size and nanoscale structural geometry on atomically-sharp crack tip dislocation emission behavior. The experiments have been designed to correspond to the theoretical limits that bound the expected crack tip response. Continuum elasticity analyses of these situations have also been carried out, in which the leading-order terms in the Williams expansion (the K and T terms) are determined, and the predictions of these continuum analyses coupled with discrete dislocation theory are compared with the experimental results. The experiments exhibit fascinating changes in crack tip dislocation emission direction with changing crack and structural size, crack location and loading conditions, as well as substantial changes in the magnitude of the resolved shear stress that drives dislocation emission. These changes are predicted well by the continuum elasticity-discrete dislocation model down to extremely small dimensions, on the order of a few atomic spacings. Preliminary experiments were performed with layered and two-atom basis rafts to establish crucial comparisons between theory and experiment that validate the applicability of continuum elasticity theory to make predictions directly related to nanoscale fracture behavior.

INTRODUCTION

The nominal fracture response of a cracked material can be considered to be a competition between cleavage crack growth and the spontaneous emission of blunting dislocations [1]. With nanoscale multilayered geometries this framework indicates potential length-scale-induced material transitions due to high densities of physical boundaries. Novel multilayered structures therefore may exhibit transitional behaviors, through the modification of strength and fracture toughness, that are not experienced on larger scales.

An alternative to discrete lattice calculations, proceeding *ab initio* from quantum mechanics, is the bubble model introduced by Bragg and Nye [2]. The nominal material behavior of the bubble model has been established through the calculation of inter-bubble potential and force law, and is shown to appropriately capture the short-range response of atomic interaction in close-packed materials, most notably copper [3, 4]. The bubble interaction characteristics have made it an attractive means of simulating microscopic phenomena [5-7].

Recently, a study was performed in which sharp cracks were introduced into perfect single crystal rafts to explore the connection between linear elastic fracture mechanics combined with discrete dislocation theory and the crack tip response of a close-packed material down to the

nanoscale [8]. This paper is an attempt to further bolster the validity of the theoretical predictions through a new series of experiments.

THEORETICAL FOUNDATION

The radial shear stress is the critical planar stress component for prediction of the edge dislocation emission angle from a sharp crack tip. Under planar loading, edge dislocations will be nucleated at a crack tip and will move away from the tip along the direction of maximum radial shear stress.

It is convenient to use the leading-order terms in the Williams crack tip stress field expansion to calculate the angular orientation that experiences the maximum radial shear stress. If more than the singular leading-order terms are retained, the direction of maximum radial shear stress is a function of radius. Choosing the dislocation core width, $\xi_0 b$, as the appropriate radius, the normalized radial shear stress for a crack that experiences loading of both Modes I and II is

$$\frac{\sigma_{r\theta}}{\sigma} = \frac{K_I}{\sigma\sqrt{2\pi\xi_0 b}} F_{r\theta}^{I}(\theta) + \frac{K_{II}}{\sigma\sqrt{2\pi\xi_0 b}} F_{r\theta}^{II}(\theta) + \frac{T}{\sigma} F_{r\theta}^{I(0)}(\theta) \tag{1}$$

where the universal dimensionless functions, $F_{r\theta}$, are

$$\begin{aligned} F_{r\theta}^{I}(\theta) &= \frac{1}{2}\cos\frac{\theta}{2}\sin\theta \\ F_{r\theta}^{II}(\theta) &= \frac{1}{2}\cos\frac{\theta}{2}(3\cos\theta - 1) \\ F_{r\theta}^{I(0)}(\theta) &= -\frac{1}{2}\sin 2\theta. \end{aligned} \tag{2}$$

K_I and K_{II} are the Mode I and Mode II stress intensity factors, respectively, and T is the T-stress for a specific far-field loading. The dislocation core width is chosen as the location to evaluate the shear stress because within this zone the stress fields are nonlinear and the linear elastic solution is invalid; the core width is determined experimentally here, as discussed in the next section.

The stress intensity factors for a specific cracked geometry can be obtained in a straightforward manner [9]. The T-stress, a non-singular constant stress that acts parallel to the crack line can also be calculated in a direct manner. These details are given in a paper in preparation [10]. For very small cracks (on the order of tens of atomic spacings) loaded in Mode I, the critical stress intensity factor for dislocation nucleation can be strongly modified through inclusion of the T-stress [11].

Figure 1 shows the representative crack geometry that will be treated analytically and experimentally. A crack of length $2a$ is parallel to and a distance, h, from a rigid boundary. For boundary displacement or traction normal to the crack K_I, K_{II}, and T have a relatively strong dependence on the normalized distance h/a as $h/a \to 0$:

$$K_I, K_{II} \propto (h/a)^{-3/2}, T \propto (h/a)^{-2}. \tag{3}$$

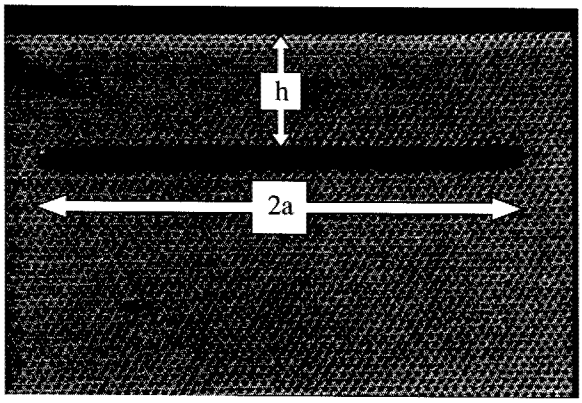


Figure 1. A sharp crack in a single crystal, at a distance, h, from the rigid upper boundary.

EXPERIMENTAL RESULTS

Experiments were performed to explore the qualitative and quantitative shift in dislocation emission from a crack tip as a function of crack location, size, and loading condition. A flat-bottomed, rectangular tray was constructed of polycarbonate to contain the liquid bubble solution. The liquid solution was prepared of soapy water and glycerol in a ratio of 50:1 [12]. Varying the air pressure through the orifice of a small-bore jet controlled the size of the blown bubbles. The bubbles were of uniform size of approximately 1.2 mm in diameter.

Uniform displacement was achieved by fashioning a crack in a perfect bubble raft between two rigid polycarbonate boundaries and then translating the upper polycarbonate boundary in the direction normal or parallel to the stationary boundary. Uniform traction was achieved by constructing a perfect raft around a polycarbonate filament, leaving the upper surface unconstrained. A polycarbonate block was drawn near the free surface to alter the local surface tension and induce normal traction loading. Digital movies of the crack tip processes were taken during the application of the uniform displacement or traction.

In the close-packed structure of the bubble raft, slip will only occur along one of the three equally inclined directions of closely packed rows. With respect to the crack line, this corresponds to emission directions of 0°, ±60°, and ±120°. Therefore, these are the only directions that must be interrogated with Eq. (1) to obtain the maximum radial shear stress.

The soap mixture used for all the bubble experiments exhibited dislocation cores, regions of crystal disregistry, which were spread out over a distance of 5-6 bubble diameters [see e.g. Figure 3] in all cases examined. This dislocation core size was used as a direct material input to solve Eq. (1) for a nanoscale crack. The calculations show that cracks of nanoscale dimension may exhibit different emission behavior than large cracks with identical h/a.

Figures 2(a) and (b) are maps of the predicted dislocation emission directions as a function of h/a for the cases of uniform normal displacement and traction, respectively. The theoretically calculated curves give the maximum shear stress normalized by the maximum shear stress near a crack tip in an infinite body, both for a macroscopic crack and a nanoscale crack. The macroscopic crack is characteristic of the case in which the crack is many orders of magnitude

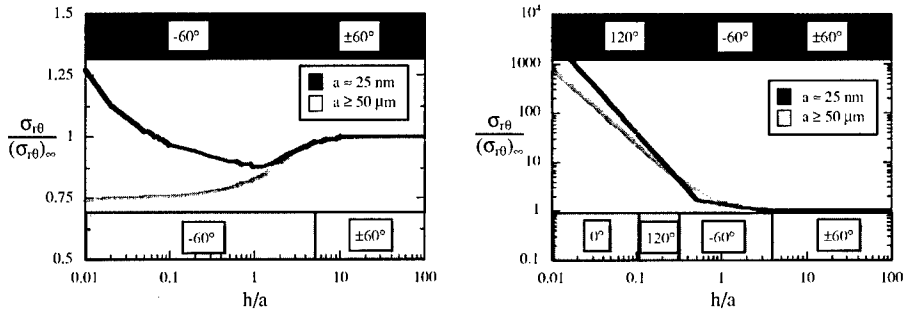


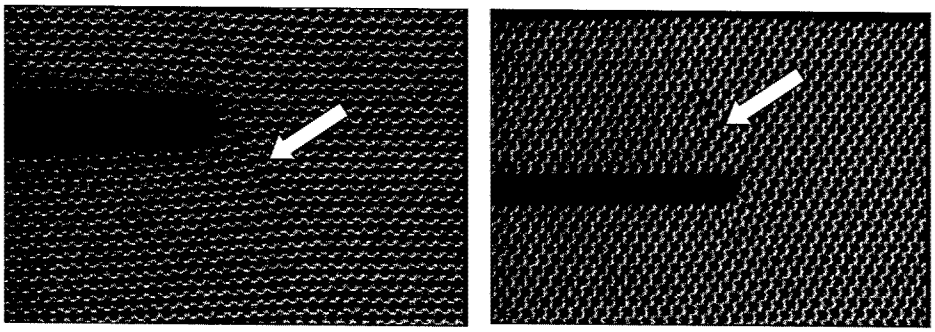
Figure 2. Dislocation emission maps in homogeneous, cracked bubble rafts. The nanoscale crack corresponds to the dark line and the transitions indicated on the upper portion of the plot. The macroscopic crack corresponds to the light line and the lower transitions. Uniform normal (a) displacement and (b) traction.

larger than the atomic spacing and therefore the T-stress is not required to accurately describe the near-tip stress field. Conversely, the T-stress is required for the nanoscale crack where the crack length is of similar order to atomic spacing. The slip direction for which the shear stress is maximized is reported in the plot for each h/a. The dark gray bar at the top and the light gray bar at the bottom indicate the angular orientation with respect to the crack line for which dislocation emission is predicted to occur for the nanoscale crack and macroscale crack respectively.

Corresponding to Figure 2(b) are several uniform normal traction bubble raft simulations. Figure 3(a) shows the case of uniform normal traction for $h/a \approx 2.0$, while Figure 3(b) shows the case for $h/a \approx 0.2$. This transition in emission behavior is expected for a crack with nanoscale dimension as illustrated by the separate emission regimes predicted theoretically for those values of h/a shown in Figure 2(b). Experimental results of uniform normal displacements have been shown previously [8], and are qualitatively similar to the results shown in Figure 3.

Although not shown here, theoretical analyses and experiments have been performed on interfacially-cracked multilayered bubble rafts [13]. The analysis involves a generalization of the homogeneous crack analysis of Eqs. (1) and (2) to the case of a crack on the interface between dissimilar materials. The bubble rafts are constructed of two distinct phases of close-packed bubbles that have different diameters and therefore different elastic moduli. Initial experimentation again shows agreement with theoretical predictions for dislocation emission behavior at a crack tip.

Preliminary investigations of crack tip response have also been made than using bubble rafts that have packing structures other than close-packed. Figure 4 shows the case of a two-atom basis crystal structure. The nature of the soap bubble interactions is essentially the same as a raft constructed of bubbles of one size. However, the dislocation emission response appears to be markedly different. This is due to the different set of allowed slip displacement directions and because the two-atom basis structure has a larger Burgers' vector magnitude and consequently a larger Peierls barrier.



(a) (b)

Figure 3. Crack tip response of bubble rafts experiencing uniform normal traction. Dislocation emission (a) at -60° for $h/a \approx 2.0$ and (b) at 120° for $h/a \approx 0.2$.

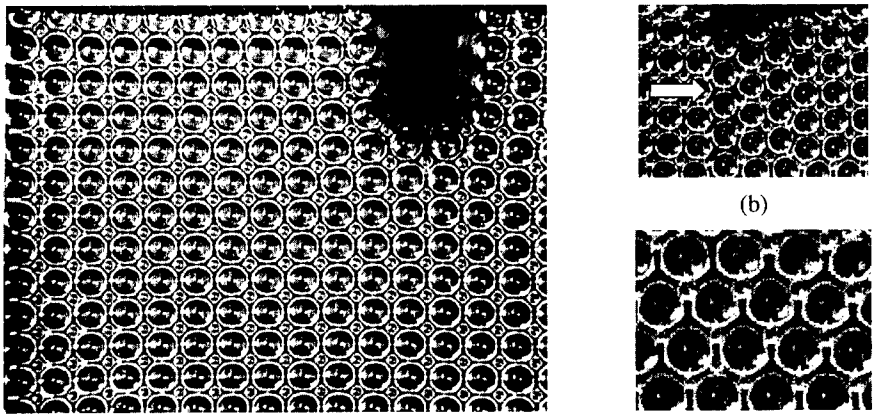
DISCUSSION

As shown through the experiments, most notably the normal traction experiment, omission of the T-stress contribution may give an incorrect prediction for preferred emission direction for nanosized cracks and/or for cracks with nanoscale proximity to a boundary. The case of uniform displacement serves as an upper bound for the response of a crack in a multilayer due to the effectively rigid boundary, while the lower bound was established through the application of uniform surface tractions (perfectly compliant boundary).

A notable feature of the uniform imposed displacement emission map of Figure 2(a) is the substantial change in the stress behavior as the crack length approaches the nanoscale. Instead of exhibiting diminishing shear stress as the crack approaches the boundary (as is the case for the macroscale crack), the maximum shear stress of the nanoscale crack reaches a local minimum for $h/a \approx 1$ and begins to grow as it approaches the boundary. This effect corresponds to a heightened propensity for the emission of a dislocation from the crack tip, and also occurs in the case of nanoscale cracks with $h/a < 0.3$ for imposed normal boundary traction.

Another intriguing implication of this work is the ability of linear elastic fracture mechanics to model the stresses on the nanoscale in such a way that theoretical predictions can be validated in an experimentally repeatable manner. Although an idealized model, continuum elasticity is shown to maintain its predictive capabilities down to a discrete atomic length scale. It may not be appropriate to draw direct parallels between the theory and actual material response in a three-dimensional multilayered material. However, theory and experiment do indicate that a significant transition, with respect to dislocation emission, occurs at a crack tip on the nanoscale.

Certain predictions seem to indicate that materials which behave in a brittle manner in bulk may undergo a transition on the nanoscale for which dislocation emission from a crack tip is preferred over cleavage [13]. These predictions are not testable via the close-packed bubble raft because it is a ductile metal analog. It is hoped that a simple brittle analog will be found that may validate theoretical predictions of a brittle-to-ductile response. The two-atom basis raft, although not a true brittle analog, may be useful as it appears to have a much larger Peierls barrier than its closed-packed counterpart and exhibits elastic response for much larger strains.



(a) (b) (c)

Figure 4. (a) "Sharp" crack in a two-atom basis packing structure that resembles the (001) plane in a "rock salt"-type crystal. (b) Atomic rearrangement along 0° to the crack line. (c) Reordered phase in a two-atom basis packing structure in the most highly strained regions of the raft.

ACKNOWLEDGEMENTS

The authors would like to thank Prof. Wendy Crone for experimental support. This research was supported by the National Science Foundation, Mechanics and Materials Program, Grant CMS-9800157 and the National Science Foundation Materials Research Science and Engineering Center at UW-Madison.

REFERENCES

1. J. R. Rice and R. Thomson, *Phil. Mag.* **29**, 73 (1974).
2. W. L. Bragg and J. F. Nye, *Proc. Roy. Soc. Lond. A*, **190**, 474 (1947).
3. W. M. Lomer, *Proc. Roy. Soc. Lond. A*, **196**, 182 (1949).
4. L. T. Shi and A. S. Argon, *Phil. Mag. A*, **46** (2), 255 (1982).
5. A. S. Argon, and L. T. Shi, *Phil. Mag. A*, **46** (2), 275 (1982).
6. F. A. McClintock and W. R. O'Day, *Proc. Int. Conf. Frac.* **1**, 75 (1965).
7. A. Gouldstone, K. J. Van Vliet, and S. Suresh, *Nature* **411**, 656 (2001).
8. M. J. Starr and W. J. Drugan (Proc. Soc. Exp. Mech., Milwaukee, WI, 2002) pp. 145-148.
9. F. Erdogan and G. Gupta, *Int. J. Solids Structures* **7**, 39 (1971).
10. M. J. Starr and W. J. Drugan, (manuscript in preparation for publication).
11. G. E. Beltz and L. L. Fischer in *Multiscale Deformation and Fracture in Materials and Structures*, edited by T.-J. Chuang and J. W. Rudnicki, (2000), pp.237-242.
12. M. J. Geselbracht, A. B. Ellis, R. L. Penn, G. C. Lisensky, and D. S. Stone, *J. Chem. Ed.* **71**, 254 (1994).
13. M. J. Starr, PhD. Thesis, University of Wisconsin-Madison, 2002.

Mat. Res. Soc. Symp. Proc. Vol. 740 © 2003 Materials Research Society I8.9

Interfacial Control of Creep Deformation in Ultrafine Lamellar TiAl

L. M. Hsiung
University of California, Lawrence Livermore National Laboratory
Chemistry and Materials Science Directorate
Livermore, CA 94551-9900, U.S.A.

ABSTRACT

Solute effect on the creep resistance of two-phase lamellar TiAl with an ultrafine microstructure creep-deformed in a low-stress (***LS***) creep regime [where a nearly linear creep behavior was observed] has been investigated. The resulted deformation substructure and in-situ TEM experiment reveals that interface sliding by the motion of pre-existing interfacial dislocations is the predominant deformation mechanism in ***LS*** creep regime. Solute segregation at interfaces and interfacial precipitation caused by the segregation result in an increase of creep resistance in ***LS*** creep regime.

INTRODUCTION

Two-phase [TiAl (γ-$L1_0$) and Ti_3Al (α_2-DO19)] lamellar TiAl alloys have recently attracted a great attention because of their low density ($\rho = 3.9$ g/cc), high specific strength, adequate oxidation resistance, and good combination of ambient-temperature and elevated-temperature mechanical properties, which are of interest for aerospace and transportation applications such as high-temperature components in turbine and combustion engines. Through alloy design and microstructural optimization, significant progress has been made to improve both room-temperature ductility/toughness and high-temperature creep resistance of the alloys [1-5]. Previous research has revealed that the alloys fabricated by hot extrusion of gas-atomized TiAl powder at 1400°C can form refined lamellar microstructures in association with interlocking colony boundaries through a shear-assisted eutectoid transformation induced by hot-extrusion process [6]. The hot-extruded lamellar alloys provide a better combination of room temperature and high-temperature mechanical properties than those of lamellar TiAl alloys fabricated by conventional ingot metallurgy. Accordingly, there is of great interest to further refine lamellar spacing of the alloys to submicron or nanometer length-scales to develop TiAl nanophase composites for engineering applications. A recent report of the formation of nanoscale lamellae (with lamellar spacing in the order of 5 to 10 nm) within a water-quenched TiAl alloy [7] revealed the feasibility of materializing the idea of fabricating TiAl nanophase composites. However, in parallel to make an effort for developing TiAl nanophase composites, there is a need to understand if further refinement of the lamellar microstructures would lead to adverse effects on high-temperature creep properties. A previous investigation [8] on the creep behavior of a Ti-47Al-2Cr-2Nb (at.%) alloy with a refined lamellar microstructure revealed that there existed two distinct creep regimes, where a nearly linear creep behavior [i.e. $\dot{\varepsilon}$ (steady-state creep rate) $= k\sigma^n$, where σ is applied creep stress] was observed in low-stress (***LS***) regime (i.e. $\sigma < 300$ MPa at 760°C), and power-law break down was observed in high-stress (***HS***) regime (i.e. $\sigma > 300$ MPa at 760°C). TEM investigation of deformation substructures within creep-deformed specimens has revealed the occurrence of interface sliding in ***LS*** regime and deformation twinning in ***HS*** regime, which has led us to propose that interface sliding associated with viscous glide of pre-existing interfacial dislocations is the predominant creep mechanism in ***LS*** regime, and interface-activated deformation twinning in γ lamellae is the predominant creep mechanism in ***HS*** regime [9, 10]. Furthermore, it is also suggested that the solute atoms segregated at lamellar interfaces can act as short-range barriers to drag the motion of interfacial dislocation arrays during interface sliding. It is also anticipated that more effective barriers to impede the interface sliding can be obtained by interfacial precipitation resulting from the solute segregation. Accordingly, the investigation has been extended to investigate the effect of alloying modification on the creep property of refined lamellar TiAl. Emphasis was placed upon the effect of solute segregation on the creep resistance in ***LS*** regime in order to facilitate the effort of developing TiAl nanophase composites for high-temperature applications.

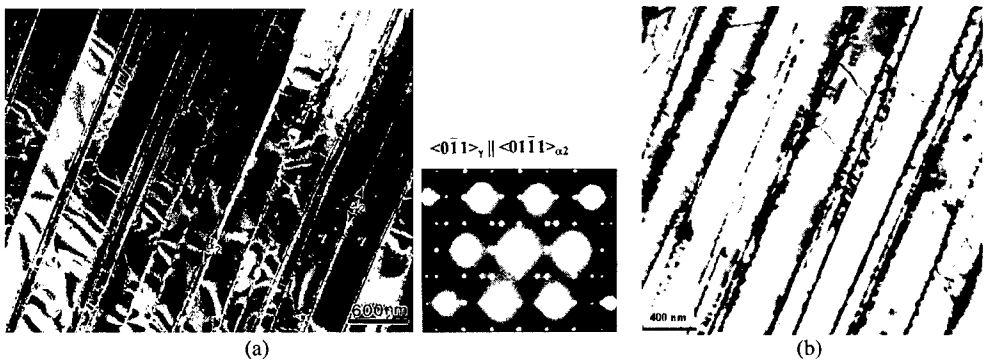
EXPERIMENTAL DETAILS

TiAl alloys with nominal compositions of Ti-47Al-2Cr-2Nb and Ti-47Al-2Cr-1Nb-0.8Ta-0.2W-0.15B (at.%) were chosen for current study. The alloys were fabricated at Oak Ridge National Laboratory by a powder metallurgy process, which involves a hot-extrusion (16:1 ratio) of gas-atomized titanium aluminide powder (particle size: - 200 mesh) canned in molybdenum billets and were subsequently hot-extruded at 1400 $^{\circ}$ C. Test specimens with a gauge dimension of 24.4 x 5.08 x 1.52 mm were prepared from the annealed alloys by electrical discharge machining. Creep tests were conducted in a dead-load creep machine with a lever arm ratio of 16:1. Tests were performed in air in a split furnace with three zones at 760 $^{\circ}$ C and 815 $^{\circ}$ C. The deformation substructures of tested specimens creep deformed in both *LS* and *HS* regimes were investigated. In-situ TEM experiment was conducted by electron-beam heating of a pre-crept sample (138 MPa, 760 $^{\circ}$ C) to study interfacial dislocation motion. TEM foils were prepared by twinjet electropolishing in a solution of 60 vol. % methanol, 35 vol. % butyl alcohol and 5 vol. % perchloric acid at ~15 V and –30 $^{\circ}$ C. The microstructures of the creep-deformed alloys were examined using a JEOL-200CX transmission electron microscope equipped with a double-tilt goniometer stage.

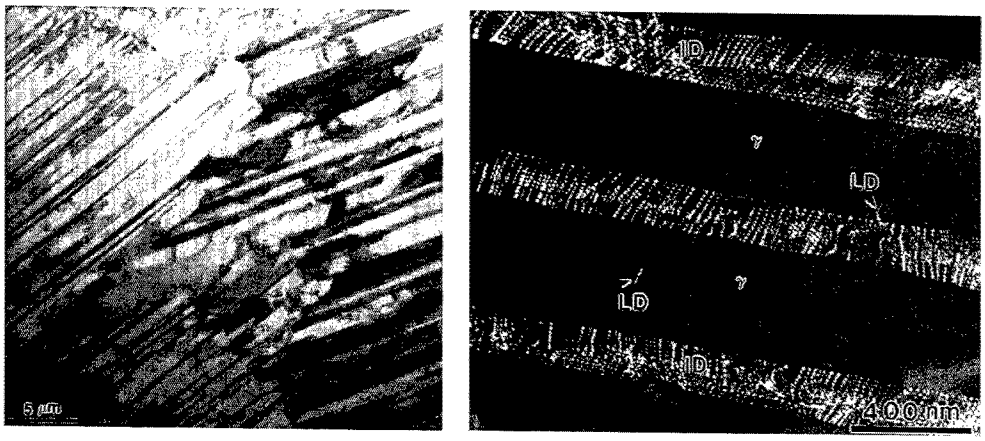
DISCUSSION

Microstructures of As-extruded alloys

Near fully lamellar microstructures [containing TiAl (γ-$L1_0$) and Ti_3Al (α_2-DO19) lamellae] with interlocking colony boundaries were developed within both Ti-47Al-2Cr-2Nb and Ti-47Al-2Cr-1Nb-0.8Ta-0.2W-0.15B alloys hot extruded at 1400 $^{\circ}$ C. Typical lamellar microstructures of Ti-47Al-2Cr-2Nb and TiAl-47Al-2Cr-1Nb-0.8Ta-0.2W-0.15B alloys are shown in Figs. 1 (a) and (b), respectively. Similar colony grain sizes (< 100 μm) and lamella widths were observed within the lamellar alloys. The width of γ lamellae varies between 100 nm and 350 nm, and the width of α_2 lamellae varies between 10 nm and 50 nm. These values are considerably finer than those in lamellar TiAl alloys fabricated by conventional processing techniques. In addition, as shown in Fig. 1 (c), interwoven-type colony boundaries were developed within these two lamellar alloys, which could effectively interlock the colony boundaries from rotation and sliding when deformed at elevated temperatures. In general, lamellar TiAl contains two types of lamellar interfaces within colony grains [11, 12]: (1) the γ/α_2 interphase interface which has an orientation relationship: $(0001)_{\alpha 2} \parallel (111)_{\gamma}$ and $<11\bar{2}0>_{\alpha 2} \parallel <1\bar{1}0>_{\gamma}$ [which can be determined from the SAD pattern shown in Fig. 1(a)], and (2) the γ/γ interfaces which include true twin, pseudo twin, and order-fault interfaces. Both pre-existing lattice dislocations (*LD*) within γ lamellae and a high density of intrinsic interfacial dislocations (*ID*) in lamellar interfaces were observed within as-fabricated lamellar TiAl [Fig. 1(d)]. While the intrinsic interfacial dislocations formed in semi-coherent γ/α_2 interfaces are $1/6<112>$ or $1/3<112>$ type misfit dislocations, those on γ/γ twin-related interfaces are $1/6[11\bar{2}]$ type twinning dislocations or geometry necessary dislocations for accommodating the departure of true-twin interface from the exact (111) twin plane [13 - 15].



(a) (b)

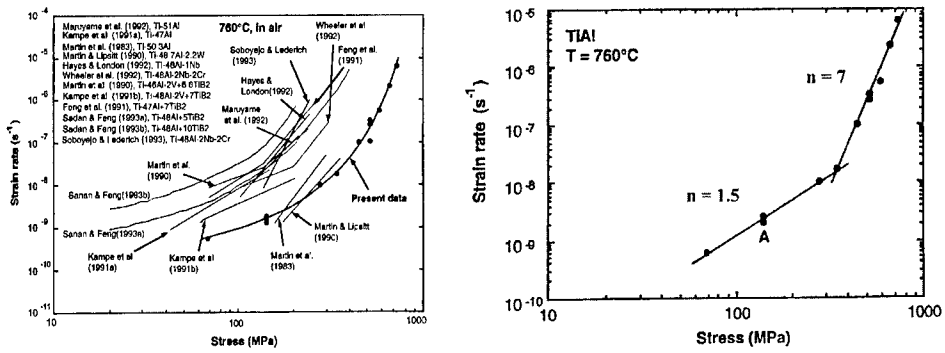


(c) (d)

Fig. 1. (a) A weak-beam dark-field TEM image showing a typical lamellar microstructure observed from Ti-47Al-2Cr-2Nb extruded at 1400 ° C, and an SAD pattern generated from the domain in (a) showing the phase relationships between γ and α_2, $\mathbf{Z} = [0\bar{1}1]_\gamma \| [01\bar{1}0]_{\alpha 2}$; (b) A bright-field TEM image showing a typical lamellar microstructure observed from Ti-47Al-2Cr-1Nb-0.8Ta-0.2W-0.15B extruded at 1400 ° C; (c) A bright-field TEM image showing a interwoven colony boundary in lamellar Ti-47Al-2Cr-1Nb-0.8Ta-0.2W-0.15B; (d) A tilt view of lamellar microstructure showing a dislocation substructure within the lamellar alloy (*LD* denotes lattice dislocation, and *ID* denotes interfacial dislocation).

Creep data and deformation substructures

Creep data of the refined lamellar Ti-47Al-2Cr-2Nb alloy tested at 760 ° C with a comparison of the creep data of conventionally processed TiAl alloys reported in the literature is shown in Fig. (a) [3]. The refined lamellar alloy demonstrates superior creep resistance among all in the high stress (*HS*) regime and relatively better (although not the best) creep resistance in the low stress (*LS*) regime. Since for engineering applications the structural components are mainly operated in *LS* regime, further investigations were conducted to understand the underlying creep mechanism in *LS* regime in order to improve the creep resistance of the lamellar alloy. By re-plotting the data to correlate the power-law creep (i.e. $\dot{\varepsilon} = k\sigma^n$) as shown in Fig. (b), a nearly linear creep behavior ($n \approx 1.5$, i.e. the steady-sate creep rate is nearly proportional to the applied stress) occurred in *LS* regime (<300 MPa), and power-law breakdown ($n \approx 7$) took place in *HS* regime (>300MPa). The corresponding deformation substructures of creep-deformed samples under conditions A (138 MPa in *LS* regime) in Fig. 2(b) is shown in Fig. 3. In general, no significant increase in dislocation density was found within the specimen deformed in *LS* regime, except that grain boundary ledges presumably formed as a result of interface sliding (caused by the motion of *ID* arrays) are shown in Fig. 3. On the other hand, as reported in [10], both the emission of dislocations from lamellar interfaces and the formation of {111} and {112}-type deformation twins (*DT*) were observed within the specimen deformed in *HS* regime. The above observations suggest that interface sliding is the predominant deformation mechanism in *LS* regime, whereas the deformation of γ lamellae by the emission of dislocations and deformation twins from lamellar interfaces becomes the predominant deformation mechanisms in *HS* regime.



(a) (b)

Fig. 2. (a) A comparison of the creep resistance at 760 ° C between the presently studied PM alloy and other TiAl alloys [3]; (b) Steady-state creep rate plotted as a function of applied stress at 760 ° C showing that there existed two distinct creep regimes, i.e. low stress (*LS*) and high stress (*HS*) regimes.



Fig. 3. A dark-field TEM image showing the formation of grain boundary ledges (marked by arrows) presumably caused interface sliding within a specimen creep-deformed at 760 ° C, 138 MPa.

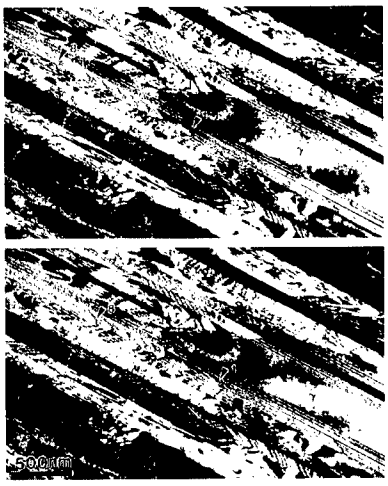


Fig. 4. Consecutive in-situ TEM images showing the motion of an interfacial dislocation array in a γ/γ interface (time period for beam heating: 20 s).

Results of in-situ TEM experiment to demonstrate the cooperative motion of interfacial dislocations in lamellar TiAl under room-temperature straining conditions have been reported elsewhere [16]. Here, results of in-situ TEM experiment from a creep-deformed sample (138MPa, 760 $^{\circ}$ C) are presented to demonstrate the motion of interfacial dislocations under an electron-beam heating condition. It is noted that a local heating of TEM sample can be achieved by spotting the focused electron-beam (several micron meters in size) onto the region of interest in the sample. Figure 4 are two consecutive in-situ images showing the cooperative motion of a dislocation array (total eight interfacial dislocations in the array) in a γ/γ interface during beam heating, and the array moved about 250 nm after beam heating for 20 seconds. The dislocation array stopped moving after re-spreading the beam onto a wide region of the TEM sample. It is also worthy to note that zigzag motion of the interfacial dislocations were observed which presumably caused by the pinning-unpinning of dislocation lines from solute atoms during their movement. These observations support the previously proposed creep mechanism [9]: interface sliding associated with a viscous glide of pre-existing interfacial dislocations is the predominant deformation mechanism for a nearly linear creep behavior observed in *LS* regime.

The interstitial atoms segregated at lamellar interfaces can act as short-range barriers for the motion of interfacial dislocations and resulting in the viscous glide of interfacial dislocations at elevated temperatures. The high population of interfacial dislocations in lamellar interfaces can act as preferential sites for solute segregation. In fact, the segregation of W solute atoms at lamellar interfaces has recently been identified from a lamellar TiAl alloy by Liu et al. using a field-ion atom probe technique [17]. It is accordingly suggested that while further refining of lamellar spacing may increase creep resistance of lamellar TiAl in *HS* regime by restraining *LD* motion within constituent lamellae and impeding *ID* motion by impinging *LD* and *DT* onto lamellar interfaces, it can cause an adverse effect on the creep resistance of lamellar TiAl in *LS* regime. The creep resistance of refined lamellar TiAl in *LS* regime may be promoted by reducing the mobility of interfacial dislocations by the segregation of low-diffusivity solutes such as Ta and W to impede the motion of interfacial dislocations. Although more rigorous investigations are needed for the effects of solute segregation at lamellar interfaces on the creep resistance in *LS* regime, a preliminary result demonstrating the promotion of creep resistance of lamellar TiAl by the addition of Ta, W, and B is shown in Fig. 5 (a). As can be seen clearly that steady state creep rates significantly decrease as a result of the solute additions of Ta, W, and B. Figure 5 (b) shows a preliminary result of TEM examination of the Ti-47Al-2Cr-1Nb-0.8Ta-0.2W-0.15B alloy sample creep-deformed at 70 MPa. Here precipitates, presumably TiB_2-type boride particles, were observed at α_2/γ interfaces. It is noted that the formation of TiB_2-type particles in similar TiAl alloys doped with boron has been previously reported elsewhere [18 - 20]. It is also noted that no interfacial precipitation was observed at γ/γ interfaces, which suggests that solute segregation phenomenon is more pronounced at α_2/γ interfaces than at γ/γ interfaces.

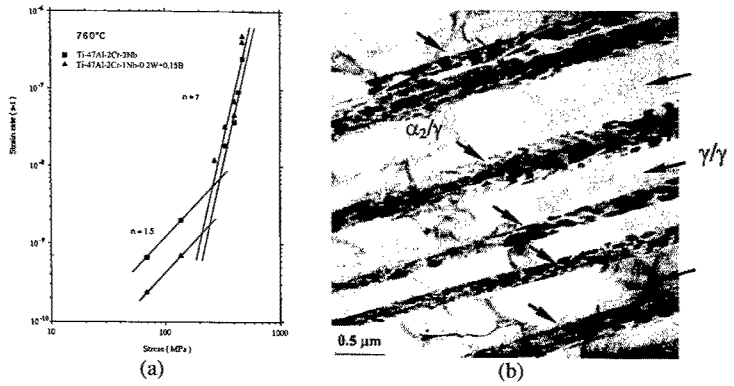


Fig. 5. (a) Creep data show the effects of alloying modification to the creep resistance of refined lamellar TiAl alloys in *LS* regime at 760 $^{\circ}$C; (b) Bright-field TEM images showing the formation of TiB_2-type boride particles at α_2/γ interfaces within a Ti-47Al-2Cr-1Nb-0.8Ta-0.2W-0.15B alloy sample creep-deformed at 760 $^{\circ}$C, 70 MPa. Notice that no precipitation was found in γ/γ interfaces which appeared as faint contrasts in (b).

CONCLUSION

A nearly linear creep behavior [i.e. $\dot{\varepsilon} = k\sigma^n$, $n \sim 1.5$] has been observed in both Ti-47Al-2Cr-2Nb and Ti-47Al-2Cr-1Nb-0.8W-0.2W-0.15B alloys with an ultrafine lamellar microstructure (γlamellae: 100 – 300 nm thick, α_2 lamellae: 10 – 50 nm thick) creep-deformed at elevated temperatures with stresses below 300 MPa. The resulted deformation substructure and in-situ TEM experiment reveal that interface sliding by the motion of pre-existing interfacial dislocations is the predominant deformation mechanism. Since the operation and multiplication of lattice dislocations within both $\gamma$and α_2 lamellae are very limited at a low stress level as a result of the refined lamellar spacing, creep mechanisms based upon glide and/or climb of lattice dislocations become insignificant, instead the mobility of interfacial dislocation arrays on γ/α_2 and γ/γinterfaces becomes predominant. It has been demonstrated that solute segregation at lamellar interfaces and interfacial precipitation caused by the segregation have a beneficial effect on the creep resistance of ultrafine lamellar TiAl in low-stress creep regime.

ACKNOWLEDGEMENTS

This work was performed under the auspices of the U.S. Department of Energy by University of California, Lawrence Livermore National Laboratory under contract No. W-7405-Eng-48. The author would like to thank Dr. T.G. Nieh for providing unpublished creep data and many helpful discussions during the course of this investigation. The author is also in debt to Dr. C. T. Liu of Oak Ridge National Laboratory for his technical guidance and providing the alloys used for this investigation.

REFERENCES

1. Y-W. Kim and D.M. Dimiduk, *JOM*, 43(8), 40 (1991).
2. Y –W. Kim, *Acta Metall. Mater.* **40**, 1121 (1992).
3. J. N. Wang, A. J. Schwartz, T. G. Nieh, C. T. Liu, V. K. Sikka and D. R. Clemens, in *Gamma Titanium Aluminides*, ed. Y-W. Kim et al., TMS (Warrendale, PA), 949, (1995).
4. C.T. Liu, J.H. Schneibel, P.J. Maziasz, J.L. Wright, D.S. Easton, *Intermetallics* **4**, 429 (1996).
5. C. T. Liu, P. J. Maziasz, J. L. Wright, *Mat. Res. Soc. Symp. Proc.*, **460**, 83 (1997).
6. L.M. Hsiung, T.G. Nieh and D.R. Clemens, *Scripta Mater.*, 36 (1997), 233.
7. K. Hono, E. Abe, T. Kumagai, H. Harada, *Scripta Mater.*, **35**, 495 (1996).
8. J. N. Wang and T. G. Nieh, *Acta Mater.*, **46**, 1887 (1998).
9. L. M. Hsiung and T. G. Nieh, *Intermetallics* **7**, 821 (1999).
10. L.M. Hsiung, T.G. Nieh, B.W. Choi, and J. Wadsworth, *Mater. Sci. Eng.*, A329-331, (2002), 637.
11. M. Yamaguchi, S.R. Nishitani, Y. Shirai, in *High Temperature Aluminides and Intermetallics*, ed. S.H. Whang et al., TMS (Warrendale, PA), 63, 1990.
12. Y. Yamamoto, M. Takeyama, T. Matsuo, *Mater. Sci. and Engrg.*, **A329 – 331**, 631 (2002).
13. G.J. Mahon and J.M. Howe, *Metall. Trans. A*, **21**, 1655 (1990).
14. L. Zhao and K. Tangri, *Acta Metall. Mater.*, **39**, 2209.
15. L. M. Hsiung and T. G. Nieh, *Mater. Sci. Engrg.*, **A239-240**, 438 (1997).
16. L. M. Hsiung, A. J. Schwartz and T. G. Nieh, *Scripta Mater.* **36**, 1017 (1997).
17. C.T. Liu, P.J. Maziasz, D.J. Larson, in *Interstitial and Substitutional Solute Effects in Intermetallics*, ed. I. Baker et al., TMS (Warrendale, PA), 179 (1998).
18. M. De Graef, D.A. Hardwick, P.L. Martin, in *Structural Intermetallics*, ed. M.V. Nathal et al., TMS (Warrendale, PA), 177 (1993).
19. D.J. Larson, C.T. Liu, M.K. Miller, *Intermetallics* **5**, 411 (1997).
20. C.T. Liu, J.L. Wright, S.C. Deevi, *Mater. Sci. and Engrg.*, **A329 – 331**, 416 (2002).

Characterization of Nanostructured Materials

Mat. Res. Soc. Symp. Proc. Vol. 740 © 2003 Materials Research Society

Structure and Characterization of Sol-gel and Aerogel Materials and Oxidation Products from the Reaction of $(CH_3O)_4Si$ and $C_{16}H_{33}Si(OCH_3)_3$

Thomas M. Tillotson and John G. Reynolds
University of California, Lawrence Livermore National Laboratory, Livermore CA 94551

ABSTRACT

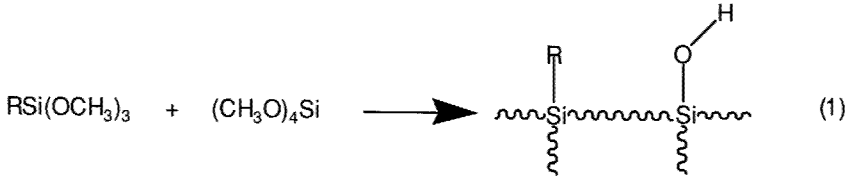
Reactions of $(CH_3O)_4Si$ and $C_{16}H_{33}Si(OCH_3)_3$ at various mole ratios were performed in methanol using base and acid catalysis. Sol-gel materials were formed that have low surface areas (~10 m^2/g). Subsequent supercritical drying using CO_2 at 40 °C produced materials that are very different than traditional aerogels, with surface areas around the same values as the corresponding sol-gels, as well as no detectable meso-pore features. In some cases, the aerogels even melted upon heating. Spectroscopic characterization, using IR, ^{29}Si and ^{13}C NMR revealed normal Si-O substitution as well as incorporation of the carbon chain into the Si framework.

Heating of the stable forms of the materials in air at different temperatures yielded, depending upon oxidation conditions, several materials with much higher surface areas, typical of aerogels. Pore size distribution measurements revealed meso-pore features with a narrow distribution around 35Å. Spectroscopic characterization revealed the disappearance of the R-Si substitution and the appearance of an oxidized intermediate.

This paper will describe the chemistry and characterization of these unusual sol-gels, aerogels, and oxidation products, as well as potential applications.

INTRODUCTION

Aerogels are open foam type materials with high surface areas (can be over 1000 m^2/g), low density (generally 0.1 to 0.3 g/cc), and high porosities (generally 90+%) [1]. These materials are extremely interesting and have found many commercial applications, such as insulators, water purification, optics, optic coating, energy storage and chemical sensing [2]. Perhaps the most notable use is in cosmic particle collectors in satellites and space shuttles.



(1)

In addition to the unusual base properties of these materials, the chemical properties can also be modified. One method is through incorporation of organic substituted siloxanes into the silica matrix through hydrolysis/condensation reactions, equation 1. This is been shown to be effective for a variety R groups, yielding new sol-gels or aerogels with modified properties [3]. For example, where R = $-CH_2CH_2CF_3$, under certain reaction conditions, produces a highly hydrophobic aerogel [4].

In efforts to understand the reaction chemistry of organic/inorganic hybrid materials, several new aerogels with different R groups have been synthesized and characterized. Here we report initial results on utilization of R = n-$C_{16}H_{33}$ in the synthesis of organic/inorganic hybrid aerogels by equation 1. Full results will be published elsewhere.

EXPERIMENTAL

The chemicals were purchased from standard chemical supply companies and used as received. The aerogels were synthesized by methods described previously in detail. The aerogel was formed by mixing 2.0 g (5.8 x 10^{-3} mol) $C_{16}H_{33}Si(OCH_3)_3$ and 2.0 g (1.3 x 10^{-2} mol) $(CH_3O)_4Si$ in 7.5 mL of methanol. 200 uL of HBF_4 was added and stirred. Two phases appear initially, but eventually became homogenized. The solution was poured into beakers and were covered with parafilm and left to gel. Gellation took a few seconds. After gellation, the samples were dried either by supercritical CO_2 to form an aerogel or air evaporation to form a xerogel. A typical supercritical extraction solvent exchange took 2 to 4 days.

The supercritical extraction of the aerogels were performed in a SPI Supplies Critical Point Drier. The IR spectra of the samples were taken on a Nicolet Impact 440 spectrometer. The samples were examined either as neat liquid between two NaCl plates or as KBr pellets. The ^{29}Si NMR were taken on a Chemagnetics 300 NMR spectrometer using a Chemagnetics solid state probe. The surface property measurements were taken on a Micromeritic ASAP 2000 upgraded to a ASAP 2010 analyzer. The samples were degassed at 200°C under vacuum before measurements. The surface areas were calculated using the BET model and the meso-pore distributions were calculated using a BHJ model. The oxidations were performed in NEY Vulcan 3-1750 temperature controlled furnace. Temperatures were held at ± 0.5°C.

RESULTS

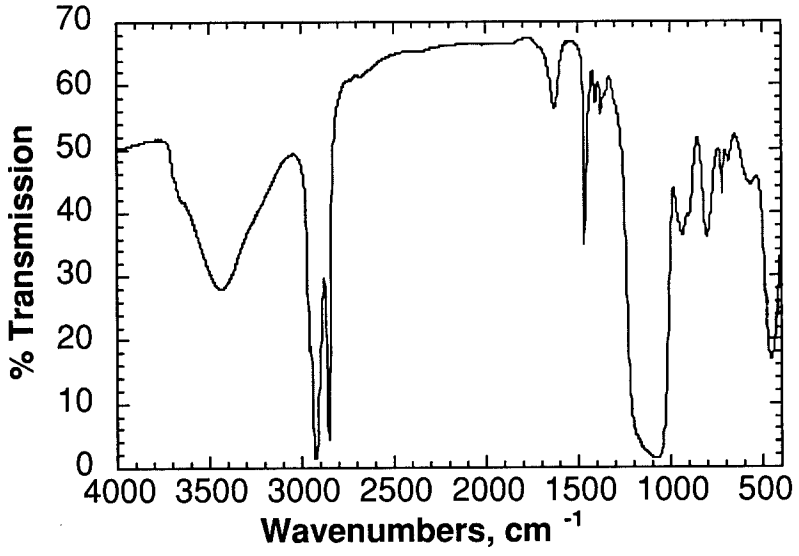


Figure 1. FTIR of the product of $C_{16}H_{33}Si(OCH_3)_3$ and $(CH_3O)_4Si$.

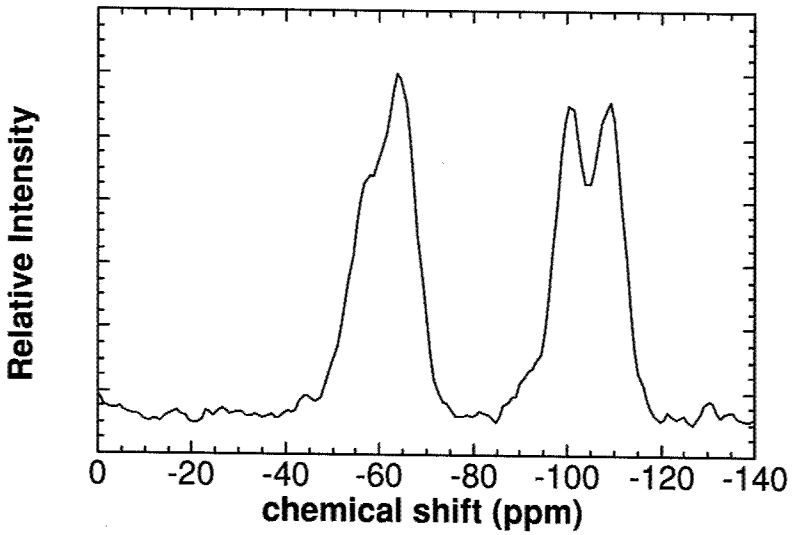


Figure 2. ^{29}Si NMR product of $C_{16}H_{33}Si(OCH_3)_3$ and $(CH_3O)_4Si$.

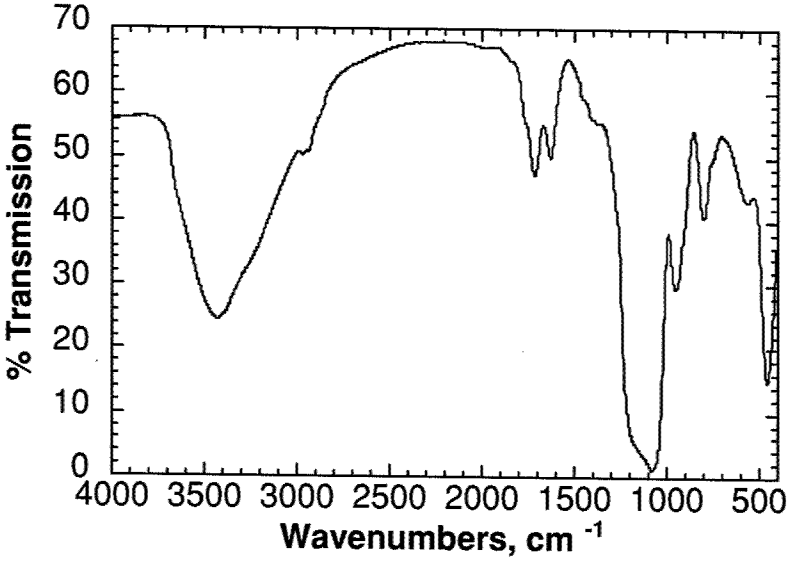


Figure 3. FTIR spectrum of the oxidation of the product of $C_{16}H_{33}Si(OCH_3)_3$ and $(CH_3O)_4Si$ at 300°C for 1h.

Figure 1 shows the IR of the aerogel formed by the reaction of $C_{16}H_{33}Si(OCH_3)_3$ and $(CH_3O)_4Si$ in methanol, shown in equation 1. Clearly evident is a very strong broad feature from

1000 to 1200 cm^{-1}. This is assigned to Si-O-Si of the silica backbone. An overtone feature is also seen at 1640 cm^{-1}. A small medium sharp feature is seen at 960 cm^{-1} assigned to Si-OH. Features indicating the incorporation of the $C_{16}H_{33}$ group are seen in the alkyl region of 2800 to 3000 cm^{-1}. A broad feature centered around 3400 cm^{-1} indicating hydrogen bonded materials.

Figure 2 shows the ^{29}Si NMR of the same sample. The features around -110 ppm correspond to the Q_1 through Q_4 substitution distribution for the silica backbone of the aerogel. The features around -60 ppm correspond to Si species with direct C bonds, most likely from the $C_{16}H_{33}$ group incorporated.

The surface area of this aerogel was found to be 9 m^2/g, and the meso-pore distribution measurement produced no pore distribution.

Figure 3 shows the IR spectrum of a sample of aerogel oxidized at 300°C for 1 hour. In addition to the features seen in the unoxidized aerogel in Figure 1, features are seen from 1600 to 1850 cm^{-1}. The overtone at 1640 cm^{-1} is now adjacent to a sharper taller feature at 1716 cm^{-1}. Deconvolution of this feature (not shown) shows this envelope contains less intense bands at 1741, 1775, and 1847 cm^{-1}. These bands are assigned to alkyl carboxylic acids, esters, and cyclic anhydrides. In addition to these bands formed by the oxidation, the alkyl features in the 2800 to 3000 cm^{-1} range are decreased in intensity.

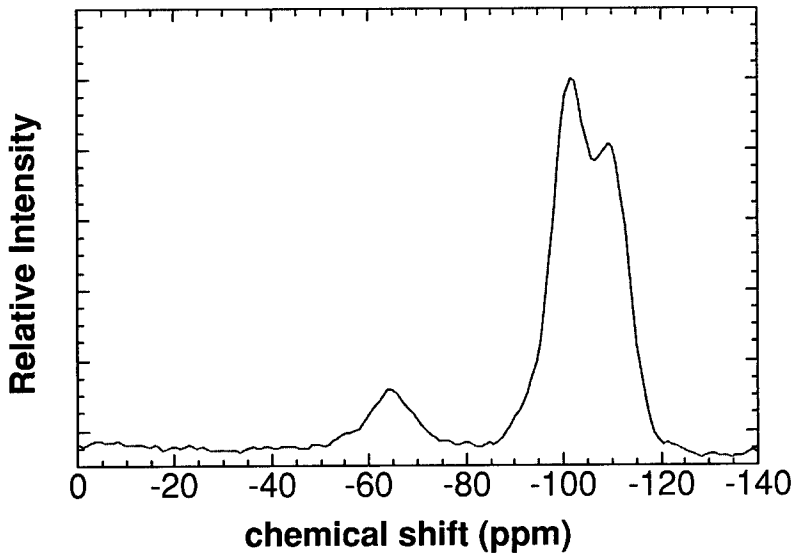


Figure 4. ^{29}Si NMR spectrum of the product of $C_{16}H_{33}Si(OCH_3)_3$ and $(CH_3O)_4Si$ oxidized at 300°C for 4 h

Figure 4 shows the ^{29}Si NMR spectrum of the aerogel oxidized at 300°C for 4 h. The resonances accounting for the Q_1 to Q_4 branching distribution are changed in proportion, but are still visible. The resonance corresponding to the Si-C bond is visible, but is greatly reduced in intensity.

Figure 5 shows the % weight loss of the aerogel at 300°C at different oxidation times. As the oxidation time increases, the amount of weight loss also increases. However, after about 100 min., the % weight appears to reach a upper limit of 45%. There is little difference between the 90 min. data point and the 240 min. data point.

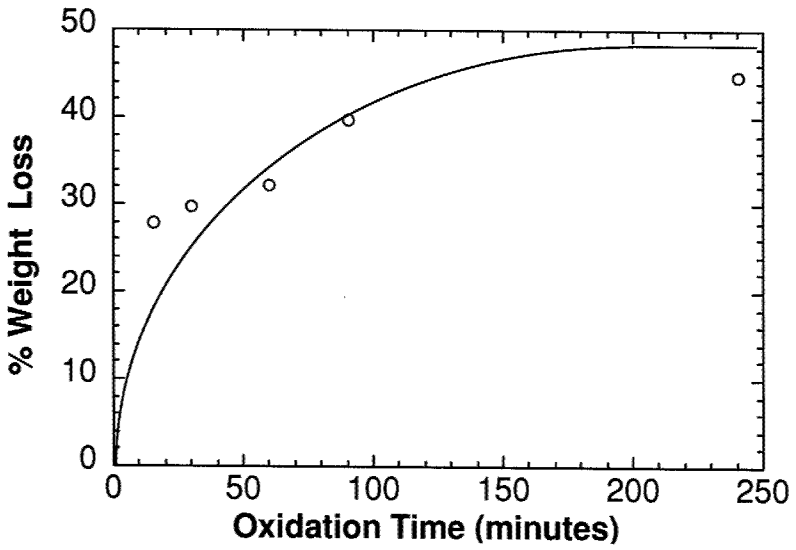


Figure 5. Weight loss of the product of $C_{16}H_{33}Si(OCH_3)_3$ and $(CH_3O)_4Si$ at different oxidation times.

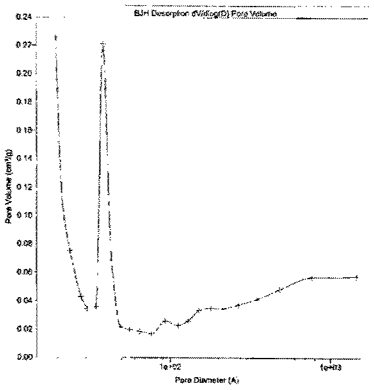


Figure 6. Meso-pore distribution for product of $C_{16}H_{33}Si(OCH_3)_3$ and $(CH_3O)_4Si$ oxidized at 300°C for 1h.

Figure 6 shows the pore size distribution for in the meso-pore range for the sample oxidized at 300°C for 1 h. A sharp pore feature centered at 35Å is visible. Other meso-pore features are seen, but at much lower intensities.

DISCUSSION

The reaction of $C_{16}H_{33}Si(OCH_3)_3$ and $(CH_3O)_4Si$ in methanol utilizing HBF_4 catalysis ultimately produced an aerogel that has the R group incorporated, verified by IR and ^{29}Si NMR. Comparison with IR spectra of the starting material and a xerogel produced by the same formulation indicate the sol-gel process incorporates the substituted

siloxane similar to results seen in preparations with other R group substitution [3,4].

Oxidation at 300°C shows various changes in the properties of the aerogel. The IR spectrum indicates carboxylic acids and other carboxylate features that are not present in the unoxidized aerogel. In addition, the alkyl features appear to be decreasing in intensity relative to the Si-O-Si features. These results suggest the oxidation is logically happening on the $C_{16}H_{33}$ group, probably forming shorter alkyl carboxylic acids esters and cyclic anhydrides. At 90 min. oxidation, most of the alkyl features in the IR are virtually absent (not shown). This corresponding to the weight loss behavior seen in Figure 5, which appears to reach a maximum around that reaction time. However, some of the carboxylate features are still seen in the 90 min. sample spectrum, although the relative intensities are much reduced compared to other features. The ^{29}Si NMR of the oxidized material supports this behavior. The 60 min. sample (not shown) also shows the presence of the Si bound directly to C, but at a much reduced intensity.

The meso-pore measurements of the oxidized aerogel show the formation of a fairly sharp pore distribution at maximum around 35Å. All the other oxidized samples exhibited the same type of pore distribution at the same place, except with different intensities. This must be a result of the oxidation because the non-oxidized aerogel has no meso-pore features. This could possibly due to the oxidation of the $C_{16}H_{33}$ group leaving a void space, or the structural rearrangement of the aerogel itself. However, the same behavior occurs when the aerogel is oxidized at 200°C suggesting aerogel structural rearrangement is unlikely.

Because of the very low surface area and non-existent meso-pore distribution of the non-oxidized aerogel, it can be argued that this material is not an aerogel. A xerogel produced by the same formulation but left to air dry has a similar surface area, and no meso-pore distribution. The oxidiation of the aerogel does produce a sharp meso-pore distribution. This suggests that in the formation of the sol-gel, the R group is so large that it fills the void spaces in the silica matrix that normally lead to standard aerogel meso-pores. The $C_{16}H_{33}$ group is long and flexible and probably folds onto itself into a ball, filling these voids. Alternatively, the group is so large that the sol-gel forms around it, forcing a structure that has no meso-pore size voids.

ACKNOWLEDGMENT

Thanks goes to Robert S. Maxwell of LLNL for useful discussion. This work was performed under the auspices of the U.S. Department of Energy by University of California Lawrence Livermore National Laboratory under contract No. W-7405-ENG-48.

REFERENCES

1. C. J. Brinker, and G. W. Scherer, Sol-Gel Science, The Physics and Chemistry of Sol-Gel Processing, Academic Press, 1989, ISBN 0-12-134970-5.
2. L. W. Hrubesh, Chem. Industry **24**, 824–827 (1989).
3. N. Hüsing, and U. Schubert, Angew. Chem. Int. Ed. **37**, 22–45 (1998).
4. J. G. Reynolds, Recent Res. Dev. Non-Cryst. Solids **1**, 133–149 (2001), ISBN 81-7895-028-6.

Mat. Res. Soc. Symp. Proc. Vol. 740 © 2003 Materials Research Society

Red Shift in Optical Absorption Tail and Superparamagnetism of γ - Fe_2O_3 Nanoparticles in a Polymer Matrix

John K. Vassiliou[1], Jens W. Otto[2], V. Mehrotra[3] and J. J. Davis[1]
[1]Department of Physics, Villanova University, Villanova, PA 19085
[2]Joint Research Center for the European Commission, B-1049 Brussels, Belgium
[3] RSC Rockwell, Thousand Oaks, CA

ABSTRACT

Well defined spherical particles of γ - Fe_2O_3 have been synthesized in the pores of a polymer matrix in the form of beads by an ion exchange and precipitation reaction. The particle size distribution is a gaussian with an average diameter of 80 A. The DC magnetic susceptibility and the magnetization of the nanocomposite has been measured between 4 and 300 K using a Faraday balance and a magnetometer, respectively. The magnetic measurements demonstrate that the particles are superparamagnetic with a blocking temperature T_b about 55 K. The optical absorption edge of the mesoscopic system is red shifted with respect to single crystal films of γ - Fe_2O_3 with an absorption tail extended deeply in the gap. Although lattice distortion and existence of excitonic states in the gap can explain the absorption behavior, the red shift can successfully be explained by the quantum confinement of an electron-hole pair in a spherical well.

INTRODUCTION

Nanophases and nanocomposite materials have been the subject of numerous studies[1-6], because of their interesting physical properties and their potential use to diverse applications such as high density magnetic recording[7], magnetic refrigeration[8], ferrofluids[9] and color imaging[10]. This activity has been triggered by the realization that the physical and chemical properties of nanophase materials are usually dramatically different from those of the bulk counterparts and that nanophase materials often exhibit novel or crossover phenomena. As a result of their small size the properties of nanoparticles are intermediate to those of molecules and bulk solids. The magnetic and optical properties of small particles are modified by the particle size effects. Below a certain critical size, magnetic particles become single domain as opposed to multidomain in the bulk[11]. Furthermore, magnetic nanoparticles exhibit unique phenomena such as superparamagnetism[12,13], quantum tunneling of magnetization[14,16] and occasionally possess unusually high coercivities. Another well known particle size effect is the blue shift of the optical absorption edge in semiconductor nanoparticles[17], due to the molecular character of the wave function of the particles. Novel magnetic and optical properties have been sought by forming nanocomposites of nanoscale magnetic particles in a nonmagnetic matrix in the form of polymer beads[18,19]. The interplay of particle size and properties is reported here.

EXPERIMENTAL

Nanometer-scale iron oxide magnetic particles were synthesized in the porous network of a cross-linked polymer matrix by ion exchange reaction and subsequent hydrolysis[18]. The

polymer matrix is a strongly acidic, cation exchange, resin containing sulfonate functional groups. It consists of sulfonated polystyrene, cross linked with divinylbenzene to form a three dimensional, porous network. We used 50X8-200 resin, marketed under the name Dowex, which is composed of an 8% cross-linked matrix, thus providing a cation exchange capacity of 5.2 meq/g. The polymer was in the form of uniform spherical beads with an approximate diameter of 150 μm. The beads were exposed to an aqueous solution of $FeCl_2$, for an hour, and subsequently washed in sodium hydroxide solution for varying times. Finally the beads were washed with deionized water and methanol and dried to 60 degrees.

Energy dispersive X-ray powder diffraction (EDXD) patterns were obtained using synchrotron radiation at the Cornell High Energy Synchrotron Source (CHESS). The data were collected using a solid germanium detector. The particle size and shape of the iron oxide was determined by transmission electron microscopy (TEM) on microtomed samples. The particle size distribution was determined from the TEM images using a graphic particle size analyzer. The DC magnetic susceptibility of the samples was measured between 4.2 and 300 K by the Faraday balance method, at magnetic field strengths ranging from 2 to 10 kG.

Magnetization measurements were performed using a vibrating sample magnetometer with a helium flow cryostat[19], as well as a Squid magnetometer. The zero field cooled measurements were taken by inserting the sample in the cryostat at zero magnetic field and letting the temperature stabilize at 10 K. A magnetic field of 200 G was applied and the magnetization was measured while increasing the temperature. The field cooled measurements were taken by taking the sample out of the cryostat warming it at room temperature and subsequently, inserting it in the cryostat with a magnetic field of 200 G applied and cooled to 10 K. The magnetization measurements were taken by gradually increasing the temperature.

Optical transmission measurements were performed on a single γ - Fe_2O_3/polymer composite bead using light from a 100 W quartz tungsten-halogen lamp. A single crystal of sapphire was used for mounting the beads. The light from the lamp was monochromated and focused onto a 20 μm spot on the sample. The transmitted light was collected and refocused onto the detector by a sapphire lens. A GaAs photomultiplier tube was used as a detector. A normalized spectrum was taken through the pristine polymer bead[19].

RESULTS AND DISCUSSION

Energy dispersive X-ray scattering identified the oxide phase as γ - Fe_2O_3 (maghemite). The diffraction peaks (Fig.1) were superimposed on a broad background from the amorphous polymer. The pattern was indexed for a cubic phase corresponding to the spinel structure $O_h^7 - Fd3m$. It could also be indexed for the tetragonal phase $P4_1 - C_4^2$. The lattice parameters obtained for the tetragonal phase are a=8.25 A^0 (8.34 A) and c=25.48 A^0 (25.02 A). The values in the parenthesis are the lattice parameters reported in the literature. The pristine beads were X-ray amorphous. Electron diffraction patterns demonstrated the crystalline nature of the particles. Transmition electron micrographs in conjunction with a particle size analyzer determined the particle size distribution to be gaussian with a particle mean radius of 42.5 A^0 and a standard deviation of 10 A^0. Magnetization measurements as function of magnetic field demonstrate that the composite is superparamagnetic between room temperature and 50 K (Fig.2,3). Below 50 K an hysteresis loop appears. The magnetic susceptibility of the nanocomposite depends upon the particle size and the strength of the magnetic field. It increases with decreasing temperature and

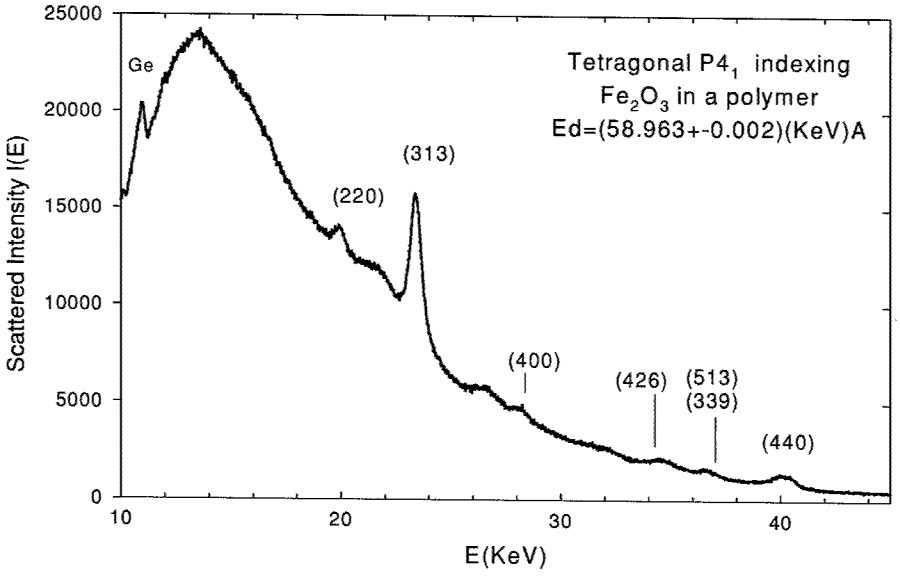


Fig.1. Energy dispersive X-ray pattern of γ - Fe_2O_3 in a polymer matrix. The indexing corresponds to the tetragonal $P4_1$ crystal group

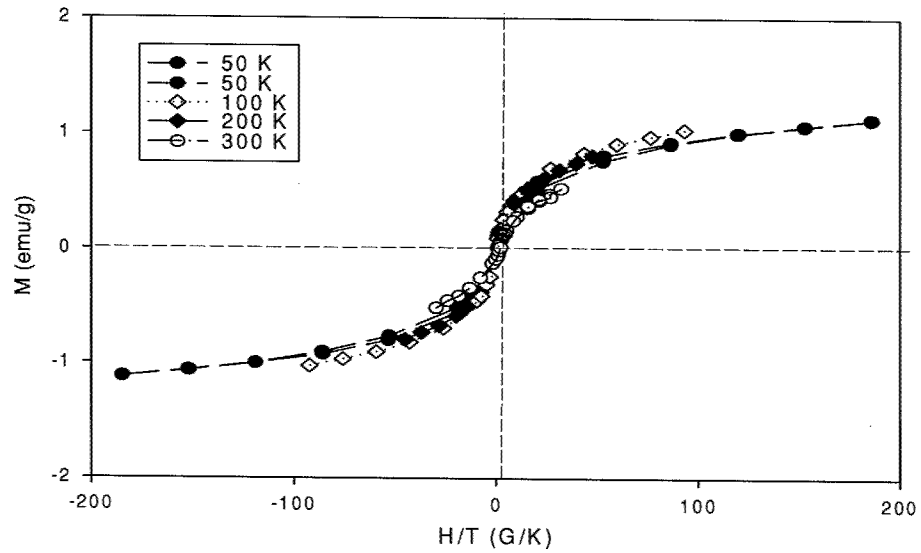


Fig.2. The H/T superposition of all magnetization data for temperatures T greater than the blocking temperature T_b demonstrating superparamagnetic behavior

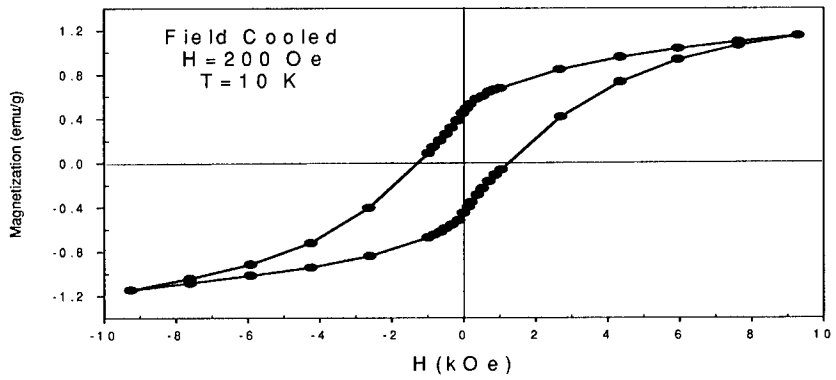


Fig. 3. Magnetization versus applied magnetic field for field cooled loop at 10 K

saturates at low temperatures. The magnitude of the susceptibility is reduced with increasing magnetic field, while the temperature dependance is unaltered[19].

The optical absorption (Fig.4) appears to be red shifted by 0.2 eV in relation to the energy gap of a crystalline film of γ - Fe_2O_3 on MgO [20]. The optical absorption tail penetrates deeply in the energy gap, suggesting the existence of localized energy states in the gap or indirect transitions. The localized states may be due to disorder, impurities, surface states or excitonic states. For a direct allowed optical transition from the valence band to the conduction band the absorption is given by the equation $a = C(E_{Pt} - E_g)^{1/2}$ where E_{Pt} is the photon energy and E_g is the direct energy gap. For indirect transitions, when direct transitions are allowed, the absorption of a photon is accompanied by the absorption or emission of a phonon. The absorption is given by the following equation $a = C_+(E_{Pt} - h\nu_{Pn} - E_{g1})^2 + C_-(E_{Pt} + h\nu_{Pn} - E_{g1})^2$, where $h\nu_{Pn}$ is the phonon energy and ν_{Pn} and h are the phonon frequency and the Planck's constant respectively. If we plot the square of the absorption versus photon energy we find the direct energy gap to be $E_g = 2.02\,\text{eV}$. By plotting the square root of the absorption tail penetrating the gap below 2.02 eV we can find the indirect energy gap $E_{g1} = 1.64\,\text{eV}$ and the involved phonon energy $E_{Pn} = 0.04\,\text{eV}$. The involved phonon's frequency is $\nu_{Pn} = 9.8\,\text{THz}$.

The red shift of the optical absorption can successfully be explained by the quantum size effects of an electron-hole pair confined in a semiconductor nanoparticle[21-23]. The energy gap E_g of a particle of radius R is determined by the following equation:

$$E_g(R) = E_g^0 + \frac{\hbar^2\pi^2}{2\mu R^2} - \frac{1.786e^2}{\varepsilon R} - \frac{0.124e^4\mu}{\hbar^2\varepsilon^2} = E_g^0 + |E_1|\left\{\frac{\pi^2}{\xi}\left(\frac{a_0}{R}\right)^2 - \frac{3.572}{\varepsilon}\left(\frac{a_0}{R}\right) - \frac{0.248\xi}{\varepsilon^2}\right\} \quad (1)$$

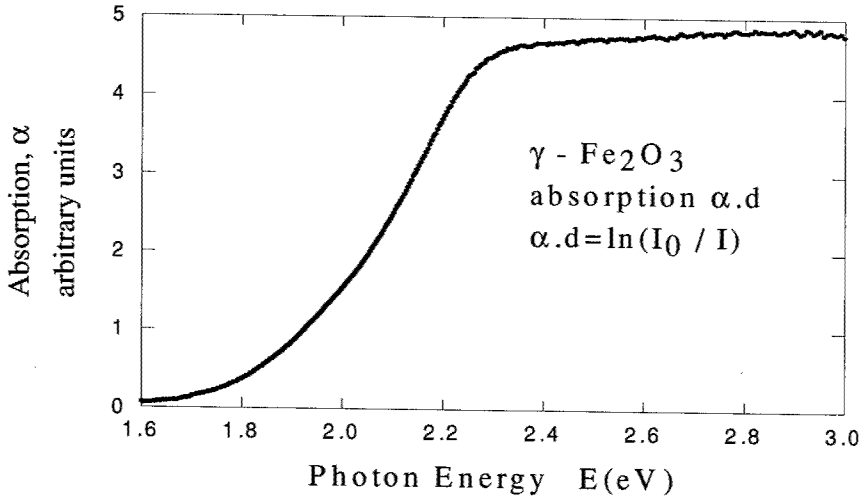


Fig.4. Optical absorption of 80 A^0 diameter particle size of γ-Fe_2O_3 nanocrystals

where E_g^0 is the bulk energy gap, ε is the dielectric constant of the material and

$$\mu = \frac{m_e^* m_h^*}{m_e^* + m_h^*}$$

is the reduced mass of the electron-hole pair. m_e^* and m_h^* are the effective masses of electron and hole, respectively. $|E_1| = \frac{1}{2}\frac{e^4 m_e}{\hbar^2} = 13.6eV$ is the hydrogen first excitation energy and $a_0 = \frac{\hbar^2}{e^2 m_e} = 0.529A$ is the hydrogen Bohr radius. The effective mass of a carrier in a semiconductor material is a fraction of the free electron mass m_e, i.e. $\mu = \xi m_e$. If we take $\xi = 0.2$ which is a typical value for semiconductors and $\varepsilon = 2.67$ the dielectric constant of the material taken from dielectric data, the red shift for a particle of the composite of average radius $R = 42.5A$ is $\Delta E_g = 0.2eV$. The red shift varies between 0.1 and 0.2 eV by varying the values of ξ, ε up to 20%. For a composite of particle size distribution the success of the equation (1) to give the red shift dependence upon the particle size is impressive. An alternative explanation to the red shift has been attributed to the compression of the material due to the surface tension. The excess pressure increases with decreasing size of the nanoparticle causing reduction of the energy gap[19].

The magnetic properties of the nanocomposite can be explained[19] in terms of Neel's[24]

theory of superparamagnetism and its generalization by Brown[25,26]. According this theory, single magnetic domain particles of volume V are characterized by a blocking temperature $T_b=KV/25k_B$. Above this temperature the particles are superparamagnetic and their magnetic moments can rotate uninhibited. Below the blocking temperature the magnetic moments of the particles are frozen out. Because of the particle size distribution the composite will have an average particle volume corresponding to a blocking temperature, below which the system shows magnetic hysteresis. In our system this temperature is around 55 K.

ACKNOWLEDGEMENT

The work was supported in part by the Physics Department at Villanova University and by the National Science Foundation under the proposal No. P621, NSF/CHESS at Cornell Synchrotron. We thank the staff at CHESS for their valuable help.

REFERENCES

1. L. E. Brus, W. L. Brown, R. P. Andres, R. S. Averback, W. A. Goddard III, A. Kaldor, S. G. Louie, M. Moskovits, P. S. Peercy, S.J. Riley, R. W. Siegel, F. A. Spaepen, Y. Wang, J. Mat. Res., 4, 704 (1089).
2. *Research Opportunities for materials with Ultrafine Microstructures*, (National Academy, Alexandria, 1989).
3. Science, 254, 1300 (1991).
4. K. Bittler and W. Ostertag, Angew. Chem. Int. Ed. Engl. 19, 190, (1980).
5. P. Ball and L. Garwin, Nature 355, 761 (1992).
6. G. D. Stucky and J. E. MaCdougall, Science 247, 669 (1990).
7. L. Gunther, Physics World, December, pp.28-34 (1990).
8. R. D. McMichael, R. D. Shull, L. J. Swartzendruder, L. H. Bennett and R. D. Watson, J. Magn. Mater. 111, 29 (1992).
9. R. E. Rosensweig, *Ferrohydrodynamics* (MIT Press, Cambridge, 1985).
10. R. F. Ziolo, U.S. Patent 4 474 866, 1984.
11. C. Kittel, Phys. Rev. 70, 965 (1946); D. J. Dunlop, Phys. Earth Planet. Inter. 26, 1 (1981).
12. C. P. Bean and J. D. Livingston, J. Appl. Phys.30, 120 (1959).
13. I. S. Jacobs and C. P. Bean, in *Magnetism III*, edited by G. T. Rado and H. Shul (Academic, New York, 1963), Chap. 6, and references therein.
14. E. M. Chudnovsky and L. Gunther, Phys. Rev. Lett. 60, 661 (1988).
15. E. M. Chudnovsky and L. Gunther, Phys. Rev. B 37, 9455 (1988).
16. A. J. Leggett, S. Chakravarty, A. T. Dorsey, M. P. A. Fisher, A. Garg, and W. Zuerger, Rev. Mod. Phys. 59, 1 (1987).
17. P. M. Fauchet, C. C. Tsai and K. Tanaka, Eds. in *Materials Issues in Microcrystalline Semiconductors* (Materials Research Society, Pittsburgh, PA, 1990).
18. J. K. Vassiliou, V. Mehrotra, M. W. Russell and E. P. Giannelis, Mater. Res. Soc. symp. Proc. 206, 561 (1991); R. F. Ziolo, E. P. Giannelis, B. A. Weinstein, M. P. O'Horo, B. N. Ganguly, V. Mehrotra, M. W. Russell, and D. R. Huffman, Science 257, 219 (1992).
19. J. K. Vassiliou, V. Mehrotra, M. W. Russell, E. M. Giannelis, R. D. McMichael, R.D. Shull, and R. F. Ziolo, J. Appl. Phys. 73, 5109 (1993).
20. H. Takey and S. Chiba, J. Phys. Soc. Jpn. 21, 1255 (1966).

21. Y. Kayanuma, Solid State Commun. 59, 405 (1986); Phys. Rev. B 38, 9797 (1988).
22. M Hayashi, T. Iwano, H. Nasu, K. Kamiya, N. Sugimotom and K. Hirao, J. Mater, Res. 12, 2552 (1997); B. Yu, C. Zhu, and F. Gan, Opt. Mater. 7, 15 (1997).
23. T. Takagahara, Phys. Rev. B 47, 4569 (1993).
24. L. Neel, Rev. Mod Phys. 25, 293 (1953); Adv. Phys. 4, 191 (1955).
25. W. F. Brown, Jr., J. Appl. Phys. 30, 130 (1959);*ibid.*,34, 1319 (1963).
26. W. F. Brown, Jr., in *Fluctuation Phenomena in Solids* (Academic, New York, 1964), p.37.

Mat. Res. Soc. Symp. Proc. Vol. 740 © 2003 Materials Research Society

Nanomechanical Characterization on Zinc and Tin Oxides Nanobelts

Minhua Zhao[1] Scott Mao[1], Zhong Lin Wang[2] Fengting Xu[3] and John A Barnard[3]
[1] Department of Mechanical Engineering, Univ. of Pittsburgh, Pittsburgh, PA 15261
[2] School of Materials Sci. & Engr. , George Institute of Technology, Atlanta, GA 30332-0245
[3] Department of Materials Sci. & Engr., Univ. of Pittsburgh, Pittsburgh, PA 15261

ABSTRACT

Nanobelts are a group of materials that have a rectangle-like cross section with typical widths of several hundred nanometers, width-to-thickness ratios of 5 to 10, and lengths of hundreds of micron meters. In this paper, nanoindentations were made on individual ZnO, SnO_2 nanobelts and (0001) bulk ZnO by using AFM and Hysitron Triboscope indenters. It was shown that the indentation size effect was still obvious for the indentation depth under 50 nm. It is also demonstrated that nanomaching is possible on nanobelt using AFM tip.

INTRODUCTION

In recent years, quasi one-dimensional (1D) solid nanostructure (nanowires and nanobelts) have stimulated considerable interest for scientific research due to their importance in mesoscopic physics studies and their potential applications. Compared to micrometer diameter whiskers and fibers, these nanostructures are expected to have remarkable optical, electrical, magnetic, and mechanical properties. Exploration of novel methods for large-scale synthesis of 1D nanostructure is a challenging research area. As n-type semiconductive materials, zinc oxide (ZnO) has received a considerable amount of attention over last few years because of many applications it has found in various fields. ZnO is now widely used as transparent conducting oxide materials and gas sensors. In particular, ZnO is regarded as a promising candidate material for flat panel displays because of its high electrical conductivity, high optical transparency as well as its low cost and easy etchability.

Recently, Wang's group [1-3] has successfully synthesized the belt-like oxides (so called nanobelts) by evaporating ZnO or SnO_2 powders at high temperatures without the presence of catalyst. The beltlike morphology is distinct from those of semiconductor nanowires. With a well-defined geometry and perfect crystallinity, the semiconducting oxide belts are likely to be a model materials family for understanding mechanical behavior at nano-scale with absence of dislocations and defects (excluding point defects). The dimension of the nanobelt as a mechanical cantilever potentially can be used as a mechanical resonator, or as electro-optical resonator. Due to its small dimension, the natural frequency (resonance) of the nanobelt, as a resonator could be very high. Since the nanobelt can be used as nanomechanical device, it is important to measure its elastic Young's modulus and strength as well as fracture stress. The nanobelts provide an ideal object for characterizing the mechanical behavior of defect-free semiconducting oxides at nano-scale. In this study, nano-scale mechanical properties of individual zinc oxide nanobelts were characterized by Nanoscope IIIa AFM and Hysitron TriboScope with homemade side view CCD camera. It was shown that the indentation size effect was still obvious for the indentation depth under 50 nm. It is also demonstrated that nanomaching is possible on nanobelt using AFM tip.

EXPERIMENTAL DETAILS

The synthesis of nanobelts was based on thermal evaporation of oxide powders under controlled conditions without presence of catalyst [1-3]. The procedures of preparing dispersed nanobelts for the study reported here are as follows [4]: first immerse the wool like nanobelts in acetone, and the mixture was dispersed by ultrasonic cleaning device. Then dip the polished silicon wafer into the solution and pull out. After drying, single nanobelt lying on silicon substrate.

The prepared nanobelt sample was investigated by two means: one is by tapping mode of Nanoscope IIIa, using diamond indenter tip with a radius of < 25 nm. The other is by STM mode of Hysitron TriboScope, an add-on force transducer from Hysitron Inc., using diamond cubic corner tip with a radius of < 40 nm. In either case, individual nanobelts were imaged, and then nanoindentations were made on the nanobelt using varied loads. After indentation, the indent was imaged in-situ using the image mode of the AFM. For nanoindentations, the hardness is normally defined as the maximum load divided by the projected area of the indenter in contact with the sample at the maximum load. Thus,

$$H = \frac{P_{MAX}}{A_C} \tag{1}$$

where H, P_{MAX} and A_C are hardness, maximum applied load and projected contact area at the maximum applied load, respectively. Since the indenter tip is not rigid during indentation, the elastic modulus can not be directly determined from the load versus displacement curve. However, the reduced elastic modulus can be determined from the unloading portion of the curve by the relation:

$$E_r = \frac{\sqrt{\pi}}{2} \cdot \frac{dP}{dh} \cdot \frac{1}{\sqrt{A_c}} \tag{2}$$

where Er and dP/dh are reduced modulus and experimentally measured stiffness, respectively.

DISCUSSIONS

Figure 1a is a three dimensional image of ZnO nanobelt before indentation. Section analysis shows the nanobelt has a rectangular section. The width of the nanobelt is about 360 nm and the height is about 65 nm. This gives a width-to-thickness ratio of 5.5. These values are typical of a single nanobelt. More investigations using transmission electron microscopy reveal that nanobelt have a rectanglelike cross section with typical widths of several hundred nanometers, width-to-thickness ratios of 5 to 10, and lengths of hundreds of micron meters by TEM. Because the material was already an oxide, it did not undergo a chemical reaction, and had a pure, flawless surface. More importantly, each belt is single crystalline without dislocation. Flawlessness is a major advantage since flaws between crystals can cause problems such as heat generated by flaws when current flows, which is important for nano-scale electronics to increase the density of devices.

After zinc oxide single nanobelt was lying on silicon substrate, the nanobelt was indented by a nanoindentor under AFM. The applied load was recorded as function of penetration. After the nanoindentation, AFM imaging was taken to study local mechanical behavior. Figure 1b is a local magnification of nanoindentations on the nanobelt, where 3 triangle nanoindentations can be found. Figure 2a shows the typical load vs. deflection curves for ZnO and SnO_2 nanobelts on

their top surfaces, which are $(2\bar{1}\,\bar{1}0)$ and $(10\bar{1})$, respectively. From the slope of the loading curves, we can find that the SnO_2 nanobelt is stiffer than ZnO nanobelt. Based on Equation (1), using load vs. deflection curves during nanoindentation, hardness of ZnO and SnO_2 nanobelts was calculated as function of indentation penetration, and the result is summarized in Fig. 2b. The hardness of ZnO is lower than that in SnO2 nanobelt. Also it can be seen that the lower penetration of the nanoindentation, the higher the hardness of the nanobelt, which is attributed to the strain gradient effect (size effect) during nanoindentation for most materials [5-6].

Comparison of ZnO nanobelt with ZnO bulk single crystal was carried out on (0001) plane by nanoindentation. As shown in Fig 3, ZnO nanobelt is little softer than that of bulk single crystal. This is likely due to that the (0001) is the most close packed plane for hexagonal structured ZnO, thus, the hardness along [0001] (the c-axis) may be higher than that along $[2\bar{1}\,\bar{1}0]$ (the a-axis), which is the normal direction of the nanobelt.

Based on Equation (2), from load vs. deflection curves, elastic modulus of ZnO and SnO_2 nanobelts are calculated as a function of the indentation penetration. As shown in Fig. 4, the elastic modulus of the SnO_2 is higher than that of ZnO. The increase of elastic modulus leads to the increase of the hardness for SnO_2 nanobelt compared to that of the ZnO nanobelt, which was given in Figure 2b.

Nano-indentation induced fracture test on SnO_2 also was carried out by increasing a large indentation loads on the nanobelt. Figure 5a shows a crack induced by nano-indenation, which was initiated from a triangle edge on the indentation. The crack propagates along [101], and the cleavage surface is (010) based on the structural information provided by electron microscopy [1]. Figure 5b is the indentation load vs. penetration curve, which indicates unstable crack propagation when 43 micro-Newton of indentation load is applied. This is probably the load at which the crack is created. After the penetration reaches 60 nm (~ belt thickness), nanoindentor starts indenting Si substrate and the load starts picking-up since Si substrate is harder than SnO_2 crystal. The fracture test on SnO_2 demonstrated the possibility to cut or machine the nanobelt under AFM down to smaller size.

CONCLUSIONS

Imaging, manipulating and testing on mechanical properties of a single nanobelt of ZnO and SnO_2, whose size is in the nano- to micron-meter range, have been performed using atomic force microscope. The hardness and elastic modulus of the ZnO nanobelt is smaller than that of SnO_2. Furthermore, the hardness of dislocation free ZnO nanobelt is slightly smaller than that of the c-axis oriented bulk ZnO single crystal, which may be attributed to the anisotropic structure of the ZnO.

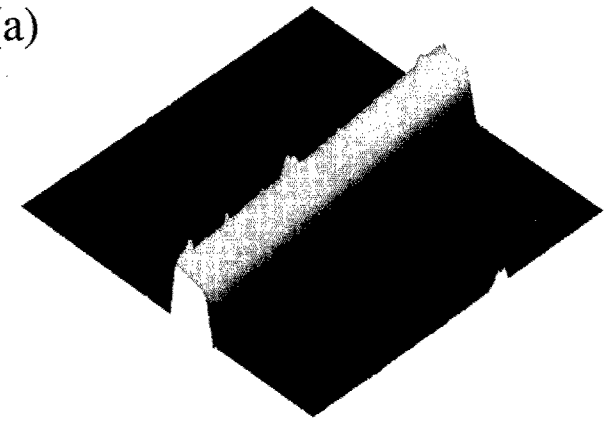
ACKNOWLEDGEMENTS

The authors are grateful to the support from NSF Grant No. CMS-0140317 to University of Pittsburgh and NSF Grant No. DMR-9733160 to Georgia Tech.

REFERENCE

1. Zheng Wei Pan, Zurong Dai and Zhong Lin Wang et al, Nanobelts of Semiconducting Oxides, Science, 9 March 2001, pp. 1947-9.
2. Z.R. Dai, Z.W. Pan and Z.L. Wang, Solid State communications 118 (2001), 351-354.
3. Z.W. Pan, Z.R. Dai and Z.L. Wang, Applied Physics Letters, Vol. 80 No.2, January 2002, P. 309
4. Scott Mao, M. Zhao, and Zhong Lin Wang, MRS 2002 fall Symposium F: Semiconductor Materials and Devices, Boston Dec. 2-6, 2002.
5. D. M. Duan, N. Wu, W.S. Slaughter, S.X. Mao, *Mat. Sci. & Eng. A. A303 (2001) 241-249*.
6. B. M. Ennis, W. Slaughter, Anita Madan and S.X. Mao, submitted to Acta Materialia.

(a)



(b)

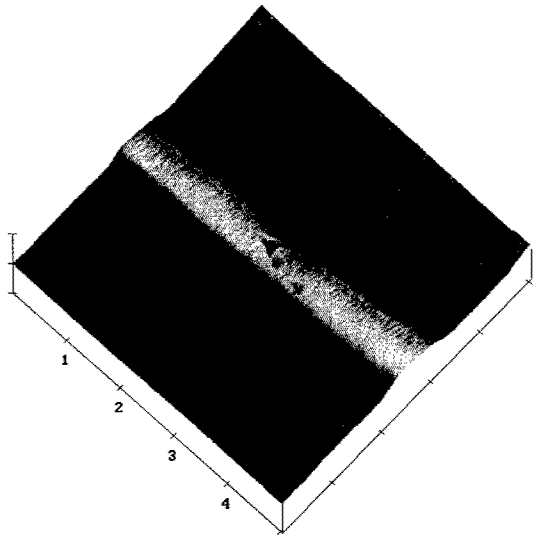
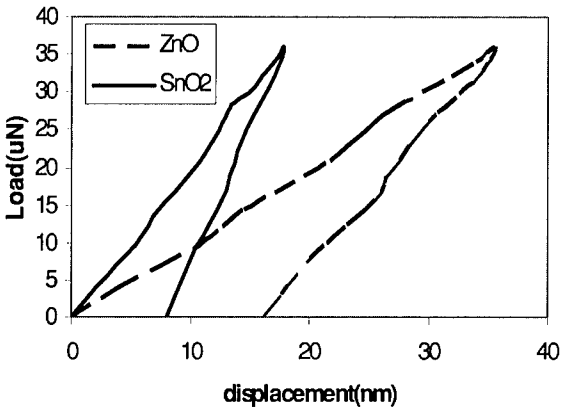


Figure 1. (a) Three dimensional image of ZnO nanobelt imaged by AFM indenter tip; (b) Indentation on ZnO nanobelt by AFM indenter.

(a)



(b)

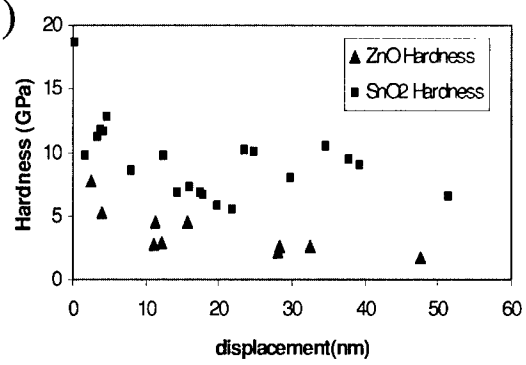


Figure 2. (a) Load vs. deflection curve during nanoindentation under AFM. The stiffness of SnO_2 is larger than that of ZnO nanobelt. (b) Hardness of ZnO and SnO_2 nanobelts as function of penetration during nanoindetation.

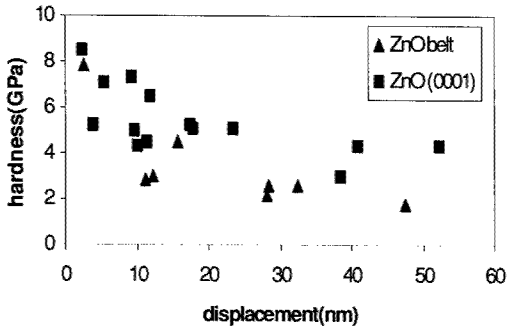


Figure 3. Hardness for ZnO nanobelt and bulk single crystal (0001).

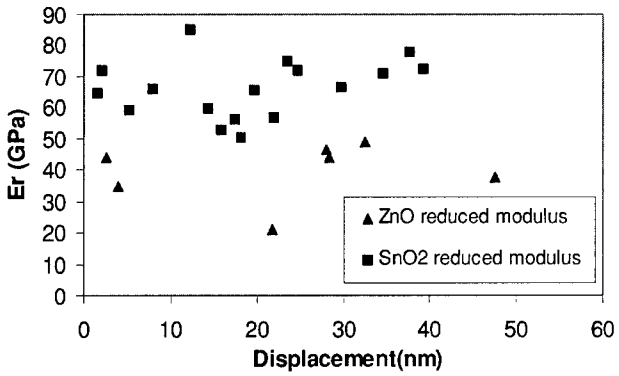
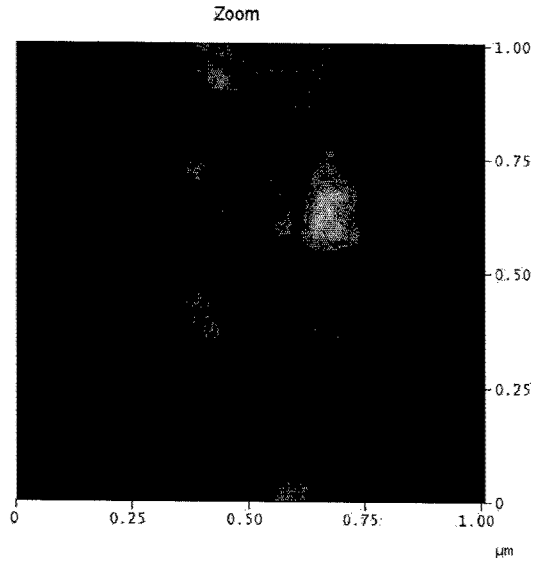


Figure 4. Elastic modulus of ZnO and SnO_2 nanobelts as function of penetration during nanoindetation



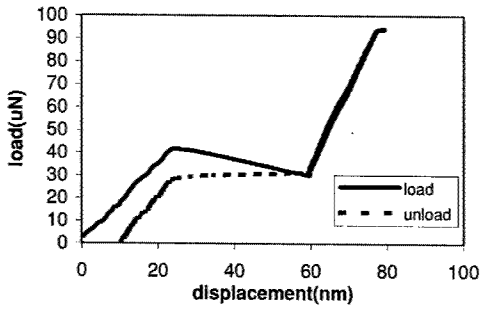


Figure 5. Crack nucleation and propagation in SnO_2 nanobelt by nanoindentation under AFM, (a) a crack induced by nano-indenation and (b) indentation load vs. penetration curve, which indicates unstable crack propagation when 43 micro-Newton of indentation load is applied.

Mat. Res. Soc. Symp. Proc. Vol. 740 © 2003 Materials Research Society I9.6

Anomalous X-ray Scattering for Determination of Nanostructured Alloy Formation and Site-specific Chemistry of Bragg Peak

G.M. Chow*
Department of Materials Science
National University of Singapore
Kent Ridge, Singapore 119260
Republic of Singapore
Email: mascgm@nus.edu.sg

* Also at Singapore-Massachusetts Institute of Technology Alliance (SMA), Republic of Singapore

ABSTRACT

The properties of nanostructured films can be tailored by many factors such as composition, structure, preferred orientation, microstructure, interphase interface and grain boundaries. Compositional control of magnetic properties of recording media depends on the miscibility of constituent elements. However, for nanostructured materials with a large surface-to-volume ratio of atoms, the miscibility at the nanoscale may not necessarily follow the prediction of conventional phase diagram that does not consider the effects of surface and interface. This limitation further complicates the prediction of phase separation at grain boundaries and interphase interface. Using anomalous x-ray scattering, the alloying and composition of a specific long range order of textured nanostructured films has been investigated. Such information may not be readily available from conventional characterization techniques.

INTRODUCTION

Nanostructured polycrystalline films have a significant amount of grain boundaries and interfaces. For many advanced materials such as those used in magnetic applications, careful control of the grain size, global composition, composition of a specific textured Bragg peak, long range order (LRO), short range order (SRO) and interphase interfaces, is of essential importance in order to achieve the desirable properties.

The empirical factors that favor the formation of a binary solid solution can be provided by the Hume-Rothery's rules [1]. The structural characterization and determination of alloys and composites by x-ray diffraction (XRD) is also well established [2]. For coarse-grained materials, the appearance of a single set of diffraction peaks and the disappearance of elemental peaks are commonly considered as a strong evidence of formation of a solid solution. The variation of lattice parameter with the composition of a random, substitutional alloy can be qualitatively followed using the Vergard's law.

When the crystallite size of a material is reduced to below a critical length scale, a nanostructured solid solution cannot be unambiguously differentiated from a nanocomposite using conventional XRD [3]. In a nanocomposite where the two phases have close lattice parameters and x-ray structural coherence, the Bragg peak of one phase has some degree of overlap with that of the other phase. Because of the effect of size broadening and the contribution to diffraction amplitude by structural coherence of the two phases, a single peak will appear for a particular Bragg reflection when the size is below a certain limit. However, this single peak has an average lattice spacing that has no correspondence in real space, and can be easily mistaken as evidence of formation of a solid solution. The critical domain size is mainly determined by the differences in scattering powers and lattice spacings of the constituent elements, and the ability to form coherence interfaces. This consideration is not limited only to XRD, and different scattering powers of different structural techniques result in different critical domain size [3]. Therefore, conventional XRD, commonly established for probing the LRO, should not be used alone to study the structure of nanostructured alloys and composites made of structurally coherent and immiscible materials.

In this paper, an overview of our work on the determination of alloying and composition of a specific Bragg peak of nanostructured magnetic films using synchrotron techniques is presented. The synchrotron techniques, due to the high brightness, flux and resolution, and tunable photon energy, are unique to provide structural and chemical information that is not available from the conventional characterization methods. Using anomalous x-ray scattering, it was shown that nanostructured NiCo films did not necessarily form solid solution as expected from their phase diagram or suggested by the results of conventional XRD [4]. The compositions of constituent elements of the textured Bragg peak of CoCrPt film were also investigated using this method [5]. The limitations of using conventional XRD alone for studying nanostructured alloys are discussed. Advantages of complementary structural investigations using anomalous x-ray scattering (for LRO) and extended x-ray absorption fine structure spectroscopy (for SRO) are presented. The limitations of applying conventional phase diagram to nanostructured materials are also addressed.

RESULTS AND DISCUSSIONS

Ni-Co films [4]

Nickel-cobalt based films find applications in decoration, protection and magnetic applications. Nickel has the fcc structure. Cobalt transforms from the hcp ε phase to the fcc α phase at about 422 °C. The Ni-Co system has complete solid solubility as the (Ni, αCo) phase at temperatures between the solidus and the solvus of the fcc $\leftrightarrow$ hcp transformation temperature. The composition of Ni in the (ε Co) phase is approximately $\leq$ 35 at. % [6]. The lattice constants for fcc Ni and fcc Co are 3.5238 Å and 3.5447 Å, respectively. The K absorption edges for Co and Ni are 7.709 keV and 8.333 keV, respectively.

The Ni_xCo_{100-x} (x = 0, 50, 90 and 100) magnetic films were deposited on Cu substrates using the non-aqueous, electroless polyol method [7]. The magnetic properties of these films can be found elsewhere [7]. Synchrotron specular x-ray scattering, anomalous x-ray scattering (AXS)

and extended x-ray absorption fine structure (EXAFS) spectroscopy were employed to investigate the LRO and SRO of these NiCo films.

Although EXAFS has been widely accepted as a very useful tool to study nanostructured metastable alloys, it is unsuitable for investigating materials consisted of elements (such as Ni and Co) with very close lattice parameters, backscattering amplitudes and phase shifts. The EXAFS results of the Ni edge and Co edge of $Ni_{90}Co_{10}$ and $Ni_{50}Co_{50}$ did not show noticeable difference from the elemental films (Fig. 1). The EXAFS data were therefore inconclusive regarding the mixing of these elements in the films.

Conventional specular XRD results showed these films were polycrystalline and had a single set of fcc diffraction peaks. No elemental separation was detected. Due to the close lattice constants of fcc Ni and fcc Co, the formation of alloy or composite could not be ascertained using XRD. The average crystallite size of Ni_{100}, Co_{100}, $Ni_{90}Co_{10}$ and $Ni_{50}Co_{50}$, as estimated from the (111) line broadening, were 64, 15, 45 and 16 nm, respectively. Only the (111) peaks that gave the strongest signal were used for AXS measurements. Powder diffraction experiments were first performed just below the respective K-edges of Ni and Co to determine the position of the (111) Bragg peak of the films at each photon energy. At the (111) reflection, only a single peak was observed in the $Ni_{50}Co_{50}$ and $Ni_{90}Co_{10}$ films. For AXS measurements, the momentum transfer was fixed to the positions of the (111) reflection, i.e. $q = 3.086 Å^{-1}$, and the scattering intensity was monitored as the x-ray energy was varied through the Ni and Co K-absorption edges, respectively. Good counting statistics was ensured in data collection.

The atomic scattering factor consists of the non-resonant Thomson scattering factor and the resonant anomalous scattering factor. In diffraction measurements, the diffraction intensity is proportional to the square of the atomic factor and shows absorption-like information. If the element in question is related to the specific Bragg peak, then the elemental absorption causes a decrease in the Bragg intensity at its absorption edge. A cusp, due to the interference between the Thomson scattering amplitude and the real part of the anomalous scattering amplitude [8], can be observed in the energy scan of the Bragg peak. This behavior was indeed observed for the Ni_{100} and Co_{100} films.

The AXS measurements of the (111) peaks of $Ni_{50}Co_{50}$ and $Ni_{90}Co_{10}$, around the K-absorption edges of Ni and Co, respectively, are shown in Figs. 2a and 2b. Both Ni and Co were related to this Bragg peak for the $Ni_{50}Co_{50}$ film. Due to their very close lattice parameters, it was not possible to determine if the peak with both elements represented an alloy or a composite. For the $Ni_{90}Co_{10}$ film, only Ni was related to the Bragg peak, whereas the Co absorption was clearly absent. The existence of Co in the $Ni_{90}Co_{10}$ sample was however indeed confirmed by the Co absorption edge in EXAFS and the chemical analysis using energy-dispersive x-ray spectroscopy. Within the detection limit of AXS, Co was not associated with the (111) Bragg peak of this film. Only Ni solely contributed to this Bragg peak. The absence of Co in the (111) Bragg peak of $Ni_{90}Co_{10}$ suggested that Co did not alloy with Ni in this atomic arrangement.

The effects of surface segregation and the correlation with the composition of the LRO need to be addressed. A thermodynamic analysis of a $Ni_{50}Co_{50}$ alloy nanoparticle was carried out to study the influence of size effect on surface compositional segregation[9]. The surface

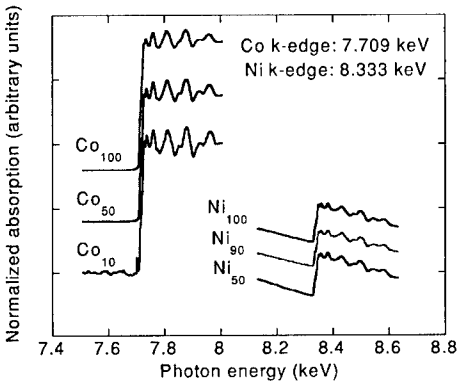


Figure 1. Normalized absorption of EXAFS of Ni-Co films, showing both Ni K- and Co K-absorption edges

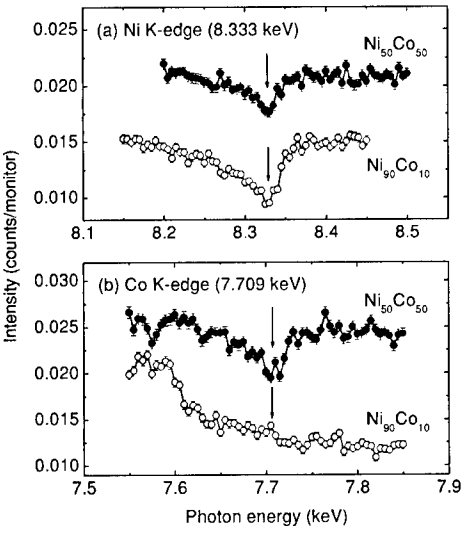


Figure 2. (a) AXS results of $Ni_{50}Co_{50}$ and $Ni_{90}Co_{10}$ films, Ni K-absorption edge. (b) AXS results of $Ni_{50}Co_{50}$ and $Ni_{90}Co_{10}$ films, Co K-absorption edge

compositions of $Ni_{50}Co_{50}$ nanoparticles were calculated based on the regular solution model, that takes into account of the size effect, and compared with that of bulk alloy particles with a larger size. The segregated surface compositions in the alloy nanoparticles (diameter of 10-100 nm) were few times larger than that of the corresponding bulk particles with the particle diameter > 100 nm. Surface segregation would eventually lead to the phase separation beyond a critical size limit for nanostructures.

CoCrPt films [5]

The magnetic properties of sputtered magnetic Co-Cr based films, as longitudinal and perpendicular recording media materials, are controlled by the alloy composition and the degree of phase separation of Co and Cr, the alignment of the columnar structures, the degree of Cr segregation at the grain boundaries and the mosaic of the texture. It is important to achieve a proper crystallographic texture with optimal composition to control the magnetocrystalline anisotropy. The magnetic properties of CoCrPt media films can be optimized by the control of Cr and Pt concentrations that can respectively reduce medium noise and enhance coercivity [10]. The segregation of Cr inhomogeneities in sputtered Co-based films has been considered as Cr segregation at grain boundaries [11], formation of Co_3Cr [12], SRO of Cr [13], formation of Cr oxide at grain boundaries [14], segregated microstructures and two-phase compositional separation [15]. The phase separation occurred by surface diffusion [16] or discontinuous precipitation via grain boundary diffusion [17].

Many characterization techniques, including TEM, x-ray microanalysis, thermo-magnetic analysis, atom-probe field ion microscopy, nuclear magnetic resonance, EXAFS, and STM, have been used to investigate the segregation of Cr. These methods however do not yield direct elemental correlation with the specific LRO of interest. In addition, structural information of compositional segregation cannot be obtained using conventional XRD or TEM, since Co and Cr have similar atomic numbers and scattering factors. It has been commonly but wrongly accepted that a single XRD Bragg peak without detectable elemental separation in these films supports that compositional segregation does not perturb the crystalline order. The conventional phase diagram may not necessarily be applicable in predicting the miscibility or phase separation of nanostructured materials, since it does not take into consideration of the significant contribution of surface and interfaces in these materials. A study was carried out to determine the elemental concentrations of the textured Bragg peak and the averaged local atomic environment of sputtered CoCrPt films using AXS and EXAFS [5].

Both magnetic $Co_{66}Cr_{18}Pt_{16}$ layer (30 nm and 60 nm thick) and Ti underlayer (25 nm thick) were deposited on glass substrates at 250 °C using dc magnetron sputtering. The argon pressure for sputtering Ti and CoCrPt were 3 and 10 mTorr, respectively. Magnetic measurements were performed using VSM. The samples were prepared for structural study without optimizing the magnetic properties.

The x-ray powder scans showed both magnetic layer and Ti underlayer were textured at (002) (Fig. 3). The weak shoulder-peak around $q = 2.959$ Å^{-1} could be assigned to (202) of Ti_2O_3, suggesting the occurrence of Ti underlayer oxidation. The (002) mosaic was obtained

from the full-width-half-maximum of the χ rocking curves. The mosaic was large for these films with poor texture. The crystal domain size (estimated from peak broadening) of Ti underlayer was 20 nm and that of30 nm (60 nm)-thick magnetic film was 30 nm (42 nm), as limited by the respective layer thickness. The VSM hysteresis loops showed these films had perpendicular magnetization orientation. The structure and perpendicular magnetic properties of these films can be found in reference 5. The M_s values were within the reported range for Co-Cr films in this Cr concentration regime [18].

For AXS study, the θ-2θ scan was first performed to determine the position of the CoCrPt (002) reflection (q = 2.984 $Å^{-1}$) at x-ray energies of 7.509 and 5.789 keV (below the respective *K*-edges of Co and Cr). There was no detectable phase separation at the (002) reflection (Fig. 3). In AXS, the momentum transfer was fixed to the position of (002) reflection at each photon energy. The scattering intensity was monitored as the x-ray energy was scanned through the Co and Cr *K*-absorption edges, respectively. The anomalous scattering of Pt was not measured due to the energy limit of the beamline used in this study.

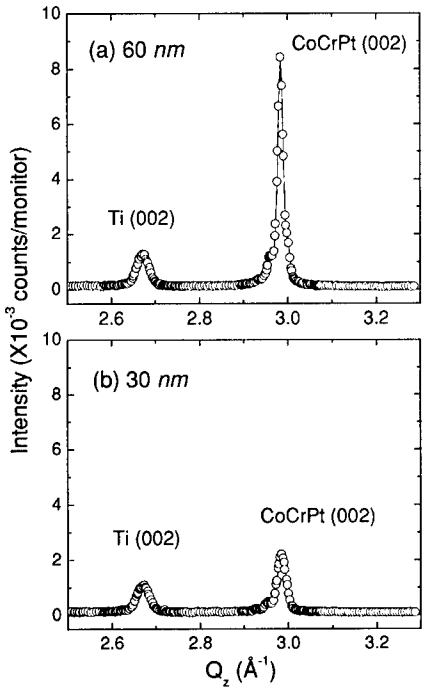


Figure 3. X-ray powder θ-2θ scans of (a) 60 nm film, and (b) 30 nm film

For a qualitative comparison, the measured AXS data was fitted using a film-thickness independent simulation, based on the kinematic approximation of intensity with random mixing of elements. The simulation only considered the concentration of elements in the specific structural order. Figures 4 and 5 show the AXS spectra of the (002) Bragg peak taken in the vicinity of Co and Cr absorption *K*-edges, respectively. The experimental data was fitted against the simulated spectra using different concentrations. The energy resolution in data collection was estimated as ~7 eV. The Co concentrations in the (002) peak for both films were ~62%, with an estimated uncertainty of ± 5 % (Fig. 4). The Cr concentration in this Bragg peak was ~25 ± 6 % for the 60 nm film, and ~ 22 ± 6 % for the 30 nm film (Fig. 5). Compared to the average global film composition, i.e. $Co_{66}Cr_{18}Pt_{16}$, the concentrations of Co decreased whereas that of Cr increased in the (002) peak.

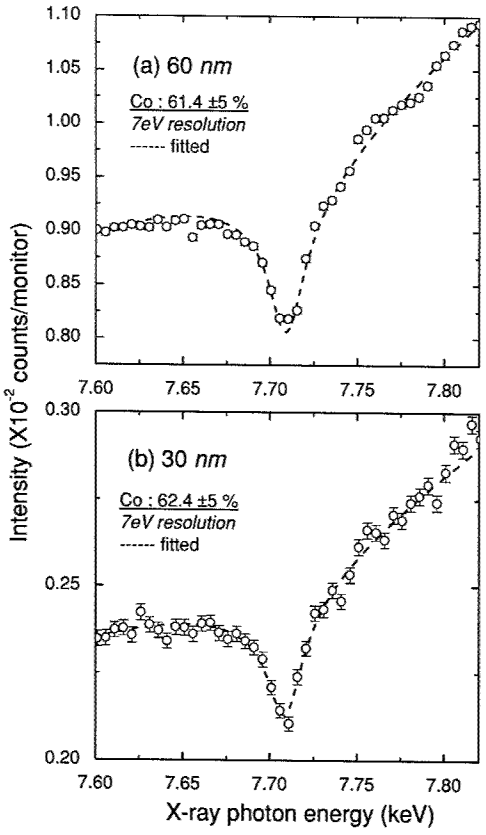


Figure 4. AXS spectra of the (002) peak in the vicinity of Co absorption *K*-edge. (a) 60 nm film. (b) 30 nm film

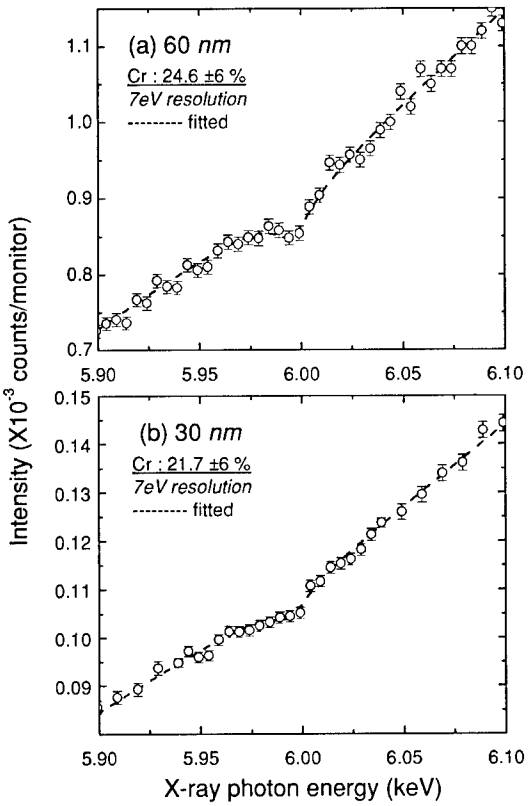


Figure 5. AXS spectra of the (002) peak in the vicinity of Cr absorption *K*-edge. (a) 60 nm film. (b) 30 nm film

The EXAFS data of Co and Cr were analyzed using a standard WinXAS 97 procedure [19]. The Pt EXAFS was too noisy for useful quantitative analysis as the absorption edge was near the operation limit of the beamline. Figure 6a shows the Fourier Transform amplitude of the Co foil standard, the 30 and 60 nm samples. The coordination number of the first shell of both magnetic films was similar but lower than that of the hcp Co foil standard. This indicated that Co had alloyed with other constituent elements. The Cr EXAFS of both films differed from that of the bcc Cr foil standard (Fig. 6.b).

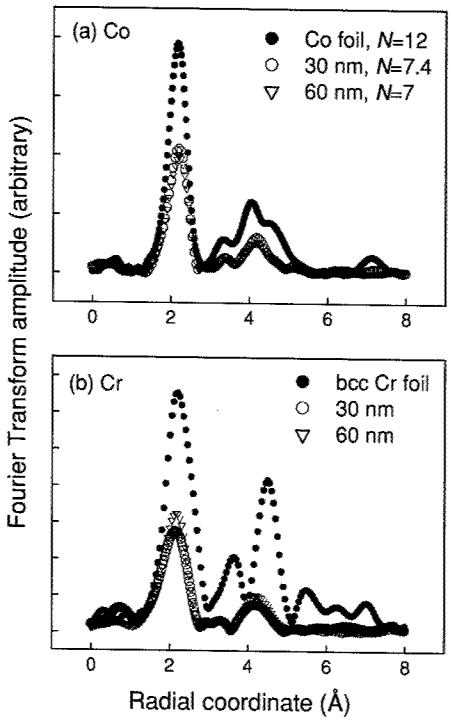


Figure 6. Fourier Transform Amplitude of (a) Co, and (b) Cr. *N* denotes the coordination number of the first shell

The AXS method only probed the elemental concentrations in the (002) peak, it did not provide the structure information besides this LRO. On the other hand, the EXAFS measurements provided averaged global information of the local atomic environment of the element in question. The AXS results revealed that Co maintained similar concentration in the (002) peak for both films. The EXAFS results showed that both films had similar Co coordination number that was lower than the bulk Co foil. A certain degree of Co alloying with Cr and perhaps Pt had therefore occurred. The dilution of Co by Cr (> 13 %) addition stabilizes perpendicular magnetization and lowers M_s. Compared to the global composition, the higher Cr concentration detected in the (002) peak for both films showed that the crystallinity of Cr was well established.

The observation of a higher Cr content in the textured peak ruled out the common assumption that a significant amount of Cr segregate to the grain boundaries, since grain boundaries are not expected to exhibit any LRO. If the segregation of Cr had resulted in two

crystalline phases, such phases must have the same *d*-spacing as the AXS measurements were fixed at the (002) momentum transfer. The segregation to two crystalline phases with the same *d*-spacing is equivalent to a single phase inhomogeneous alloy. Since Cr did not preferentially segregate to grain boundaries, a resultant higher magnetic exchange coupling [20] and reduced magnetocrystalline anisotropy constant [21] would reduce the coercivity. Since Pt is known to increase the local disorder and thus coercivity by increasing the magnetocrystalline anisotropy [22], the lower coercivity of 60 nm film [5] suggested that less Pt existed in the CoCrPt (002) Bragg peak, compared with that of 30 nm film. This argument is consistent with the observed higher Cr content (Fig. 5) and higher Fourier transform amplitude of Cr edge (Fig. 6b) of the 60 nm thick film. The low sputtering temperature and pressure used in this study could be responsible for inefficient Cr segregation in the grain boundaries [23].

SUMMARY

Conventional x-ray diffraction failed to provide correct information on alloying of materials made of elements with close lattice parameters, even for elements (such as Ni and Co) that are commonly accepted to have miscibility. Using anomalous x-ray scattering, we showed that nanostructured NiCo films did not necessarily form solid solution as expected from their phase diagram or suggested by the results of conventional x-ray diffraction.

The correlation of elemental chemistry with a particular LRO in question cannot be obtained by common conventional characterization techniques. The elemental concentrations of the textured Bragg peak and the averaged local atomic environment of sputtered CoCrPt films were investigated using anomalous x-ray scattering and extended x-ray absorption fine structures. The compositions of constituent elements of the textured peak in these polycrystalline nanostructured films differed from the average film composition. The higher Cr concentration in the textured peak showed that a significant amount of Cr did not segregate to the grain boundaries, as a result of low sputtering temperature and pressure used.

ACKNOWLEDGMENTS

The support of this research by the Academic Research Fund of the National University of Singapore and the grant from the Office of Naval Research (USA) is gratefully acknowledged. The synchrotron experiments were performed in Pohang Light Source, S. Korea, and Synchrotron Radiation Research Center, Taiwan.

REFERENCES

1. P. Haasen, Physical Metallurgy, 2nd edition, Cambridge University Press, Cambridge, UK, 1986, p. 125.
2. B.D. Cullity, Elements of x-ray diffraction, 2nd edition, Addison-Wesley Publishing Co. Inc., USA, 1978, p. 375.

3. C. Michaelsen, *Phil. Mag. A*, **72**, 813 (1995).
4. G.M. Chow, W.C. Goh, Y.K. Hwu, T.S. Cho, J.H. Je, H.H. Lee, H.C. Kang, D.Y. Noh, C. K. Lin and W. D. Chang, *Appl. Phys. Lett.* **75**,2503 (1999).
5. G.M. Chow, C.J. Sun, E.W. Soo, J.P. Wang, H.H. Lee, D.Y. Noh, T.S. Cho, J.H. Je and Y.K. Hwu, *Appl. Phys. Lett.* **80**,1607 (2002).
6. T. B. Massalski (ed.), Binary alloy phase diagrams, second edition, ASM International, USA, 1990, p. 1214.
7. G.M. Chow, J. Ding, J. Zhang, K.Y. Lee, D. Surani and S.H. Lawrence, *Appl. Phys. Lett.* **74**, 1889 (1999).
8. H. Stragier, J.O. Cross, J.J. Rehr, L.B. Sorensen, C.E. Bouldin and C.E. Woicik, *Phys. Rev. Lett*, **69**, 3064 (1992).
9. R. Jayaganthan and G.M. Chow, *Mater. Sci. Eng. B.* **95**, 116 (2002).
10. M.F. Doerner, T. Yogi, D.S. Parker, S. Lambert, B. Hermsmeier and O.C. Allegranza, *IEEE Trans. Magn.* **29**, 3667 (1993).
11. K. Ouchi and S. Iwasaki, *J. Appl. Phys.* **57**, 4013 (1985).
12. T. Chen, G.B. Charlan and T. Yamashita, *J. Appl. Phys.* **54**, 5103 (1983).
13. W. G. Haines, *J. Appl. Phys.* **55**, 2263 (1984).
14. J.W. Smits, S.B. Luitjens, and F.J.A. den Broeder, *J. Appl. Phys.* **55**, 2260 (1984).
15. D. J. Rogers, Y.Maeda, K. M. Krishnan, *J. Magn. Mag. Mater.* **163**, 393 (1997).
16. K. Hono, K. Yeh, Y. Maeda and T. Sakurai, *Appl. Phys. Lett.* **66**, 1686 (1995).
17. A. Pundt and C. Michaelsen, *Phys. Rev. B.* **56**, 14352 (1997).
18. C.W. Chen, *J. Mater. Sci.* **26**, 1705 (1991).
19. T. Ressler, *J. Physique IV 7*, C2-269 (1997).
20. J. G. Zhu, and H. N. Bertram, *J. Appl. Phys.* **63**, 3248 (1988).
21. I.M. Song, S. Ishio, M. Ishizuka, T. Tsunoda and M. Takahashi, *J. Magn. Magn. Mater.* **119**, 261 (1993).
22. K.M. Kemner, V.G. Harris, W.T. Elam, Y.C. Feng, D.E. Laughlin, J.C. Woicik, and J.C. Lodder, *J. Appl. Phys.* **82**, 2912 (1997).
23. N. Honda, J. Ariake, K. Ouchi and S. Iwasaki, *J. Magn. Magn. Mater.* **155**, 154 (1996).

Synthesis of Nanostructured Materials I

Mat. Res. Soc. Symp. Proc. Vol. 740 © 2003 Materials Research Society

Fabrication of isolated ferroelectric nanostructures

S. Bhattacharyya[a], Soma Chattopadhyay[•] and M. Alexe
Max Planck Institute of Microstructure Physics
Weinberg 2, D-06120 Halle, Germany

ABSTRACT

In this report, we explore the possibilities of the fabrication and characterization of ferroelectric nano-structures by various methods. Techniques include the self-assembly route and direct electron beam lithography. The chemical self-assembly route, which adopted the microemulsion-mediated synthesis, appeared to be very encouraging for producing very small monodispersed nano particles and powders, with sizes of 10-60 nm. The possibility to form a two dimensional arrangement of these micro droplets was explored with a suitable choice of the substrate material, and the method of coating. For the patterns prepared by the e-beam technique, a strong coupling between two closely spaced nano elements was observed, the spacing between them was found to be the key factor in tailoring their interaction, i.e., whether they would arrange themselves in rod-like pattern or a two dimensional array of isolated squares or circles.

INTRODUCTION

The quest for understanding nano particle processing methods is a natural consequence of the extensive activities carried out in the last decade that resulted in decreasing the size of electronic devices [1,2]. At present there are many ongoing research activities to explore the most rational and reproducible means of fabricating nano-patterns in a controlled manner [3,4]. Ferroelectrics are known to be a special class of functional materials that are promising for nano-scale applications such as in high density memory devices, miniaturized sensors and transducers [5,6]. It is therefore highly relevant to the scientific community to fabricate and study ferroelectric materials at the nanoscale level. In this paper, we are comparing the results of our attempts to fabricate ferroelectric nanostructures using both "top down" and "bottom up" approaches. The systems chosen were simple perovskites such as $BaTiO_3$, and $Pb(Zr_{0.40},Ti_{0.60})O_3$, for their relative ease of fabrication. In the chemical "self assembly" route, we have employed the microemulsion mediated synthesis [7,8] of monodispersed nano-particles (dispersed in a liquid medium). Although getting a regular arrangement of these particles on a solid surface is still in its infancy, it is possible to get isolated nano dots with reasonably uniform sizes. There was an agglomeration problem associated with the highly reactive fine particles which could be overcome by the method of peptization [9]. The "top down" method used was electron beam lithography, and the subsequent developing of appropriately prepared films. The substrate material, the electron beam intensity, the interval between the e-beam irradiated regions, and the choice of precursor were the deciding factors in the final size of the nano dots.

[a] Contact author: sudipta@mpi-halle.de
[•] CSRRI-IIT, MRCAT Sector 10, Advanced Photon Source, Building 433B, Argonne National Lab, Argonne, IL60439, USA.

EXPERIMENTAL

Synthesis by the self assembly route:

The microemulsion mediated synthesis involved the hydrolysis of the metallic alkoxides within nanosized water droplets in a cyclohexane/Brij 30 (Polyethylene glycol dodecyl ether)/H_2O water in oil medium, as suggested by Hempelmann and Herrig [8]. The microemulsion was first optimized for the maximum amount of water that could be accommodated in this system, and then, the microemulsion was slowly added to the appropriate amount of bimetallic precursor (Barium titanium ethylhexano-isopropoxide (Alfa Aeser), for BaTiO3 particles, for instance). The precursor reacted with the water droplets present in the microemulsion and formed the oxide particles. The reaction was confined within the water droplets. The mixture was then mechanically stirred for one hour until a slightly cloudy solution appeared. This solution was stable for a few weeks. The freshly prepared solution was heat dried to form a black residue which turned into a yellowish powder upon a further heat treatment (450 °C for 60 minutes). The as prepared powder was checked by SEM and XRD. To avoid agglomeration between the nano particles, we added tetrabutylammonium hydroxide as a peptizing agent.

e-beam lithography:

In the e-beam lithography process, a thin layer (approximately 70-100 nm thick after drying) of the precursor was deposited on a single crystalline strontium titanate (STO) substrate followed by a low temperature (80 °C) drying in order to evaporate the organic liquids. This sample was then exposed to a focussed electron beam programmed to hit the sample surface at regular spatial intervals. The interval was chosen to vary from 200 nm to 1 μm. The size of each exposed dot was also varied with the distance between them, as shown later. Two different solutions were chosen for the preparation of e-beam samples. The first one was a commercially available PZT precursor (from Chemat Corporation) and the other was a laboratory made solution, which was prepared by dissolving the individual metal alkoxides in a common solvent such as 2-methoxyethanol and xylene.

RESULTS AND DISCUSSION

An SEM picture of the microemulsion-derived barium titanate powder is shown in figure 1. It could be seen that the as-dried powder was made of almost monodispersed particles with a size centered around 700 nm. After ultrasonicating the specimens, the particles revealed themselves as well defined cubic grains with sizes of about 200-500 nm (Fig. 2). This external morphology of the grains confirmed the presence of perovskite $BaTiO_3$. The XRD of the as prepared nano powder is shown in figure 3. It was evident from the result presented in Fig. 3 that the powder was phase pure $BaTiO_3$. The formation of $BaTiO_3$ phase at such low temperature (~450 °C) had been possible due of the enhanced reactivity of the nano-particles. However, there were a few grains that showed a fine structure, i.e. they looked like a cluster of much finer grains (Fig. 4). Each cluster was approximately 800 nm in size, which was close to the particle size in the as prepared powder (Fig. 1). The individual particles forming the agglomerates were of size less than 50 nm. This was also a consequence of the ultra-fine grain structure of the as prepared particles which caused a significant increase in the number of unsaturated bonds terminating on their surfaces. It was therefore much more favorable for them to form larger agglomerates. These



Figure 1. Microemulsion derived $BaTiO_3$ nano powder (dried at 450°C)



Figure 2. Dried $BaTiO_3$ nano powder, after ultrasonic dispersion.

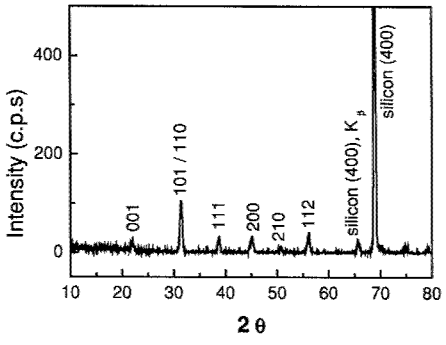


Figure 3. XRD of the $BaTiO_3$ nano-powder. The strong peak at 69° was from the silicon wafer on which the powder was glued.



Figure 4. Agglomerated $BaTiO_3$ nanoparticles.

finer particles were believed to be the product of the microemulsion mediated synthesis. However, it was seen that the precursor itself was also soluble in cyclohexane (without any surfactant). Therefore, it was thought that there could still have remained some amount of precursor dissolved in the liquid phase that were not intercepted by any water droplet. The bigger particles had most probably originated from the remaining (dissolved) precursor which could not be accommodated by the water droplets of the microemulsion. The as prepared microemulsion (before burning out the oil and surfactant) was coated on a bare silicon substrate followed by a low temperature annealing at 450 °C for 60 minutes. It was observed that the microemulsion formed a layer of interconnected particles on the silicon surface (as shown in Fig. 5). In the liquid phase, the equilibrium was maintained by the surface tensions of the oil and the surfactant. While drying, the oil phase evaporated first due to its lower boiling point, and the surfactant then drew the particles closer and formed the agglomerates. In order to remove the surfactants, the

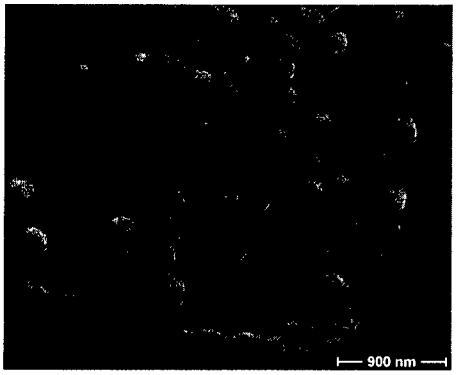


Figure 5. As prepared microemulsion sample coated on silicon and dried at 400°C.

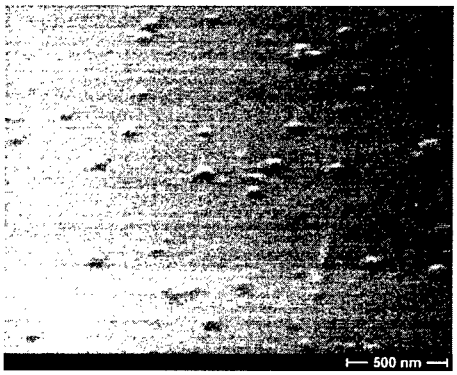
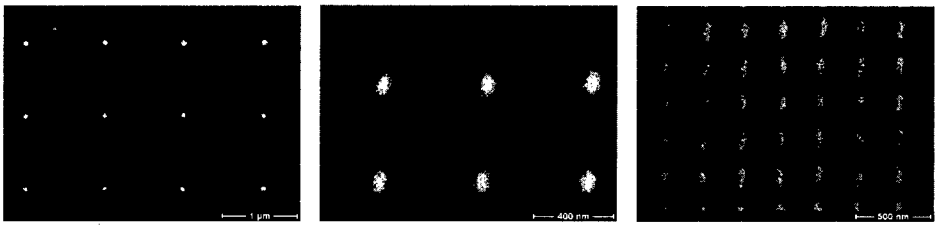


Figure 6. SEM image of the ultrasonicated microemulsion after coating & annealing.

solution was washed with acetone followed by ultrasonic dispersion. This was further filtered, and coated on a silicon substrate again. After drying, the continuous layer revealed itself as made of well separated isolated particles. The SEM image of the sample coated with the ultrasonicated solution is shown in Fig. 6. It was observed that there was a distribution in the size of these particles, the average size was in the range of 50-60 nm. The same solution was also coated on Nb doped $SrTiO_3$ substrates with (001) orientation, and both SEM and AFM images were consistent with the previous observations, demonstrating that these particles were truly a result of the microemulsion assisted synthesis and not due to any artifact associated with the oxidation of the substrate. The heights of the microemulsion derived particles were in the range of 20-30 nm. There was however, no regularity observed in the positions of the nano droplets on the solid surface. The size of the particles were still too big for self assembly. The crystal field needs a size below 10 nm to lock the nano-dots at some preferred sites. Studies are in progress to achieve much finer particles on heat treated substrates.

While the microemulsion route promised a very fine nano structure, the e-beam lithography technique was the alternative to achieve a well defined array of nanoparticles with controllable size and inter-particle distance. Figure 7 shows the e-beam patterned nano-dots with different



(a) (b) (c)

Figure 7. SEM images of the e-beam lithographic patterns as a function of the repetition distance (a) 1 µm, (b) 0.5 µm, and (c) 0.2 µm.

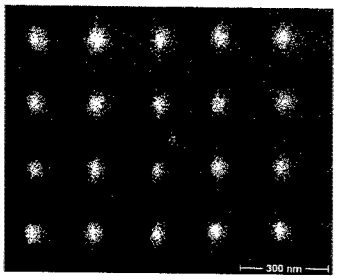


Figure 8. Patterns fabricated from the laboratory- prepared solution

intervals using a commercial solution. It can be seen from the micrographs that, for the case of the polymer precursor derived structure, there was a strong proximity effect between adjacent dots when they were placed at distances less than 0.5 micron. The dots did not remain as isolated dots, but joined together to form one dimensional arrays. The direction of the axis along which they joined was coincident with the e-beam scan direction. This was probably a result of the long-chain internal structure of the polymer solution. When such a solution was exposed to the e-beam, the exposed region would also affect the neighboring regions which were not exposed, but were lying on the same chain. This would limit the actual resolution of the e-beam lithography. On the other hand, figure 8 presents the image obtained from the e-beam pattern made from the prepared solution (containing individual precursors in the solvent matrix). It clearly demonstrated that one could get isolated nano-dots placed at regular intervals, even down to a size ~150 nm. It was demonstrated experimentally [10] for the case of PZT nano-dots that the as developed lithographic patterns change their shapes upon annealing at moderately high temperature (~650 °C). It was thought to be a consequence of the enhanced surface energy contribution at smaller sizes. A similar observation was reported by Lange *et al.* [11] in which they showed that a continuous thin film goes through a shape-change upon annealing and breaks into smaller islands of pyramidal shape. Calculations based on purely thermodynamic considerations showed that, the system indeed lowered its energy while transforming to a pyramidal shape from an initially cubic shape [11]. A detailed calculation involving the growth kinetics of nano islands starting from an initially amorphous state is under way.

CONCLUSIONS

We have successfully synthesized using the microemulsion route phase-pure nano-powders as well as isolated nano-structures on solid substrates. The size was around 50 nm. Studies are in progress in order to shrink the size further and to register these nanostructures in a regular fashion. On the other hand, the top down approach using e-beam lithography proved to be quite effective in fabricating regular arrays of ferroelectric nano-structures. The laboratory prepared solution was superior to the commercially available (polymer) solution, and could produce arrays of distinct nano-sized dots, the size being 60-70 nm which was due to the presence of shorter molecular chains present in the laboratory prepared solution.

ACKNOWLEDGEMENT

Part of this work has been supported by the Volkswagen Stiffstung Project 'Nano-sized Ferroelectric Hybrids' under contract no. 5/77737.

REFERENCES

[1] Y. V. Nastaushev, T. Gavrilova, M. Kachanova, L. Nenasheva, V. Kolosanov, O. V. Naumova, V. P. Popov and A. L. Aseev, Materials Science & Engineering C: Biomimetic Materials, Sensors & Systems, **C19**, 189 (2002).
[2] J. Nishizawa, P. Plotka and T. Kurabayashi, IEEE Transactions on Electron Devices, **49**, 1102 (2002).
[3] V. Millar, C. I. Pakes, A. Cimmino, D. Brett, D. N. Jamieson, S. D. Prawer, C. J. Yang, B. Rout, R. P. McKinnon, A. S. Dzurak and R. G. Clark, Proceedings of SPIE, **4590,** 173 (2001).
[4] E. A. Guliants, C. Ji and W. A. Anderson, Journal of Electronic Materials, **31**, 466 (2002).
[5] G. Braun, H. Hoenigschmid, T. Schlager, and W. Weber, J. Sol.-St. Circuits. **35,** 691 (2000).
[6] V. Giurgiutiu, and Z. AN, Journal of Vibration & Acoustics-Transactions of the ASME, **124,** 116 (2002).
[7] M. Bonini, U. Bardi, D. Berti, C. Neto, P. Baglioni, J. Phys. Chem. **B 106,** 6178 (2002).
[8] H. Herrig and R. Hempelmann, Mat. Lett. **27,** 287 (1996).
[9] J. Yang, S. Mei, J. M. F. Ferreira, Mat. Sci. and Engg. **C 15,** 183 (2001).
[10] M. Alexe, C. Harnagea, A. Vişnou, A. Pignolet, D. Hesse and U. Gösele, Scripta. Mater. **44,** 1175 (2001).
[11] A. Seifert, A. Vojta, J. S. Speck, and F. F. Lange, J. Mat. Res., **11,** 1470 (1996).

Mat. Res. Soc. Symp. Proc. Vol. 740 © 2003 Materials Research Society I10.4

Formation, Mechanical and Electrical Properties of Ni-based Amorphous alloys and their Nanocrystalline Structure

Xiangcheng Sun[1] and Tiemin Zhao[2]

[1]Center for Materials for Information Technology, The University of Alabama, Tuscaloosa, Alabama, 35487-0209
[2]Lab of RSA, Institute of Metal Research, CAS, Shenyang, P. R. China

ABSTRACT

A Ni-based amorphous alloy in $Ni_{60}Ti_{20}Zr_{20}$ system was prepared by melting spinning. The glass transition temperature (T_g) was as high as about 760 K, the supercooled liquid region was quite wide, ΔT_x = 50 K (ΔT_x= T_x-T_g, T_x crystallization temperature), and the reduced glass transition temperature (T_g/T_m) was 0.60. The amorphous alloys exhibited a high tensile strength (σ_f= 1015 MPa) at room temperature. The electrical conductivity obeyed a $T^{1/2}$ law over the range of 15 K< T < 300 K, which can be explained by an electron-electron interaction model. After annealing the amorphous alloy into primary crystallization, a nanocomposites consisted of metastable Ti_2Ni and Zr_2Ni nanophases with size less than 15 nm embedded in the amorphous matrix was appeared.

INTRODUCTION

Binary alloys can be stabilized by adding a third element which has an atomic size different from the other two elements [1], and, if that element has a very low heat of mixing with one of the other elements. Ni-Ti [2], and Ni-Zr [3] binary alloy systems have been prepared by mechanically alloying (MA) over wide composition ranges due to the large negative heat of mixing. From the related studies [4, 5], one expects that if an appropriate amount of Zr was added into Ni-Ti or Ti was added into Ni-Zr binary alloys, the glass forming ability (GFA) both Ni-Ti and Ni-Zr may be greatly enhanced. As important engineering materials, a number of Ni-based amorphous ternary alloys had ever been produced in Ni-Fe-B [6], Ni-Si-P-B [7] and Zr-Ni-M (M=Pd, Au, Pt) [8, 9] by melting spinning. It is rather important for the future progress of bulk amorphous alloys to fabricate new Ni-based amorphous alloys that high glass forming ability (GFA), good mechanical properties and high corrosion resistance. On the other hand, it is also the aim of the present work to investigate the amorphization possibility and their corresponding mechanical and physical properties. From both fundamental and technological points of view, it will be useful to optimize the microstructure, and to develop economic bulk Ni-based amorphous alloys.

EXPERIMENTAL

99.99% pure Ni, Zr, and Ti were melted and cast into ingots of nominal composition $Ni_{60}Ti_{20}Zr_{20}$ by non-consumable arc melting under a highly pure argon atmosphere. Amorphous alloy ribbons (about 3 mm wide, 0.02 mm thick) were derived by melt spinning onto a copper wheel from the $Ni_{60}Ti_{20}Zr_{20}$ ingots.

The thermal properties were measured by differential scanning calorimetry (DSC, TA Instruments model) at a heating rate of 40 K/min. The values of the glass transition temperature T_g, the onset temperature for first crystallization peak T_x, were determined from the DSC curves with an accuracy of ±1 K. Isothermal annealing of the alloys ribbon samples encapsulated in quartz tubes was carried out in vacuum of 1×10^{-5} Torr. The phase and structure of as-quenched and annealed samples were determined by x-ray diffraction with Cu K_α radiation and transmission electron microscopy (TEM, JEOL2010, operated at 200kV). The d.c. resistance was measured by the conventional four-probe method over a temperature range of 15 to 300 K. The voltages were recorded by a nanovoltmeter (model 182, Keithley Inc.) and the temperature was controlled within an accuracy of ± 0.5 K. Mechanical properties were measured at room temperature at a strain rate of 10^{-4} s^{-1} using a Gleeble 1500 testing machine. The amorphous $Ni_{60}Ti_{20}Zr_{20}$ ribbon samples with width of 3 mm and length of 5~5.5 mm were polished carefully before testing. Tensile fracture surface morphology of the samples was observed by scanning electron microscopy (SEM).

RESULTS AND DISCUSSION

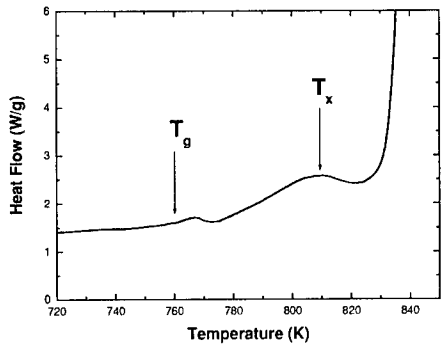


Figure 1. DSC curve of the as-quenched $Ni_{60}Ti_{20}Zr_{20}$ amorphous ribbon at the heating rate of 40K/min.

Fig. 1 shows a DSC curve of the as-quenched $Ni_{60}Ti_{20}Zr_{20}$ amorphous alloys. The glass transition is observed and its onset temperature, T_g is 760 K. The crystallization proceeds with a single exdothermic peak of which the onset temperature, T_x is 810K. It has been predicted that from kinetic considerations [6, 11], the tendency to form the amorphous phase is closely related to the reduced glass temperature (T_g/T_m, where T_m is the melting temperature) of alloys. The larger the value of T_g/T_m, the greater tendency to form the amorphous. It is evident that this Ni-based metallic amorphous alloys exhibit a wide supercooled liquid region, which reaches ΔT_x = 50K ($\Delta T_x = T_x - T_g$, where T_x is crystallization temperature), and high reduced glass transition temperature (T_g/T_m, T_m measured as 1260 K) is 0.60.

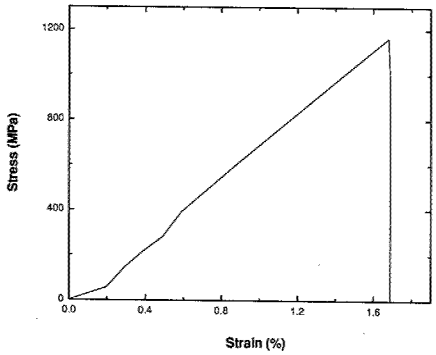


Figure 2. Stress-strain curves at room temperature for the as-quenched $Ni_{60}Ti_{20}Zr_{20}$ ribbon.

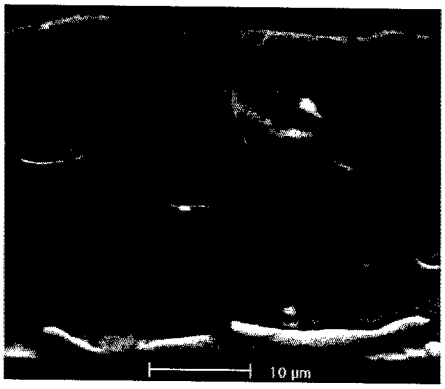


Figure 3. Scanning electron micrograph of the tensile fracture surface for the as-quenched $Ni_{60}Ti_{20}Zr_{20}$ amorphous ribbon, that clear vein patterns are visible.

Fig. 2 shows the stress-strain curve for the cylindrical samples (3 mm diameter × 5mm length) in as-quenched amorphous single-phase. It is clear that this $Ni_{60}Ti_{20}Zr_{20}$ metallic amorphous alloys exhibits high yield strength of 1015 MPa and relatively small plastic elongation of about 1.62%, where the good bending ductility is maintained in the $Ni_{60}Ti_{20}Zr_{20}$ metallic amorphous alloys. Usually, tensile fracture occurs along the maximum shear plane, which is declined by about 45° to the direction of tensile load and the fracture surface consists mainly of a vein pattern [10]. The SEM image in Fig. 3 shows that the tensile fracture surface is rather smooth on a macroscopic scale and consists mainly of well-developed vein patterns. In agreement with the model predicted by Inoue [12], the intergranular amorphous phase keeps good ductile nature and the fracture occurs preferentially along the intergranular amorphous region.

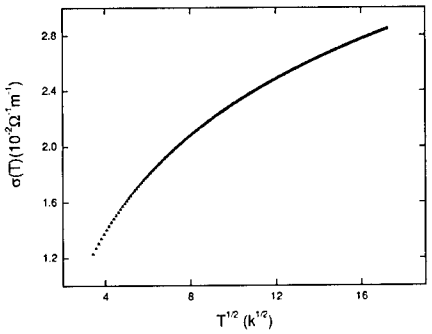


Figure 4. Electrical conductivity as a function of $T^{1/2}$ for the as-quenched $Ni_{60}Ti_{20}Zr_{20}$ amorphous ribbon.

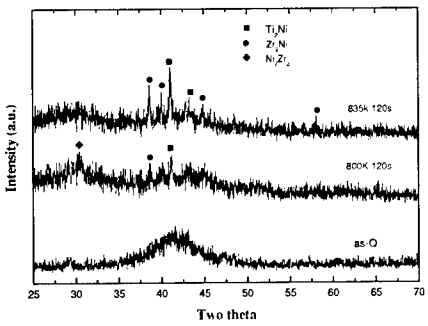


Figure 5. X-ray diffraction patterns for as-quenched and annealed $Ni_{60}Ti_{20}Zr_{20}$ alloy ribbons.

The d. c. conductivity σ (T) (Fig.4) increases with increasing temperatures range from 15 to 300K obeys a $T^{1/2}$ law; exhibiting non-metallic behavior; which can be explained by an electron-electron interaction model [13]. Such a $T^{1/2}$ law was observed for three-dimensional disordered or amorphous systems [14], in other words, this confirms the amorphous nature of the $Ni_{60}Ti_{20}Zr_{20}$ metallic alloys from 15K to 300K.

The diffraction pattern (Fig.5) of the as-quenched sample consists only of a broad peak, indicating that it is composed of an amorphous phase. For the sample annealed at 800K, the temperature just after the first crystallization peak, several very weak crystalline peaks are observed; corresponding to the tetragonal Zr_2Ni (space group I 4/mcm, a= 0.649 nm, C= 0.528 nm) and the cubic Ti_2Ni (space group, Fd3m, a= 1.1278 nm) phases. One weak peak of Ni_7Zr_2 was also found in Fig. 5(b). The broad half widths of these peaks indicate that the precipitated crystals are very fine. Zr_2Ni, Ti_2Ni and Ni_7Zr_2 phases are

metastable and these small particles should grow into larger particles upon further annealing [15]. After annealing the sample at 835K for 120s, the peaks of the Zr_2Ni and Ti_2Ni phases indeed showed higher intensity and the peak of the metastable Ni_7Zr_2 phase disappeared.

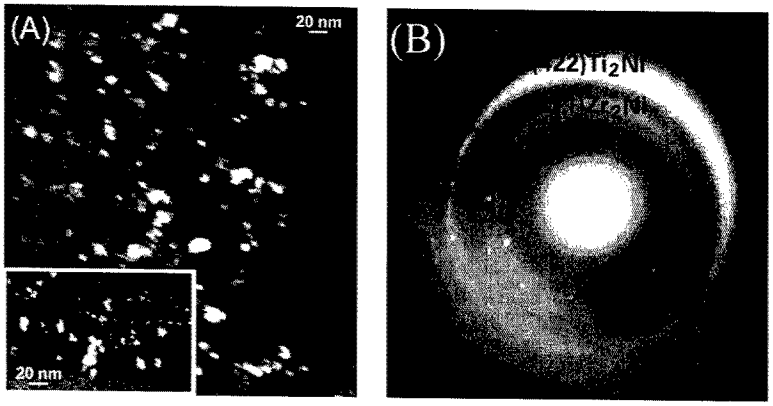


Figure 6. Dark-field TEM image (**a**) and selected area electron diffraction pattern (**b**) of the $Ni_{60}Ti_{20}Zr_{20}$ amorphous ribbon annealed at 835 K for 120 s.

The dark-field TEM image (Fig.6a) and selected-area electron diffraction pattern (Fig. 6b) of the ribbons after primary crystallization by annealing at 835K for 120s shows very fine particles with an average diameter value of 15nm surrounded by the residual amorphous phase. The particles were distributed homogeneously and had a nearly spherical morphology. The selected-area electron diffraction patterns demonstrate that these nanophases were metastable crystalline phases of Ti_2Ni and Zr_2Ni. Furthermore, together from the above XRD patterns for the samples with different temperature treatments, only a little fraction of Ti_2Ni and Zr_2Ni phases had been observed after annealed at 800k at 120s. This indicated, within the exdothermic peak, there was more metastable crystalline phase precipitated (i.e. Ni_7Zr_2 phase appeared) from the amorphous matrix. This suggested that the reaction in the DSC curve corresponded to the formation of the primary Ti_2Ni and Zr_2Ni phases [16].

CONCLUSIONS

A new Ni-based amorphous alloy ($Ni_{60}Ti_{20}Zr_{20}$) having a wide supercooled liquid region was successfully prepared. The amorphous alloy exhibited good ductility with a tensile strength (σ_f) as high as 1015 MPa at room temperature. Electrical conductivity measurement confirmed the amorphous nature of this alloy. After primary crystallization, a nanocomposite composed of two metastable Ti_2Ni and $NiZr_2$ nanophases embedded in the amorphous matrix was formed. The formation of this kind of Ni-based amorphous alloy, together with a large supercooled liquid region and high glass-forming ability, offer us

good opportunities for the future development of bulk Ni-based amorphous alloys as basic science and engineering materials.

REFERENCES

1. R. B. Schwarz and C. C. Koch, *Appl. Phys. Lett.* **49**, 146 (1986).
2. K. Y. Wang, T. D. Shen, H. G. Jiang, M. X. Quan and W. D. Wei, *Mater. Sci. Eng.* **A179/A180**, 215 (1994).
3. P. Y. Lee and C. C. Koch, *J. Mater. Sci.* **23**, 2837 (1988).
4. K. Amiya, N. Nishiyama, A. Inoue and T. Masumoto, *Mater. Sci. Eng.* **A179/A180**, 692 (1994).
5. V. V. Molokanov, V. N. Chebotnikov, *J. Non-Crystalline Solids* **117/118**,789 (1990).
6. Y. Waseda, S. Ueno, M. Hagiwara and K.T. Aust, Prog. Mater. Sci. **34**, 149 (1990).
7. F. E. Luborsky, *Mater. Sci. Eng.* **28**, 139 (1977).
8. J. Saida, M. Matsushita, C. Li and A. Inoue, *Appl. Phys. Lett.* **76**, 3558 (2000).
9. B. S. Murty, D. H. Ping, K. Hono and A. Inoue, *Appl. Phys. Lett.* **76**, 55 (2000).
10. M. W. Chen, T. Zhang, A. Inoue, A. Sakai and T. Sakurai, *Appl. Phys. Lett.* **75**,1382 (1999).
11. D. Turnbull, *Contempt. Phys.* **10**, 473 (1969).
12. A. Inoue, *Acta Mater.* **58**, 279 (2000).
13. K. Lal, A. K. Meikap, S. K. Chattopadhyay, S. K. Chatterjee, M. Ghosh, A. Barman and S. Chatterjee, *Solid State Commun.* **113**, 533 (2000).
14. A. K. Meikap, A. Das, S. Chatterjee, M. Digar and S. N. Bhattacharyya, *Phys. Rev.* **B47**, 1340 (1993).
15. C. Fan, C. F. Li and A. Inoue, *J. Non-Crystalline Solids* **270**, 28 (2000).
16. J. G. Wang, B. W. Wang, B. W. Choi, T. G. Niegh and C. T. Liu, *J. Mater. Res.* **15**, 798 (2000).

Mat. Res. Soc. Symp. Proc. Vol. 740 © 2003 Materials Research Society I10.9

Synthesis of Novel Vanadium Oxide Nanotubes and Nanofibers

Samuel T. Lutta, Hong Dong, Peter Y. Zavalij, and M. Stanley Whittingham*

Chemistry Department and the Institute for Materials Research,
State University of NewYork at Binghamton,
Binghamton, NewYork 13902-6016, U.S.A.

ABSTRACT

We are exploring the synthesis and properties of structured vanadium oxides mainly nanotubes and nanorods. Nanotubes initially formed with surfactant templates have been readily exchanged with simple cations without change of the basal-plane structure. These compounds contain δ-like vanadium oxide layers with the vanadium in VO_6 octahedra. This structure is particularly suitable for redox reactions. In this paper we report on synthesis of vanadium oxide, $(NH_4)_xV_2O_{5-\delta}{\cdot}nH_2O$ rods using organic polymer as template. This compound has been synthesized by sol-gel reaction and subsequent hydrothermal treatment. TGA, SEM, XRD and FTIR were used to characterize this compound. Thermal analysis of this compound shows that the fibrous morphology is maintained when it is heated in nitrogen and oxygen above 300 °C. However, in both cases the size of the fibers decreases. Performance of this compound as cathode material in secondary electrolyte has been investigated using $LiPF_6$ as electrolyte. A capacity of 140 mAh/g was obtained which remained fairly constant with up to at least 10 cycles. We also investigated electrochemical behavior of thermal products.

INTRODUCTION

There has been much recent interest in preparing new vanadium oxides owing to their promise as cathodes and anodes in secondary lithium batteries and electrochromic devices [1-2]. Also the catalytic behavior of vanadium oxides make these materials viable candidates as heterogeneous catalysts [3]. The physical and chemical properties of substances might well be altered when they are prepared on a nanoscopic scale and thus this phenomenon opens up a completely new perspective for material design that benefits from the introduction of particle size as a new, powerful parameter [4]. Thus fabrication of vanadium oxides in nanostructured form and with anisotropic morphology appears to be a particularly attractive goal.

The first successful approach to make a tubular vanadium oxide was use of carbon nanotubes as a template [5]; it was found possible to coat crystalline layers of V_2O_5-structures on the external surfaces of the carbon nanotubes. Recently, new type of vanadium oxide nanotubes was obtained by a soft-chemistry synthesis involving amines with long alkyl chains as molecular, structure directing template [6]. This material consisted of scrolls of vanadium oxide layers within which the alkyl amines were embedded. The structure of the double-sheet layer in this material is similar to $BaV_7O_{16}{\cdot}nH_2O$ [7]. In our attempts to make structured vanadium oxides, we have developed a new method to make novel vanadium oxide tubes and nanorods using an organic polymer as template. The synthetic approach involved sol-gel and hydrothermal techniques. This method allows us to

* Contact author; stanwhit@binghamton.edu

form one-dimenional materials or thin films metal oxide materials. This paper reports on the syntheses, characterization and electrochemical behavior of these novel vanadium oxide nanostructures.

EXPERIMENTAL DETAILS

Polylactide (PLA) is a biodegradable polymer derivered from renewable resources. It can be synthesized from either a condensation polymerization of lactic acid or ring opening polymerization of lactide, a cyclic dimmer of lactic acid [8]. Polylactide fibers were prepared here by an electro-spun technique using literature method [9]. The fibers used in this experiment were on average about 700 nm in diameter.

A piece of polylactide fiber about 2 cm × 2 cm was placed into 50 ml of 1M-ammonium vanadate solution. The pH of the solution was then adjusted to 3.4 using glacial acetic acid. The resulting mixture was transferred to a 125-ml Teflon–lined autoclave (Parr Bomb), sealed, and reacted hydrothermally for 3 days at 160 °C. A golden yellow solid formed which was washed with distilled water to remove acetic acid and any undecomposed products. Heating the hydrothermal product in nitrogen and oxygen resulted in the formation of $V_2O_{4.8}$ and V_2O_5 nanofibers respectively.

X-ray diffraction was performed using CuKα radiation on a Scintag θ-θ diffractometer. The FTIR data was obtained on a Perkin-Elmer 1500 series spectrometer. The morphology and the structure of the nanotubes were investigated by using XRD and SEM. Thermal stability of the fiber was investigated using TGA in oxygen and nitrogen.

The performance of these compounds as positive electrode was tested by galvanostatic cycling in the potential range 2.0-4.2 V vs Li/Li^+. In all cases the cathode consisted of about 80% sample, 10% carbon black, and 10% Teflon™.The carbon black was used to make the sample conductive since the samples of interest were not good electronic conductors. The Teflon™ was used as a binding agent to keep the pellet intact during the experiments. The cathode material was then hot pressed onto a stainless steel Exmet™ grid at 110 °C to dehydrate the sample. A metallic lithium sheet served as both the counter and reference electrode. A 1M solution of $LiPF_6$ in a 1:1 ethylene carbonate (EC) /1,2-dimethylcarbonate was used as electrolyte.

DISCUSSION

The role of the polylactide as template was confirmed from two control experiments. In one experiment 50 ml of 1M ammonium vanadate solution acidified with acetic acid to a pH of 3.4 was treated hydrothermally at 160 °C for 3 days and the product was crystalline $NH_4V_3O_8$. In the second control experiment, PLA fiber was placed in 50 ml of acetic acid solution at a pH of 3.4; then the mixture treated as above. In this case the fiber was found to have dissolved forming a colorless solution after hydrothermal treatment. The diameter of the vanadium oxide formed after hydrothermal treatment was smaller than that of the initial template suggesting that the product is formed by growing within the fiber and not by coating around it.

Thermo gravimetric analysis

This study showed the absence of the template in the hydrothermal product for two reasons namely; one, the TGA profile of the product remained the same after it was washed in a DMF/

CH_2Cl_2 mixture, which easily dissolves the template. Secondly, thermograph of the hydrothermal product was similar to that of δ-like V_2O_5 synthesized in our group. Thermo gravimetric analysis of hydrothermal product showed that it was possible to maintain the fibrous morphology by heating it in nitrogen and oxygen at 250 °C and 350 °C respectively. Figure 1 shows the thermographs of the hydrothermal product in oxygen and nitrogen.

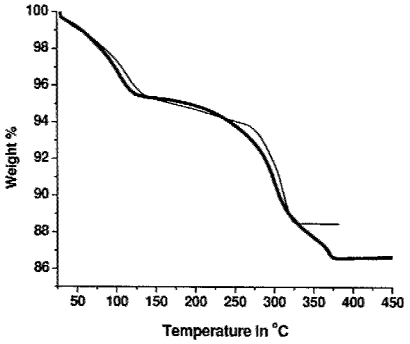


Figure 1. TGA of the hydrothermal product under nitrogen (light line) and oxygen (thick line).

Fourier transformed infrared spectroscopy

FTIR confirmed the absence of the PLA template in the hydrothermal product as the characteristic peaks for C=O at 1754 and C-H at 1392 and 1183 cm^{-1} of the template were not seen in the spectrum of the final product. Both the hydrothermal product and the vanadium oxides formed by heating it in oxygen and nitrogen showed characteristic V-O vibrations peaks between 1021 cm^{-1} and 500 cm^{-1}. Some FTIR spectra are shown in figure 2 below.

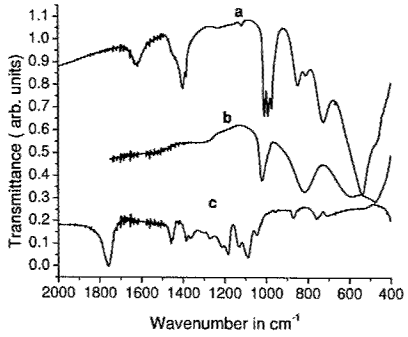


Figure 2. FTIR spectra of a) hydrothermal product, b) heated hydrothermal product in nitrogen and c) polylactide fiber.

X-ray diffraction

X-ray diffraction pattern of the hydrothermal product showed that its structure is similar to that of a δ-V_2O_5 recently made in our group [10] .The cell parameter of this compound shows similarity with other δ-V_2O_5 phases [11-12]. X-ray also confirmed that heating of the hydrothermal product in oxygen results in the formation of pure V_2O_5 nanofibers. Thus on heating in oxygen the structure changes from the double sheet of the δ-phase to the single sheet typical of V_2O_5 itself. X-ray diffraction pattern of compound formed by heating the hydrothermal product was poorly resolved and showed that it was predominantly VO_2.

Scanning electron microscopy

SEM shows that the hydrothermal product consists of fibers with the outer diameter ranging from 150-200 nm, while their lengths vary from 500 nm to a maximum of 16 μm. Closer examination of this material reveals smaller particles deposited on the surface (Figure 3a). The average diameter of the starting polylactide fibers is 700 nm, which is larger than that of the final product. This supports our earlier proposal that the product grows somehow inside the template

The SEM of the product obtained by heating the hydrothermal product in oxygen shows ribbon-like morphology and randomly orientation. The fibers exhibit a wide range of lengths and widths. Their diameters vary between 30 and 140 nm. SEM micrographs show only the presence of vanadium oxide. In some regions, fibers are curved and tangled together forming bundles. The SEM micrographs further show that the tips of these fibers are round. The SEM image of the hydrothermal product after heating in nitrogen (see figure 3 left) was investigated and typical image of the compound represented a general view of the fibrous morphology. Interestingly, the diameters of this material are longer on average than the one heated in oxygen. In some regions it appears that the fibers might be open ended. The SEM also confirmed that it is possible to heat the hydrothermal product in oxygen and nitrogen to at least 500 °C and still preserve the fibrous morphology. X-ray diffraction however shows that the fibers convert to single sheet V_2O_5 after heating in oxygen.



Figure 3. Typical SEM images of hydrothermal product (left) showing the fibrous morphology, after heating in nitrogen (middle) and V_2O_5 nanofibers (right) (product of heating the hydrothermal product in oxygen).

Electrochemistry

The cell performance of vanadium oxide fibers was investigated at a current density of 0.1 mA/cm^2 using as electrolyte $LiPF_6$ dissolved in a 1:1 mixture of ethylene carbonate (EC) and dimethyl carbonate (DMC); pure lithium metal was used as the counter and reference electrode. The electrochemical behavior of the hydrothermal product is shown in Figure 4. Its cycling is good with an average discharge profile around 2.0 volts and little capacity loss after multiple lithium insertions and removal. The XRD pattern of the compound after electrochemistry indicated that the structure had changed from the double sheet of the δ-phase to the single sheet of V_2O_5. Low angle peaks disappeared showing that the d spacing of the compound was reduced after electrochemistry. Probably large ions like water and /or ammonium are replaced by smaller lithium ions. The electrochemical behavior of the hydrothermal product heated in nitrogen (figure not shown) was also investigated. The compound was also electrochemically active and had a capacity of about 120 mAh/g, which remained fairly constant through 10 cycles. The compound did not change structure during these reactions.

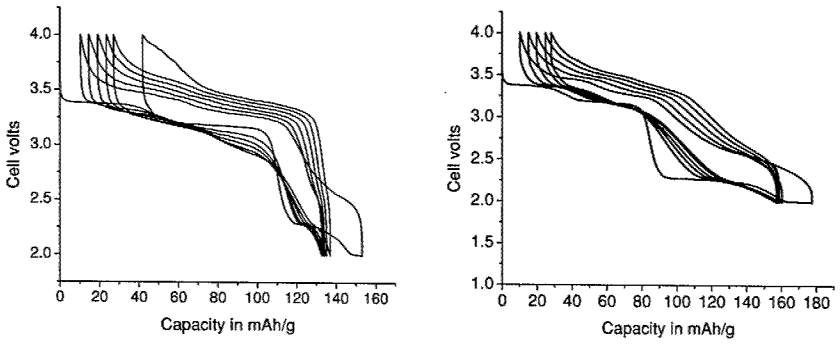


Figure 4. Electrochemical cycling of the vanadium oxide fibers in the $LiAsF_6$ based electrolyte of (left) the hydrothermal product and (right) after heating in oxygen.

Comparison of the electrochemical behavior of V_2O_5 fibers formed by heating the hydrothermal product in oxygen to pure V_2O_5 from Aldrich reveals the effect of particle size and morphology on redox performance of V_2O_5. The fibrous nano V_2O_5 shows a better redox behavior than the bulk V_2O_5; this may be associated with the much smaller distances that the Li^+ ion must diffuse in V_2O_5 fiber as the fiber is only 30 nm compared to the 60 μm of bulk V_2O_5. This observation has also been reported elsewhere with V_2O_5 cathodes [13]. The data shows that it is possible to use the template method to prepare nanostructured electrodes with improved capacity and cyclability. A challenge that remains is to develop a method for mass production of such materials.

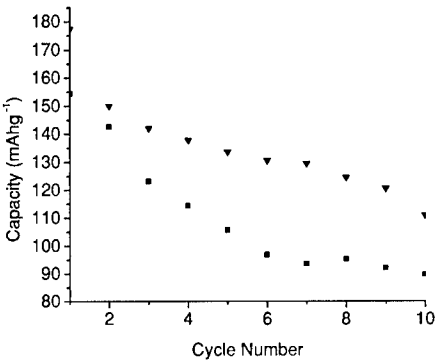


Figure 5. Electrochemical cycling of the hydrothermal product in $LiAsF_6$ salt before (■) and V_2O_5 fibers (▼) in $LiAsF_6$ salt

CONCLUSIONS

For the first time nanostructured vanadium oxides have been synthesized using organic polymer as template .We have also shown that the morphology of vanadium oxides can be preserved at temperature above 300 °C and 500 °C in oxygen and nitrogen respectively. Electrochemical studies of these compounds in lithium cell shows that they are redox active for lithium insertion.

ACKNOWLEDGEMENTS

The authors would like to thank National Science Foundation for support of this work through grant DMR-9810198. We also thank Professor Wayne E. Jones for helpful discussions on the polylactide fibers and Henry Eichelberger for help with the TEM experiments.

References:

1. C.R. Walk in *Lithium Batteries*, Academic Press, NewYork (1983).
2. M.S. Whittingham, *J. Electrochem. Soc.* **123**, 315-320 (1976).
3. B.E. Koene, N.J. Taylor, and L.F. Nazar, *Angew. Chem. Int. Ed.* **19**, 2888 (1999).
4. G.R Patzke, F. Krumeich, and R. Nesper, *Angew. Chem. Int. Ed.* **41**, 2446 (2002).
5. P.M. Ajayan, O. Stephan, P. Redlich, and C. Colliex, *Nature*. **375**, 564 (1995).
6. F. Krumeich, H. J. Muhr, M. Niederberger, F. Bieri, B. Schnyder, and R. Nesper, *J. Am. Chem. Soc.* **121**, 8324 (1999).
7. X. Wang, L.Liu, R.Bontchev, and A. J. Jacobson, *Chem. Commun.* 1009-1010 (1998)
8. C.Boswell, *Chemical Market Reporter*.**268**, No8, August20-27, 2001
9. A.G. MacDiarmid, W.E. Jones, Jr, I.D. Norris, J.Gao, A.T. Johnson, Jr., N.J. Pinto, J. Hone, B. Han, F.K. Ko, H. Okuzaki, and M. Liaguno, *Synthetic Metals*. **119,** 27 (2001).
10. K. Ngala, J. Schutle, P.Y. Zavalij, and M.S. Whittingham, To be published.
11. T. Yao, Y. Oka, N. Yamamoto, *Mater. Res. Bull.* **27**, 669 (1992).
12. F. Zhang, P.Y. Zavalij, and M.S. Whittingham, *Mater. Res. Bull.* **32**, 701 (1997).
13. C.J. Patrissi and C.R. Martin, *J. Electrochem. Soc.* **148,** A1247, (2001).

Mat. Res. Soc. Symp. Proc. Vol. 740 © 2003 Materials Research Society I10.11

Silver Nanodisk: Synthesis, Characterization and Self-Assembly

Sihai Chen, Zhiyong Fan and David L. Carroll
Laboratory for Nanotechnology, School of Materials Science and Engineering, Clemson University, Clemson, SC 29634, U.S.A.
Email: chens@clemson.edu

ABSTRACT

A new form of silver nanostructured materials, a silver nanodisk, is generated by a solution-phase approach. In this method, two main steps are applied: the first is the generation of the truncated triangular silver nanoplates, which are obtained by seed-mediated growth of silver particles using cetyltrimethylammonium bromide (CTAB) as the soft templates. The second is the mild aging of the above triangular silver nanoplate solution at 40 °C to get the desired silver nanodisks. Transmission electron microscopy and atomic force microscopy studies show that the nanodisk has a thickness of the order of 20 - 30 nm, and a diameter around 60 nm. X-ray and electron diffraction analysis reveal that the nanodisk is single crystal and with its basal plane as (111) lattice plane. These nanodisks display a strong surface plasmon absorption band at 475 nm; this band can be continuously tuned within 420 nm to 560 nm through adjusting the aging time. The formation of self-assembled monolayer of CTAB on the basal plane is suggested to account for both the anisotropic growth from triangular nanoplates to nanodisks, and the formation of large-scale necklace-like structures.

INTRODUCTION

Due to the strong surface plasmon resonant absorption band, silver nanoparticles have attracted wide attention. More interestingly, this surface plasmon band are shape sensitive. For example, Schultz et al [1] have shown that triangular particles can display the peak plasmon resonance wavelength mainly in the range of 600 – 700 nm while that of pentagons in the range of 500 – 560 nm. Mirkin et al [2] have also succeeded in the preparation of triangular nanoprisms which displayed a strong in-plane dipole plasmon resonance at 670 nm. These shape sensitive optical properties render silver hot materials for application in optics [1] surface enhanced Raman spectroscopy (SERS) [3], biological label and diagnosis [4].

Shaped silver nanostructures have been observed or synthesized using various chemical approaches. These include spherical particles [5] tetrahedral [6] cubic [7], triangular [8], pentagonal [1], hexagonal [9], decahedral [10], icosahedral, cuboctahedral [11], as well as nanorods and wires [12]. Also, dentritic nanostructures of silver have been generated [13]. Here, we wish to report a new kind of silver nanostructure, i.e., silver nanodisks, which are generated in large quantities using a solution-phase chemical approach. We found that the nanodisks display a strong surface plasmon band at around 475 nm. Furthermore, we can tune this band within 420 nm to 560 nm through a mild aging process. In addition, since the top surface of these nanodisks is covered with a self-assembled monolayer of long chain organic molecules, they provide an ideal model system that mimics the self-assembled monolayer on surface. Due to their nanoscale sizes, they are expected to be applicable as building blocks in the modern nanoelectronics.

EXPERIMENTAL DETAILS

Materials. $NaBH_4$ (98%), $AgNO_3$ (99.9%), sodium citrate (99%), CTAB (99%), NaOH (99.996%), L-ascorbic acid (99%), are all from Alfa Aesar and used as received.
Ag seeds formation. 0.6 mL of 10 mM $NaBH_4$ was rapidly injected into the stirring mixture containing 0.5 mL of 10 mM $AgNO_3$ and 20 mL of 1.25 mM sodium citrate. The resultant solution was slowly stirred for 3 min and aged for 2 h before use. The particle sizes are 15 ± 6 nm.
Ag nanodisk formation. A particle growth solution was prepared: 2.5 mL of 10 mM $AgNO_3$, 5 mL of 100 mM L-ascorbic acid 73 mL of 0.1 M CTAB and 2.5 mL of silver seeds. To this solution, 1 mL of 1M NaOH was rapidly added. With gently shacking, the color of the solution changed from light yellow to brown, red and finally to green within 5 min. With further 4 days of aging at ambient condition (20 °C), the final nanodisks are obtained by aging of the triangular silver nanoplate solution at 40 °C for 4 hours.
Instrumentation. A Hitachi H-7000 transmission electron microscope (TEM), operated at 100 kV was used to observe the images. The specimens were prepared by dropping the solution (centrifuged at 3000g for 10 min to remove the surfactant) on the copper grids covered with Formvar and amorphous carbon, and let dry in air. Atomic force microscopic (AFM) studies are conducted with a Topometrix TM 2010, operated with non-contact mode. The sample is prepared by dropping the solution on a silicon wafer and dry in air. UV-Vis absorption spectra were obtained on a Perkin-Elmer Lambda 900 spectrophotometer. Oriented particulate monolayer X-ray diffraction (OPML-XRD) was used to determine the Miller induces of the basal plane of the nanoplates, performed on a Scintag DXS 2000 diffractometer with the X-ray generator (Cu K_α radiation, λ= 0.15418 nm) operated at 40 kV and 30 mA. The samples were prepared by dispersing the nanoplates into 3% gelatin (at 40 °C) on a glass plate, spreading the solution evenly with a glass stick, and let dry naturally in air.

RESULTS AND DISCUSSION

Figure 1a shows the TEM image of the obtained silver nanodisks lying flat on the substrate. Most of the particles show clear outlines of round circles. The mean diameter and standard

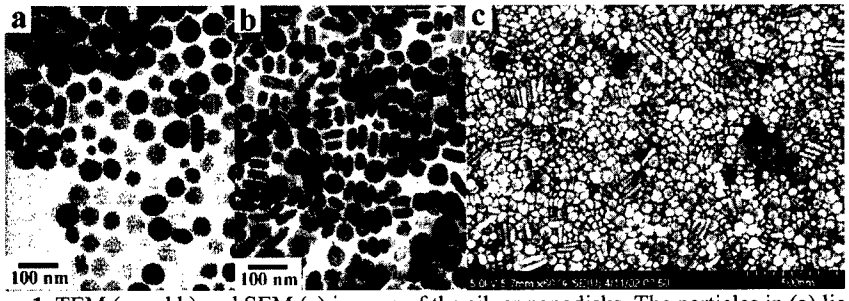


Figure 1. TEM (a and b) and SEM (c) images of the silver nanodisks. The particles in (a) lie flat on the substrates, while those in (b) stack together.

deviation of the particles are 59 ± 10 nm. The thickness of these particles are obtained by observing the closely packed particles, as shown in Figure 1b, the thickness is estimated their as 26 ± 3.4 nm. This further demonstrates the plate-like nature of these particles. Observed from the side view, these nanoplates are round in edges and also look like rods; the aspect ratios of these images are between 2 and 3, which are consistent with the value of 2.3 obtained with average disk diameter divided by their thickness. Note that there are still gaps between the packed neighboring nanodisks with an average distance of 3 - 3.6 nm, since the average molecular length of the C_{16} chain is about 1.8 – 1.9 nm [14], this gap distance is almost double the length of the CTAB long alkyl chain. It suggests that the basal plane of each nanodisk may be covered with a monolayer of CTAB molecules, most likely, with its CH_3-N^+ headgroup bound to the silver surface, and its long alkyl hydrophobic chain toward outside. It is the strong hydrophobic interactions between long alkyl chains on neighboring plates that cause the stacking of the nanodisks. The similar double alkyl layer structures for CTAB have already been suggested on Au nanorod surface [15].

Structure information is obtained with electron diffraction and oriented particulate monolayer X-ray diffraction (OPML-XRD) analysis. Electron diffraction of individual silver nanodisk gives spot points with a hexagonal arrangement indicating that the particle is a single crystal. The XRD patterns for the flat-lying nanodisks with their basal plane parallel to the substrate only show an overwhelmingly intensive diffraction peak at $2\Theta = 38.05$, which is from the (111) lattice plane of face-centered cubic (fcc) silver. This clearly demonstrates that the particles are made of pure silver and their basal plane, i.e., the top crystal plane, should be the (111) plane.

The formation process was studied by combined TEM and absorption methods. Immediately after the addition of NaOH, sampling was conducted by taking small aliquot which is quenched by HCl solution, the TEM photos of the samples taken at 30s, 90s and 300s are shown in Figure 2. One can see that at 30s, the most of the particles are small and spherical; the triangular particles formed at about 90s, and continue to grow at 300s. This process can be clearly seen from the absorption spectra shown in Figure 3. At 30s, the spectrum displays two peaks, one at 430 nm; another at around 520 nm, the former is due to the formation of spherical particles, the latter to the triangular shaped one. As the time increased, the latter peak shifted to longer wavelength, indicating the formation of triangular particles. Noted that the intensity of the 430 nm peaks increased during this time, this shows that spherical particles may produce continuously.

After aging for 4 days at room temperature, we found that the 430 nm peak decreased in



Figure 2. TEM images of the silver particles obtained at 30s (a), 90s (b) and 300s (c) after adding NaOH solution. The scale bar in (a) applies to all images.

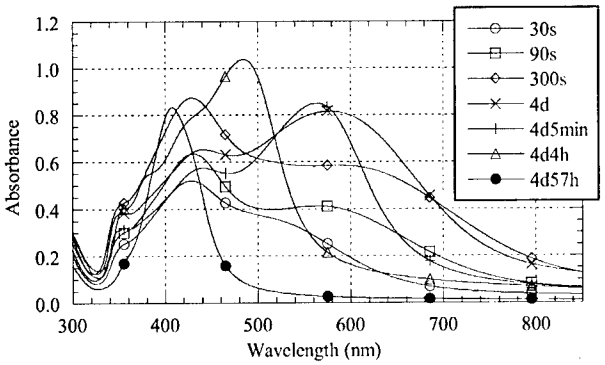


Figure 3. Absorption spectra of the samples at 30s, 90s, and 300s after the addition of NaOH solution. And that after 4 days of aging at 20 °C, then aged at 40 °C for 5 min, 4 h, and 57 h.

intensity at the expense of that of the long wavelength peak (Figure 3), implying that spherical particles continuously grow to triangular particles. The aging process at 40 °C is found to exert a strong influence on the shape transformation of the silver particles. As the aging time increased from 5 min to 4 h (Figure 4a and b), the particle shape changed from triangular to circles. On the other hand, the particle thickness is essentially unchanged (24 ± 8 nm at 5 min vs. 26 ± 3.4 nm at 4 h), similar OPML-XRD patterns are observed for the not aged, 5 min and 4 h aged samples, implying that the (111) basal plane is not altered during this aging process. This shows that the isotropic growth of silver mainly occurred within the basal plane.

It is reasonable to suggest that CTAB molecules play a critical role in this isotropic growth. Well-defined SAM layer of CTAB on the (111) plane should prevent this plane from further growth, leading to the rounding of the triangular particles.

Interestingly, after long time (e.g. 57 h) of aging, as shown in Figure 4c, the particles shrank in size to 44 ± 8 nm and changed to spherical in shape. Since this size is larger than the thickness of the nanodisks, particle growth normal to the basal plane should occur due to desorption or destruction of the CTAB self-assembled monolayers. Similar aging effects are also reported for the gold nanorod [16]. On the other hand, particle dissolution is also found for the basal plane. This phenomenon is more apparent when aging is carried out at a higher temperature, such as 80 or 95 °C. In some cases, particles are completely dissolved, giving a colorless transparent solution.

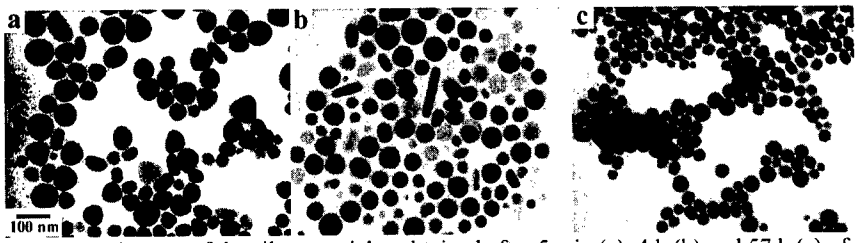


Figure 4. TEM images of the silver particles obtained after 5 min (a), 4 h (b) and 57 h (c) of aging at 40 °C. The scale bar in (a) applies to all images.

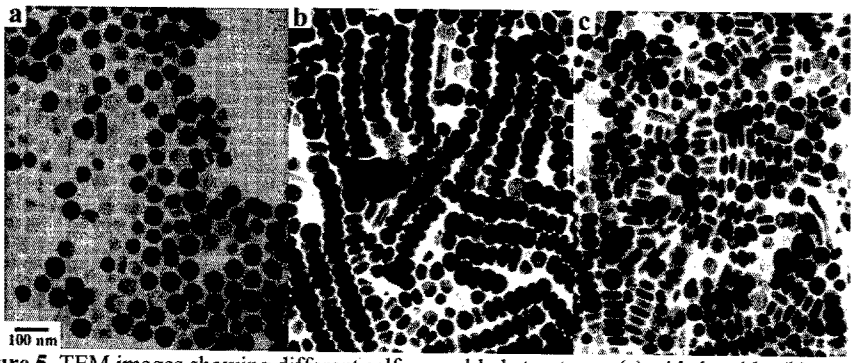


Figure 5. TEM images showing different self-assembled structures. (a), side by side. (b) shoulder to shoulder, and (c) head to head. The scale bar in (a) applies to all images.

The above shape changes are reflected in the absorption spectra (Figure 3). Before aging, truncated triangular particles display mainly three absorption peaks at 584 nm, 444 nm and 351 nm. According to the theoretical calculation of Schatz et al. [2], these peaks are assigned to in-plane dipole, out-of-plane dipole and quadrupole plasmon bands, respectively. When aging time changed from 5 min to 4 h, the first 584 nm peak quickly blue-shifted (see Figure 3), corresponding to the in-plane transformation of the triangles to circles. At the same time, the peak position of the two out-of-plane peaks are kept almost unchanged due to the constant thickness of the nanoplates. Continuous aging to 57 h finally give a single absorption band which belongs to the spherical particles.

The nanodisks are found to form different kind of large-area self-assembled nanostructures on the copper grid (Figure 5). From the optical microscopy, it is found that the aggregation occurs during the dry of the solvent. Also, two factors can be considered as prerequisites for generating these structures: one is the existence of the SAM layer on the basal plane of the nanodisks, which provides the hydrophobic interactions between neighboring particles. Another is the monodispersity of the nanodisks. One can see that nanodisks in the trains are similar in sizes. From Figure 5, at least three kinds of self-assembled structures can be defined; they are side by side (nanodisks sit at the same plane, forming associated structures), shoulder by shoulder (partial overlap) and head to head (close packing). These self-assembled structures provide an interesting example showing that nanodisks can be used as very useful building blocks in constructing devices in future nanoelectronics.

CONCLUSION

In summary, silver nanodisks have, for the first time, been generated in large quantities by a solution-phase approach. These particles have a thickness of 26 nm, and a diameter around 60 nm. They are single crystal and with their basal plane as (111) lattice plane. The formation of self-assembled monolayer of CTAB on the basal plane is likely to be very important not only in explaining the anisotropic growth from triangular nanoplates to nanodisks, but also the formation of large-area necklace-like structures. A strong surface plasmon absorption band at 475 nm is

found for these nanodisks. In addition, a simple mild aging method is provided to systematically control the surface plasmon band of silver particles within 420 nm to 560 nm.

ACKNOWLEDGEMENTS

Supports from DARPA through grant N66001-01-1-8938 (the Laboratory for Advanced Photonic Composites), and through the Center for Optical Materials Science and Engineering Technologies (COMSET) at Clemson University is grateful acknowledged.

REFERENCES

1. J. J. Mock, M. Barbic, D. R. Smith, D. A. Schultz and S. Schultz, *J. Chem. Phys.* **116**, 6755 (2002).
2. R. C. Jin, Y. W. Cao, C. A.; Mirkin, K. L. Kelly, G. C. Schatz and J. G. Zheng, *Science* **294**, 1901 (2001).
3. S. Nie and S. R. Emory, *Science* **275**, 1102 (1997).
4. S. Schultz, D. R. Smith, J. J. Mock and D. A. Schultz, *Proc. Natl. Acad. Sci. U. S. A.* **97**, 996 (2000).
5. S. Schneider, P. Halbig, H. Grau and U. Nickel, *Photochem. Photobiol.* **60**, 605 (1994).
6. S. A. Harfenist, Z. L. Wang, M. M. Alvarez, I. Vezmar and R. L. Whetten, *J. Phys. Chem.* **100**, 13 904 (1996).
7. Y. Sun, B. T. Mayers and Y. Xia, *Nano Lett.* **2**, 481 (2002).
8. A. I. Kirkland, D. A. Jefferson, D. G. Duff, P. P. Edward, Gameson, B. F. G. Johnson and D. J. Smith, *Proc. R. Soc. London A* **440**, 589 (1993).
9. T. Klaus, R. Joerger, E. Olsson and C.-G. Granqvist, *Proc. Natl. Acad. Sci. U. S. A.* **96**, 13611 (1999).
10. D. G. Duff, A. C. Curtis, P. P. Edwards, D. A. Jefferson, B. F. G. Johnson and D. E. Logan, *J. Chem. Soc. Chem. Commun.* 1264 (1987).
11. S. Giorgio and J. Urban, *J. Phys. F: Met. Phys.* **18**, L147 (1988).
12. B. H. Hong, S. C. Bae, C.-W. Lee, S. Jeong and K. S. Kim, *Science* **294**, 348 (2001).
13. J. Xiao, Y. Xie, R. Tang, M. Chen and X. Tian, *Adv. Mater.* **13**, 1887 (2001).
14. R. H. Terrill, T. A. Postlethwaite, C. Chen, C. Poon, A. Terzis, A. Chen, J. E. Hutchison, M. R. Clark, G. Wignall, J. D. Londono, R. Superfine, M. Falvo, C. S. Johnson, E. T. Samulski, Jr. and R. W. Murray, *J. Am. Chem. Soc.* **117**, 12537 (1995).
15. M. B. Mikoobakht and M. A. El-Sayed, *Langmuir* **17**, 6368 (2001).
16. M. B. Mikoobakht, K. Z. Ismail, S. Link and M. A. El-Sayed, *J. Phys. Chem. B* **102**, 9370 (1998).

Synthesis of Nanostructured Materials II

Mat. Res. Soc. Symp. Proc. Vol. 740 © 2003 Materials Research Society I11.2

Radiolytic Synthesis of Bimetallic Nanoparticles with High Aspect Ratio

C. M. Doudna[1], M. F. Bertino[1], S. Pillalamarri[2], F. D. Blum[2], A. T. Tokuhiro[3], S. Chattopadhyay[4], and J. Terry[4]

[1] Department of Physics, University of Missouri-Rolla, Rolla, MO 65409; [2] Department of Chemistry, University of Missouri-Rolla, Rolla, MO 65409; [3] Department of Nuclear Engineering, University of Missouri-Rolla, Rolla, MO 65409; [4] Biological, Chemical, and Physical Sciences, Illinois Institute of Technology, Chicago, IL 60616

ABSTRACT

We present a technique to synthesize high aspect ratio metallic nanostructures based on the radiolysis method. In our experiments, we use gamma rays to irradiate aqueous solutions containing Ag and Pt ions and a water-soluble polymer. The aspect ratio of the nanoparticles is controlled by varying the radiation dose rate, the type of polymer, and the type of counter ions. Transmission electron microscopy shows that wire-like structures composed of grains with a face centered cubic (fcc) structure can be formed with a length of up to 3.5μm and typical diameters between 5 and 12nm. X-Ray absorption spectroscopy shows that Ag and Pt do not form an alloy, but remain segregated.

INTRODUCTION

Metallic nanostructures with high aspect ratios are promising candidates for the development of sensors [1], nanoscopic electrical connections, and catalysts [2]. Several techniques have been developed to synthesize nanoparticles with predefined aspect ratios and crystalline habits [3-12]. The mechanism of nanowire formation is not clear in its details; however, most synthesis techniques [3-12] share common features. In general, a noble metal is reduced at a slow rate in the presence of pre-formed metal clusters, which act as nucleation seeds, and a capping polymer. Reduction often takes place in a micellar environment [3-8]. We show here that nanoparticles with high aspect ratios can also be produced with the radiolysis method [3,11-14]. A large number of experiments were carried out to determine the parameters affecting nanowire formation. Parameters included total gamma ray dose, type of counter ions added to the solution, total and relative metal concentration, and polymer type and concentration.

EXPERIMENTAL DETAILS

Sample preparation

Metal salts used to prepare aqueous solutions were $AgNO_3$, Ag_2SO_4, H_2PtCl_6, and K_2PtCl_4. Solutions had a typical total metal ion concentration between 0.5 and $2x10^{-3}$ mol/l. Samples were prepared with Ag/Pt mole ratios varying from 100% to 0% Ag in steps of 10%. To scavenge $H^{\bullet}$ and $OH^{\bullet}$ radicals generated during irradiation, 0.2 mol/l of 2-propanol was added to the solutions. Poly(vinyl alcohol) (PVA) of varying molecular weight and degree of hydrolysis was used as a capping polymer. The characteristics of the capping polymers are reported in Table I. Polymer concentrations were varied between 2 and 12 g/l, corresponding to a concentration of monomer units between 0.09 and 0.5 mol/l. Due to their photosensitivity, the samples were stored in the dark after mixing. Before and after irradiation, the solutions were free of precipitates.

Table I. Types of poly(vinyl alcohol) polymers employed in the experiments. Molecular weights indicated with * are estimated from a viscosity-molecular weight conversion table available from Celanese Chemicals

Poly(vinyl alcohol) (brand name)	Hydrolysis (%)	Molecular Weight (amu)	Supplier
Celvol 540	87-89	146 000 – 186 000 *	Celanese
-	87-89	88 000 - 97 000	Alfa Aesar
Celvol 205 and 502	87-89	13 000 - 52 000 *	Celanese
Celvol 165 and HA-70	99.3+	146 000 - 186,000+ *	Celanese
-	98-99	88 000 - 97 000	Alfa Aesar

Radiolysis of aqueous solutions is an efficient method for the reduction of metal ions and formation of homo- and hetero- nuclear clusters of transition metals [3,11-13]. In the radiolysis method, aqueous solutions are exposed to γ-rays, as shown in equation 1, to create solvated electrons, e^-_{aq} [14]. The solvated electrons reduce the metal ions, as shown in equations 2 – 3. The metal atoms coalesce to form clusters as shown in equation 4.

$$H_2O \xrightarrow{\gamma\text{-radiation}} e^-_{aq},\ H_3O^+,\ H^\bullet,\ OH^\bullet,\ H_2O_2 \quad (1)$$

$$e^-_{aq} + M^{m+} \longrightarrow M^{(m-1)+} \quad (2)$$

$$e^-_{aq} + M^{+} \longrightarrow M_0 \quad (3)$$

$$nM_0 \longrightarrow M_2 \longrightarrow \ldots\ldots M_n \quad (4)$$

Samples were irradiated with gamma radiation from the fission products of the University of Missouri-Rolla's pool nuclear reactor. In the experiments described here, the dose rate decreased exponentially from a value of about 0.5 kGy/h in the first hour to about 0.05 kGy/h 48 hours after shutdown. Exposure to a total dose between 3 and 3.5 kGy typically required 36 to 48 hours. Total doses were measured with Thermoluminescent Dosimeters (TLD) placed in vials adjacent to the samples to be irradiated.

Characterization

TEM measurements were carried out with a Philips EM430T microscope operated at 300 keV. Selected area electron diffraction (SAED) was employed for structural characterization. The chemical composition of the nanoparticles was determined with energy dispersive X-ray chemical analysis (EDS). SAED and EDS had a spatial resolution of 150 nm. X-ray Absorption Fine Structure (XAFS) was performed at the MR-CAT undulator beamline at Advanced Photon Source, Argonne National Laboratory. A double crystal Si(111) monochromator was utilized for energy selectivity and a Rh harmonic rejection mirror was used to eliminate the higher harmonics of the desired energy range (Pt L_3-edge). XAFS measurements were performed in fluorescence mode using a 13-element Ge detector. The incident photon intensity was measured by an ion chamber filled with 80% He, 20% N_2 gas mixture.

DISCUSSION

A bright-field TEM micrograph showing typical nanoparticles produced is shown in Figure 1. These particles were produced by irradiating a solution with a total metal concentration of $2x10^{-3}$ mol/l, and a mole ratio of 70%Ag, 30%Pt with 0.5 kGy. Nearly spherical particles, with diameters in the 20-30 nm range, were observed. EDS showed that these particles were composed of pure Ag, and SAED

yielded diffraction rings characteristic of a fcc structure. The fact that Ag was reduced first can be explained based on electrochemical arguments. Reduction of $Pt^{IV}Cl_6^{2-}$ to Pt metal occurs in two steps. The first step, $Pt^{IV}Cl_6^{2-}/ Pt^{II}Cl_4^{2-}$, has a reduction potential of 0.68V and the second step, $Pt^{II}Cl_4^{2-}/ Pt^0$, has a reduction potential of 0.74V. The reduction potential of Ag^+ to Ag metal in acidic solution is E^0 = +0.79 V, and is more positive than both Pt reduction steps. Thus, Ag^+ is the more noble species in our solutions. When ionizing radiation at low dose rates is employed to reduce metal ions in aqueous solutions, clusters of the more noble metal (Ag in our case) form first because charge is transferred from the less noble to the more noble species [12,13].

Figure 1b shows typical nanoparticles obtained after exposure to a total dose of 3.5 kGy for solutions with the same total metal ion concentration as those shown in Figure 1a. Nanowires are evident, and they are typically made up of thin filaments, with diameters of 2-5 nm, that join large particles, with typical diameters of 20-30 nm. Nanoparticle chemical composition was determined with EDS. The spatial resolution of our instrument (about 150 nm) prevented a precise determination of individual cluster composition. We did establish, however, that regions surrounding the large particles have a typical composition of 80-90 at% Ag. Regions containing only filaments have a typical composition close to 50 at% Ag. The EDS results suggest that the larger particles are made from the Ag particles that form in the early stages of reduction, and that Pt-rich filaments nucleate out of these Ag particles. Figure 1c shows a SAED obtained from a filament region. Diffraction spots are distributed on rings, and indicate that the filaments are polycrystalline. The rings are consistent with fcc structures, and indicate that the filaments are made up of fcc grains. The low particle density of the filaments and their small diameter resulted in a small number of broad diffraction spots, and prevented an accurate determination of lattice parameters with SAED. The upper left quadrant of Figure 1c, shows the rings expected for the (111) and (200) reflections of bulk Ag and Pt. Some diffraction spots are broader than the distance between the Ag and Pt rings. It is not possible to determine if the spots originate from reflections of isolated Pt and Ag particles, or, for example, from a Ag-Pt alloy with a lattice parameter intermediate between those of Ag and Pt. SAED taken from regions surrounding the larger particles yielded results comparable to those obtained for the filaments.

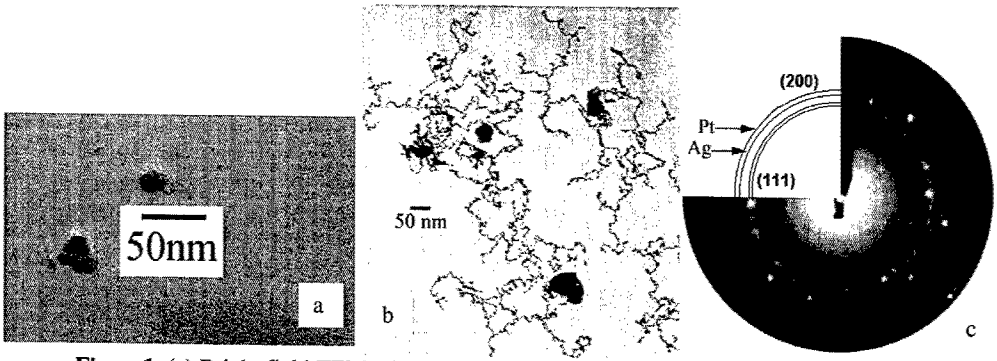


Figure1. (a) Bright field TEM micrograph of nanoparticles obtained after exposure to a total dose of 0.5 kGy. Spherical particles are 20-40nm in diameter (b) Bright field TEM micrographs of nanoparticles obtained after exposure to a dose of 3.5 kGy. Larger spherical particles are 20-35nm while the smaller clusters are on the order of 1 or 2nm (c) Typical SAED of a filament region. All samples were made with 70at% Ag and 30at% Pt nominal concentration, 8mg/ml PVA (MW 88,600-97,000, 87-89% hydrolysis), and a total metal ion concentration of 2×10^{-3}.

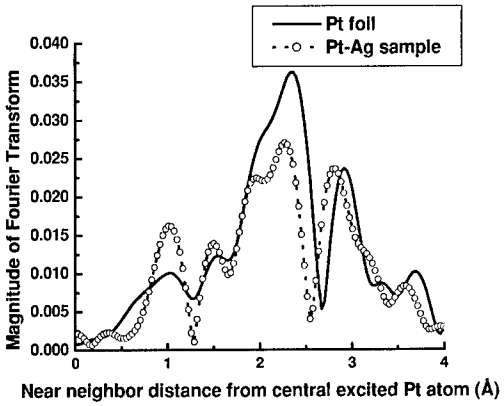


Figure 2. Fourier transform of Pt foil data (solid) and of a 60/40 at% Ag/Pt sample (dot) over the k-range 3 - 11.8 $Å^{-1}$.

To determine whether or not the grains making up the filaments were Ag-Pt homogeneous alloys, XAFS of a 60/40 at% Ag/Pt sample was measured. The period of observed oscillations is a function of the bond-lengths of the neighbors of the absorbing atom, and the amplitude depends on the coordination number. The oscillations were extracted from the spectrum by a background subtraction and then Fourier-transforming the oscillations into real space. A Pt foil was first measured in transmission mode XAFS and as compared to the same type of measurements of the Ag/Pt sample. The first shell did not show any conspicuous trace of Ag; only Pt atoms coordinate the central Pt. This apparent reduction in bond length can be explained by the effect of disorder in XAFS [15-17], which suggests that the Pt atoms in this sample are in a disordered state compared to the Pt foil. Formation of a homogeneous Ag-Pt alloy would lead to an expansion of the lattice parameter of Pt, as expected from Vegard's law, and experimentally observed [16]. The absence of an expansion ruled out alloying. Rather, we observed a contraction in the Pt first shell bond length by 0.05 Å, as seen in Figure 2. The coordination number is much lower compared to that of the bulk Pt, which is a reasonable characteristic of nanoparticle systems.

The high aspect ratio of the nanoparticles produced in our experiments is at odds with previous experiments, where radiolysis yielded nearly spherical Ag-Pt bimetallic clusters [12]. To better understand the nanowire formation mechanism, we varied numerous parameters, such as total and relative metal and polymer concentrations, counter ions, and type and molecular mass of the polymer. The effects of these parameters on the aspect ratio of the nanoparticles are summarized in Table II. For example, when K_2PtCl_4 was employed, spherical particles resulted. Similarly, nanowires did not form when $AgNO_3$ was employed instead of Ag_2SO_4. Nanowires also did not form when the Ag^+ concentration was lower than 20% or higher than 80% of the total metal ion concentration. The degree of hydrolysis of the capping polymer PVA also played an important role. When PVA hydrolysis was on the order of 98-99%, spherical aggregates resulted. High aspect ratio nanoparticles were produced only with 87-89% hydrolyzed PVA with a molecular weight of at least 31,000.

Our results suggest that polymer-metal complexes (and possibly micelles) are being formed. Partially hydrolyzed PVA can be envisaged as a copolymer, where hydrophilic vinyl alcohol groups are broken up by less hydrophilic, un-hydrolyzed vinyl acetate groups. The un-hydrolyzed groups are likely to aggregate in aqueous solution, presumably around hydrophilic species such as metal clusters or metal ions, possibly like a swollen micelle. The sensitivity of the synthesis to the presence of SO_4^{2-} and $PtCl_6^{2-}$ ions also indicates polymer-ion complex formation. For example, polymer gels of modified PVA show great sensitivity to the presence of ions such as sulfate [19]. These specific interactions probably enhance the interaction of the metal ions (and ultimately particles) with PVA.

Table II. List of metal compounds, type of capping polymers and Ag/Pt mole ratios leading to, or preventing, nanowire formation. All conditions in the second row must be met to produce nanowires, any condition met in the third row prevents nanowire formation. The aspect ratio of the nanoparticles did not depend on the total metal ion concentration (tested range: 1×10^{-4} to 2×10^{-3} mol/l), or the polymer concentration (tested range: 2 to 12 g/l). Solutions were exposed to a total dose of 3.5 kGy.

PVA molecular mass (amu), hydrolysis degree (%)	**Ag/Pt mole ratio**	**Ag, Pt compounds**	**Wire formed**
MW: 31000-170000 and Hydrolysis: 87-89%	80/20 to 20/80	H_2PtCl_6 and Ag_2SO_4	Yes
MW: 20000 or Hydrolysis: 98%	100/0 or 90/10, or 10/90 or 0/100	K_2PtCl_4 or $AgNO_3$	No

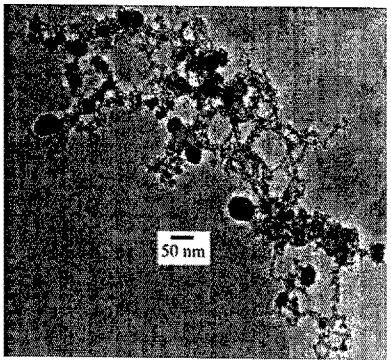


Figure 3. Bright field TEM micrographs of nanoparticles obtained after exposure to a dose of 3.5 kGy. The larger spherical particles are 30-45 nm while the filaments are on the order of 3 to 6 nm. Samples were made with 60 at% Ag and 40at% Pt nominal concentration, 5.7mg/ml PEO-block-PPO, and a total metal ion concentration of 2×10^{-3}.

The polymer-metal complexes might be micelles, since there is experimental evidence that copolymers made up of hydrophilic and hydrophobic blocks such as poly(ethylene oxide) – block – poly(methacrylic acid) [5], coordinated with metal ions of Ag, can give rise to micelles [20]. In Figure 3, we show preliminary results obtained by replacing PVA with a co-block polymer, poly(ethelene oxide) – block – poly(propylene oxide) (PEO-block-PPO). PEO is the hydrophilic part while PPO is the hydrophobic part of the polymer. Solutions containing a 2×10^{-3} total metal ion concentration of 60at% Ag and 40at%Pt were prepared with 57 g/l of PEO-block-PPO. The resulting nanoparticle structure alternated with large spherical particles and thin, filament-like aggregates. Regions where small clusters aggregated to give rise to large patches of high cluster density were also evident and were not detected when PVA was employed. The results suggest that alternating hydrophilic and hydrophobic groups in the capping polymer is a necessary condition for filament formation. The precise morphology of the nanoparticles, however, probably has a complex dependence on the compositions of the solutions.

CONCLUSION

We describe a technique to synthesize high aspect ratio bimetallic nanostructures. We employed radiolysis to reduce metal ions in aqueous solution and generate filament-like nanostructures that can be as long as several microns, with a diameter of a few nanometers. The filaments are polycrystalline, and are made up of grains with fcc structure. The grains have a Ag core-Pt shell structure, homogeneous alloying being ruled out by XAFS. Key parameters for nanowire formation are the mole ratio between

the two metals, the type of counter ions in solution, and the presence of hydrophobic groups in the capping polymer.

ACKNOWLEDGMENT

We thank William Bonzer for his assistance in irradiating our samples. We also thank Dr. S. Miller for his assistance with TEM measurements. A. T. Tokuhiro, Director of the University of Missouri-Rolla Reactor (UMRR) Facility, thanks the Department of Energy for continued support of UMRR through the Reactor Instrumentation and Reactor Sharing Grant programs. The MRCAT beamline is supported by the US DOE under grant number DEFG0200ER45811.

REFERENCES

(1) S.R. Nicewarner-Pena, R.G. Freeman, B.D. Reiss, L. He, D.J. Pena, I.D. Walton, R. Cromer, C.D. Keating, M.J. Natan, *Science* **294**, 137 (2001).
(2) A. Fukuoka, N. Higashimoto, Y. Sakamoto, S. Inagaki, Y. Fukushima, M. Ichikawa, *Topics in Catalysis* **18**, 73 (2000).
(3) A. Filankembo, M.P. Pileni, *J. Phys. Chem. B.* **104**, 5866 (2000).
(4) M.P. Pileni, *Langmuir* **13**, 3266 (1997).
(5) D. Zhang, L. Qi, J. Ma, H. Cheng, *Chem. Mater.* **13**, 2753 (2001).
(6) N.R. Jana, L. Gearheart, C.J. Murphy, *Chem. Mater.* **13**, 2313 (2001).
(7) C.J. Murphy, N.R. Jana, *Adv. Mater.* **14**, 80 (2002).
(8) N.R. Jana, L. Gearheart, C.J. Murphy, *J. Phys. Chem. B.* **105**. 4065 (2001).
(9) Y. Sun, B. Gates, B. Mayers, Y. Xia, *Nanoletters* **2**, 165 (2002).
(10) Y. Zhou, S.H. Yu, C.Y. Wang, X.G. Li, Y.R. Zhu, Z.Y. Chen, *Adv. Mater.* **11**, 850 (1999).
(11) J. Belloni, M. Mostafavi, H. Remita, J.L. Marignier, M.O. Delcourt, *New J. Chem.* 1239 (1998).
(12) M. Treguer, C. de Cointet, S. Remita, M. Khatouri, M. Mostafavi, J. Amblard, J. Belloni, J. *Phys. Chem. B.* **102**, 4310 (1998).
(13) H. Remita, M. Mostafavi, M.O. Delcourt, Radiat. *Phys. Chem.* **47**, 275 (1996).
(14) A. Henglein, *Israel J. Chem.* **33**, 77 (1993).
(15) M. Newville, B. Ravel, D. Haskel, J.J. Rehr, E.A. Stern, Y. Yacobi, *Physica B* **208 & 209**, 154 (1998).
(16) G. Dalba, P. Fornasini, R. Grisenti, D. Pasqualini, D. Diop, F. Monti, *Phys. Rev. B* **58**, 4793 (1995).
(17) H. Rossner, H.J. Krappe, *Syn. Rad.* **8**, 261 (2001).
(18) K. Torigoe, Y. Nakajima, K. Esumi, *J. Phys. Chem.* **97**, 8304 (1993).
(19) Y. Okazaki, K. Ishizuki, S. Kawauchi, M. Satoh, Komiyama, *J. Macromolecules* **29**, 8391 (1996).
(20) H. Colfen, *Macromol. Rapid Commun.* **22,** 219 (2001).

Mat. Res. Soc. Symp. Proc. Vol. 740 © 2003 Materials Research Society I11.6

Fluorinated Single Wall Nanotube/Polyethylene Composites for Multifunctional Radiation Protection

Merlyn X. Pulikkathara[1], Meisha L. Shofner[2], Richard T. Wilkins[1], Jesus G. Vera[2], Enrique V. Barrera[2], Fernando J. Rodríguez-Macías[3], Ranji K. Vaidyanathan[4], Catherine E. Green[4], Clay G. Condon[4]
[1]Center for Applied Radiation Research, Prairie View A&M University, Prairie View, TX 77446, U.S.A.
[2]Department of Mechanical Engineering and Material Science, Rice University, Houston, TX 77005, U.S.A.
[3]Department of Chemistry, Rice University, Houston, TX 77005, U.S.A.
[4]Advanced Ceramics Research, E. Hemisphere Loop, Tucson, AZ 85706, U.S.A.

ABSTRACT

Fluorinated Single Wall Nanotubes (f-SWNTs) have been processed in polyethylene by an incipient wetting technique to achieve a well dispersed nanocomposite for radiation protection. In some cases, samples were further processed using the rapid prototyping method of extrusion freeform fabrication. Composites were exposed to 40 MeV proton radiation with a flux of about $1.7x10^7$ protons/cm^2/sec to a total fluence of $3x10^{10}$ protons/cm^2 .This exposure is consistent with a long-term space mission in low earth orbit. The samples were evaluated by means of Raman spectroscopy and thermogravimetric analysis (TGA). These results were compared to the unexposed composite and unfilled polymer samples. This study has focused on the stability of the nanotube composites when exposed to radiation and prior to hydrogen exposure. It was shown that the stability of the functional group is not constant with SWNTs produced by different processes and that radiation exposure is capable of defluorinating SWNTs in polyethylene.

INTRODUCTION

Since the discovery of single wall carbon nanotubes (SWNTs) in 1993 [1, 2], research has been conducted to exploit their unique mechanical, electrical, and thermal properties to create multifunctional composite materials [3]. Previous research has shown that SWNTs have the highest measured electrical conductivity of any known fiber [4], a higher thermal conductivity than diamond [5], and the highest stiffness of any known fiber [6]. Due to the provocative geometry and other remarkable properties of carbon nanotubes, they are of interest to the aerospace and radiation communities [7-10]. The possibility of nanotubes serving as a storage medium for hydrogen is of particular interest for future spacecraft, and hydrogen-rich and other low atomic mass materials are believed to minimize radiation exposure in the space environment [11]. It is expected that nanotube polymer composites will be effective radiation protection shielding when prepared to contain hydrogen.

Fluorinated and purified SWNTs were used in this work to prepare polyethylene composites. Fluorination is seen as a near term approach for achieving un-roped nanotubes for composite applications, and it may even shorten the tube lengths. As an extension of the work presented in this paper, a sample of f-SWNT/polyethylene composite material was processed and further prepared by extrusion freeform fabrication [12] and submitted to the Materials International

Space Station Experiment (MISSE). Panels containing candidate materials for use in space are installed on the International Space Station (ISS) and exposed to space radiation for approximately three years. The first set of materials, containing the single wall carbon nanocomposites, will be on board the ISS in March 2003 for an eighteen month evaluation. The results of this study will provide a deeper insight into the capabilities of such materials in future space applications.

However, long term space based experiments, are not a practical way of accessing the radiation characteristics of materials, and studies using ground-based energetic particles relevant to the space environment have been limited [13]. In this experiment, SWNT composites were irradiated with 40 MeV protons at Texas A&M University Cyclotron Institute (TAMCI). The proton energies and the total particle fluence used in our work are consistent with the radiation environment of low earth orbit (LEO); such as the environment encountered by the astronauts and electronics of the ISS. To characterize the effects of proton irradiation on nanotubes, the samples were characterized by thermogravimetric analysis (TGA) and Raman spectroscopy. This paper describes some initial results of an ongoing study on the radiation properties of carbon nanotube reinforced materials.

EXPERIMENTAL DETAILS

The SWNTs used in this research were purchased from Tubes@Rice and Carbon Nanotechnologies, Inc. in purified form. These nanotubes were produced by the pulsed laser vaporization [14] and High Pressure Carbon Monoxide (HiPCO) [15] processes respectively. The nanotubes were used in purified (P-SWNT) and fluorinated (f-SWNT) conditions. The fluorination was performed by previously described methods [16]. Medium density polyethylene (MDPE) was obtained from Aldrich in powder form to create the composites. The MDPE had a molecular weight of 6000 and a melting point between 109-111°C. The composite compositions studied are found in Table 1.

The composites were processed by incipient wetting followed by Banbury mixing. The incipient wetting technique creates an initial level of dispersion by coating the polymer with nanotubes [3, 17]. A polymer powder and a nanotube solution were combined and heated in an oil bath to remove the solvent. The remaining material is dried in a furnace to remove the remaining solvent. The over coated polymer is subsequently processed by Banbury mixing and pressed into sheets by heated compression molding. The unfilled polymer was processed in the same manner for consistency.

Each composite sample was placed between two sheets of thin Mylar to facilitate positioning in the proton beam. The samples were irradiated with 40 MeV protons at a flux rate of about 1.7×10^7 p/cm^2/sec to a total fluence of 3×10^{10} p/cm^2 (except in one case). The fluence was chosen to be consistent with the expected exposure during a long-term LEO mission. The irradiations were performed at room temperature in a vacuum of about 5×10^{-5} Torr. The irradiation conditions for the samples are summarized in Table 1.

The samples were characterized by Raman spectroscopy pre- and post-irradiation. The Raman spectroscopy measurements utilized a Renishaw Micro Raman spectrometer with 780.6 nm diode laser and a resolution of 2 cm^{-1} was used. The objective used was 50X with a 0.55 μm aperture. In addition, pieces of each sample were used to perform thermogravimetric analysis (TGA). Both pre-and post-irradiation samples were studied. TGA was performed in a nitrogen atmosphere to ascertain any damage to the polymer caused by the radiation exposure. The

apparatus used was a SDT 2960 from TA Instruments. Weight loss and temperature difference values were used to evaluate the materials.

Table I. Samples studied and radiation conditions.

Sample	Fluence
1.5% wt. SWNT/ MDPE (purified HiPCO)	$3x10^{10}$ protons/cm^2
5% wt. SWNT/MDPE (purified HiPCO)	$3x10^{10}$ protons/cm^2
1.5% wt. f-SWNT/MDPE (laser Tubes@Rice)	$3x10^{10}$ protons/cm^2
5% wt. f-SWNT/MDPE (HiPCO)	$3x10^{10}$ protons/cm^2
1.5% wt. f-SWNT/MDPE (HiPCO)	$4.7x10^{10}$ protons/cm^2
MDPE	$3x10^{10}$ protons/cm^2

RESULTS AND DISCUSSION

Raman spectroscopy results shown in Figures 1-3 of the composites suggest that the proton radiation had a different effect on the samples containing laser generated f-SWNTs compared with the samples containing the HiPCO f-SWNTs. The pre-irradiation spectra of both laser and HiPCO f-SWNT composites were similar as can be seen by the marked peaks of the breathing mode and G band in both curves. The significant features of the pre-irradiation Raman spectra, specifically the broad breathing mode (254.5cm^{-1}) and broad G band (1595cm^{-1}) in Figure 1 of the laser f-SWNTs (Tubes@Rice) composite are still observed in the post-irradiation spectra with no significant change.

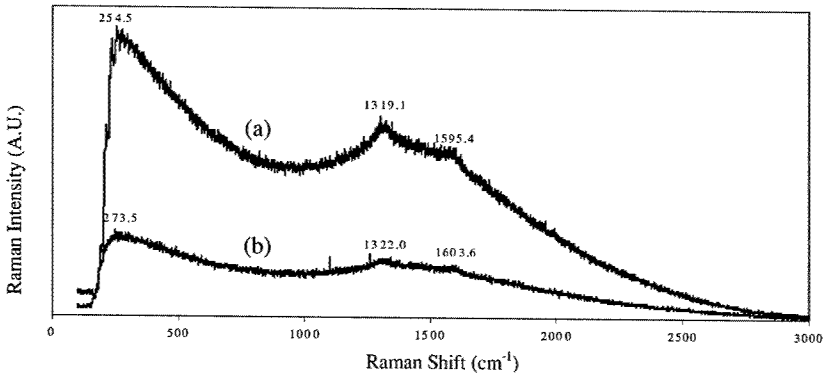


Figure 1. Raman spectra of (a) pre- and (b) post-irradiation of 1.5% wt. fluorinated-SWNT/MDPE (Tubes@Rice, laser).

However, the HiPCO f-SWNT composites appear to defluorinate after radiation. This is observed by comparing the spectra of the irradiated HiPCO f-SWNT composites (Figure 2) with the spectra of both pre- and post-irradiated non-fluorinated HiPCO SWNT composites (Figure 3). The broad features of the pre-irradiated fluorinated composites change to the familiar sharp

and strong lines (around 1590-1600 cm^{-1}) post-irradiation. The non-fluorinated SWNT composites showed no remarkable change in the relevant peaks pre- and post- irradiation as seen in Figure 3. The spectra in Figures 2 and 3 show that percent weight of the SWNTs in the composites played no role in the materials' response to the radiation. The spectra of a control sample of unfilled PE showed no significant change after irradiation.

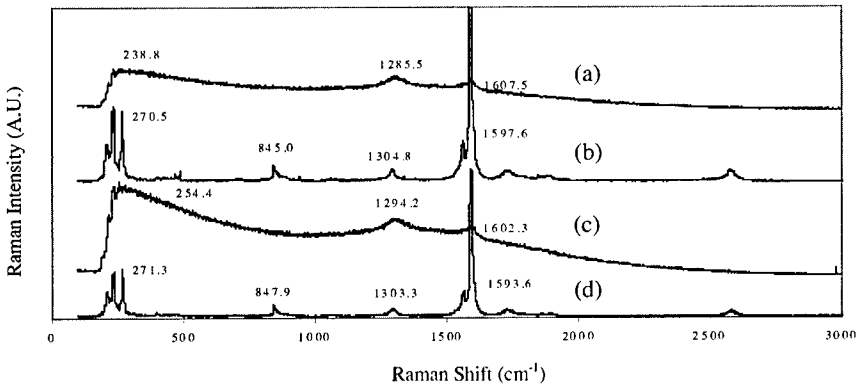


Figure 2. Raman spectra of (a) pre- and (b)post-irradiation of 5% wt. and (c) pre- and (d)post-irradiation of 1.5% fluorinated- SWNT/MDPE (HiPCO).

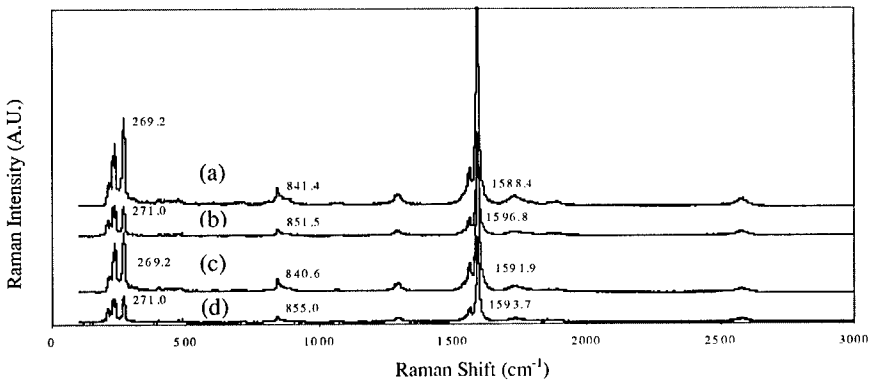


Figure 3. Raman spectra of (a)Pre- and (b)post-irradiation of 1.5% and (c)pre- and (d)post-irradiation of 5% wt. non-fluorinated SWNT/MDPE (HiPCO).

The TGA results in Figure 4, show that no detrimental changes in the thermal degradation properties of the unfilled polymer or the composites occurred due to radiation exposure. All

samples decomposed in one step with the maximum weight loss occurring at a temperature between 469°C and 479°C. The composite containing P-SWNTs and Tubes@Rice f-SWNTs did not show any appreciable change in the temperature where this peak occurred, but the peak position for the composites containing fluorinated HiPCO SWNTs shifted to a higher temperature. In both the 1.5 wt.% and 5 wt.% f-SWNT composites, the inflection point shifted approximately 4°C to correspond with their P-SWNT counterparts corroborating the defluorination observed in the Raman spectra. Figure 4 shows the % weight loss curves and the derivative % weight loss curves in the inset plotted against temperature for the composites containing 5 wt. % P-SWNTs and 5 wt. % f-SWNTs. The curves for the other materials; unfilled polyethylene, 1.5 wt. % f-SWNT (Tubes@Rice)/MDPE, 1.5 wt. % P-SWNT/MDPE, and 5 wt. % P-SWNT/MDPE; agreed within one degree, indicating no radiation-induced damage was observed in these materials.

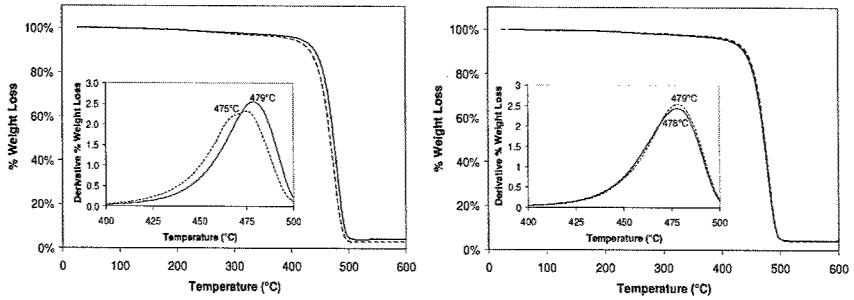


Figure 4. TGA results for the composites containing 5 wt. % f-SWNTs (dashed lines) and 5 wt. % P-SWNTs (solid lines). The left graph shows the TGA data for the composite materials prior to radiation exposure and the right graph shows the TGA data for the materials following radiation exposure. The curves for the composite containing f-SWNTs shift to higher temperatures following radiation exposure suggesting that the fluorine functional groups are removed by the radiation.

CONCLUSIONS

These initial results indicate that radiation exposure with 40MeV protons induces defluorination of the HiPCO SWNTs, as evidenced in the Raman spectra and by TGA results. The proton exposures were consistent with a long-term mission in LEO. This is significant since it would serve as a basis to explore future applications of SWNTs in space. A similar effect is not observed in the Tubes@Rice fluorinated SWNTs processed by the pulsed laser vaporization. Further experiments are planned to study the mechanism behind the defluorination. These results may provide the basis for exploring beneficial attributes of radiation on multifunctional nanotube materials.

ACKNOWLEDGEMENTS

This work has been partially supported by the NASA SBIR No. NAS1-02001 and NASA Grant No. NCC 9-114. Merlyn X. Pulikkathara is a NASA Harriett G. Jenkins Fellow and

Meisha L. Shofner is supported by a NSF Graduate Fellowship. A portion of this work was supported by the Welch Foundation Grant No. C-1494.

REFERENCES

1. S. Iijima and T. Ichihashi, *Nature* **363**, pp. 603-605, 1993.
2. D. S. Bethune, C. H. Kiang, M. S. deVries, G. Gorman, R. Savoy, J. Vasquez, and R. Beyers, *Nature* **363**, pp. 605-607, 1993.
3. E. V. Barrera, *JOM* **52**, pp. 38-42, 2000.
4. A. Thess, R. Lee, P. Nikolaev, H. Dai, P. Petit, J. Robert, C. Xu, Y. H. Lee, S. G. Kim, A. G. Rinzler, D. T. Colbert, G. E. Scuseria, D. Tomanek, J. E. Fischer, and R. E. Smalley, *Science* **273**, pp. 483-487, 1996.
5. J. Hone, M. C. Liaguno, N. M. Nemes, A. T. Johnson, J. E. Fischer, D. A. Walters, M. J. Casavant, J. Schmidt, and R. E. Smalley, *Applied Physics Letters* **77**, pp. 666-668, 2000.
6. M.-F. Yu, B. S. Files, S. Arepalli, and R. S. Ruoff, *Physical Review Letters* **84**, pp. 5552-5555, 2000.
7. M. O'Rourke, L. Clayton, D. D'Angelo, J.P. Harmon, J.Mater.Res., **17** (10) 2002.
8. V.V. Klimov, V.S. Letokhov, Physics Letters A **226** pp. 244-252 (1997).
9. F.Z. Cui, Z.H. Chen, J. Ma, G.R. Xia, Y. Zhai, Physics Letters A **295** pp. 55-59 (2002).
10. E. Salonen, A.V. Krasheninnikov, K. Nordlund, Nuclear Instruments and Method in Physics Research B **193** pp. 603-608 (2002).
11. Edited by J.W. Wilson, J. Miller, A. Konradi, and F.A.Cucinotta, *Shielding Strategies for Human Space Exploration* NASA Conference Publication 3360. (1997) pp.17-28.
12. R. Vaidyanathan, J. Walish, J. L. Lombardi, S. Kasichainula, P. Calvert, and K. C. Cooper, *JOM* **52**, pp. 34-37, 2000.
13. M.X. Pulikkathara, R. Wilkins, J. Vera, L. Fotedar, E.V. Barrera, T. Reese, H. Huff, R. Singleterry, B. Syed, "Radiation Effect Risk Analysis and Mitigation of Carbon Nanomaterials and Nanocomposites", American Nuclear Society Radiation Protection Shielding Division Topical Conference. Published on Proceeding CD, 2002.
14. A. G. Rinzler, J. Liu, H. Dai, P. Nikolaev, C. B. Huffman, F. J. Rodríguez-Macías, P. J. Boul, A. H. Lu, D. Heymann, D. T. Colbert, R. S. Lee, J. E. Fischer, A. M. Rao, P. C. Eckland, and R. E. Smalley, *Applied Physics A* **67**, pp. 29-37, 1998.
15. M. Bronikowski, P. A. Willis, D. T. Colbert, K. A. Smith, and R. E. Smalley, *Journal of Vacuum Science and Technology A* **19**, pp. 1800-1805, 2001.
16. I. W. Chiang, R. K. Saini, E. T. Mickelson, W. E. Billups, R. H. Hauge, and J. L. Margrave, "Covalent Sidewall Functionalization of Single Wall Carbon Nanotubes," presented at Applied Diamond Conference/Second Frontier Carbon Joint Conference Proceedings, 2001.
17. C. A. Cooper, D. Ravich, D. Lips, J. Mayer, and H. D. Wagner, *Composites Science and Technology* **62**, pp. 1105-1112, 2002.

Mat. Res. Soc. Symp. Proc. Vol. 740 © 2003 Materials Research Society I11.11

Damping and Stiffness Enhancement in Composite Systems with Carbon Nanotubes Films

E. A. Lass†, N. A. Koratkar‡, P. M. Ajayan†, B. Q. Wei†, and P. Keblinski†
†-Department of Materials Science and Engineering
‡-Department of Mechanical, Aerospace and Nuclear Engineering
Rensselaer Polytechnic Institute, Troy, NY 12180-3590, USA

ABSTRACT

Structural damping is an essential design parameter for many engineering applications. We demonstrate here the potential for the use of multi-walled carbon nanotube films in structural systems where vibrational energy dissipation is important. These films can provide a light weight, minimally intrusive alternative to conventional damping materials such as visco-elastic polymers. In addition, because of their multifaceted properties, damping materials utilizing carbon nanotubes are expected to be superior to traditional materials and may enhance the performance of the system by increasing structural stiffness and thermal stability.

INTRODUCTION

Carbon nanotubes (CNTs) have been shown to possess an amazing blend of mechanical properties such as high elastic modulus (~1TPa), strength (~50GPa) and low density (1.3g/cm^3) [1-5]. Due to this extraordinary combination, carbon nanotubes are being heavily researched for use as structural components in engineering systems. However the potential of augmenting damping in structural systems by using CNTs has not yet been fully explored in the literature.

Structural damping is an important aspect of many engineering applications. Traditional damping materials, being polymeric materials, perform well in terms of energy dissipation and damping, but only at low temperatures (below 60°C). Another limitation is that when damping films are integrated into composite systems, mechanical properties and structural integrity are often sacrificed [6-9]. This is due to the low modulus and strength of polymeric materials. CNTs, which possess high modulus and strength to weight ratios, along with good thermal stability, and a large surface area to volume ratio, show promise as a damping material. Minimally intrusive CNT films could potentially be seamlessly integrated into composite systems without a decrease in stiffness/strength of the host structure. The mechanical properties of the composite system may even be enhanced rather than diminished by such reinforcement due to the outstanding mechanical properties of CNTs. Also, because CNTs are thermally stable up to temperatures around 800°C, CNT-damping films may far exceed the operating temperatures of traditional polymeric materials.

EXPERIMENTAL DETAILS

Aligned multi-walled carbon nanotube (MWNT) arrays were produced on silica (SiO_2) substrates (25.4×25.4mm in size) using catalytic thermal chemical vapor deposition (CVD) of a xylene/ferrocene mixture at 800°C for a time of 15 minutes (detailed in Refs. [10, 11]). This process yielded a film of CNT with a length of ~50μm. Silica was used as a substrate because it can be readily used for the growth of aligned MWNT films as shown in the scanning electron microscopy (SEM) image shown in figure 1.



Figure 1. SEM image of aligned CVD grown CNT film.

A piezoelectric sheet was bonded to the CNT film (anchored on SiO_2 substrate) with an acrylic adhesive by the application of uniform pressure of 0.5MPa. The piezoelectric material was used because by applying a sinusoidal voltage, it provided for a convenient method of inducing a dynamic bending in the composite beam. A baseline beam was also created in a similar fashion by sandwiching a silica substrate and piezoelectric sheet together without the CNT film. The dimensions of the beams are shown in figure 2.

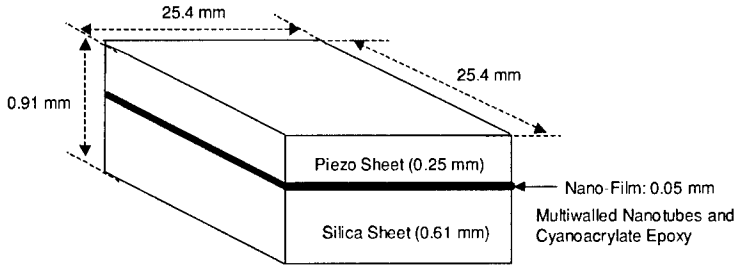


Figure 2. Schematic of sandwich test samples for damping characterization.

Both the beams were tested in the same manner. First, one end was rigidly clamped, creating a cantilever system. The dimensions of the setup were the same for both beams; cross-sectional dimensions of 25.4x0.91mm and cantilever length of 22.9mm. The piezoelectric sheet was excited by applying an alternating voltage and sweeping from low to high frequency, creating a bending moment in the beam. The response to this bending moment was measured with strain gauges mounted at the root of the beam [12]. A finite element model was developed in order to quantify the observed behavior.

RESULTS

Experimental observations and Beam Modeling

The composite beams were tested in a flat-wise bending mode by applying an alternating voltage to the piezoelectric sheet, and sweeping it from low to high frequency. Figure 3 shows the strain response of the baseline and CNT reinforced beams for an input of 50Vrms to the

piezoelectric sheet (along with finite element beam modeling calculations). It can be seen that the magnitude of the beam root strain at resonance is significantly reduced by CNT reinforcement. This qualitatively corresponds to an increase in the damping of the system. In addition, the shift in the bending mode frequency from 700Hz to 840Hz suggests an increase in composite beam stiffness.

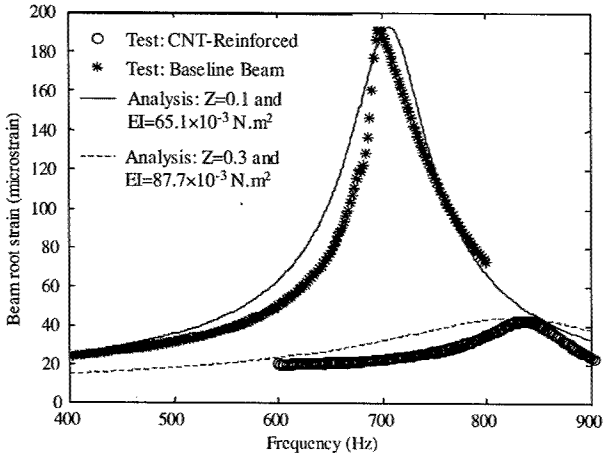


Figure 3. Experimental data of beam response and comparison to modeling results.

In order to quantify the increase in damping and stiffness observed in the experimental results, a finite element beam model was developed. The cross-sectional bending stiffness, EI, and mass per unit length, ρA were calculated from the data in table 1. From this model, the equation of motion for the beam is given as:

$$[M_b]\{\ddot{w}\}+[(1+Z_b.j).K_b]\{w\}=Q_b \tag{1}$$

where Q_b and Z_b are the piezoelectric force moment and structural damping ratio, respectively. M_b and K_b are the global mass and stiffness matrices as described in Reference 13. The beam bending strain can then be found from the solution for w, the beam response, and is found to be:

$$\varepsilon_{zz}(x) = z\frac{\partial^2 w}{\partial x^2} \tag{2}$$

where x is the longitudinal axis and z is the thickness direction of the beam. A detailed discussion of the model is developed in reference 13.

Table I. Properties of Composite Beam Materials

Sandwich Beam Components (25.4 mm × 25.4 mm)	Young's Modulus (GPa)	Thickness (μm)	Density g/cm^3
PZT-5H	69	250	7.8
Silica	131	610	2.33
Multiwalled Nanotubes that comprise the Nano-Film	1000 (data for individual tubes)	50	1.1-1.5
Adhesive Layer	3	50	0.8

The analysis of the baseline composite beam resulted in a cross-sectional bending stiffness of $65.1\times10^{-3}Nm^2$ and a mass per unit length of 0.12g/mm. A good correlation between the beam model and observed data is seen for a damping ratio (Z_b) of 0.1, where both the correct bending mode frequency (700 Hz) and strain were predicted ($\sim40\times10^{-6}$). The CNT reinforced beam analysis also showed a good correlation with the experimental data for a damping ratio of 0.3. The cross-sectional stiffness was found to be $87.7\times10^{-3}Nm^2$. The results of the model are also shown in figure 3 and compared to the experimental data. From this, it can be concluded that the CNT reinforcement increases the composite damping by 200% and the stiffness by 30% compared to the baseline beam.

Analysis of Film Microstructure

SEM was used to investigate the microstructure of the nanotube layer in the composite structure. Figure 5 reveals that the CNT film contained a network of densely-packed, cross-linked nanotube clusters. This unusual film morphology is not characteristic of CVD grown CNT arrays and is a result of the applied pressure (~0.5 MPa) during the curing of the acrylic adhesive. The connectivity of the CNTs in the film suggests that these strong interactions between the tubes are a primary source of energy dissipation when adjacent clusters are displaced relative to one another. As a consequence, the CNT reinforced film exhibits a significant increase in damping. In addition, the cross-links between tubes offer an effective method of load transfer between tubes resulting in improved beam stiffness

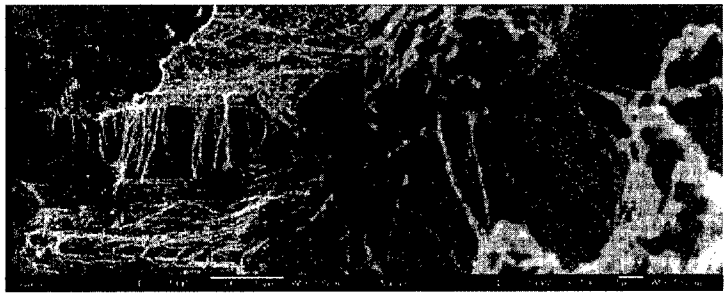


Figure 4. SEM image of cross-linked network morphology of CNT film after application of uniform pressure of 0.5 MPa.

Molecular Dynamics Simulations

Molecular dynamics simulations were conducted in order to better understand the role of inter-tube friction on the damping response. Four aligned single walled nanotubes with an inter-tube separation of 3.35Å were considered. A momentum impulse was applied along the axial direction of one tube. Figure 5 demonstrates the reduction in impulse velocity as a function of time for the system for externally applied pressures of 0GPa, 0.5GPa, and 1.0GPa. This decrease in velocity is due to energy dissipation caused by inter-tube friction. It can be seen from figure 5 that damping of the impulse is greatly enhanced as the external pressure is increased.

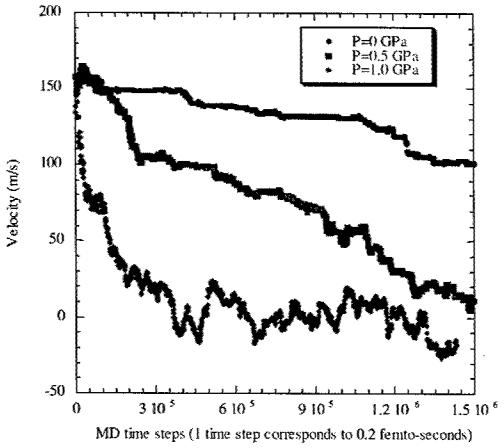


Figure 5. MD simulation showing increased damping characteristics of SWNT upon application of external pressure.

Properties Comparison with Conventional Damping Materials

Table 2 lists the properties of two commercially available damping polymers, 3M 1SD-112 (acrylic) [14] and Soundcoat Dyad-606 (polyurethane) [15], along with the properties that have been determined for the CNT damping film. The density of the damping film is similar to that of the commercial polymers. Conventional polymeric materials also degrade at higher temperatures and can only be used at temperatures below ~100°C. CNTs however, are thermally stable at temperatures as high as 800°C. The modulus of the CNT damping film is 100 times higher than the Soundcoat polymer, adding mechanical integrity to any system where it is utilized. The thickness of the CNT film was also much less that the two commercial materials.

Table II. Property Comparison with Commercial Damping Materials

Property	3M-ISD-112	Soundcoat Dyad-606	Nano-Film
Modulus at 850 Hz and room temperature	400 psi (2.75 MPa)	4.5×10^4 psi (0.3 GPa)	41.2×10^6 psi (284 GPa)
Density	0.9 gm/cm^3	1.2 gm/cm^3	1.1 gm/cm^3
Thickness	127 μm	500 μm	50 μm
Temperature Limit	65º C	70º C	~600º C
Frequency Limit	1 KHz	1 KHz	Tested up to 4 KHz

CONCLUSION

The use of carbon nanotube films in damping applications show potential for several advantages over traditional polymeric materials. The experimental data presented here shows that such a film may provide a 200% increase in damping over a baseline system. SEM analysis of the film microstructure suggests energy dissipation is a result of strong inter-tube connectivity caused by the application of pressure during sample fabrication. Finite element modeling of the composite system showed good correlation with experimental data. Molecular dynamics simulations indicated that inter-tube friction was the dominant mechanism for damping within the nanotube film. In addition to providing this energy dissipation, these films are minimally intrusive, thermally stable, light weight, and may increase the stiffness and strength of the system.

ACKNOWLEDGEMENTS

This Research Project was funded by the National Science Foundation (Division of Civil and Mechanical Systems), Award Number CMS 0210124, with Dr. Ken Chong and Dr. Oscar Dillon serving as the technical monitors.

REFERENCES

1. J.P. Lu, Phys. Rev. Lett. **79**, 1297 (1997).
2. E. Hernandez, C. Goze, P. Bernier, A. Rubio, Phys. Rev. Lett. **80**, 4502 (1998).
3. M. M. J. Treacy, T. W. Ebbesen, J. M. Gibson, Nature **381**, 678 (1996).
4. P. Poncharal, Z.L. Wang, D. Ugarte, W.A. de Heer, Science **283**, 1513 (1999).
5. M. Yu, O. Lourie, M. J. Dyer, K. Moloni, T. F. Kelley, R. S. Ruoff, Science **287**, 637(2000).
6. W. H. Liao, K. W. Wang, Journal of Sound and Vibration **207**, 319 (1997).
7. C. Brackbill, L. E. Ruhl, G. A. Lesieutre, E. C. Smith, Journal of the American Helicopter Society **45**, 34 (2000).
8. A. Baz, S. Poh, Journal of Shock and Vibration **7**, 81 (2000).
9. C. L. Davis, G. A. Lesieutre, Journal of Sound and Vibration **232**, 601 (2000).
10. Z. J. Zhang, B. Q. Wei, G. Ramanath, P. M. Ajayan, Appl. Phys. Lett. **77**, 3764 (2000).
11. B. Q. Wei, Z. J. Zhang, G. Ramanath, P. M. Ajayan, Appl. Phys. Lett. **77**, 2985 (2000).
12. B. Q. Wei, N. Koratkar, P. M. Ajayan, "Non-intrusive damping films featuring carbon nanotubes", Proceedings of the 43rd AIAA/ASME/ASCE/AHS/ASC Structures, Structural Dynamics, and Materials Conference, Denver, Colorado, April 22-25, 2002.
13. N. Koratkar, I. Chopra, AIAA Journal **38**, 1113 (2000).
14. 3M Bonding Systems Division, "Material Data Sheets", 3M Center, Building 220-7E-01, St. Paul, MN, 55144-1000, February 1999.
15. J. M. Biggerstaff, J. B. Kosmatka, J. Comp. Mater. **32**, 21 (1998).

Mat. Res. Soc. Symp. Proc. Vol. 740 © 2003 Materials Research Society I11.12

In-situ preparation of polymer-coated zirconia nanoparticles by decomposition of zirconium-tert-butoxide

Michael Schallehn, Volker Lorenzen, Johannes Seydel* and Horst Hahn*
SusTech GmbH&Co. KG, Petersenstrasse 20, 64287 Darmstadt, Germany
*Institute of Materials Science, Darmstadt University of Technology, Petersenstrasse 23, 64287 Darmstadt, Germany

Abstract

Nanocrystalline zirconia particles coated with polymers have been prepared by a two step Chemical Vapor Synthesis process using a hot wall reactor to synthesize the nanocrystalline ceramic core and a subsequent RF plasma reactor for the polymer coating. The polymer coating is built up of organic byproducts of the pyrolysis of the zirconia precursor. By using continuous and pulsed plasma deposition and variation of the plasma parameters, such as RF power, period and duty-cycle, the structure and thickness of the polymer coating can be influenced. Typical particle radii are in the range of 3 to 4 nm with radii of the ceramic core in the range of 2 nm and a coating thickness in the range of 1 to 2 nm. The powders have been characterized by FT-IR, XRD, BET and HRTEM. Consequences for the dispersibility are reported.

Introduction

Nanocrystalline powders are characterized by a very large surface area (of the order of several hundred m^2/g) and surface-to-volume ratio (of the order of 10^8 / m). Therefore, it can be expected that coatings on these ultrafine particles substantially change their characteristics such as chemical reactivity, or catalytic, optical, magnetic and electronic properties[1].

A special field are polymer coated nanocrystalline ceramic particles. The polymer coating could have the function as a spacer to avoid direct contact of the nanoscaled ceramic particles preventing agglomeration[2]. This can have consequences for the dispersibility of treated and untreated nanoparticles in aequous and organic solvents. Furthermore, this preserves special particle properties even after the fabrication of a bulk material, e.g. superparamagnetism in soft magnets[2]. The use of polymer coated nanocrystalline particles as fillers in polymer nanocomposites could be twofold: 1. due to the lack of scattering of visible light the nanocomposite can be transparent even at high volume fraction of nanoparticles; 2. the improvement of the ceramic-polymer interface could result in better mechanical properties.

In this paper the in-situ formation of a polymershell on oxide nanoparticles synthesized by Chemical Vapor Synthesis (CVS) by using a pulsed or continuous plasma is described. The byproducts of the precursor are used for the polymerization. A second route to obtain polymer coatings by using a monomer such as ethene introduced additionally into the plasma reactor will be described in a separate paper[3].

Experimental

The powders are prepared by a modular CVS reactor (Fig. 1), which is similar to assemblies described earlier[3, 4]. It is equipped with a second reaction zone (RF plasma reactor), where the polymer coating takes place. With the first reaction zone, the hot wall reactor, it is

possible to prepare oxide nanoparticles of small grain size (of the order of a few nanometers), narrow size distribution and low degree of agglomeration[4]. Argon gas is bubbled through a container with the zirconia precursor (zirconium-tert-butoxide, ZTB, $Zr(OC_4H_9)_4$) controlled by a MKS thermal mass flow controller (50 sccm). The bubbler is held at a temperature of 75°C by means of a water bath. As the gas flow through the bubbler is not sufficient for maintaining the process pressure of 10 hPa an additional argon gas flow is used (1000 sccm). The first reaction zone consists of an alumina tube with an inner diameter of 19 mm heated by a furnace to 1100°C for the production of zirconia nanoparticles by pyrolysis of ZTB. A mixed flux of argon, organic byproducts of the pyrolysis of ZTB and zirconia nanoparticles enters the plasma reactor which consists of a quartz tube with an inner diameter of 34 mm. The electric field generating the plasma is supplied by two electrodes. A stainless steel rod is used as power electrode in the center of the tube. A flexible copper tape is wrapped several times around the tube acting as mass electrode. The high frequency alternating electric field (13.56 MHz) is generated by a RF-Generator. In addition a so called matchbox is used for minimizing the power reflected by the plasma. The pulses are generated by an arbitrary function generator which is connected to the RF-Generator. The ultrafine particles act as seeds for the heterogeneous formation of the polymer films. The coated nanoparticles are separated from the gas stream by thermophoresis due to a thermal gradient between the hot quartz lamps and the water cooled wall of the collecting zone. The pumping unit consists of a sliding vane pump.

Nanoparticles are collected at two different positions in the system. Most powder is deposited in the collecting zone after both reaction zones (position **2**). Due to the temperature gradient between the hot wall and the plasma reactor, a small amount of zirconia particles is deposited in the components between the hotwall and the RF plasma reactor (position **1**). These powders, which had no contact with the plasma were used as a reference for the modified powders. The powders collected have a very low tap density similar to aerogels[5]. The production rate of the laboratory reactor is about 0.5 to 1g per hour at a yield of about 40%. Most probably the yield is limited by the collection efficiency of the thermophoretic collector.

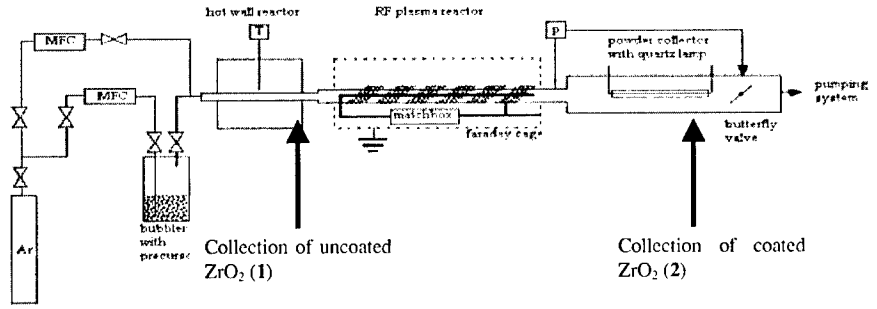


Figure 1: CVS apparatus for the production of polymer-coated nanopowders. The arrows indicate the positions 1 and 2 where uncoated and coated powders were collected, respectively.

The powders were examined by infra-red spectroscopy (Perkin-Elmer 1750) in the range between 4000-400 cm^{-1} and by X-ray diffraction (STOE STADI P) using Ni-filtered Cu-Kα radiation. The specific surface area of the powder was measured by nitrogen absorption with a

Quantachrom Autosorb-3B instrument. High resolution transmission electron microscopy (HRTEM) micrographs were obtained using a Philips CM20 microscope operated at 200 kV.

Results and Discussion

Metal oxide nanopowders are usually prepared using CVS by decomposition of a metal alkoxide precursor in a mixture of an inert gas and oxygen,[5] where the oxygen is used to reduce the amount of carbonaceous impurities in the product. However, it is evident that for the deposition of polymers in the plasma reactor free oxygen which would oxidize the monomer has to be absent. Therefore, an additional oxygen gas flow cannot be used to prepare the zirconia nanoparticles. Fortunately, stochiometric ZrO_2 is can be prepared by pyrolysis of zirconium-t-butoxide ($Zr(OC_4H_9)_4$) in the hot wall reactor according to the reaction.

$$Zr(OC_4H_9)_4) \rightarrow ZrO_2 + \text{2-butanol} + \text{butene} + \text{water} + \text{other byproducts.} \quad (1)$$

In our new approach the byproducts, such as butanol and especially butene are used as monomers for the deposition of the polymer coating. Uncoated zirconia particles were collected at position **1** in the reactor and plasma treated zirconia at position **2** as indicated in figure 1. Different conditions were employed in the plasma zone: continuous plasma, pulsed plasma with different frequencies and duty cycles. Table 1 summarizes the different conditions. The values of the average power are calculated by equation (2), with $t_{on}/(t_{on} + t_{off})$ corresponding to the duty cycle [6].

$$P_{av} = P_P * \frac{t_{on}}{(t_{on} + t_{off})} \quad (2)$$

X-ray diffractograms of the powders (Fig. 2) show the formation of crystalline ZrO_2 in the tetragonal phase. However, due to the line broadening, it is not possible to distinguish it definitely from the cubic phase at these small grain sizes. The coated powders collected at position **2** after passing the plasma zone have a yellow colour which is typical for polymer coated nanopowders[3]. The yellow tone gets more and more intense with increasing average power. Powders prepared using a continuous plasma (A) are dark yellow and the particles coated under conditions C are slightly yellow coloured. The zirconia powders collected at position **1** is white.

Table I: Plasma parameters of the experiments

	Peak Power [W]	Pulse on [ms]	Pulse off [ms]	Period [ms]	Duty Cycle [%]	Average Power [W]
A (cont.)	47	-	-	-	-	47
B (pulsed)	105	10	30	40	25	26,3
C (pulsed)	99	1	39	40	2,5	2,5

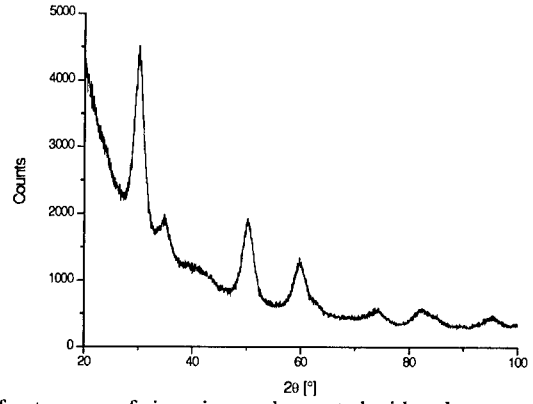


Figure 2: XRD diffractrogram of zirconia powder coated with polymer

Zirconia nanoparticles collected from position **2** from experiments without any plasma do not show any absorption bands in the ranges from 1350-1500 cm^{-1} and 2850-3000 cm^{-1}. Zirconia nanoparticles from position **1** from the plasma experiments (condition A, B, C) are almost identical to that pure zirconia. There are small differences in the range from 1350-1500 cm^{-1} due to small amounts of organic adsorbants (not shown). Figure 3 shows IR spectra of different zirconia nanopowders coated under conditions A, B, C and collected at position **2**. It is clearly visible that new absorption bands develop in the plasma zone which get more and more intense with increasing average plasma power. These bands can be attributed to C-H stretching vibrations (2956 cm^{-1}, 2932 cm^{-1} and 2870 cm^{-1}) and to CH_2 and CH_3 groups bending vibrations (1456 cm^{-1} and 1378 cm^{-1}), which are typical for plasma polymers out of hydrocarbon monomers [7]. The adsorption bands at 1576 cm^{-1} and at 1626 cm^{-1} originate from carboxylate groups and physisorbed water, respectively[8], and are found in spectra of other ceramic nanoparticles prepared under these conditions, too [3].

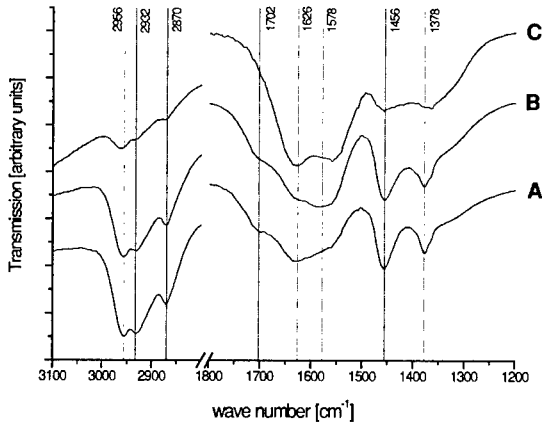


Figure 3: FTIR spectra of plasma treated zirconia powders collected at position **2** (coated) prepared under A) continuous plasma B) pulsed plasma 10/30 and C) pulsed plasma 1/39

The shoulder at 1702 cm^{-1} in the spectra A and B is due to carbonyl stretching vibrations. The IR spectra clearly show that the amount of polymer produced next to the zirconia nanoparticles increases with increasing average plasma power.

The evidence of the coating of the nanoparticles is gained from the HRTEM micrographs in Figure 4. The micrographs are taken from two powders collected at the positions **1** (left) and **2** (right) prepared under the conditions A. In the left micrograph crystalline, non-spherical particles with lattice fringes up to the particles surfaces can be detected. The crystalline particles in the right micrograph are embedded in an amorphous matrix, which is interpreted to be the polymer detected in the IR-spectrum. Again, all particles collected at position **1** result in similar TEM-micrographs even if the experiment was performed under conditions B or C. However, the micrographs of particles from position **2** differ from the right micrograph shown here. Particles prepared under condition B have only very thin amorphous layers (micrograph not shown). On micrographs of powder from the condition C experiment no amorphous areas were detected (not shown), although some polymer bands are visible in the IR-spectrum of these particles.

Table 2 gives an overview of different grain sizes and particle sizes calculated from XRD line broadening (Scherrer formula) and nitrogen adsorption (BET), respectively. The particle sizes at position **1** are in the same order of the grain sizes derived from the XRD. They are all smaller than the particles at position **2**.

The plasma treatment changes the macroscopic properties of the nanoparticles such as dispersibility and wetting behaviour. The zirconia from position **1** is dispersable in acidic water (pH-value 2) to 80 nm (not shown). However, the plasma treated powder of the experiments A and B is not wettable in water, but in acetone or ethanol. Unfortunatly, the dispersibility is lost. The powder prepared under the C-conditions is dispersable in acidic water, but only to 140 nm. A continuous plasma (A) forms thick polymer coatings around the zirconia nanoparticles which let the particles loose their hydrophilic character. Under pulsed conditions with a medium average power (B) a thin (nearly invisible in TEM micrographs) polymer shell is deposited on the particles. However, this coating is sufficient to change the dispersibility of the particles completely. The particles prepared under conditions C show nearly no differences in the TEM micrographs and dispersibility compared to untreated zirconia, although the colour of the particles and the IR spectra indicates small amounts of polymer.

Table II: Grain size (diameter) of zirconia and polymer coated zirconia determined from XRD line broadening and nitrogen adsorption (BET) for the different experimental conditions

	C (pulsed plasma)	B (pulsed plasma)	A (continuous plasma)
Grain Size (XRD) [nm]	3,8	3,9	3,9
Particle Size Position 1 (BET) [nm]	4,5	4,8	4,1
Particle Size Position 2 (BET) [nm]	4,7	6,1	4,8

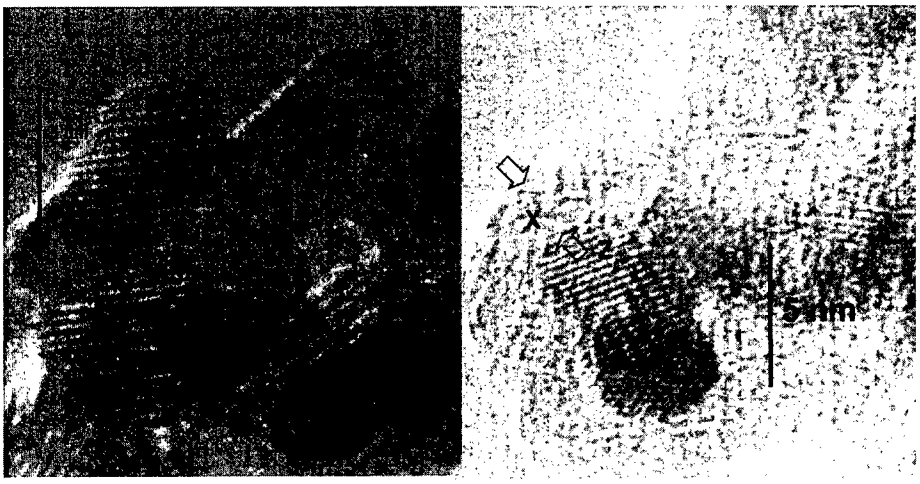


Figure 4: Transmission electron micrographs of powders collected at position **1** (left) and **2** (right) prepared under conditions A. The markers indicate a shell structure X around a core Z.

Conclusions

From the combined results of FTIR, XRD, BET and TEM experiments it is concluded that the plasma polymerization of the pyrolysis byproducts of the zirconia precursor leads to a polymer coating of the zirconia nanoparticles without the addition of any monomer. The thickness of the coatings depends on the plasma parameters and decreases with decreasing average power, adjustable by using continuous and pulsed plasmas with variable duty cycles.

This result has important consequences for the functionalization of ceramic nanoparticles. If additional monomers with functional groups are used in the plasma polymerization , the role of the byproducts of the monomer pyrolysis, forming a polymer shell itself, has to be considered.

Acknowledgement

The authors thank the Center of Materials Characterization for the XRD of the zirconia. The financial support of the Deutsche Forschungsgemeinschaft is gratefully acknowledged.

References

[1] Q. H. Powell, T. T. Kodas, and B. M. Anderson, *Chem. Vap. Deposition* **1996**, *2*, 179
[2] D. Vollath, and D. V. Szabo, J. Fuchs, *Nanostruct. Mater.* **1999**, *12*, 433
[3] M. Schallehn, M. Winterer, T. Weirich, U. Keiderling, H. Hahn, *Chem. Vap. Deposition* **2003**, 9, No. 1
[4] V. Srdic, M. Winterer, A. Möller, G. Miehe, H. Hahn, *J. Am. Ceram. Soc.*, **2001** *84*, 2771
[5] M. Winterer, *Nanocrystalline Ceramics – Synthesis and Structure*, Springer Heidelberg **2002**,
[6] K. Nakajima, A. T. Bell, M. Shen, *J. Polym. Sci., Polym. Chem. Ed.* **1979**, 23, 2627
[7] M. Shen, A. T. Bell, A Review of Recent Advances in Plasma Polymerization, American Chemical Society, *ACS symposium series* **1979**, *108*, 1
[8] R. O. Kagel, J. Phys. Chem. **1967**, *71*, 844

Poster Session

Mat. Res. Soc. Symp. Proc. Vol. 740 © 2003 Materials Research Society I12.1

Simulation of Carbon Nanotube Pull-out When Bonded to a Polymer Matrix

S. J. V. Frankland[1] and V. M. Harik[2]
[1]ICASE, M/S 132C, NASA Langley Research Center, Hampton, VA 23681-2199
[2]Swales Aerospace, M/S 186A, NASA Langley Research Center, Hampton, VA 23681-2199

ABSTRACT

A carbon nanotube pulling through a polyethylene matrix was simulated using molecular dynamics. The interfacial sliding was characterized in terms of a nanoscale friction model, which is parametrized from the molecular dynamics simulation, and involves determining the critical pull-out force on the nanotube and the effective viscosity at the nanotube/polymer interface. Comparison was made of the pull-out behavior of non-bonded and functionalized nanotube composites. Chemical bonds between the polymer and the nanotube increased the critical pull-out force, the resistance to interfacial sliding, and the interfacial viscosity.

INTRODUCTION

In polymer-nanotube composites, the strength of the interface between the polymer and the nanotube (NT) may be enhanced by chemically bonding the NTs to the polymer. Chemical functionalization of NTs remains a challenge [1, 2], but in some polymer-NT composites, where significant load transfer between the polymer and the nanotube has been observed, chemical bonding with the NT may occur [3].

In traditional fiber-reinforced composites, the fiber-matrix interfacial shear strength is often characterized by fiber pull-out experiments [4]. Analogous nanoscale pull-out experiments have been carried out with atomic force microscopy for the sliding of NTs in multi-walled NTs [5] and in bundles of single-walled NTs [6]. A simulated pull-through test has also been devised for polymer-NT composites via molecular dynamics (MD) to determine the interfacial shear strength while a force is applied to the NT. These simulations have indicated an increase in the interfacial shear strength with the addition of chemical bonds between the polymer and a NT [7]. Furthermore, the simulations have been extended to study the interfacial sliding of the NT during pull-out in non-bonded composites, and to characterize the effective interfacial viscosity due to the van der Waals interactions of the polymer and the NT [8, 9].

In this work, the interfacial sliding during pull-out of a NT chemically bonded to a crystalline polymer matrix was modeled with MD simulations. The objective was to show some of the mechanisms which may serve to enhance its ability to transfer mechanical load within the composite. First, a description of the composite structure will be given with details of the MD simulations. Then stages encountered by the NT during interfacial sliding will be analyzed. Finally, the sliding velocity will be interpreted by using the interfacial viscosity model [8, 9].

MOLECULAR DYNAMICS SIMULATION

The simulated polymer-NT composite consisted of a (10,10) carbon nanotube embedded in a crystalline polyethylene (PE) matrix (Figure 1a). The NT was chemically bonded at three

locations to one of the nearby polymer chains (Figure 1b). Each attachment included a direct bond to the NT, two CH_2 groups and a direct bond to the chain (Figure 1d). In the MD simulations, all the chemical bonding, including the chemical bonds between the NT and the PE, was represented with the same hydrocarbon potential [10]. The non-bonded interactions were represented with the Lennard-Jones potential [11]. The system was replicated across periodic boundaries in each of the 3-dimensions, making the NT and the PE chains infinitely long. This composite was similar to the crystalline polyethylene used in previous work [7], and the detailed chemical description is kept for consistency.

To simulate the interfacial sliding of the NT, force was added to each atom of the NT in the axial direction. As the system was periodic, the NT moved through the polymer into the next periodic image when it began to slide. The applied force was incremented over time. The simulation is run for about 210,000 MD steps of 0.05 fs each. The size of the force increment was increased by a factor of 2.5 at 105,000 steps. The displacements and velocities of the NT, the attached chains, and the nearby chains were monitored under increasing force. The attached chain exhibited a breakage before the initial force loading due to reactivity included in the hydrocarbon potential, and retained that configuration throughout the rest of the simulation (Figure 1c). The initial configuration also included attachments to a second chain on the opposite side of the NT, but this attached chain did not survive past 40,000 steps. Only a third of this chain survived the initial NT pull-out force intact. This incident had marginal effect of the investigated interfacial sliding after the onset of pull-out; that sliding was dominated by the friction along the entire surface area and the chemical bonding of the first chain.

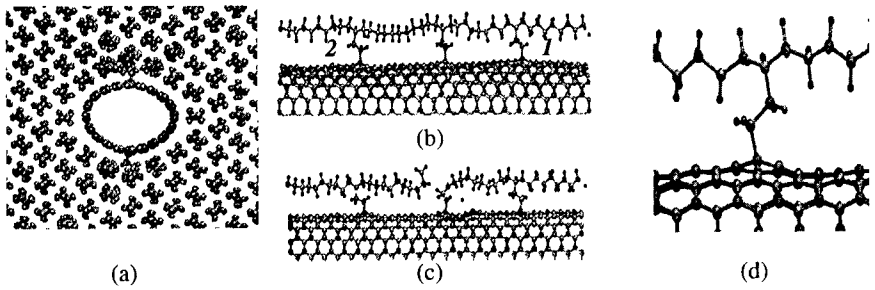


Figure 1. The structure of the functionalized polymer-nanotube composite (a) cross-sectional view, (b) side view of the starting structure with links 1 and 2 and (c) the actual structure of NT and the attached chain with one breakage (d) close-up of an attachment.

RESULTS AND DISCUSSION

Interfacial Sliding

The velocity profile of the NT under load is plotted in Figure 2. Several stages were observed in the interfacial sliding of the NT through this composite. However, the interfacial sliding of the NT in this composite is significantly different from that observed previously for the non-bonded PE/NT composite [8, 9]. Initially, the NT experienced thermal vibrations and

interacts with the adjacent polymer chains in equilibrium at 300 K. At 0.17 nN enough force was exerted on the NT for interfacial sliding to begin. This initial pull-out force was higher than that observed for the onset of NT sliding in a non-bonded composite. The next difference between the composites occurred when the NT velocity peaked just past 20,000 steps and then decreased again almost to zero. At this point, the NT was under the constraint of the chemical bonds attaching it to the chain. Increasing the force on the NT beyond this point caused it to drift about 0.5 A as shown by the NT displacement in Figure 3. At about 57,000 steps, the NT began to accelerate on average until about 141,000 steps. Although the size of the force increment was increased in this range, the relation of force to velocity maintained the same slope (Figure 4).

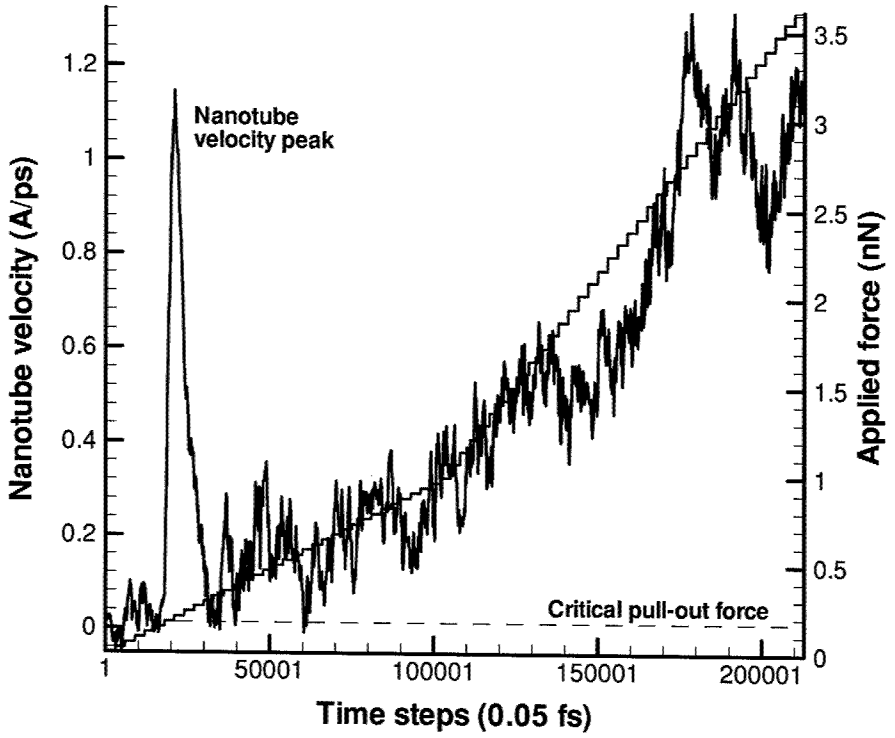


FIGURE 2. *Velocity of the center of mass of a carbon NT during the simulated pull-out.*

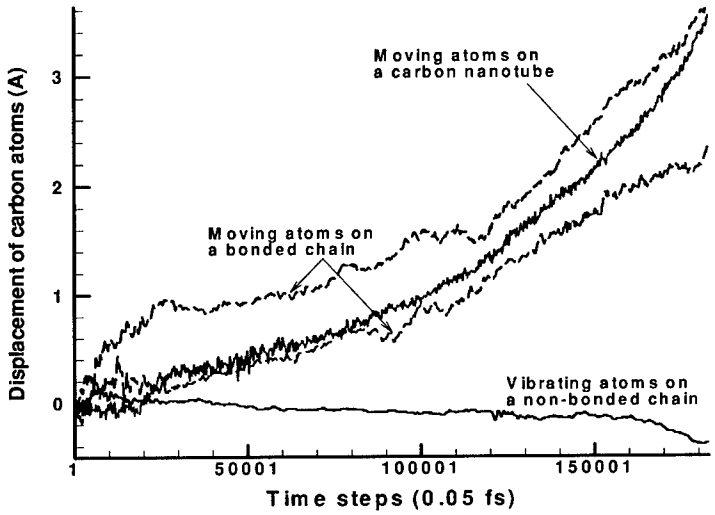


FIGURE 3. *Displacement of individual carbon atoms of the NT during the simulated pull-out.*

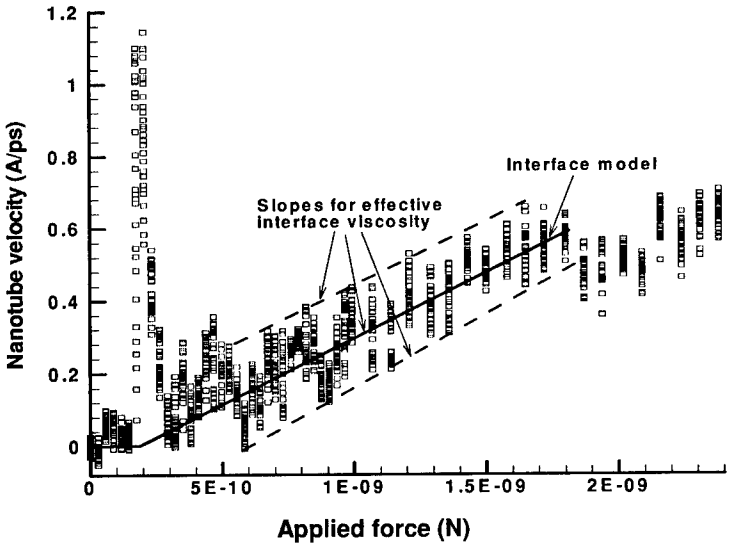


FIGURE 4. *The force-velocity relation for the simulated NT pull-out.*

In this range, one of the links (Link 1 in Figure (1b)) of the chain engaged part of the chain nearby to move with the NT. The chain was loose enough that the part near Link 1 moved with the NT while the rest of chain progressively slowed down in the vicinity of Link 2. Link 2 was moving with the NT, but it was loose enough that it did not engage its part of the chain into motion. The linkages and the chains had significantly more degrees of freedom and could move differently relative to one another and the NT. A transition took place at about 141,000 steps, where Link 2 broke releasing its part of the chain. This transition was followed by two peaks in NT velocity (Figure 2) indicating continued acceleration of the NT and the attached chain.

In Figure 3, the displacement of individual carbon atoms associated with the sliding NT, the bonded chain and a non-bonded chain are shown as the applied force increased up to 3 nN. The bonded polymer chain moved along with the NT pulled by force, while a non-bonded chain vibrated around its initial position without significant motion in the direction of NT axis.

Interfacial viscosity

The NT pull-out process, in general, and interfacial sliding, in particular, can be described by an interfacial friction model [9], which is analogous to a Bingham-type model for viscoplastic failure of the interface including the concept of interfacial viscosity [12,13]. The model describes the dependence of the average applied force, $\langle f \rangle_{pull}$, on the average NT velocity, $\langle V_z \rangle$, in the z-direction of the NT axis:

(1) $$\langle f \rangle_{pull} = f_0 + \chi_{eff} \langle V_z \rangle,$$

where f_0 is the critical pull-out force and χ_{eff} is the effective viscosity coefficient, which can be obtained from the MD simulation. The effective viscosity, χ_{eff}, of the NT/polymer interface is defined as a proportionality constant in the force-velocity relation that characterizes the interfacial momentum transfer. NT velocity variations shown in Figure 2 are plotted in Figure 4 for every incremental force loading. Once the critical pull-out force, f_0, at 0.17 nN was reached, the force-velocity dependence could be approximated by a linear relation (the solid line). The inverse of the slope of the resulting line is the coefficient χ_{eff}, which is 2.3±0.2 (nN ps)/A. This slope can be estimated from dashed lines like those shown in Figure 4, which bound the NT velocity variations during NT sliding.

The average applied force, $\langle f \rangle_{pull}$, in equation (1) is related to the average shear stress, $\langle \tau \rangle$, for sliding interactions by the force balance: $\langle \tau \rangle \approx \langle f \rangle_{pull} / A_i$, where A_i is the interfacial area between the NT and polymer. During the NT pull-out, the applied force is balanced by the interfacial friction characterized by the effective viscosity, μ_{eff}, and the induced shear stress, $\langle \tau \rangle$. The effective viscosity coefficient, χ_{eff}, is related to the effective viscosity μ_{eff} via

(2) $$\mu_{eff} = \frac{\chi_{eff} \bar{h}_{vdW}}{A_i},$$

where $\bar{h}_{vdW}$ is the van der Waals separation between the stationary polymer and the sliding NT. Therefore, the effective viscosity, μ_{eff}, is 0.27 cP, which is 50% higher than that of the non-bonded NT composite, 0.18 cP [8, 9].

CONCLUDING REMARKS

The interfacial sliding of a carbon nanotube (NT) chemically bonded to a local chain in a polymer matrix is simulated with molecular dynamics (MD) and the results fit an interfacial friction model for NT pull-out. The interfacial sliding in this composite differs from a non-bonded composite in at least two major ways. First, the NT is observed to be constrained by the chemical linkages. Second, as the linkages are flexible, they engage separately in motion with the NT at different times and force loadings. These differences result in higher interfacial shear strengths and higher interfacial viscosities than in the non-bonded composite, yielding qualitative information for the design of NT-reinforced polymer composites.

ACKNOWLEDGMENT

This research was supported by National Aeronautics and Space Administration under NASA Contract No. NAS1-97046 while S. J. V. Frankland was at ICASE, NASA Langley Research Center, Hampton, VA. V. M. Harik was partially supported by the NASA URETI for Bio-inspired Nanostructured Multifunctional Materials (award No. NCC-1-02037). The molecular dynamics simulations were carried out with DL-POLY which is a package of molecular simulations subroutines written by W. Smith and T. R. Forester, copyright The Council for the Central Laboratory of the Research Councils, Daresbury Laboratory at Daresbury, Nr. Warrington, England, UK, 1996.

REFERENCES

1. P. J. Boul, J. Liu, E. T. Mickelson, C. B. Huffman, L. M. Ericson, I. W. Chiang, K. A. Smith, D. T. Colbert, R. H. Hauge, J. L. Margrave, and R.E. Smalley, *Chem. Phys. Lett.* **310,** 367 (1999).
2. Y. Chen, R. C. Haddon, S. Fang, A.M. Rao, P. C. Eklund, W. H. Lee, E. C. Dickey, E. A. Grulke, J. C. Pendergrass, A. Chavan, B. E. Haley, and R. E. Smalley, *J. Mat. Res.* **13**, 2423 (1998).
3. H. D. Wagner, O. Lourie, Y. Feldman, and R. Tenne, *Appl. Phys. Lett.* **72**, 188 (1998).
4. V. T. Bechtel and N. R. Sottos, *Comp. Sci & Techn.* **58,** 1727 (1998).
5. M. F. Yu, B. I. Yakobson, and R. S. Ruoff, *J. Phys. Chem. B* **104**, 8764 (2000).
6. M. F. Yu, B. S. Files, S. Arepalli and R. S. Ruoff, *Phys. Rev. Lett.* **84,** 5552 (2000).
7. S. J. V. Frankland, A. Caglar, D. W. Brenner, M. Griebel, *J. Phys. Chem. B* **106**, 3046 (2002).
8. S. J. V. Frankland, V. M. Harik, *Mat. Res. Soc. Symp. Proc.* **733** E. T6.2.1 (2002).
9. S. J. V. Frankland, V. M. Harik, *Surf. Sci. Lett.* (2003), in press.
10. D. W. Brenner, O. A. Shenderova, J. A. Harrison, S. J. Stuart, B. Ni, and S. B. Sinnott, *J. Phys C: Condensed Matter* **14,** 783 (2002).
11. M. P. Allen and D. J. Tildesley, *Computer Simulation of Liquids*, (Clarendon Press, Oxford, 1987).
12. V. M. Harik, *Experimental and Theoretical Studies of Interfacial Effects in Multiphase Media*, Ph.D. Thesis, University of Delaware, Newark, DE, 1997.
13. V. M. Harik and R. A. Cairncross, *Mech. Mater.* **32**, 807 (2000).

Mat. Res. Soc. Symp. Proc. Vol. 740 © 2003 Materials Research Society I12.3

A Study of Hydrogen Adsorption in Pretreated Nanocarbon

Sang Moon Lee*, Satoshi Ohshima, Kunio Uchida and Motoo Yumura
*Japan Fine Ceramics Center, AIST Tsukuba Central 5, Tsukuba, Ibaraki 305–8565, Japan
Nanostructured Materials Team, Research Center for Advanced Carbon Materials, AIST Tsukuba Central 5, Tsukuba, Ibaraki 305–8565, Japan

ABSTRACT

A thermal treatment was applied with CO_2 and air for the development of a porous structure. Adsorption isotherms of nitrogen were measured on well-characterized Ni-C nanoparticles. The thermal treatment with CO_2 increased the total surface area and micropore volume. In addition, the thermal treatment with CO_2 increased the hydrogen adsorption.

INTRODUCTION

In recent years, the preparation of new materials, such as carbon nanotubes[1], carbon nanoparticles[2], and nanofibers[3] has been receiving much attention. These carbon nanomaterials are of interest from scientific and technological points of view, and they are expected to hold a great potential for application in various fields. In particular, the reversible storage of hydrogen on carbon nanotubes and nanofiber has been studied extensively[4-6]. Moreover, for adsorption utilization, opening of the potential adsorption space of nanotubes has been studied[7-8]. However, there has not been a study of gas adsorption on nanoparticles. Therefore, we investigated the pore structure, which plays an essential role in gas adsorption, as well as the properties of hydrogen adsorption and the surface properties of Ni-C nanoparticles. Ni-C nanoparticles with a diameter of 5-20nm were synthesized by the arc-discharge method. The particles were stable under the atmosphere because they were surrounded with a graphite sheet and amorphous carbon. Because Ni-C nanoparticles are nearly nonporous, the thermal treatment was applied with CO_2 and air in order to develop a porous structure. After that, the pore structure parameters of Ni-C nanoparticles before and after thermal treatment were investigated by high-resolution N_2 adsorption measurement at 77K. In addition, the surface properties of Ni-C nanoparticles were investigated by X-ray Photoelectron Spectroscopy (XPS). Hydrogen adsorption studies were performed using a gravimetric method in which weight changes in samples with gas adsorption were measured using a balance.

EXPERIMENTAL

Ni-C particles were synthesized by the arc-discharge method. Ni-C nanoparticles have a diameter of 5-20nm. Thermal treatment was respectively performed by CO_2 and air for development of a porous structure. Ni-C nanoparticles were heated in a CO_2 flow of 200mL/min at 1173K for 15min using a tubular furnace and in air atmosphere at 623K for 15min using a box furnace. Prior to the thermal treatment, TGA analysis of Ni-C nanoparticles was carried out to determine the temperature of thermal treatment in CO_2 and air, respectively. The micropore structures were determined by adsorption of N_2 at 77K using volumetric equipment (Quantachrome AS-1-MP) after preevacuation at 573K and 10^{-4} Pa for 24hr. IUPAC recommends the classification of pores according to pore width(w): micropores (w<2nm), mesopores (2<w<50nm), and macropores (w> 50nm). The micropore structural parameters were obtained form a high-resolution α_s-plot[9] using the standard adsorption data of highly crystalline nonporous carbon black (Mitsubishi 4040B). X-ray photoelectron spectroscopy (XPS) was used to determine the oxygen and nickel content on the surface of Ni-C nanoparticles. XPS spectra were measured using a PHI ESCA model 5800 (Physical Electronics Co.). The measurements were performed with Al Kα under a vacuum pressure of <10-6 Pa at room temperature. The power of the monochromatized X-ray source was 100W.

Hydrogen adsorption studies were performed using a gravimetric method in which weight changes in samples with gas adsorption were measured using a balance. The high-pressure hydrogen adsorption isotherm was measured at 298K using a magnetic suspension balance (Mettler AT 261, resolution 0.01mg). High-purity hydrogen gas (99.99999%) was used after purification with a liquid nitrogen trap. The pretreatment prior to the adsorption measurement was performed under a vacuum (10^{-4} kPa) and a temperature of 573K for 2hr.

DISCUSSION

To predict the temperature of the thermal treatment, TGA analysis of Ni-C nanoparticles was carried out in air and CO_2. Figure 1 shows the TGA results of Ni-C nanoparticles. When air was used, the weight decreased sharply at around 818K. In a CO_2 atmosphere, however, the weight decreased at a much slower rate, and no significant reaction was observed below 1000K. Considering the TGA results in air and CO_2, thermal treatment was carried out at a temperature over 818K for air oxidation and 1173K for CO_2 oxidation.

The adsorption isotherms of N_2 at 77K for Ni-C nanoparticles, as-received and thermal-treated in air and CO_2, are given in Figure 2. Ni-C nanoparticles exhibit an isotherm of type II according to IUPAC classification without hysteresis. The Ni-C2 sample exhibits an isotherm

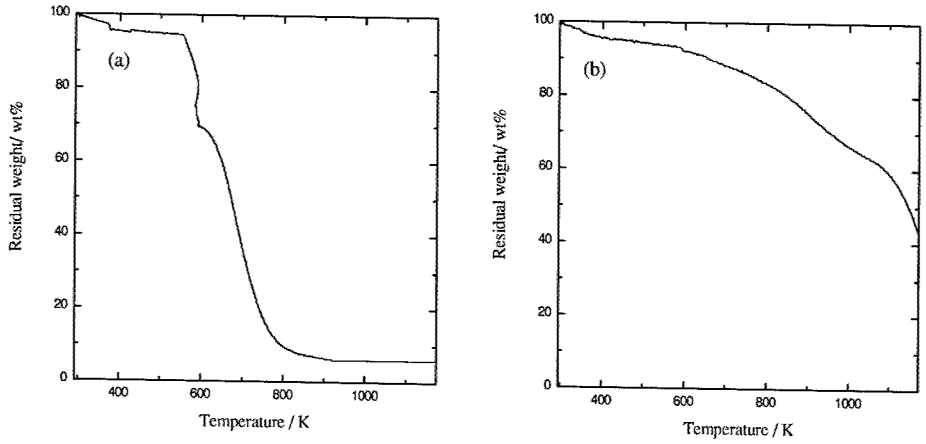


Figure 1. The TGA results of Ni-C nanoparticles: (a) in air, (b) in CO_2.

with a relatively high plateau. The high uptake in the adsorption isotherm at a relatively low pressure indicates the presence of micropores. The adsorption isotherms were analyzed with the subtracting pore effect (SPE) for a high-resolution α_s-plot. The α_s-plot on highly crystalline nonporous carbon black (Mitsubishi 4040B) was used as a standard isotherm. The pore structure parameters estimated by SPE are summarized in Table 1. The thermal treatment with air and CO_2 is accompanied with a substantial increase of the total surface area. In addition, the number of micropores increased significantly after the thermal treatment. Thus, the micropore volume of the Ni-C nanoparticle after oxidation in CO_2 at 1173K increased 2.7 times. The mesopore volume, V_{me}, estimated as the difference between the total pore (the volume filled at P/P_0=0.98) and micropore volume, is also given in Table 1. The mesopore volume increased after the thermal treatment. The mesopore volume ratio of Ni-C after the thermal treatment in air at 623K was much greater than that of Ni-C after thermal treatment in CO_2 at 1173K.

The surface chemical changes of Ni-C nanoparticles after the thermal treatment were examined by XPS. Figure 3 (a) shows that the XPS spectral change of the C1s peak coincides with that of graphitic carbon (284.6eV). All samples show a sharp graphitic carbon peak and a broad peak at 287-290eV. Figure 3 (b) shows the Ni2p XPS spectra of Ni-C nanoparticles. The as-received Ni-C nanoparticle (Ni-C0) has no Ni2p XPS peak, although the TGA result showed 6% of the residual amount. These results suggest that the Ni in the nanoparticle is coated with a graphene sheet. However, thermal-treated Ni-C nanoparticles (Ni-C1, Ni-C2) show typical Ni2p peaks of

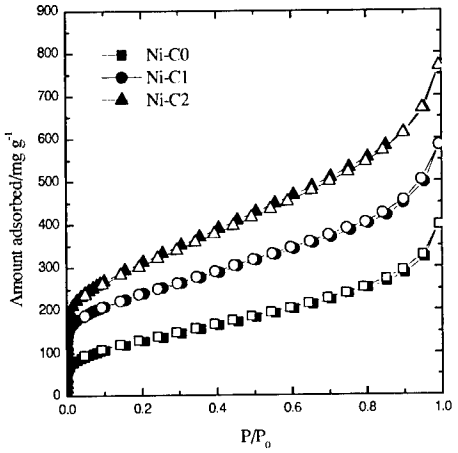


Figure 2. N_2 adsorption isotherms on as-received and thermal-treated Ni-C nanoparticles at 77K. Ni-C0: as-received sample; Ni-C1: thermal-treated Ni-C in air; Ni-C2: thermal-treated Ni-C in CO_2. The solid and open symbols indicate adsorption and desorption, respectively.

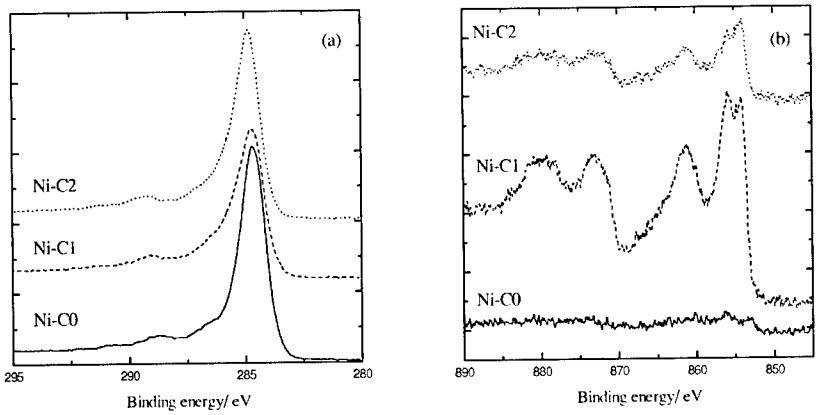


Figure 3. XPS spectra of as-received and thermal-treated Ni-C nanoparticles: (a) C1s, (b) Ni2p.

Table I. Pore structure of as-received Ni-C nanoparticles and thermal-treated Ni-C nanoparticles determined by the SPE method.

sample	pretreatment condition	S_t [a] ($m^2 g^{-1}$)	S_{ext} [b] ($m^2 g^{-1}$)	V_t [c] ($mL g^{-1}$)	V_{mi} [d] ($mL g^{-1}$)	V_{me} ($mL g^{-1}$)
Ni-C0	As-received	248	192	0.47	0.09	0.38
Ni-C1	air, 623K, 15min	548	342	0.68	0.15	0.53
Ni-C2	CO_2, 1173K, 15min	637	273	0.77	0.24	0.53

[a] Total specific surface area, [b] External surface area, [c] Total pore volume, [d] Micropore volume.

NiO or Ni_2O_3 at 854.3 and 855.8 eV[10]. These results are due to the surface-etching effect by the thermal treatment with air and CO_2.

Figure 4 shows hydrogen adsorption isotherms at 298K on thermal-treated Ni-C nanoparticles. The adsorption equilibrium was achieved very quickly within 15min, and the adsorption was reversible. Consequently, hydrogen is adsorbed by physical adsorption. Thermal-treated Ni-C nanoparticles show an increase in the amount of hydrogen adsorption. The CO_2 treatment significantly improved the hydrogen adsorption because the micropores were developed more by the CO_2 than by the air treatment. Furthermore, an increase of the hydrogen adsorption was observed with increasing the specific surface area of Ni-C nanoparticles. Therefore, for increasing hydrogen adsorption, an enlargement of the specific surface area by the development of micropores was required.

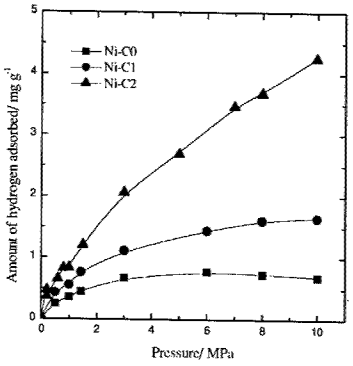


Figure 4. Hydrogen adsorption isotherms at 298K on thermal-treated Ni-C nanoparticles at 298K. Ni-C0: as-received samples; Ni-C1: thermal-treated Ni-C in air; Ni-C2: thermal-treated Ni-C in CO_2.

CONCLUSIONS

The hydrogen adsorption of as-received and thermal-treated Ni-C nanoparticles has been measured. The maximum hydrogen adsorption observed at 298K and 10M Pa is less than 5mg g^{-1}. Hydrogen is adsorbed by physical adsorption. Thermal-treated Ni-C nanoparticles show an increased hydrogen adsorption. The amount of adsorbed hydrogen in Ni-C nanoparticles can be described as a function-specific surface area and micropore volume.

REFERENCES

1. R. H. Baughman, A. A. Zakhidov, W. A. de Heer, *Science* **297**, 787-792 (2002).
2. X. Li, L. Liu, S. Shen, *Carbon* **39**, 2335-2338 (2001).
3. A. Chambers, C. Park, R.T.K. Baker, N. M. Rodriguez. *J. Phys. Chem.* **B102**, 4253-4256 (1998)
4. G. G. Tibbetts, G. P. Meisner, C. H. Olk, *Carbon* **39**, 2291-2301 (2001).
5. V. V. Simonyan, J. K. Johnson, *J. Alloys and Compounds* **330-332**, 659-665 (2002).
6. F. L. Darkrim, P. Malbrunot, G.P. Tartaglia, *Int. J. of Hydrogen Energy* **27**, 193-202 (2002).
7. S.C. Tsang, P.J.F. Harris, M.L.H. Green, *Nature* **362**, 520-522 (1993).
8. P.M. Ajayan, T.W. Ebbesen, T. Ichihashi, S. Iijima, K. Tanigaki, H. Hiura, *Nature* **362**, 522-525 (1993).
9. K. Kaneko, C. Ishi, *Colloid Surf.* **67**, 203-12 (1992).
10. Handbook of X-ray Photoelectron Spectroscopy, Physical Electronics Inc., USA.

Mat. Res. Soc. Symp. Proc. Vol. 740 © 2003 Materials Research Society

An Approach to Nanoglasses through Anodic Oxidation of Sputtered Aluminum on Glass Surface

Satoru Inoue, Song-Zhu Chu, Kenji Wada
National Institute for Materials Science, Advanced Materials Laboratory,
Namiki 1-1, Tsukuba, Ibaraki, 305-0044, Japan

ABSTRACT

The new processes for the preparation of nanoglasses have been developed through anodic oxidation. The aluminum thin film sputtered on the ITO thin film on the glass surface was decomposed into alumina by anodic oxidation technique. The alumina layer possessed nanometer size pore array standing on the glass surface. The sizes of the pore was widened by acid etching from 10~20nm to a few hundred nm. The glass substrate having the alumina nanostructures on the surface could transmit the UV and visible light at the wavelength range of 200 ~ 800nm. The TiO_2 sol was impregnated into the pores of alumina layer and the sample was heated at ~ 400 ºC for 2 hr, converted into TiO_2 nanotubes of anatase phase. The acid etching could remove the alumina skeletons, leaving the TiO_2 nanotube array on the glass surface. These glasses were transparent to the light in UV-visible region. The electro deposition technique was applied to the introduction of Ni metal into pores, giving Ni nanorod array on the glass surface. The glass samples possessing TiO_2 nanotube array showed very good catalytic function on the decomposition of acetaldehyde gas under the irradiation of UV light. The effect of the dimensions of the Ni nanorods on the magnetization was investigated.

INTRODUCTION

The anodic oxidation of aluminum has been used as the method to convert the aluminum surface into alumina for the improvement of the chemical durability. The anodic oxidation technique is known as the self organization process to generate the porous alumina where the nanopores are arranged as perpendicular to the substrate. Recently nanostructured materials have attracted great interest for their potentiality leading to the unique functions in the optical properties, electronic properties, magnetic properties and mechanical properties. In these years, the porous anodic alumina has been studied to fabricate the nanostructured materials [1~5]. The anodic oxidation of the thin aluminum film has been studied recently on the sputtered aluminum film on the Ta [6] and the Si [7] substrate, resulting in the oxidation of the aluminum layer followed by the oxidation of the substrate.

The authors have been studying the formation of the nanostructures on glass surfaces and have developed the new process in which the sputtered alumina film on the conductive layer (tin-doped indium oxide (ITO)) on the glass substrate was converted into the nanostructures by anodic oxidation [8]. The authors have also been studying the processes to introduce other compounds into nanopores of the anodic alumina using sol-gel technique and electro deposition. The TiO_2 component could be introduced by sol-gel process [9,10] giving the high efficiency photo catalytic function [11]. The density of the nanopores of the alumina nanostructures on the glass surface was estimated to be about 1000 Gbit / inch^2 and the introduction of the magnetic components possessing easy magnetization axis perpendicular to the substrate would be applicable to the ultra high density magnetic recording media. The introduction of Ni metal could be attained by electro deposition process and the magnetization characteristics of the Ni nanorods were investigated [12].

In this paper, the new processes approaching to the nanoglasses which might work as the high efficiency photo catalysts or the ultra high density new magnetic recording media have been reviewed.

EXPERIMENTAL DETAILS

Specimens

Pure aluminum (99.99%) was deposited on a soda-lime-silica glass substrate coated with ITO and SiO_2 protection thin film by RF sputtering technique. The size of the substrate was 20 x 100 x 1.1 mm. The thickness of the ITO film and SiO_2 film were 100 ~ 130 nm and ~ 15 nm, respectively. The sheet resistivity of the ITO film was ~ 20 ohm. The aluminum layer was deposited at the rate of ~1.5 nm/s in 2.5 cycles (0.8 μm per cycle) under the pressure of 1.0 x 10^{-5} Torr to reach ~ 2 μm in the thickness.

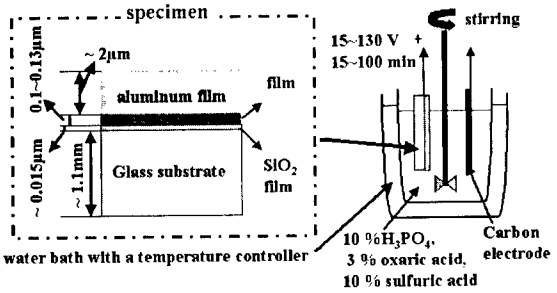


Figure 1. Setup for the anodic oxidation of aluminum film

Anodic oxidation [8]

The aluminum thin film was anodized by a regulated dc power supply in a 10 vol.% phosphoric acid solution or in a 3 % oxalic acid solution or in a 10 % sulfuric acid solution. The specimens were washed by ultrasonic-cleaning in ethanol for 10 min and were anodized in phosphoric acid at a voltage of 130 V at 280 K, in oxalic acid at 40 V at 293 K and in sulfuric acid at 15 V at 283 K. To avoid repetition, the anodic oxide films prepared in phosphoric, oxalic and sulfuric acid solutions are quoted as phosphoric films, oxalic films and sulfuric films, respectively. The setup for the anodization was shown in Figure 1. The part of the films on the substrate was enlarged and the scale of the specimen did not show the real dimensions. The anodized specimens were etched in a 5 vol% phosphoric acid at 30°C for 2 ~ 15 min to enlarge the pore size and remove the anodic alumina barrier layers at the bottoms of the pores (to expose the ITO layer to the electrolyte) for the smooth electro deposition of Ni metal.

Sol-gel process [9,10]

The TiO_2 sol (~5 wt%) was prepared from reagent grade titanium isopropoxide, acetylacetone, ethanol and distilled water at a mole ratio of 1:1:20:3. The reaction was carried out at room temperature in the open air. The mixture was stirred for 2 h and stored in a brown bottle at room temperature. Prior to the experiments, the sol solution was aged for 1 week ~ 1 month. Though the color of the sol changed gradually from light yellow to dark yellow, nothing precipitated and the solution was very stable.

In the introduction of TiO_2 sol into the nanopores of the anodic alumina, the specimens were first immersed in ethanol for 10 min and then dipped in the TiO_2 sol at room temperature for 20 min. After 20 min dipping, the specimens were lifted up slowly from the solution. The TiO_2 sol on the back side of the specimen was washed away with ethanol. The specimens dipped in the TiO_2 sol were dried in the air at room temperature for more than 2 h. To obtain porous alumina/titania structure, the specimens were heated in the furnace at 100°C for 1 h and at 400°C for 2 h where the heating rate was 2°C/min. To get TiO_2 nanotube array, the anodic alumina skeletons were removed with the etching by 5 % phosphoric acid and 2 % CrO_3 solution at 75°C for 5 ~ 8 min.

Electro deposition process [12]

The electrolyte solution for the Ni electro deposition consisted of 0.38 M $NiSO_4$, 0.13 M $NiCl_2$, 0.65 M H_3BO_4 and 60 ppm $CH_3(CH_2)_{11}OSO_3Na$, and was adjusted to PH 5.2 with a 20 % NaOH solution. The specimens were immersed in distilled water for 1 min to push out the air in the pores with applying ultrasonic wave prior to the electro deposition. The Ni electro deposition was performed at 1.0 ~ 1.5 V and 30°C for 2 ~ 10 min, with stirring. The counter electrode was a pure nickel plate. To get Ni nanorods, the alumina skeletons of the specimens were removed with the etching by 5 % NaOH solution

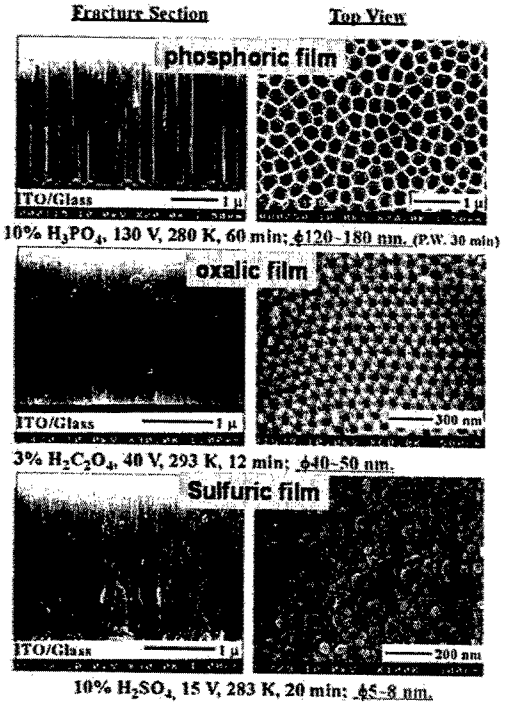


Figure 2. SEM photos of the anodic alumina on the glass surfaces.

Characterizations

The morphology of the samples were observed with a field emission scanning electron microscope (FESEM, S-500, Hitachi) with an energy-dispersion X-ray analyzer (EDXA). The thin coating of osmium was applied on the sample surfaces for the discharge during observations. The UV-visible transmission spectra were recorded by a spectrophtometer (U-3500, Hitachi). The crystalline phases were identified with an X-ray diffractometer (XRD, RINT-2000/PC, Cu Ka, 40 V / 40 mA). The transmission electron microscope (TEM, JEM-1010, 100 kV) was used to observe the structures of Ni nanorods. Magnetization curves were measured by a vibrating sample magnetameter (USM, Lake Shore model 7300). The evaluation of the photo catalysis of the TiO_2 nanotube array was performed by monitoring the volume of the CO_2 gas released in the decomposition of acetaldehyde [11]. The popular and high performance photo catalysis, Degussa P25, was used as the reference sample. The UV light source was a 200W Hg-Xe lamp possessing the peak emission at 365nm.

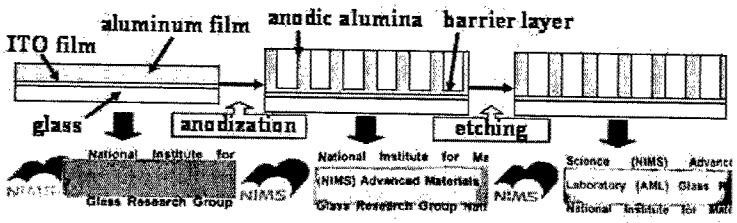


Figure 3. The photos of the specimen and the anodic alumina on the glass substrate.

RESULTS AND DISCUSSION

Nanostructures on the glass surface [8]

The FESEM photos of the anodic alumina prepared under various conditions were shown in Figure 2. The details of the preparation processes were given in the reference [12]. The pore sizes of the phosphoric film were 120 ~ 180 nm in the diameter after 30 min pore widening treatment. The pore diameters of the anodic film were 40 ~ 50 nm in the oxalic film and 5 ~ 8 nm for the sulfuric film. The pores were arranged as perpendicular to the glass substrate. The photos of the specimens were shown in Figure 3. The specimen became transparent after the anodization. The transmission spectrum of the phosphoric film was given in Figure 4 [9]. The anodic alumina film on the glass gave ~ 90 % transmission in the visible region. The waving of the spectra originated from the interference taking place within the specimen.

Introduction of TiO_2 sol into nanopores [9]

Figure 5 shows the schematic illustrations, the photos of the specimens and the SEM photos tin he process for the synthesis of the TiO_2 nanotube array on the glass. After widening of the pores, the sol was introduced into pores. The SEM photo indicated that the inside wall of the pores were coated with the sol. The photo showed that the transparency was kept after the impregnation. The transmission spectrum was given in Figure 4 as "Al_2O_3/ TiO_2 Nanostructure", showing the transmission of 30 ~ 80 % in the visible region. The specimen was converted into the TiO_2 nanotube array after dissolution of the alumina skeletons. The dimensions of the nanutubes were ~ 200 nm in the outside diameter and ~ 140 nm in the inside diame-

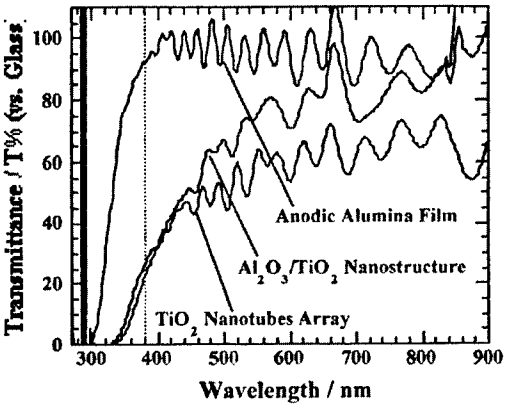


Figure 4. Transmission spectra of the nanostructures on the glass surfaces.

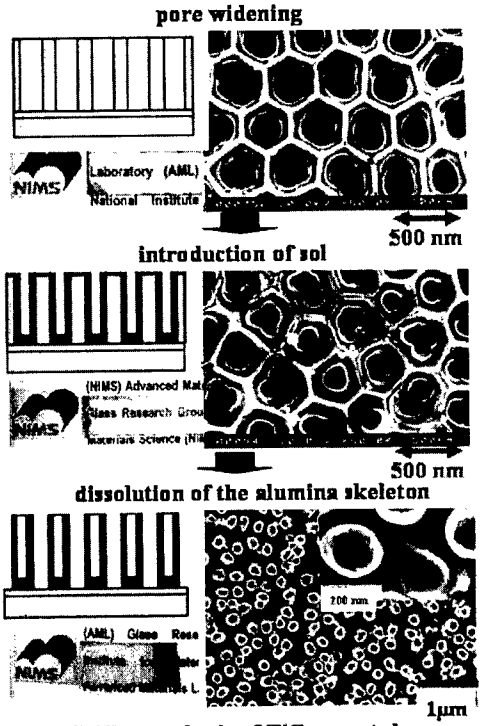


Figure 5. The synthesis of TiO_2 nanotube array.

ter. The length of the nanotube s correspondd the thickness of the anodic alumina film and were ~ 3 μm. The translucency of the specimen was kept but the transmittance decreased a little as shown in Figure 4, where the spectrum was quoted as "TiO_2 Nanotube Array". The transmittance was ~ 60 % in the visible region and decreased gradually in the UV region. The surface area of the specimen was estimated to increase by ~ 45 times from the calculation based on the simple geometry. The TiO_2 formed in the process was identified to be anatase phase by the X-ray diffraction.

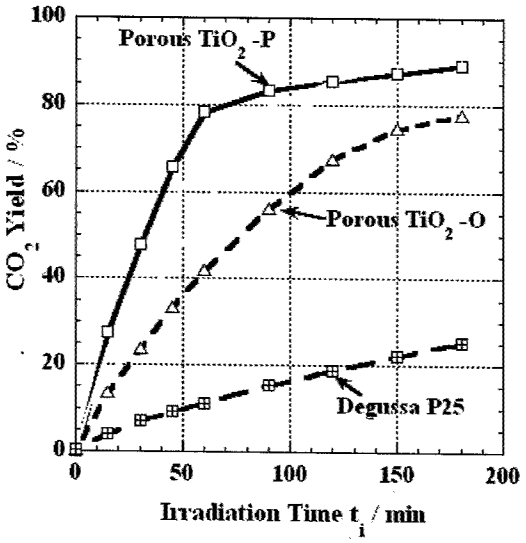


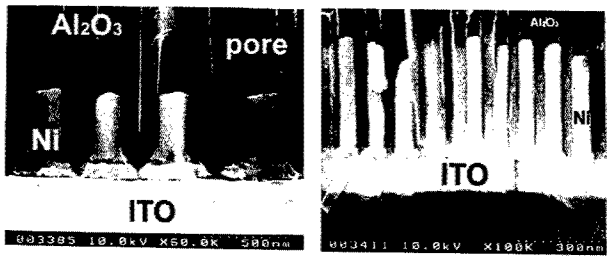
Figure 6. Evaluation of photo calatytic function.

Evaluation of photo catalytic function [11]

The relative value of the volume of the released CO_2 gas was plotted against the irradiation time of UV light in Figure 6. All the data were normalized to the specimen area of 1cm^2. The impregnated anodic film on the glass gave photo catalytic function better than Degussa P25. "Porus TiO_2-P",which is the impregnated phosphoric film, showed the decomposition rate larger by ~ 13 times than that of Degussa P25. The catalytic function of the TiO_2 nanotube array has not yet been finished, but would be better for the increase of the surface area. The sulfuric film impregnated with TiO_2 sol did not seem to have open pores and was not taken in the catalytic function test.

Introduction of Ni into nanopores [12]

In Figure 7, the cross sectional SEM photos were shown for the cases of the phosphoric film and oxalic film. The Ni deposition was performed directly on the ITO film. When the anodic alumina barrier layer remained, the electro deposition could not be performed. The SEM photos of the Ni nanorod arrays, which were obtained after dissolution of anodic alumina skeletons, were summarized in Figure 8. The phosphoric film, the oxalic film and the sulfuric film gave the nanorods of ~ 150 nm, ~ 50 nm and ~ 18 nm in the diameter, respectively. The Figure 9



phosphoric film oxalic film

Figure 7. The cross sectional SEM photo at the interface between the Ni and ITO film. Deposition time: 2min

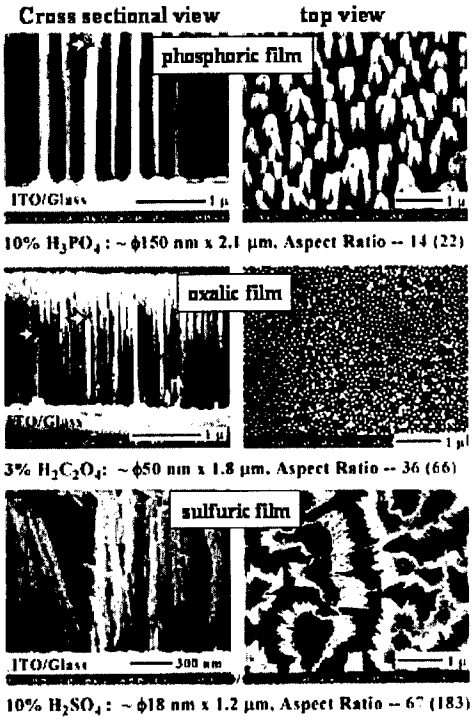


Figure 8. SEM photos of the Ni nanorod array.

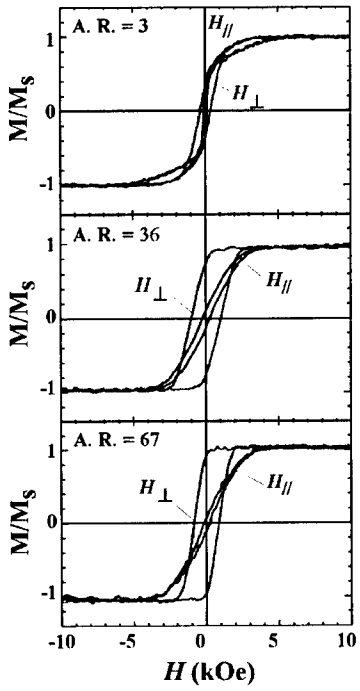


Figure 9. Magnetization curves of the Ni nanorod arrays.

shows the magnetization curves for the Ni nanorod embedded in the anodic alumina skeletons. In the figures, A.R. indicates the average aspect ratio of the Ni nanorods. The top one is for the phosphoric film, the middle one for the oxalic film and the bottom one for the sulfuric film. The figure indicated that the easy axis of magnetization changed from in-plane to perpendicular direction with the increase of the aspect ratio of the nanorod. In other words, The magnetization perpendicular to the substrate became dominant over the in-plane magnetization. Taking that the density of the pores of the anodic films were about 1000 Gbit / inch^2 into account, the anodic films embedded with appropriate magnetic substances could be applied to the ultra high density magnetic recording media.

CONCLUSIONS

The anodic oxidation of the sputtered alumina on the glass substrate was fruitful process to build up the nanostructures on the glass surface. The introduction of the compounds into pores could be attained with the sol-gel processing and electro deposition technique. The embedding of the components into the nanopores could endow the glasses the photo catalytic functions and would be applicable to the ultra high density magnetic recording. The photo catalyst prepared in this study showed the decomposition rate of acetaldehyde larger by an order of one than that of the Degussa P25. The anodic oxidation process, the sol-gel coating process and the electro deposition process are principally applicable to general curved substrates and large substrates. The new process does not require the special and expensive apparatuses like

high power lasers, nanometer range precise manipulators etc. Therefore the process is believed to have an advantage over the other nanomachining processes in the applications and the commercial productions.

REFERENCES

1. A. Huczko, Appl. Phys. **70**, 365 (2000).
2. T. Kyotani and A. Tomita, Bull. Chem. Soc. Jpn. **72**, 1957 (1999).
3. M. Zhang, Y. Bando, K. Wada and K. Kurashima, J. Mater. Sci. Lett. **18**, 1911 (1999).
4. B. B. Lakshmi, P. K. Dorhout and C. R. Martin, Chem. Mater. **9**, 857 (1997).
5. H. Masuda and K. Fukuda, Science **268**, 1466 (1995).
6. for example; A. Mozalev, A. Surganov and H. Imai, Electrochim. Acta **46**, 2825 (2001).
7. for example; D. Crouse, Y. Lo, A. E. Miller and M. Crouse, Appl. Phys. Lett. **76**, 49 (2000).
8. S. Z. Chu, K. Wada, S. Inoue and S. Todoroki, J. Electrochem. Soc. **149**(7), B321 (2002).
9. S. Z. Chu, K. Wada, S. Inoue and S. Todoroki, Chem Mater. **14**, 266 (2002).
10. S. Z. Chu, K. Wada and S. Inoue, Advanced Materials, **14**[23] , 1752 (2002)
11. S. Z. Chu, S. Inoue, K. Wada, Di Li and H. Haneda, J. Mater. Chem., (in press) (2003), also published as an Advanced Article on the RSC web site (http://www.rsc.org/is/journals/current/jmc/mappub.htm) on Feb. 7, 2003.
12. S. Z. Chu, K. Wada, S. Inoue and S. Todoroki, Chem. Mater., **14**, 4595 (2002).

Mat. Res. Soc. Symp. Proc. Vol. 740 © 2003 Materials Research Society

GROWTH OF CARBON NANOFIBERS ON ELECTROLESS Ni-P ALLOY CATALYST

T.K. Tsai, W.L. Liu, S.H. Hsieh, and W.J. Chen

Department of Materials Science and Engineering, National Huwei Institute of Technology, Huwei, Yunlin, Taiwan 632, Republic of China

Abstrate

Carbon nanotubes (CNTs) were grown by electroless Ni–P plated on silicon substrate in a microwave heating chemical vapor deposition (CVD) system with methane gas at 700 ℃. The CNTs grown on Ni–P catalyst showed random orientation and small diameter around 15~30 nm. Field emission test results indicated that the Ni–P catalyzed–CNTs exhibited excellent field emission properties. The turn–on field was about 0.56 V/μm with an emission current density 10 μA/cm^2 and the threshold field was 4.4 V/μm with an emission current density 10 mA/cm^2. These excellent field emission properties may be attributed to the random orientation and small diameter of CNTs.

1. Introduction

Since the discovery of carbon nanotubes (CNTs) in 1991,[1] this kind of carbon nanostructures has attracted extensive attention and study, due to their novel properties and potential applications, such as in high–performing nano–materials, nanoelectronics, high–efficiency energy storage and cold field emitter.[2-5] One of the most potential applications of CNTs is as electron emitter for flat plane displays. Because CNTs have excellent field emission properties, i.e., good emission stability, long emitter lifetime and low voltage for operating. Therefore, many researchs have been done on the fabrication of field emission display (FED) and other electronic devices.

Several synthesizing methods for the fabrication of CNTs have been developed by researchers, such as arc discharge, laser evaporation, pyrolysis of hydrocarbon gases and plasma–enhanced or thermal CVD.[5-10] Among these methods, the CVD possessed simple process, selective growth, high purity, high yield and vertical alignment characteristics. Thus CVD was widely accepted by many investigators. In the CVD method, the transition metal, e.g., Ni, Co, Fe, plays an important and indispensable role for the growth of CNTs, because it works as a catalyst of the CNTs' growth. The chemical composition and nanoparticle size of the catalyst determine the structure, property and diameter of the CNTs. Since the catalyst nanoparticles are essential for both initial nucleation and subsequent growth of CNTs in CVD, many investigations have been developed to prepare catalyst nanoparticles. The techniques include filling metallic catalyst nanoparticle in nanoporous or mesoporous zeolite, [11] silicon[5] and anodic alumina[12] by evaporation or impregnation, chemically synthesized catalyst metal nanoparticle by reverse micelle method,[13] and etching the catalyst metal–coated substrate by laser ablation,[8] plasma[9] or NH_3 treatment.[14] Choi et al.[15] deposited Ni using rf magnetron sputtering on Si substrate. Sohn et al.[16] deposited Fe on Si (100) substrate by pulse–laser deposition. Avigal et al.[17] coated Co on n–type Si by e–beam, and Kim et al.[14] coated Ni using electroplating on soda–lime glass, etc. However, there is little literature mentioned about electroless plating Ni deposited on substrate for fabricating CNTs. Electroless plating technique has been applied for ohmic contacts with silicon in semiconductor devices and for contact filling in very large scale integrated (VLSI) [18] for several years. This technique is a useful process for microelectronics, because it is simple and easy to manage.

In the present study, we have deposited Ni as catalyst metal on the silicon substrate by a low cost and simple method – electroless plating technique. The CNTs with excellent field emission property grown on electroless plating Ni has fabricated

successfully by using a microwave heat CVD system. We believe the cheap and simple process of growing CNTs has potential for the fabrication of flat plane displays and other electronic devices.

2. Experimental

A Ni–P thin film was deposited by using electroless plating technique on p–type (100) silicon wafer (1–20 ohm cm). Prior to the electroless plating process, it is necessary to pretreat the silicon surface. This pretreatment consisted of the following four steps; (1) degrease cleaning of the surface using a weak base solution (aceton) by ultrasonic; (2) roughening the surface by etching in an acid solution of HNO_3, HF and deionized (DI) water; (3) sensitizing in a solution of $SnCl_2$ and HCl; and (4) catalyzing by deposition of Pd in a solution of $PdCl_2$ and HCl. A rinse with DI water was carried out at the end of each step. The plating solution was composed of a mixture of $NiSO_4$, NaH_2PO_2, $Na_2C_4H_4O_4$ and $Pb(NO_3)_2$; where $NiSO_4$ as the main nickel source, NaH_2PO_2 as the reducing agent, $Na_2C_4H_4O_4$ and $Pb(NO_3)_2$ as buffer and complexing agent for nickel. Since NaH_2PO_2 is used as a reducer, the electroless plated nickel structures always incorporated with phosphorus. The composition of plating solution and experimental condition are list in Table Ⅰ.

A microwave heating CVD system has been utilized for growth of CNTs. The electroless Ni deposited-silicon substrate was placed on a ceramic holder, which was heated to 700 ℃ by controlling the microwave power and CNTs were grown on the substrate using methane gas as the source of carbon with its flow rate 200 cc/min for 10 min. The CNTs were observed by field emission scanning electron microscope (FESEM). Field emission was measured by taking voltage – current (V– I) curve with Keithley 237 in a vacuum chamber.

3. Result and discussion

Figure 1 is a SEM micrograph showing the surface morphology of CNTs grown on the silicon substrate. The SEM image shows the CNTs are not vertically aligned but randomly tangled. The diameter of the most CNTs are 15~30 nm, only few CNTs around 60~80 nm. This result is consistent with the previous report that the size of Ni nanoparticle suitable for CNTs growth is limited to around 20~30 nm.[19] Figure 1 also illustrates a large amount of nanoparticles at tip of the tubes. Energy dispersive x-ray (EDX) spectra carried out during FESEM measurements showed that the nanoparticle consists of Ni, P and carbon. This phenomenon may be indicated the nucleation and growth mechanism have correlation with the process conditions and the morphology of the Ni–P nanoparticles on the surface of substrate. Although many nucleation and growth mechanisms about Ni catalyst for CNTs have been proposed, [20-22]the CNTs formation mechanism for catalyst by electroless plating Ni was not clear yet. Further studies are required for investigating the catalyst effect of Ni–P alloy for CNTs.

Field emission properties were measured at room temperature in a vacuum chamber with a 10^{-6} torr by applying voltages up to 1100 V. The distance between the indium–tin oxide (ITO) film and the CNTs tips is 180 μm. Figure 2 illustrates the electron emission current density versus electric field curve of the CNTs. The turn–on field, for an emission current density of 10 $\mu A/cm^2$, is 0.56 V/μm. The threshold field, for an emission current density of 10 mA/cm^2, is 4.4 V/μm. Bonard et al.[23] has reviewed emission characteristics of carbon nanotube; the lowest turn–on field 0.75 V/μm was reported by Rao and co–workers. Our result shows the CNTs catalyzed by Ni–P alloy have very good field emission properties, especially the extremely low turn–on field, 0.56 V/μm. The Fowler–Nordheim equation was used to analyze the field emission data obtained from V–I curve. Figure 3 shows the corresponding F–N plot of Figure 2. The plot of $\ln | I/V^2 |$ versus $| 1/V |$ is approximately straight line, indicating that the emitting electrons mainly follow field emission process.

The field emission characteristics of CNTs are determined by its intrinsic structure, chemical properties, aligned density and orientation of the tubes. These excellent field emission properties of Ni–P catalyzed–CNTs may be attributed to the random orientation and small diameter of CNTs. As Davydov and co–workers[24] pointed out, perfectly aligned carbon nanotubes were less efficient field emitters and

had lower field enhancement than chaotic carbon nanotubes. Groning and co–workers[25] also suggested that some random CNTs exhibited better field emission properties than aligned CNTs. These results are good evidence to our supposition.

4. Conclusion

We have grown CNTs on Ni–P catalyst electroless plated on silicon substrate in a microwave heating CVD system with methane at 700 ℃. The CNTs grown on Ni–P catalyst shows random orientation and small diameter about 15~30 nm. Field emission results indicated the Ni–P catalyzed–CNTs exhibits excellent field emission properties, the turn–on field was about 0.56 V/μm with an emission current density of 10 $\mu A/cm^2$ and the threshold field was 4.4 V/μm with an emission current density of 10 mA/cm^2. These excellent field emission properties may be attributed to the random orientation and small diameter of CNTs. The electroless plating technique not only provides a cheap and easy process for fabricating CNTs, but also promotes the field emission property of CNTs. The electroless plating technique for CNTs growth has potential for the fabrication of flat plane displays and the other electronic device industries.

References

[1] S. Iijima, Nature (London) **354**, 56 (1991)
[2] S. Wong, E. Joselevich, A. T. Wolley, C. L.Cheung, and C. M. Lieber, Nature (London) **394**, 52 (1998)
[3] S. J. Tans, A. R. M. Verschueren, and C. Dekker, Nature (London) **393**, 49 (1998)
[4] C. Liu, Y. Y. Fan, M. Liu, H. T. Cong, H. M. Chen, and M. S. Dresselhaus, Science **286**, 1127 (1999)
[5] S. Fan, M. G. Chapline, N. R. Franklin, T. W. Tombler, A. M. Cassel, and H. Dai, Science **283**, 512 (1999)
[6] S. Iijima and T. Ichihashi, Nature (London) **363**, 603 (1993)
[7] A. Thess, R. Lee, P. Nikolaev, H. Dai, P. Petit, J. Robert, C. Xu, Y. H. Lee, S. G. Kim, D. T. Colbert, G. Scuseria, D. Tomanek, J. E. Fisher, and R. E. Smalley, Science **273**, 483 (1996)
[8] M. Terrines, N. Grobert, J. Olivares, J. P. Zhang, H. Terrones, K. Kordatos, W. K. Hsu, J. P. Hare. P. D. Townsend, K. Prassides, A. K. Cheetham, H. W. Kroto, and D. R. M. Walton, Nature (London) **388**, 52 (1997)
[9] Z. F. Ren, Z. P. Huang, J. W. Xu, J. H. Wang, P. Bush, M. P. Siegal, and P. N. Provencio, Science **282**, 1105 (1998)
[10] W. Z. Li, S. S. Xie, L. X. Qian, B. H. Chang, B. S. Zou, W. Y. Zhou, R. A. Zhao, and G. Wang, Science **274**, 1701 (1996)
[11] K. Mukhopadhyay, A. Koshio, T. Sugai, N. Tanaka, H. Shinohara, Z. Konya, and J. B. Nagy, Chem. Phys. Lett. **303**, 117 (1999)
[12] J. Li, C. Papadopoulos, J. M. Xu, and M. Moskovits, Appl. Phys. Lett. **75**, 367 (1999)
[13] H. Ago, T. Komatsu, S. Ohshima, Y. Kuriki, and M. Yumura, Appl. Phys. Lett. **77**, 79 (2000)
[14] J. Kim, K. No, and C. J. Lee, J. Appl. Phys. **90**, 2591 (2001)
[15] Y. C. Choi, D. J. Bae, Y. H. Lee, B. S. Lee, G. S. Park, W. B. Choi, N. S. Lee, and J. M. Kim, J. Vac. Sci. Technol. A **18**. 1864 (2000)
[16] J. I. Sohn, C. J. Choi, S. Lee, and T. Y. Seong, Appl. Phys. Lett. **78**, 3130 (2001)
[17] Y. Avigal and R. Kalish, Appl. Phys. Lett. **78**, 2291 (2001)
[18] C. H. Ting and H. Paunovic, J. Electrochem. Soc. **136**, 456 (1989)
[19] M. Yudasaka, R. Kikuchi, T. Matsui, Y. Ohki, S. Yoshimura, and E. Ota , Appl. Phys. Lett. **67**, 2477 (1995)
[20] M. Yudasaka, R. Kikuchi, Y. Ohki, E. Ota, and S. Yoshimura, Appl. Phys. Lett. **70**, 1817 (1997)
[21] A. N. Andriotis, M. Menon, and G. Froudakis, Phys. Rev. Lett. **85**, 3193 (2000)
[22] F. Banhart, J. -C. Charlier, and P. M. Ajayan, Phys. Rev. Lett. **84**, 686 (2000)
[23] J. -M. Bonard, H. Kind, T. Stőckli, and L.-O. Nilsson, Solid-State Electronics **45**, 893 (2001)

[24] D. N. Davydov, P. A. Sattari, D. AlMawlawi, A. Osika, T. L. Haslett, and M. Moskovits, J. Appl. Phys. **86,** 3983 (1999)
[25] O. Groning, O. M. Kuttle, C. Emmenegger, P. Groning, and L. Shlapbach, J. Vac. Sci. Technol. B **18**, 665 (2000)

TABLE I. The composition of plating solution and experimental condition for electroless Ni–P plating.

Chemicals	concentration (g/l)
$NiSO_4 \cdot 6H_2O$	8
$NaH_2PO_2 \cdot H_2O$	27
$Na_2C_4H_4O_4 \cdot 6H_2O$	16
$Pb(NO_3)_2$	1 ppm
PH = 4.5	
Temperature 70℃	

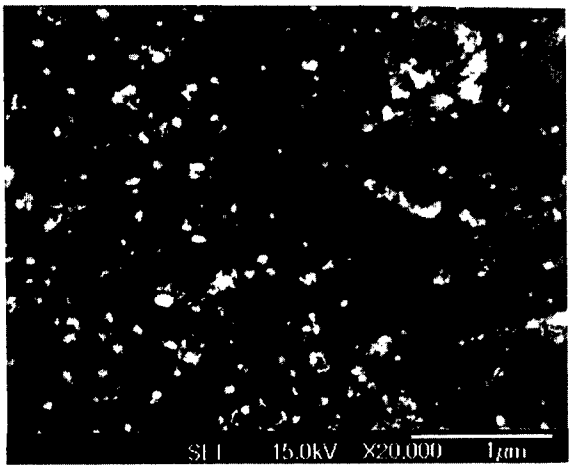


Fig. 1. FESEM image of the surface morphology of CNTs. The CNTs grown on Ni–P catalyst shows random orientation and small diameter about 15~30 nm, few CNTs' diameter is around 60~80 nm. There is a large amount of nanoparticles at tip of the tubes.

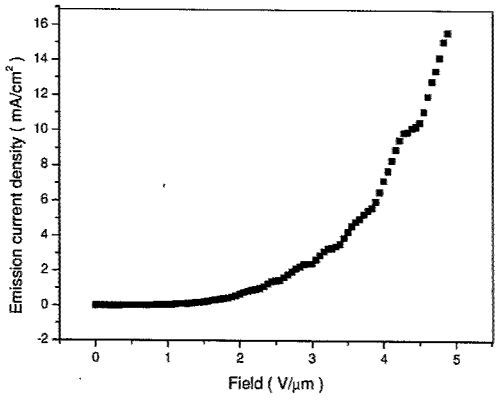


Fig. 2. Electron emission current density versus electric field (I–V) curve of CNTs. The turn–on field was about 0.56 V/μm with an emission current density 10 μA/cm^2 and the threshold field was 4.4 V/μm with an emission current density 10 mA/cm^2.

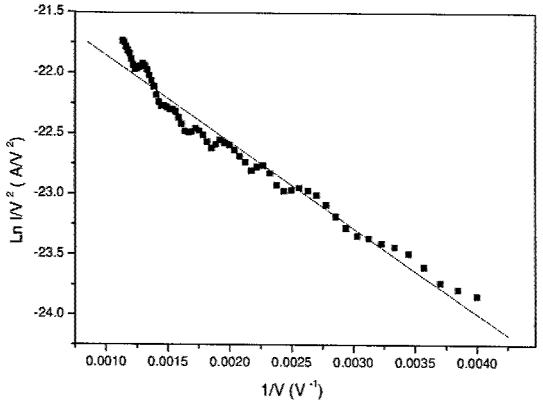


Fig. 3. The corresponding F–N plot of Figure 2. The plot of ln | I/V^2 | versus | 1/v | is approximately straight line.

Mat. Res. Soc. Symp. Proc. Vol. 740 © 2003 Materials Research Society

Material Properties and Process Compatibility of Spin-on Nano-foamed Polybenzoxazole for Copper Damascene Process

Takashi Enoki, Kenzo Maejima, Hidenori Saito, and Akifumi Katsumura
Fundamental Research Laboratory, Research Department, Sumitomo Bakelite Co., Ltd., 495, Akiba-cho, Totsuka-ku, Yokohama, 245-0052, JAPAN

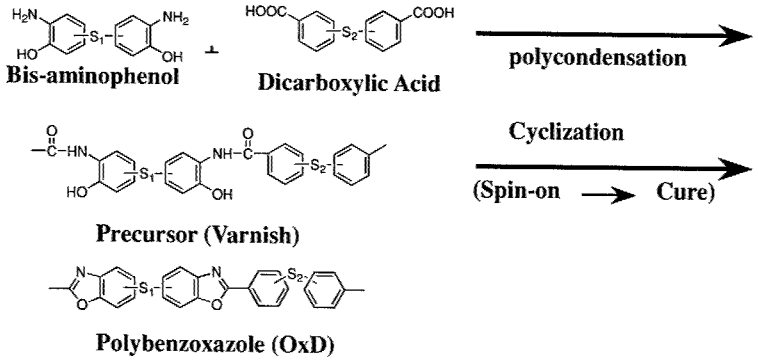
ABSTRACT

We have developed nano-foamed OxD which has good properties such as dielectric constant=2.2, homogeneous distributed nano pores, smooth surface based on polybenzoxazole chemistry and nano-foaming technology. The nano-foamed OxD also has excellent thermal stability, chemical stability and etching property. The developed nano-foamed OxD is one of good candidates for copper damascene structure to achieve shrinking dimensions of future semi-conductor devices.

INTRODUCTION

In shrinking dimensions of future semi-conductor devices, lower dielectric constant (k) material is strongly required in Cu/low k damascene structure. According to the International Technology Roadmap for Semiconductors (ITRS) 2001, ultra low-k interlayer dielectric materials (k < 2.4) will be needed around 2005 [1]. Because the k value of air is one, nano-foaming with air is possible solution to provide lower k material.

Polybenzoxazole [2] is one of excellent heat resistant polymers and is synthesized via cyclization of its precursor (poly(o-hydroxy)amide) by polycondensation between bis-o-amino-phenol and dicarboxylic acid derivative monomers (Scheme 1.).



Scheme 1. Chemistry of Polybenzoxazole. S_1 and S_2 = Spacers

The precursor shows good solubility to several organic solvents, which allows us

spin-on application. Once the polybenzoxazole is obtained by cyclization from spun-on precursor by heat, it becomes insoluble and shows high thermal stability. We have designed a spin-on nano-foamed OxD (Oxazole Dielectrics) by taking advantage of polybenzoxazole chemistry considering nano-foaming process [3,4].

In this work, we will report material and process properties of nano-foamed OxD which are important to consider Cu damascene process. We will discuss pore size, surface roughness, thermal stability, chemical stability, process compatibility such as etching property and so on.

EXPERIMENTAL DETAILS

OxD precursor varnishes were spin coated onto silicon wafers to form films from 0.4 um to 1.0 um thick. The films were cured for 1 hour at 250°C and 1 hour at 425°C in N_2 atmosphere. The thickness and refractive index of the films were measured with a spectrometric reflectance tool, n & k analyzer 1500 (n&k Technology, Inc.). All the electrical measurements were done using Hg probe (Automatic Mercury Probe CV System SSM 495, Solid State Measurements Co.,Ltd.). Surface roughness of the film was analyzed by atomic force microscopy (AFM), Nano Scope IIIa (Digital Instruments). Determination of pore size was examined by TEM (transmission electron microscopy and Small Angle X-Ray Scattering (SAXS: Advanced Thin Film X-ray System ATX-G, Rigaku Corporation). Hardness and modulus of the films were determined by nano Indenter XP (MTS Systems Corporation). Thermal stability was examined by Thermal Desorption Spectrometer, EMD-WA1000S (ESCO Ltd.). Chemical stability was examined by Fourier transform-infrared spectrometer, IRus-II (Spectra-tech, Inc.). Etching was done using dry etching system, L-201D-L (Anelva Corporation).

RERULTS & DISCUSSION

Film Properties

Table 1 shows film properties of nano-foamed OxD on 200mm wafers. Dielectric constant is 2.2. A standard deviation of the measurement around 0.7% is found, indicating that the dielectric constant is constant over the wafer. Dielectric constant did not change for 3 months at 25°C for 50 % RH. The leak current value is below $9.1E^{-9}$ A/cm^2 and the films did not show breakdown up to fields of 2.7 MV/cm. Leak current and dielectric breakdown of the nano-foamed OxD are comparable to those of Aromatic organic, hydroxyl silsesquioxane (HSQ), and methyl silsesquioxane (MSQ) [5]. The nano-foamed OxD exhibited good adhesion to various substrate surfaces such as SiC, SiO_2, and Si in a tape pull test.

Standard deviation on film thickness by n&k analyzer was below 0.3% which showed that the nano-foamed OxD was fabricated uniformly. The surface roughness was analyzed by AFM. Roughness was measured over different spots on the sample and the scans were done in 0.5 x 0.5 um^2 areas. Figure 1 shows a 3D image of the film surface. The root means square (RMS) was 1.67 nm, and this value is independent of the area measured.

Table 1. Properties of nano-foamed OxD.

Properties	Unit	Method	Value
Dielectric constant	at 1MHz	Hg probe	2.2
Dielectric breakdown	MV/cm(0.4 um)	Hg probe	2.68
Leak Current at 1MV/cm	A/cm^2 (0.4 um)	Hg probe	$9.1E^{-9}$
Refractive index		n&k analyzer	1.40
Young's modulus	GPa	Nanoindentation	1.5
Hardness	GPa	Nanoindentation	0.12
Thermal Stability	A	TDS	$<1.0E^{-10}$
Adhesion (SiC, SiO_2, Si)		Tape pull test	Pass
Average pore size	nm	SAXS	6.6

Therefore, the nano-foamed OxD has good film qualities (roughness and uniformity) [6] in addition to its good electrical properties.

Pore size was examined by FIB-TEM, and SAXS measurements shown in Figure 2. FIB-TEM picture (Figure 2 (a)) shows that pores whose sizes were below 10nm distributed uniformly. Figure 2 (b) shows pore size distribution by SAXS. The average pore size is 6.6nm with very narrow distributions in which pore sizes are below 12nm.

Thermal stability was demonstrated by TDS measurement. Figure 3 shows thermal desorption spectrum of the nano-foamed OxD. The film shows excellent thermal stability up to 450°C.

Chemical stability is important to consider Cu damascene integration process. The changes in thickness and refractive index of the nano-foamed OxD films were less than 1% after the films were immersed in 10% sulfuric acid, 3% hydrogen peroxide, 2.38%

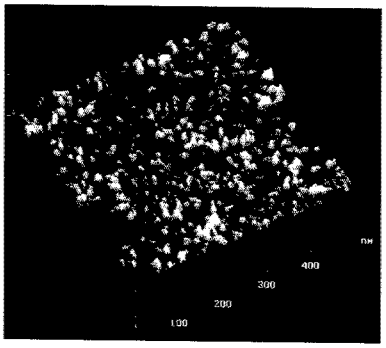


Figure 1. AFM image of the nano-foamed OxD, RMS = 1.67 nm.

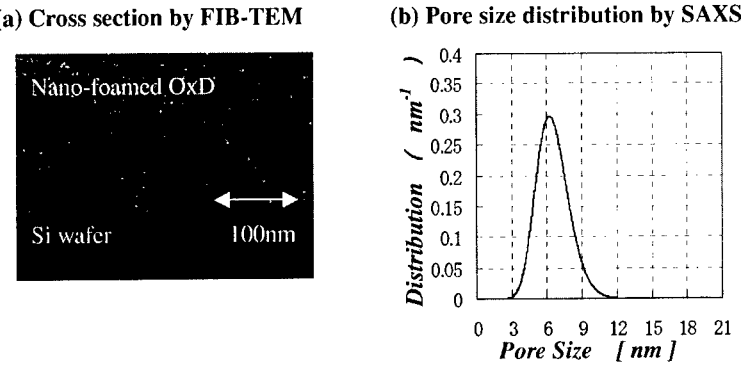


Figure 2. FIB-TEM (a), and SAXS (b) data of the nano-foamed OxD.

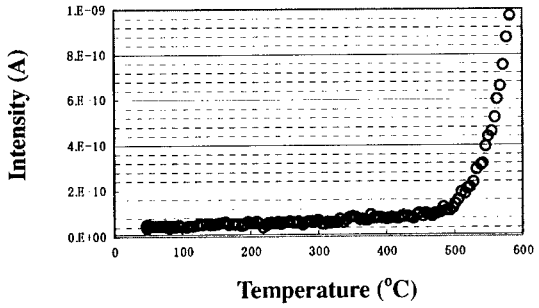


Figure 3. Thermal behavior of the nano-foamed OxD by TDS measurement.

tetra-methyl ammonium hydroxide, 1,1,1,3,3,3-hexamethyldisilazane, organic solvents such as N-methyl-2-pyrrolidone, isopropyl alcohol, 1-methoxy-2-propanol acetate, ethanolamine, respectively at 25°C for 10 minutes and rinsed with diionized water and dried at 200°C for 10 minutes. The nano-foamed OxD shows good chemical stabilities because of its chemical structure.

Compatibility to integration process

Nano-foamed OxD can be dry-etched by N_2 / H_2 chemistry [7] with sufficient etching selectivity against plasma-deposited tetra-ethoxy silane (TEOS) which indicates that SiO_2 can be used as etch stopper for OxD in damascene process. The combination of nano-foamed OxD and SiO_2 also leads to lower effective dielectric constant. The nano-foamed OxD is attractive as dielectrics due to sufficient etching selectivity [8] and possible lower effective dielectric constant.

Figure 5 shows behaviors of dielectric constant and refractive index during N_2 / H_2 reactive ion etching (RIE) and resist stripper treatment (cleaning). The film thickness decreased during etching, but it did not change after resist stripper treatment. The dielectric constant and the refractive index did not change during both RIE etching and resist stripper treatment. The chemical composition did not change supported by the IR spectra of the films which were the same through the processes (Figure 6). Figure 7 shows the etched profile on nano-foamed OxD after N_2:H_2 etching. The nano-foamed OxD was etched perpendicularly. Etched residues were cleaned with ACT-NE-14. Therefore, it is suggested that the nano-foamed OxD has compatibility to N_2 / H_2 etching process and cleaning.

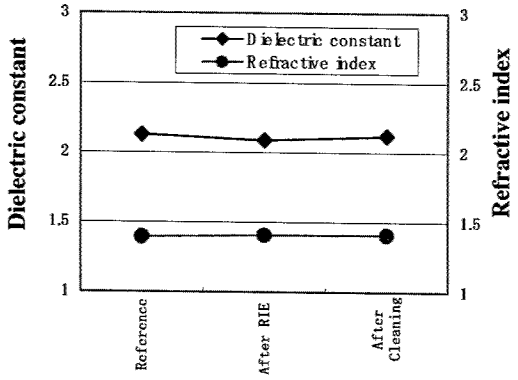


Figure 5. Behaviors of refractive index and film thickness on the nano-foamed OxD film during RIE and cleaning: etching gas: N_2 : H_2 = 2.5 sccm : 7.5 sccm, RF output = 10W, etching time = 30 sec.; cleaning: the film was immersed in resist stripper, ACT-NE-14 (Ashland Specially Chemical Company) at 25°C for 30 minutes, rinsed with deionized water, dried at 130°C for 10 minutes.

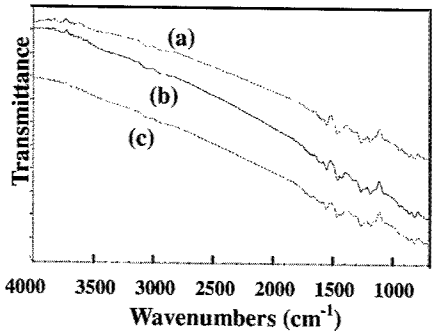


Figure 6. FT-IR spectra of nano-foamed OxD film: (a) reference, (b) after RIE, and (c) after cleaning.

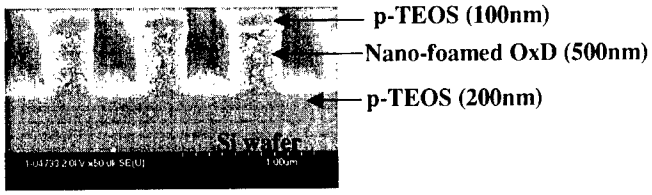


Figure 7. SEM micrograph of etched profile on nano-foamed OxD after N_2:H_2 etching.

CONCLUSIONS

It is demonstrated that the nano-foamed OxD shows excellent film properties such as film uniformity, thermal stability, adhesion, chemical stability with k=2.2 and homogeneous nano-order pores. In addition, the nano-foamed OxD shows chemical stability during N_2:H_2 etching and cleaning and is etched perpendicularly, suggesting compatibility to copper damascene process.

ACKNOWLEGEMENTS

The authors would like to thank Venture Business Laboratory (VBL) and Department of Machine Intelligence and Systems Engineering in Tohoku University.

REFERENCES

1. The National Technology Roadmap for Semiconductors, Semiconductor Industry Association, San Jose, CA, 2001.
2. K. Lowack, G. Schmid, A. Maltenberger, R. Sezi, and W. Radlik in *Issues for CMOS Process Integration of OxD, the Innovative Low k Interlayer Dielectric*, edited by H. S. Sachdev, M. M. Khojasteh, D. McHerron, (Proceedings of the seventh International conference on Polymers in Electronic Packaging, McAfee, NJ, USA, October 18-20, 2000) pp. 113-119.
3. Yuhuan Xu, et. al, Applied Physics Letter, 75, 853-855 (1999).
4. K. R. Carter, et. al., Mat. Res. Soc. Symp. Proc., Vol. 431,487-495 (1996).
5. M. Tada, J. Kawahara, and Y. Hayashi, Conference Proceedings ULSI XVI (2001), Materials Research Society, pp. 579-585.
6. E. K. Lin, W. Wu, C. Jin, and J. T. Wetzel, Mat. Res. Soc. Symp. Proc., **612** (2000) D4.1.1-D4.1.8.
7. K. Maejima, A. Katsumura, J. C. Shin, H. Kurino, and M. Koyanagi, (the 63rd Autumn Meeting, 2002, the Japan Society of Applied Physics), p766.
8. N. Aoi et al., Symposium on VLSI Technology Digest of Technical Papers, pp.41-42, 1999.

Mat. Res. Soc. Symp. Proc. Vol. 740 © 2003 Materials Research Society

Ferromagnetic Shape Memory of Nanostructure Fe-Pd Alloy: The Texture Observation Study by Laser and Electronic Microscopes

T. Okazaki, T. Kubota, Y. Furuya, S. Kajiwara[1] and T. Kikuchi[1]

Faculty of Science and Technology, Hirosaki University, Hirosaki 036-8561, Japan.
[1] National Institute for Materials Science, Tsukuba 305-0047, Japan

ABSTRACT

Ferromagnetic shape memory Fe-29.6at%Pd alloy ribbon (about 60 μm thickness) prepared by the rapid solidification melt-spinning method, has a large magnetostriction of 1.0×10^{-3} when a magnetic field of 10 kOe is applied normal to the ribbon surface at room temperature. The strain induced by magnetic field is caused by the conversion of variants in the martensite phase, and increases with temperature and has a maximum at phase transformation temperature of 380-400 K. However, the mechanically shape recovery effect of the ribbon has two-step phase transformation temperature of 300-330 K and 380-420 K. To investigate the origin, we observed the texture by using laser microscope and high resolution electronic microscope. The cross section of ribbon shows columnar structure of about 10μm in width. The ribbon consists of three parts: both upper and bottom surfaces have small grains of 2-3 μm with strong [100] texture and the inner part has fine layer-structures of 30-40 nm thickness in grains. It can be concluded that this nano-scale composite structure makes phase transformation temperature increase from 300 K in surface to 380-400 K in inner part.

INTRODUCTION

Ferromagnetic shape memory alloy (FSMA) Fe-Pd is expected to be useful as a magnetic-field-drive sensor/actuator material for a micro-machine and intelligent/smart material system. The FMSA exhibits a large strain caused by martensitic twin's initiations and its movements, i.e., a new type of mangetostriction [1]. Although Fe-31.2at%Pd single crystal [2] and polycrystalline bulk [3] samples exhibit large magnetostriction, phase transformation temperatures are low than room temperature. In previous study [4, 5], we showed that Fe-29.6at%Pd alloy ribbon prepared by the rapidly solidification melt-spinning method has stronger crystal anisotropy and giant magnetostriction of 1.0×10^{-3} at room temperature with good shape memory effect. The magnetostriction of this ribbon is 10 times as large as polycrystalline bulk value. Its value increases with temperature and has a maximum at the phase transformation temperature of 380-400 K, though the austenite finishing temperature A_f of Fe-29.6at%Pd single crystal is 320-330 K [6].

In the present study, to investigate the origin of the temperature discrepancy, we observed the texture of ribbon sample by using laser microscope and high resolution electronic microscopes. We found that the martensite twin in the inner part of ribbon consists of fine layer-structures of 30-40 nm thickness.

EXPERIMENTAL DETAILS

The rapidly solidified Fe–29.6at%Pd ribbon sample with 60 μm in thickness, was prepared by originally designed electro-magnetic melt-spinning single-roll method from bulk alloy [4]. Some of ribbon was annealed at 1173 K for 1 h in vacuum atmosphere to study the effect of heat treatment on magnetostriction. The structure of ribbon was researched by XRD method with Cu Kα radiation. The microstructure of texture of ribbon was observed by

using laser and high resolution electronic microscopes. The magnetization M vs. applied magnetic field H loop was measured by VSM.

The magnetostriction ε was measured by a strain-gauge attached on the sample (see Fig.4(a)). The magnetic field was applied perpendicular to the rolling direction (RD) and strain changes were measured along RD. The shape memory effect was evaluated from the changes of shape recovery of the curled ribbon with temperature.

RESULTS AND DISCUSSION

Microstructure of ribbon

Figure 1 shows laser microscope photographs of (a) the contact surface and (b) the free surface of as-spun ribbon. Microstructure of roll contacting surface, which is covered by roller traces, is observed in (a). As seen in (b), the free surface consists of microstructure of grains with about 3 μm size.

Figure 2 shows (a) the schematic diagram of the rapidly solidification apparatus and processed ribbon sample, (b) the micrograph of as-spun Fe-29.6at%Pd ribbon. The cross section of ribbon shows unevenness of columnar texture of about 20 μm. Moreover, there is a fine chilled region of 10-15 μm on roll contacting side.

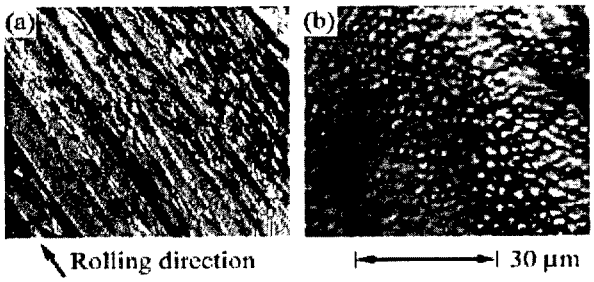


Fig. 1 Laser microscope photographs of (a) the contact surface and (b) the free surface of as-spun Fe-29.6at%Pd ribbon.

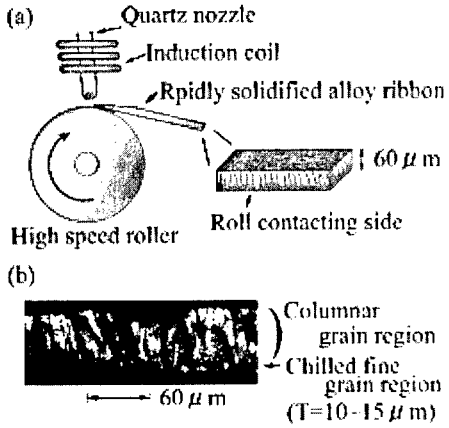


Fig.2 (a) Schematic diagram of the rapidly solidification apparatus and processed ribbon sample, (b) a micrograph of as-spun Fe-29.6at%Pd ribbon.

Figure 3 shows the XRD profiles of (a) roll contact surface and (b) free surface for as-spun and annealed ribbons. The fct martensite and fcc austenite phases coexist in the ribbon because fcc and fct {111} peak at near 2θ=42 K, fct(200), (020), fcc{200} and fct(002) peaks at 47 K<2θ<52 K arise in Fig.3. The second and third peaks are larger than the first one for the free surface, indicating that the ribbon has strong [100]-oriented texture. Moreover, the fct(200), (020) and fct(002) peaks characteristic of martensite phase increases after annealing at 1173 K for 1 h.

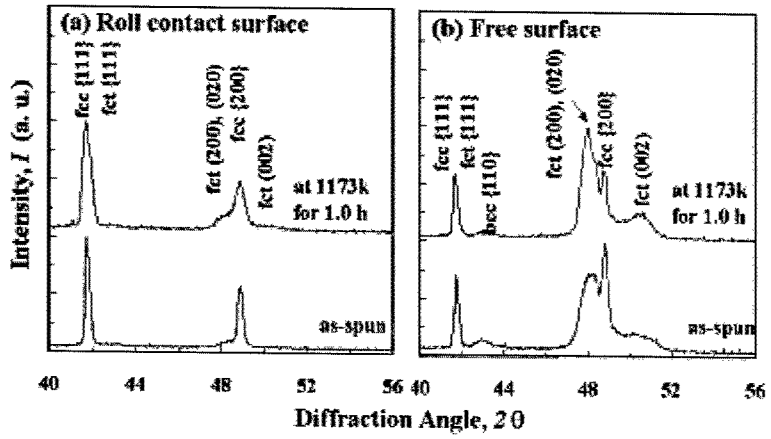


Fig. 3 XRD profiles on (a) roll contact surface and (b) free surface of as-spun and annealed Fe-29.6at%Pd ribbons.

Magnetic and magnetostriction properties

Figure 4(a) is the M–H loops of as-spun ribbon, where θ is the rotation angle between the transverse direction of ribbon and H, and θ=0 K and 90 K denote H parallel and perpendicular to plate of ribbon.

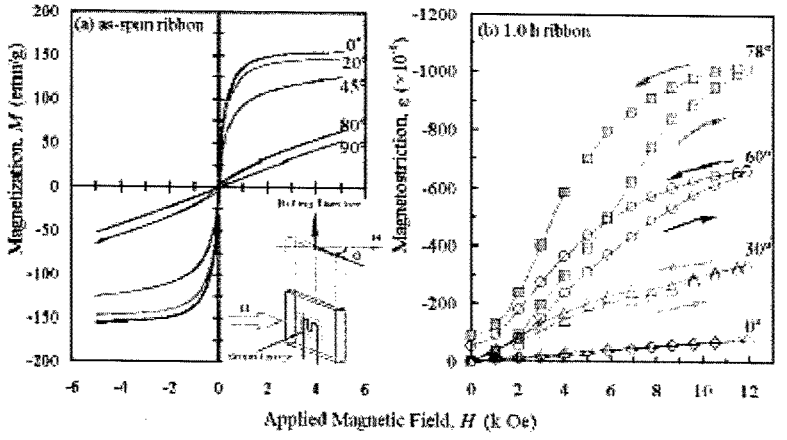


Fig. 4 (a) M–H loops of as-spun Fe-29.6at%Pd ribbon and (b) magnetostriction vs. H curves after annealing for 1 h at 1173K.

When H=2.5 kOe parallel to plate, the saturation magnetization Ms of ribbon is 153 emu/g, indicating that it is ferromagnetic. When H of 5 kOe applies to the θ=90 Kcase, the magnetization of ribbon can not be saturated because of a large demagnetizing field and the coercive force (Hc) is 65 Oe, which is larger than one for θ=0 K The above results indicate that the ribbon has magnetic anisotoropy. Figure 4(b) shows the magnetostriction ε vs. H curves of the ribbon annealed for 1 h at 1173 K, which measures change in strain in RD. The value depends remarkably on θ, and has a maximum of - 0.1 % strain at θ=78 Kdirection. The strain decreases with H and goes almost back to the H=0 value. The reason that the maximum arises at thickness direction is considered to be that [100] directions of the texture of ribbon are distributed around the center of pole figure [7].

Phase transition temperature

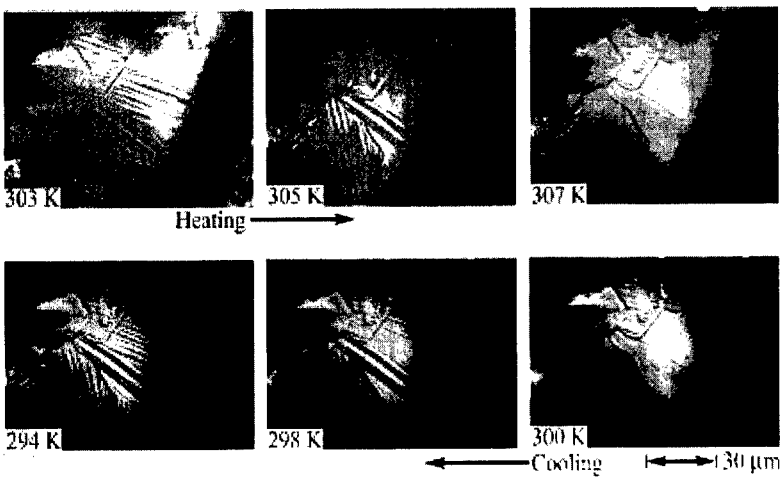


Fig. 5 Laser microscope photographs on surface of coarse grain (about 30μm).

Figure 5 shows the laser microscope photographs of surface of coarse grain (about 30 μm). On heating process, the martensite twin observed at 303 K disappears at 307 K. On cooling process, the same martensite twin is recovered at 298 K. From these results, A_f and the martensite starting temperature M_s of the grain are determined to be 307 K and 298 K, respectively, in almost agreement with the values obtained from XRD measurement for the same ribbon [4] and single crystals [6].

Dependence of the magnetostriction and shape recovery ratio of as-spun ribbon on temperature is shown in Fig. 6(a). The magnetostriction increases from 3.2×10^{-4} at room temperature to 7.0×10^{-4} at 376 K with temperature. In the range of T>376 K, the strain decreases and suddenly falls to 1.6×10^{-4}. We consider that this phenomenon is closely related with the mobility of martensite twin, that is, the mobility of variants is activated by heating, and a maximum strain arises near the phase transformation temperature, A_s. A_s and A_f of the ribbon are found to be 376 K and 450 K, respectively. Moreover, the shape recovery ratio Φ_{T2}/Φ_{T1} increases with temperature, where Φ_{T1} and Φ_{T2} are diameters of curled ribbon at 300 K and T K, respectively (see Fig. 6(b)). The variation is rapid in temperature ranges of 300-330 K and 380-420 K. These results suggest that the ribbon has two-step phase transformations from martensite phase to austenite one. Low A_s-A_f, 300-330 K is consistent

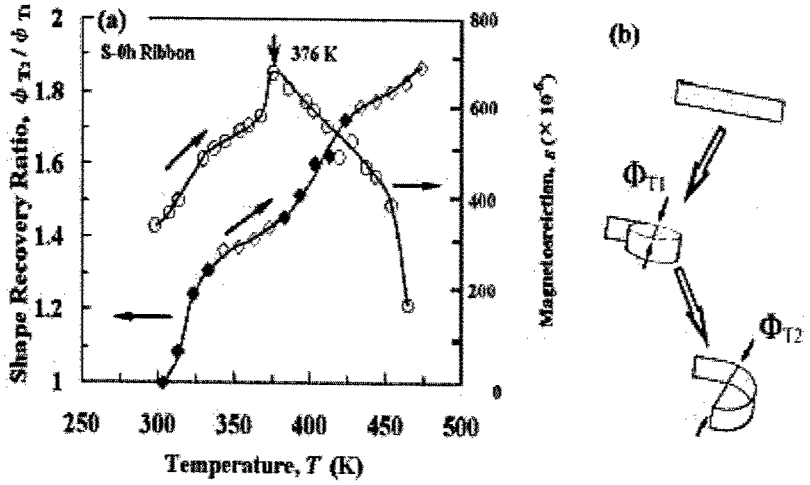


Fig. 6 Temperature dependence of the magnetostriction and shape recovery ratio of as-spun Fe-29.6at%Pd ribbon.

with the value obtained from laser microscope observation of the surface in Fig.5 and XRD [4]. Therefore, the low A_s-A_f is net phase transformation temperature of Fe-29.6at%Pd alloy. Note that high A_s-A_f, 380-420 K is peculiar to rapidly solidification ribbon.

Nano-scale composite structure



Fig. 7 High-resolution electron-microscope photograph of the inner part of ribbon.

To investigate the origin of high A_s-A_f, we observed inner part of ribbon by using high resolution electronic microscope. The observed photograph is shown in Fig.7. There, it is seen that grains of about 1μm size consist of fine layer-structures of 30–40 nm thickness. That is , they are martensite twins because the widths of dark and light layers are in the ratio of about 2 to 1. These nano-scale layers are parallel to the columnar structure which is in the same direction of thermal diffusion on roll. This nano-scale composite structure is stress-induced martensite twin. Therefore, it can be considered that nano-scale martensite twins make phase-transformation temperature increase from 300-330 K in surface to 380-420 K in inner part.

CONCLUSION

Rapidly solidification FSMA Fe-29.6at%Pd ribbon has two-step phase transformation temperatures. To investigate the origin, we observed the texture by using laser and high resolution electron microscopes. The cross-section of ribbon has columnar structure of about 10 μm in width. The ribbon consists of three parts: both upper and bottom surfaces have small grains of 2-3 μm with strong [100] texture and the inner part has fine layer-structures of 30–40 nm thickness in grains. It can be concluded that this nano-scale structure makes phase-transformation temperature increase.

REFERENCES

[1] K.Ullakko, J.K.Huang, V.V.Kokorin and R.C.O'Handley, Scr. Matter, 36, 1133 (1997).
[2] J.Koeda,Y.Nakamura, T.Fukuda, T.Kakeshita,T.Takeuchi and K.Kishio, Trans. Mater. Res. Soc.Jpn., 26, 215 (2001).
[3] H.Y.Yasuda, N.Komoto, M.Ueda and Y.Umakoshi, Sci.Tec.Adv. Mater., (2002) in press.
[4] T.Kubota, T.Okazaki, Y.Furuya and T. Watanabe, J.Magn. Magn. Mater., 239, 551 (2002).
[5] T.Kubota, T.Okazaki, H.Kimura, T. Watanabe, M.Wuttig and Y.Furuya, Sci.Tec.Adv. Mater., 2, 201 (2002).
[6] M.Sugiyama, R.Ohshima and F.E.Fujita, Trans.Mater.JIM, 25,585(1984).
[7] Y.Furuya, N.W.Hagood, H.Kimura and T.Watanabe, Trans.Mater.JIM, 39, 1248 (1998).

Mat. Res. Soc. Symp. Proc. Vol. 740 © 2003 Materials Research Society I12.17

Stoichiometry, crystallinity, and nano-scale surface morphology of the graded calcium phosphate-based bio-ceramic interlayer on Ti-Al-V

J. D. Long, K. Ostrikov, and S. Xu
Advanced Materials and Nanostructures Laboratory, Natural
Sciences, Nanyang Technological University, 637616 Singapore

V. Ligatchev
School of Electrical and Electronic Engineering,
Nanyang Technological University, Nanyang Avenue,
Singapore 639798, Singapore

ABSTRACT

A plasma-assisted concurrent Rf sputtering technique for fabrication of biocompatible, functionally graded CaP-based interlayer on Ti-6Al-4V orthopedic alloy is reported. Each layer in the coating is designed to meet a specific functionality. The adherent to the metal layer features elevated content of Ti and supports excellent ceramic-metal interfacial stability. The middle layer features nanocrystalline structure and mimics natural bone apatites. The technique allows one to reproduce Ca/P ratios intrinsic to major natural calcium phosphates. Surface morphology of the outer, a few to few tens of nanometers thick, layer, has been tailored to fit the requirements for the bio-molecule/protein attachment factors. Various material and surface characterization techniques confirm that the optimal surface morphology of the outer layer is achieved for the process conditions yielding nanocrystalline structure of the middle layer. Preliminary cell culturing tests confirm the link between the tailored nano-scale surface morphology, parameters of the middle nanostructured layer, and overall biocompatibility of the coating.

INTRODUCTION

Calcium phosphate-based bio-ceramics have recently attracted a great deal of interest as functional surface coatings in dental and orthopedic implants because of excellent bio-activity, bio-compatibility, chemical and mechanical properties [1-5]. In particular, hydroxyapatite (HA, $Ca_{10}(PO_4)_6(OH)_2$, Ca/P=1.67) coatings reveal inspiring clinical advantages in promoting efficient implant fixation and implant-to-bone adhesion shortly after the implantation, as well as faster bone remodeling due to enhanced bi-directional growth and formation of a bonding interlayer between bone and implant [1]. Furthermore, calcium phosphates with apatite-like structure are the major constituents of the bone mineral phase, are compatible with various soft and muscular tissue types, and can efficiently sustain protein attachment and growth [1]. Clinical applications of CaP-based bio-ceramics for improved fixation between bone and implant pose a number of challenges for tailoring the coating quality specifications. The key quality factors include stoichiometry, crystallinity, microstructure, metal-implant interfacial stability and several others [6]. In addition, a successful technique for fabrication of a viable biocompatible

coating would intrinsically imply a certain degree of replication of biological apatites, featuring nano-crystalline structures in bone and dentin materials. Above all, surface morphology with nano-scale features and excellent island uniformity, appears to be a critical factor in promoting bio-molecule/protein - surface interactions.

Thus, fabrication of a graded bioceramic-implant structure capable of simultaneously satisfying the basic requirements for the interfacial stability at the coating-implant interface, controllable stoichiometry and crystallinity in the bulk, and the optimized, from the point of view of sustained protein attachment and growth, nano-scaled surface morphology, is a critical problem in the biomaterials research. In particular, a large number of the existing techniques for CaP-based films (including HA) deposition suffer from poor coating-metal implant interfacial bonding strength, excessive amorphosity or larger, than in natural apatites, crystal size in the bulk, as well as irregular surface morphology features typically in the micrometer range.

EXPERIMENTAL DETAILS

Here, we report on a new and efficient technique for synthesis of a graded CaP-based biocompatible interlayer on orthopedic alloy Ti-6Al-4V, consistently satisfying all the above requirements. The essential part of the method is a concurrent low-temperature plasma-assisted Rf magnetron sputtering (PA-RFMS) of crystalline HA and metallic titanium targets in low-pressure discharges of reactive gas mixtures of argon and water vapor sustained in PSAC/PA-RFMS facility. The titanium target has purposely been introduced to create a titanium-rich layer adjacent and stronger adhering to the implant-simulating metallic sample. The discharges were sustained in the range of Rf powers of P_{in} = 300 - 700 W applied to a water-chilled Rf magnetron electrode with several rows of concentrically positioned permanent magnets with specific polarities. The working pressure p_0 was typically maintained in the range of 10 to 70 mTorr. In this pressure and power range, large DC sheath potentials near the HA/Ti target surface, promoting high sputtering yields, and eventually high film deposition rates, can be achieved. An electrically floating substrate heater powered by an external temperature controller supports the Ti-6Al-4V samples, with the surface being coated facing downwards, approximately 6 cm above the HA/Ti sputtering target. In the experiments, the substrates were negatively biased with V_b = 25 - 200 V. Chemical composition and elemental bonding states in the interlayer were studied by VG ESCALAB 220i-XL spectrometer (XPS). The crystal structure was characterized using SIEMENS D5005 X-Ray diffractometer (XRD) in a lock coupled ($\theta - 2\theta$) mode with an incident x-ray wavelength of 1.540A (Cu Kα line). Cross-sectional structure of the functionally graded structure was examined with the Field Emission Scanning Electron Microscopy (FESEM). Nano-scaled features of the surface morphology were studied by the Atomic Force Microscope in a contact mode (AFM). Bio-ceramic-metal interfacial bonding strength was assessed via a Micro-scratch teste. Further details of the PSAC/PA-RFMS sputtering facility, routine steps in pre-deposition substrate treatment, as well as film characterization instruments and techniques, can be found elsewhere [7,8].

RESULTS AND DISCUSSION

XPS layer-by layer analysis of the composition and chemical bonding states reveals clear presence of Ca, P, O, and Ti in the film, the concentration of the latter being gradually increased towards the bottom layer of the coating. In addition, varying the DC substrate bias V_b and deposition pressure p_0, one can efficiently control the elemental composition and Ca/P ratio (Fig.1), which is a key factor defining the phases of apatite. In particular, a near-stoichiometric HA (Ca/P ~ 1.67) can simply be achieved by applying DC bias of V_b= -100 V at p_0=70 mTorr. The elemental presence in the bulk of the coating is measured to be approximately Ca (27 %), P (15 %), O (50 %), and Ti (5 %). Furthermore, most of calcium and phosphorus in the film enter calcium phosphate phase, whereas titanium is predominantly a part of $CaTiO_3$ and TiO_2. Formation of the phosphate phases is further supported by the results of FTIR analysis (Perkin Elmer Spectrum I spectrometer) showing the characteristic absorption peaks of PO_4^{3-}. Thus, the results of the XPS and FTIR analysis confirm that stoichiometry, elemental composition, and bonding states in the coating in question can indeed be tailored by varying the substrate bias, and under certain conditions the near-stiochiometric phase of HA can be synthesized.

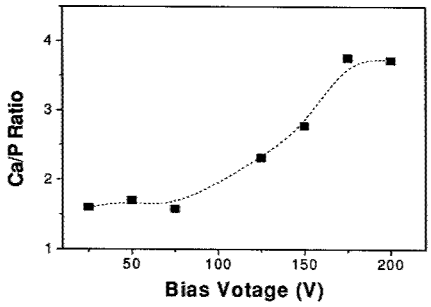


Figure 1. Ca/P ratio versus DC bias voltage

The XRD spectrum of the film prepared at P_{in}=700 W and p_0=70 mTorr is presented in Fig.2, suggesting preferential crystal growth along (130) or (132) planes depending on deposition parameters. Furthermore, the diffraction pattern suggests presence of monoclinic crystalline tetracalcium phosphate $Ca_4P_2O_9$ (TTCP) structure. It is remarkable that the diffraction pattern is strongly affected by variation of the substrate bias and working pressure. An amorphous phase is observed to be characteristic to weakly biased films. A close examination of the broadening nature of the diffraction peaks reveals that the films prepared at higher negative bias feature clear nanocrystal structures (see, for example, (132) plane), and the (132) direction becomes a preferential crystal growth plane at substrate biases exceeding 150 V. It is also worth noting that a high crystallinity of the coating can be achieved at lower working pressures and moderate substrate biases.

Cross-sectional structure of the graded CaP-based film on Ti-6Al-4V has been analyzed using FE SEM. The total thickness of the CaP-based interlayer appears to be approximately 200 nm, and it contains three major areas namely, adjacent to the implant alloy, bulk area, and outer surface area (the latter to be in contact with bone tissues). Furthermore, cross-sectional SEM imaging (not shown here) suggests about formation of a functionally-graded titanium-embedded CaP-based graded coating on Ti-6Al-4V alloy.

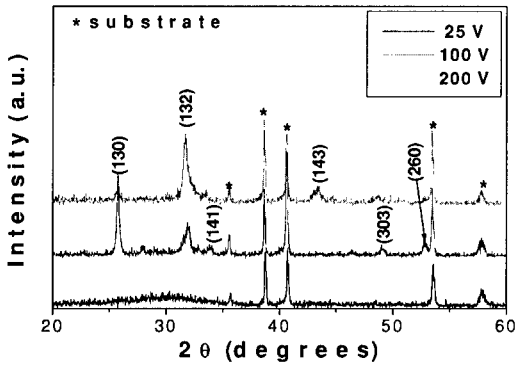


Figure 2. Typical XRD spectra from Ca-P-Ti thin films at different DC substrate bias.

Nano-scaled surface morphology of graded CaP-based crystalline interlayers was analyzed with the Atomic Force Microscopy. Fig.3 demonstrates remarkable changes in surface morphology with variation of the substrate bias. Indeed, V_b affects homogeneity of distribution and architecture (e.g. sharpness) of the elements of morphology as well as inter-element spacing and surface areas in the "humps" and "dips". We note that homogeneous distribution of very much similar by shape and size nano-sized morphology elements over the micro-scaled surface area is ideal for promoting biomolecule/protein attachment and growth. Furthermore, sharp "humps" and smooth "dips" are especially desirable for this purpose, which has recently been confirmed by cell culturing experiments on ordered arrays of sharp pillars. The inspiring conclusion that can be drawn from the AFM analysis is that all the above quality factors of the surface morphology of the outer functional layer are met for the films prepared at V_b = -100 V (Fig.3a). The latter suggests direct link between the origin of nano-crystalline structure reflected in Fig.2, and self-organization of the outer functional layer, which can be inferred as a possible reason for preferred nano-crystalline self-assembly of natural apatites in various bone embodiments. The AFM data thus confirm a challenging opportunity of controlling the nano-scale surface morphology of the outer layer of the graded structure by varying the process parameters.

Meanwhile, the entire coating strongly adheres to the Ti-6Al-4V alloy, which has convincingly been confirmed by the interfacial bonding strength measurement with the Mi-

croscratch test. The critical load that the coating can withstand ranges from 2.0 N to 5.7 N. It is notable that the best interfacial strength is achieved for moderately-biased and higher pressure-grown coatings with well-resolved nano-features. We remark that higher gas pressures favor enhanced sputtering of the titanium target, thus eventually improved doping of the bottom layer by titanium/titania in the atomic/molecular or nanocluster states.

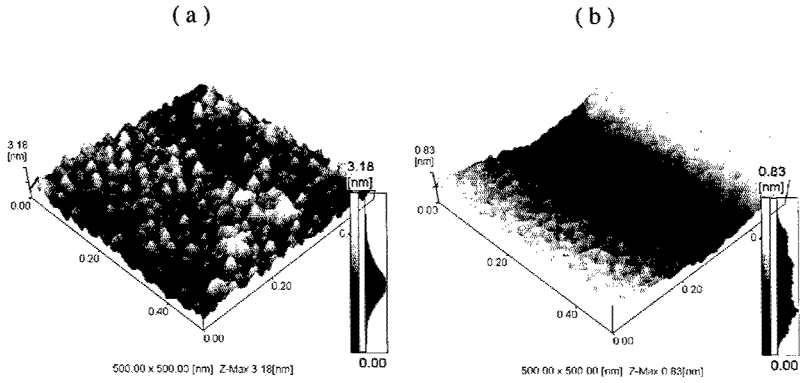


Figure 3. AFM images of the outer nano-sized layer of Ca-P-Ti coating deposited at –100 V (a) and –50 V (b) DC bias.

It is notable that preliminary *in-vitro* cell culturing tests on the graded CaP-based interlayer suggest promising biocompatibility of the coating. The relevant imaging reveals well-preserved cyto-sceletal structure of COS7 monkey kidney cell series after up to 48 hours after cell culturing. The work is continuing into *in-vivo* assessments of these bioactive HA films.

CONCLUSION

In summary, the plasma-assisted concurrent Rf sputtering in low-temperature, low-pressure reactive environment offers a great deal of control of the major coating quality parameters, including functional grading, stoichiometry, phase purity, chemical composition, crystallinity, crystal size, interfacial bonding strength, as well as of tailoring the nano-scale features of the surface morphology of the outer thin (few nm) layer with specific bio-active functionality. Another unique features of this technique include, but are not limited to, low-temperature, no need for post-treatment, easy deposition process control, etc. From practical considerations, the technique proposed is indeed promising to mimic a number of the basic parameters of natural bone minerals via tailoring certain features at nano-scales, such as nano-crystalline structure and surface morphology. Successful cell culturing tests have demonstrated excellent *in-vitro* biocompatibility, which sounds favorably in view of future *in-vivo* studies. Finally, the results obtained have further supported the usefulness of nano-scale approach for assembly of functionally graded

coatings and give us a hope that such an approach will soon be widely adopted for a wider class of nano- and bio-materials.

ACKNOWLEDGMENTS

This work was supported in part by the Agency for Science, Technology, and Research of Singapore (Project No. 012 101 00247). The authors are grateful to J. H. Lu for his assistance in in-vitro analyses of the films. Fruitful discussions with N. Voelcker, S. Kumar, I. Brown, and C. H. Diong are also gratefully acknowledged.

REFERENCES

1. L. Sun, C. C. Berndt, K. A. Gross, A. Kucuk, *Journ. Biomed. Mater. Res.: Appl. Biomater.* **58**, 570 (2001).
2. C. C. Berndt, G. H. Haddad, A. J. D. Farmer, K. A. Gross, *Mater. Forum* **14**, 161 (1990).
3. Y. C. Tsui, C. Doyle, T. W. Clyne, *Biomaterials* **19**, 2031 (1998).
4. C. K. Wang, J. N. Chern Lin, C. P. Ju, H. C. Ong, P. R. H. Chang, *Biomaterials* **18**, 1331 (1997).
5. R. G. T. Geesink, K. D. Groot, C. P. A. T. Klein, *Journ. Bone Jt. Surg.* **70-B**, 17 (1988).
6. J. Gomez-Morales, J. Torrent-Burgues, T. Boix, J. Fraile, R. Rodrigues-Clemente, *Cryst. Res. Technol.* **36**, 15 (2001).
7. S. Xu, J. D. Long, J. H. Lu, K. N. Ostrikov, and C. H. Diong, *IEEE Trans. Plasma Sci.* **30**, 118 (2002).
8. S. Xu, J. D. Long, K. N. Ostrikov, and H. Y. Foo, *Key Eng. Mater.* **240**, 307 (2002).

Mat. Res. Soc. Symp. Proc. Vol. 740 © 2003 Materials Research Society I12.21

PREFERRED ORIENTATION IN FIBERS OF HIPCO SINGLE WALL CARBON NANOTUBES FROM DIFFUSE X-RAY SCATTERING

W. Zhou, K. I. Winey, J. E. Fischer
Department of Materials Science and Engineering, University of Pennsylvania, Philadelphia PA;
S. Ramesh, R. K. Saini, L. M. Ericson, V. A. Davis, M. Pasquali, R. H. Hauge, R. E. Smalley
Center for Nanoscale Science and Technology, Rice University, Houston TX.

ABSTRACT

Neat Fibers of HiPco single wall carbon nanotubes extruded from strong acid suspensions exhibit preferred orientation along fiber axes. We characterize the extrusion-induced alignment using x-ray fiber diagrams and polarized Raman scattering, using a model which allows for some fraction of the sample to remain completely unaligned. We show that both x-ray and Raman data are required for a complete texture analysis of SWNT fibers.

INTRODUCTION

Macroscopic oriented arrays of single wall carbon nanotubes (SWNT) [1-4] could be the starting point for the construction of useful structures which maintain a high degree of the excellent axial properties expected from perfect SWNT. Such nanotubes produced by the HiPco process [5] offer promise for high strength, light weight, electrically conducting structural elements at lower cost than other nanotube forms. The properties of HiPco fibers will depend on the degree of SWNT alignment [6]. In this paper we study the preferred orientation by combining diffuse x-ray and polarized Raman scattering [7].

EXPERIMENTAL DETAILS

Fibers were produced from purified HiPco SWNT [8] containing less than 1 at.% residual metal catalyst. Nanotubes were mixed with oleum or 100% sulfuric acid, concentrations up to 8 wt.%, at ~110°C for 24 hours with constant argon flow to eliminate moisture. Mixing at low concentration was achieved by a low shear magnetic stirring while medium shear double helix mixer was used for high concentrations. Fibers were then extruded into a coagulation bath using a syringe with no drawing applied. Different diameter fibers were produced by using syringe needles with different inside diameters. Detailed description can be found elsewhere [9].

Texture analysis was done on 3 fibers, all produced from HiPco batch 93 (purified) under different experimental conditions. HPR93a was extruded from 8% SWNT in 100% sulfuric acid through a 500 micron syringe needle; HPR93b was 6% SWNT through a 125 micron syringe; HPR93c was 6% SWNT through a 250 micron syringe. No mechanical stretching was applied during or after coagulation. The diameters of 3 fibers were 220, 60 and 110μm respectively, about a factor of two smaller than orifice due to collapse of the gel state. The nanotubes in neat fibers are heavily p-doped by sulfuric acid. To measure the intrinsic properties we annealed neat fibers either in flowing argon at 1100°C for 24 hours or in vacuum at 1150°C for 2 hours using a slow temperature ramp [10]. Most acid residue and some amorphous carbon were expected to be removed in the annealing process.

Texture analysis was done on neat and annealed fibers by combining x-ray diffuse and polarized Raman scattering. X-ray scattering was performed on a multi-angle diffractometer equipped with Cu rotating anode, double-focusing optics, evacuated flight path and 2-D wire detector. All samples were measured in transmission for 2 hours. For large diameter fibers, a single piece gave enough signal; for small diameters several pieces were carefully assembled parallel to each other. Polarized Raman measurements were done in VV geometry on a Renishaw Ramanscope 1000 system using 514.4 nm excitation. Both x-ray and Raman data were analyzed with a "2-phase" model described here, to account for both aligned and unaligned SWNT.

RESULTS AND DISCUSSION

HiPco SWNT exhibit weak or no x-ray Bragg intensity due to the broad diameter distribution [11]. Our fibers of HiPco also exhibit poor crystallinity, and the x-ray scattering in the wide angle region (Q>0.1) is made up of diffuse scattering from isolated tubes and poorly crystallized large bundles, plus the low Q tail of small-angle x-ray scattering (SAXS) from uncorrelated pores, impurity particles etc. The SWNT-related diffuse scattering should in principle follow the Bessel function form factor of a cylindrical shell of charge [12], but the oscillations are smeared out and we observe monotonically decreasing intensity with increasing Q which cannot be separated from non-SWNT-related scattering. On the other hand it is reasonable to assume that only the SWNTs contribute to the observed anisotropy. Therefore we can obtain reliable distribution widths that characterize the aligned SWNTs, but we learn nothing about unaligned SWNTs. In previous studies the on fibers or mats diffuse scattering was classified with the sample-independent background and only the weak Bragg intensity was considered [3].

X-ray profiles (obtained by azimuthal integration of the 2D data) from neat HPR93a fibers are shown in Fig.1. No Bragg peaks were detected from the neat fiber; the broad peak at Q ~ 1.6 A^{-1} is most likely due to acid residues since amorphous carbon is effectively removed by the purification scheme. After vacuum annealing we observe stronger low-Q scattering, 3 weak Bragg peaks near 0.45, 0.75 and 1.1 A^{-1}, and the disappearance of the broad peak at 1.6 A^{-1}. We attribute these changes to removal of acid residues and partial reorganization of tubes within bundles. Although vacuum annealing improved the crystallinity of nanotubes to some extent, the main contribution to SWNT scattering remains diffuse.

From the 2D data sets, we take sectors along the radial Q direction out of 1^{o} wedges and plot their intensity vs. azimuthal angle χ. Preferred orientation is then deduced in the range of $0.35 < Q < 0.55$. In Fig.2(a) we show the result from the neat fiber HPR93c. The solid curve is the least squares fit to Gaussians centered near χ=0° and 180° plus a constant, where the fiber axis is perpendicular to these maxima. The constant corresponds to isotropic scattering from both non-SWNT constituents and unaligned tubes. The Gaussians are fully attributed to nanotube alignment. We term this analysis the "2-phase" model. The fitted Gaussian FWHMs are 63°, 55° and 45° for neat fibers a, c and b respectively, where b was spun from 6% SWNT through the 125 μm orifice. Similar results were obtained from the annealed counterparts. Fitted values are collected in Table I.

Texture is also revealed in the small angle diffuse scattering. Figure 2(b) shows the azimuthal dependence of the Q-integrated intensity from 0.035 to 0.070 A^{-1} for annealed sample c. The corresponding FWHM, 58°, was only slightly larger than the high Q result. Since the scattering bodies are rod-like nanotube bundles or aggregates, we assign the anisotropic SAXS to the preferred orientation along the fiber axis of these rod-like objects.

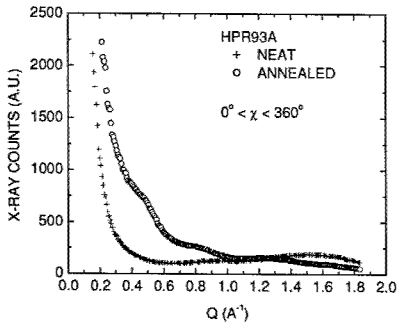


Figure 1. X-ray scattering from neat and annealed fiber HPR93a. Samples are in transmission geometry. Profiles are obtained by azimuthal integration of the 2D data.

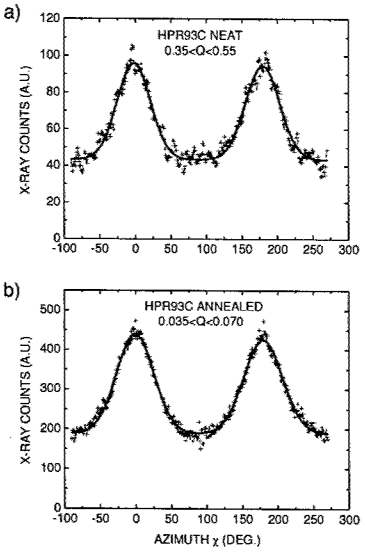


Figure 2. Background-subtracted X-ray counts, summed over certain Q intervals, every 1° in χ. Data are the symbols; fits to two Gaussians plus a constant are the smooth curves. Top: neat HPR93c; Bottom: annealed HPR93c.

Raman measurements using VV polarization were carried out at many angles Ψ between the fiber axis and polarization vector, to obtain a characteristic distribution analogous to x-ray fiber diagrams [6,10]. We used the same "2-phase" model as for our x-ray analysis. The fibers are axially symmetric so the distribution function has cylindrical symmetry. We accounted for

anisotropic optical attenuation by the nanotubes; $f_{abs} \propto 1/(\cos\phi + K \sin\phi)$ where ϕ is the angle between polarization vector and *nanotube* axis and $K = \alpha_\perp / \alpha_\parallel$ ($\alpha_\parallel$ and $\alpha_\perp$ are the components of polarized absorption coefficients) [3]. It is believed that K is between 0 and ¼ for the wavelength of interest. In principle, both the aligned fraction A and FWHM are obtained by fitting the deviation from a $f_{abs}\cos^4\Psi$ law for 100% perfectly aligned tubes. Due to the large error bar of the Raman data, it's almost impossible to reliably fit A and FWHM simultaneously. Thus, we input the FWHM from the x-ray analysis and perform a one-parameter fit to the Raman data that optimizes A.

Peak intensities of the tangential Raman G_2-band at 1590 cm^{-1} were recorded from 3 different 2 μm spots to account for inhomogeneity in the fiber, at each of 7 Ψ values. Analysis is shown in Fig.3. Least squares fits assuming K=1/8 show that the aligned fractions for neat HPR93 a, c and b are 0.83, 0.90 and 0.94 respectively. Slightly smaller or larger values result from assuming K=0 and ¼ respectively, from which we estimate the error on A to be ±0.02. Note that A decreases with decreasing orifice diameter. An obvious explanation is that smaller orifices do a better job of excluding or breaking up the undispersed aggregates. Small increases in A were observed after annealing, Table I.

From Raman spectra, it is also found that the shapes of the RBM band and G band are quite different for neat and annealed fibers, as shown in Fig.4. This is mainly because neat and annealed samples are under different resonance conditions. The neat fibers are heavily p-doped and the doping shifts the Fermi energy, thus certain tubes in neat fibers lost Raman resonance. The annealing process at high temperature de-doped the nanotubes so that the Raman spectra of annealed fibers resemble those of ordinary HiPco materials [11].

SUMMARY

HiPco fibers produced by simply extruding a strong acid suspension of SWNT exhibit moderate nanotube alignment. Further improvements may be expected by applying additional extensional flow or stretching in the gel state [13]. Structural analysis by combining x-ray and Raman scattering unambiguously shows that more dilute SWNT suspension and smaller diameter syringe needle generally result in fibers with better alignment. The synthesis parameters and texture analysis fit parameters for both neat and annealed fibers are summarized in Table I. For the first time, we show that fiber diagrams can be obtained from diffuse X-ray scattering of nanotubes. We also show that a complete fiber texture can be determined by combining x-ray fiber diagram and Polarized Raman scattering, using a "2-phase" model which allows for a fraction of the sample to remain completely unaligned. Results of this analysis are used to optimize the fiber process. Correlation between texture and anisotropic thermal and electrical properties will be reported elsewhere.

ACKNOWLEDGEMENTS

This research was supported by the Office of Naval Research Grant No. N000140010720 and N000140010657.

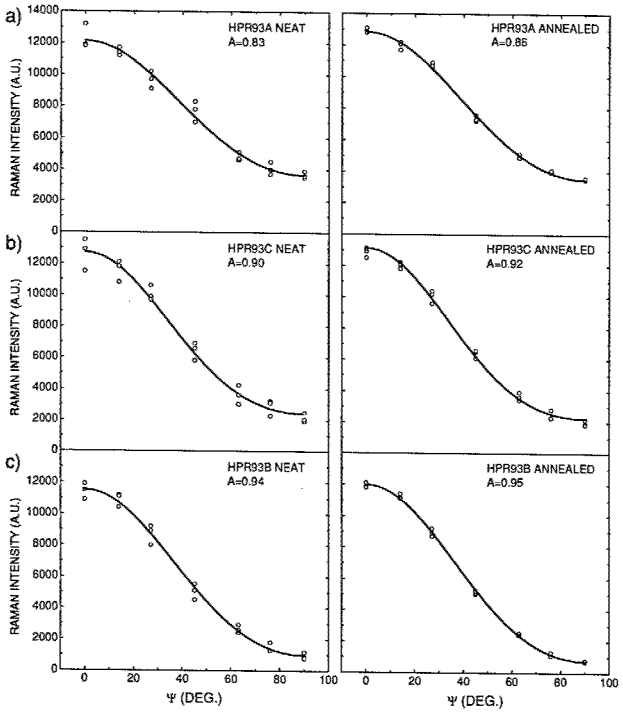


Figure 3. Analysis of polarized Raman spectra. Symboles are Raman G2-band intensities, measured on 3 spots on the sample, versus the angle between polarization and fiber axis for HPR93A (top), C (middle) and B (bottom). Solid curves are least square fits to the model described in the text, with fitted aligned fraction indicated in the figures.

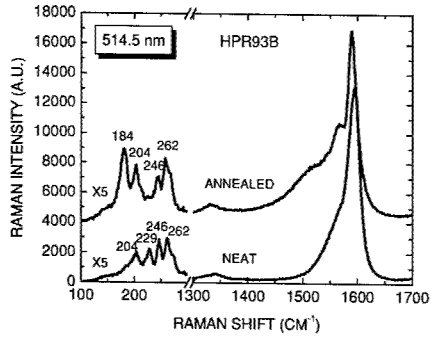


Figure 4. Raman spectra of neat and annealed fiber HPR93B. Note the difference of both RBM band and G band between neat and annealed fibers.

Table I. Summary of the synthesis parameters, texture analysis fit parameters for neat and annealed HiPco fibers.

	HPR93A		HPR93C		HPR93B	
Concentration	8 wt.%		6 wt.%		6 wt.%	
Orifice (μm)	500		250		125	
	Neat	Annealed	Neat	Annealed	Neat	Annealed
FWHM(deg.)	63	64	55	54	45	43
Aligned Fraction, A (±0.02)	0.83	0.86	0.90	0.92	0.94	0.95

REFERENCES

1. L. Jin, C. Bower and O. Zhou, Appl. Phys. Lett. **3**, 1197 (1998).
2. J. C. Hone, M. C. Llaguno, N. M. Nemes, J. E. Fischer, D. E. Walters, M. J. Casavant, J. Schmidt and R. E. Smalley, *Appl. Phys. Lett.* **77**, 666 (2000).
3. P. Launois, A. Marucci, B. Vigolo, A. Derre and P. Poulin, J. Nanoscience and Nanotechnology Vol. 1 (2001) pp125-128.
4. J. E. Fischer, W. Zhou, J. Vavro, M. C. Llaguno, C. Guthy, R. Haggenmueller, K. I. Winey, M. J. Casavant and R. E. Smalley, J. Appl. Phys. (Submitted)
5. Michael J. Bronikowski, Peter A. Willis, Daniel T. Colbert, K. A. Smith, and Richard E. Smalley, J. Vac. Sci. Technol. A **19**, 1800 (2001)
6. R. Haggenmueller, H. H. Gommans, A. G. Rinzler, J. E. Fischer and K. I. Winey, Chem. Phys. Lett. **330,** 219 (2000).
7. H. H. Gommans, J. W. Alldredge, H. Tashiro, J. Park, J. Magnuson and A. G. Rinzler, J. Appl. Phys. 88, (2000) 2509.
8. I. W. Chiang, B. E. Brinson, A. Y. Huang, P. A. Willis, M. J. Bronikowski, J. L. Margrave, R. E. Smalley, and R. H. Hauge, J. Phys. Chem. B, 105(35), 8297 (2001)
9. Virginia A. Davis, Lars M. Ericson, Rajesh Saini, Ramesh Sivarajan, R. H. Hauge, Richard E. Smalley and Matteo Pasquali, AIChE proceedings (2001)
10. A. G. Rinzler, J. Liu, P. Nikolaev, C. B. Huffman, F. J. Rodriguez-Macias, P. J. Boul, A. H. Lu, D. Heymann, D. T. Colbert, R. S. Lee, J. E. Fischer, A. M. Rao, P. C. Eklund, and R. E. Smalley, Applied Physics A **67**, 29 (1998).
11. W. Zhou, Y. H. Ooi, R. Russo, P. Papanek, D. E. Luzzi, J. E. Fischer, M. J. Bronikowski, P. A. Willis and R. E. Smalley, Chem. Phys. Lett. **350,** 6 (2001).
12. A. Thess, R. Lee, P. Nikolaev, H. Dai, P. Petit, J. Robert, C. Xu, H. Lee, S.G. Kim, D. T. Colbert, G. Scuseria, D. Tomanek, J. E. Fischer and R. E, Smalley, Science **273**, 483 (1996).
13. Brigitte Vigolo, Pascale Launois, Marcel Lucas, Stéphane Badaire, Patrick Bernier, and Philippe Poulin, Mat.Res.Soc.Symp.Proc., 706, Z1.4.1 (2002)

Mat. Res. Soc. Symp. Proc. Vol. 740 © 2003 Materials Research Society I12.24

Polymer-Attached Functional Inorganic-Organic Hybrid Nano-composite Aerogels

Xipeng Liu, Mingzhe Wang and William M. Risen, Jr.
Department of Chemistry, Brown University, Providence, RI 02912-9108, USA

ABSTACT

Novel materials in which modified inorganic-organic hybrid silica aerogels are attached to polymer chains have been synthesized. The aerogels are based on chitosan, a bioderived polymer from chitin, and they contain silica. The first stage of the modifications includes attachment of isocyanate, amine onto the chitosan chains embedded within the aerogel. These groups are employed in the second stage to develop the reactions required to "string" aerogel particles along functionalized linear polymers or to employ these polymers to crosslink the composite aerogels. The initial chitosan-silica aerogel particles have an ultimate size of about 2nm, and their functionally modified forms were reacted at sizes up to 1 μm. These aerogels can take up and hold dyes and water-soluble drugs. The chemistry to synthesize polyamino-siloxane based aerogel composite was discussed. In addition, two approaches to synthesize PHEMA aerogel hybrid were studied.

INTRODUCTION

Chitosan silica aerogels in transparent or translucent monolithic solid form have been synthesized by an initial sol-gel process, followed by extraction with supercritical CO_2 [1-6]. The chitosan silica aerogels have high porosity, up to 95%(v/v), and densities ranging from 0.2 to 0.3g/cm^3. The chitosan silica aerogels have average pore size of 3-5nm[2-3]. They have a three dimensional network which can be thought of as a Si-O-Si bonded framework with the chitosan polymer winding through the network like a snake that interacts with silica by both hydrogen bonds and Si-O-C bonds.

In recent work, we have demonstrated that the amine groups on the chitosan in the silica network are able to react with externally provided compounds. Thus, it is possible to carry out reactions on the chitosan molecule that is essentially suspended in the dry aerogel space. That makes it feasible to do chemical reactions where water must be excluded on a molecule (chitosan) that otherwise would only be available in solvents with active hydrogen [7]. Small molecules such as bis (4-isocynatocyclohexyl) methane (HMDI), succinic anhydride (SA), isocyanatoethyl methacrylate (IEMA), and dansyl chloride (DC) have been used in this work to modify the chitosan in aerogel through chemical reactions with amines present in chitosan [7].

Of particular interest are the reaction of HMDI with chitosan silica aerogel, which results in a new -NCO terminated material, and, the reaction of IEMA with chitosan silica aerogel to produce a methacrylate terminated new aerogel material. They are valuable not only because they have new physical properties, but also because they bring new functional groups into these aerogels, making it possible to carry out new chemistries. This should lead to novel materials with varied properties.

One possibility is to attach these -NCO terminated aerogel particles in the 100nm to 1μm size range to linear polymers such as poly (allyamine), aminopropylmethylsiloxane-dimethylsiloxane copolymer, or poly (2-hydroxyethyl methacrylate) (PHEMA).

The aminopropylmethylsiloxane-co-dimethylsiloxane copolymers are soluble in organic solvents that do not have active hydrogen, so it should be possible to carry out the reaction

between chitosan-silica aerogel particles with pendant -NCO-containing moieties, on one the hand, and amine groups on the substituted siloxane copolymer, on the other. However, poly (allyamine) and PHEMA are not very soluble in non-polar organic solvents that do not have active hydrogen atoms. Thus, reactions between pendant -NCO and $-NH_2$ or -OH groups, in which water has to be excluded, have been carried out in neat phases. Through such reactions, novel materials have been formed consisting of the polymer chain with aerogel attached, as shown conceptually in Figure 1.

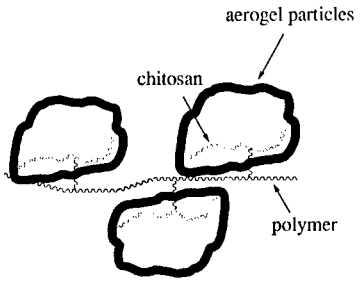


Figure.1 Schematically showing the structure of aerogel particles attached linear polymer.

The PHEMA polymer is an important polymer, which is widely used in biomedical applications due to its biocompatibility, high permeability and hydrophilicity. An aerogel attached PHEMA, could combine many of the valuable properties of this polymer and of chitosan-silica aerogel, and useful to investigate. It has been approached by combining the solid aerogel phase with solid polymers, and by two additional methods involving copolymerization of monomer 2-hydroxyethyl-methacrylate and methacrylate-terminated aerogel.

By grinding monolithic chitosan-silica aerogel pieces, particles of aerogel can be obtained so that a functional group on a chitosan silica aerogel particle can react with a polymer molecule. It is useful to explore the reaction under concentration conditions that tend to favor a particle attached to a polymer molecule over these that favor a networks structure with chitosan silica aerogel particles serving as the crosslinking reagents. In this paper, we address the synthesis of two types of polymer-chitosan aerogel hybrid bonds. The first involves -NCO terminated aerogel reacting with aminopropylmethylsiloxane-dimethylsiloxane copolymer, and the second two methods are used to form chitosan aerogel PHEMA hybrids.

EXPERIMENTAL SECTION

1. Synthesis of isocyanate terminated chitosan-silica aerogel, X-SiO_2-NCO

The 10%(w/w) chitosan-silica aerogel was synthesized in our previous work [7]. The bulk pieces of these aerogel were ground into fine powder. The 0.176 g of the powder was combined with 0.360 g dicyclohexylmethane-4, 4' diisocyanate (HMDI, Bayer Corp.) in a 20 ml glass vial and 2ml THF was added to serve as solvent. After the mixture reacted for 3hrs at room temperature, the product was washed by THF for 6 times. For each time, 15 ml fresh THF was added and after 30 mins, the supernatant solvent was discarded. After it was washed, the product was dried in vacuum and its FT-IR spectrum was measured.

2. Reaction of X-SiO_2-NCO with amine pendant siloxane copolymer

A 0.06 g NCO-terminated aerogel was mixed with 0.6 g 4-5% aminopropylmethylsiloxane-dimethylsiloxane copolymer (AMS-152, Gelest, INC.) in a 20ml glass vial. After reacting for 40 minutes at room temperature, the mixture was washed by THF using the technique described above. Then the product was dried in vacuum and its FT-IR spectrum was measured. To make it clear that there is no interference from trace of water during the washing process, a blank sample of the isocyanate-terminated aerogel was washed the same way as a control.

3. Reactions of X-SiO_2-NCO with HEMA monomers

First, 0.0366 g HMDI modified chitosan silica aerogel, X-SiO_2-NCO, calculated amount of 2-hydroxyethyl methacrylate (HEMA, Aldrich) monomer and dibutyltin dilaurate catalyst were mixed in a 20 ml glass vial. After it was heated at 67^{0}C for 7 hrs, the mixture was washed by THF and then vacuum dried.

Second, 0.057 g HMDI modified chitosan silica aerogel, X-SiO_2-NCO, was mixed with calculated amount of HEMA and dibutyltin dilaurate catalyst. After it was heated at 67^{0}C for 12 hrs, the mixture was washed by THF, and vacuum dried.

4. Synthesis of chitosan-silica aerogel pendant PHEMA hybrid composite by copolymerizing methacrylate terminated aerogel with HEMA monomer.

First, 0.2 g chitosan silica aerogel particles were mixed with 0.2 g isocyanatoethylmethacrylate (IEMA, Aldrich) in 5ml THF and reacted for 30 minutes at room temperature. The mixture was washed by THF and vacuum dried. A methacrylate-terminated aerogel was obtained. Second, 0.047 g this product was mixed with 0.57g HEMA monomers and 0.014g AIBN in 5 ml THF. The mixture was heated at 62°C for 30 minutes, then cooled down to room temperature for another 3 hours. Then the product was washed by THF and dried in vacuum. And its FT-IR spectrum was measured.

Infrared (FT-IR) spectra were measured on all samples using a Perkin Elmer 1600 spectrometer.

RESULTS AND DISCUSSION

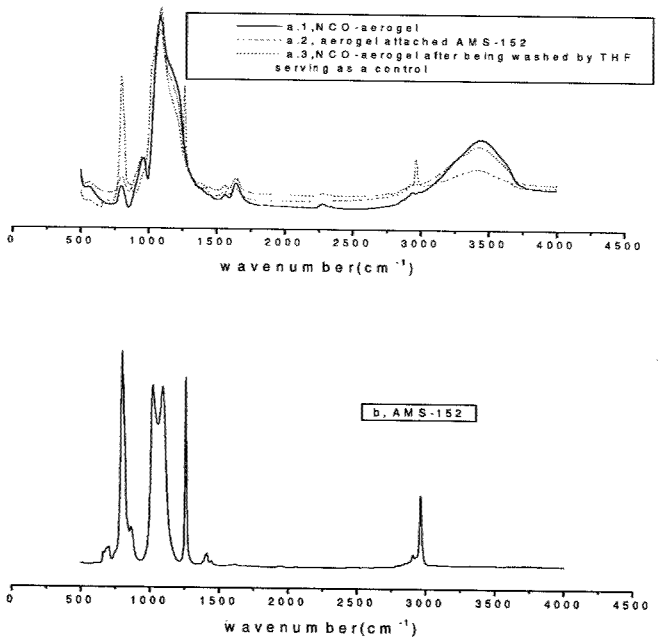


Figure 2, FT-IR spectra of (a.1) NCO-aerogel; (a.2) aerogel attached AMS-152; (a.3) NCO-aerogel after being washed by THF severing as a control of a.2; (b), AMS-

In the reaction of X-SiO_2 aerogel with HMDI, the amine groups on chitosan reacted with one isocyanate group of each HMDI. Thus, a urea linkage -NH-(C=O)-NH-, which has characteristic absorptions at 1660 cm^{-1} and 1560 cm^{-1}, is formed at one end of each HMDI. However, on some of the HMDI molecules, one NCO is unreacted and available for further reaction [7]. This is shown in Figure 2.a.1, which has a peak at 2272 cm^{-1}, due to the stretching vibration of NCO.

This unreacted NCO group was utilized to react with amine groups that are on the amine pendant siloxane copolymer (AMS-152). The aerogel particles were attached to the siloxane polymer chain through urea linkage. In Figure 2.a.2, the disappearance of the peak for NCO at 2272 cm^{-1} and the appearance of peak at 1262 cm^{-1} (due to the symmetric CH_3 deformation vibration in Si-$(CH_3)_2$ from the silicone copolymer), the increased intensities at 800 cm^{-1} (due to the symmetric Si-C stretching of Si-$(CH_3)_2$) and at 2963 cm^{-1}(due to C-H) and the change in shape of the band in the range from 900 cm^{-1} to 1200 cm^{-1} due to addition of absorption bands at 1028 cm^{-1} to 1102 cm^{-1}, all support this identification. Figure 2.a.3 shows that the NCO in the control product remained. This showed that water was not introduced during the THF washing process, which is effective in washing off the unreacted siloxane polymer.

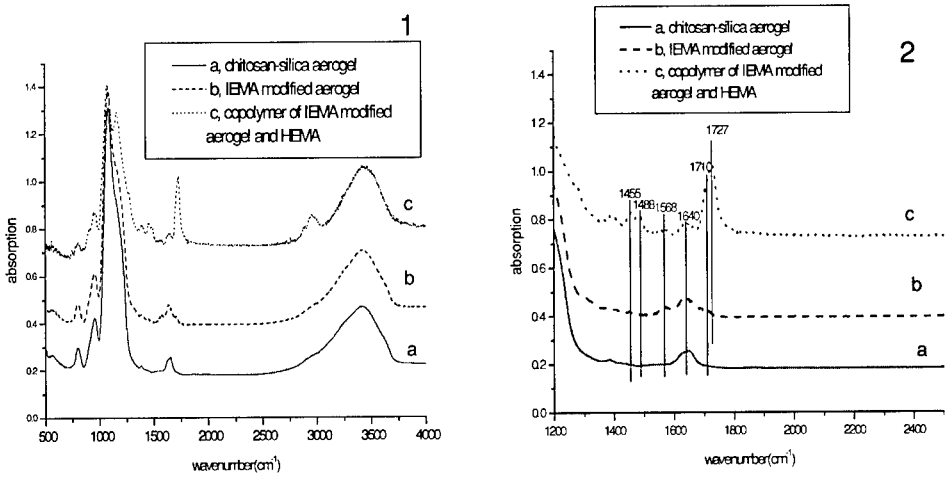


Figure 3, FT-IR spectra of (a), chitosan-silica-aerogel; (b), IEMA modified aerogel, the product after chitosan-silica-aerogel reacted with IEMA at room temperature for 30mins; (c), PHEMA aerogel hybrid, the product after (b) reacted with HEMA at 62^0C for 30 minutes, then at room temperature for another 3 hours.

Reactions of IEMA with the chitosan-silica aerogel were successful. IEMA, which has an isocyanate group at one end and methacrylate group at the other end, was attached to chitosan within chitosan-silica-aerogel by forming a urea linkage between the isocyanate group and the amine on chitosan. Thus, the methacrylate group was attached and available for further chemistry. In Figure.3, spectrum b has peaks at 1568 cm^{-1} and 1710 cm^{-1} which spectrum a does not have. The peak at 1568 cm^{-1} is due to the combination of the bending of N-H and the stretching of C-N in the newly formed urea linkage. The urea linkage also has a characteristic peak at 1660 cm^{-1} due to -(C=O)-N-, but it is merged into the strong O-H bending vibration of H_2O at 1630 cm^{-1} [3]. The stretching of -C=C also contributes to the band at 1640 cm^{-1}. The peak at 1710 cm^{-1} on spectrum b is due to the -O-C(=O)-C=C in the methacrylate group [7]. The resultant methacrylate terminated aerogel was copolymerized with monomer HEMA. In a certain circumstance, such as the right size of the aerogel particles and the right temperature, methacrylate terminated aerogel acted as a difunctional monomer, copolymerizing with monomer HEMA, and forming a linear hybrid, which contained a long chain with aerogel particles pendant along it. In Figure 3, new peaks at 1727 cm^{-1}, 1488 cm^{-1} and 1455 cm^{-1} appear in spectrum c. The strong peak at 1727 cm^{-1} is shifted from 1710 cm^{-1}, due to formation of -O-C(=O)-C-C- from polymerization of -O-C(=O)-C=C groups. Peaks at 1488 cm^{-1} and 1455 cm^{-1} are due to vibration of C-H of the PHEMA formed.

The HMDI modified chitosan-silica-aerogel was used to react with HEMA at ca. 60^0C. The -NCO group reacts with the -OH of HEMA to form urethane linkages. As shown in Figure 4, the

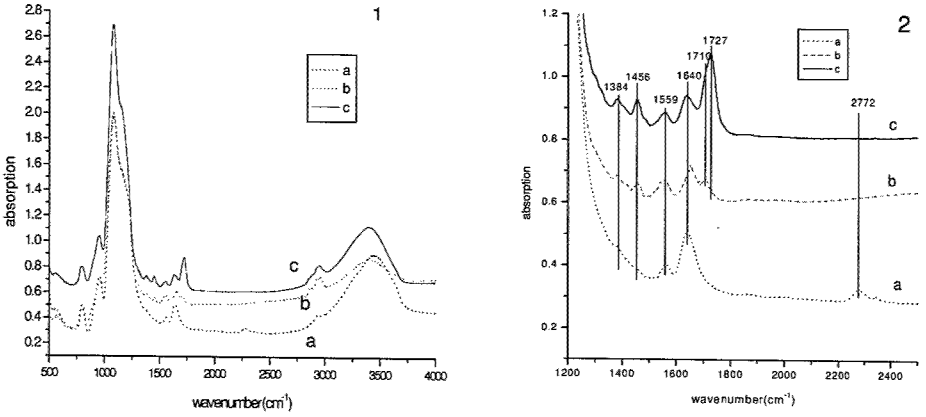


Figure 4, FT-IR spectra of (a), NCO-aerogel (X-SiO_2-NCO, the product of reaction of chitosan silica aerogel with HMDI); (b), HEMA terminated aerogel (the product of the reaction of NCO-aerogel with HEMA at 67^0C for 7 hrs); (c), aerogel-PHEMA hybrid (the product of the reaction of NCO-aerogel with HEMA at 67^0C for 12 hrs).

band at 2272 cm^{-1} due to NCO in spectrum a, is absent in spectrum b, and in b the 1559cm^{-1} band is increased in relative intensity due to formation of the urethane linkage. Both the unpolymerized methacrylate group from HEMA and the formed urethane linkage contribute to the band at 1710 cm^{-1}. Thus, after heating the mixture of NCO terminated aerogel and HEMA at 67^0C for 7 hours, HEMA molecules attached the aerogel by urethane linkage formed between hydroxyl groups on HEMA and NCO groups of the modified aerogel. This treatment caused addition but not much polymerization, as shown by the relatively weak peak at 1727 cm^{-1} for the -O-C(=O)-C-C groups. However, when the heating time is increased to 12 hours, the peak at 1727 cm^{-1} in spectrum c became stronger, meaning that the HEMA terminated aerogel copolymerized with HEMA monomers, and formed an aerogel PHEMA hybrid material. The shoulder at 1710 cm^{-1} showed that there were still some methacrylate groups left unreacted within the hybrid.

CONCLUSION

This study has shown that the small molecule modified chitosan-silica-aerogels, especially NCO-terminated and methacrylate terminated aerogels can be used either to combine with functional polymers or combine with other functional monomers to produce copolymers. Materials that contain polymer chains with aerogel particles attached to them have been prepared and could be quite interesting, because they combine the properties of the polymer and of the chitosan-silica aerogel. This work has shown that this kind of hybrid materials can be produced chemically. Future work will relate to investigation of the physical properties of these new materials.

REFERENCE:

1. X. Hu, S. Ji and K. Littrell and W. M. Risen, Jr., in *Nanophase and Nanocomposite Materials III*, edited by S. Komarneni, J. C. Parker and H. Hahn, (Mater. Res. Soc. Symp. Proc. **581**, Boston, MA 2000), pp 353 – 362 (2000).
2. X. Hu, K. Littrell, S. Ji, D. Pickles and W. M. Risen, Jr., *J. Non-Cryst. Solids* **288** 184 (2001).
3. Shuang Ji, Ph. D. Thesis, Brown University, 2001.
4. W. M. Risen, Jr., S. Ji, X. Hu, and R. Zhang, U. S. Patent 6,303,046 B1.
5. X. Hu, Ph. D. Thesis, Brown University, 2002.
6. M. R. Ayers and A. J. Hunt, *J. Non-Cryst. Solids* **285**, 123 (2001).
7. M. Wang, X. Liu, S. Ji and W.M. Risen, Jr., Mat. Res. Soc. Symp. Proc. Vol. 702(Advanced Fibers, Plastics, Laminates and Composites), 77-85 (2002).

Mat. Res. Soc. Symp. Proc. Vol. 740 © 2003 Materials Research Society I12.28

Nanocomposite Fibers

Yong K. Kim, Armand F. Lewis, Prabir K. Patra, Steven B. Warner, Shamal K. Mhetre, Mithun A. Shah and Daejin Nam
Department of Textile Sciences, College of Engineering, University of Massachusetts-Dartmouth, Dartmouth, MA 02747-2300, USA

ABSTRACT

Nanocomposite fibers involve the concept of integrally dispersing nanosized particles of the second phase inorganic material into fiber forming polymers such as nylon or polyester. The material goal involves obtaining bi-phasic fibers with high mechanical stiffness and strength, electrical conductivity and/or enhanced other features such as thermal stability. Thus far, the main difficulties toward achieving nanocomposite fibers are: (1) the inability of obtaining large quantities of nanoparticles in a pure, un-agglomerated state and (2) obtaining a uniform, intimate dispersion of single entity nanoparticles in a fiber polymer matrix. These problems have been approached in the context of studying the properties of experimentally prepared nano-silica reinforced fibers and attempts to prepare carbon nanotube, CNT, containing fiber material. Modulus and tenacity tests on experimentally prepared nanosilica filled PET (polyethyleneterephthalate) fibers showed the silica nanoparticles reduced the modulus and tenacity (tensile strength) of the filled PET fiber materials. DSC and shrinkage studies on nano-silica/PET fiber show that polymer crystallinity is influenced by the presence of the silica nano-particles. Heats of melting are found to increase as the filler loading increases. In further shrinkage studies, the "shrinkage modulus" of these nanosilica/PET fibers was found to increase by the addition of silica nanoparticles. Attempts to prepare nylon reinforced CNTs (multi-wall) from a commercially available CNT/nylon resin "concentrate" failed due to the poor melt dispersion processing of the blended polymer. Only very weak CNT reinforced nylon fibers could be prepared.

INTRODUCTION

This paper focuses on the understanding of creating nanocomposite Fibers. Here one must determine ways of intimately blending individual entities of nanofibers, such as carbon nanotubes and SiC whiskers, silica and clay, into polymers with the goal of producing new forms of textile fibers. The properties of these presumed nanocomposite fibers are widely different from the spectrum of fiber forming polymers that now exist. One might expect the modulus and strength of existing fiber polymers to be greatly enhanced by the addition of nanofiber reinforcement. For example, if carbon nanotube (CNT) particle implanted fibers are used, one would expect a great increase in the electrical conductivity of the so-reinforced fibers since CNTs themselves are electrically conducting. Nanofiber particle reinforced fiber polymers such as nylon, polyester, acrylic, cellulose etc. are the more obvious fiber composites to study as the more traditional choice of fiber producing polymer. However, the fabrication of nanocomposite fibers from these polymeric media is not a direct process.

EXPERIMENTAL DETAILS

1. General Sources of Nanoparticles and Other Materials

(1) Carbon Nanotubes (CNT) –CarboLex AP, Carbolex Inc. Lexington, KY; Graphite Nano-Fibers, (GNF), Catalytic Materials, LLD, Holliston, MA
(2) Nano-Silica Filled PET Fibers - Supplied by Albany International, Mansfield, MA
(3) 20% Concentrate of multiwall CNTs in nylon 66 – Fibril® nylon 66, Hyperion Catalyst Inc. (HCI), Cambridge, MA
(4) 15% Concentrate of multiwall CNTs in polybutyleneterephthalate Fibril® (PBT) from HCI
(5) Graphitic Carbon Black - Black Pearls 2000, Cabot Corp., Boston, MA

The nanosilica/PET blended fibers were prepared from in-situ polymerized with varying nanosilica loading of 1%, 1.5%, 3% and 5% by extruding in a twin screw extruder. These prepared fibers were used in the study. Studies were conducted in an effort to determine if commercially available CNT "concentrated" manufactured by Hyperion Catalysts, Inc (HCI), Cambridge, MA could be formulated to form fiber producing polymer material. To this end, nanotubes (multiwall CNTs) in a 20% nylon concentrate form (Nylon 66, Fibril™) and PolyButyleneTerephthalate (PBT) in a 15% CNT concentrate form (PBT Fibril™) were obtained. The approach was to compound these HCI concentrates with virgin (fiber grade) nylon or PBT resin to form CNT containing resin molding compounds having good electrical and mechanical properties. These compounded materials were extruded into fibers.

DISCUSSION

Novel Carbon Nano-Particles

Catalytic Materials, Ltd., Holliston, MA has developed a process for the synthesis of a similar material to carbon nanotubes, "tubular" graphite nano-fibers (GNF), which are produced from the decomposition of carbon monoxide/hydrogen mixtures over selected metal surfaces at temperatures over the range 600 to 750°C [1]. It has been found that by judicious choice of the catalyst and control of the parameters involved in the synthesis, it is possible to control the morphology and the crystallinity of the structure [2]. High-resolution transmission microscopy studies have revealed that GNF consist of well-ordered graphite platelets, aligned at various angles with respect to the fiber axis. We can now produce "faceted tubes", "ribbons", "platelets" and "herring-bone" conformations, which are generated by the correct choice of catalyst system and reaction conditions [3-6].

Nanoparticle Reinforced Fibers

PET/Silica Nanocomposite Fibers

The polymer material properties of PET/nanoparticle silica composites were studied. Nanocomposite fibers made from several blends of PET/Silica (Nyacol DP6100, average particle diameter = 100 nm or less) were acquired from Albany International,

Mansfield, MA. DSC measurements were carried out on the polymer/silica blends containing 0% (neat PET), 1.5%, 3% and 5% (by weight) silica. Here, the crystallization endotherm temperature was not significantly changed by the presence of the various weight concentrations of silica. Endothermic peak (melting) temperatures ranging from 252 to 254°C were observed. Also the general shapes of all the DSC curves were not too much different from each other. However, upon furthe4 analysis, a trend was found in the (normalized) heat of melting, Qm, of these composites. Correcting the determined heat of melting according to the percent polymer mass in the nano-composite fiber, created a linear trend in the data as shown in Figure 1. Qm is found to increase as the concentration of the silica increases. This suggests that the silica-PET interfacial (boundary layer phase) material formed in these composites has a strong influence on the heat of fusion. Hence, the higher loading of nano-silica composite fiber has a higher interfacial area than that of the "neat" PET polymer. In turn, heat of fusion increases as the filler loading increases.

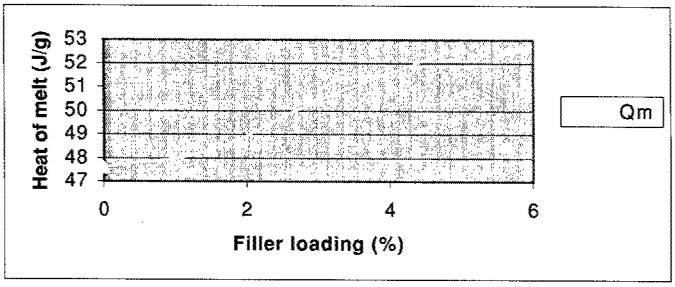


Figure 1. Effect of Filler on Heat of Melting, Qm, of PET/Silica Nanocomposite Fibers

In additional work, the tensile modulus and inherent shrinkage of nanosilica/PET (figure 2) composite fibers were measured for filler loadings of 0.5, 1, 1.5, 3 and 5% (by weight). The average force and shrinkage of all the samples were measured using the FST 2000 apparatus (Lawson and Hemphill). Dispersion of the nanoparticles with in the polymer matrix was observed through polarized light microscope and SEM. The silica nanoparticles were found to be well dispersed. The shrinkage test involves securing a yarn or fiber sample at a fixed length, in a constant temperature chamber under a constant load. The shrinkage peak force can be better explained as an intrinsic property of the polymeric fiber and the 'treatments' imposed during fiber spinning process. Fiber formation process generally occurs in three broad stages flow deformation, crystalline orientation and plastic deformation. The crystalline orientation of polyethyleneterephthalte (PET) occurs very rapidly accompanied by neck-like deformation and release of latent heat. Higher filler concentrations may induce "additional" crystallinity in the fiber as evident in higher silica loading. At the high temperatures there appears to be a rapid change in the fiber's fine structure that determines its properties. There is a change in degree of molecular orientation that may have arisen out of interaction between filler and fiber matrix. A frozen-in stress contributes greatly to peak force. Many molecules of the materials become frozen in an

oriented conformation. Such a conformation is unnatural to "neat" polymer molecules, which continuously strive to take up a randomly coiled state. So there is a frozen-in stress corresponding to frozen-in strain due to molecular orientation to enhance the peak force. Another factor that corresponds largely to the peak force is the defects in the fiber yarn or there may be a very poor dispersion of the silica in the molecular level to avoid the defects in 0.5% loaded composite fiber.

In additional experiments, all the samples were held at 177 °C for 2 min and then allowed to come down to room temperature and then shrinkage of the samples were measured. To our expectation, no shrinkage was observed in any case. Under high temperature (177 °C), all the samples underwent a molecular re-orientation process, an annealing, that resulted in reducing the entropy of the system and fiber shrinkage at lower temperature comes to nil. Heating the samples to 177°C perhaps takes care of induced orientation suppressing the marginal effect of fillers towards crystallization. However, crystallinity is not the only factor that could be responsible for reduction in shrinkage. Larger crystallites and a lower degree of orientation in the amorphous zone leads to reduced shrinkage. The mechanism of nanocomposite fiber shrinkage phenomena is still under investigation.

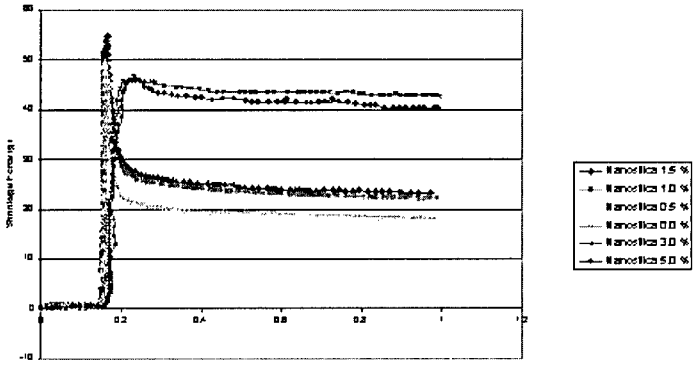


Figure 2. Variation of shrinkage force of the composite fiber with time

Table1 Mechanical properties of PET/nanosilica composite fibers

Denier	Tenacity (g/den)	Modulus (g/den)	%elongation	Silica loading (% wt)
240	4	120	26	0
240	3.85	100	28	1
240	3.95	90	26	1.5
420	3.11	30	50	3
420	3.23	36	55	5

Additional amorphous content with increase in silica loading is probably responsible for increase in elongation at break and observed decrease in modulus of the samples as silica loading increases. The original crystalline melting point decreases marginally with filler loading however normalized melting energy increases. This may well be because of increased amorphous content with increased nanosilica in PET/silica nanocomposite.

Shrinkage Vs temperature of PET/silica nanocomposite fibers

The shrinkage of the PET/nanosilica was measured in FST 3000 force shrinkage tester from 150°C to 200°C at 5°C/min ramp and then cooled to 150°C. As shown in figure 3 the shrinkage of the PET fibers increases with increasing filler loading and the fibers with highest filler loading shows the maximum shrinkage value. Owing to very small size large number of amorphous nanosilica molecules may give rise to increased non-crystalline area at the polymer-filler interface. This extent of formation of such non-crystalline region increases with increase in silica loading and probably that contributes to the increase in percentage shrinkage value with increased filler loading. Once we heat the samples it seems that non-crystalline regions try to orient themselves causing shrinkage in the materials. However it needs further exploration to properly corroborate the findings.

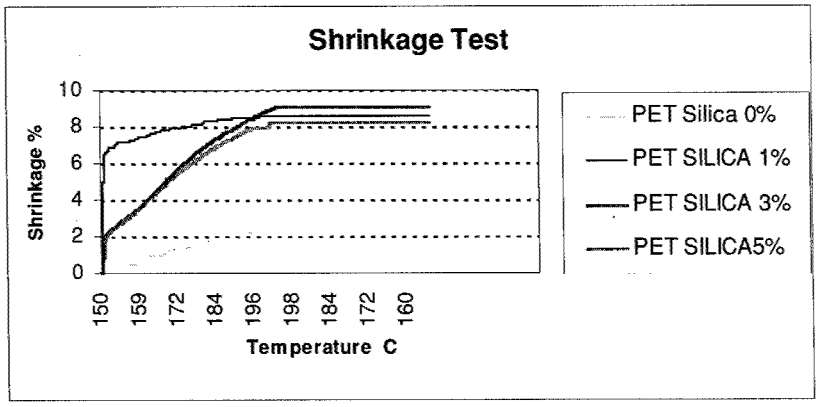


Figure 3. The variation in Shrinkage (%) of PET/nanosilica composite fibers with temperature

Nylon and PBT Based CNT Fibers

In the first experiment, a master batch sample of CNT/nylon 66 (20% of CNT concentration) was diluted to a 4% CNT concentration with fiber grade nylon 66. This material was then placed in a twin-screw extruder (at Albany international) to obtain fiber. Several problems were encountered while extruding the fiber. Overall, the fibers were formed with great difficulty. Any fiber produced was found to be very weak. The dispersion of the CNT was observed to be poor. Lumps of CNT particles were observed in specific areas of the fiber causing material discontinuity. The polymer matrix continuity needed for fiber (or film) formation was not present. Here there appears to be

poor dispersion of the CNTs in the polymer matrix. This agglomeration of CNT particles is considered to be a major problem in the extrusion of CNT containing fibers. Attempting to prepare PBT fibers with the PBT "concentrate" met with the same problems as was observed for the nylon based polymer/fiber studies. Better nanoparticle/polymer matrix melt dispersion techniques are needed.

CONCLUSIONS

The development of nanocomposite fibers is in its infancy. There are many facets to this technology that are yet to be addressed. It is observed that the crystallinity and hence the mechanical properties of the PET was found to be influenced by the presence of the nano-silica. Higher nanosilica loading gives higher amorphous content and hence reduced crystallinity. This is manifested in observations: Increased filler loading increases the shrinkage of the composite fiber with increased temperature ramp. At higher silica loading the strength reduced moderately upto 25% but modulus was drastically reduced. The preparation of CNT reinforced fiber polymers has not yet been successful. CNT/polymer dispersion problems remain. Present studies on a new form of CNT, namely, Graphite Nano-Fibers, GNF show some promise. GNFs are commercially available in a relatively pure state and at a relatively low cost.

ACKNOWLEDGMENT

Authors are thankful to National Textile Center for funding the project under US Department of Commerce grants.

REFERENCES

1. Rodriguez, N. M. J. Mater. Res. **8,** 3233 (1993).
2. Rodriguez, N. M., Chambers, A. and Baker, R. T. K. Langmuir **11**, 3862 (1995).
3. Kim, M. S., Rodriguez, N. M. and Baker, R. T. K. J. Catal. **131**, 60 (1991).
4. Rodriguez, N. M., Kim, M. S. and Baker, R. T. K. J. Catal. **144**, 93 (1993).
5. Owens, W. T., Rodriguez, N. M. and Baker, R. T. K. J. Phys. Chem. **96**, 5048 (1992).
6. Krishnankutty, N., Rodriguez, N. M. and Baker, R. T. K. J. Catal. **158**, 217 (1996)

Mat. Res. Soc. Symp. Proc. Vol. 740 © 2003 Materials Research Society I12.29

Simulation of Morphology and Surface Vibration in Copper and Gold Nanoparticles

Y. Kogure, Y. Kato, T. Nozaki and M. Doyama
Teikyo University of Science & Technology
Uenohara, Yamanashi 409-0193, Japan

ABSTRACT

Formation and vibrational states in nanoparticles have been investigated by means of molecular dynamics simulation. The embedded atom method potentials for Cu and Au were adopted to express the interaction between atoms in the crystals. The nanoparticles were formed by cooling the atomic systems of molten states. Surface morphology of the nanoparticles were represented by highlighting the surface atoms, which were distinguished by the potential energy. Simulated surface morphology is not so symmetric as natural nanoparticles. The radial distribution function and the cross sectional view of the particles were also derived to characterize the internal structure. Thermal vibration of sample atoms at elevated temperatures was analyzed and the power spectra were calculated. Excitation of phonon mode is seen in the spectra.

INTRODUCTION

Morphology of metallic nanoparticles produced by gas-evaporation technique has extensively been investigated by means of electron microscope observations [1]. Those particles are 10-1000 nm in diameter and have highly symmetric external shape. The static morphology of these particles is strongly affected from surface energy and compared with the Wulff polyhedron. A theoretical calculation of Wulff polyhedron based on the Morse potentials has also been reported [2]. Recently, the embedded atom method (EAM) potentials have been developed [3,4], which can realize the many body nature of the atomic interaction in metals and has successfully been applied to the problems of surface and defects. Molecular dynamics simulations using the EAM potential are performed in the present study, and the process of formation and dynamical nature of the nanoparticles are investigated. The nanoparticle is a suitable system for the molecular dynamics simulation because it is consisted of manageable number of atoms by a computer. The formation of nanoparticles are related with the fundamental nature of crystal growth, and final purpose of the present study is to find the fundamental mechanisms of self-organization in the nanostructures.

METHOD OF SIMULATION

In the molecular dynamics simulation of glassy state, dynamics of 5300 atom systems are treated under free boundary condition. The motion of each atom is traced by integrating the Newton's equation of motion. The time interval Δt for the molecular dynamics simulation is chosen to be 5×10^{-15}s, which is about 1/100 of the period of the maximum atomic vibration frequency.

The potential function used in the present study has been developed by the present authors [5,6], and has been applied to the simulation of nanoparticles [7]. The potential energy for i-th atom is expressed as

$$E_i = F(\rho_i) + \frac{1}{2}\sum_{j\neq i}\phi(r_{ij}). \tag{1}$$

Where $F(\rho_i)$ is the embedding energy for i-th atom. ρ_i is the electron density function and it is a sum of the density of the neighbor atoms labeled by j. These are expressed as,

$$F(\rho_i) = D\rho_i \ln \rho_i, \qquad \rho_i = \sum_{i\neq j} f(r_{ij}). \tag{2}$$

The functions $\phi(r)$ and $f(r)$ are

$$\phi(r) = A(r_{c1} - r)^2 \exp(-c_1 r), \tag{3}$$

$$f(r) = B(r_{c2} - r)^2 \exp(-c_2 r), \tag{4}$$

where r_{c1} and r_{c2} is the truncation distance of the potential. The value of r_{c1} is chosen to be 1.65 r_0 and r_{c2} is1.95 r_0 in the simulation, where r_0 is the nearest neighbor distance. For the perfect fcc crystal, 42 atoms are involved in the present truncation r_{c2}. The other parameters are determined by fitting the potential function to the experimental values of the lattice parameter, the elastic constants, the cohesive energy, and the vacancy formation energy. The determined potential parameters for Cu and Au are shown in Table I.

Table I. EAM potential parameters

	Cu	Au
A [eV]	8289.46	5.18022×10^5
B [eV]	0.0183251	0.0183066
c_1	10.7273 r_0	15.5771 r_0
c_2	0.319759 r_0	1.28671×10^{-5} r_0
D [eV]	13.0792	11.9318

RESULTS AND DISCUSSION

Formation of nanoparticles

The process to produce copper nanoparticle is shown in Figure 1, where the external forms and the radial distribution functions are shown. Atoms on surfaces have larger potential energy

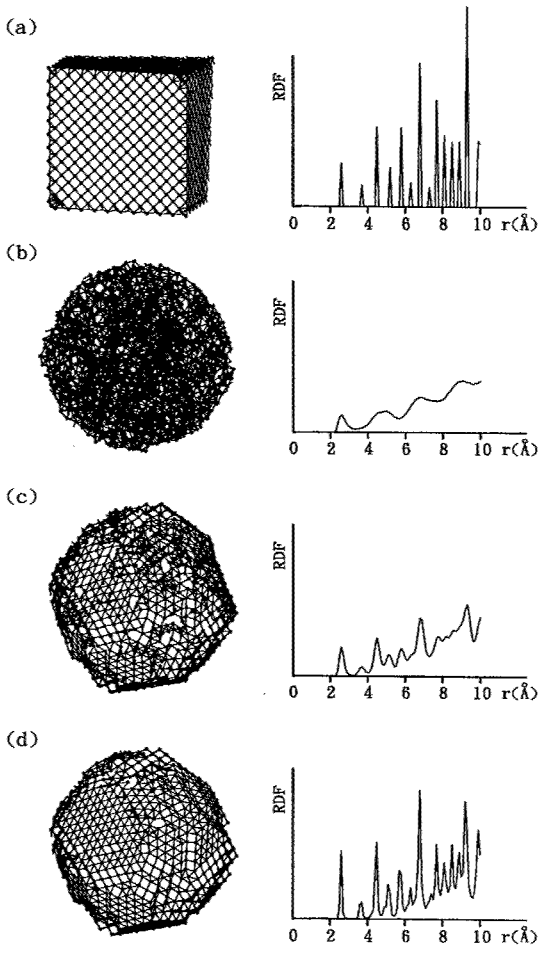


Figure 1. External form and radial distribution function in the course of producing copper nanoparticle in molecular dynamics simulation. (a) Initial fcc crystal, (b) melted state at 1470 K, (c) cooled state at 460 K and (d) final polycrystalline state at 0 K.

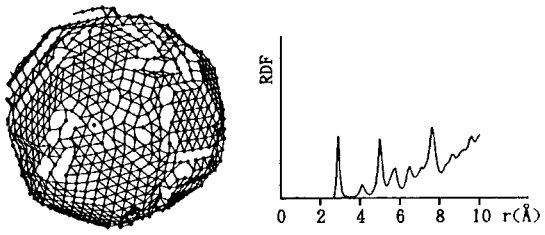


Figure 2. External form and radial distribution function of gold nanoparticle.

than internal atoms, and those are selected to show the external forms of the particle. Initially, atoms are arranged as a fcc crystal with {100} faces. When the temperature of the system is increased above 2000 K, the system is melted and external form become spherical. Then the temperature is decreased slowly at a rate of 0.02 K/step. The external form becomes asymmetrical polyhedron and the radial distribution function recovers crystalline sharp peaks with decreasing temperature. Finally obtained external surfaces of the nanoparticle is mostly covered by {111} surfaces, which has lower energy than {110} and {100} surfaces. Similar results are also obtained for gold nanoparticle, and the result is shown in figure 2. Sharpness of the RDF peak for gold nanoparticle is even dull compared with that for copper shown in figure 1. (d). This may be due to the technical problem of simulation. Heavy mass of gold atom slows down the relaxation in simulation. The cross sectional views of copper and gold nanoparticles are shown in figure 3. It is seen that the nanoparticles are consisted of several grains of fcc structure. The atoms shown by solid circles near the center and the surface of the nanoparticles are samples to monitor the vibrational states.

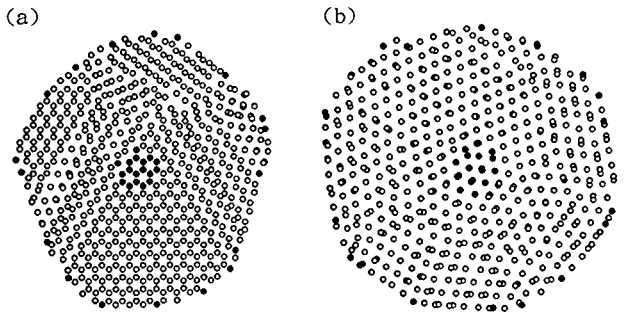


Figure 3. Cross sectional view of (a) copper and (b) gold nanoparticle.

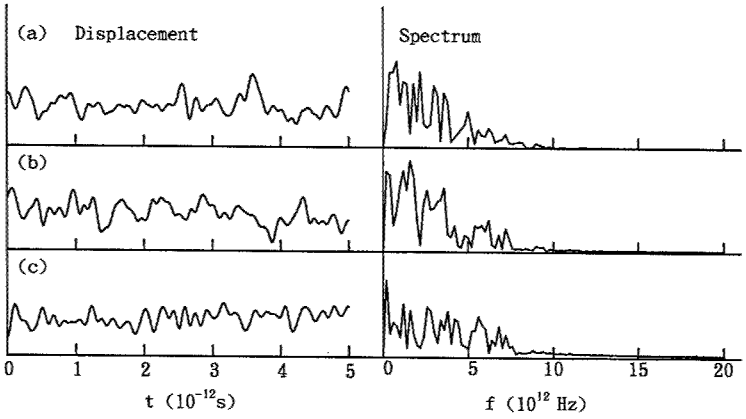


Figure 4. Examples of time variation of displacements and its power spectra. (a) Displacement of a surface atom in radial direction. (b) displacement of a surface atom in azimuthal direction , and (c) displacement of a central atoms in radial direction.

Thus obtained nanoparticles has rather asymmetric configuration than experimentally observed particles. This is due to the difference of the cooling rate. A time to cool the 2000 K sample to 0 K is about 1 ns, and this is much faster than experiments. Namely, it is difficult to attain the real equilibrium by the simulation.

Thermal vibration

Time variations of displacement of atoms are Fourier transformed and power spectra for the thermal vibration at 100 K are derived. Some examples of the displacements and power spectra are shown in figure 4. Vibrational amplitude is larger in lower frequency for surface atoms.

Mean value of power spectra for 18 sample atoms are obtained for copper and gold nanoparticles. Their logarithmic plots are shown in figure 5. Overall behavior of the spectra is inversely proportional to the frequency ($U \propto 1/f$), which is characteristic to complex or disordered systems. The solid lines in the figures show $1/f$ dependence. Vibrational amplitude deviates from the $1/f$ dependence at lower frequency, where a broad peak seems to be piled up. The peak frequency is higher for copper nanoparticle than the frequency for gold. The peak is anticipated to be due to the excitation of the thermal phonon mode. As the Debye temperature is 343 K and 165 K for Cu and Au, respectively, the frequency of thermal phonon in copper should be larger than in gold.

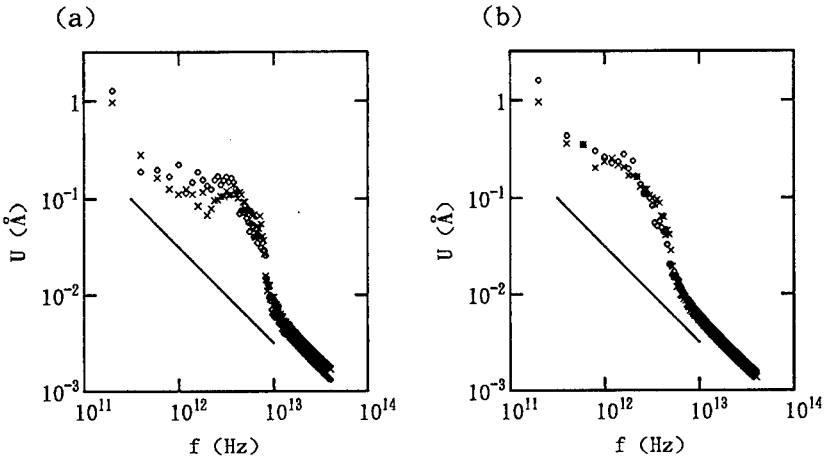


Figure 5. Power spectra of atomic vibration in (a) copper and (b) gold samples. The circles show the spectra for surface atoms and crosses for central atoms.

CONCLUSION

Formation and thermal vibration of nanoparticles were simulated. Surface morphology of simulated nanoparticles was not so symmetric as the particles experimentally produced by gas-evaporation technique. The time to form the nanoprticle in the simulation is order of 1 ns, and this may be too short the system to attain a mechanical equilibrium. The system may be a proper system to test the annealing efficiency of the simulation. The power spectra for the thermal vibration seem to consist of two components. One is phonon mode excitation and the other component is proportional to $1/f$, but the origin is not known.

REFERENCES

1. R. Uyeda, J. Cryst. Growth 24/25, 69 (1974)
2. Y. Saito, J. Cryst. Growth 53, 273 (1981)
3. M. S. Dow and M. I. Baskes, Phys. Rev. B29 (1984) 6443.
4. M. W. Finnis and J. E. Sinclair, Philos. Mag. A50 (1984) 45
5. M. Doyama and Y. Kogure, Radiation Effects and Defects in Solid, 142 ,107 (1997)
6. M. Doyama and Y. Kogure, Compt. Mater. Sci. 14, 80 (1999)
7. Y. Kogure, Physica B 263/264, 482 (1999)

Mat. Res. Soc. Symp. Proc. Vol. 740 © 2003 Materials Research Society I12.31

COMPRESSIVE BEHAVIOR FOR SURFACE-NANOCRYSTALLIZED AL-ALLOY MATERIAL

Yueguang Wei, Chen Zhu, Xiaolei Wu
LNM, Institute of Mechanics, Chinese Academy of Sciences, Beijing 100080, P.R. China

ABSTRACT

Mechanical behavior of the surface-nanocrystallized material fabricated by the ultrasonic shot peening method is investigated experimentally and theoretically. In the experimental research, based on microscopic observations, the compressive specimens are designed and machined considering the material features, and the compressive experiments are performed. Furthermore the compressive stress-strain curves are measured. In the theoretical research, a microstructure cell model is presented considering the material microscopic organization observed from experiments, and the compressive stress-strain relations are simulated. Both experimental and theoretical results display the strong size effect on the material behavior.

INTRODUCTION

Recent researches have shown that the high-quality nano-structured materials can be fabricated by some advanced techniques, and the some conventional materials can be improved in quality by a surface-nanocrystalline technique. For example, using so called the severe plastic deformation (SPD) method, the nanocrystalline material has been fabricated [1-5]. The adopted severe plastic deformation method mainly includes the large torsion [1], large pressing [4] and the ultrasonic shot peening [5], etc. The advantages of the nano-structured materials and the surface-nanocrystallized materials are displayed with material regular microstructures globally or locally. The size of the microstructure is measured from several ten nanometers to several hundred nanometers even to several microns. Within the length scales, materials usually behave strong size effect. On the research of the size effect, many investigations have been performed for the micro-indentation tests of the single crystal metals previously. Through theoretical and experimental researches for the micro-indentation test, one found that with decreasing applied load, or with decreasing the indentation depth, the obtained hardness curve displayed a going up trend, i.e., the size effect. The size effect could be described using the strain gradient theories [6-9], and the prediction results were consistent with the experimental measurement. The research showed that the microscale length parameter for the single crystal metal materials was taken in an order of microns [10,11]. However, the case is complicated for a nano-crystallized material, about which besides the above size effect, basically the influences of the crystal grain size and its shape distribution, i.e., the effect of the micro-structure features on the material behavior must be considered. In author's previous research for systems of the nano-polycrystal Al and the thin film/substrate [12], the effects of the crystal grain size and its shape distribution were called geometrical effects, for differing from the size effect. Based on the microstructure cell model and the strain gradient plasticity, the size effect and geometrical effect (when the microstructure size was in micron or sub-micron order) have been studied [12].

In the present research, the mechanical behavior of the surface-nanocrystallized Al-alloy

material (SNCAA) fabricated by the ultrasonic shot peening method [5] will be studied experimentally and theoretically. In experimental research, test specimen is designed and prepared according to microstructure features, and compressive experiments will be performed. The compressive stress-strain curves are measured. In theoretical research, simplified mechanics model will be presented and discussed in detail, and a microstructure cell model is developed to describe the material behavior. Using the cell model and the strain gradient plasticity theory, the compressive stress-strain relations with related model and material parameters will be analyzed. During simulation, some parameter values are come from experimental measurements, and others are determined through comparing experimental result with theoretical result.

MICROSCOPIC OBSERVATION AND ANALYSIS FOR THE SNCAA MATERIAL

Photos of the conventional and high-resolution electron microscopy and TEM about the SNCAA fabricated by the ultrasonic shot peening show in Figure 1. The material fabrication was carried out in the Metal Material Institute, Chinese Academy of Sciences [13]. The nanocrystalline principle is sketched in Figure 1(a). Figure 1(b) shows TEM photo of the distribution of nano-crystallized grains. From Figure 1(b), the most grain size is in an order of about several ten of nano-meters. Basically, the distribution of the grain size is uniform locally. Figure 1(c) shows photo of the high-resolution electron microscopy about the nano-crystal grain boundary. Clearly, the grain boundary region is in an orderly structure. Figure 1(d) is another high-resolution photo of electron microscopy, shows the distributed dislocations in a nano-crystal. Using these microscopic observations, one obtains a basic understanding to the SNCAA material.

COMPRESSIVE EXPERIMENTAL STRESS-STRAIN CURVES

It is an expectation that the specimen design and preparation for a compressive test can basically display the mechanical behavior for the surface-nanocrystallized material. For this reason, two types of specimens are designed, which are the fully influenced specimens by nano-crystallization, and the uninfluenced specimens in the nano-crystallization, respectively. Two type specimens were cut in an order respectively from nanocrystalline surface toward inside the material, as shown in Figure 2. Since each specimen is a cubic column, 1mm x 1mm x 2mm, so that the second kind specimens are nearly uninfluenced by the nanocrystalline procedure. After each specimen was cut, it was ground and polished with number 600~1200 sand sheets smoothly. Each type consists of 6 specimens. Compressive experiments were performed at the Laboratory of the Mechanics and Engineering Department, Peking University. During the compressive experiments, displacement loading was adopted. Figure 3 shows the compressive stress-strain curves, measured from experiments based on the above mentioned two type specimens. Each type has 6 specimens, and the measured curves have the small differences from Figure 3. The compressive stress-strain curves obtained from the SNCAA specimens are clearly higher than those of uninfluenced specimens.

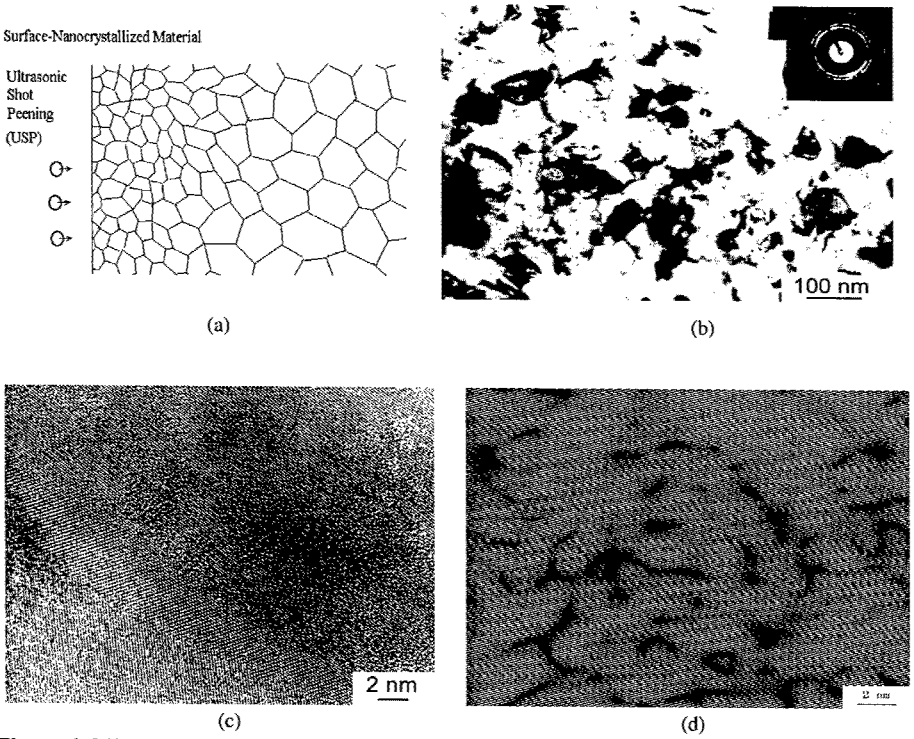


Figure 1. Microscopic organization features of the surface-nanocrystallized Al-alloy material. (a) Surface-nanocrystalline method-ultrasonic shot peening method, (b) the formed new grains, (c) the profile of the grain boundary zone, and (d) the formed dislocations within a grain.

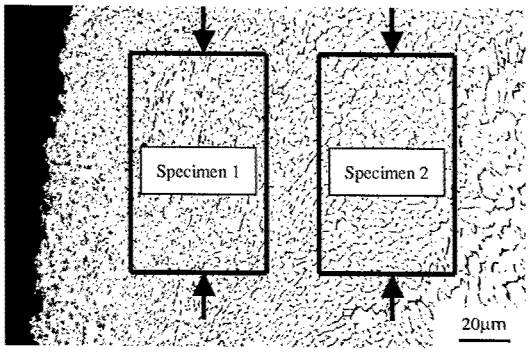


Figure 2. The specimen design for compressive experiment

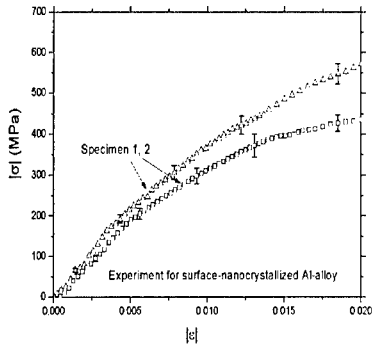


Figure 3. Compressive stress-strain curves of two types of specimens, influenced and uninfluenced specimens by nanocrystalline

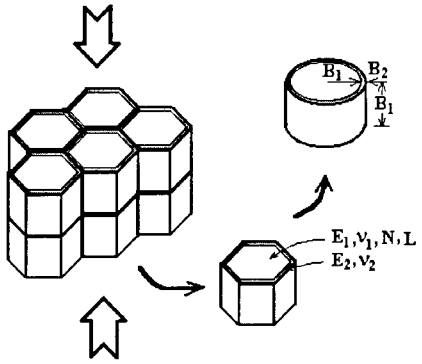


Figure 4. The microstructure cell model of compressive experiment for nano-crystallized material

The material size effect can not be predicted from conventional elastic-plastic theory. Therefore, we use the strain gradient plasticity theory[6] combined with a microstructure cell model considering the compressive test feature to simulate the compressive stress-strain relations of the SNCAA material. The foundalmental relations of Fleck-Hutchinson strain gradient plasticity theory can be referred to literatures [6,7,11,12]. Comparing with conventional elastic-plastic theory, the strain gradient plasticity theory includes an additional length parameter L, which can be used to characterize the strain gradient effect. In macroscale, the strain gradient effect is much weak so that it can be neglected, however in the microscale (specifically in the order of micron or sub-micron), the strain gradient effect is important. The length parameter L is sometimes called micro-scale parameter.

By examining the microstructure characteristics of the SNCAA material shown in Figure 1(b)~(d) and in Figure 2 (specimen orientation and location), a microstructure cell model for compressive test is presented and shown in Figure 4. Grain shape is simplified as a six-edge column, and distributed inside material periodically. Each column is connected with another by a thin layer material, which characterizes the grain boundary layer. For further simplicity, the grain shape is simplified as a cylinder. Effective radius and height of a representative grain is described by B_1. Thickness of the grain boundary layer is denoted by $2B_2$. Through microscopic observation and analysis of the SNCAA material, during nano-crystallization process, the original large grains were broken down into many small grains, and inside the grain a large number of dislocations were produced and moved to gather around the new grain boundaries. Therefore, in the simplified model, grain is taken as an elastic-plastic material, and characterized by the strain gradient plasticity theory, while grain boundary layer is taken as an elastic material

and characterized by conventional elastic theory. The related parameters for grain material are E_1 (Young's modulus), ν_1 (Poisson ratio), N (strain hardening exponent) and L (length scale parameter), while the related parameters for grain boundary layer are E_2 and ν_2. The size ratio of the elastic-plastic material zone with the elastic material zone is B_1/B_2, which can be used to characterize the volume fractions of the grain region and the grain boundary region.

The compressive stress-strain relation with independent parameters can be expressed as

$$\frac{|\sigma|}{\sigma_Y} = f(|\varepsilon|;\ \frac{E_1}{\sigma_Y}, \frac{E_2}{E_1}, \nu_1, \nu_2, N, \frac{B_2}{B_1}, \frac{L}{B_1}) \tag{1}$$

One can carry out the finite element simulation for the compressive experiments using the microstructure cell model (see Figure 4) and the strain gradient plasticity theory. For the axisymmetrical simplified model shown in Figure 4, nine-node isoparametric displacement element with 2x2 Gauss points is adopted. Figure 5 shows the simulated compressive stress-strain curves with several cell sizes and several material parameters. Considering the metal material, some material parameters taken in the simulation are shown in Figure 5. On the model parameter B_1/B_2 value, from the observation of microscopic organization of SNCAA it is about 0.03~0.06, therefore in the simulation it is taken as 0.03 and 0.06, respectively. Figure 5 shows the compressive stress-strain curves for several values of L/B_1. When grain size is very large (or L/B_1 is very small), the compressive stress-strain curve is very low. However, with decreasing the grain size it goes up. Furthermore, when grain size decreases until it is comparable with material length parameter L, to continue decreasing the grain size has only a small influence on the material strength (or stress-strain relations).

Figure 6 shows both comparisons of the simulated with average experimental stress-strain relations, for L=0.5 micron and B_1=0.1 and 100 microns respectively. From Figure 6, the prediction results and the experimental results are basically consistent with each other for the proper selections of model parameters and material parameters.

CONCLUSION

A system study for the surface-nanocrystallized Al-alloy has been performed in this paper. The research includes the following contents. Mechanical behavior of the surface-nanocrystallized material fabricated by using the ultrasonic shot peening method has been investigated experimentally and theoretically. In the experimental research, high-resolution electron microscopy observations are performed, and based on the observation, the compressive specimens were designed and machined considering the material features. The compressive experiments have been carried out, and the compressive stress-strain curves have been measured. In the theoretical research, a microstructure cell model has been presented considering the material microscopic organization features observed from experiments, and the compressive stress-strain relations have been simulated. Both experimental and theoretical results have shown the strong size effect on the material behavior.

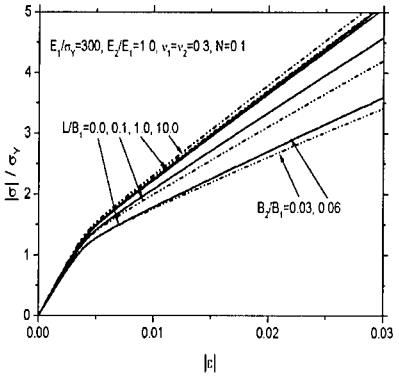


Figure 5. The simulated compressive stress-strain relations for several model parameters

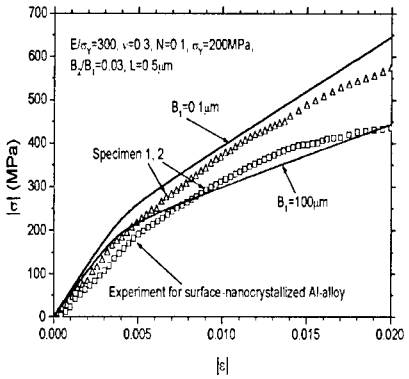


Figure 6. The comparison of compressive stress-strain relations from experiment and simulation

ACKNOWLEDGMENTS

This work was supported by the National Natural Science Foundation of China through Grant 19925211, and jointly supported by the Chinese Academy of Sciences through "Bai Ren Plan".

REFERENCES

1 Valiev RZ, Korznikov AV, Mulyukov RR. *Mater. Sci. Eng.*, **A168**, 141(1993).
2 Valiev RZ, Ivanisenko YV, Rauch EF, Baudelet B. *Acta Mater.*, **44**, 4705 (1996).
3 Valiev RZ, Islamgaliev RK. *Mater. Sci. Forum*, **304**, 39 (1999).
4 Valiev RZ, Islamgaliev RK, Alexandrov IV. *Prog. in Mater. Sci.*, **45**, 103 (2000).
5 Lu K, Lu J. *J. Mater. Sci & Tech*, **15**, 193 (1999).
6 Fleck NA, Hutchinson JW. *Adv. in Appl. Mech.*, **33**, 295 (1997).
7 Wei Y, Hutchinson JW. *J. Mech. Phys. Solids*, **45**, 1253 (1997).
8 Gao H, Huang Y, Nix W D, Hutchinson J W. *J. Mech. Phys. Solids*, **47**, 1239 (1999).
9 Chen S, Wang TC. *Acta Mater.*, **48**, 3997 (2000).
10 Begley M, Hutchinson J W. *J. Mech. Phys. Solids*, **46**, 1029 (1998).
11 Wei Y, Wang X, Wu X, Bai Y. *Science in China (Series A)*, **44**, 74 (2001).
12 Wei Y, Wang X, Zhao M, Cheng CM, Bai Y. *Acta Mechanica Sinica*, **19**, No.1, (2003).
13 Zhu C. Master Thesis, Institute of Mechanics, Chinese Academy of Sciences, June, (2002).

Synthesis of Nanostructured Materials III

Mat. Res. Soc. Symp. Proc. Vol. 740 © 2003 Materials Research Society I13.4

Plastic Relaxation Mechanics in Systems with a Twist-Bonded Layer

Catherine Priester[1] and Geneviève Grenet[2],
[1] IEMN/ISEN, CNRS-UMR 8520, BP 69 F-59625,
Villeneuve d'Ascq Cedex, FRANCE.
[2] ECL/LEOM, CNRS-UMR 5512, BP 163 F-69131,
Ecully, Cedex, FRANCE

ABSTRACT

With a view to investigating how a thin film twist-bonded to a host substrate can have compliant behavior from a plasticity point of view, the onset and spread of edge dislocations throughout a mesa are studied. The discussion focuses on the energy relaxed by such dislocations in a mesa made from two coherently bonded lattice-mismatched layers twist-bonded onto a host substrate and patterned down to the film/host substrate interface. Our theoretical results show that the confinement of threading dislocations into a thin twist-bonded film is energetically favorable allowing the overgrowth of a mismatched layer exempt of any threading dislocation at least as far as mesas are concerned.

INTRODUCTION

Manufacturing high-performance optoelectronic devices requires the growth of semiconductor heterostructures exempt of any defects, especially those that result from stress relaxation. Actually, such manufacture is inhibited by the lack of appropriate substrates allowing the growth of highly lattice-mismatched heterostructures. Indeed, when a film is grown lattice-mismatched on a substrate by techniques like MBE (Molecular Beam Epitaxy), its stress energy increases with thickness up to a critical point beyond which it has to be released by either an elastic (formation of dots) or a plastic (formation of dislocations) process. Therefore, engineering a somewhat "universal" substrate, i.e., "compliant" with any kind of epitaxial growth is currently one of the most challenging goals in materials research for optoelectronics [1-5]. In 1991, Lo [1] initiated the subject by suggesting the use of a thin film as substrate. As a matter of fact, the law ruling the way the elastic energy is shared by the two films means the thicker will impose its own lattice parameter onto the thinner, which will therefore sustain most of the defects arising from stress relaxation. The next problem to be solved is the unavoidable curvature and the difficult mechanical handling of such an ultra thin heterostructure. Several solutions have already been proposed to tackle this problem, most of them involve sticking the compliant substrate on a thick host substrate. The way this sticking is done reveals the way the relaxation is presumed to act. If an intermediate viscous layer is used to stick the compliant layer to its host substrate, an elastic relaxation is guessed acting [6,7] whereas any attempt to weaken the interface by for example twisting and/or tilting the compliant axes relative to the host substrate ones means that some kind of plastic relaxation is expected [8-13].

In this study, we concentrate on the plastic relaxation undergone by a heterostructure made of two lattice-mismatched layers, twist-bonded to a host substrate. At this point, it is worth noting that when dealing with the concept of compliance, the film cannot be considered as laterally infinite but must be regarded as a finite mesa because edges are the most favourable places for a dislocation to initiate or end. This paper is the second one dedicated to the subject. In

the first one [14], we made use of a Keating formalism to describe the chemical bonding at the twist-bonded interface for twist angles smaller than 16°. As far as rectilinear edge dislocations are concerned, their energetically best locations have been proved to be at the heterointerface and not at the twist-bonded interface. Besides, we have proposed a new type of dislocations called "kinked edge dislocations" shaped to better fit the twist-bonded interface features than rectilinear edge dislocations do. Both rectilinear edge dislocations and kinked edge dislocations have to face a significant energy barrier when penetrating from a mesa edge towards the mesa center, either at the heterointerface or at the twisted interface. In the present paper, we will continue this study with special attention paid to the role played by the threading dislocations on the edge dislocation spreading into the sample, the latter being among the most damaging defects for optoelectronics applications.

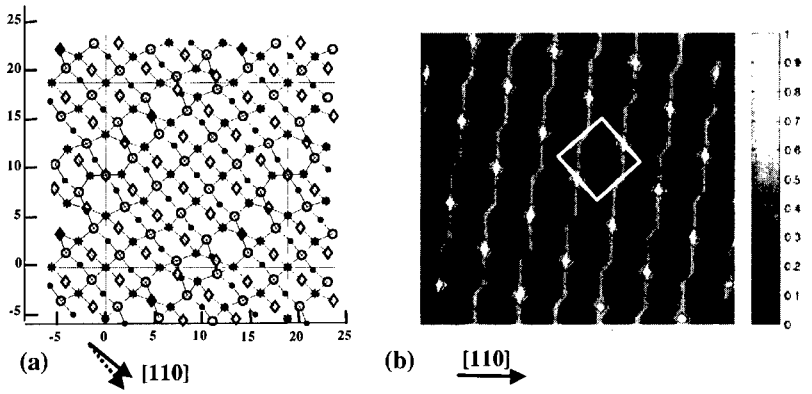


Figure 1. a) The Σ_{25} (θ=16.26°) twist-bonded interface: P- and In-atoms are tagged by circles and points in the host substrate, by star and square in the twist-bonded layer, respectively. The sp^3 bonds are marked by lines. Dashed and solid arrows indicate the [110] direction for the host substrate and the twist bonded layer, respectively. **b)** Energy map for the Σ_{25} (θ=16.26°) twist-bonded interface. The white square indicates the Σ_{25} period boundaries

METHODOLOGY

To study compliance effects a model structure is constructed out of a heterostructure made of two (001) zinc-blende mismatched layers twist-bonded to a (001) host substrate. The whole structure is made of material having the same InP stretching force constants but the uppermost layer is stressed by assuming a lattice parameter 4% greater than that of the other two. The thickness is 32 atomic layers for the stressed layer (thus beyond the usual plastic critical thickness) but only 8 atomic layers for the twist bonded layer (thus below the usual plastic critical thickness). The system displays two interfaces along the [001] axis: i) a heterointerface between the lattice-mismatched layer and the twist-bonded layer and ii) a twist-bonded interface between this twist-bonded layer and the host substrate below. The position of rows of atoms above (below) the twist-bonded interface is denoted by integer numbers n_1 and n_2 (n_3 and n_4) in surface lattice units along the [110] and [1-10] directions. The twist-bonded layer and the host substrate

are rotated one with respect to the other around the [001] axis by 16.26° that corresponds to the grain boundary Σ_{25}. The relaxed Σ_{25} atomic positions in the twist-bonded interface and the corresponding map energy are shown in Figure 1. This interface is stabilized, assuming that no dangling bonds remain. Afterwards, a 100-atomic-row wide square mesa is designed by patterning the so-defined heterostructure down to the twist-bonded interface as shown in Figure 2a.

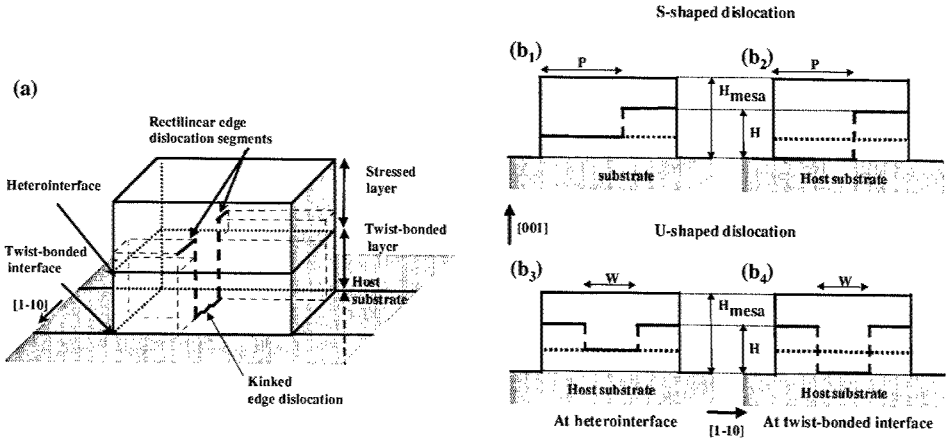


Figure 2. a) Schematic diagram of a mesa formed from a heteroepitaxial film deposited on a twist-bonded substrate on a thick host substrate. **b)** Diagram showing S-shaped dislocations and U-shaped dislocations bottomed either at the heterointerface or at the twist-bonded interface. The bottom segment is either rectilinear at the heterointerface or kinked at the twist-bonded interface.

The next step in our theoretical approach addresses the way threading dislocations could be confined in a twist-bonded layer. We define in Figure 2b two kinds of dislocations, namely, the "S-shaped» and the "U-shaped" dislocations. As can be seen in Figure 2b, "S-shaped" dislocations consist of a edge (rectilinear) dislocation segment located on the twist-bonded interface (heterointerface), starting at a mesa edge, penetrating into the mesa up to depth P and ended by a threading dislocation gliding up to height H towards the surface. Another rectilinear edge dislocation segment starts from this threading dislocation extremity, goes and reaches the other mesa edge. Indeed, the strong interaction between close dislocations forbids the return to the same mesa edge. Note that some "S-shaped" dislocations have a special pattern: i) a threading dislocation ending at a height H equal to the mesa height (H_{mesa} =40 atomic rows) signifies a threading dislocation emerging at the mesa surface and thus a pattern devoid of a second edge dislocation segment. These special S-shaped dislocations will be named "L-shaped" in the following, ii) a null penetration depth P corresponds to a system without any kind of edge (for H= H_{mesa}) or threading dislocations (for H<H_{mesa}), iii) a penetration depth P equal to the mesa width (100 atomic rows) means an edge dislocation heading straight through the whole mesa and thus a system with no threading dislocations. Let us consider now "U-shaped" dislocations they involve a edge dislocation segment (width W) also lying on the twist-bonded interface but now set

symmetrically relative to the mesa middle. Therefore, two threading dislocations emerge one at each of the segment ends and travel through the mesa toward the surface up to height H. The pattern is completed by two edge dislocation segments placed on both sides of the initial segment and finishing at the opposite mesa edges for the same reason as above. Here again, there are some special cases of interest: i) if width W is zero, the pattern contains no dislocation at all, ii) if the segment width is equal to the mesa width, there is just a single transverse edge dislocation, and finally iii) if height H is equal to the mesa height, the system includes two surface-ended threading dislocations enabling us to give an estimation of a threading dislocation cost. The bottom segment is always of the kinked type if at the twist-bonded interface, but of the rectilinear kind elsewhere.

RESULTS AND DISCUSSION

Figure 3 displays the reduced energy (energy normalized by the average atom number contained in a mesa plane) for various kinds of dislocations making their way into the mesa along the [1 –1 0] direction. In Figure 3a, the curve marked by circles shows the reduced energy variation versus the penetration depth P for an L-shaped rectilinear edge dislocation located at the heterointerface (schematized in Fig $2b_1$, with $H=H_{mesa}$). A simple look at this curve indicates that the dislocation faces a 30-atomic-row wide and 15meV-high energy barrier to break into the mesa. Actually, this barrier energy is thought to be small enough to be overcome especially in a growth process. If so, the more the dislocation progresses into the mesa the more the mesa elastic energy will be released. In the same Figure 3a, the curve labeled by points deals with an L-shaped dislocation with a bottom kinked edge segment at the twist-bonded interface (schematized in Fig $2b_2$, with $H=H_{mesa}$). The periodic oscillations shown by this curve result from the crossing by the dislocation of regularly spaced strongly (light gray in Fig.1b) and weakly (dark gray in Fig.1b) stressed regions according to Σ_{25} periodicity. This oscillating behavior allows the original energy barrier to be split into a succession of lower (few meV) and narrower (4 atomic rows) ones and thus makes it easier to pass through via a step-by-step process. However, note that the ensuing progression enables less energy to be released than in the previous case for penetration depths greater than 25 atomic rows.

Let us turn now to the hypothesis of a dislocation nucleation in the mesa core itself. Figure 3b presents reduced energy curves versus dislocation width for mesa-centered U-shaped dislocations with a bottom rectilinear segment at the heterointerface (circles) or a bottom kinked segment at the twist-bonded interface (points) schematized in Fig.$2b_3$ or Fig.$2b_4$, respectively. In both cases, the associated threading dislocations end at the surface. When comparing Figure 3b with Figure 3a, it is clear that the curves are on the whole shifted towards higher energy because of the cost in energy required by two threading dislocations now instead of only one as previously. Second, in both cases, the energy decreases as the U-dislocation bottom widens, that is to say, when the interaction between the threading dislocations diminishes as they move apart and the elastic strain is relaxed on a larger area. These two points clearly underline the key role played by threading dislocations in the total energy balance: their cost in energy in a nucleation process protects the system from any kind of dislocation nucleation inside a mesa when other relaxation processes such as introduction from edges are available.

In other respects, limiting the threading dislocation extension itself can also be of importance in terms of reduced energy. Figure 3c highlights this point by showing the reduced energy of an S-shaped dislocation for P=11 atomic rows (circles) and P=45 atomic rows (points) on the one hand, and on the other hand of 60-atomic-row wide U-shaped dislocation (diamonds) as a

function of their height H. The common trend of these three curves is that the energy decreases with height down to a minimum when threading dislocations are confined in the twist-bonded layer, viz, for H=8 atomic rows. In Figure 3d, the variation of S-shaped dislocation topped with a rectilinear edge dislocation segment at the heterointerface and bottomed with a kinked edge dislocation segment at the twist -bonded interface (see Fig.2b_2 with $H=H_{mesa}$) is shown as a function of the penetration depth P, i.e. the lateral position of the threading dislocation into the twist-bonded layer. As expected, the energy increases linearly as the kinked edge dislocation segment penetrates deeper and deeper into the twist-bonded interface, indicating by the way that the most suitable location for edge dislocation is at the heterointerface.

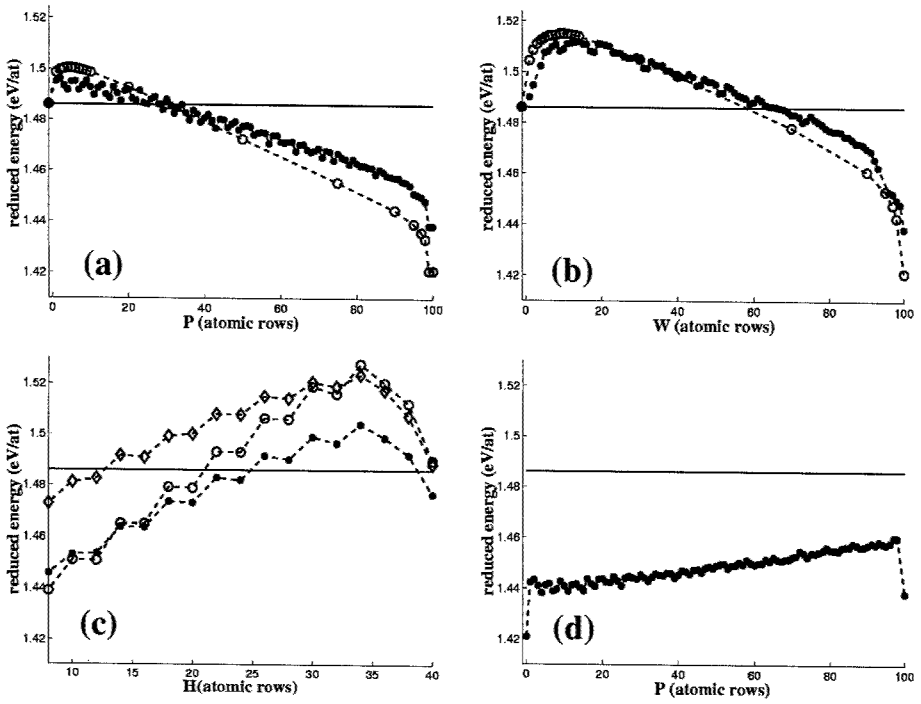


Figure 3: Reduced energy **a)** versus penetration depth P for an L-shaped dislocation located either at the heterointerface (circles) or at the twist bonded interface (points). **b)** versus width W for a U-shape dislocation located either at the heterointerface (circles) or at the twist bonded interface (points), the threading dislocations emerging at the surface (H=40). **c)** versus height H for an S-shaped dislocation for P=11 atomic rows (circles) and P=43 atomic rows (points) and for U-shaped dislocation with W=60 atomic rows (diamonds). **d)** versus threading dislocation location P (see text) for S-shaped dislocations with H=8 atomic layers. The horizontal solid line indicates the reduced energy for a mesa without any dislocation.

CONCLUDING REMARKS

In this paper, we have dealt with questions about plastic relaxation in a so-called compliant systems. For this, we have considered a mesa cut out of a heterostructure twist-bonded to a host substrate and we have focused on misfit dislocations in such a system. The latter displays two interfaces where misfit edge dislocation can originate, viz, a heterointerface and a twist-bonded interface. At both these locations, edge dislocations have to confront an energy barrier prior to moving ahead through the mesa. It appears that misfit dislocations located at this twist-bonded interface enter in an easier way from the edge of the sample than those located at the heterointerface. Actually not all edge dislocations totally cross through the sample and residual threading dislocations are usually present. Their cost in energy is the key point in compliance mechanisms. We have thus studied several different types of misfit dislocations, ended by threading dislocations, located either in the overlayer or in the twist-bonded layer. It turns out that the best design for releasing stress energy is an S-shaped dislocation fully confined within the twist-bonded layer. The unavoidable residual threading dislocations are thus kept away from the overlayer what is most important for technological applications.

ACKNOWLEDGMENTS

This work is partially supported by "Région Rhône-Alpes" under contracts 00815050 and 00815165. The authors thank G. Hollinger (ECL-LEOM) and F. Mollot (IEMN) for fruitful discussions. IEMN, Institut Supérieur d'Electronique, de Microélectronique et de Nanotechnologie is Unité Mixte de Recherche - CNRS 8520 and LEOM, Laboratoire d'Electronique, Optoélectronique et Microsystèmes is Unité Mixte de Recherche - CNRS 5512

REFERENCES

1. Y.H. Lo, *Appl. Phys. Lett.* **59**, 2311(1991)
2. G. Kästner and U. Gösele, *J. Appl. Phys.* **88**, 4048, (2000).
3. A.S. Brown and W.A. Doolittle, *Appl. Surf. Sci.*, **166**, 392, (2000).
4. A. Bourret, Appl. *Surf. Sci.*, **164**, 3, (2000).
5. K. Vanhollebeke, I. Moerman, P. Van Daele and P. Demeester, *Progress in Crystal Growth and Characterization of materials* **41**,1 (2000).
6. N. Sridhar, D.J. Srolovitz, Z. Suo , *Appl. Phys. Lett.* **78**, 2482 (2001).
7. H.Yin, R. Huang, K.D. Hobart, Z. Suo, T.S. Kuan, C.K. Inoki, S.R. Shieh, T.S. Duffy, F.J. Kub, and J.C. Sturm, *J. Appl. Phys.* **91**, 9716 (2002)
8. F.E. Ejeckam, Y.H. Lo, S. Subramania, H.Q. Hou, and B.E. Hammons, *Appl. Phys. Lett.* **70**, 1685(1997).
9. F.E. Ejeckam, M.L. Seaford, Y.H. Lo, H.Q. Hou, and B.E. Hammons, *Appl. Phys. Lett.* **71**, 776 (1997).
10. Z.H. Zhu, R. Zhou, F.E. Ejeckam, Z. Zhang, J. Zhang, J. Greenberg, Y.H. Lo, H.Q. Hou, and B.E. Hammons, *Appl. Phys. Lett.* **72**, 2598 (1998).
11. T.Y. Tan, and U. Gösele, *Appl. Phys. A* **64**, 631 (1997).
12. G. Kästner, T.Y. Tan, and U. Gösele, *Appl. Phys. A* **66**, 13 (1998).
13. Y. Obayashi and K. Shintani, *J. Appl. Phys* **88**, 105 (2000); *J. Appl. Phys* **88**, 5623 (2000).
14. S. Rohart, G. Grenet and C. Priester, *Appl. Surf. Sci.*, **188,** 193 (2002)

AUTHOR INDEX

Abot, Jandro L., 75, 167
Agrawal, D.C., 57
Aguilar, Juan A., 255
Ajayan, P.M., 371
Alexe, M., 333

Baghai-Anaraki, Mana, 147
Barnard, A.S., 69
Barnard, John A., 309
Barrera, Enrique V., 365
Batt, Carl A., 141
Bertino, Massimo F., 235, 359
Bhattacharyya, S., 333
Bizios, Rena, 161
Blum, F.D., 359

Carlsson, Mats, 173
Carroll, David L., 351
Carter, C. Barry, 87, 133
Cavaillé, J.-Y., 155
Chabert, E., 155
Chattopadhyay, S., 359
Chattopadhyay, Soma, 333
Chazeau, L., 155
Chen, Sihai, 351
Chen, W.J., 405
Chow, G.M., 319
Chu, Song-Zhu, 397
Clegg, W.J., 81
Coia, George M., 101
Condon, Clay G., 365

Daniel, Isaac M., 75, 167
Davis, J.J., 301
Davis, V.A., 429
Dendievel, R., 155
Djenizian, T., 205
Dobal, P.S., 57
Dong, Hong, 345
Doudna, C.M., 359
Doyama, M., 447
Drugan, Walter J., 281
Dulgar Tulloch, Aaron J., 161

Eiff, Isabelle M., 113
Einarsson, Erik, 101
Embury, J.D., 49
Enoki, Takashi, 411
Ericson, L.M., 429

Fan, Qinguo, 113
Fan, Zhiyong, 351
Farmer, B.L., 81
Farmer, John, 235
Feng, C.R., 15
Fischer, J.E., 429
Frankland, S.J.V., 385
Fukai, Kumiko, 125
Furuya, Y., 417

García, Monserrat, 33
Gauthier, C., 155
Gerberich, William W., 87
Giannelis, Emmanuel P., 141
Gidwani, Ashok, 133
Gill, S.J., 15
Girshick, S.L., 133
Green, Catherine E., 365
Grenet, Geneviève, 461

Hahn, Horst, 377
Harik, V.M., 385
Hauge, R.H., 429
He, Peng, 93
Heberlein, J.V.R., 133
Hebert, Rainer J., 267
Higashi, Kenji, 119
Ho, Derek L., 147
Hoagland, R.G., 49
Holmes, D.M., 81
Hsieh, S.H., 405
Hsiung, L.M., 287
Hund, Jared F., 235

Inoue, Satoru, 397
Iwasaki, Hajime, 119
Iwata, Nobuyuki, 125

Jiao, Jun, 101
Johnsson, Mats, 173
Jones, H.N., 15

Kajiwara, S., 417
Katiyar, R.S., 57
Kato, Y., 447
Katsumura, Akifumi, 411
Keblinski, P., 371
Kecskes, L.J., 199
Kharissova, Oxana V., 255
Kikuchi, T., 417
Kim, D.K., 217
Kim, Sung-Duck, 107
Kim, Yong K., 441
Kireitseu, Maksim V., 211, 223, 229
Klotz, B.R., 199
Kogure, Y., 447
Koratkar, N.A., 371
Kubota, T., 417
Kung, H., 49
Kuntz, Joshua D., 41

Lass, E.A., 371
Lavernia, Enrique J., 21
Ledneva, Olga A., 261
Lee, Gil-Geun, 107
Lee, Sang Moon, 391
Lee, Zonghoon, 21
Leventis, Nicholas, 235
Levin, Vadim M., 187, 261
Lewis, Armand F., 441
Lian, Jie, 93
Ligatchev, V., 423
Liu, W.L., 405
Liu, Xipeng, 435
Long, J.D., 423
Lopez, Israel Nieto, 255
Lopez-Garcia, Maria d. C., 281
Lorenzen, Volker, 377
Love, Logan, 101
Lutta, Samuel T., 345

Maejima, Kenzo, 411
Maiti, Pralay, 141
Majumder, S.B., 57
Mani, Gopinath, 113
Manning, M.P., 241
Mao, Scott, 309
Marks, N.A., 69
Marla, Krishna T., 193
Mast, David, 93
Masumura, R.A., 3
Matsuo, Kohji, 125
McMurry, P.H., 133
Mehrotra, V., 301
Méndez, Ubaldo Ortiz, 255
Meredith, James C., 193
Mhetre, Shamal K., 441
Mikhaylova, M., 217
Misra, A., 49
Mook, William M., 87
Muhammed, M., 217
Mukherjee, Amiya K., 41
Mukherjee, Rajesh, 133

Nam, Daejin, 441
Namkung, Min, 249
Nastasi, M., 49
Nemerenco, Ion, 223
Nieh, T.G., 27, 119
Nozaki, T., 447
Nutt, Steven R., 21

Ohkubo, Manabu, 125
Ohshima, Satoshi, 391
Okazaki, T., 417
Ostrikov, K., 423
Otto, Jens W., 301
Ozmusul, Murat S., 275

Paik, Sun Mok, 249
Pakstis, Lisa, 179
Pande, C.S., 3
Pao, P.S., 15
Pasquali, M., 429
Patra, Prabir K., 441
Perepezko, John H., 267
Perrey, Christopher R., 87, 133
Petronyuk, Julia S., 187, 261
Petty, Jeremy, 101
Picu, Catalin R., 275
Pillalamarri, S., 359
Pohl, Annika, 173
Ponomareva, Inna V., 187
Popov, Anatolii A., 261
Pradhan, Anshu A., 179
Prado, Josie, 101

Priadilova, Olga V., 261
Priester, Catherine, 461
Pulikkathara, Merlyn X., 365

Ramesh, S., 429
Renault, Thierry, 133
Reynolds, John G., 295
Risen Jr., William M., 435
Rivera, Moisés Hinojosa, 255
Rodríguez-Macías, Fernando J., 365
Russo, S.P., 69

Sacco Jr., A., 241
Saini, R.K., 429
Saito, Hidenori, 411
Santinacci, L., 205
Sarvestani, Alireza, 275
Schallehn, Michael, 377
Schmidt, A.D., 57
Schmuki, P., 205
Schuh, Christopher A., 27
Schulz, Mark, 93
Scierka, Stephanie, 147
Seydel, Johannes, 377
Shah, Mithun A., 441
Shah, S. Ismat, 179
Shen, Y., 241
Shi, Donglu, 93
Shofner, Meisha L., 365
Siegel, Richard W., 161
Smalley, R.E., 429
Snook, I.K., 69
Sotiriou-Leventis, Chariklia, 235
Starr, Michael J., 281
Stearn, R.J., 81
Stone, Donald S., 281
Sun, Xiangcheng, 339
Sung, Li-Piin, 147

ten Bosch, A., 63
Terry, J., 359
Thompson, Ryan, 133
Tillotson, Thomas M., 295
Tokuhiro, Akira T., 235, 359
Toprak, M., 217
Tsai, T.K., 405

Uchida, Kunio, 391
Ugbolue, Samuel C., 113

Vaidyanathan, Ranji K., 365
Vandeperre, L.J., 81
van Ooij, Wim J., 93
van Zyl, Werner E., 33
Vassiliou, John K., 301
Vera, Jesus G., 365
Verweij, Henk, 33

Wada, Kenji, 397
Wan, Julin, 41
Wang, H., 49
Wang, Lumin, 93
Wang, Mingzhe, 435
Wang, Zhong Lin, 309
Warner, Steven B., 441
Warzywoda, J., 241
Wei, B.Q., 371
Wei, Yueguang, 453
Whittingham, M. Stanley, 345
Wilkins, Richard T., 365
Wincheski, Buzz, 249
Winey, K.I., 429
Witkin, David B., 21
Woodman, R.H., 199
Wu, Xiaolei, 453

Xu, Fengting, 309
Xu, S., 423

Yamamoto, Hiroshi, 125
Yasmin, Asma, 75, 167
Yumura, Motoo, 391

Zavalij, Peter Y., 345
Zhan, Guo-Dong, 41
Zhang, Guohui, 235
Zhang, X., 49
Zhao, Minhua, 309
Zhao, Tiemin, 339
Zhou, W., 429
Zhu, Chen, 453

SUBJECT INDEX

acoustic microscopy, 261
adsorption, 391
aerogels, 235, 295
AFM, 205
Al-7.5Mg alloy, 21
aluminum, 267
    alloys, 15
amorphous, 267
anodic oxidation, 397
anomalous x-ray scattering, 319
arc plasma, 107
atomic(-)
    force microscopy, 255
    scale simulation, 461

bamboo, 81
bimodal microstructure, 21
bio-ceramic, 423
biocompatibility, 423
biodegradation, 141
biomaterial, 161

calculation of elastic properties, 187
carbon, 81, 187
    coils, 101
    nanotube(s), 255, 371, 385, 405
ceramics, 41, 57
characterization, 295
chemical
    modification, 435
    potentials, 193
    vapor deposition, 405
chitosan-silica aerogel, 435
clay, 113
CNT, 441
coated powder, 57
coating, 93, 223
Coble creep, 3
co-condensation, 179
cold-rolling, 267
colloid-polymer, 193
compliant substrates, 461
composite(s), 41, 211, 223, 229
compression, 453
continuum mechanics modeling, 281
copper, 447
copper-304 stainless steel, 49
creep deformation, 287
cryomilled nanocrystalline metal, 21

damping, 371
density functional theory, 69
diffuse x-ray scattering, 429
dislocation emission, 281
dispersoids, 249
dynamic mechanical analysis, 155

elastic properties, 261
electrochemical deposition, 205
electrodeposition, 119
    Ni catalyst, 101
electroless plating, 405
electron beam lithography, 333
epoxy, 167
EXAFS, 319
extrusion, 441

failure, 211
fatigue, 15
Fe-29.6at%Pd, 417
Fe_2O_3 nanoparticles, 301
ferroelectrics, 333
ferromagnetic shape memory, 417
fluorine, 365
FT-IR, 435

glass forming ability, 339
GNF, 441
gold, 235, 447
grain
    boundary, 119
    growth, 199

Hall-Petch relationship, 27
hardness, 223
homogenization, 275

immiscible polymer, 261
in situ polymerization, 441
interface, 385
    sliding, 287
intermetallics, 249

iron, 107

magnetron sputtering, 49
mechanical modeling, 155
mechanics, 229
mechanism, 81
metal clusters, 235
microwaves, 255
molecular dynamics, 249
    simulation, 385, 447
multilayer, 217

nanobelt, 309
nanocomposite(s), 75, 141, 167, 197, 217, 441
nanocrystalline, 15
    materials, 3
    metals, 27
    nickel alloy, 119
    structure, 339
nanocrystallinity, 423
nanocrystallized material, 453
nanocrystals, 241
nanodiamond, 69
nanofiber, 345
nano-foamed polybenzoxazole, 411
nanoglasses, 397
nanoindentation, 27, 49, 87, 211, 309
nanomaterials, 41
nanoparticle(s), 133, 179, 391
nanophase, 161
nanopowder, 107, 199
nanoscale experiments, 281
nanostructure(s), 141, 187, 333
nanostructured alloy films, 319
nanotube, 93
Ni-based amorphous alloys, 339
nucleation and growth: theory, 63
nylon-6, 33

optical absorption, 301
organoclay, 75
oxidation, 295

particle size, 113
patterning, 205
PET/nanosilica, 441
phase behavior, 193
plasma, 93
    deposition, 133
    polymerization, 377
platinum, 359
polylactide, 345
polymer
    coating, 377
    interfaces, 275
    nanocomposites, 275
polystyrene/polybutylacrylate blends, 155
preferred orientation, 429

radiation, 365
radiolysis, 359
Raman spectroscopy, 365
rapid solidification melt-spinning method, 417
Re oxide, 125
resistivity, 125
rheology, 229

self-assembly, 217, 351
shear mixing, 75
SiC nanoparticles, 173
silica, 33
silicon, 87
silver, 235, 351, 359
single walled nanotube, 365
sintering, 199
size effect, 453
small angle
    neutron scattering, 147
    x-ray scattering, 411
sol-gel, 57
    synthesis, 147
sputtered aluminum on glass, 397
sputtering, 125
structural enhancement, 371

submicron alumina, 173
superparamagnetism, 301
surfaces and interfaces, 63
SWNT fiber, 429
synthesis, 241

TEM, 87, 133
thermal
    gravimetric analysis, 365
    treatment, 391
thermomechanical properties, 167
thin film growth, 63
three-dimensional, 161
TiN nanoparticles, 173
TiO_2 nanostructure, 147
transmission electron microscopy, 33, 351
tungsten substrate, 101

ultrafine lamellar TiAl, 287
ultrasonication, 113

vanadium oxide, 345

Wannier functions, 69

yield stress, 3

zeolite Y, 241
zinc and tin oxides, 309
zirconia nanoparticles, 377